Transactions of the ASME®

Technical Editor
H. D. NELSON (2001)

Associate Technical Editors
Advanced Energy Systems
M. J. MORAN (1999)
Gas Turbine
D. COOKE (1999)
H. NELSON (1999)
J. PETERS (1999)
Internal Combustion Engines
D. ASSANIS (1999)
Nuclear
R. DUFFEY (2001)
Power
D. LOU (1998)

BOARD ON COMMUNICATIONS
Chairman and Vice President
R. K. SHAH

OFFICERS OF THE ASME
President, **W. M. PHILLIPS**
Executive Director, **D. L. BELDEN**
Treasurer, **J. A. MASON**

PUBLISHING STAFF
Managing Director, Engineering
CHARLES W. BEARDSLEY
Director, Technical Publishing
PHILIP DI VIETRO
Managing Editor, Technical Publishing
CYNTHIA B. CLARK
Managing Editor, Transactions
CORNELIA MONAHAN
Production Coordinator
COLIN MCATEER
Production Assistant
MARISOL ANDINO

Transactions of the ASME, Journal of Engineering for Gas Turbines and Power (ISSN 0742-4795) is published quarterly (Jan., April, July, Oct.) for $205.00 per year by The American Society of Mechanical Engineers, Three Park Avenue, New York, NY 10016. Periodicals postage paid at New York, NY and additional mailing offices. POSTMASTER: Send address changes to Transactions of the ASME, Journal of Engineering for Gas Turbines and Power, c/o THE AMERICAN SOCIETY OF MECHANICAL ENGINEERS, 22 Law Drive, Box 2300, Fairfield, NJ 07007-2300.
CHANGES OF ADDRESS must be received at Society headquarters seven weeks before they are to be effective. Please send old label and new address.
PRICES: To members, $40.00, annually: to nonmembers, $205.00. Add $40.00 for postage to countries outside the United States and Canada.
STATEMENT from By-Laws. The Society shall not be responsible for statements or opinions advanced in papers or ... printed in its publications (B7.1, par. 3).

INDEXED by Applied Mechanics Reviews and Engineering Information, Inc. Canadian Goods & Services Tax Registration #126148048

Journal of Engineering for Gas Turbines and Power

Published Quarterly by The American Society of Mechanical Engineers

VOLUME 120 • NUMBER 4 • OCTOBER 1998

TECHNICAL PAPERS

(Contents continued on outside back cover)

This journal is printed on acid-free paper, which exceeds the ANSI Z39.48-1992 specification for permanence of paper and library materials. ♾ ™

♻ 85% recycled content, including 10% post-consumer fibers.

(Contents continued)

ANNOUNCEMENTS

J. F. Kikstra
Delft University of Technology,
Faculty of Mechanical Eng.,
P. O. Box 5037,
2600 GA Delft, The Netherlands

B. Roffel
University of Twente,
Faculty of Chemical Eng.,
P. O. Box 217,
7500 AE Enschede, The Netherlands

P. Schoen
Stork Engineers & Contractors,
Radarweg 60,
1043 NT Amsterdam,
The Netherlands

Model Predictive Control of a Combined Heat and Power Plant Using Local Linear Models

Model predictive control has been applied to control of a combined heat and power plant. One of the main features of this plant is that it exhibits nonlinear process behavior due to large throughput swings. In this application, the operating window of the plant has been divided into a number of smaller windows in which the nonlinear process behavior has been approximated by linear behavior. For each operating window, linear step weight models were developed from a detailed nonlinear first principles model, and the model prediction is calculated based on interpolation between these linear models. The model output at each operating point can then be calculated from four basic linear models, and the required control action can subsequently be calculated with the standard model predictive control approach using quadratic programming.

Introduction

Model predictive control (MPC) has been successfully applied in industry to control processes which behave in a more or less linear fashion (Garcia et al., 1989; Cutler, 1983; Biegler and Cuthrell, 1985; Ricker, 1985). The technique has also been applied to control of nonlinear processes (Economou, Morari, and Palsson, 1986; Wright and Edgar, 1994), and adaptive and neural network based extensions have been reported (Morningred et al., 1993; Maiti et al., 1995; Bhat and McAvoy, 1990; Psichogios and Ungar, 1991); however, industrial applications of nonlinear model predictive control have been limited and are much fewer in number than the applications of the linear counterpart.

Control is based on a predictive model of the process; the block diagram is shown in Fig. 1. The process model predicts the process output y_m^* over a so-called output horizon, which is the number of prediction steps into the future. The model also calculates the prediction of the current process output y_m, which is compared to the actual process output y. The control algorithm is essentially the process model inverse.

The basic model equation which is used in model predictive control is

$$y_{m,k} = a_1\Delta u_{k-1} + a_2\Delta u_{k-2} + a_3\Delta u_{k-3} + \ldots + a_n\Delta u_{k-n} \quad (1)$$

in which

$y_{m,k}$ = process output at time k-steady state value
Δu_{k-1} = change in process input at time $k-1 = u_{k-1} - u_{k-2}$
a_i = stepweights of the process, describing the process output to a unit change in input

The stepweights of the process are a representation of the model of the process. If the process input would change from zero to one at time zero, then a_1 would be the process output at time one, a_2 the process output at time two, and so forth.

According to Eq. (1), the process output at the present time k will depend on the input moves that have been made in the past ($k-1, \ldots k-n$). Equation (1) can also be used to predict the value of y_m one step into the future (by simply replacing k by $k+1$).

Similarly, we could write expressions for y_m up to P steps into the future. The vector of future values of the process output can then be written as a matrix times a vector of past input moves and another matrix, called the dynamic matrix $\mathbf{A}$, multiplied by a vector of future input moves.

$$\mathbf{A} = \begin{bmatrix} a_1 & 0 & 0 & 0 & \cdots \\ a_2 & a_1 & 0 & 0 & \cdots \\ a_3 & a_2 & a_1 & 0 & \cdots \\ a_4 & a_3 & a_2 & a_1 & \cdots \\ \cdots & \cdots & \cdots & \cdots & \cdots \end{bmatrix} \quad (2)$$

It can be shown that if there are no process constraints, the control problem can be solved analytically.

The result is

$$\Delta u(k+i-1), i = 1, \ldots M = (\mathbf{A}^T\Gamma\mathbf{A} + \Gamma_m)^{-1}\mathbf{A}^T\Gamma e(k+i), i = 1, \ldots P \quad (3)$$

in which

Γ = output weighting matrix, indicating the relative importance of the process outputs
Γ_m = input weighting matrix, limiting excessive moves
e = predicted error = setpoint—predicted process output
M = process input horizon or control horizon
P = prediction horizon or process output horizon

When there are process constraints, the controller cannot be solved analytically, but a linear or quadratic program is usually used to find the optimal process input moves at each execution interval of the controller.

Equation (1) can also be used for identification. If the values of the process outputs and process inputs are known, we could solve the coefficients a_i, amongst others, by using a least squares algorithm.

Applications of MPC in the power industry are limited partly because of the nonlinear nature of these plants. As electricity or steam demand increases, plant throughput increases, and it is not uncommon that a plant experiences throughput swings in the order of 40 to 100 percent and vice versa on a particular day (characteristic is 3–10 percent per minute maximum change). Because of these throughput swings and the associated nonlinear process behavior, complicated control schemes have often been encountered in power plants. Consequently, there is a desire to develop a more integrated and simplified control approach if possible. Therefore, a study was undertaken with the

Contributed by the International Gas Turbine Institute. Manuscript received by the ASME Headquarters July 1, 1997. Associate Technical Editor: H. Simmons.

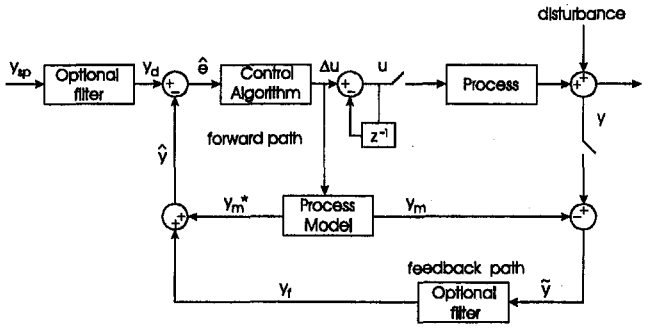

Fig. 1 Basic structure of model predictive control

objective to investigate whether this could be achieved, using model predictive control. An added benefit of applying MPC is that process constraints can be easily incorporated in the control scheme.

Process Description

A simplified diagram of the process part under investigation is shown in Fig. 2. For reasons of simplicity, single loop $PI(D)$ controllers are not shown. These controllers operate well without interaction from other controllers. The process input and output variables that were chosen to be part of a multivariable control structure either functioned poorly or showed much interaction from other controllers. The output variables that were chosen are the drum level, the pressure in the steam net, the temperature of the steam after the secondary superheater, the flow of the steam to consumer two, the flow of the steam to consumer one, and the temperature of the steam to consumer one (indicated by $y_1 \ldots y_6$). The process input variables that were chosen for control are the speed of the feed water pump, the flow to the injection cooler of the secondary super heater, the boiler fuel flow, the position of the valve in the consumer two steam flow, the steam flow to the turbine and the position of the valve in the water flow to the spray attemperator (indicated by $u_1 \ldots u_6$). The six listed output variables are presently controlled by the six listed input variables, however, the control scheme is rather complex because of feed-forward actions, decouplers, and gain scheduling. Moreover, it is felt that another approach might improve the current closed loop behavior in terms of maximum deviation from setpoint and speed of response.

Determination of Process Interaction

Using step weight models and a model reduction based on Hankel singular values, a dynamic relative gain analysis

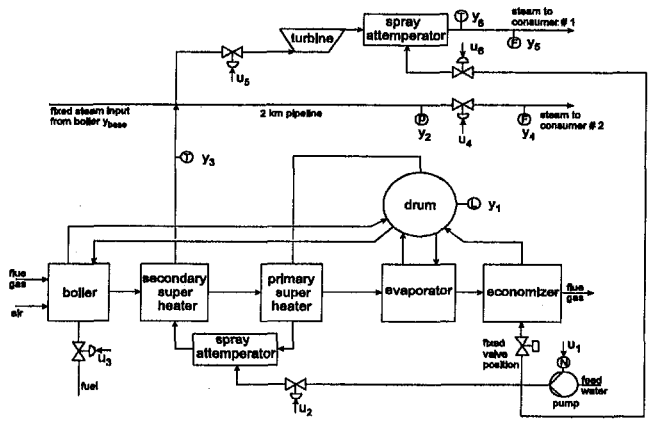

Fig. 2 Process flow diagram of the high pressure part of a combined heat and power plant

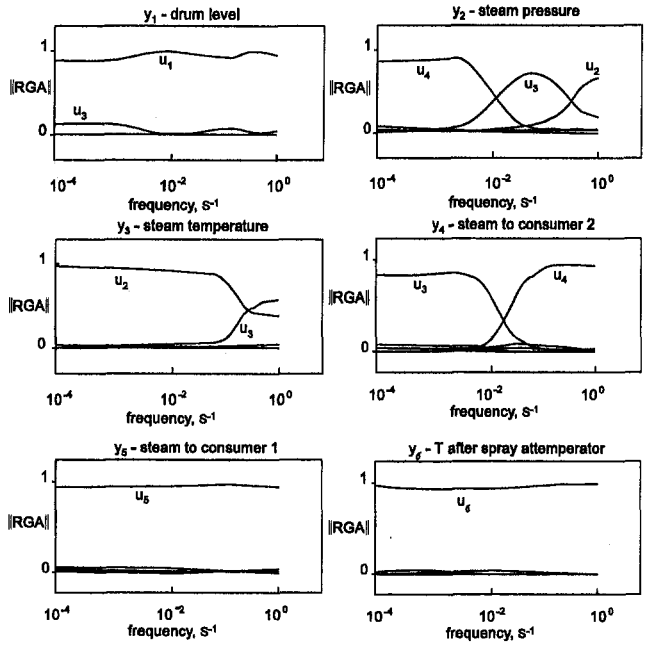

Fig. 3 Dynamic relative gain analysis to determine process interaction, u_1 = speed feed water pump, u_2 = flow to injection cooler, u_3 = boiler feed flow, u_4 = valve position consumer 2 flow, u_5 = flow to turbine, and u_6 = valve position flow to spray attemperator

(DRGA) was made in order to determine what the interaction between the variables is. Because the drum level shows integrating behavior for the DRGA analysis, a model describing the time derivative of the level instead of the level itself was used. The result is shown in Fig. 3. From this analysis it can be seen that y_5 (steam to consumer number one) and y_6 (temperature of the steam to consumer one) can be very well controlled by the turbine inlet valve (u_5) and the injection cooler inlet valve (u_6). However, since some of the models change considerably when the turbine inlet valve (u_5) changes, it was decided to leave the steam flow y_5 and the turbine inlet valve u_5 in the multivariable control strategy and only remove the temperature y_6 and valve position u_6 from the control strategy by using a PID controller for the pair (y_6, u_6). Hence, the remaining variables to be controlled are $y_1 \ldots y_5$ with $u_1 \ldots u_5$ as manipulated variables. From the DRGA analysis it is clear that the drum level depends primarily on the speed of the feed water pump, although there is some impact of the boiler fuel flow. The other process output variables are clearly influenced by more than one process input.

Model Predictive Control at Normal Operating Conditions

For the 5 × 5 system, step weight models were determined at normal operating conditions (NOC). The results are output horizon $P = 30$ and a control input horizon $M = 3$. After 750 seconds all nonintegrating processes have reached a steady state. In order to keep the models manageable, it was decided to use 50 stepweights for each model (the software does not require the number of stepweights to be the same for all models), hence to run the multivariable controller every 15 seconds.

During the controller design process it was found that multivariable control worked well for the process shown in Figure 4; however, when the process nonlinearity is also taken into consideration, a lower value of P gives improved results, it was therefore decided to choose $P = 5$ (75 seconds). This also worked well at NOC.

It was found that 0.01 m level variation raised the same concern as 10^4 kPa pressure variation, 0.1 degree temperature deviation and 0.1 kg/s flow variation. Using equal concern

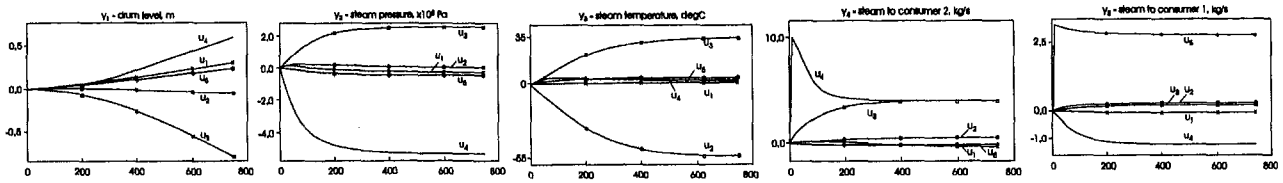

Fig. 4 Stepweight models at normal operating conditions, u_1 = speed feed water pump, u_2 = flow to injection cooler, u_3 = boiler feed flow, u_4 = valve position consumer 2 flow, u_5 = flow to turbine, and u_6 = valve position flow to spray attemperator

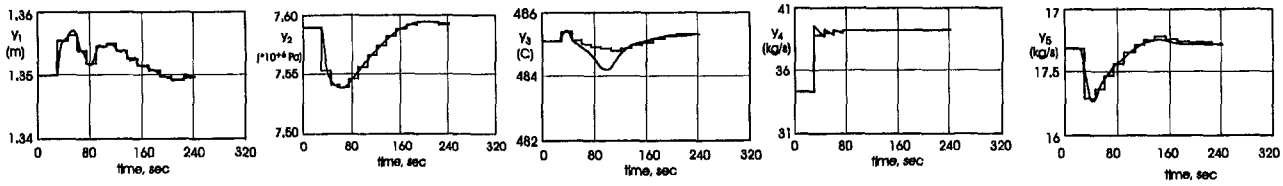

Fig. 5 Prediction and process response to a setpoint change in y_4, the steam flow to consumer 2

considerations (Cutler, 1983), it was decided to choose a set of process output variable weights of [10000, 0.01, 1000, 1000, 1000]. Based on considerations of maximum allowable input change per controller step, a set of input variable weights was chosen equal to [1, 10000, 10000, 1, 1]. There are also some process constraints that should be taken into account, these are the process input constraints such as minimum and maximum valve openings and pump speed, a maximum rate of change constraint for the feed water pump.

Other constraints are process output constraints that are not critical as long as the process outputs are maintained close to their setpoint values. Figure 5 shows the predicted and real process output behavior for a setpoint change in y_4 of 14 percent.

It can be seen that all models predict well except there is some process-model mismatch in the temperature y_3. Therefore a filter was used in the feedback path of y_3.

Process Nonlinearity

One of the main problems of the combined heat and power plant is that the load of the boiler varies considerably. As a result, the models at NOC are not valid over the entire operating region of the plant.

As the load increases, the responses will become faster due to a decrease in residence time. However, also at small valve openings and large valve openings the effect of changes will be different.

For example, the effect of a change in spray attemperator valve position u_2 on the temperature y_3 is more pronounced at high load since the feed water pump flow is then much higher and the pressure drop across the spray attemperator is larger. As a result, there will be a larger change in flow through the valve at high load and a correspondingly larger effect on the temperature.

Figure 6 shows the step responses of some of the models at different load conditions. As already mentioned, the steam load of the system will have a major impact on the models. The load can be estimated from:

load = steam flow to consumer 1

$$+ \text{ steam flow to consumer 2} - \text{base steam flow} \quad (4)$$

It was also found that the steam flow to consumer one changes over a large range, which has a major impact on the turbine inlet valve u_5. The gain from u_5 to y_5 varies with a factor of ten when the flow to consumer one changes from its maximum to its minimum value. This is mainly due to the valve characteristic of u_5 whose position varies from totally open to almost closed.

After thorough investigation it was concluded that changes in the load and the steam flow to consumer one were responsible for most of the changes in the process models. It was therefore evident that the different process models could be determined for different combinations of these two process variables. If the process models that were developed at NOC are used for control at low and high boiler load, most of the process outputs start to oscillate. Hence, there will be a need to update the process models for other operating conditions. The operating window was divided into six smaller operating windows. For each sub window process models were determined (Fig. 7).

The load of the process varies between b_1 and b_2, and the flow to consumer one varies between f_1 and f_2. Since the impact of the flow to consumer one has the largest impact on the change of the models, three divisions were made for this flow and only two divisions for the load. How many local linear models are required to describe the nonlinear process behavior is not immediately evident and could be a theme for further investigation.

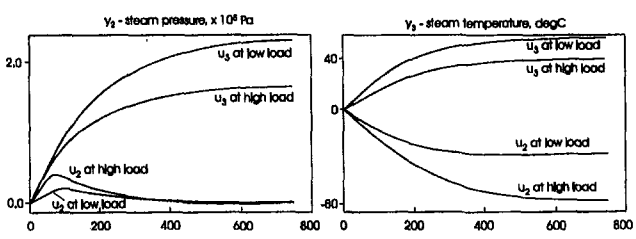

Fig. 6 Some process step response models at different process conditions

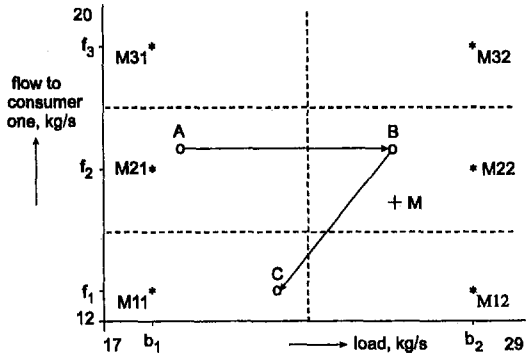

Fig. 7 Linear models in different operating windows

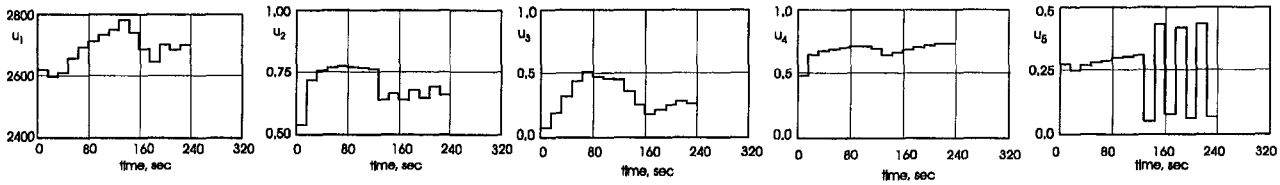

Fig. 8(*a*) Process input responses to setpoint changes with fixed models, u_1 = speed feed water pump, u_2 = flow to injection cooler, u_3 = boiler feed flow, u_4 = valve position consumer 2 flow, and u_5 = flow to turbine

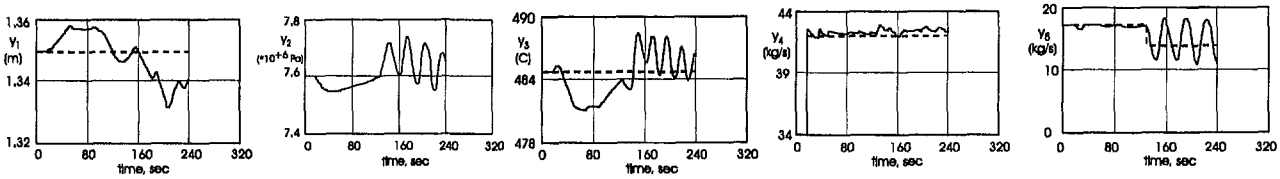

Fig. 8(*b*) Process output responses to setpoint changes with fixed models, y_1 = drum level, y_2 = steam pressure, y_3 = steam temperature, y_4 = steam to consumer 2, and y_5 = steam to consumer 1

In this study, it was important to achieve a fast solution of the control problem, hence the issue of the number of linear local models was not further investigated. The six standard linear step weight models are $\mathbf{M}_{11}$, $\mathbf{M}_{12}$, $\mathbf{M}_{21}$, $\mathbf{M}_{22}$, $\mathbf{M}_{31}$ and $\mathbf{M}_{32}$. For an arbitrary operating point $\mathbf{M}$ (see Fig. 7) the step weight models can be obtained by interpolation:

$$\mathbf{M} = c_{11}\mathbf{M}_{11} + c_{12}\mathbf{M}_{12} + c_{21}\mathbf{M}_{21} + c_{22}\mathbf{M}_{22} \qquad (5)$$

in which

$$c_{11} = (f_2 - f)*(b_2 - b)/((f_2 - f_1)*(b_2 - b_1))$$
$$c_{12} = (f_2 - f)*(b - b_1)/((f_2 - f_1)*(b_2 - b_1))$$
$$c_{21} = (f - f_1)*(b_2 - b)/((f_2 - f_1)*(b_2 - b_1))$$
$$c_{22} = (f - f_1)*(b - b_1)/((f_2 - f_1)*(b_2 - b_1)) \qquad (6)$$

Similar approximations are used when the steam flow to consumer one is between f_2 and f_3.

In order to determine what the present operating point is, the present actual values of load and steam flow to consumer one could be used. However, if the setpoints of the load and/or flow change, the process will change from one state to another, hence the actual state of the process will be somewhere in between the original state and the final state. Therefore, the following approximations were used:

$$\text{load } b(k) = \alpha PV\_b(k-1) + (1-\alpha)SP\_b(k)$$
$$\text{flow } f(k) = \beta PV\_f(k-1) + (1-\beta)SP\_f(k), \qquad (7)$$

where α and β are suitable weighting factors; it was found that the best values were $\alpha = 0.5$ and $\beta = 0.3$. PV represents the measured process value and SP the setpoint. Equation (7) is essential since on a change of setpoint it is essential that the right operating point is determined; hence, the right models are used (the calculated load b and flow f are calculated by using simple first order filters when the setpoint changes to a new value).

Figure 8 shows control with two shifts in operating point, at $t = 15$ seconds the flow to consumer two (i.e., the load) changes with +20 percent; at $t = 120$ seconds the flow to consumer one (i.e., the load and the flow) changes with −22 percent.

The starting point corresponds with point A in Fig. 7, the setpoint change at $t = 15$ corresponds with point B and the setpoint change at $t = 120$ corresponds with point C. In point A the best model is calculated from the models M_{21}, M_{22}, M_{31}, and M_{32}. Since this point is very close to the basic model point M_{21}, the model will also be very close to the model for this point.

This model is not updated; hence, the same model is used for control at point B and C as for point A. From Fig. 8 it can be seen that from A to B the response is still stable even though the model changes, however, from point B to point C control becomes unstable.

Figure 9 shows the same setpoint changes, now with an update of the model at every controller execution interval. In this case control is somewhat better from point A to point B, especially the temperature and level that are controlled tighter with

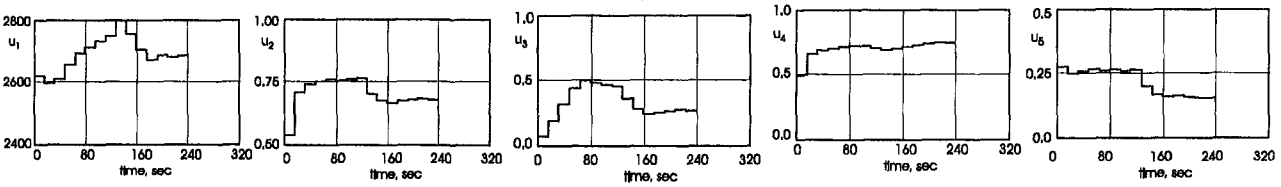

Fig. 9(*a*) Process input responses to setpoint changes using different linear models

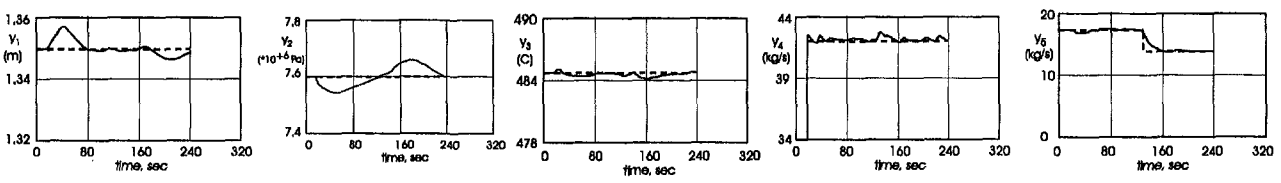

Fig. 9(*b*) Process output responses to setpoint changes using different linear models

Table 1 Comparison of PID with MPC control using model update

maximum deviation in:	MPC	PID
temperature, degC	1	3.1
pressure, bar	1.5	7.9

model update. The biggest change can be seen when the operating point shifts from B to C.

With model update, the controller is stable and control is tight, while without model update control is unstable. The controller design procedure with and without model update were the same, i.e., the control horizon, process output horizon, and input and output weighting parameters were not changed. If the changes in the response time of the system would be large, there might be room for some further improvement by changing, for example, the process output horizon. However, in this project there appeared to be no need to adjust the controller parameters.

Comparison With Conventional Control

The plant is currently controlled by single loop PID controllers with decouplers and gain schedulers. Hence, it is useful to compare the closed loop behavior of the plant model under control of the conventional control scheme to the results obtained with multivariable control using local linear models.

This was done for the situation where consumer two required an increase in steam flow of +20 percent.

The results for the steam temperature and pressure are given in Table 1. PID control is stable; however, some control loops cannot be tuned tightly, resulting in slowly damped responses with a long period.

For example, the temperature response in case of PID control would show a damped response with $\frac{1}{4}$ decay and a period of 1100 seconds, the pressure response in case of PID control would show a damped response with $\frac{1}{2}$ decay and a period of approximately 1400 seconds.

Responses to Disturbances

In a combined heat and power plant, there are many disturbances that can affect the process. In one case, the enthalpy of combustion of the fuel was about 75 percent of its original value, hence a process-model mismatch will exist for several process models. A setpoint change in y_4 (steam to consumer two) was given of +20 percent, and the case of "no", process-model mismatch was compared to the case where the process-model mismatch (pmm) existed. The results are shown in Table 2.

The speed of response with and without process-model mismatch was the same; it can be concluded that the temperature response suffers the most from the decrease in the heat of combustion. The temperature drops significantly because the fuel delivers less heat than predicted according to the model. In all cases, however, stable responses were obtained.

Table 2 Results of process-model mismatch

maximum deviation in:	no pmm	with pmm
drum level y1, m	0.015	0.02
steam pressure y2, bar	0.8	1
steam temperature y3, degC	0.9	2.5
steam to consumer 2 y4, kg/s	2	3
steam to consumer 1 y5, kg/s	0.4	0.25

Conclusions

In this work, the use of local linear models in multivariable predictive control was investigated. It was demonstrated that this idea could be successfully used to obtain stable process responses with excellent speed of response. Improvements compared to conventional PID control are significant. The combined heat and power plant was nonlinear to such an extent that the use of fixed models over the entire operating region would give unstable control.

One disadvantage of using local linear models is that an increased number of step weight models have to be determined, hence it will require an increased modeling effort.

If, however, a detailed nonlinear and experimentally verified process model is available, the step weight models can easily be generated from this model.

References

Garcia, C. E., Prett, D. M., and Morari, M., 1989, "Model-Predictive Control, Theory and Practice—A Survey," *Automatica,* Vol. 25, No. 3, pp. 335–348.

Cutler, C. R., 1983, "Dynamic Matrix Control, an Optimal Multivariable Control Algorithm," Ph.D. thesis, University of Houston, Houston, TX.

Biegler, L. T., and Cuthrell, J. E., 1985, "Improved Infeasible Path Optimization for Sequential Modular Simulators: II—The Optimization Algorithm," *Comp. Chem. Eng.,* Vol. 9, pp. 257–267.

Ricker, N. L., 1992, "Model Predictive Control: State of the Art," proceedings, 4th International Conference on Chem. Proc. Control, AIChE/CACHE Sheraton South Padre Island, Texas.

Economou, C. G., Morari, M., and Palsson, B. O., 1986, "Internal Model Control: 5—Extensions to nonlinear Systems," *Ind. Eng. Chem. Process Des. Dev. 25,* pp. 403–411.

Wright, G. T., and Edgar, T. F., 1994, "Nonlinear Model Predictive Control of a Fixed Bed Water-Gas Shift Reactor: An Experimental Study," *Comp. Chem. Eng.,* Vol. 18, No. 2, pp. 83–102.

Morningred, J. D., Mellichamp, D. A., and Seborg, D. E., 1993, "Experimental Evaluation of a Multivariable Nonlinear Predictive Controller," *J. Proc. Control,* Vol. 3, No. 2, pp. 125–134.

Maiti, S. N., Ganguly, S., and Saraf, D. N., 1995, "Some New Approaches for the Control of a Distillation Column and Their Experimental Evaluation on a Pilot Plant," *Comp. Chem. Eng. Suppl.,* Vol. 19, pp. S399–S404.

Bhat, N. V., and McAvoy, T. J., 1990, "Use of Neural Networks for Dynamic Modelling and Control of Chemical Process Systems," *Comp. Chem. Eng. 14,* pp. 573–583.

Psichogios, D. C., and Ungar, L. H., 1991, "Direct and Indirect Model-Based Control Using Artificial Neural Networks," *Ind. Eng. Chem. Res. 30,* pp. 2564–2573.

A Fast-Response Total Temperature Probe for Unsteady Compressible Flows

D. R. Buttsworth

T. V. Jones

Department of Engineering Science,
University of Oxford,
Parks Road,
Oxford, OX1 3PJ, United Kingdom

A fast-response probe for the measurement of total temperature in unsteady or fluctuating compressible flows is discussed. The operation of the device is based on the measurement of transient heat flux at different probe operating temperatures. The heat flux gauges used in the present investigation were thin film platinum resistance thermometers painted onto the stagnation region of hemispherical fused quartz probes. The quartz probes had a diameter of approximately 3 mm. Uncertainty estimates indicate that temperature measurements with an accuracy of better than ±3 K are possible. As a demonstration of the accuracy and utility of the device, total temperature and convective heat transfer coefficient measurements were obtained in a number of supersonic nozzle tests and in a compressible turbulent jet experiment.

Introduction

The flow temperature is clearly a fundamental variable of interest in many processes and experiments. In principle, a variety of methods could generally be employed to obtain the same measurement of the flow temperature. In practice, however, physical and economic constraints limit the availability of certain techniques.

Remote sensing techniques such as line reversal, classical spectroscopy, Raman and Rayleigh scattering, coherent anti-Stokes Raman spectroscopy, laser-induced fluorescence, photodetection spectroscopy, and tomography offer a nonintrusive measurement of the flow temperature (e.g., Timnat, 1989). Furthermore, as the instrumentation need not be exposed to the frequently adverse environment of interest, the life and accuracy of the equipment can be preserved. However, as many of these techniques require expensive equipment and optical access is not always possible, probe and surface mounted temperature measuring devices are often utilized.

Thermocouples are used extensively to provide an accurate and low cost measurement of temperature. However, the practical frequency limit for unshielded thermocouples is around 1 kHz due to thermal inertia effects (Forney et al., 1993). Thus, the utility of thermocouple devices in unsteady or fluctuating compressible flows is somewhat restricted. Higher frequency temperature measurements are possible using thin wire devices. Bremhorst and Graham (1990) described the electronic compensation of a constant-current anemometer for the measurement of temperature fluctuations in an unsteady incompressible air jet. Multiple hot wire anemometers operated in the constant temperature mode have also been used for temperature measurements in relatively low speed flows (e.g., Eklund and Dobbins, 1977; Fabris, 1978). However, the practical extension of such techniques to unsteady or fluctuating compressible flows is difficult, since the density, velocity, temperature, and pressure may all vary independently with time. An additional difficulty that frequently arises in compressible flows is that of wire breakage, since the pressure and particle impact loading on the wire are often significant.

Compressible total temperature measurements are possible with the aspirating probe described by Ng and Epstein (1983). This device consists of two constant temperature hot wires located upstream of a choked orifice. The external diameter of the probe used by Ng and Epstein was 3 mm, and the internal channel upstream of the choked orifice had a diameter of 1.5 mm. The drag loading on the wires is greatly reduced relative to an exposed hot wire of identical dimensions in the same compressible flow, due to the reduction of the dynamic pressure within the channel. By operating the wires at different overheat ratios, it is possible to temporally resolve both pitot pressure and total temperature variations in unsteady or fluctuating compressible flows (e.g., Ng and Epstein, 1983; Alday et al., 1993). The successful operation of the probe is dependent on establishing a steady flow in the channel leading up to and including the choked orifice. Calculation of such flow establishment times and experimental measurements at the exit of a transonic compressor suggest that the upper frequency limit for this device is approximately 20 kHz (Ng and Epstein, 1983).

Techniques based on the measurement of transient heat transfer rate using thin film gauges and calorimeters can also be used to deduce the total temperature in compressible flows (e.g., Edney, 1967), provided the convective heat transfer coefficient is known for the particular probe and flow configuration being considered. Optical fibre Fabry–Perot interferometers have been used to deduce high frequency gas temperature fluctuations in compressible flows (Kidd et al., 1994). However, assumptions regarding the value of the heat transfer coefficient were again necessary in that study, since the total temperature was inferred from measurements of the surface heat transfer rate.

The purpose of the current paper is to describe a probe that offers a high-frequency measurement of total temperature in unsteady compressible flows. The present total temperature device utilizes the measurement of transient heat transfer rate at different probe operating temperatures. It is superior to many other devices in that both the flow total temperature and the convective heat transfer coefficient are determined from the experimental measurements. Thus, with the present device, it is not necessary to calibrate the probe to determine the constants in an empirical heat transfer relationship (as is the case with devices based on thin wire anemometry), and neither is it necessary to make assumptions regarding the value of the convective heat transfer coefficient (as is the case when the flow temperature is inferred from surface heat flux measurements obtained at a single probe operating temperature).

Principle of Operation

The convective heat transfer rate is approximately proportional to the difference between the surface temperature of the

Contributed by the International Gas Turbine Institute and presented at the 41st International Gas Turbine and Aeroengine Congress and Exhibition, Birmingham, United Kingdom, June 10–13, 1996. Manuscript received by the ASME Headquarters November 20, 1995. Paper No. 96-GT-350. Associate Technical Editor: J. N. Shinn.

body and the total temperature of the flow (or the recovery temperature in cases where viscous dissipation is significant). Therefore, if the convective heat transfer is measured at two known surface temperatures, the total or recovery temperature may be deduced. This is the fundamental operating principle of the current total temperature probe. In the present work, the heat flux was measured with thin film heat transfer gauges at the stagnation point of hemispherical fused quartz probes. The operating principles of thin film gauges are detailed in other publications (e.g., Schultz and Jones, 1973).

For measurements obtained at a stagnation point, the appropriate relationship between the heat transfer rate and the driving temperature difference is

$$q = h(T_t - T_w). \tag{1}$$

The flow total temperature, rather than recovery temperature, appears in this relationship because there is no viscous dissipation within the stagnation point boundary layer, even in relatively high speed compressible flows. It should be noted that there is no loss of total temperature when a normal shock wave forms ahead of the probe, in contrast to the loss of total pressure that affects supersonic pitot pressure measurements.

The convective heat transfer coefficient, h, is a property of the stagnation point boundary layer and is thus a function of the probe geometry and the upstream flow conditions. It has been found that the convective heat transfer coefficient is only a weak function of the surface temperature of the probe at the stagnation point. For example, in a steady flow with low free-stream turbulence, the convective heat transfer coefficient can be expressed in the form of a Nusselt number as (from White, 1991, p. 516),

$$\mathrm{Nu} = 0.763\ \mathrm{Pr}^{0.4}\ \mathrm{Re}^{0.5} C^{0.1} \sqrt{\frac{KD}{u_\infty}}, \tag{2}$$

where

$$\mathrm{Nu} = \frac{hD}{k_e},\ \mathrm{Pr} = \frac{c_p \mu_e}{k_e},\ \mathrm{Re} = \frac{\rho_e u_\infty D}{\mu_e},\ K = \frac{du_e}{dx},$$

$$\text{and } C = \frac{\rho_w \mu_w}{\rho_e \mu_e}.$$

Upon evaluation of the above result under typical conditions, it is found that the ratio, T_t/T_w can vary by a factor of 2, while the convective heat transfer coefficient remains constant to within approximately 1 percent. Thus, the convective heat transfer coefficient in Eq. (1) can be treated as being independent of T_w.

The flow total temperature and convective heat transfer coefficient can therefore be determined by measuring the stagnation point convective heat flux at two different probe operating temperatures. That is, at the two measured surface temperatures, the physics of the heat transfer process can be described by

$$q_1 = h(T_t - T_{w1}) \tag{3}$$

and

$$q_2 = h(T_t - T_{w2}). \tag{4}$$

Equations (3) and (4) can therefore be solved to obtain the convective heat transfer coefficient and total temperature as follows:

$$h = (q_1 - q_2)/(T_{w2} - T_{w1}) \tag{5}$$

$$T_t = T_{w1} + q_1(T_{w2} - T_{w1})/(q_1 - q_2) \tag{6}$$

The above method provides a measurement of the flow total temperature that is independent of other flow parameters such as the Mach number, Reynolds number, pressure, and the flow composition. The assumption that steady, low-turbulence flow conditions prevail (which is associated with the use of a heat transfer relationship such as Eq. 2), is not made with the present method (c.f. Edney, 1967 and Kidd et al., 1994). This is a significant advantage of the present method because it means that accurate total temperature measurements can now be obtained in unsteady compressible turbulent flow environments in which the steady, low-turbulence flow assumptions are inappropriate. The total temperature probe does not rely on pitot pressure measurements. A further advantage of the present device is that it can be used to determine total temperatures in flows of arbitrary composition.

In principle, a similar method could be used with thin wire anemometry to obtain temperature measurements (e.g., Eklund

Nomenclature

c = specific heat of the substrate ($\mathrm{J \cdot kg^{-1} \cdot K^{-1}}$)
c_p = specific heat of the flow
c_1 = constant in turbulent boundary layer correlation
C = Chapman-Rubesin parameter
d = internal diameter of the gun tunnel barrel
D = probe diameter
h = convective heat transfer coefficient
k = conductivity of the flow or substrate ($\mathrm{W \cdot m^{-1} \cdot K^{-1}}$)
K = stagnation point velocity gradient
l_b = gun tunnel barrel length
l_{be} = effective gun tunnel barrel length
Nu = Nusselt number
p = pressure
p_{pit} = pitot pressure
Pr = Prandtl number
q = surface heat transfer rate ($\mathrm{W \cdot m^{-2}}$)
r = gun tunnel boundary layer recovery factor
R = radius of the probe or resistance of the thin film
R_0 = resistance of the thin film at 20°C
Re = Reynolds number
t = time
T = temperature of the flow or substrate (K)
T_0 = room temperature, taken as 20°C.
T_r = recovery temperature behind first gun tunnel barrel shock
u = flow velocity
x = distance from stagnation point or start of gun tunnel barrel
y = distance from the centerline of the mixing region
α_R = linear coefficient in the temperature-resistance calibration
β_R = nonlinear coefficient in the temperature-resistance calibration
δ = boundary layer thickness at the stagnation point
ρ = density of the flow or substrate material
μ = flow viscosity

Subscripts

e = stagnation point boundary layer edge value
i = index for either probe 1 or 2
p = gun tunnel piston
$s1$, $s2$ = first and second gun tunnel shocks
t = total or stagnation condition
w = value at probe surface or gun tunnel barrel wall
1, 2 = first and second ("hot" and "cold") probes
2 = value behind first gun tunnel barrel shock
∞ = undisturbed value upstream of probe

Superscripts

$'$ = fluctuating component
$(\bar{\ })$ = time-averaged or mean component

and Dobbins, 1977). However, if the necessary data is obtained using two wires operated at different overheat ratios, then additional calibrations will be needed since the physical variations between two nominally identical wires are generally sufficient to cause a difference in the heat transfer coefficients of the two wires (e.g., Lomas, 1986, p. 77). With thin film heat transfer gauges located at the stagnation point of hemispherical probes, such calibrations are unnecessary because it is relatively easy to generate identical heat transfer coefficients by producing substrates for the thin film gauges with essentially the same radius of curvature.

Probe Design, Calibration, and Operation

Design. In the present investigation, the heat transfer probes consisted of platinum thin film resistance thermometers painted onto fused quartz substrates, as illustrated in Fig. 1. The platinum films had an estimated thickness of approximately 0.5 μm, and a resistance of around 20 Ω. The rise time (0 to 90 percent) of such a gauge for a step in heat flux is approximately 30 μs (Schultz and Jones, 1973). However, the bandwidth of the present total temperature device is not necessarily restricted to around 50 kHz (the 3 dB point for 0.5 μm platinum films on quartz) because it is possible (in principle) to either use thinner films, or to compensate for the effects of the thermal inertia of the platinum.

The quartz probes had a diameter of approximately 3 mm and the thin films had a length of approximately 1 mm. It is known that the magnitude of the convective heat flux decreases at locations away from the stagnation point (e.g., Kemp et al., 1959). The average heat flux across the length of the film was calculated (using results from Kemp et al.) to be 2.4 percent lower than the stagnation point value. Convective heat flux results presented in this paper have been adjusted by this amount so that they correspond to the stagnation point values. However, it should be noted that, provided the two films have the same length, such corrections are generally unnecessary for the accurate measurement of total temperature because the two films will have the same overall convective heat transfer coefficient.

During routine operation, high temperatures were induced at the thin film end of the probes. Electrical leads formed by a gold paste that ran to the cool end of the probes, and permitted the sustained integrity of the solder, which joined the electrical wires to the probes. The probes were mounted in macor collars (which provided electrical and thermal insulation for the probes) prior to their installation in the total temperature measurement device shown in Fig. 2.

Temperature-Resistance Calibration. It is essential to calibrate thin film gauges over the whole range of anticipated operating temperatures (which presently is from approximately 300 K to 700 K), due to the nonlinearity of the temperature-resistance relationship. Calibrations were performed in air at temperatures up to approximately 700 K. Six gauges were calibrated simultaneously in the small calibration rig shown in Fig. 3. This rig was inserted into the inspection port of a conventional furnace and the gauge resistances were measured at various temperatures (measured with the thermocouple shown in Fig. 3), while the furnace and the rig slowly cooled to room temperature.

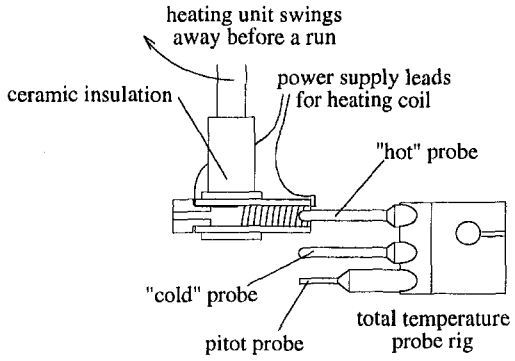

Fig. 2 Total temperature measurement device and preheating unit

Temperature-resistance calibrations can be expressed in the form (e.g., Schultz and Jones, 1973; Lomas, 1986, p. 36),

$$\frac{R}{R_0} = 1 + \alpha_R(T - T_0) + \beta_R(T - T_0)^2 \qquad (7)$$

Frequently, however, the nonlinear coefficient, β_R is neglected. In Fig. 4, results from a calibration of a typical thin film are presented. The values of the nonlinear coefficient, β_R, derived from the present calibrations, are in reasonable agreement with results obtained in other platinum thin film investigations (Bogdan, 1963). The significance of the nonlinear coefficient is clearly illustrated in Fig. 4. It is encouraging that calibrations performed before and after experimental use of the thin film gauges yielded essentially the same values of α_R and β_R, even though there was a slight increase in ambient resistance ($\bar{R}_0$) that was accumulated throughout the series of experiments. The increase in film resistance can be attributed to small air-borne particles that cause some abrasive wear of the films. However, in the present experiments, film wear did not significantly degrade the accuracy of the results because the resistance change during any one experiment was barely perceptible (typically less than 0.1 percent).

Operation. To generate the necessary difference in the surface temperature of the probes, the preheating unit shown schematically in Fig. 2 was utilized. Power was supplied to the unit through an aluchrom heating coil which had a resistance of approximately 2 Ω, using a typical excitation of around 7 V. Thermal insulation for the heating coil was provided by an oxide ceramic material. During the preheating of the "hot" heat flux probe, the temperature of the "cold" probe also in-

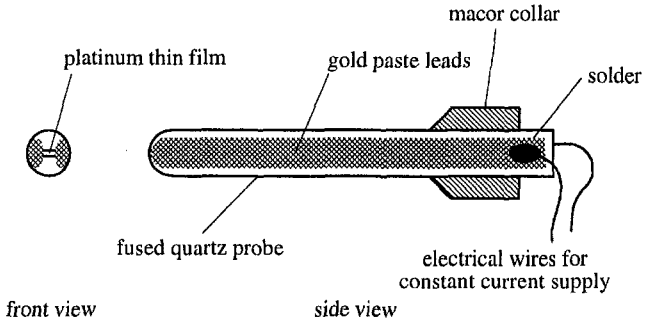

Fig. 1 Schematic illustration of the thin film heat flux sensors

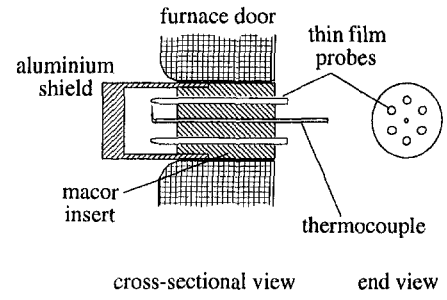

Fig. 3 Temperature-resistance calibration rig in the inspection port of the furnace

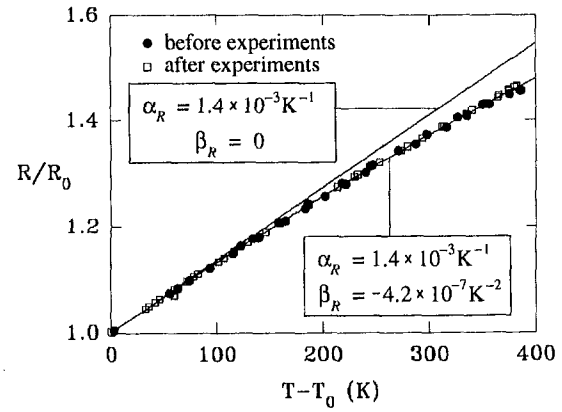

Fig. 4 Results from the temperature-resistance calibration of a thin film gauge

creased due mainly to radiation from the heating unit. Immediately before a run, the heating unit was swung clear of the probes and thus allowed the measuring device to be driven into position or to traverse the flow as required. To provide additional flow data, a pitot probe was mounted parallel to the heat flux probes (as illustrated in Fig. 2). However, it should be noted that the pitot pressure probe is not an essential feature of the total temperature measuring device. The thin film gauges were powered with a constant current supply of around 20 mA.

Accuracy Considerations. The derivation of total temperature is based on the measurement of two different probe surface temperatures and the associated convective heat transfer rates. Thus, the accuracy with which the total temperature can be determined will depend on the uncertainties associated with measurement of the temperatures and heat transfer rates.

The convective heat transfer rate is determined from measurements of the change in the surface temperature of each probe and a knowledge of the thermal properties of the probe substrate (e.g., Schultz and Jones, 1973). For the present uncertainty analysis, it is assumed that the relationship for a constant convective heat flux to a semi-infinite flat plate is appropriate. Therefore, the expression

$$q_i = \frac{\sqrt{\pi}}{2}\frac{\sqrt{(\rho c k)_i}}{\sqrt{\Delta t}}\Delta T_i \quad (\text{for } i = 1, 2) \tag{8}$$

is utilized (e.g., Schultz and Jones, 1973). Thus, it is assumed that the fundamental independent variables relevant to the present uncertainty analysis are T_1, ΔT_1, T_2, ΔT_2, $\sqrt{(\rho ck)_1}$, and $\sqrt{(\rho ck)_2}$. (It is assumed that Δt is accurately measured during the experiments.)

Therefore, the uncertainties in the derived quantities, h and T_t, can be estimated using the expressions (e.g., Holman, 1984, p. 50)

$$\frac{\delta h}{h} = \left[\left(\frac{T_1}{h}\frac{\partial h}{\partial T_1}\frac{\delta T_1}{T_1}\right)^2 + \left(\frac{\Delta T_1}{h}\frac{\partial h}{\partial \Delta T_1}\frac{\delta(\Delta T_1)}{\Delta T_1}\right)^2 + \ldots\right]^{1/2} \tag{9}$$

$$\frac{\delta T_t}{T_t} = \left[\left(\frac{T_1}{T_t}\frac{\partial T_t}{\partial T_1}\frac{\delta T_1}{T_1}\right)^2 + \left(\frac{\Delta T_1}{T_t}\frac{\partial T_t}{\partial \Delta T_1}\frac{\delta(\Delta T_1)}{\Delta T_1}\right)^2 + \ldots\right]^{1/2}. \tag{10}$$

(The pattern established in the first two terms of Eqs. 9 and 10 simply continues on for the remaining variables.) The partial derivatives that appear in Eqs. (9) and (10) can be obtained analytically from Eqs. (5), (6), and (8). The relative uncertainties in the fundamental quantities (i.e., $\delta T_1/T_1$, $\delta(\Delta T_1)/\Delta T_1$, etc.), which appear in Eqs. (9) and (10), are estimated below.

Due to slight spatial variations of the air temperature within the temperature-resistance calibration rig, uncertainties in the thermocouple calibration, and uncertainties associated with the measurement of the ambient film temperature it is estimated that the relative uncertainty of the absolute temperature measurement can be expressed as

$$\frac{\delta T_i}{T_i} = 0.005\left(1 - \frac{T_0}{T_i}\right) + \frac{0.5}{T_i}. \tag{11}$$

Therefore, the relative uncertainty in the temperature changes will be

$$\frac{\delta(\Delta T_i)}{\Delta T_i} = 0.005. \tag{12}$$

The uncertainty in the thermal product, $\sqrt{\rho ck}$ for fused quartz is assessed by considering the uncertainties in the individual quantities, ρ, c, and k. Quoted values for the density of fused quartz vary between 2190 and 2210 kg · m^{-3} (e.g., Miller, 1981; Schultz and Jones, 1973). Therefore, the density of fused quartz is currently taken to be ρ = 2200 kg · m^{-3} ± 0.5 percent.

A curve fit for the fused quartz specific heat data presented in Toulokian (1970) is

$$c = -7.8331 \times 10^{-10} T^4 + 3.3153 \times 10^{-6} T^3 - 5.3008 \times 10^{-3} T^2 + 4.0143\, T - 7.3221 \times 10^{1}, \tag{13}$$

which is valid for $100 < T < 1000$ K. Values from the above expression have been plotted in Fig. 5 along with representative data from Toulokian (1970). Based on the deviations of the data presented in Fig. 5, the uncertainty of the curve fit for the specific heat of fused quartz (Eq. 13) is estimated to be ±2 percent over the range 200 to 800 K.

Recommended values for the conductivity of fused quartz (from Toulokian, 1970) are also presented in Fig. 5 along with a curve fit given by

$$k = -7.5685 \times 10^{-12} T^4 + 2.2634 \times 10^{-8} T^3 - 2.1557 \times 10^{-5} T^2 + 9.4079 \times 10^{-3} T - 5.0808 \times 10^{-2}. \tag{14}$$

Again, the valid temperature range for the curve fit is $100 < T < 1000$ K. It is stated (Toulokian, 1970) that, ". . . the uncertainty of the recommended values is thought to be within ±3 percent at temperatures from 200 to 500 K and increase to about

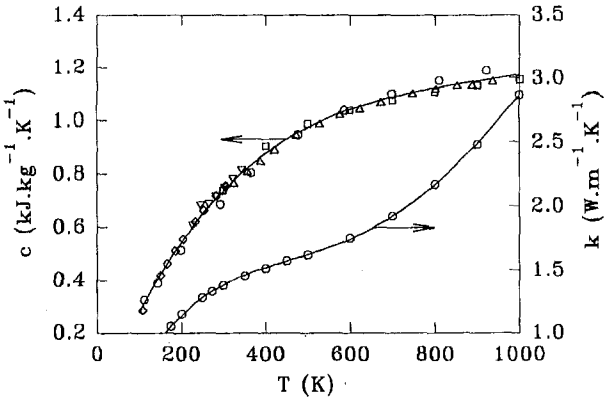

Fig. 5 Thermal properties of fused quartz based on bulk values from Toulokian (1970)

±8 percent at 50 K and 900 K and ±15 percent below 10 K and near 1400 K."

The relative uncertainty of the thermal product can be expressed as

$$\frac{\delta(\sqrt{\rho ck})}{\sqrt{\rho ck}} = \left[\left(\frac{1}{2}\frac{\delta\rho}{\rho}\right)^2 + \left(\frac{1}{2}\frac{\delta c}{c}\right)^2 + \left(\frac{1}{2}\frac{\delta k}{k}\right)^2\right]^{1/2}. \quad (15)$$

On evaluating the above expression, the uncertainty in $\sqrt{\rho ck}$ is presently estimated to be ±1.8 percent for temperatures between 200 and 500 K, and increases to ±3.5 percent at 800 K.

Using the above estimates, and assuming probe operating temperatures of 700 K and 400 K, Eqs. (9) and (10) were evaluated for the range of flow total temperatures shown in Fig. 6. Clearly, the flow total temperature measurement is more accurate when it corresponds to the operating temperature of one of the probes. For the case considered, uncertainties of less than ±3 K are possible provided the flow total temperature falls between the two probe operating temperatures. For flow total temperatures that lie outside the range of the probe temperatures, larger uncertainties are anticipated. However, for T_1 = 700 K and T_2 = 400 K, a reasonable level of accuracy is maintained for flow total temperatures over the range $300 < T_t < 800$ K (Fig. 6).

In the above analysis, it was assumed that no additional uncertainties arose due to the thermal modeling of the substrate. For the probe configurations and flow conditions considered in the present investigation, the usual one-dimensional semi-infinite flat-plate solution with constant thermal properties is, in general, inappropriate (although it remains adequate for the purposes of determining uncertainties in derived quantities). In the next section, the practical analysis of the measured surface temperature histories is discussed. Experimental results testing the accuracy of the current thermal modeling and analysis are also presented.

Results

Mach 5 Nozzle Flow Experiments. As an initial demonstration of the total temperature probe, experiments were performed using a small Mach 5 conical nozzle. The Mach 5 nozzle had a throat diameter of 6.05 mm, an exit diameter of 30.5 mm, and an expansion half-angle of 10.2 deg. A piezoelectric pressure transducer and a 0.0005 in. diameter K-type exposed thermocouple measured the flow stagnation properties within the plenum chamber upstream of the Mach 5 nozzle, as shown in Fig. 7. Signals from the pressure transducer, the thermocouple, and the "hot" heat flux probe, obtained during a preliminary experiment, are presented in Fig. 8.

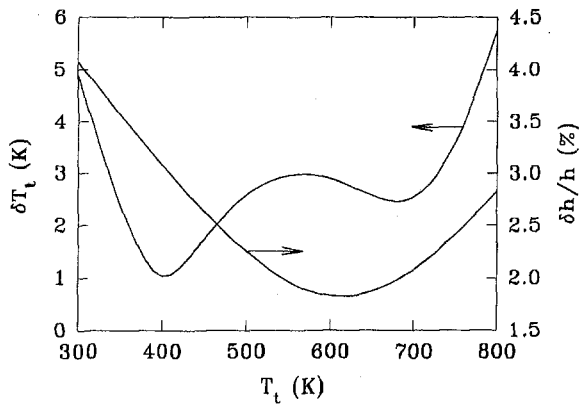

Fig. 6 Uncertainty estimates for the measurement of total temperature and convective heat transfer coefficient assuming T_1 = 700 K and T_2 = 400 K

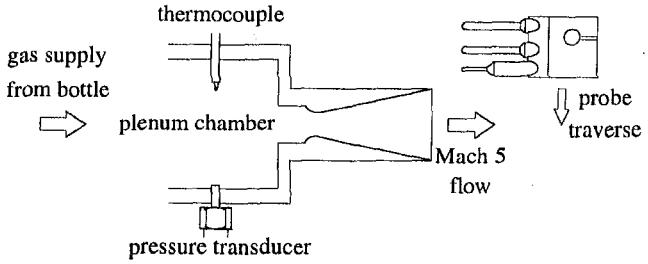

Fig. 7 Arrangement for the Mach 5 nozzle flow experiments

At approximately 0.22 s on the scale in Fig. 8, the heater unit (Fig. 2) was removed, causing the probe temperature to fall due to radiation and conduction effects. Referring again to Fig. 8, at approximately 0.05 s, the nitrogen supply valve was opened and the flow reached a steady operating state at approximately 0.50 s. The measurement of heat flux began at approximately 0.55 s, when the probe was traversed into position on the centerline of the Mach 5 flow at a location 10 mm downstream of the nozzle exit plane.

The linearity of the heat diffusion equation makes it possible to separate the temperature history due to the convective heat flux (T_{conv}) from the temperature history due to the radiation and conduction effects ($T_{rad+cond}$) that operate both prior to, and during, a run (see Fig. 8(*b*)). To determine the convective heat flux, a curve fit was applied to the temperature signal prior to the start of the convective heating. The difference between the curve fit and the measured temperature history was then obtained (T_{conv} in Fig. 8).

The convective heat flux was inferred from this measured temperature difference (T_{conv}) using a finite difference routine (Buttsworth, 1996) that accurately accounted for variable thermal property and curvature effects (including lateral conduction) within the fused quartz substrate. It is important to account for the temperature dependency of the thermal properties of the quartz in cases where the surface temperature change is significant (e.g., Schultz and Jones, 1973). It should be noted that strictly, the variable thermal property form of the heat diffusion equation (as used in the finite difference routine) is

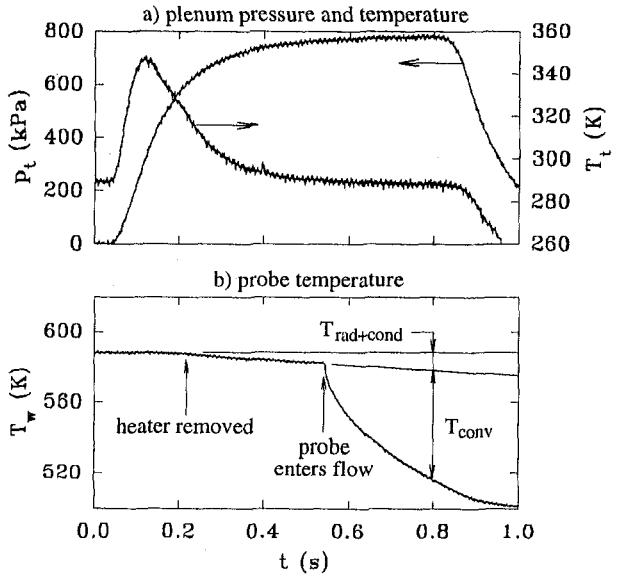

Fig. 8 Example of signals obtained from the pressure transducer, thermocouple, and hot heat flux probe using the Mach 5 nozzle flow rig

nonlinear. In practice, however, this nonlinearity is weak enough for the temperature separation procedure discussed above to remain valid.

To validate the techniques that were established to account for radiation and conduction, variable thermal properties, and curvature effects, experiments in which the probe was traversed right through the Mach 5 flow were conducted. The "hot" probe was operated at a number of different initial temperatures using nitrogen as the test gas. In general, during a traverse of the nozzle flow (which took around 0.1 s), the probe temperature, and, hence, the measured heat flux, varied significantly. Measurements from these experiments (obtained while the probe remained in the core of the Mach 5 nozzle flow) are plotted in Fig. 9 in terms of the instantaneous measured heat flux versus the measured temperature at that point in time. The gradient of the line formed by the data is thus proportional to the convective heat transfer coefficient and the temperature-axis intercept is a measurement of the total temperature (see Eq. (1)). Included in Fig. 9 is a theoretical prediction based on Eqs. (1) and (2), the measured plenum temperature (290.0 K), and the result

$$\frac{du_e}{dx} = \frac{1}{R}\sqrt{\frac{2p_{\text{pit}}}{\rho_e}}, \tag{16}$$

(e.g., Anderson, 1989, p. 256) which is valid in hypersonic flows.

With some manipulation, the theoretical result (Eqs. (1), (2), and (16)) shows that the measured heat flux varies in proportion to $\sqrt{p_{\text{pit}}/R}$. For the present experiments, the average pitot pressure was 27.5 kPa, and the radius of curvature of the probe at the stagnation point was 1.3 mm. As there was a slight run-to-run variation in the measured pitot pressure and the actual radius of curvature differed from the nominal value of 1.5 mm, the heat flux results have been normalized using $\sqrt{p_{\text{pit}}/R}$, as shown in Fig. 9.

For the present experiments, the average flow total temperature (measured with the plenum chamber thermocouple) was 290.0 K (with a maximum deviation from this value of 1 K for any particular run). From Fig. 9 it is observed that the theoretical prediction is a very good fit to the experimental data. Thus, the total temperature probe indicates a flow total temperature that is in very close agreement with the measured plenum value. Furthermore, there exists a similar degree of agreement between the experimental and theoretical values of the convective heat transfer coefficient. It may also be observed that the agreement between theoretical and experimental results spans the entire measured temperature range ($360 < T_w < 640$ K), even when the surface temperature change during a run is as large as 50 K. Thus, it is concluded that the present approach to the measurement of total temperature, and in particular, the current modeling of the substrate's variable thermal properties and curvature effects, is accurate and valid in a practical sense.

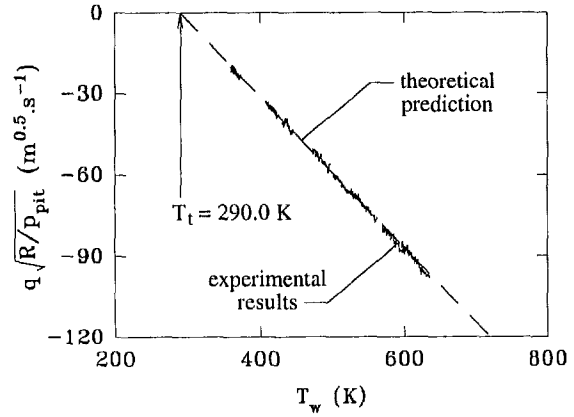

Fig. 9 Normalized heat flux versus probe temperature results from the Mach 5 nozzle flow experiments

A single Mach 5 nozzle flow run was also performed using helium as the test gas. Large differences between the measured convective heat transfer coefficients for the nitrogen and helium test gases were observed, and these differences were accurately predicted by the theoretical results. Therefore, the Mach 5 nozzle flow experiments also demonstrated that, in cases where Eq. (2) is applicable, the total temperature probe can be used to define the composition of a binary gas mixture (provided the two gases which form the mixture are sufficiently dissimilar).

Hypersonic Gun Tunnel. Having established the reliability of the total temperature device under well-defined flow conditions, the probe was then applied to the measurement of total temperature in the University of Oxford gun tunnel facility. In the past, shielded thermocouple devices (East and Perry, 1966) have been used to measure gun tunnel total temperatures. However, such probes generally have relatively poor frequency response characteristics. Probe measurements of gun tunnel total temperature have also been obtained using stagnation point heat transfer methods, as discussed previously (Edney, 1969). However, in general, Edney was only concerned with the time-averaged results and thus did not utilize the high frequency response characteristics of such devices.

For the present experiments, the University of Oxford gun tunnel was operated using the Mach 7 nozzle with an air driver (having an initial pressure of 4.9 MPa) and nitrogen in the barrel (at an initial pressures of 162 kPa). The stagnation pressure of the flow was measured with a piezoelectric transducer located 153 mm upstream from the end of the barrel, Fig. 10. The Mach 7 nozzle was contoured with an exit diameter of 211 mm and a throat diameter of 19.1 mm. The barrel was 9.14 m long with an internal diameter of 96 mm. Further details of the University of Oxford gun tunnel facility have been reported by Cain (1991). For the present experiments, the "hot" heat flux probe was located 10.3 mm above the nozzle centerline, the "cold" heat flux probe was located on the centerline, and the pitot probe was 8.2 mm below the centerline during the gun tunnel runs. All of the probes were 148 mm downstream of the Mach 7 nozzle exit plane.

Five nominally identical gun tunnel runs were performed, each with different probe operating temperatures. The measured stagnation pressures for each of the five runs were within approximately ±1 percent of the averaged result which is presented in Fig. 11(*a*). The repeatability of the gun tunnel and, in particular, the ability to generate consistent total temperatures were confirmed by measurements of the flow duration. (The flow duration is the time that it takes the test gas to drain from the barrel; this parameter is sensitive to the stagnation temperature generated by the gun tunnel.) An average flow duration of 71.5 ms ± 0.7 percent was indicated by the nozzle exit pitot pressure measurements for the five runs.

The temperatures (in K) of the "hot" and "cold" probes near the start of each of the gun tunnel runs were (T_1, T_2) = (726, 405); (608, 372); (522, 349); (445, 335); and (626, 379). Heat flux results were again inferred from the measured temperatures using the finite difference heat transfer routine discussed previously (Buttsworth, 1996). By calculating an instantaneous linear regression for the heat flux versus temperature data at each sample point, the measured total temperature history in Fig. 11(*b*) was obtained from the value of the temperature axis intercept. In Fig. 11(*b*), the theoretical predictions of total temperature were obtained from the stagnation pressure history (Fig. 11(*a*)) assuming that the entropy rise within the test gas was generated by 3 shock waves that generated the pressure levels (1, 2, and 3) indicated in Fig. 11(*a*). The lower theoretical prediction in Fig. 11(*b*) is again based on the mea-

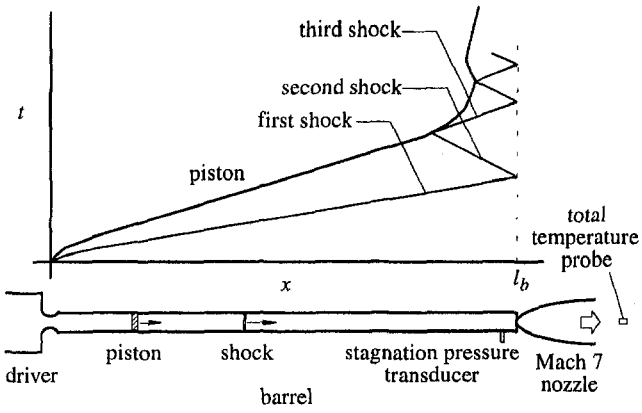

Fig. 10 Schematic diagram of the gun tunnel and sketch of the *x-t* diagram for the compression process

sured stagnation pressure history, but also includes a model for the boundary layer cooling effects (which is introduced below).

Edney (1967) utilized the turbulent boundary layer correlation of Hartunian et al. (1960) to obtain an expression for the average temperature drop due to boundary layer cooling in a gun tunnel. A more general expression, giving the spatial distribution of the temperature loss within the barrel is (referring to Fig. 10)

$$\Delta T_t = 5c_1(T_r - T_w)\,\mathrm{Re}^{-1/5}\,\frac{u_p}{u_{s1}}\left(\frac{u_{s1}}{u_{s1}-u_p}\right)^{-1/5}\left(\frac{l_{be}-x}{d}\right)^{4/5}, \tag{17}$$

where $c_1 = 3.7 \times 10^{-2}$ (from Hartunian et al., 1960)

$$T_r = T_2 + \frac{1}{2}\frac{ru_2^2}{c_p}$$

$$r = \mathrm{Pr}^{0.39-0.023u_{s1}/(u_{s1}-u_2)}$$

$$\mathrm{Re} = \frac{\rho_2 u_p d}{\mu_2}$$

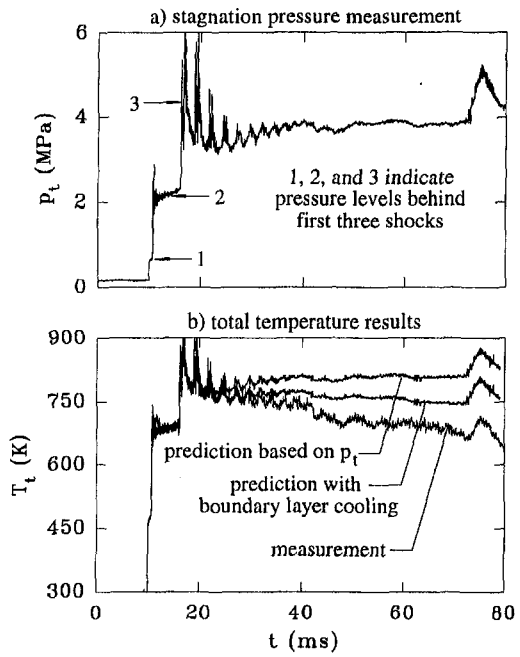

Fig. 11 Results from the gun tunnel experiments

$$l_{be} = \frac{l_b(u_{s1}-u_{s2}) - x(u_{s1}-u_p)}{u_p + u_{s2}}$$

In the derivation of Eq. (17), it was assumed that the boundary layer cooling continues until the reflected shock stagnates the test gas, in contrast to the Edney result which assumes that the cooling process continues only until the first shock reaches the end of the barrel.

Figure 11(*b*) indicates that the measured gun tunnel total temperature is in good agreement with inviscid predictions at the start of the run, but decays more rapidly throughout the run than is predicted by the simple turbulent boundary layer cooling model. The additional cooling of the test gas may arise due to shock wave-boundary layer interactions and the formation of vortices near the piston and at the end of the barrel (since such effects are not incorporated in the simple cooling model). Therefore, the apparent under-prediction of the test gas cooling within the barrel appears reasonable. The results in Fig. 11(*b*) indicate that the unsteady total temperature fluctuations near the start of the run (between approximately 15 and 30 ms on the scale in Fig. 11) are accurately detected with the total temperature probe.

Compressible Turbulent Jet. As a further demonstration of the present total temperature measuring device, experiments were also performed in a compressible turbulent jet. The jet was formed by injecting nitrogen (with a total temperature approximately equal to the room temperature) from a contoured Mach 4 nozzle (exit diameter of 30.5 mm and throat diameter of 9.5 mm) into low pressure quiescent air, as illustrated in Fig. 12. The background air pressure was approximately 1 kPa and the static pressure of the injected nitrogen was chosen to match this value. A Ludwieg tube (length 25 m and bore 25.4 mm) fitted with a fast-acting valve, generated a constant injection pressure gas supply for approximately 100 ms (Morris, 1995). During this steady flow period, the total temperature probe traversed the centerline of the jet at a location 150 mm downstream of the nozzle exit plane. During the mixing region traverse, the total temperature probe was moving at approximately 3 $\mathrm{m \cdot s^{-1}}$, and the maximum surface temperature change experienced by the heat flux probes was 25 K. The average temperature of the "hot" and "cold" probes were 662 and 416 K, respectively, during the mixing region traverse.

In Fig. 13(*a*) measurements from the "hot" and "cold" heat flux probes are presented. This data was obtained directly from a heat transfer analogue unit (Oldfield et al., 1982), and was sampled at 100 kHz. An analytical curvature correction (Buttsworth and Jones, 1996) was applied to the heat flux data and it was assumed that the thermal properties of the "hot" and "cold" probes remained equal to their pretraverse values. The constant thermal properties assumption does not significantly compromise the accuracy of the present data due to the relatively small surface temperature changes experienced in the current experiment.

By separating the quantities that appear in Eq. (1) into their mean and fluctuating components (e.g., $q = \bar{q} + q'$), and assuming that $\overline{h' \cdot T_t'} \ll \bar{h} \cdot \bar{T}_t$, $|T_w'| \ll |T_t'|$, and that second order terms such as $h' \cdot T_t'$ can be neglected relative to terms such as $h' \cdot \bar{T}_t$ and $\bar{h} \cdot T_t'$, the fluctuations in the heat transfer rate can be written as

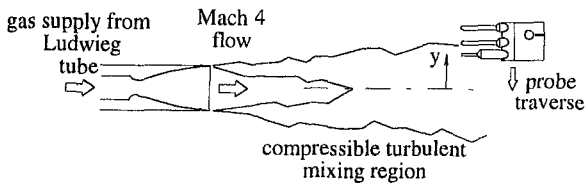

Fig. 12 Arrangement for the compressible turbulent jet experiment

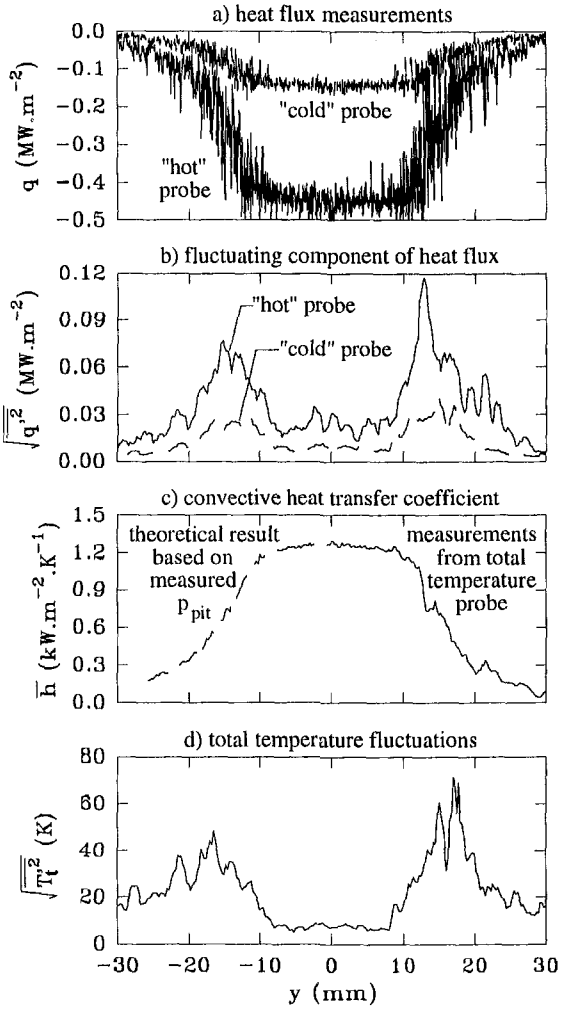

Fig. 13 Results from the compressible turbulent jet experiment

$$q' = \bar{h}T_t' + h'(\bar{T}_t - \bar{T}_w). \tag{18}$$

By squaring Eq. (18) and taking time averages, the following expression is obtained

$$\overline{q'^2} = \overline{T_t'^2}\bar{h}^2 + \overline{h'T_t'}\bar{q} + \overline{h'^2}\bar{q}^2/\bar{h}^2. \tag{19}$$

Values of $\sqrt{\overline{q'^2}}$ for the "hot" and "cold" probes have been plotted in Fig. 13(b). To obtain these results, an averaging window of 40 data points was applied to the data in Fig. 13(a) to determine $\bar{q}$. The value of $q'^2 = (q - \bar{q})^2$ was then determined for each data sample, and the averaging window of 40 data points was again applied to determine $\overline{q'^2}$.

Values of $\bar{h}$ obtained using Eq. (5) are given in the $y > 0$ half of Fig. 13(c). In the $y < 0$ portion of Fig. 13(c), theoretical values of $\bar{h}$ determined from Eq. (2) and the measured pitot pressure have been plotted. (It should be noted that Eq. 2 can be rearranged so that $\bar{h}$ is expressed simply as a function of the pitot pressure for a given flow static pressure and composition.) A high degree of symmetry may be observed in the results presented in Fig. 13(c). The observed agreement between the experimental and theoretical results in Fig. 13(c) indicates that, in the present experiment, the presence of turbulent fluctuations has not significantly increased the convective heat transfer coefficient.

It is known (Dullenkopf and Mayle, 1994) that laminar stagnation point boundary layers are sensitive to free stream turbulent fluctuations only within a relatively narrow band of frequencies. For lower frequencies, the boundary layer responds to the changing flow conditions in a quasi-steady manner, and for higher frequencies, the effects are damped by the viscosity. From stability theory it can be estimated that the maximum effect occurs at a frequency of approximately 0.03 u_∞/δ, or an eddy length scale of around 16δ (Dullenkopf and Mayle). For the present flow conditions, the thickness of the stagnation point boundary layer is estimated as $\delta \approx 35$ μm (White, 1991, p. 157). Based on incompressible free jet results it appears that the length scale of the turbulent fluctuations might reasonably be estimated as 10 percent of the mixing region half width (Wilcox, 1993, p. 42) that, for the present case, equates to a length of about 3 mm. As this length scale is around 5 times larger than the maximum boundary layer sensitivity length scale ($\approx$16δ, or 0.56 mm in the present case), it may be concluded that the majority of the turbulent fluctuations have only a quasi-steady effect on the convective heat transfer coefficient (Dullenkopf and Mayle, 1994). That is, the time-averaged heat transport is likely to remain unaffected by the fluctuations. Thus, the observed agreement between the nonturbulent theoretical prediction and the experimental results in Fig. 13(c) is indeed plausible.

From the probe measurements, it has been possible to determine the terms $\bar{q}$, $\overline{q'^2}$, and $\bar{h}$ in Eq. (19) for two probe operating temperatures. Thus, two equations are available, but there remain three unknowns ($\overline{T_t'^2}$, $\overline{h'T_t'}$, and $\overline{h'^2}$). To precisely determine the values of these remaining quantities, additional data using a probe operating at a temperature different to either the "hot" or the "cold" probe is therefore necessary. However, it is possible to assume that, when the mean heat flux is very low ($\bar{q} \to 0$ in Eq. 19), the total temperature fluctuations are given by,

$$\overline{T_t'^2} = \overline{q'^2}/\bar{h}^2. \tag{20}$$

Results based on Eq. (20) for the "cold" probe are presented in Fig. 13(d). It appears that large fluctuation in total temperature occur within the present compressible jet, even though the total temperature of the jet at the exit of the Mach 4 nozzle is close to that of the ambient surroundings. Probe measurements with a finite, nonzero value of $\bar{q}$ were used to obtain the results in Fig. 13(d). The validity of these results was examined by assuming that a perfect correlation existed between the total temperature fluctuations and the convective heat transfer coefficient fluctuations. Thus, the number of unknowns in Eq. (19) was reduced from three ($\overline{T_t'^2}$, $\overline{h'T_t'}$, and $\overline{h'^2}$) to two ($\overline{T_t'^2}$ and $\overline{h'^2}$), allowing a solution for $\overline{T_t'^2}$ from the "hot" and "cold" probe measurements. From this analysis, it was concluded that the estimates of the total temperature fluctuations presented in Fig. 13(d) may be in error by up to 10 percent. In future turbulent fluctuation measurements, additional probe operating temperatures could be utilized so that both $\overline{T_t'^2}$, and $\overline{h'^2}$ can be accurately determined without making unnecessarily restrictive assumptions.

Conclusions

The current experiments have demonstrated the viability of using transient convective heat flux measurements at differing probe temperatures to determine the total temperature of the flow. The present device provides a measurement of the flow total temperature that is independent of other flow parameters such as the Mach number, Reynolds number, pressure, and flow composition. The total temperature probe, therefore, has considerable versatility—for example, it may be used to measure the total temperature in a flow of arbitrary composition. No calibration is necessary, apart from the mandatory temperature-resistance calibration which should ideally be performed over the entire operating temperature range of the probe.

Uncertainty estimates suggest that it is possible to measure the total temperature with the current device to within approxi-

mately ±3 K for $300 < T_t < 800$ K, depending somewhat on the chosen probe operating temperatures. The accuracy of the device (and thus the validity of the thermal modeling and the analysis of the measured temperature histories) was demonstrated at low total temperatures using a small Mach 5 blowdown rig and at high total temperatures using the University of Oxford gun tunnel facility.

Because the total temperature device is based on the measurement of transient heat flux using platinum thin film gauges, the probe has a high frequency response that allows the measurement of fluctuating and rapidly varying total temperatures. The high frequency response of the probe was demonstrated through the accurate measurement of the total temperature during the unsteady shock compression processes in the University of Oxford gun tunnel facility. As a further demonstration of the potential for high frequency measurements, the probe was also used to obtain fluctuation measurements in a Mach 4 turbulent jet. Based on the thermal inertia of the platinum films, the bandwidth of the present measurements is restricted to approximately 50 kHz. However, in future experiments it may be possible to account for the thermal inertia of the platinum, in which case the upper frequency limit of the device would be in the MHz range.

To improve the versatility of the total temperature device, a new configuration in which two films are mounted on a single quartz probe is being investigated. It is anticipated that the difference in the surface temperature of the two films will be generated by pulsing a relatively large current through one of the films.

Acknowledgments

Financial support for the work described in this paper was provided by DRA Farnborough.

References

Alday, J., Osborne, D. J., Morris, M. B., Ng, W., and Gertz, J., 1993, "Flow Randomness and Tip Losses in Transonic Rotors," ASME Paper 93-GT-189.

Anderson, J. D., 1989, *Hypersonic and High Temperature Gas Dynamics,* McGraw-Hill, New York.

Bogdan, L., 1963, "Thermal and Electrical Properties of Thin-Film Resistance Gauges Used for Heat Transfer Measurements," *AIAA J.,* Vol. 1, No. 9, pp. 2172–2173.

Bremhorst, K., and Graham, L. J. W., 1990, "A Fully Compensated Hot/Cold Wire Anemometer System for Unsteady Flow Velocity and Temperature Measurements," *Meas. Sci. Technol.,* Vol. 1, pp. 425–430.

Buttsworth, D. R., 1996, A Finite Difference Routine for the Solution of Transient One-Dimensional Heat Conduction Problems with Varying Thermal Property and Curvature Effects, report, Department of Engineering Science, University of Oxford, United Kingdom.

Buttsworth, D. R., and Jones, T. V., 1996, "Radial Conduction Effects in Transient Heat Transfer Experiments," *Aeronautical Journal,* Vol. 101, No. 1005, pp. 209–212.

Cain, T. M., 1991, "An Experimental Study of Underexpanded Jets," D. Phil. thesis, Dept. Eng. Sci., University of Oxford, United Kingdom.

Dullenkopf, K., and Mayle, R. E., "An Account of Free-Stream-Turbulence Length Scale on Laminar Heat Transfer," ASME Paper 94-GT-174.

East, R. A., and Perry, J. H., 1966, "A Short Time Response Stagnation Temperature Probe," Report No. 264, Department of Aeronautics and Astronautics, University of Southampton, United Kingdom.

Edney, B. E., 1967, "Temperature Measurements in a Hypersonic Gun Tunnel Using Heat-Transfer Methods," *J. Fluid Mech.,* Vol. 27, pp. 503–512.

Eklund, T. I., and Dobbins, R. A., 1977, "Application of the Hot Wire Anemometer to Temperature Measurement in Transient Gas Flows," *Int. J. Heat Mass Transfer,* Vol. 20, pp. 1051–1058.

Fabris, G., 1978, "Probe and Method for Simultaneous Measurement of True Instantaneous Temperature and Three Velocity Components in Turbulent Flow," *Rev. Sci. Instrum.,* Vol. 49, No. 5, pp. 654–664.

Forney, L. J., Meeks, E. L., Ma, J., and Fralick, G. C., 1993, "Measurement of Frequency Response in Short Thermocouple Wires," *Rev. Sci. Instrum.,* Vol. 64, pp. 1280–1286.

Hartunian, R. A., Russo, A. L., and Marrone, P. V., 1960, "Boundary–Layer Transition and Heat Transfer in Shock Tubes," *J. Aerospace Sci.,* Vol. 27, pp. 587–594.

Holman, J. P., 1984, *Experimental Methods for Engineers,* 4th ed., McGraw-Hill, New York.

Kemp, N. H., Rose, P. H., and Detra, R. W., 1959, "Laminar Heat Transfer Around Blunt Bodies in Dissociated Air," *J. Aero/Space Sci.,* Vol. 26, pp. 421–430.

Kidd, S. R., Barton, J. S., Meredith, P., Jones, J. D. C., Cherrett, M. A., and Chana, K. S., 1994, "A Fibre Optic Probe for Gas Total Temperature Measurement in Turbomachinery," ASME Paper 94-GT-34.

Lomas, C. G., 1986, *Fundamental of Hot Wire Anemometry,* Cambridge University Press, London, United Kingdom.

Miller, C. G., 1981, "Comparison of Thin-Film Resistance Gages with Thin-Skin Transient Calorimeter Gages in Conventional Hypersonic Wind Tunnels," NASA TM-83197.

Morris, N. A., 1995, "An Experimental and Computational Study of Moderately Under-Expanded Rocket Exhaust Plumes in a Co-Flowing Hypersonic Stream," D. Phil. thesis, Dept. Eng. Sci., University of Oxford, United Kingdom.

Ng, W. F., and Epstein, A. H., 1983, "High-Frequency Temperature and Pressure Probe for Unsteady Compressible Flows," *Rev. Sci. Instrum.,* Vol. 54, No. 12, pp. 1678–1683.

Oldfield, M. L. G., Burd, H. J., and Doe, N. G., 1982, "Design of Wide-Bandwidth Analogue Circuits for Heat Transfer Instrumentation in Transient Wind Tunnels," *16th Symp. of International Centre for Heat and Mass Transfer,* Hemisphere Publishing, Bristol, PA, pp. 233–257.

Schultz, D. L., and Jones, T. V., 1973, "Heat–Transfer Measurements in Short–Duration Hypersonic Facilities," Agardograph No. 165.

Timnat, Y. M., 1989, "Diagnostic Techniques for Propulsion Systems," *Prog. Aerospace Sci.,* Vol. 26, pp. 153–168.

Toulokian, Y. S., ed., 1970, *Thermophysical Properties of Matter,* The TPRC Data Series: Vol. 2, *Thermal Conductivity Nonmetallic Solids;* Vol. 5, *Specific Heat Nonmetallic Solids,* Ifi/Plenum, New York.

White, F. M., 1991, *Viscous Fluid Flow,* 2nd. ed., McGraw-Hill, New York.

Wilcox, D. C., *Turbulence Modeling for CFD,* DCW Industries, La Canada, CA.

Evaluation of CH_4/NO_x Reduced Mechanisms Used for Modeling Lean Premixed Turbulent Combustion of Natural Gas

H. P. Mallampalli

T. H. Fletcher

Chemical Engineering Department,
Brigham Young University,
Provo, UT 84602-4100

J. Y. Chen

Mechanical Engineering Department,
University of California,
Berkeley, CA 94720

This study has identified useful reduced kinetic schemes that can be used in comprehensive multidimensional gas-turbine combustor models. Reduced mechanisms lessen computational cost and possess the capability to accurately predict the overall flame structure, including gas temperatures and key intermediate species such as CH_4, CO, and NO_x. In this study, four new global mechanisms with five, six, seven, and nine steps based on the full GRI 2.11 mechanism, were developed and evaluated for their potential to model natural gas chemistry (including NO_x chemistry) in gas turbine combustors. These new reduced mechanisms were optimized to model the high pressure and fuel-lean conditions found in gas turbines operating in the lean premixed mode. Based on perfectly stirred reactor (PSR) and premixed code calculations, the five-step reduced mechanism was identified as a promising model that can be used in a multidimensional gas-turbine code for modeling lean-premixed, high-pressure turbulent combustion of natural gas. Predictions of temperature, CO, CH_4, and NO from the five- to nine-step reduced mechanisms agree within 5 percent of the predictions from the full kinetic model for $1 <$ pressure (atm) < 30, and $0.6 < \phi < 1.0$. If computational costs due to additional global steps are not severe, the newly developed nine step global mechanism, which is a little more accurate and provided the least convergence problems, can be used. Future experimental research in gas turbine combustion will provide more accurate data, which will allow the formulation of better full and reduced mechanisms. Also, improvement in computational approaches and capabilities will allow the use of reduced mechanisms with larger global steps, perhaps full mechanisms.

Introduction

Lean premixed combustion (LPC) of natural gas is a promising method to achieve low emissions from advanced gas turbines. However, no comprehensive computer models are presently available to model LPC of natural gas that include the full set of chemical mechanisms along with turbulent interactions (Correa, 1992b). Methods have been presented in the literature that include complex chemistry in turbulence models, but these models require enormous computing time and are limited to simpler chemical systems such as H_2 combustion (Borghi, 1988). Therefore, simplified kinetic schemes with four to five global reaction steps are being developed for use in turbulent combustion (Maas and Pope, 1992a; Maas and Pope, 1992b). Many reduced mechanisms based on full mechanisms have been developed and published in literature (e.g., Bilger et al., 1990; Chen and Dibble, 1991; Glarborg et al., 1992b; Treviño and Mendéz, 1992; Wang and Frenklach, 1991; Polifke et al., 1995). However, relatively few reduced mechanisms have been developed specifically for lean premixed conditions, and, hence, cannot accurately predict CO and NO_x concentrations from modern gas turbine combustors.

In addition to reduced mechanisms, which are generally based on (*a*) subsets of elementary reaction steps and (*b*) steady-state approximations for intermediate species, global mechanisms have been developed to predict overall species in limited ranges of temperature, equivalence ratio, and pressure. Such global mechanisms do not attempt to use elementary step reactions, but can be very useful when computational constraints do not permit more sophisticated mechanisms. Global mechanisms pertaining to combustion of methane are reviewed in a recent paper by Nicol et al. (1997, 1998). Nicol and coworkers note that previously published global mechanisms are not pertinent to lean premixed combustion, and do not include NO formation. The global model presented by Nicol and coworkers uses three global steps for CH_4 oxidation and two steps for NO formation, and is good at atmospheric pressure for $0.45 < \phi < 0.70$. A proprietary model for combustion at elevated pressures is also mentioned by Nicol and coworkers.

Full mechanisms are usually validated using experimental measurements. These full mechanisms are then used as benchmarks to evaluate reduced mechanisms. Alternatively, reduced mechanisms can be compared to actual data, when the data are obtained in systems that can be easily modeled. However, lack of pertinent experimental data in lean premixed systems at high pressure warrants the use of full mechanisms for evaluation of reduced mechanisms. For example, Nicol et al. (1997, 1998) report agreement between their global mechanism and the full Miller-Bowman mechanism (Miller and Bowman, 1989) that is generally within 5 percent (and a maximum of 20 percent difference).

Reduced and global mechanisms have been applied in comprehensive computational fluid dynamics models with mixed success, since turbulence and turbulence–chemistry models are limited. For example, the global mechanism of Nicol et al. (1997, 1998) was applied in a commercial CFD code using the eddy breakup model for turbulence chemistry. More sophisticated chemistry models will obviously require advanced turbulence–chemistry models to describe important details of the combustion process in gas turbine combustors.

Contributed by the Gas Turbine Division. Manuscript received by the ASME Headquarters October 3, 1997. Associate Technical Editor: J. E. Peters.

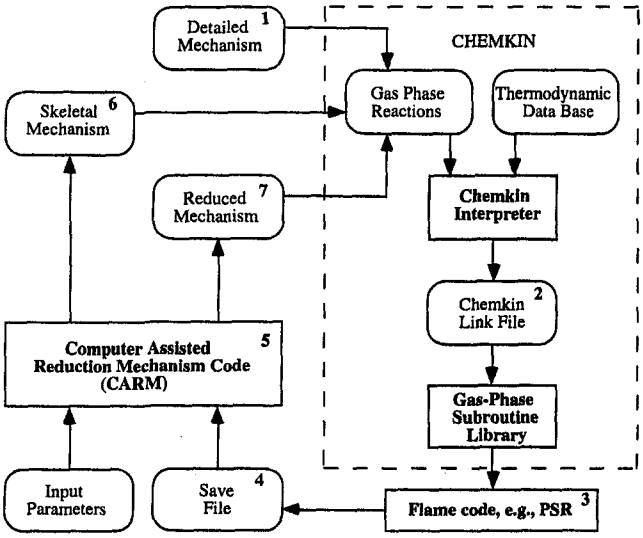

Fig. 1 Flow diagram illustrating the relationship between the CARM code, the Flame code, and CHEMKIN preprocessor package (Chang, 1995)

Pollutant Formation in Lean Premixed Combustion (LPC)

NO_x, CO, and unburned hydrocarbons (UHC) are the three common pollutants in lean premixed combustion (LPC) of natural gas. NO_x emissions decrease at lean premixed conditions because of low peak-flame temperatures; such conditions may also cause flame instabilities, which result in high CO formation. CO and UHC emissions are usually caused by incomplete or inefficient combustion, where the oxidation reaction of CO to CO_2 is quenched (Anand and Gouldin, 1985). This quenching may occur at (*a*) low gas temperatures found in lean premixed conditions, (*b*) boundary layers adjacent to combustor walls, and (*c*) sometimes in the dilution zone, where air is introduced for cooling (Correa, 1992a). Also, CO emissions may increase due to the CH_x species present in the flame; the CH_x species react with the oxidizing radicals more rapidly than CO, and cause the CO to oxidize at later times in the flame (Correa, 1992a). Thus, increased emissions of CO at very lean conditions, due to low temperatures or flame instabilities, is one of the factors that limits the ultimate NO_x reduction attainable by lean premixed combustion.

In lean premixed laminar flames at high pressure, NO_x is formed predominantly by the nitrous oxide mechanism with little contribution from prompt NO_x or thermal NO_x (Correa, 1992b; Polifke et al., 1995; Nicol et al., 1993; Steele et al., 1994). Jet-stirred reactor data suggest that the contribution to total NO_x formation from the prompt NO_x mechanism increases at atmospheric pressure, and cannot be neglected (Polifke et al., 1995). Calculations in a perfectly stirred reactor (PSR) code (Glarborg et al., 1992a) and comparisons to PSR data can be useful in evaluating the characteristics of NO_x formation in lean premixed turbulent flames (Correa, 1992b). The PSR modeling seems to indicate that the nitrous oxide (N_2O) mechanism significantly contributes to the total NO_x in premixed turbulent flames (Correa, 1992a; Davis and Washam, 1989). PSR calculations do not account for turbulence–chemistry interactions, but allow for a perfectly mixed condition, where the rate of the chemical process is controlled by the chemical kinetic rates and not by the mixing process.

Table 1 Five-step global mechanism

Reaction Number	Global Reaction
R1	$3H_2 + O_2 + CO_2 = 3H_2O + CO$
R2	$H_2 + 2OH = 2\,H_2O$
R3	$3\,H_2 + CO = H_2O + CH_4$
R4	$H_2 + CO_2 = H_2O + CO$
R5	$3\,H_2 + CO_2 + 2NO = 3\,H_2O + CO + N_2$

Table 2 Nine-step global mechanism

Reaction Number	Global Reaction
R1	$H_2 + O = H + OH$
R2	$4H + O_2 = H_2 + 2OH$
R3	$H + O = OH$
R4	$H_2 + 2O + CH_3 = 4H + OH + CO$
R5	$O + CH_4 = OH + CH_3$
R6	$H + OH + CO = H_2 + CO_2$
R7	$H + OH = H_2O$
R8	$5H + 2NO = 2\,H_2 + O + OH + N_2$
R9	$O + N_2O = O_2 + N_2$

Table 3 Global rates of the five-step mechanism

$R1 = +\omega_4 - \omega_{33} - \omega_{35} - \omega_{36} + \omega_{38} + \omega_{45} + 2\,\omega_{46} - 2\,\omega_{85} + \omega_{87} + \omega_{122} + \omega_{125} + \omega_{135} + \omega_{144} + \omega_{145} + \omega_{155} - \omega_{168} - \omega_{169} - \omega_{170} + \omega_{171} + \omega_{173} + \omega_{176} + \omega_{179} - \omega_{181} + \omega_{186} - \omega_{187} + \omega_{189} - \omega_{192} - \omega_{197} - \omega_{201} - \omega_{206} - \omega_{212} + \omega_{213} + \omega_{214} + \omega_{215} + \omega_{220} + \omega_{259}$
$R2 = +\omega_7 + \omega_{11} + \omega_{15} + \omega_{33} + \omega_{35} + \omega_{36} - \omega_{38} + \omega_{43} - \omega_{46} + \omega_{53} + \omega_{58} + \omega_{61} + \omega_{62} + \omega_{66} + \omega_{71} + 2\,\omega_{85} + \omega_{93} + \omega_{98} + \omega_{101} - \omega_{122} - \omega_{125} - \omega_{126} - \omega_{127} + \omega_{130} + \omega_{137} + \omega_{138} + \omega_{140} - \omega_{144} - 2\,\omega_{155} + \omega_{158} - \omega_{160} - \omega_{166} - \omega_{167} + \omega_{169} + \omega_{170} - \omega_{173} - \omega_{176} + \omega_{180} - \omega_{183} - 2\,\omega_{185} + 2\,\omega_{187} - \omega_{189} + \omega_{190} + \omega_{192} + \omega_{197} + \omega_{199} + \omega_{201} - \omega_{204} - \omega_{205} + \omega_{212} - \omega_{220} + \omega_{222} - \omega_{227} - \omega_{240} - \omega_{246} - \omega_{247} - \omega_{248} - \omega_{256} - \omega_{259}$
$R3 = +\omega_{10} - \omega_{11} - \omega_{15} - \omega_{25} + \omega_{52} - \omega_{53} - \omega_{56} - \omega_{57} - \omega_{58} - \omega_{75} + \omega_{83} + \omega_{92} - \omega_{98} - \omega_{101} - \omega_{112} + \omega_{127} - \omega_{132} + \omega_{138} + \omega_{152} + \omega_{158} + \omega_{159} + \omega_{160} + \omega_{169} + \omega_{170} + \omega_{173}$
$R4 = +\omega_{23} + \omega_{28} - \omega_{38} - \omega_{46} - \omega_{56} - \omega_{57} + \omega_{61} + \omega_{66} - \omega_{75} + \omega_{81} + \omega_{85} - \omega_{95} - \omega_{97} - \omega_{99} - \omega_{112} - \omega_{122} - \omega_{125} + \omega_{132} - \omega_{133} - \omega_{135} - \omega_{137} - \omega_{140} + \omega_{142} + \omega_{146} + \omega_{148} + 2\,\omega_{153} - 2\,\omega_{155} + \omega_{169} + \omega_{170} + \omega_{180} - \omega_{183} - \omega_{185} + \omega_{187} - \omega_{189} + \omega_{190} + \omega_{192} + \omega_{197} + \omega_{199} + \omega_{201} - \omega_{220} + \omega_{222} + \omega_{224} - \omega_{240} - \omega_{246} - \omega_{247} - \omega_{248} - \omega_{249} - \omega_{250} - \omega_{251} - \omega_{255} - \omega_{256} - \omega_{259} - \omega_{262} - \omega_{268}$
$R5 = +\omega_{178} + \omega_{181} + \omega_{183} + \omega_{185} - \omega_{208} - \omega_{240}$

Objectives and Approach

The GRI 2.11 mechanism (Bowman et al., 1995) developed by the Gas Research Institute (GRI) is currently considered one of the best mechanisms that accurately describes CH_4/NO_x chemistry for natural gas combustion. The objective of this work was to find a reduced mechanism based on the GRI 2.11 mechanism that would describe lean premixed CH_4/air combustion systems. The full GRI 2.11 mechanism was reduced using a computer code that first eliminated unimportant species (for a desired condition) and then applied steady-state approximations for short-lived species (Chen, 1988). This resulted in five- to nine-step reduced mechanisms of CH_4 combustion coupled with NO_x chemistry. The GRI 2.11 mechanism was then used as a benchmark to test the global mechanisms using both a PSR code (Glarborg et al., 1995) and a premixed code (Kee et al., 1992a). Predictions of these global mechanisms were also compared with predictions of CH_4 chemistry obtained using

Table 4 Steady-state species for the five and nine-step mechanisms

5-Step Mechanism	9-Step Mechanism
C_2H, H_2CN, HCNN, C_2H3, C_2H_2, C, CH_2O, CH, CN, N, C_2H_6, NH, HCCO, NNH, CH_2OH, NH_2, HCCOH, $CH_2(S)$, NCO, C_2H_5, HOCN, C_2H_4, HNO, HCO, CH_2CO, NO_2, CH_3, CH_3OH, H_2O_2, HCNO, HO_2, HNCO, HCN, CH_2O, CH_3, N_2O, H, and O	C_2H, H_2CN, HCNN, C_2H3, C_2H_2, C, CH_2O, CH, CN, N, C_2H_6, NH, HCCO, NNH, CH_2OH, NH_2, HCCOH, $CH_2(S)$, NCO, C_2H_5, HOCN, C_2H_4, HNO, HCO, CH_2CO, NO_2, CH_3, CH_3OH, H_2O_2, HCNO, HO_2, HNCO, HCN, CH_2O, and CH_3

Table 5 PSR code test variables

Pressure (atm)	Equivalence Ratio (ϕ)	Inlet Temperature (K)	Residence Time (ms)
1	0.4	600	2
15	0.60	1200	5
30	0.85	1800	10
	1.00		

Table 6 Premixed code test matrix

Pressure (atm)	Equivalence Ratio (ϕ)
1	0.60
15	0.85
30	1.00

the four-step Seshadri–Peters reduced mechanism (Chen and Dibble, 1991) (for PSR cases), which appeared to be the best reduced mechanism for lean premixed natural gas combustion previously available in literature. The four-step Seshadri–Peters mechanism for CH_4 combustion is based on a 25-step skeletal mechanism developed by Smooke and Giovangigli (1991), and does not include NO_x chemistry.

The global rates of the five- and nine-step global mechanisms were derived from a skeletal mechanism based on the 276-step full GRI 2.11 mechanism (Bowman et al., 1995) using the computer-assisted reduction mechanism (CARM) code (Chen, 1988; Chang, 1995). CARM is an interactive program that runs in conjunction with CHEMKIN-II (Kee et al., 1992b) and flame codes such as the perfectly stirred reactor (PSR) code (Glarborg et al., 1992a) and the premixed code (Kee et al., 1992a). The PSR program is more commonly used due to its simplicity, and also because it provides solutions to flame problems more quickly. Figure 1 shows the schematic diagram that explains the interaction between the CARM code, CHEMKIN, and a flame code such as the PSR code.

As shown in Fig. 1, the detailed GRI mechanism (1) is first provided to the CHEMKIN interpreter. This produces a linking file (2) that is utilized by the PSR code (3) to solve the required problem. The solution from the PSR code is stored in a "save file" (4) which is read by the CARM program (5). The "save file" contains important information related to species concentrations, sensitivity coefficients, and other variables. Based on the relative importance of elementary reactions provided by the user, a skeletal mechanism (6) is generated for the given conditions by eliminating fast reactions which are usually not very important (Chang, 1995).

To obtain a suitable skeletal mechanism for the required range of applicability, the CARM code allows the comparison of predictions between the skeletal mechanism and the detailed mechanism. After a solution using the skeletal mechanism is obtained from the PSR code, the CARM code reads the results from the "save file," and then compares the results from the skeletal mechanism to the previously obtained solution from the detailed mechanism. When the error bounds between the skeletal and detailed schemes for the required range of applicability are within the specified limits (usually within 5 percent), the performance of the skeletal mechanism is accepted. Therefore, the CARM code eliminates unimportant elementary reactions and species for the specified range and conditions; however, the eliminated species and elementary reactions may be important for other operating conditions. If required, the intermediate step used in obtaining the skeletal mechanism can be avoided, and it is possible to develop a reduced mechanism for a wider range of applicability using the complete reaction scheme. However, this may result in extremely complicated algebraic expressions with associated convergence problems (Chang, 1995).

The next step in the development of a reduced mechanism involves the subsequent algebraic manipulation of the skeletal mechanism to the desired five to nine global reactions. This

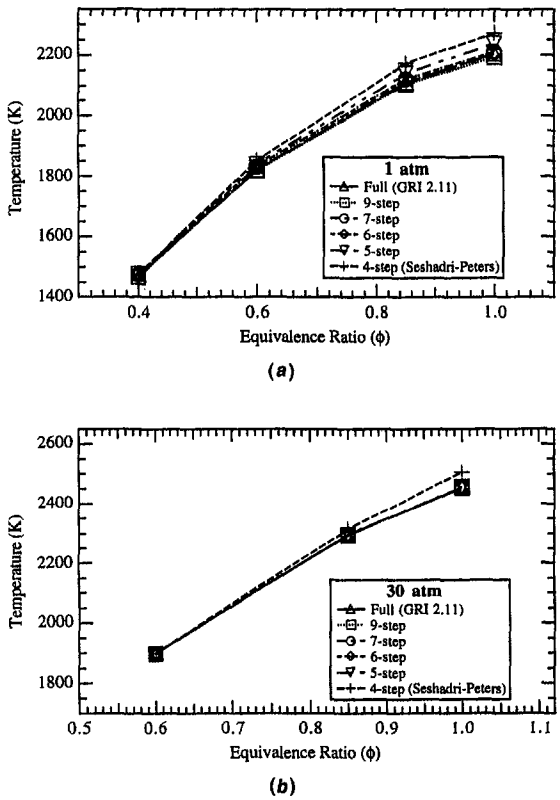

Fig. 2 PSR calculations of temperature as a function of equivalence ratio at 1 and 30 atm (T_{inlet} = 600 K; τ = 2 ms): (*a*) temperature versus equivalence ratio, 1 atm, T_{inlet} = 600 K, and τ = 2 ms; (*b*) temperature versus equivalence ratio, 30 atm, T_{inlet} = 600 K, and τ = 2 ms.

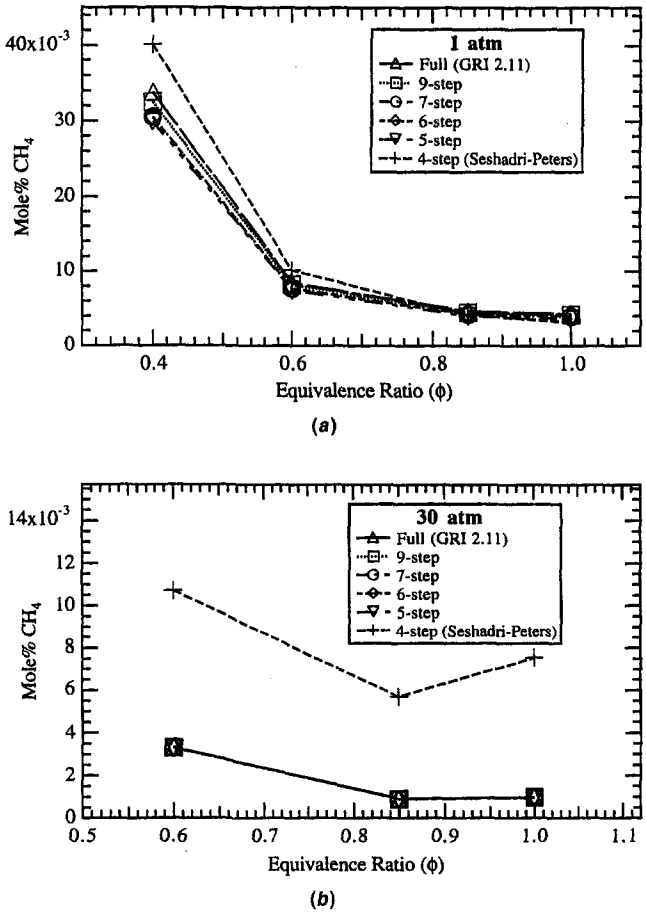

Fig. 3 PSR calculations of mole% CH_4 as a function of equivalence ratio at 1 and 30 atm (T_{inlet} = 600 K; τ = 2 ms): (*a*) Mole% CH_4 versus equivalence ratio, 1 atm, T_{inlet} = 600 K, and τ = 2 ms; (*b*) Mole% CH_4 versus equivalence ratio, 30 atm, T_{inlet} = 600 K, and τ = 2 ms.

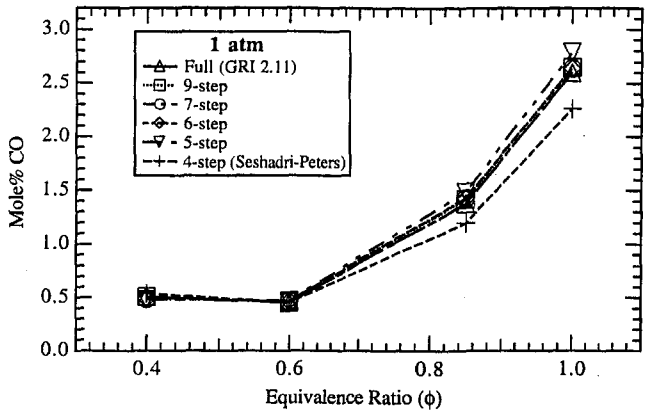

(a)

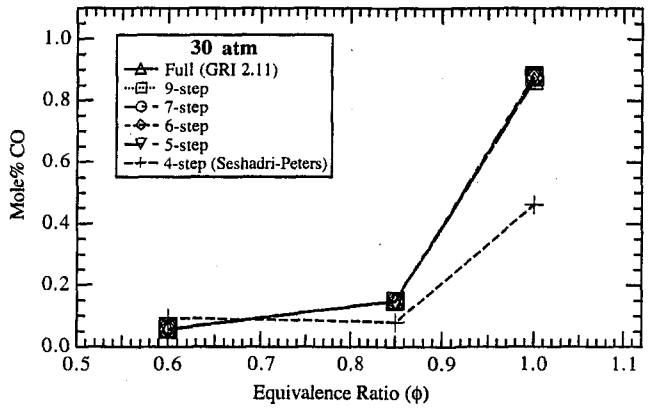

(b)

Fig. 4 PSR calculations of mole% CO as a function of equivalence ratio at 1 and 30 atm (T_{inlet} = 600 K; τ = 2 ms): (a) Mole% CO versus equivalence ratio, 1 atm, T_{inlet} = 600 K, and τ = 2 ms; (b) Mole% CO versus equivalence ratio, 30 atm, T_{inlet} = 600 K, and τ = 2 ms.

was done by first selecting the species that are used for the steady-state assumption. These species are usually intermediate species which have small concentration levels when compared to the initial reactants and final products. Secondly, a set of elementary reactions was selected which was used to eliminate the steady-state species and to formulate the reduced mechanism. The CARM program (Chang, 1995) performed these algebraic manipulations and utilized an iteration scheme to provide the final form of the reduced mechanism. The reduced mechanisms were obtained with relative ease, and required approximately 50 iterations for the lean flame.

Results and Discussion

Four new global mechanisms with five, six, seven, and nine steps were developed and optimized to agree with PSR calculations using the GRI 2.11 mechanism at 30 atm and equivalence ratios ranging from ϕ = 0.4 to 0.6. These newly developed global mechanisms contain both CH_4 chemistry (including C_2 chemistry) and NO_x chemistry that is present in lean premixed turbulent combustion of natural gas. Only a description of the five-step and nine-step global mechanisms is presented here; additional details are described by Mallampalli (1996).

Five and Nine-Step Global Mechanisms. Tables 1 and 2 show the global steps of the five- and nine-step reduced mechanisms. Here, thermal NO_x, prompt NO_x, and NO_x formed via the nitrous oxide pathway are all included through the steady-state approximations for intermediate species. The global rates of the above five- and nine-step reactions are functions of the rate constants and species present in the skeletal mechanism generated from the full GRI 2.11 mechanism. For example, the global rates for the five-step mechanism are shown in Table 3 where ω_i, is the reaction rate for the ith elemental reaction in the GRI 2.11 mechanism. These elementary steps include both the forward and backward rates. For both the five-step and nine-step global mechanisms, the net global rates (R_i) were calculated assuming that the species in Table 4 are in steady state. Due to length considerations, the steady-state expressions for the five- and nine-step mechanisms are found elsewhere (Mallampalli, 1996; Mallampalli et al., 1996). Similarly, the skeletal mechanism that contains the elementary reactions is also found elsewhere (Mallampalli, 1996). The mechanisms can be also obtained on the internet in complete form (http://www.et.byu.edu/~tom/Papers/Hemant-WSS96/WSS.html).

PSR Code Calculations. The four newly developed global mechanisms were evaluated according to the test matrix shown in Table 5; 108 PSR cases were performed using the full GRI 2.11 mechanism (Bowman et al., 1995), the Seshadri–Peters global mechanism (Chen and Dibble, 1991), and each of the four newly developed reduced mechanisms (648 total cases) in order to examine the effects of pressure, equivalence ratio, inlet temperature, and residence time. The one inlet temperature of

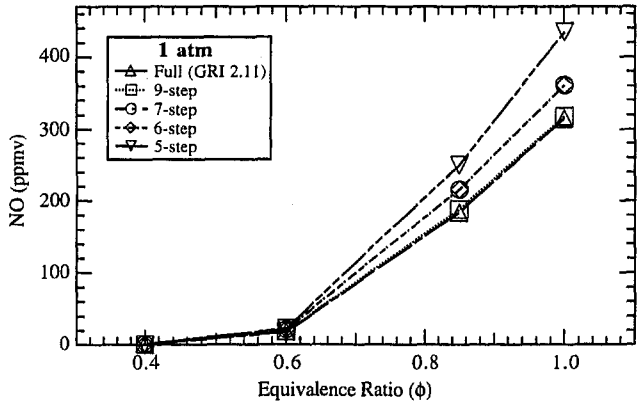

(a)

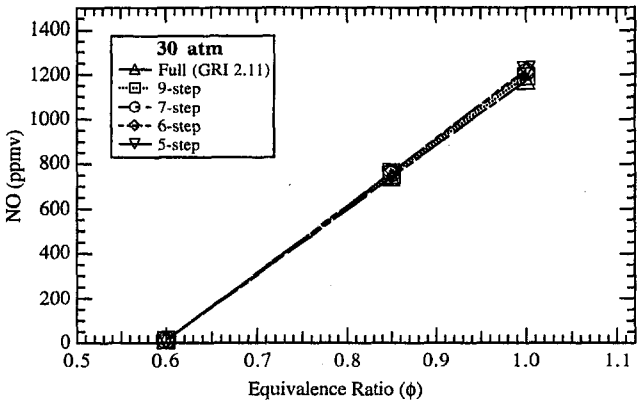

(b)

Fig. 5 PSR calculations of NO (ppmv) as a function of equivalence ratio at 1 and 30 atm (T_{inlet} = 600 K; τ = 2 ms): (a) NO (ppmv) versus equivalence ratio, 1 atm, T_{inlet} = 600 K, and τ = 2 ms; (b) NO (ppmv) versus equivalence ratio, 30 atm, T_{inlet} = 600 K, and τ = 2 ms.

1800 K shown in Table 6 is unrealistically high, but was used to allow testing of the mechanisms at extreme temperatures. The conditions for these calculations were selected to be non-equilibrium conditions in order to emphasize the importance of chemical kinetics. Neither the full GRI 2.11 mechanism nor the four newly developed reduced mechanisms converged to a solution for 3 test cases (i.e., at 30 atm, $\phi = 0.4$, $T_{inlet} = 600$ K and different residence times of 2 ms, 5 ms, and 10 ms), since the lean blow out limit was reached at these conditions.

Figures 2(*a*) and 2(*b*) show predictions of temperature in a PSR as a function of equivalence ratio for pressures of 1 and 30 atmospheres, respectively ($T_{inlet} = 600$ K, $\tau = 2$ ms). It is seen from Figs. 2(*a*) and 2(*b*) that the four newly developed reduced mechanisms yield excellent agreement with the full GRI 2.11 mechanism at both pressures (maximum relative error ~1.6 percent). The four-step Seshadri–Peters global mechanism predictions also show good agreement; the Seshadri–Peters mechanism deviates from the full mechanism by less than 50 K at high pressures and high equivalence ratios (maximum relative error ~3 percent).

Figures 3(*a*) and 3(*b*) show predictions of CH_4 concentrations in a PSR for pressures of 1 and 30 atm ($T_{inlet} = 600$ K, $\tau = 2$ ms). It is again seen from Fig. 3(*a*) that the four newly developed global mechanisms give very good predictions for mole% CH_4 in fuel-lean mixtures and atmospheric pressures (maximum relative error ~15 percent). Comparatively, at 1 atm pressure, the four-step Seshadri–Peters global mechanism predictions agree within 26 percent (on a relative basis). At 30 atm, Fig. 3(*b*) shows that the five to nine-step mechanisms give identical predictions for all conditions (maximum relative error 3 percent), but the Seshadri–Peters mechanism does not show similar agreement (maximum relative error ~650 percent). At high pressures, C_2 chemistry appears to be vital for predicting flame chemistry, and the newly developed reduced mechanisms include C_2 chemistry, whereas the Seshadri–Peters mechanism does not.

Figures 4(*a*) and 4(*b*) show predictions of mole% CO in a PSR for pressures of 1 and 30 atm ($T_{inlet} = 600$ K, $\tau = 2$ ms). Figure 4(*a*) shows that at atmospheric pressure, the full GRI 2.11 mechanism and the four newly developed reduced mechanisms are in good agreement (maximum relative error ~7 percent), while slightly less agreement was achieved using the four-step Seshadri–Peters global mechanism (maximum relative error ~12 percent). Figure 4(*b*) shows that at 30 atm, the newly developed reduced mechanisms perform very well at all equivalence ratios (maximum relative error ~2 percent), but the Seshadri–Peters mechanism significantly differs from the full GRI 2.11 mechanism predictions (relative maximum error 65 percent). As expected, the lack of C_2 chemistry causes more pronounced deviations between the Seshadri–Peters mechanism and the full GRI 2.11 mechanism at high pressures. Figure 4(*a*) shows that CO emissions, relative to $\phi = 0.6$, increase dramatically in rich mixtures and slightly leaner mixtures. At near stoichiometric conditions, CO emissions are higher because the higher gas temperatures result in the dissociation of CO_2 to CO (Anand and Gouldin, 1985). At very lean mixtures, CO does not completely oxidize to CO_2 because the low gas temperatures at these conditions quenches the oxidation reaction of CO (Anand and Gouldin, 1985). The Seshadri–Peters mechanism also exhibits this quenching effect at high pressures and low equivalence ratios, which results in slightly higher predictions of CO concentrations at $\phi = 0.4$ than at $\phi = 0.6$.

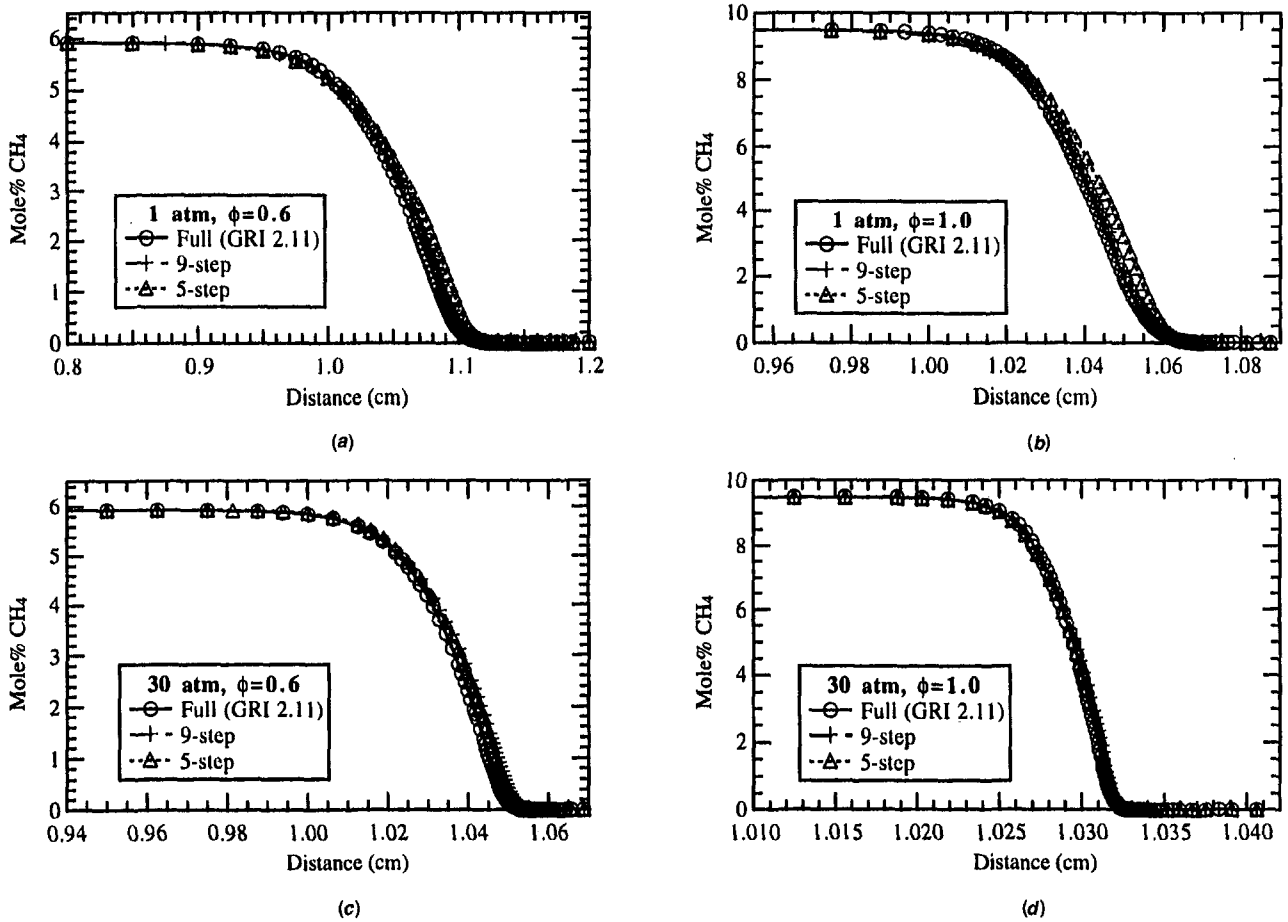

Fig. 6 Premixed calculations of mole% CH_4 ($T_{inlet} = 300$ K): (*a*) Mole% CH_4 versus distance, 1 atm, $\phi = 0.6$; (*b*) Mole% CH_4 versus distance, 1 atm, $\phi = 1.0$; (*c*) Mole% CH_4 versus distance, 30 atm, $\phi = 0.6$; and (*d*) Mole% CH_4 versus distance, 30 atm, $\phi = 1.0$.

Figures 5(a) and 5(b) show the predicted NO concentrations in a PSR as a function of equivalence ratio at 1 and 30 atmospheres (T_{inlet} = 600 K, τ = 2 ms). It is seen that although the predictions of all four newly developed reduced mechanisms are extremely good at high pressures (Fig. 5(b)) for all equivalence ratios (maximum relative error ~5 percent), the five, six, and seven-step global mechanisms are less accurate for atmospheric pressure (Fig. 5(a)) at high equivalence ratios (maximum relative error ~38 percent). This occurs because these five, six, and seven-step global mechanisms were optimized for high pressure and low equivalence ratio conditions found in lean premixed gas turbine combustion. At these and all other conditions, the nine-step global mechanism is the most accurate reduced mechanism (as expected). Since the four-step Seshadri–Peters mechanism (Chen and Dibble, 1991) does not contain NO_x chemistry, it could not be used for this comparison.

Premixed Code Calculations. Premixed flames are effectively one-dimensional, and experimentally they can be made very steady so that detailed temperature and species concentrations can be measured. The four newly developed reduced mechanisms were further tested using the premixed code that predicts species profiles using the burner-stabilized flame option (Kee et al., 1992a) and a user-specified temperature profile. Some convergence problems were encountered, especially for the five-step mechanism; the presence of small concentrations of intermediate species at low temperatures created numerical instabilities in the iterative solution procedure. This problem was effectively resolved by temporarily setting such intermediate species to zero at temperatures below 1200 K for atmospheric cases and below 1450 K for 30 atm cases, since their concentrations are too low to significantly affect overall flame structure. At higher temperatures, where flames are more stable, these intermediate species are present in significant quantities and hence do not cause convergence problems. This numerical convergence problem for low concentrations of intermediates is a subject of ongoing research, but does not seem to have an adverse effect on gas turbine combustor simulations (Cannon et al., 1996).

Comparatively, the nine-step global mechanism converged to premixed code solutions more easily than the smaller mechanisms. The nine-step global mechanism contains a large number of algebraic expressions for intermediate species, just like the smaller mechanisms, but the algebraic steady-state relationships are less complicated. The test matrix shown in Table 6 was used to evaluate the performance of the five and nine-step global mechanisms in comparison to the full GRI 2.11 mechanism (Bowman et al., 1995); the six and seven-step mechanisms showed similar agreement (Mallampalli, 1996). In these premixed calculations, the length of the reactor was adjusted to provide adequate residence time for the major species to reach thermodynamic equilibrium.

Figure 6 shows predictions of CH_4 concentration along the length of the premixed flow reactor for pressures of 1 and 30 atm for ϕ = 0.6 and 1.0 (T_{inlet} = 300 K). The combustion rates predicted by the nine-step and five-step global mechanisms are similar to the full GRI 2.11 mechanism at all pressures and equivalence ratios. Further, increases in pressure for a given equivalence ratio increase the combustion rate, which is predicted by all three mechanisms (note the change in scale in the horizontal axes in Fig. 6).

Figure 7 shows the predicted CO and CO_2 concentrations as a function of distance in a premixed flow reactor for pressures

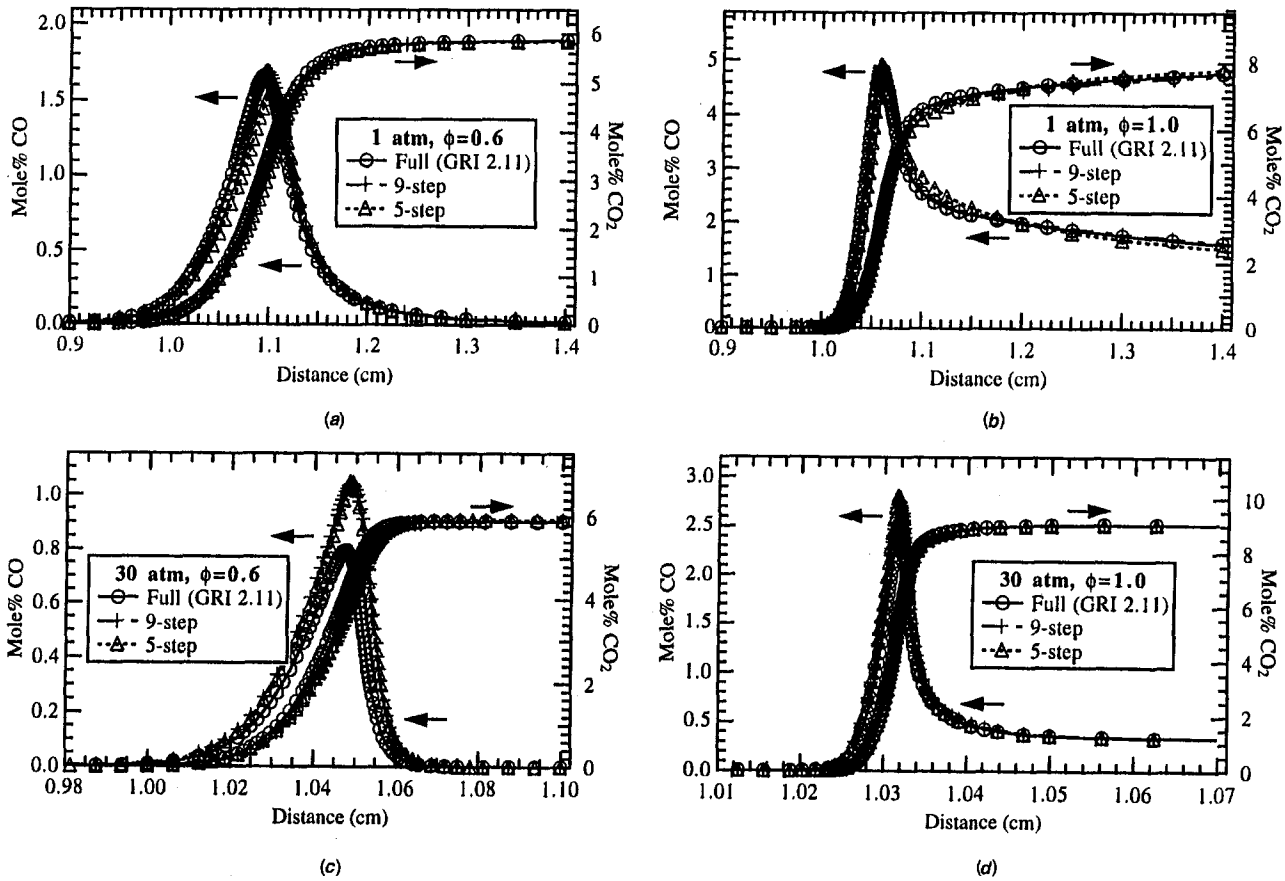

Fig. 7 Premixed calculations of mole% CO and CO_2 (T_{inlet} = 300 K): (a) Mole% CO, CO_2 versus distance, 1 atm, ϕ = 0.6; (b) Mole% CO, CO_2 versus distance, 1 atm, ϕ = 1.0; (c) Mole% CO, CO_2 versus distance, 30 atm, ϕ = 0.6; and (d) Mole% CO, CO_2 versus distance, 30 atm, ϕ = 1.0.

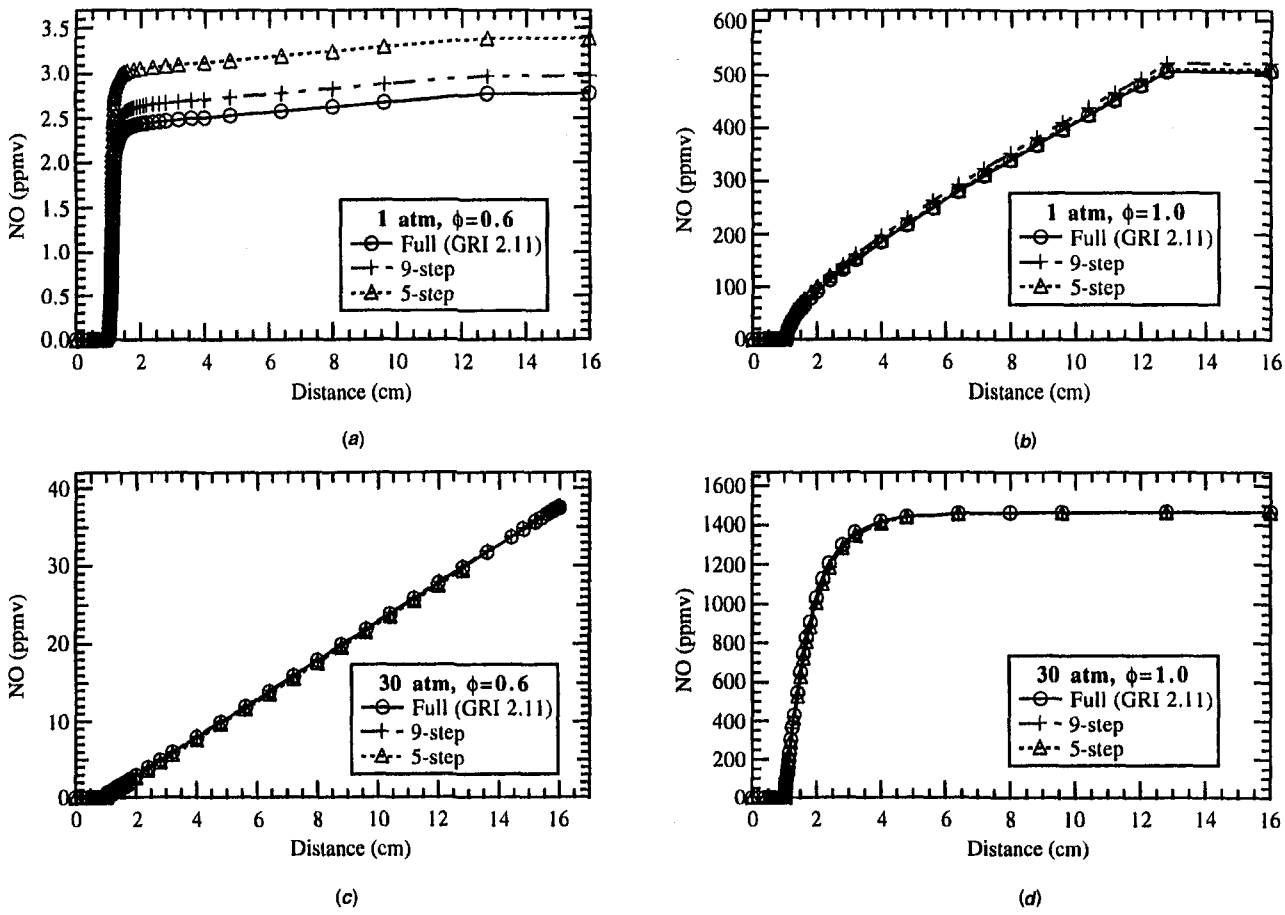

Fig. 8 Premixed calculations of NO (ppmv) (T_{inlet} = 300 K): (*a*) Mole% NO versus distance, 1 atm, ϕ = 0.6; (*b*) Mole% NO versus distance, 1 atm, ϕ = 1.0; (*c*) Mole% NO versus distance, 30 atm, ϕ = 0.6; and (*d*) Mole% NO versus distance, 30 atm, ϕ = 1.0.

of both 1 and 30 atm at equivalence ratios of 0.6 and 1.0 (T_{inlet} = 300 K). At 1 atm, the predicted peak CO concentration using the nine-step and five-step reduced mechanisms are similar to the full GRI 2.11 mechanism for both ϕ = 0.6 and ϕ = 1.0 (maximum relative error ~2 percent). At 30 atm, the peak CO concentrations predicted using the reduced mechanisms are higher than the full GRI 2.11 mechanism predictions (maximum relative error ~30 percent). The CO_2 formation rate is similar for the reduced and full mechanisms at all conditions shown, included the effect of pressure.

Equilibrium conditions were reached for all conditions shown in Fig. 7, except for predictions shown in Fig. 7(*a*) (CO reached ~9.3 ppm). For CO, equilibrium values vary with both pressure and equivalence ratio. At low equivalence ratios of ϕ = 0.6 (Figs. 7(*a*) and 7(*c*)), the equilibrium CO concentration is <5 ppm for both atmospheric and 30 atm pressures. However, at stoichiometric conditions (Figs. 7(*b*) and 7(*d*)), equilibrium values decreased with increases in pressure. At 1 atm, the equilibrium concentration of CO is ~14,300 ppm, while at 30 atm, the equilibrium concentration of CO is ~7,200 ppm (roughly half).

Figure 8 shows predicted NO concentrations as a function of distance along the premixed flow reactor (T_{inlet} = 300 K). The NO formation rate is largely dependent on the other conditions within the reactor (i.e., temperature, major and minor gas species concentrations). Figure 8(*a*) shows that at 1 atm and ϕ = 0.6, the peak NO concentration is ~3 ppm, which is predicted reasonably well by both the nine-step and five-step reduced mechanism. Increases in NO are predicted when the equivalence ratio is increased from ϕ = 0.6 (Fig. 8(*a*)) to ϕ = 1.0 (Fig. 8(*b*)). Increasing the flame equivalence ratio raises the gas temperatures, which directly increases the thermal NO_x, and, hence, increases the total NO_x formed. Figure 8(*c*) shows that at low equivalence ratios (ϕ = 0.6), increases in pressure (compared to Fig. 8(*a*)) increase NO_x emissions. Figure 8(*d*) shows that predicted NO_x values are high at high pressures and ϕ = 1.0.

Equilibrium conditions were not reached for NO in any of the predictions shown in Fig. 8. Also for NO, equilibrium values vary with both pressure and equivalence ratio. At low equivalence ratios of ϕ = 0.6 (Figs. 8(*a*) and 8(*c*)), the equilibrium NO concentration is 500 ppm for both atmospheric (not reached with τ = 0.45 sec) and 30 atm pressures (not reached with τ = 3.85 sec). However, at stoichiometric conditions of ϕ = 1.0 (Figs. 8(*b*) and 8(*d*)), thermodynamic equilibrium values decrease with increased pressure. At atmospheric pressure, the equilibrium concentration of NO is 3200 ppm (not reached with τ = 0.13 sec), while at 30 atm, the equilibrium concentration of NO is 2500 ppm (not reached with τ = 0.95 sec).

Discussion. In order to properly understand NO_x emissions from gas turbine combustors, it is essential to understand the relative importance of the three individual pathways and mechanisms that contribute to the total NO_x formed. Starting from the full GRI 2.11 mechanism and the five-step global mechanism, the individual NO_x contributions for the tested cases were obtained in the PSR code by using a simple three-step procedure suggested by Nicol et al. (1993):

1 The prompt NO contribution was obtained by eliminating both the thermal NO_x and the NO_x due to nitrous oxide pathway from both the full GRI 2.11 mechanism and the five-step global mechanism. Thermal NO_x was eliminated by removing the main reaction (N + NO = N2 + O). Other

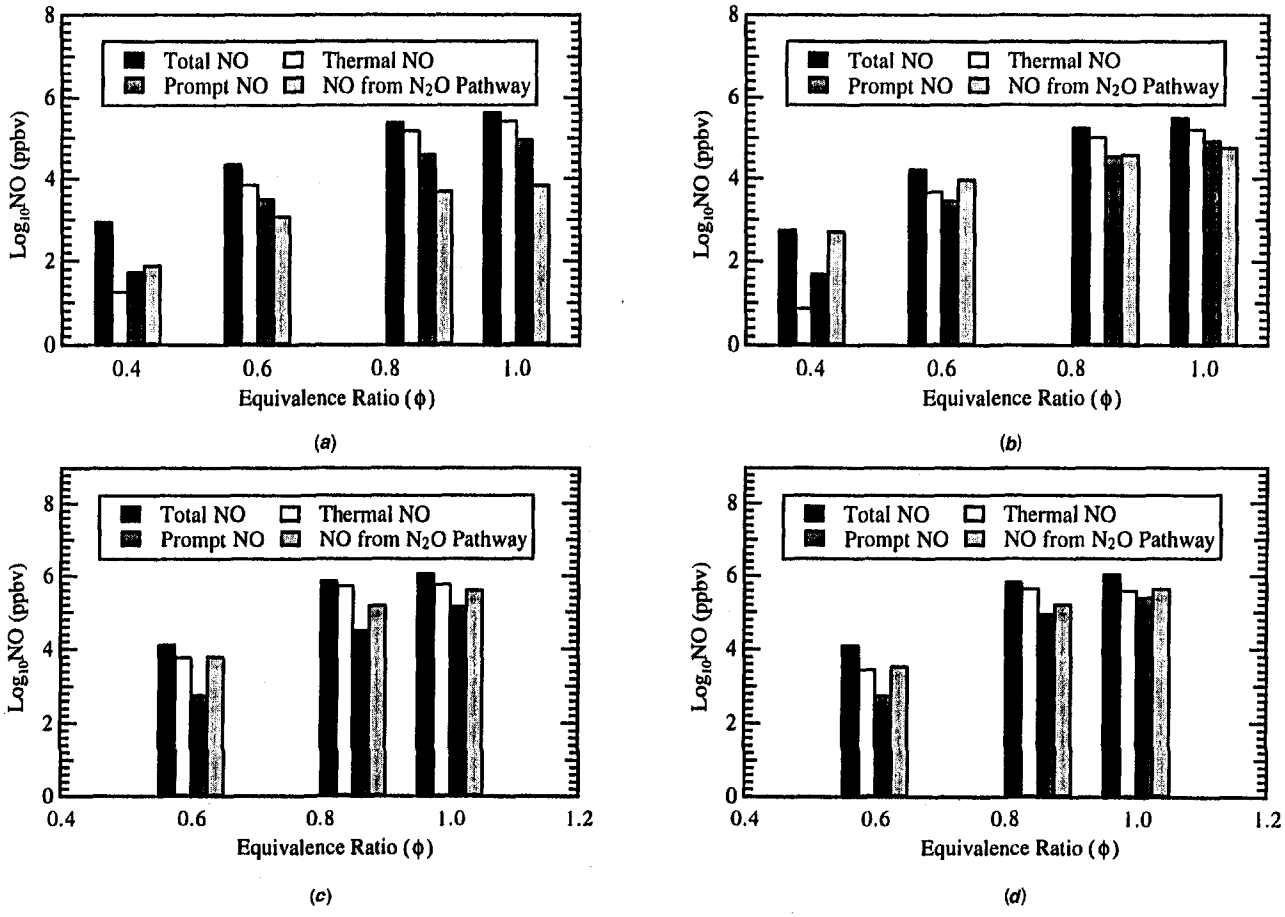

Fig. 9 PSR calculations of Log_{10} NO (ppbv) as a function of equivalence ratio (at ϕ = 0.4, ϕ = 0.6, ϕ = 0.85, and ϕ = 1.0) at 1 and 30 atm (T_{inlet} = 600 K; τ = 2 ms): (*a*) five-step global mechanism, 1 atm; (*b*) full GRI 2.11 mechanism, 1 atm; (*c*) five-step global mechanism, 30 atm; and (*d*) full GRI 2.11 mechanism, 30 atm.

less important reactions contributing to thermal NO_x were also removed. The nitrous oxide pathway was eliminated by removing the main reactions ($N_2O + M = N_2 + O + M$) and ($N_2O + M = N_2 + O(^1D) + M$). Some of the other lesser contributing reactions were also removed (see Mallampalli, 1996).

2 The NO contribution from the nitrous oxide pathway was obtained by eliminating thermal NO_x and prompt NO_x mechanisms from both the full GRI 2.11 mechanism and the five-step global mechanism. Thermal NO_x was eliminated by removing reactions as explained above. Prompt NO_x was eliminated by removing the main initiation reaction ($CH + N_2 = HCN + N$) for the formation of prompt NO_x. Other less important reactions contributing to prompt NO_x, such as ($CH + NO = HCN + O$) were also eliminated (see Mallampalli, 1996).

3 In the final step, thermal NO was obtained by subtracting the individual NO_x contributions from the prompt NO_x and NO_x from the nitrous oxide pathway from the total NO_x obtained for both the full GRI 2.11 mechanism and the five-step global mechanism.

Figure 9 shows comparisons of predicted thermal NO, prompt NO, NO from the nitrous oxide pathway, and total NO concentrations in a PSR for the five-step global mechanism and full GRI 2.11 mechanism at 1 and 30 atmospheres (τ = 2 ms, T_{inlet} = 600 K). At atmospheric conditions, the five-step mechanism shows similar trends in the relative contributions of thermal NO versus prompt NO versus the N_2O pathway (compare Fig. 9(*a*) and 9(*b*)) for ϕ = 0.8 and ϕ = 1.0. However, at the lower two equivalence ratios, the correct value of NO is predicted by the five-step mechanism without matching the correct trend in pathway. In the 30 atm predictions, the five-step mechanism seems to predict the correct trend in NO formation pathway for all equivalence ratios examined. The fact that better predictions are made at the higher pressure are consistent with the fact that the five-step model was specifically tuned to work best for the high pressure lean cases.

All of the calculations shown in this paper simulate ideal mixing conditions (no flame instabilities). In actual burners, flame instabilities occur at low equivalence ratios, and local extinction or flame blowout out may occur which can greatly increase the formation of CO. Since NO_x is known to decrease at lower equivalence ratios, increases in CO at these low equivalence ratios can limit the ultimate potential lean premixed combustion for NO_x reduction. Obviously, these newly developed reduced mechanisms only mimic the predictions obtained from the full GRI 2.11 mechanism, which is in a continuous state of improvement (especially at high pressure). All of the new reduced mechanisms presented here reproduce the behavior of the GRI 2.11 mechanism over a wide range of equivalence ratios for total pressures from 1 to 30 atm. The reason for the agreement is due to the use of a large set of complicated steady-state expressions for the intermediate species. Comparisons with individual laminar flame data sets have been performed extensively in the literature using the GRI 2.11 mechanism, and are not repeated here. The ultimate goal is the application of the reduced mechanisms to turbulent lean premixed flames, with subsequent comparison with data. Cannon et al. (1996, 1998) and Cannon, 1997 have shown that the five-step and nine-step global mechanisms provide a good representation of the flame

chemistry in (a) a partially stirred reactor, and (b) a comprehensive gas-turbine computer model. Predictions from the comprehensive model were compared with laser-based data obtained in an axisymmetric laboratory-scale gas turbine combustor. Their method used an in-situ adaptive look-up table for the chemical reactions; these five to nine-step reduced mechanisms greatly reduced the computational requirements for gas-turbine combustion modeling. It is anticipated that these reduced mechanisms will be of value to many other applications in lean premixed combustion simulations.

Further research in this area will likely result in better detailed mechanisms for modeling CH_4 and NO_x chemistry in lean premixed turbulent natural gas combustion. As computer technology advances, faster computers will become available that will perhaps permit the use of larger elementary reaction schemes in practical geometries. Until then, methods such as the computer reduction methods will gain popularity, and will be used for modeling natural gas combustion. The reduced mechanisms presented here are robust and perform well at relevant conditions to lean premixed gas turbine combustion.

Summary and Conclusions

A major focus of this project was to develop reduced mechanisms of CH_4 combustion and NO_x formation that describe lean premixed turbulent combustion of natural gas. This included identifying a useful comprehensive mechanism and then comparing the reduced mechanisms to the full mechanism in idealized codes at practical experimental conditions. The potential reduced mechanisms tested were expected to predict gas temperature and concentrations of key pollutant species such as NO_x and CO.

New five to nine-step reduced mechanisms of CH_4 and NO_x were developed from the recently released GRI 2.11 mechanism, which incorporates detailed NO_x kinetics for combustion of natural gas along with detailed CH_4 chemistry. The newly developed five to nine-step reduced mechanisms were evaluated by comparing key species and gas temperature predictions in these mechanisms to the full GRI 2.11 mechanism. The four-step Seshadri–Peters global mechanism (Chen and Dibble, 1991) found in the literature was also examined. Using the full GRI 2.11 mechanism as a standard, predictions made using the five-step reduced mechanism were more accurate than the four-step Seshadri–Peters reduced mechanism, especially at lean premixed high pressure conditions. Predictions using the five-step reduced mechanism agreed within 5 percent at all conditions for $0.4 < \phi < 0.6$ and $1 <$ pressure (atm) < 30.

Based on the PSR and premixed code calculations performed in this study, it is thus concluded that the five-step global mechanism appears to be a promising reduced mechanism that can be used in multidimensional codes for modeling lean premixed turbulent combustion of natural gas. The five-step global mechanism is reasonably accurate for both NO_x and CH_4 chemistry, based on comparisons with the validated full GRI 2.11 mechanism for pressures from 1 to 30 atm and equivalence ratios from 0.4 to 1.0. However, if computational costs due to additional global steps are not severe, the newly developed nine-step global mechanism could be used, since it was a little more accurate and provides the fewest convergence problems. The four-step Seshadri–Peters global mechanism is useful at low equivalence ratios and atmospheric pressures, and should be used if the computational time due to the additional NO_x step in the five-step global mechanism is a limiting factor. However, the four-step Seshadri–Peters reduced mechanism lacks C_2 chemistry and is, thus, less accurate at high pressures.

Acknowledgment

This work was supported by the U.S. Department of Energy—Federal Energy Technology Center through a cooperative agreement with the South Carolina Energy Research and Development Center at Clemson University under Contract No. DE-FC21-92MC29061.

References

Anand, M. S., and Gouldin, F. C., 1985, "Combustion Efficiency of a Premixed Continuous Flow Combustor," ASME JOURNAL OF ENGINEERING FOR GAS TURBINES AND POWER, Vol. 107, pp. 695–705.

Bilger, R. W., Stårner, S. H., and Kee, R. J., 1990, "On Reduced Mechanisms for Methane–Air Combustion in Nonpremixed Flames," *Combustion and Flame,* Vol. 80, pp. 135–149.

Borghi, R., 1988, "Turbulent Combustion Modelling," *Progress in Energy and Combustion Science,* Vol. 14, pp. 245–292.

Bowman, C. T., Hanson, R. K., Gardiner, W. C., Lissianski, V., Frenklach, M., Goldenberg, M., Smith, G. P., Crosley, D. R., Golden, D. M., 1995, GRI Mech 2.11, 1995, http://www.gri.org.

Cannon, S. M., Brewster, B. S., and Smoot, L. D., 1996, "Prediction of CO and NO_x in Lean Premixed Turbulent Combustion," presented at the Fall 1996 Meeting of the Western States Section/Combustion Institute, University of Southern California, Los Angeles, CA.

Cannon, S. M., 1997, "Modeling of Lean Premixed Gaseous Turbulent Combustion," Ph.D. dissertation, Mechanical Engineering Department, Brigham Young University, Provo, UT.

Cannon, S. M., Brewster, B. S., and Smoot, L. D., 1998, "Stochastic Modeling of CO and NO in Premixed Methane Combustion," *Combustion and Flame,* Vol. 113, pp. 137–146.

Chen, J. Y., and Dibble, R. W., 1991, "Applications of Reduced Chemical Mechanisms for the Prediction of Turbulent Nonpremixed Methane Jet Flames," in *Reduced Chemical Mechanisms and Asymptotic Approximations for Methane-Air Flames,* M. D. Smooke, ed., Springer-Verlag, New York, pp. 193–226.

Chen, J. Y., 1988, "A General Procedure for Constructing Reduced Reaction Mechanisms with Given Independent Reactions," *Combustion Science and Technology,* Vol. 57, pp. 89–94.

Chang, W. C., 1995, "Modeling of NO_x Formation in Turbulent Flames—Development of Reduced Mechanisms and Mixing Models," Ph.D. thesis, University of California at Berkeley.

Correa, S. M., 1992a, "Carbon Monoxide Emissions in Lean Premixed Combustion," *Journal of Propulsion and Power,* Vol. 8, pp. 1144–1151.

Correa, S. M., 1992b, "A Review of NO_x Formation Under Gas-Turbine Combustion Conditions," *Combustion Science and Technology,* Vol. 87, pp. 329–362.

Davis, L. B., and Washam, R. M., 1989, "Development of a Dry Low NO_x Combustor," presented at the Gas Turbine and Aeroengine Congress and Exposition, June 4–8, Toronto, Canada.

Glarborg, P., Kee, R. J., Grcar, J. F., and Miller, J. A., 1992a, "PSR: A Fortran Program for Modeling Well-Stirred Reactors," report, SAND86-8209. UC-4, Sandia National Laboratories. Livermore, CA.

Glarborg, P., Lilleheie, N. I., Byggstoyl, S., Magnüssen, B. F., Kilpinen, P., and Hupa, M., 1992b, "A Reduced Mechanism for Nitrogen Chemistry in Methane Combustion," *Twenty-Fourth Symposium (International) on Combustion,* The Combustion Institute, Pittsburgh, PA, pp. 889–898.

Kee, R. J., Grcar, J. F., Smooke, M. D., and Miller, J. A., 1992a, "A Fortran Program for Modeling Steady Laminar One-Dimensional Premixed Flames," report, SAND85-8240.UC-401, Sandia National Laboratories, New Mexico.

Kee, R. J., Rupley, F. M., and Miller, J. A., 1992b, "Chemkin-II: A Fortran Chemical Kinetics Package for the Analysis of Gas-Phase Chemical Kinetics," report, SAND89-8009B.UC706, Sandia National Laboratories, New Mexico.

Maas, U., and Pope, S. B., 1992a, "Implementation of Simplified Chemical Kinetics Based on Intrinsic Low-Dimensional Manifolds," *Twenty-Fourth Symposium (International) on Combustion, The Combustion Institute,* Pittsburgh, PA, pp. 103–112.

Maas, U., and Pope, S. B., 1992b, "Simplifying Chemical Kinetics: Intrinsic Low-Dimensional Manifolds in Composition Space," *Combustion and Flame,* Vol. 88, pp. 239–264.

Mallampalli, H., 1996, "Evaluation of Global CH_4/NO_x Mechanisms for Modeling Lean Premixed Turbulent Combustion of Natural Gas," M.S. thesis, Brigham Young University, Provo, UT.

Mallampalli, H., Fletcher, T. H., Chen, J. Y., 1996, "Evaluation of Global CH_4/NO_x Mechanisms for Modeling Lean Premixed Turbulent Combustion of Natural Gas," Paper 96F-098, Western States Section of the Combustion Institute, University of Southern California, Los Angeles, CA; see also: http://www.et.byu.edu/~tom/Papers/Hemant-WSS96/WSS.html

Miller, J. A., and Bowman, C. T., 1989, "Mechanism and Modeling of Nitrogen Chemistry in Combustion," *Progress in Energy and Combustion Science,* Vol. 15, pp. 287–338.

Nicol, D. G., Steele, R. C., Marinov, N. M., and Malte, P. C., 1993, "The Importance of Nitrous Oxide Pathway to NO_x in Lean Premixed Combustion," presented at the ASME International Gas Turbine and Aeroengine Congress and Exposition, Cincinnati, Ohio.

Nicol, D. G., Malte, P. C., Hamer, A., Roby, R. J., and Steele, R. C., 1997, "A Five-Step Global Mechanism for Methane Oxidation with NO Formation for Lean-Premixed Combustion: Development of the Mechanism and Application to a Gas Turbine Combustor," presented at the Western States Section of the Combustion Institute, April 14–15, Paper 97S-039, Livermore, CA.

Nicol, D. G., Malte, P. C., Hamer, A., Roby, R. J., and Steele, R. C., 1998, "Development of a Five-Step Global Methane Oxidation—NO Formation Mechanism for Lean-Premixed Gas Turbine Combustion," accepted for the ASME International Gas Turbine and Aeroengine Congress, Stokholm, Sweden.

Polifke, W., Dobbeling, K., Sattlemayer, T., Nicol, D. G., and Malte, P. C., 1995, "A NO_x Prediction Scheme for Lean Premixed Gas Turbine Combustion based on Detailed Chemical Kinetics," *International Gas Turbine and Aeroengine Congress and Exposition,* ASME, New York, NY.

Smooke, M. D., and Giovangigli, V., 1991, "Formulation of the Premixed and Nonpremixed Test Problems," *Reduced Chemical Mechanisms and Asymptotic Approximations for Methane-Air Flames,* M. D. Smooke, ed., Springer-Verlag, New York, pp. 1–28.

Steele, R. C., Malte, P. C., Nicol, D. G., and Kramlich, J. C., 1994, "NO_x and N_2O in Lean Premixed Jet-Stirred Flames," *Combustion and Flame,* Vol. 100, No. 3, pp. 440–449.

Treviño, C., and Mendéz, F., 1992, "Reduced Kinetic Mechanism for Methane Ignition," *Twenty-Fourth Symposium (International) on Combustion,* The Combustion Institute, Pittsburgh, PA, pp. 121–12.

Wang, H., and Frenklach, M., 1991, "Detailed Reduction of Reaction Mechanisms for Flame Modeling," *Combustion and Flame,* Vol. 87, pp. 365–370.

Numerical Prediction of the Dynamic Behavior of Turbulent Diffusion Flames

D. Bohn

G. Deutsch

Aachen University of Technology,
Teemplergraben 55,
Institute of Steam and Gas Turbines,
Aachen, D-52056, Germany

U. Krüger

B&B-AGEMA GmbH,
Jülicher Str. 338,
Aachen D-52070, Germany

Environmental compatibility requires low-emission burners for gas turbine power plants as well as for jet engines. In the past, significant progress has been made developing low NO_x and CO burners. Unfortunately, these burners often have a more pronounced tendency than conventional burner designs to produce combustion driven oscillations. The oscillations may be excited to such an extent that pronounced pulsation may possibly occur; this is associated with a risk of engine failure. The stability of a burner system can be investigated by means of a stability analysis under the assumption of acoustical behavior. The problem with all these algorithms is the transfer function of the flame. A new method is presented here to predict the dynamic flame behavior by means of a full Navier-Stokes simulation of the complex combustion process. The first step is to get a steady-state solution of a flame configuration. After that a transient simulation follows with a sudden change in the mass flow rate at the flame inlet. The time-dependent answer of the flame to this disturbance is then transformed into the frequency space by a Laplace Transformation. This leads, in turn, to the frequency response representing the dynamic behavior of the flame. In principle, this method can be adapted for both diffusion as well as premixed flame systems. However, due to the fact that diffusion flames are more controlled by the mixing process than by the chemical kinetic, the method has first been used for the prediction of the dynamic behavior of turbulent diffusion flames. The combustion has been modelled by a mixed-is-burnt model. The influence of the turbulence has been taken into account by a modified k-ϵ model and the turbulence influences the combustion rate by presumed probability density functions (pdf). The steady state as well as the transient results have been compared with experimental data for two different diffusion flame configurations. Although the burner configuration is relatively complex, the steady-state results collaborate very well with the experiments for velocity, temperature, and species distribution. The most important result is that the heat release that drives the oscillations can be modeled sufficiently accurately. The effect of using different pdf models has been discussed and the best model has been used for the transient calculations of the dynamic flame behavior. The results for the frequency response of the flame are very encouraging. The principal behavior of the flame—higher order time element with a delay time—can be predicted with sufficient precision. In addition, the qualitative results collaborate fairly well with the experiments.

Introduction

Due to the need for environmental compatibility, combustion is a very important field of research in gas turbine development. In the past, significant progress has been made developing low NO_x and CO burners. In addition, the power output of heavy-duty gas turbines has increased significantly, with the result that the thermal power of the combustion chamber is greater. Unfortunately, these advanced burners and combustion chambers often have a more pronounced tendency to produce combustion-driven oscillations than conventional burner designs. The oscillations may be excited to such an extent that pronounced pulsation may possibly occur; this is associated with a risk of engine failure. They can lead to higher levels of pollution, and result in very high noise emissions. Therefore, there is an urgent need to develop a design tool for the prediction of these instabilities. It is important to understand that they are not sympathetic vibrations, so variations of geometry will not prevent them automatically [1].

The stability of a burner system can be investigated by means of a stability analysis under the assumption of acoustical behavior. At the Institute of Steam and Gas Turbines, RWTH Aachen, an acoustical model has been developed to predict the stability range of a combustor [2, 3]. The combustor is therefore split up into several units, as shown in principle in Fig. 1. The whole combustor works as a feedback system leading to self-induced oscillation under special assumptions. This model was successfully tested and verified with experimental data taken from a test combustor. For further details see [2]. However, in order to predict the instabilities of real gas turbine burners, a thorough understanding of the dynamic behavior of the flame that works as an amplifier in this oscillating circuit is required.

Some experimental work in this area can be mentioned. Lenz [4] and Lang [5] have investigated the dynamic behavior of turbulent premixed flames. Matsui [15] and Sugimoto and Matsui [16] did further experimental work on laminar premixed flames. Priesmeier [6] did experiments on the dynamic behavior of diffusion flame systems. All authors deduced that the frequency response of flames can be described as a higher-order time element with a delay time. The behavior of the flame

Contributed by the International Gas Turbine Institute and presented at the 41st International Gas Turbine and Aeroengine Congress and Exhibition, Birmingham, United Kingdom, June 10–13, 1996. Manuscript received by the ASME Headquarters March 3, 1996. Paper No. 96-GT-133. Associate Technical Editor: J. N. Shinn.

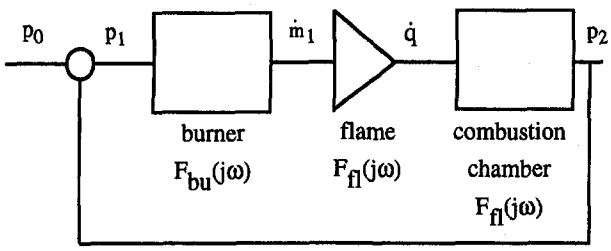

Fig. 1 Oscillating circuit of a combustor system

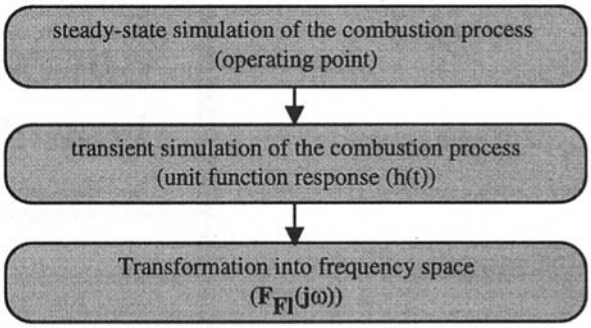

Fig. 2 Numerical simulation of the dynamical behavior

depends strongly on the geometry of the burner, the type of flame, the equivalence ratio, and the thermal power.

Some theoretical work has been done by Merk [7], Becker and Günther [8], Lenz [4] and Bohn and Deuker [2]. In combination with the experimental work mentioned above, these analytical works are very helpful for describing the principles of dynamic flame behavior. In the case of practical flames, which are characterized by complex geometries, and highly turbulent fluid flows, however, these analyses are not precise enough because many assumptions have to be postulated in order to derive the frequency response of flames.

In this paper, a new method is used (first described in Bohn and Krüger [9]) that derives the frequency response by means of a transient numerical simulation of the complex combustion process.

Derivation of the Flame Frequency Response

The principal method used to calculate the frequency response of a flame by numerical simulation of the combustion process is sketched in Fig. 2. First, the steady-state combustion process of a given configuration has to be calculated. After that, transient calculations are carried out that give the time-dependent unit function response of the flame ($h(t)$) to a sudden increase in the mass flow rate of air at the burner inlet, as follows:

$$h(t) = \frac{\Delta \dot{q}_{\text{flame}}}{\Delta \dot{m}}. \tag{1}$$

This response is then transferred into frequency space by a Laplace Transformation to obtain the frequency response of the flame $F_{fl}(j\omega)$:

$$F_{fl}(j\omega) = j\omega \int_0^\infty h(t) \cdot e^{-j\omega t} dt. \tag{2}$$

In the case of diffusion flames, it is expedient to define the ratio of the transient heat release of the flame to the mass flow jump of air—mass flow rate of air is much larger than that of fuel—at the burner inlet as the characteristic value for the dynamic behavior of the flame. The advantage of this definition is that this ratio is independent of the computational domain. The definition (1) is compatible with that used by Priesmeier [6].

Due to the thermal inertia of the system, this procedure cannot be used for experimental investigations. Therefore, the flame is perturbed by harmonic disturbance, i.e., a sinusoidal variation of the inlet mass flow. In order to obtain the frequency response, many discrete frequencies have to be investigated; this means that a lot of effort has to be invested in experimental work. These two different methods for obtaining the frequency responses of a dynamic system are absolutely equivalent under the assumption of linear systems, which is really true for the beginning of self-induced oscillations [1].

Numerical Procedure

Basic Equations. Under the assumption of fast chemistry, which means that the turbulent mixing of fuel and oxidant dominates the combustion process, the combustion chemistry can be given by only one simple reaction equation:

$$\underbrace{1 \text{ kg F}}_{\text{Fuel}} + \underbrace{\alpha \text{ kg O}}_{\text{Oxidant}} \rightarrow \underbrace{(1+\alpha) \text{ kg P}}_{\text{Product}}. \tag{3}$$

Neglecting the chemical kinetic effects, fuel is burnt infinitesimal fast, consuming all available oxidant. This model that is often used for diffusion flame systems is called the mixed-is-burnt model.

Then, the entire combustion process of a turbulent diffusion flame can be described by the Favre-averaged transient and

Nomenclature

C = general constant
c_p = specific heat capacity
F = frequency response
F = fuel
f = mixture fraction
g = variance of mixture fraction
H_u = net calorific power
h = unit function response
h = enthalpy
j = complex variable
k = turbulent kinetic energy
M = molecular weight
$\dot{m}$ = mass flow rate
$\Delta\dot{m}$ = jump function
O = oxidant
P = product
p = pressure
p = probability density function
$\dot{q}$ = transient heat release
R = gas constant
t = time
T = temperature
Tu = turbulence intensity
$\vec{v}$ = velocity vector
u, v, w = axial, radial and circumferential velocity component
x, r, ϕ = axial, radial and circumferential coordinate
α = stoichiometric oxidant mass
ϵ = turbulent dissipation rate
μ = viscosity
ρ = density
ξ = mass fraction
ψ = mole fraction
φ = phase angle
ϕ = equivalence ratio
ω = angular frequency

Subscripts

F = fuel
fl = flame
O = oxidant
P = product
st = stoichiometric
t = total
$\underline{T}$ = turbulent
$\bar{}$ = average value

compressible Navier-Stokes equations (4–6), the equations for the turbulence quantities k (7) and ϵ (8), the mixture fraction f (9), and the variance of the mixture fraction g (10):

$$p(f) = \delta(f - \bar{f}) \tag{11}$$

Double Delta Function (2δ-pdf).

$$p(f) = \begin{cases} \frac{1}{2}\delta(f - (\bar{f} + \sqrt{\bar{g}})) + \frac{1}{2}\delta(f - (\bar{f} - \sqrt{\bar{g}})) & \text{if} \quad (\bar{g} \le (1-\bar{f})^2) \wedge (\bar{g} \le \bar{f}^2) \\ \frac{\bar{g}}{\bar{f}^2 + \bar{g}}\delta(f) + \frac{\bar{f}^2}{\bar{f}^2 + \bar{g}}\delta\left(f - \left(\bar{f} + \frac{\bar{g}}{\bar{f}}\right)\right) & \text{if} \quad \bar{f}^2 \le \bar{g} \le \bar{f}(1-\bar{f}) \\ \frac{\bar{g}}{(1-\bar{f})^2 + \bar{g}}\delta(f-1) + \frac{(1-\bar{f})^2}{(1-\bar{f})^2 + \bar{g}}\delta\left(f - \left(\bar{f} - \frac{\bar{g}}{(1-f)}\right)\right) & \text{if} \quad (1-\bar{f})^2 \le \bar{g} \le \bar{f}(1-\bar{f}) \end{cases} \tag{12}$$

$$\frac{\partial \rho}{\partial t} + \nabla\cdot(\rho\vec{v}) = 0 \tag{4}$$

$$\frac{\partial \rho\vec{v}}{\partial t} + \nabla\cdot(\rho\vec{v}\times\vec{v} - (\mu + \mu_T)\nabla\vec{v}) = -\nabla\left(p + \frac{2}{3}\rho k\right) + \nabla\cdot((\mu + \mu_T)(\nabla\vec{v})^T) \tag{5}$$

$$\frac{\partial \rho h_t}{\partial t} + \nabla\cdot\left(\rho\vec{v}h_t - \left(\frac{\lambda}{c_p} + \frac{\mu_T}{\sigma_{Tht}}\right)\nabla h_t\right) = \frac{\partial p}{\partial t} \tag{6}$$

$$\frac{\partial \rho k}{\partial t} + \nabla\cdot\left(\rho\vec{v}k - \left(\mu + \frac{\mu_T}{\sigma_{Tk}}\right)\nabla k\right) = P - \rho\epsilon \tag{7}$$

$$\frac{\partial \rho \epsilon}{\partial t} + \nabla\cdot\left(\rho\vec{v}\epsilon - \left(\mu + \frac{\mu_T}{\sigma_{T\epsilon}}\right)\nabla\epsilon\right) = C_1\frac{\epsilon}{k}P - C_2\rho\frac{\epsilon^2}{k} \tag{8}$$

$$\frac{\partial \rho f}{\partial t} + \nabla\cdot\left(\rho\vec{v}f - \left(\frac{\mu}{\sigma_f} + \frac{\mu_T}{\sigma_{Tf}}\right)\nabla f\right) = 0 \tag{9}$$

$$\frac{\partial \rho g}{\partial t} + \nabla\cdot\left(\rho\vec{v}g - \left(\frac{\mu}{\sigma_g} + \frac{\mu_T}{\sigma_{Tg}}\right)\nabla g\right) = C_{g1}\frac{\mu_T}{\sigma_T}(\nabla f)^2 - C_{g2}\rho\frac{\epsilon}{k}g \tag{10}$$

P is the production term of turbulence energy and turbulence dissipation due to shear forces. There are several empirical constants appearing in both the turbulence and the combustion model. In Table 1, the used values of these constants are listed; however, these values are all known as standard values, apart from C_1 that appears in the epsilon equation (8). This number has been changed from 1.44 to 1.6, which is often used for problems with free jets. As shown in Table 1, this also has consequences on the turbulent Prandtl number $\sigma_{T\epsilon}$ of the epsilon equation. The effects of this change will be discussed later on. The influence of turbulence on the mixture fraction representing the combustion progress is taken into account by presumed probability density functions (see Fig. 3). Three different forms have been used and tested:

Single Delta Function (δ-pdf).

Table 1 Constants of the numerical scheme

C_1	C_2	C_{g1}	C_{g2}	σ_{Tht}	σ_{Tk}	$\sigma_{T\epsilon}$	σ_f	σ_{Tf}	σ_g	σ_{Tg}
(1.44)1.6	1.92	2.22	2	0.9	1	$\frac{0.4187^2}{(C_2 - C_1)\sqrt{0.09}}$	0.7	0.9	0.7	0.9

Beta Function (β-pdf).

$$p(f) = \frac{\Gamma(a+b)}{\Gamma(a)\Gamma(b)}f^{a-1}(1-f)^{b-1}, \tag{13}$$

where

$$a = \frac{\bar{f}}{\bar{g}}(\bar{f}(1-\bar{f}) - \bar{g}) \quad \text{and}$$

$$b = \frac{(1-\bar{f})}{\bar{g}}(\bar{f}(1-\bar{f}) - \bar{g}). \tag{13a}$$

Then, the mass fractions of fuel, oxidant and product are given by the following:

$$\xi_F = \int_0^1 \max\left(\frac{f - f_{st}}{1 - f_{st}}, 0\right)p(f)df \tag{14}$$

$$\xi_O = \int_0^1 \max\left(1 - \frac{f}{f_{st}}, 0\right)p(f)df \tag{15}$$

$$\xi_P = 1 - \xi_F - \xi_O \tag{16}$$

The stoichiometric mixture fraction f_{st} depends on the fuel used; (here, all investigations are carried out with methane (α = 17.2), leading to a value of f_{st} = 0.055) and is defined as follows:

$$f_{st} = \frac{1}{1 + \alpha}. \tag{17}$$

The set of 9 coupled differential equations (4–10) is closed by the equation of state for ideal gases (18) and the constitutive equation for ideal gases (19):

$$\rho = \frac{p}{RT} \tag{18}$$

$$h = \int_{T_{ref}}^{T} c_p(\xi_i, T)dT + \xi_F H_u \tag{19}$$

In equation (19), the second term represents the heat release

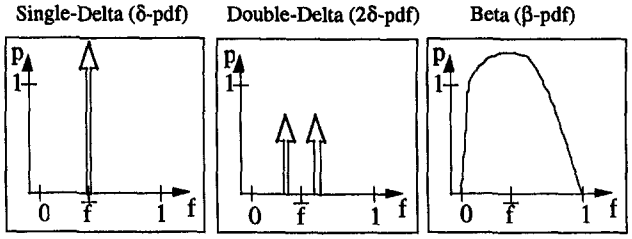

Fig. 3 Different probability density functions (PDFs)

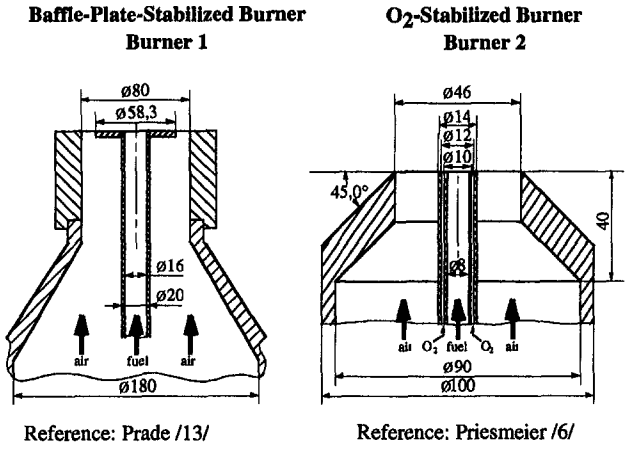

Fig. 4 Burner configurations

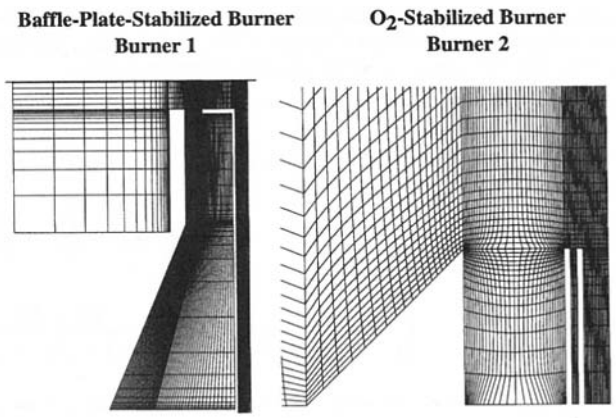

Fig. 5 Computational grids

as a result of the combustion process, where H_u is the net calorific value.

Finally, for ideal gas mixtures (here the mixture consists of fuel (ξ_F), oxidant (ξ_O), and product (ξ_P)) the specific gas constant and the specific heat capacity are defined as

$$R = \frac{\mathcal{R}}{\bar{M}} \quad \text{where} \quad \frac{1}{\bar{M}} = \sum_{i=1}^{n} \frac{\xi_i}{M_i} \tag{20}$$

$$c_p(\xi_i, T) = \sum_{i=1}^{n} \xi_i c_{p,i}(T). \tag{21}$$

Solution Method. A fully implicit finite-volume scheme has been used for solving the coupled equations (4) – (10). The SIMPLEC pressure-correction algorithm [10] is adapted on a nonstaggered grid, while avoiding the chequerboard oscillations by using the improved Rhie-Chow interpolation method [11, 12]. For diffusion terms, a central differencing scheme is used, while advection terms are discretised by upwind differencing. A fully backward difference time stepping procedure is employed. Therefore, in principle, the time step is not bound to CFL stability restrictions; this is a very important feature for numerical investigations of transient combustion phenomena.

Burner Geometries.

Two different burner geometries have been used for testing the steady-state as well as the transient flow with and without combustion included. A cutout of the two-burner configurations is shown in Fig. 4 (for clarity, only the head ends of the combustion chambers where the reactants are introduced and the flame is stabilized are plotted). The main difference between these two burners is the stabilizing mechanism. The flame of burner 1 is stabilized by a baffle plate at the burner exit. Methane (fuel) is flowing through the inner duct, while the air (oxidant) is flowing through the outer one. The acceleration induced by the baffle plate leads to a radial component at the burner exit and two antispin vortices downstream of the exit. This vortices stabilize the flame due to the low flow velocities that have to be on the order of the burning velocity of the flame. Burner 2 is characterized by a different stabilizing method. A very small pilot flame is produced directly at the burner exit. Therefore, between the inner fuel jet and the outer air jet, there is a third nozzle through which pure oxygen O_2 is flowing. The burner can therefore be referred to as O_2-stabilized. Oxygen is used for the pilot flames instead of air due to the fact that O_2 flames have a higher adiabatic flame temperature.

Both burners have been developed and experimentally investigated at the University of Karlsruhe [6, 13]. For burner 1, steady-state investigations for the cold flow configuration as well as for the combustion configuration are available. The velocities were measured by a LDV-measurement technique, concentration profiles were measured by watercooled probes, and the temperatures were obtained by Pt/Pr-Ro thermocouples. Experimental results of the dynamic flame behavior are available only for burner 2, for which the transient heat release is measured by OH-radiant technique.

Grid and Boundary Conditions. In Fig. 5 a cut of the structured computational grids for the two burners are shown. Using the multiblock technique it is possible to take into account not only the domain downstream of the burner exit but also the internal flow of the burner itself. This is more general as one can give boundary conditions at the burner inlet and no information is needed about the very important, and in most cases unknown, flow conditions at the burner exit. This is an essential cause of the very complex flow situation especially in the case of burner 1.

The boundary conditions for the steady-state calculations are shown in Fig. 6. For burner 1 these values lead to an air mass flow rate of 32.4 g/s and to a fuel mass flow rate of 3.14 g/s (equivalence ratio $\phi = 1.66$). For burner 2 the air mass flow rate is 21.2 g/s, the fuel mass flow rate is 1.18 g/s and the oxygen mass flow rate of the pilot flame is 0.056 g/s. Neglecting the oxygen flame this results in an equivalence ratio of $\phi = 0.95$. For the transient calculations of burner 2, the mass flow rate of air is increased by 20 percent of the steady-state value.

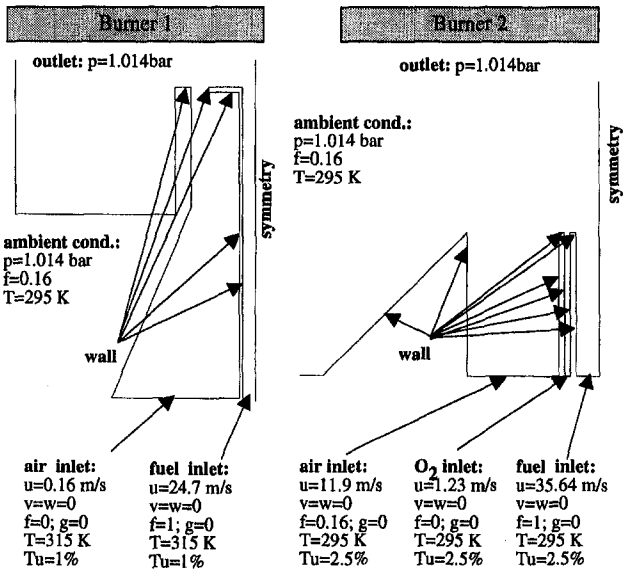

Fig. 6 Boundary conditions

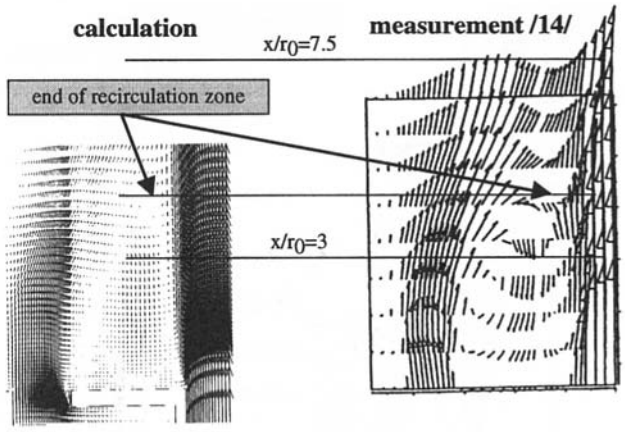

Fig. 7 Velocity-vectorplot: comparison between measurement and calculation

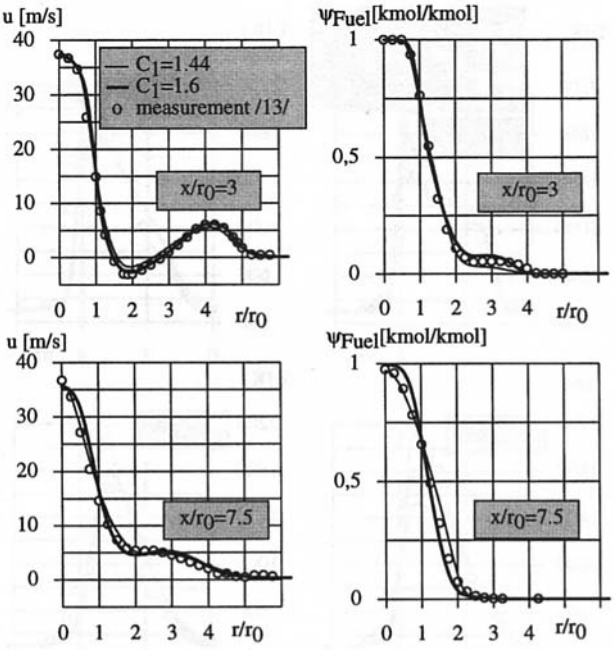

Fig. 8 Validation of turbulence model

Results

Before starting the transient calculations, two main topics have to be investigated. Firstly, the flow has turbulent character, with the result that the turbulence modeling has to be evaluated. To separate the effects, it is worthwhile to validate this on cold flow configurations. This has been done for both burners. However, due to the fact that burner 1 has the more complex geometry, results will be presented for this configuration only. Secondly, the combustion process itself and the interaction with turbulent mixing has to be evaluated. The temperature distribution in particular is of great interest because this is essential for the transient heat release during the combustion process following a sudden jump in the mass flow rate at the burner exit.

Cold Flow. The principal flow pattern of the baffle stabilized burner (burner 1) can be illustrated by Fig. 7 in which the velocity vectors are shown near the burner exit. In principle, the numerical results collaborate well with the measured one. The two vortices of the return flow can be clearly identified. These vortices are very important for the stabilization mechanism of this burner. Apart from the advantage that no information about the boundary conditions at the burner exit is needed, the fact that such important details as the separation of the air jet at the baffle plate can be predicted makes it straightforward to take into account the internal flow of the burner.

In order to evaluate the used standard k-ϵ model, the quantitative results of the numerical simulation of the isotherm flow are presented in Fig. 8. The axial velocity u and the concentration of methane ψ_{Fuel} are plotted against the dimensionless radius (the radius is normalized by the radius of the fuel nozzle r_0) for two different axial positions 24 mm ($x/r_0 = 3$) and 60 mm ($r/r_0 = 7.5$) downstream of the burner nozzle. Two different values of the C_1 parameter of the ϵ-equation (Eq. (8)) are used: the standard value of 1.44 and a value of 1.6, which is often used for free jet configurations. It is clearly shown that for both axial positions, the calculations with $C_1 = 1.6$ match the measurements almost perfectly. In particular, the most important region in which flow return between fuel and air jet occurs is calculated extremely precisely. This is also true for the prediction of the fuel species that is characterized by the turbulent mixing process. The results discussed above show that the standard k-ϵ turbulence model, with the correction of the parameter C_1 in the ϵ-equation, is suitable for the prediction of the flow pattern in a multijet, multicomponent diffusion flame system.

Steady-State Combustion. The steady-state combustion process for the turbulent diffusion flame system has been calculated for the purpose of validating the combustion model and in particular, the probability density function used. In addition, the calculation serves to obtain a steady-state operating point to start the transient calculation for getting the frequency response of the flame.

In Fig. 9 the distribution of temperature and the mass fraction of the fuel is shown for the entire burner system of burner 1. The reaction zone can be clearly detected by the strong temperature gradients. As is typical for diffusion flames, the reaction zone is displaced on the lean air side. The influence of the radial component of velocity at the air exit of the burner on the distribution is given by the s-shaped reaction zone.

To evaluate the quality of the numerical results and to decide which pdf (see Eq. (11–13)) to choose for predicting the heat release in Fig. 10, a comparison between measurements [14] and three calculations with different pdfs is shown for four different axial positions (16 mm ($x/r_0 = 2$), 32 mm ($x/r_0 = 4$), 54 mm (x/r_0) = 6.8), and 64 mm ($x/r_0 = 8$) downstream of the burner exit). The single delta function (Eq. (11)) is not

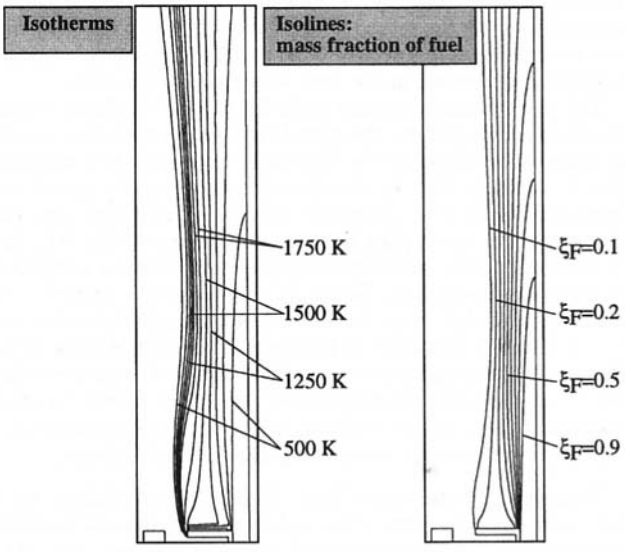

Fig. 9 Baffle-plate-stabilized burner: steady-state calculation

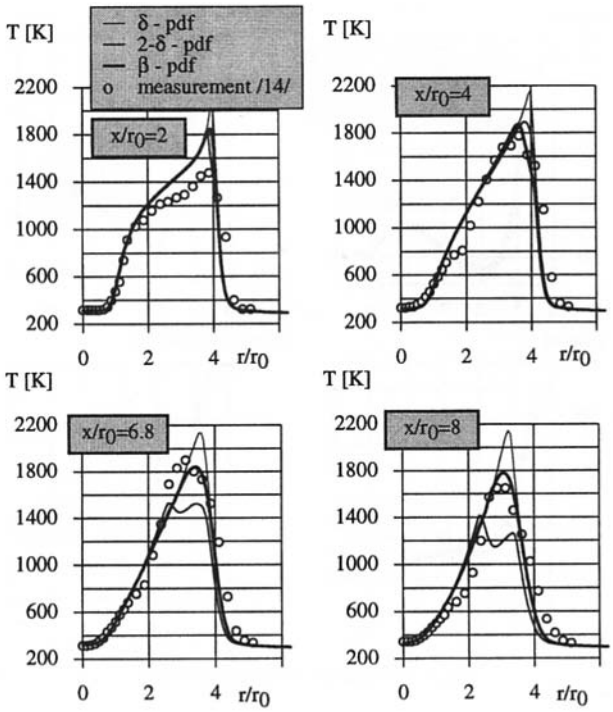

Fig. 10 Validation of the combustion model

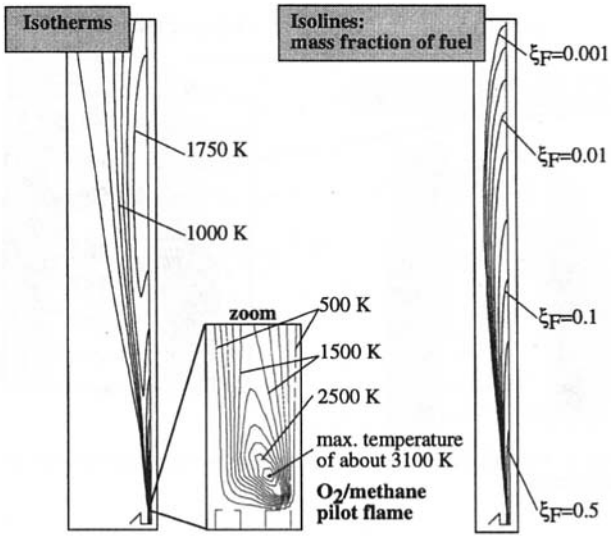

Fig. 11 O_2-stabilized burner: steady-state calculation

suitable for predicting the temperature distribution correctly. Due to the nature of this pdf, the effects of turbulence on the mixture fraction f are neglected. Consequently, the predicted temperatures are too high compared to reality. The maximum temperature of 2200 K is almost equal to the adiabatic flame temperature of methane. This result shows how important it is to consider the interaction between turbulence and combustion, especially for gas turbine combustors.

Near the burner exit, there is no significant difference between the double delta function (Eq. (12)) and the beta function (Eq. (13)). This changes further downstream of the burner. For some reason, the double delta function tends to underestimate the temperature and shows two similar peaks one on the lean side and one on the rich side of the flame. These results demonstrate that the beta-pdf gives the best results for the important temperature distribution. The calculated temperature only overestimates measurements very near to the burner exit. This can be explained by the fact that chemical kinetic effects are neglected by the mixed is burnt model and by the temperature measurement that seems to have a slight tendency to underestimate temperature in the very rich zone of the flame.

The steady-state operation point for the O_2-stabilized burner has been calculated by the turbulence and combustion model as discussed in detail above. The temperature and fuel distribution is shown in Fig. 11. Some modification of the model has been introduced due to the fact that three jets (fuel, air, and O_2) exist. The small pilot flame is also shown in Fig. 11. The O_2-methane flame produces very high temperatures compared to the main air-methane flame. As proven by the experiments of Priesmeier [6], this pilot flame has no significant influence on the dynamic behavior of the main flame, but instead stabilizes the flame at the burner exit. It is important to mention that only $\frac{1}{4}$ of the entire computational domain is shown in axial direction in this figure. Because of the lean configuration, all fuel is burnt inside the complete computational domain.

Transient Flame Modeling. Transient calculations have been performed for burner 2 in order to obtain the unit function response that can be transferred into frequency space by a Laplace Transformation. Therefore, after the converged steady-state solution is obtained, the mass flow rate at the air inlet has been increased by 20 percent of the operation point mass flow rate. One attempt has also been made to check the linearity of the system with 5 percent jump height, but the result, the unit function response, shows no significant difference. Thus, it can be concluded that linearity of the system exists, at least for a jump height up to 20 percent. Figure 12 displays the unit function response $h(t)$ calculated, which is defined as the ratio of the heat release to the mass flow jump at the burner inlet (Eq. 1). For a time of zero, $h(t)$ is zero by definition—if we remember that $\dot{q}_{\text{flame}}$ is only the difference between the transient heat release and the steady-state heat release of the operation point. For times going to infinity, $h(t)$ is again zero, which is due to the fact that all methane is burnt inside the computational domain. The unit function response can be divided into three parts, as is shown in Fig. 12. In part 1, the time is in the order of the length of the computational domain (2 m) divided by the sound velocity, which differs between 350.0 m/s for the unburnt and 850.0 m/s for the hottest zones of the exhaust gas. In this part there is a short period of low amplification (from $t = 0$ s to $t = 6$ ms). This can be explained by the transportation of the disturbance with sound velocity. After this period the combustion process is disturbed; this leads to a lower heat release than the steady-state heat release. In the third part, the combustion process is strongly amplified leading to higher heat release. After 0.5 s, the steady-state condition is reached again and the flame produces the same heat release as before. Integrating $h(t)$ over the time, there is much more heat produced. This can be explained by looking at the shape of the flame. After increasing the air mass flow, the mixing process is improved resulting in a shorter flame than the flame before the jump. This means that

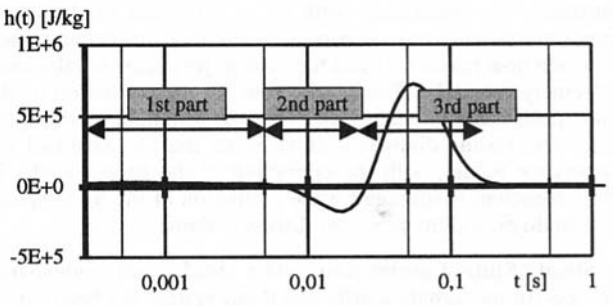

Fig. 12 Unit function of the turbulent diffusion flame

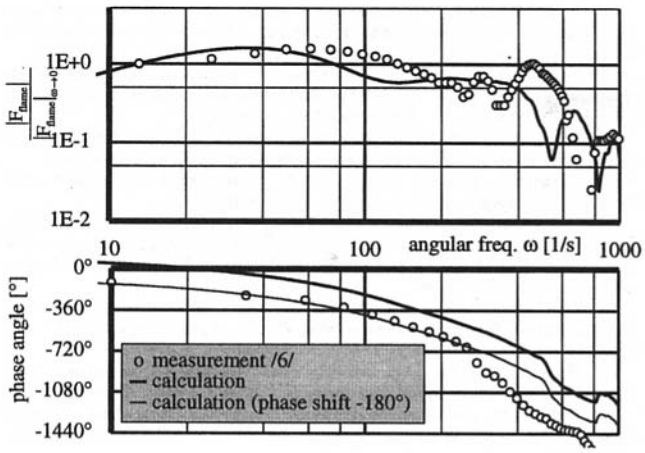

Fig. 13 Flame frequency response

less unburnt methane is stored and the difference must have been burnt, thus producing heat.

The third part is most significant for the dynamic behavior of the flame; this can be clearly seen by looking at the frequency response shown in Fig. 13 in Bode's diagram. In this figure, the experimental results [6] can be compared to the numerical calculation of the dynamic behavior. The magnitude of the frequency response is normalized by the magnitude for low frequencies [6]. The principle behavior of the flame, which is characterized by a higher-order time element with a delay time, can be described sufficiently accurately. The magnitude of the frequency response shows high values up to an angular frequency of about 100 1/s. After that, there is only a small decrease in the magnitude up to an angular frequency of about 400 1/s, which can be identified as the sharp cutoff. This means that, in principle, this turbulent diffusion flame can amplify self-induced oscillations over a wide angular-frequency range. The comparison between the magnitude of the frequency response calculated with the measured one shows fairly good agreement. Some discrepancies of the phase angle between measurement and calculation have to be mentioned. Up to an angular frequency of 250 1/s there exists a constant phase shift of −180 deg between the measurement and the calculation. This is corresponding to a sign change in the frequency response, which can perhaps be explained by different definitions of the normalization. In any case, the principal behavior of the phase of the frequency response can be predicted perfectly. The flame shows the characteristics of a perfect delay time element up to an angular frequency of 500 1/s. For higher frequencies, the phase angle decreases faster because part 2 of the unit function response becomes dominant. This behavior has also been measured by Priesmeier [6], but the significant angular frequency is smaller (250 1/s). This can be explained due to the fact that kinetic effects are neglected, the flame reacts faster to a disturbance near the burner exit than in reality. To summarize, for low angular frequencies the dynamic behavior of the turbulent diffusion flame can be described almost perfectly with the mixed is burnt model used; for higher angular frequencies (corresponding to the region near the burner exit) the influence of chemical kinetics becomes more important. Therefore, future work should concentrate on this influence in combination with turbulence transport mechanisms.

Nevertheless, the results are very encouraging. Flame frequency responses are the most important factor in investigations on self-induced combustion-driven oscillations. The results show that the numerical mechanism discussed above is suitable for predicting the dynamic behavior of such complex flame configurations. In addition, with experimental work, the principal influences of changing burner configurations, combustion parameters, etc. can now be discussed much more easily.

All results were obtained on an HP715 workstation. Almost 30 percent of computer time was needed to calculate the steady-state operation point. Having the experience with this model, it is now possible to obtain a frequency response of a turbulent diffusion flame in less than one month using modern state of the art workstation hardware.

Summary and Conclusion

A new method has been presented for the numerical prediction of the dynamic behavior of flames. Frequency responses which describe this behavior are the most important element of investigations on self-induced, combustion-driven oscillations. Due to a reliable operation of a gas turbine, these oscillations must be provided.

To obtain the frequency response, numerical simulation (using a three-dimensional Navier-Stokes Code) of the steady-state operation point is performed, followed by a transient simulation of the combustion process following a sudden increase in the mass flow rate at the burner inlet. This simulation leads to the unit function response that can be transferred into frequency space by a Laplace transformation. The method which, in principle, is suitable for both premixed and diffusion flame systems has first been adapted for turbulent diffusion flames.

To evaluate the turbulence and the combustion models and to obtain the steady-state operation point, simulations of the cold and hot steady-state flow of two different diffusion flame systems were initially performed. The results can be summarized as follows:

1. The standard k-ϵ turbulence model is suitable for these systems with a well-known correction of the production term in the dissipation equation. The complex flow configuration including the internal flow inside the burner can be predicted extremely precisely.
2. Using the beta-pdf to take into account turbulence effects on the combustion process, the important heat release can be predicted sufficiently accurately. There is only one region where the temperature is overpredicted, i.e., very near to the burner exit. This can be explained using the mixed-is-burnt model, which neglects chemical kinetics.

After a sudden jump in the air mass flow rate at the inlet, transient numerical simulation generates the unit function response of the flame. The important characteristics of the dynamic behavior of the flame can be discussed, as follows:

1. Up to a delay time of 5 ms only low amplification exists.
2. After a period in which the combustion process is disturbed (less heat is released compared to the steady-state operation point) high amplification follows. This amplification starts after 0.02 s.
3. After 0.5 s the steady-state operation point is reached again.
4. Integrated over time, more heat is released due to the fact that the flame is shorter after the jump, leading to less fuel stored. The difference must have been burnt during the time period.

The frequency response is obtained by a Laplace Transformation of the unit function response. It can be compared with measurements of this diffusion flame system. It can be concluded that:

1. The principal behavior of the flame collaborates well with the measurements.
2. Due to the high values of the frequency response, the possibility of amplification of self-induced combustion driven oscillations exists.
3. The phase angle shows the typical trend of an element with a delay time. Compared to the measurements the phase angle correlates almost perfectly up to a special angular frequency. After that the predicted delay time is too small.

This can again be explained by the fact that the chemical kinetics are neglected.

Nevertheless, the results show the feasibility of the procedure and help to clarify the dynamic flame behavior in much more detail. Future work should also concentrate on the influence of chemical kinetics on diffusion flames, which are mainly controlled by the turbulent mixing process. A second very important aspect is the influence of high pressure on the dynamic flame behavior that is typical for gas turbine applications.

Acknowledgment

The authors would like to thank the "Deutsche Forschungsgemeinschaft" for sponsoring this work by the Graduiertenkolleg "Turbulenz und Verbrennung" at the RWTH Aachen.

References

1 Baade, P. K., 1974, "Selbsterregte Schwingungen in Gasbrennern," Klima Kälte Ingenieur.

2 Bohn, D., and Deuker, E., 1993, "An Acoustical Model to Predict Combustion Driven Oscillations," presented at the 20th International Congress on Combustion Engines (CIMAC), London.

3 Deuker, E., 1995, "Ein Beitrag zur Vorausberechnung des akustischen Stabilitätsverhaltens von Gasturbinenbrennkammern mittels theoretischer und experimenteller Analyse von Brennkammerschwingungen," Ph.D. thesis, RWTH Aachen, Germany.

4 Lenz, W., 1980, "Die dynamischen Eigenschaften von Flammen und ihr Einfluß auf die Entstehung selbsterregter Brennkammer-schwingungen," Ph.D. thesis, Uni Karlsruhe (T.H.), Germany.

5 Lang, W., 1986, "Dynamik und Stabilität selbsterregter Verbrennungsschwingungen beim Auftreten mehrerer Frequenzen. Ein erweitertes Stabilitätskriterium" Ph.D. thesis, TU München, Germany.

6 Priesmeier, U., 1987, "Das dynamische Verhalten von Axialstrahl-Diffusionsflammen und dessen Bedeutung für selbsterregte Brennkammerschwingungen," Ph.D. thesis, Uni Karlsruhe (T.H.), Germany.

7 Merk, H. J., 1956, "An Analysis of Unstable Combustion of Premixed Gases," presented at the Sixth Symposium (International) on Combustion.

8 Becker, R., and Günther, R., 1973, "Niederfrequente nichtakustische Druckschwingungen in Brennkammern," Chemie-Ing.-Techn.

9 Bohn, D., and Krüger, U., 1994, "Experimental and Theoretical Investigations on the Dynamic Behaviour of Flames Typical Used in Gas Turbine Combustors," Numerical Modelling in Continuum Mechanics, Proceedings of the 2nd Summer Conference, Prague.

10 Van Dormal, J. P., and Raithby, G. D., 1984, "Enhancements of the SIMPLE Method for Predicting Incompressible Flows," *Numer. Heat Transfer,* Vol. 7, pp. 147–163.

11 Rhie, C. M., 1981, "A numerical study of the flow past an isolated airfoil with separation," Ph.D. thesis, University of Illinois at Urbana-Champaign, IL.

12 Rhie, C. M., and Chow, W. L., 1983, "Numerical Study of the Turbulent Flow Past an Airfoil With Trailing Edge Separation," *AIAA J1,* Vol. 21, pp. 1527–1532.

13 Prade, B., 1993, "Experimentelle und theoretische Untersuchung zum Abblaseverhalten von turbulenten Stauscheibendiffusionsflammen," Ph.D. thesis, Uni Karlsruhe (T.H.), Germany.

14 Leuckel, W., "SFB 169—Hochbelastete Brennräume—stationäre Gleichdruckverbrennung," Uni Karlsruhe (T.H.), Germany.

15 Matsui, Y., 1981, "An Experimental Study on Pyro-Acoustic Amplification of Premixed Laminar Flames," *Combustion and Flame,* Vol. 43, pp. 199–2009.

16 Sugimoto, T., and Matsui, Y., 1982, "An Experimental Study on the Dynamic Behavior of Premixed Laminar Flames," presented at the Nineteenth Symposium (International) on Combustion/The Combustion Institute, pp. 245–250.

J. R. Seume

N. Vortmeyer

W. Krause

Siemens Power Generation (KWU),
10553 Berlin, Germany

J. Hermann

C.-C. Hantschk

P. Zangl

S. Gleis

D. Vortmeyer

Lehrstuhl B. Fuer Thermodynamik,
Technical University of Munich, Germany

A. Orthmann

pad Software,
Haar-Salmdorf, Germany

Application of Active Combustion Instability Control to a Heavy Duty Gas Turbine

During the prototype shop tests, the Model V84.3A ring combustor gas turbine unexpectedly exhibited a noticeable "humming" caused by self-excited flame vibrations in the combustion chamber for certain operating conditions. The amplitudes of the pressure fluctuations in the combustor were unusually high when compared to the previous experience with silo combustor machines. As part of the optimization program, the humming was investigated and analyzed. To date, combustion instabilities in real, complex combustors cannot be predicted analytically during the design phase. Therefore, and as a preventive measure against future surprises by "humming", a feedback system was developed which counteracts combustion instabilities by modulation of the fuel flow rate with rapid valves (active instability control, AIC). The AIC achieved a reduction of combustion-induced pressure amplitudes by 86 percent. The combustion instability in the Model V84.3A gas turbine was eliminated by changes of the combustor design. Therefore, the AIC is not required for the operation of customer gas turbines.

Introduction

The Model V84.3A was shop tested and optimized in the Berlin test facility (Boehm et al., 1996) as the first of the Vx4.3A Series gas turbines (Fig. 1) with a new ring combustor design (Becker et al., 1996). The machine unexpectedly exhibited self-excited combustion oscillations under certain operating conditions in the premixed gas combustion mode. The pressure oscillations in the combustion chamber reached several hundred mbar, which is an unusually high value that had not been observed in silo combustor machines.

The instabilities were studied and subsequently resolved by passive design measures. To allow a quick and flexible response to future flame instabilities, an active combustion instability control system was developed in parallel with the combustion optimization work. This Active Instability Control system is the subject of the present paper.

Self-Excited Combustion Instabilities

In closed combustion systems, a feedback between the heat release rate of the flame and the acoustics in the combustion chamber can occur. Fluctuations in the heat release of the combustion excite an acoustic pressure field in the combustion chamber that, in turn, causes new fluctuations of the heat release rate. If the fluctuations of the pressure are nearly in phase with those of the energy release rate, i.e., if the Rayleigh criterion (Rayleigh 1878) is fulfilled, a self-amplification of the oscillations occurs. This phenomenon is called self-excited combustion instability or self-excited combustion oscillation.

Combustion instabilities often cause high pressure amplitudes and are accompanied by an increased heat transfer to the combustion chamber walls which impose high mechanical and thermal loads on the system. Combustion oscillations can lead to high noise emissions as well as to damage to parts of the machine. Their suppression or elimination, therefore, is an important task in engineering.

Analysis of Combustion Oscillations in the Model V84.3A Gas Turbine

To be able to resolve the problem in the Model V84.3A gas turbine, the phenomenon was investigated experimentally.

The focus of the investigations was the measurement of the dynamic pressure at different locations in the combustion chamber along with the simultaneous measurement of the rate of heat release in the combustion at these locations. The oscillations of heat release were detected by measuring the C_2 emission intensity at a wavelength of 516.7 nm. The radiation of the C_2 radical, which is an intermediate product of the combustion, is approximately proportional to the heat release rate. The wavelength was filtered from the spectrum of the combustion radiation with a band-pass filter and was measured by a photomultiplier. An optical fiber was used to observe the flame radiation in the combustion chamber.

The pressure oscillations in the combustion chamber were measured by means of piezoelectrical pressure transducers. Special water-cooled probes were developed for the fiber optics and pressure transducers because of the high temperatures and pressure in the combustion chamber (up to approximately 1500°C and 17 bars).

Contributed by the International Gas Turbine Institute and presented at the ASME ASIA '97 Congress and Exhibition, September 30–October 2, 1997. Manuscript received by the ASME Headquarters July 1997. Paper No. 97-AA-119. Associate Technical Editor: H. A. Kidd.

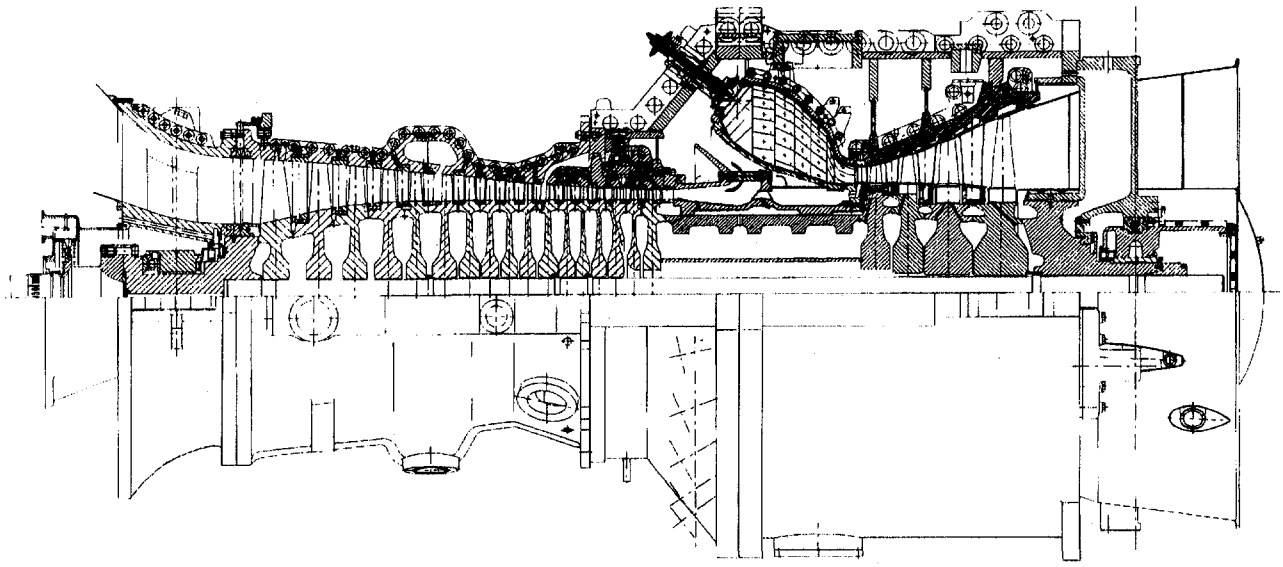

Fig. 1 Gas turbine: Vx4.3A Series

A frequency analysis of the measured signals showed 217 Hz and 433 Hz as the dominant frequencies excited in the combustion oscillations. Subsequently, several cross-power density spectra and transfer functions were calculated, each derived from two dynamic pressure signals measured at different locations of the combustion chamber. This modal analysis showed that the oscillations excite standing sound waves in the combustion chamber.

These standing waves typically consist of alternating regions of high and low sound-pressure amplitudes (pressure "antinodes" separated by "nodes") that are related to each other by a characteristic difference in phase. In case of the ring combustor, these regions are distributed along its circumferential coordinate and will be called azimuthal modes below (Fig. 2).

With a mean diameter of the ring combustor of approximately $d = 2.5$ m and a speed of sound of $c = 844$ m/s (assuming the mean temperature in the combustion chamber to be 1500°C) the relation

$$f_n = \frac{n \cdot c}{\pi \cdot d}$$

yields 215 Hz and 430 Hz for the frequency of the second and fourth azimuthal harmonic, respectively, which is in good agreement with the measurements. At the frequency of the first and third harmonic (108 Hz and 326 Hz) no significant amplitudes could be detected.

Potential Remedies

To date, it has been impossible to predict self-excited combustion oscillations in complex systems, and, thus, to take measures against them while still in the developing stage. If oscillations occur in systems in use, two approaches are available to deal with the problem.

Passive Versus Active Methods. Passive methods use changes in the operating parameters (e.g., the equivalence ratio), the design, or the geometry of the combustion system to hinder the self-excitation mechanism. They may reduce the prevailing sound pressure amplitudes to a tolerable level by dissipative measures, e.g., by mufflers or baffles (Culick, 1988).

Active methods, by contrast, use a feedback control loop. A quantity that is characteristic for the oscillating combustion is measured (e.g., pressure and/or heat release rate in the combustion chamber), processed by a controller, and used as the input signal for an actuator. This actuator influences the oscillating combustion in a way that is exactly counteracting the process of self-excitation, i.e., it acts anticyclically on the self-excited oscillations. This system is called active instability control (AIC). Two excellent reviews on AIC have been given recently by Candel (1992) and McManus et al. (1993).

Gas turbine experience reported by Scalzo, Sharkey, and Emmerling (1990), Vortmeyer et al. (1996) for coal gasification applications, and by Konrad et al. (1996) in an aeroengine show

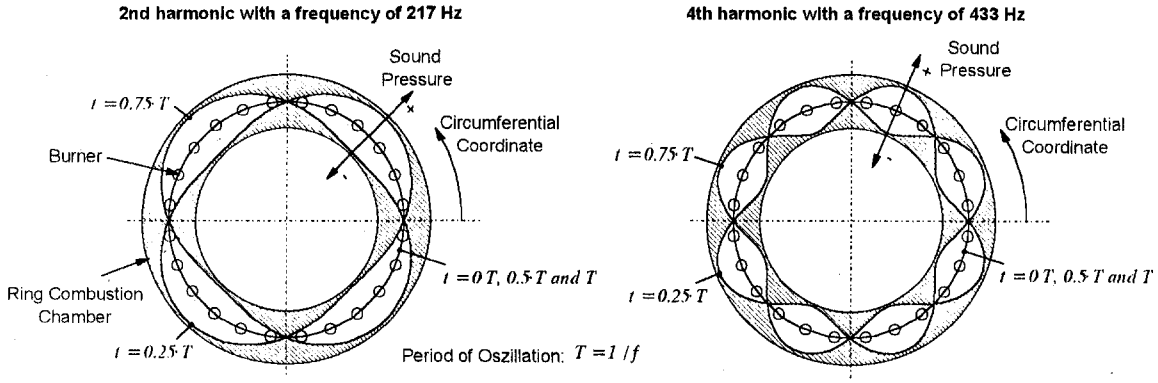

Fig. 2 Excited azimuthal modes in the combustion chamber

the successful application of passive measures, e.g., by changing combustor flow patterns as to avoid forced excitation of fluid vibrations.

In the present case, the following passive means were successfully applied: change of the operating parameters (e.g., pilot fuel); use of asymmetry in the fuel and air supply system (e.g., different pilot fuel orifices in neighboring burners); and acoustic decoupling of the interacting burners which oscillate with a characteristic phase shift (e.g., the mutual excitation of neighboring burners is reduced by baffels in the fuel supply lines connecting them).

In addition to such passive measures, the system for the active control of the combustion oscillations was developed and successfully implemented in the V84.3A in order to investigate the potential of the AIC, in general, and as a preventive measure against future instability problems that might occur again when greatly changing the operating range of the gas turbine. Since the AIC is implemented in the fuel system, the gas turbine itself need not be changed. Therefore, it is potentially implemented more quickly than design changes in the combustor.

In general, active measures against combustion oscillations influence either the fuel supply or the air/exhaust gas stream of the combustion process. When modulating the air or exhaust gases, the pressure oscillations caused by the combustion instability are eliminated by inversed sound pressure oscillations (''antisound''), e.g., induced by a loudspeaker. This method is limited to rather small combustion systems (Lang 1987; Poinsot 1988) because of the large amounts of air or exhaust gas that must be modulated in large combustors. This is certainly true in case of the V84.3A with a design exhaust mass flow rate of 445 kg/s.

Combustion oscillations can also be suppressed by modulation of the fuel flow rate, if the rate of fuel reaching the flame is kept anticyclical to the oscillations of the heat release rate of the flame. The advantage of this technique is that only rather moderate volume flow rates must be modulated (Hermann 1996; Hermann et al., 1996; Hantschk et al., 1996).

Due to the principle of the AIC, the modulation of either air/exhaust gas or fuel flow rate must take place at the frequency of the self-excited combustion oscillations. As these can often reach more than 1000 Hz, suitable actuators that meet these requirements must be found.

Selection of the AIC. The AIC system implemented with the V84.3A gas turbine works as follows: a pressure transducer measures the pressure oscillations in the combustion chamber. This signal is used as the input signal for the control unit which derives an input signal for the actuator that modulates the fuel flow rate. As described above, the resulting flow-rate oscillation affects the heat release rate in the combustion zone exactly opposite to the oscillation of the heat release rate caused by the self-excitation process. Thus, the actuator counteracts the combustion oscillations and at the same time those of the related quantities, e.g., the pressure.

To date, AIC had only been successful on a laboratory scale, i.e., with combustors of a thermal power of up to 1 MW. Furthermore, no experiences existed concerning the special requirements for an application of the AIC to systems similar to the ring combustor under consideration. The following three basic problems had to be solved for the operation on a ring combustor gas turbine:

1 In the premixed mode and at base load, the V84.3A uses about 9 kg/s of gas. Because of this high mass flow rate even a modulation of the fuel flow cannot be accomplished with existing actuators at the observed frequencies (217 Hz and 433 Hz). In general, possible actuators will be valves or magnetostrictive and piezoelectrical devices (Hantschk et al., 1996; Hermann et al., 1996; Hermann, 1996).
2 In case of the ring combustor machine, several control systems consisting of sensor, controller, and actuator are located in different positions along the circumference of the combustion chamber. Because of the azimuthal modes of the combustion instabilities, this means that the control devices are situated in different regions of the excited acoustic field. The prevailing oscillating quantities at these positions can strongly differ in their amplitude and phase, depending on the excited mode.
3 High temperature and pressure in the combustion chamber and limited accessibility are stringent requirements for the probes that can be used to obtain the input signal for the controller, i.e., the pressure.

Implementation of the AIC With the Model V84.3A Gas Turbine

Active Control Through Pilot Flames. In the premixed gas mode, each burner of the V84.3A operates with small additional diffusion flames that contribute approximately 10 percent of the total thermal power of the burner. These pilot flames stabilize the main premixed flame. Investigations of the dynamic behaviour of the combustion in the premixed gas mode showed a distinct dependence of the heat release of the main flame on the heat release of the smaller pilot flames.

By modulating the heat released by the pilot flames, e.g., by modulating the fuel flow rate, the heat release in the main flame can be influenced accordingly. Therefore, the AIC can modulate the large flame by controlling a small fraction of the fuel instead of the entire gas flow (Fig. 3).

A special high-speed valve, the direct drive valve (DDV) manufactured by MOOG Germany serves as an actuator for the modulation of the pilot gas flow. Due to its special design, the DDV can be used with frequencies of up to 400 Hz with a loss in amplitude of only about 4 dB.

Tuning the Pilot Gas System. The success of the AIC is strongly dependent on the pressure amplitudes in the pilot gas pipes that can be induced with the actuator. Higher pressure amplitudes in the pilot gas lines cause higher modulation amplitudes of the pilot gas flow into the combustion chamber, and, correspondingly, increase the heat release in the flame. To obtain high pressure amplitudes in the pilot gas supply system, it is of great importance to tune the pipe length acoustically to the frequency to be controlled, as the acoustics play an important role in these pipes with the frequencies in question.

The DDV induces an acoustic pressure field in these pipes. The amplitudes that can be obtained in this field depend on the resonance behavior of the pilot gas pipe connecting the DDV to the burner. This resonant behavior, in turn, is mainly a function of the pipe geometry, especially its length. Since the complex pilot gas piping system makes the tuning difficult and also causes additional damping, it is useful to install a suitable device

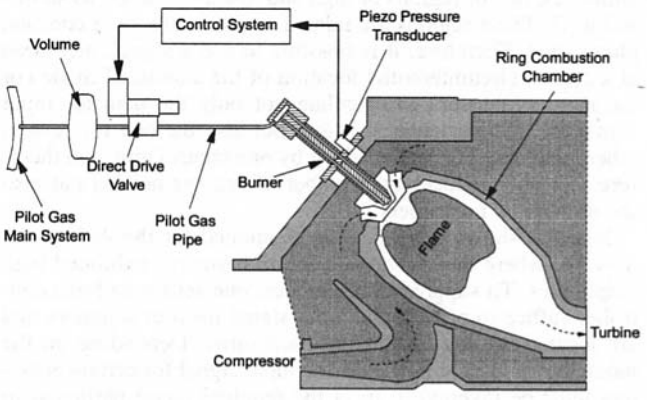

Fig. 3 Schematic of the AIC applied to the Model V84.3A gas turbine

for the acoustic decoupling of those sections of the pilot gas system which are located upstream of the actuator (Hantschk et al., 1996; Hermann, 1996).

Retuned Acoustics or Active Control? The attention given above to the acoustics of the pilot gas system and the observed sensitivity of the main flame to the behavior of the pilot flames might lead to the conclusion that the observed combustion oscillations are caused by the interaction between the pilot gas and the combustion chamber itself, with the pilot flames as the coupling elements between acoustics and combustion.

If the pilot gas system and the combustion chamber were interacting with each other in the way described above, then the ocurrence of self-excited combustion oscillations and the characteristics of these would strongly depend on the acoustics in the pilot gas system. Any change in the acoustic behavior of the pilot gas system would most likely cause a significant change in the behavior of the combustion oscillations including their onset or disappearance. This was not observed.

During the prototype tests of Model V84.3A, the pilot gas system underwent various changes in the geometry prior and during the implementation of the AIC, e.g., different overall lengths of the pilot gas tubes were used at different times for design reasons, a plenum chamber ("volume" in Fig. 3) for the acoustic decoupling was inserted, the valves were inserted, and tests with different sizes of valve openings were performed. Each of these measures causes a significant change in the acoustic characteristics of the pilot gas systems. Nevertheless, with the AIC turned off, neither of these measures caused any significant change in the combustion oscillations, which shows that these are based on an excitation mechanism that is independent on the pilot gas tubes' acoustics. The latter, however, are important for the amplitude of modulation of the pilot gas flow as outlined above.

Use of Symmetry to Reduce Feedback Loops. Each of the 24 burners of the V84.3A was equipped with a DDV valve for the AIC. Due to the nature of the excited azimuthal modes, the actuators are located in different regions of the acoustic field where different phases and amplitudes of the combustion oscillation must be controlled. To cope with this problem, each burner could be supplied with an independent control unit together with the corresponding sensor and actuator. In this case, the input signal for a certain DDV valve could be obtained from the pressure signal measured at the same location, ensuring that the induced modulation of the heat release rate is indeed anticyclical to the self-excited heat release oscillation at this actual location. This approach would require 24 feedback control loops.

The number of necessary sensors and control units may be reduced by using the symmetry of azimuthal modes. This symmetry is marked by a characteristic distribution of nodes and antinodes, i.e., of regions of high and low amplitudes, as shown in Fig. 3. These regions are related to each other by a constant phase shift. Therefore, it is possible to use a signal, measured at a certain circumferential location of the azimuthal mode (or the ring combustor) to calculate not only the actuator input signal for this particular location, but also the one for several other locations. This can be done by one control unit, and therefore, not only reduces the number of sensors needed but also the number of controllers.

Figure 4 shows this principle as applied for the AIC of the V84.3A, where the second and fourth harmonic exhibited high amplitudes. To suppress these modes, one sensor and one controller suffice to provide the input signal for four actuators that are located 90 deg apart from each other. Depending on the mode that is to be suppressed, the input signal for certain actuators must be inverted to meet the required phase particular to the position of the actuator. In summary, the configuration the

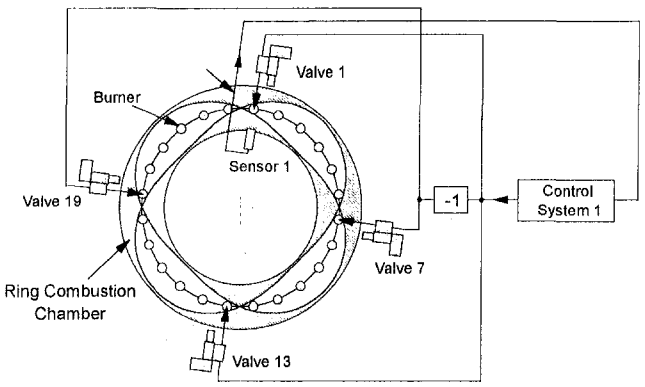

Fig. 4 Advantageous use of the symmetry of azimuthal modes, here shown for the second harmonic. One sensor and one controller provide input signals for four actuators.

AIC for the V84.3A was implemented using six independent control loops each consisting of a pressure sensor and a control unit as well as 4 valves as actuators, resulting in a total of 24 actuators. The essential part of the control unit is the signal processor that is based on a control algorithm working in the frequency domain.

Choice of the AIC Controller Input-Signal. Various sensors and probes were tested for the acquisition of a suitable input signal for the controller. As a measure for the heat release rate in the combustion, the OH radical emission may be used as the input signal for the controller. This signal requires the observation of the entire combustion zone of one burner at all times. This is a very difficult task as only fiber optics that have a very limited view angle can access the combustion chamber.

The pressure in the combustion chamber, by contrast, can be measured indirectly under favourable circumstances. If the location of the measurement is chosen well, a pressure signal which is proportional to the pressure in the combustion chamber may be measured outside the combustion chamber itself, in a location which is more accessible.

In case of the V84.3A, the pressure was measured with water cooled probes at positions close to the burners that are acoustically coupled to the combustion chamber through the air supply system, but are located outside of the actual combustion chamber. These indirect pressure signals were first compared to those inside the combustor to ensure that amplitude and phase of the signals are sufficiently correlated to yield a suitable controller input for the AIC.

Results and Discussion

Typical AIC Performance. During prototype shop tests of the 170 MW Model V84.3A ring combustor gas turbine, self-excited combustion oscillations were observed in the premixed-gas mode at base load. The AIC system described above reduced these oscillations at the dominant frequency of 433 Hz by up to 17 dB. With the active control turned off, the measured sound pressure amplitudes rose to 210 mbar (corresponding to a sound pressure level of 177 dB), while they fell as low as 30 mbar with the AIC system active.

Operating Parameters Observed. Figure 5 shows the relevant quantities versus time during test operation. Note that these measurements were taken at base load with all working conditions kept constant, except for the AIC parameters. Also, the mean total mass flow rate of the pilot gas is kept constant at all times, independently of the modulation of the pilot gas with the AIC. The following quantities are presented in Figure 5: the control parameters (gain and phase shift between the actuator input signal

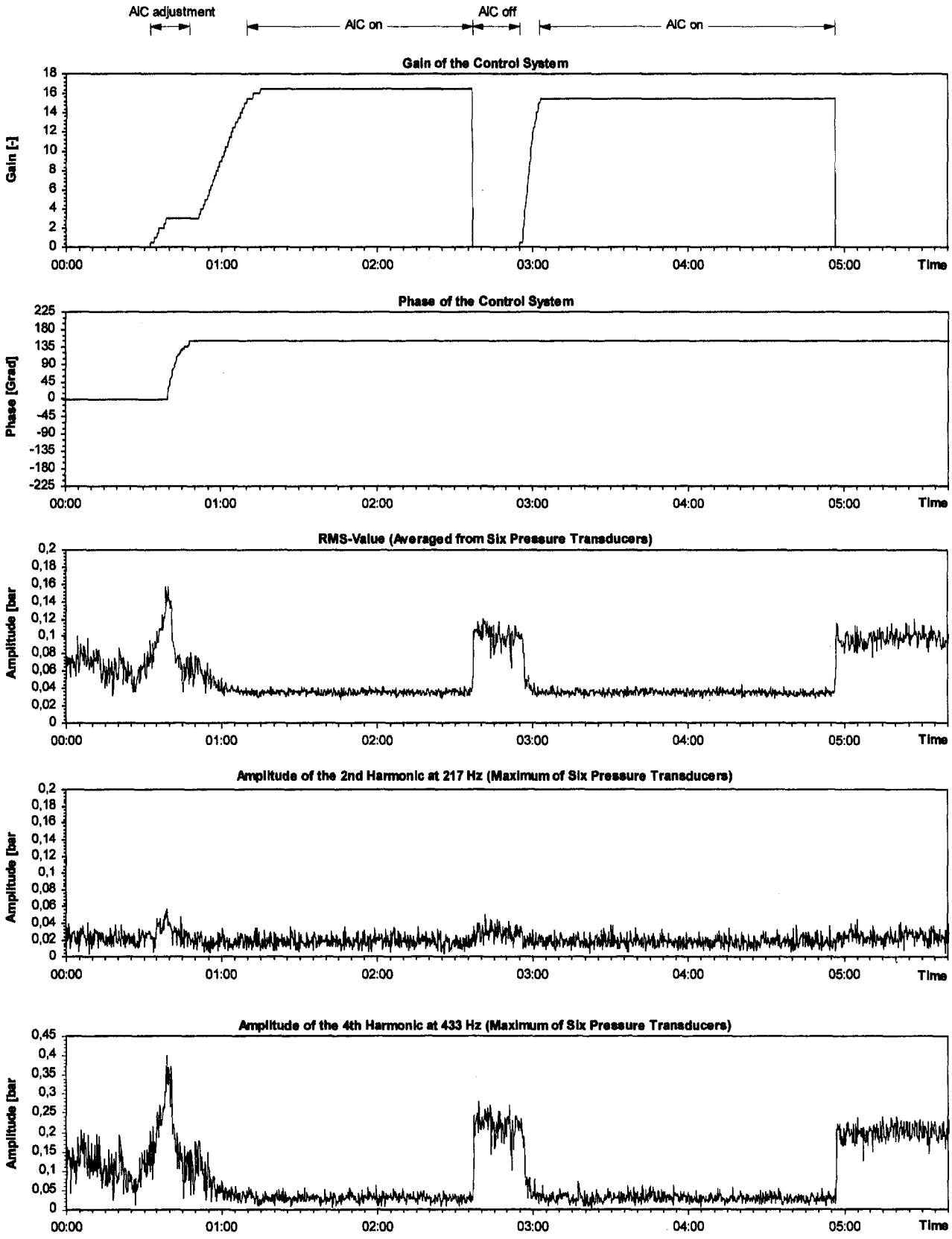

Fig. 5 Test operation of the AIC at base load

and the combustor pressure which is the input to the controller); the RMS-value of the sound pressure in the combustion chamber (average of six pressure transducers); and the maximum amplitude (among the 6 transducers) for the two dominant harmonics (217 Hz and 433 Hz) of the sound pressure in the combustion chamber. "Gain" above denotes a factor by which the DDV driver module multiplies the output signal of the valve controller. It is therefore given without units.

Discussion of the Results. During the first 32 sec of the shown period, the gain is set to zero and the pressure amplitudes in the combustion chamber are high due to the combustion oscillations. Short intervals of a few seconds with comparatively low amplitudes that can be observed do not indicate stable operating conditions. Usually small perturbations that are always present in the system cause the immediate recommencement of the oscillations. These conditions do not allow a safe, steady operation of the machine.

In the beginning of the tests, the controller parameters are adjusted for the frequency of the fourth harmonic at 433 Hz. After a first increase of the gain to about 3 with the phase shift still at 0 deg, a slight augmentation of the oscillations can be observed. With the phase shift adjusted to 150 deg, the oscillations are significantly suppressed. The dependence of the effect of the system on the phase shift is apparent. This shows that the suppression is the result of real feedback by the control loop, and is not caused by arbitrarily disturbing the self-excitation process. Increasing the gain to about 17 leads to a further reduction of the amplitudes of the combustion oscillations. Subsequently the amplification is switched off, which leads to the immediate resurgence of strong oscillations. These subside instantly after the gain is reset to the previous level.

Limitations and Further Development. Further investigations of the effects of the AIC showed a dependence of the required control parameters (gain and phase shift) on the operating conditions of the gas turbine (e.g., power level, pilot gas fraction). AIC operating parameters, which result in a clear reduction of the oscillations for certain gas turbine operating conditions, can cause a significant loss in performance of the control system during other gas turbine operating conditions. In the worst case, the heat release rate modulation induced by the controller can be in phase with the one resulting from the self-excitation, which results in a positive feedback and a further amplification of the undesired oscillations. Therefore, the control parameters must be adjusted to the operating condition quickly. Since the control parameters were set manually, difficulties arose when the operating conditions were subject to sudden changes. Therefore, an adaptive control algorithm is being developed that seeks the optimum settings for gain and phase shift.

The AIC controller used in the present study is only capable of controlling oscillations at one frequency. If more than one dominant frequency exists, the performance dropped noticeably for some operating conditions. Current projects address the development of an AIC system for the simultaneous suppression of multiple frequencies.

Future investigations must also address the influence of the AIC on the emission of pollutants. During the experiments presented above, the individual periods during which the AIC-System was active were too short to allow sound conclusions from measurements of these emissions.

Summary and Conclusions

Self-excited combustion instabilities in a ring combustor gas turbine were successfully reduced: during the prototype shop tests, the 170 MW Model V84.3A heavy duty gas turbine exhibited strong self-excited combustion oscillations in the premixed gas mode with pressure amplitudes reaching several hundred mbar in the ring combustor. The oscillations were eliminated by design changes to the combustor and the machine now operates without combustion instabilities.

Despite this success, investigations and tests were carried out to develop an active instability control by means of a feedback control loop that anticyclically influences the combustion. This AIC serves as both a research tool to gain further understanding of the mechanisms of combustion instabilities and as an additional option for the control of combustion instabilities in the future.

Due to the geometry of the ring combustor, azimuthal acoustic modes are excited by the oscillations. These azimuthal modes permit the use symmetry in reducing the number of control loops. The considerable mass flow rates of air and fuel encountered in gas turbines of this size require the implementation of an effective active control by way of the pilot gas system.

The AIC system implemented achieved a reduction of the observed combustion-induced pressure amplitudes by 86 percent or 17 dB. Thus, the AIC method was taken beyond the laboratory scale and successfully applied to a heavy duty gas turbine. However, two further steps of development must be taken prior to a successful industrial application:

1 The AIC control algorithm must be extended to operate with multiple simultaneous frequencies.
2 The suitable control parameters proved to be dependent upon the operating conditions of the gas turbine. Therefore, further work focusses on the development of a adaptive control strategy.

With these two improvements, the AIC will represent a technically viable, short-term alternative to combustor design changes during gas turbine trials and combustor development work.

References

Becker, B., Schulten, W., Schetter, B., 1996, "Combustion System Development for Dry Low-NO_x Emission And High Turbine Inlet Temperature," ASME Paper No. 96-TA-26, presented November 5–7, 1996 at he ASME Turbo Asia Conference, Jakarta, Indonesia.

Boehm, W., Raake, D., Regnery, D., Seume, J., and Terjung, K., 1996, "Testing the Model V84.3A Gas Turbine—Experimental Techniques and Results," ASME Paper No. 96-TA-14, presented November 5–7, 1996 at the ASME Turbo Asia Conference, Jakarta, Indonesia.

Culick, F. E. C., 1988, "Combustion Instabilities in Liquid-Fuelled Propulsion Systems—An Overview," AGARD Conference on Combustion Instabilities in Liquid-Fuelled Propulsion Systems, Bath, AGARD-CP-450, pp. 1-1–1-73.

Candel, S. M., 1992, "Combustion Instability Coupled by Pressure Waves and their Active Control," invited general lecture, 25th Int. Symp. on Combustion, Sydney, Australia.

Hantschk, C., Hermann, J., and Vortmeyer, D., 1996, "Active Instability Control with Direct Drive Servo Valves in Liquid-Fuelled Combustion Systems," *26th Int. Symp. on Combustion,* Naples, Italy.

Hermann, J., Gleis, S., and Vortmeyer, D., 1996, "Active Instability Control (AIC) of Spray Combustors by Modulation of the Liquid Fuel Flow Rate," *Combust. Sci. and Tech.,* Vol. 118, pp. 1–25.

Hermann, J., 1996, "Anregungsmechanismen und aktive Dämpfung (AIC) selbsterregter Verbrennungsschwingungen in Flüssigkraftstoffsystemen," dissertation, TU München.

Konrad, W., Brehm, B., Kameier, F., Freeman, C., Day, I. J., 1996, "Combustion Instability Investigations On The BR710 Jet Engine," ASME Paper No. 96-TA-36, presented November 5–7, 1996 at the ASME Turbo Asia Conference, Jakarta, Indonesia.

Lang, W., Poinsot, T., and Candel, S., 1987, "Active Control of Combustion Instability," *Combustion and Flame,* Vol. 70, pp. 281–289.

McManus, K. R., Poinsot, T., Candel, S. M., 1993, "A Review of Active Control of Combustion Instabilities," *Prog. Energy Combust. Sci.,* Vol. 19, pp. 1–29.

Poinsot, T., Veynante, Bourienne, F., Candel, S., and Esposito, E., 1988, "Initiation and Suppression of Combustion Instabilities by Active Control," *22nd Symposium (International) on Combustion,* Seattle, pp. 1363–1370.

Rayleigh, Lord J. W. S., 1878, "The Explanation of Certain Acoustical Phenomena," *Nature,* July 18, pp. 319–321.

Scalzo, A. J., Sharkey, W. T., Emmerling, W. C., 1996, "Solution of Combustor Noise in a Coal Gasification Cogeneration Application of 100-MW-Class Combustion Turbines," ASME JOURNAL OF ENGINEERING FOR GAS TURBINES AND POWER, Vol. 112, pp. 39.

Vortmeyer, N., Huth, M., Becker, B., Karg, J., Emsperger, W., 1996, "Experience in the Design and Operation of Syngas Gas Turbines," presented October 2–4, at the EPRI 1996 Gasification Technologies Conference, San Francisco, California.

Industrial Gas Turbine Performance Uprates: Tips, Tricks, and Traps

T. L. Ragland
Engine Performance Group Leader,
Solar Turbines Incorporated,
2200 Pacific Hwy.,
P.O. Box 85376, MS C-9,
San Diego, CA 92186-5376

After industrial gas turbines have been in production for some amount of time, there is often an opportunity to improve or uprate the engine's output power, cycle efficiency, or both. Typically, the manufacturer would like to provide these uprates without compromising the proven reliability and durability of the product. Further, the manufacturer would like the development of this uprate to be low cost, low risk, and result in an improvement in customer value over that of the original design. This paper describes several options available for enhancing the performance of an existing industrial gas turbine engine, and discusses the implications for each option. Advantages and disadvantages of each option are given along with considerations that should be taken into account in selecting one option over another. Specific options discussed include dimensional scaling, improving component efficiencies, increasing massflow compressor zero staging, increasing firing temperature (thermal uprate), adding a recuperator, increasing cycle pressure ratio, and converting to a single shaft design. The implications on output power, cycle efficiency, off-design performance engine life or time between overhaul (TBO), engine cost, development time and cost, auxiliary requirements, and product support issues are discussed. Several examples are provided where these options have been successfully implemented in industrial gas turbine engines.

Introduction

High on the priority list of every gas turbine manufacturer is continuous improvements. Continuous improvements apply to every phase of the business process; technologies, products, processes, and business relationships. This paper discusses product improvements; specifically, those programs that improve engine output power and/or efficiency. These engine improvements are often referred to as engine uprates, but are also referred to as product improvements or product improvement programs (PIPs). Regardless of what name they go by, these programs have always been and will continue to be a major part of the gas turbine engine business.

Most design engineers that have worked on aircraft engine designs have probably noticed that aircraft power requirements tend to increase with time. This seemed to happen in the aircraft design and development phase when the total drag and total weight inevitably came out higher than projected and even after the aircraft was in production when mission requirements were expanded. Even after an aircraft was in service and mature, competitive and economic forces always dictated a need for more power and improved fuel efficiency while not compromising cost. A similar trend exists with industrial gas turbines. Regardless of the power size or application, customers' power needs tend to increase with time. Also, every user's need to improve profits puts pressure on industrial gas turbine suppliers to reduce fuel consumption and improve cost per unit of power, both on first cost and life cycle cost basis. This paper describes several methods for improving the performance of a mature industrial gas turbine engines. Both the advantages and disadvantages are discussed along with general comments on relative risks and impact on costs.

For comparison purposes, a fictional industrial gas turbine engine, which will be called the base engine, is described, and used as a basis for comparison between the different uprate methods. This will allow the performance improvements to be quantified and the different methods to be compared. Quantitatively, these improvements cannot be translated directly to other engines, but their trends in performance improvements, cost impacts, and risk should apply to most of todays industrial engines.

The incentive behind most gas turbine uprates is to be able to offer more value to the end users of the gas turbine. In evaluating a performance uprate to an engine with an established reputation, customers will first want to know how engine durability will be affected. In most cases, customers are not willing to accept noticeable reductions in either reliability, availability, or maintainability (RAM). Therefore, uprates that are perceived as putting established durability at risk will be more difficult to get accepted in the market place. This is why maintaining or improving existing durability is a key goal in all uprate programs.

Base Engine

To help make the discussion more meaningful, a fictional engine will be defined that will be called the base engine. We will assume that this engine is a mature product that was designed about 15 years ago with a good durability record and a good initial cost basis. As with most engines of this type, it can be assumed that it does not have state-of-the-art component or cycle efficiencies and that it does not take advantage of the most recent materials and manufacturing developments. A schematic of this base engine is shown in Fig. 1. The main cycle parameters for this base engine are listed in Table 1.

With this base engine defined, the various options available to provide uprates can now be evaluated.

Dimensional Scaling

One popular method of expanding a product line is dimensional scaling, which has been used successfully by several engine manufacturers. The goal of dimensional scaling is to get

Contributed by the International Gas Turbine Institute and presented at the International Gas Turbine and Aeroengine Congress and Exhibition, Orlando, FL, June 2–5, 1997. Manuscript received by the ASME Headquarters July 1997. Paper No. 97-GT-409. Associate Technical Editor: H. A. Kidd.

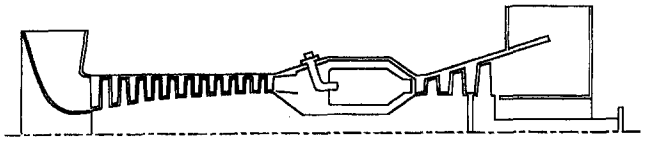

Fig. 1 Schematic of fictional base engine

a different size engine, usually larger (but can be smaller), that requires minimal development and retains the proven durability of the existing design. In its simplest form, dimensional scaling means that all the linear dimensions of an existing design are scaled (usually up) by a constant factor. The general rules of scaling are shown in Table 2.

When these rules of scaling are followed, most of the original aerodynamics and most of the original mechanical safety margins are not changed. This means that the original aerodynamic values of Mach numbers, velocity triangles, gas temperatures, and gas pressures are maintained in the new design. It also means that the original stress margins and the percent vibration and critical speed margins are maintained.

It would be nice if scaling would be as simple as adding a multiplier to all of the dimensions of the drawings, but it is not that simple. One important area of the design that does not scale is heat transfer characteristics, especially in the turbine cooling system. This area always has to be re-analyzed and usually requires some design modifications. However, these modifications can usually be limited to slight changes in the cooling flow percentages and small to moderate changes to the airfoil cooling passages.

The combustion system may also require some modifications. The scaled combustor case and combustor liner will usually work fine, but the amount and size of the liner dilution holes may require further modifications if the radial temperature profile entering the first stage turbine blade is to be maintained. In order to maintain or improve the original combustor exit pattern factor, the design and number of fuel injectors may also need to be changed. Scaling up a dry low NO_x (DLN) combustor could require a significant amount of redesign.

Any area of the design that uses standard hardware such as fasteners, tubing, connectors, etc. will usually need to be modified to accommodate available standard parts that are close to the scaled sizes.

From the rules of scaling, one would expect the power to be changed by the square of the scale factor and the cycle efficiency to remain unchanged. In practice, however, there are size-affected dimensions that will have small effects on performance. Mechanical tolerances and surface finishes usually do not scale. Mechanical tolerances can usually be improved as a design is scaled up, and airfoil surface finishes can usually be kept the same as airfoils are scaled up. Tip clearances and seal clearances may or may not scale depending on what mechanism sets the minimum values. Also, airfoil leading and trailing edge thicknesses usually have a minimum value in order to maintain adequate material properties. When airfoils are scaled up there is often a chance to reduce leading and trailing edges as a percentage of chord, thus improving airfoil efficiencies. Just the opposite happens when airfoils are scaled down. Often, the scaled-down leading and trailing edge values are too small to maintain adequate material properties during casting or they become very expensive to manufacture and must be increased. This usually results in a slight performance penalty.

Table 1 Main cycle parameters for base engine

Cycle Parameter	Value
Compressor Airflow (ω)	50.0 lb/sec (22.7 kg/sec)
Compressor Pressure Ratio (P/P)	10:1
Compressor Efficiency (η_c)	85%
Gas Producer Speed ($N_{G/P}$)	13,500 RPM
Turbine Rotor Inlet Temp. (TRIT)	1900°F (1038°C)
Gas Producer Turbine Efficiency ($\eta_{G/P}$)	88%
Power Turbine Efficiency ($\eta_{P/T}$)	89%
Power Turbine Speed ($N_{P/T}$)	13,000 RPM
Cycle Efficiency (η_{cy})	31.5%
Shaft Output Power (Hp_s)	7800 HP (5816 Kw)

Table 2 Rules of scaling

1. Linear dimensions scale directly with the scale factor.
2. Rotor speeds scale inversely with the scale factor.
3. Flows scale with the square of the scale factor.
4. Power scales with the square of the scale factor.
5. Weight and volume scale with the cube of the scale factor.

This leads to one of the subtle traps of dimensional scaling. It is nearly impossible to complete a scaled design without finding things in the design that can be improved. Many of these changes are legitimate and some are "must do," but the design team must be careful not to take on so many design improvements that they lose the proven integrity of the original design, and, at the same time, exceed their design and development schedule and budget.

If we were to apply a 1.5 scale factor to our base engine we would expect to get an engine that is 50 percent longer with 50 percent larger diameters that would have performance of 17,550 Hp (13,087 Kw) and 31.5 percent cycle efficiency, as shown in Table 3.

If we make some allowances for size effects (reduced tip clearances, constant surface finish, and reduced leakages through improved tolerances) on performance, we should be able to produce around 17,900 Hp (13,348 Kw) at a cycle efficiency of 32.0 percent.

Figure 2 shows an isometric view of a 1.5× scaled airfoil and Fig. 3 shows a schematic view of the original engine and a 1.5× scale of that schematic. These figures are included to point out that the volume of a part like the volume of an engine increases by the cube of the linear scaling factor.

One additional factor that does not scale is the manufacturer's recurring engine cost. This cost is a difficult factor to predict and each project will have to be evaluated independently. It stands to reason, however, that by scaling an engine up, the cost per unit of power (dollars per horsepower) should decrease. Figure 4 can be used to understand the trends in engine cost as a given design is scaled up or down. This figure indicates that for a given design (i.e., fixed complexity and technology level), the cost per unit of power decreases as the engine gets larger. The rate at which cost decreases will depend on the technology level or complexity of the design. Figure 4 also helps explain why we see the most advanced technologies in the largest engines. When new but expensive technologies become available, it is usually more cost effective to apply these technologies in the larger engines first.

Component Efficiency Improvements

As analytical tools, design methods, and manufacturing processes advance, it is often possible to improve the efficiency of

Table 3 Approximate performance for a 1.5× base engine

	Original	1.5X Scale (Direct)	1.5X Scale (Improved)
Output Power	7800 Hp (5816 Kw)	17,550 Hp (13,087 Kw)	17,900 Hp (13,348 Kw)
Cycle Eff.	31.5%	31.5%	32.0%
Airflow	50.0 lb/sec (22.7 Kg/sec)	112.5 lb/sec (51.0 Kg/sec)	113.0 lb/sec (51.3 Kg/sec)

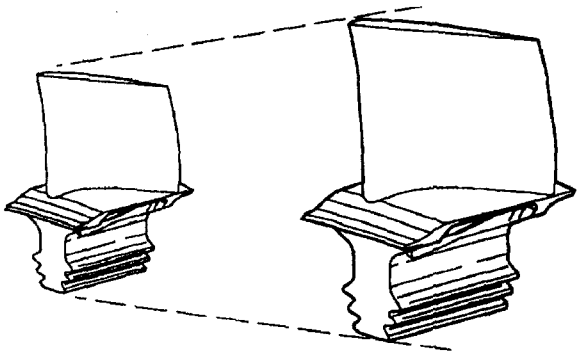

Fig. 2 Comparison of a base airfoil and a 1.5× scaled airfoil

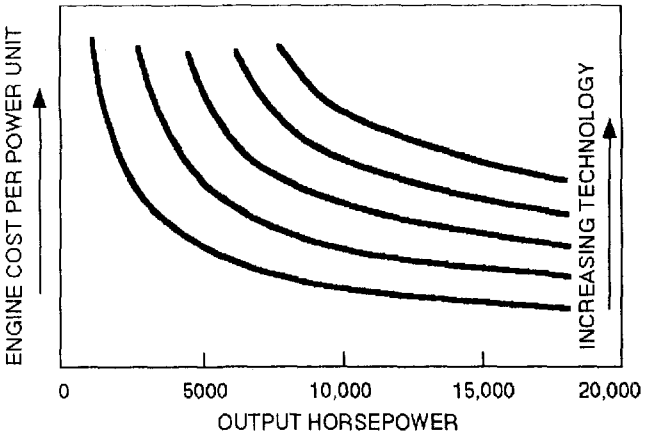

Fig. 4 Engine recurring cost trends

one or more components of a mature design. Referring back to our base engine, we can examine the results of various component improvements. If we assume a 1.0 percent efficiency improvement in the compressor, the gas producer turbine, and the power turbine, we can generate the values shown in Table 4. This table gives the performance improvements of our base engine if these improvements were made individually and if they were made concurrently.

For these methods of increasing performance to be attractive, the components in the existing design must first of all have room to be improved. Also, the cost of these improvements must be justified by the performance gains. If, for example, a completely new compressor must be designed and developed just to pick up one point in efficiency, this effort would be hard to justify. On the other hand, if one point in compressor efficiency could be gained just by reducing tip clearances and seal leakages, this might be easy to justify.

A good example of the latter is what Solar Turbines Incorporated did with their latest Taurus™ 60 uprate (Van Leuven, 1994). This engine was uprated from the T6500 model to the T7000 model with a power increase of 7.1 percent from 6500 Hp (4847 Kw) to 6960 Hp (5190 Kw) and with a 3.1 percent reduction in heatrate. This was accomplished primarily by tip clearance reductions in the compressor and turbine sections plus about a 3.4 percent increase in flow obtained by slightly untwisting the first compressor blade. This uprate was successful because it provided improved performance while maintaining the proven durability of the engine. The recurring cost was kept low because minimal changes were made to only a few parts. The durability of the product was maintained because there was no change in firing temperature and other operating conditions remained essentially the same.

Increased Airflow

If the airflow of an engine can be increased without a significant falloff in component efficiencies, the power of the engine will increase, and the engine's durability can usually be maintained. This is usually done by increasing the flowpath height in the first few compressor stages. This may also be accomplished by other means such as redesigning the first stage airfoils, untwisting the compressor first stage blades, setting the first stage blades at an increased broach angle, and sometimes by simply opening up the compressor's inlet guide vanes (IGV's). These procedures are sometimes referred to as high flowing a compressor.

These types of uprates are usually limited to under 10 percent flow increases. These uprates are usually successful because minimal amounts of parts are changed and the core part of the engine operates at conditions very near to those of the original engine. There are some conditions, however, that can restrict the use of this uprating method.

First of all, the compressor must have adequate surge margin to accommodate the increased pressure ratio that occurs with the increased airflow. If the gas producer turbine remains unchanged and the firing temperature is kept the same, then the engine pressure ratio will increase proportional to the airflow increase. This could reduce the surge margin of the compressor to an unacceptable level. Other results of the increased pressure ratio are increased loads on the thrust bearings and a slightly higher cooling air temperature.

Another often overlooked effect of this high-flowing method of uprating engines is the impact on performance at high ambient temperatures. Usually the front end of a compressor can be redesigned to provide the additional flow without a major loss in compressor efficiency at design point but not at all off-design points. A typical compressor map is shown in Fig. 5. With this type of map, it is easy to see that we would expect compressor efficiencies to increase slightly as we move down the operating line. The compressor map shown in Fig. 6 shows what tends to happen when the front end of a compressor is redesigned for increased airflow, but the remaining stages are not redesigned and must operate off-design. With this type of compressor map, efficiency actually drops slightly as we move down the operating line. Figure 7 shows how the compressor efficiency

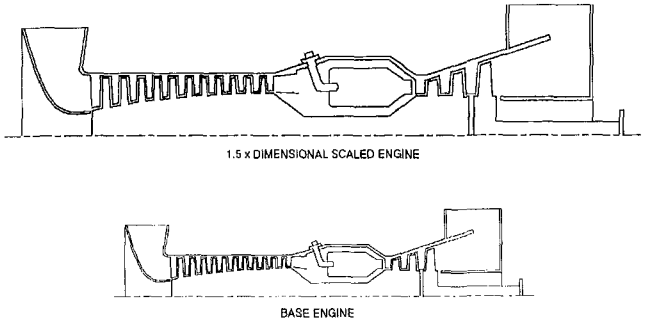

Fig. 3 Relative comparison of the base engine and a 1.5× scaled-up version

Table 4 Base engine improvements with component efficiency improvements

Component	Eff. Improvement	Power Increase	Cycle Eff. Incrse.
Compressor Eff.	1.0% Point	+1.4%, 113 Hp (84 Kw)	0.31 points (1.0%)
G/P Turbine Eff.	1.0% Point	+1.1%, 84 Hp (63 Kw)	0.34 points (1.1%)
Power Turbine Eff.	1.0% Point	+1.1%, 88 Hp (66 Kw)	0.35 points (1.1%)
All Three Improvements Combined		+3.6%, 285 Hp (213 Kw)	1.00 points (3.2%)

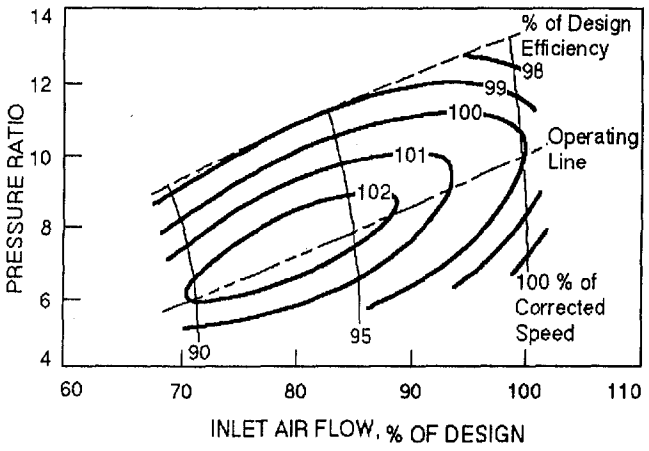

Fig. 5 Typical compressor map

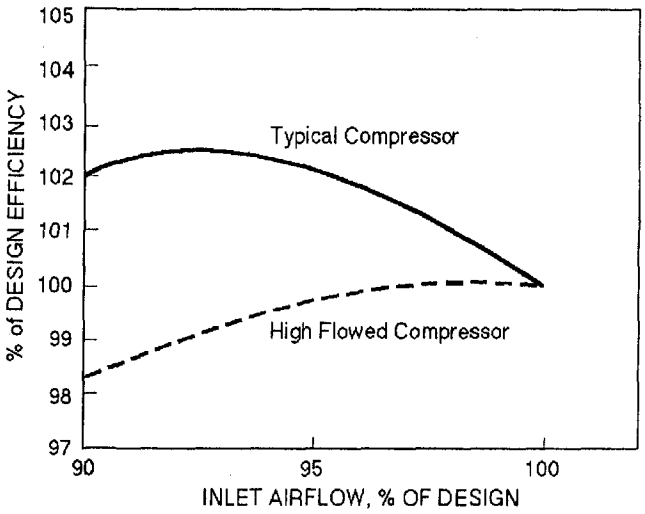

Fig. 7 Comparison of compressor operating line efficiency

curves of a typical compressor and a high-flowed compressor tend to compare. What this means is that uprated engines with a high-flowed compressor may not produce the same percentage improvement in engine performance at 122°F (50°C) ambients as they do at 59°F (15°C) ambients. Solar Turbines Incorporated has been successful in recovering most of the extra falloff in high ambient performance by using a variable guide vane control system. This control system keeps the gas producer speed up near 100 percent mechanical speed at ambients above 59°F (15°C).

A high-flowed compressor will also have an effect on the turbine section. The flow rate entering the gas producer turbine will go up, but the pressure will go up by the same proportion. Since the firing temperature remains unchanged, the Mach number entering this turbine will be essentially unchanged. Almost all of the increased pressure ratio available for the full turbine section will be required by the gas producer turbine to provide the extra power required to drive the higher pressure ratio compressor. The results is that this turbine will operate at a slightly higher pressure ratio but should not experience a large drop-off in efficiency at its new operating conditions.

The power turbine will see the increased flow at almost its original pressure levels since the gas producer turbine requires most of the cycle's increased pressure ratio. Also, since the firing temperature of the engine stays the same, the temperature entering the power turbine will only be slightly reduced due to the increased pressure drop through the gas producer turbine. As a result, the Mach numbers throughout the power turbine will increase, and the power turbine efficiency levels will usually drop off more than for the gas producer turbine. Increased losses may also be experienced in the exhaust diffuser and collector section due to the increased velocities.

Anytime the pressure ratio of an engine is increased without increasing the firing temperature, the temperature of the exhaust gas will be reduced. In this uprate option, the engine exhaust conditions will change to reflect the increased airflow, but at a slightly reduced temperature.

In evaluating this high-flowed concept for a performance uprate, the design team must decide how much additional airflow can be designed for before the component losses reach the point where the uprate does not make sense.

Looking at a possible high-flowed compressor uprate for our base engine, we might try to increase the airflow by 5.0 percent by redesigning the first two compressor stages with a slightly opened-up flowpath. We should be able to hold the design point efficiency of the compressor but we could loose 0.1 percent efficiency in the gas producer turbine and 0.5 percent in the power turbine. With these assumptions, our base engine performance should increase by 340 Hp (254 Kw)/(4.4 percent) with a slight improvement in heatrate (0.5 percent). The exhaust gas temperature would be decreased by 11°F (5°C).

This is the uprate method that was selected by Solar Turbines Incorporation for the latest Mars™ 90 and Mars 100 uprates. In this case, the first two compressor airfoil stages and the IGV were redesigned for a slightly more open flowpath, and no other parts in the engine were changed. For the Mars 100 engine, the T14000 model was uprated to the T15000 model. This resulted in almost 9 percent more flow and a performance increase of 900 Hp (671 Kw)/(6.4 percent) and a heatrate improvement of 1.5 percent. The compressor efficiency in the uprated engine actually increased by 0.6 percentage points as a result of using more modern aerodynamic design tools. The overall turbine efficiency dropped by 0.25 points, and the compressor pressure ratio increased from 16:1 to 17.4:1. This engine did not get the same percentage improvement at the high ambient conditions as it did at 59°F (15°C), but by incorporating compressor variable guide vane controls, the engine achieved a power gain of 5.0 percent at 122°F (50°C) ambients.

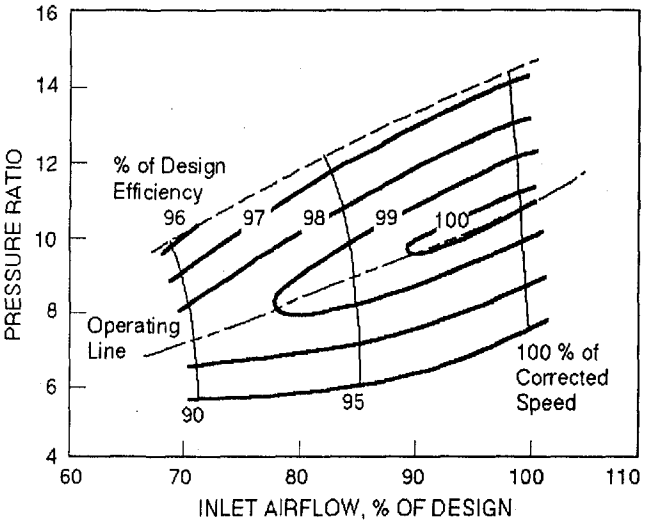

Fig. 6 Typical high flowed compressor map

Zero Staging

The process of adding an axial compressor stage in front of an existing compressor has commonly been referred to as zero

staging. To avoid having to rename many existing parts and changing even more drawings, this new stage has usually been called stage zero or the zero stage.

The main principal behind this type of uprate is to try to increase the output of an existing engine with few or no changes to the center core of the engine. The center core is almost always the most expensive, the most development intensive, and the most durability limiting section of a turbine engine. The aircraft engine industry has used this basic principle very successfully by using a well proven, high pressure core and matching it with several different size fans and low pressure turbines.

By the use of zero staging, the performance of an engine can usually be increased with minor or no changes to the existing compressor, the combustor, and the gas producer turbine. This is usually done by adding a single axial stage in front of the compressor, and opening up or completely redesigning the power turbine. This approach results in an engine program that needs to develop a single axial compressor stage and a new or modified power turbine. Both of these tasks are usually fairly predictable and relatively low risk. When these new components are applied to the existing engine, the results can be a new engine that has a large number of parts in common with the original engine and a percentage cost increase that is much less than the percentage increase in power.

The durability of the new engine can usually be maintained close to that of the engine being uprated. This is done primarily by keeping the firing temperature unchanged. Even though the pressure levels in the high pressure area of the engine will be increased and thrust loads will go up, the Mach numbers will stay about the same and the temperature levels in the high pressure turbine area will stay about the same. This helps maintain the proven durability of the original design because the high-pressure and high-temperature sections of the engine (the engine core) are relatively unchanged, and this is the most durability sensitive section of the engine.

When adding a zero stage to an existing compressor, it would be ideal if the mechanical speed of the gas producer shaft could be increased so that the corrected speed ($RPM/\sqrt{Temp}$) at the inlet to what was originally the first stage remained unchanged. This would keep all the velocity triangles and corrected conditions throughout the compressor unchanged. This would require that the original design have a 3 to 4 percent speed margin in the gas producer spool. This usually is not available unless the original design took into account the need for a zero stage uprate at some future date. Even if no increase in mechanical speed is possible, a zero stage design should be able to increase the compressor's airflow by about 20 percent without a significant falloff in compressor design point efficiency.

When a zero stage is applied to an existing engine, the original components react in the same manner as they do with the high-flow option described above, but to an even greater extent. With the original compressor stages running at the original mechanical speed but with the increased flow, they will be running off-design, and some drop in compressor efficiency should be expected.

Before a zero staged design can be released to the field, several issues resulting from the increased airflow must be addressed. These include increased thrust loads, increased cooling air temperature, increased power falloff at high ambient temperatures, reduced exhaust temperatures, and increased inlet filtration and exhaust silencing requirements.

With the gas producer turbine unchanged and the same firing temperature, the cycle pressure ratio will increase in proportion to the airflow. This means that the combustor will operate at a higher pressure, but the Mach numbers will be about the same. The combustor may work in the new engine cycle with only modifications to the fuel injectors. DLN (Dry-Low-NO_x) combustors, however, will probably require further modifications.

The aerodynamic conditions entering the gas producer turbine will be about the same as in the original engine but with an increased pressure ratio across the turbine. With this increased loading in the gas producer turbine section, the efficiency will probably decrease somewhat but not drastically. The power turbine, however, will be heavily impacted. The velocities throughout the power turbine will increase, and the velocities entering the diffuser/collector section will increase almost in proportion to the flow increase. It is unrealistic to expect the efficiency of the power turbine not to fall off.

When an engine is uprated by zero staging, the power turbine will usually have to be redesigned. At least the flowpath annulus area needs to be increased to get low loss velocities through the turbine and the diffuser/collector section. In some cases an additional turbine stage may need to be added and the shaft speed reduced in order to get reasonable power turbine efficiencies. The reduced output shaft speed may actually help since driven equipment at a higher power range usually wants to run a bit slower.

To see what a zero staged uprate option could do for our base engine, we can assume that the zero stage will increase airflow by 20 percent, but must run at the original mechanical speed. Under these conditions, the compressor efficiency may drop by 1.0 percent. The gas producer turbine will also drop in efficiency, but only about 0.3 percent. We will assume that the power turbine can be redesigned and opened up so that the total-to-static efficiency of the power turbine and diffuser/collector system will not change. If these assumptions can be met, we should have an uprated engine with a 1350 Hp (1007 Kw)/(+17.3 percent) increase in power with a little over 2.0 percent improved heat rate. The exhaust conditions would have 20 percent more massflow but the gas temperature would be reduced by 50°F (28°C).

The Taurus 60 product was created at Solar by zero staging the Centaur™ 50 engine. In addition to the zero-staged compressor, the only other major modification to the Centaur 50 engine was a new power turbine. A lower speed, two-stage power turbine was designed for the two-shaft Taurus 60 and a single, more open, third turbine stage was designed for the single-shaft version. The last eleven compressor stages, the combustor section, and the gas producer turbine are all identical on these two engines.

The zero-staged compressor provided an increase in airflow of approximately 17 percent. This increased airflow and the corresponding cycle pressure ratio increase from 9.5:1 to 11:1 combined with a more efficient power turbine to produce a power increase of 1000 Hp (746 Kw)/(+18.2 percent) and a heatrate reduction of 5.3 percent.

By keeping the firing temperature of these two engines the same, it was felt that the durability of the zero-staged Taurus 60 engine would be as good as it was on the developed Centaur 50 engine and this turned out to be true.

Increased Firing Temperature

Probably the most common way of uprating gas turbine engines is by increasing the firing temperature (thermal uprate). The main attraction of this method is that the increased performance usually comes with no change in external dimensions. This makes the uprate very attractive for retrofitting into existing installations.

From a manufacturer's point of view, this can be one of the more difficult uprates to develop. In many cases a manufacturer will introduce a new engine at a derated firing temperature to build up field experience to identify any weak areas in the hot section. After the engine has enough field experience to identify any weakness in the hot section design and these weaknesses, if any, have been corrected, it is then easy to increase the firing temperature to the original design level. This should not be considered a true thermal uprate.

In other cases, the firing temperature of an existing engine may be increased by upgrading the material of the life-limiting part or parts of the hot section. For example, if the first stage turbine blade is the life-limiting part of an existing design, it maybe possible to change from a normally cast material to a single crystal alloy, and then allow a higher firing temperature. These types of uprates can usually be done with low risk to the durability of the engine as long as temperature increase is small and the other hot section parts have adequate life margins.

For a substantial increase in firing temperature of a mature engine, the gas producer turbine and its airfoil cooling system usually have to be redesigned. This type of uprate usually carries extra cost, risk, and development time. In most cases, the turbine aerodynamics have to be redesigned, additional airfoil rows require cooling, the airfoil cooling schemes have to be redesigned, materials often have to be upgraded, the gas producer turbine flowpath may have to be changed, plus the power turbine has to be modified or even redesigned.

As an example, we could look at what would be involved in doing a thermal uprate for our base engine. For this example we will assume that we want to increase the turbine rotor inlet temperature (TRIT) from 1900°F (1038°C) to 2100°F (1149°C). To retain the engine retrofitable option we will assume that we want to keep the engine outside dimension unchanged. With this amount of change in TRIT, the gas producer turbine and power turbine will need to be redesigned. In addition to cooling the first turbine nozzle and rotor, the second turbine nozzle will now have to be cooled. The combustor case can probably be saved, but the combustor liner will have to be redesigned or at least modified.

With new state-of-the-art design tools, we should be able to improve the aerodynamics of the turbine section. In the gas producer turbine section, however, the increased amount of cooling air will hurt efficiency so we will probably end up with no gain in gas producer turbine efficiency. Similarly, with the power turbine we should be able to improve the total-to-total efficiency at optimum speed, but most likely the optimum aerodynamic speed will be beyond the maximum mechanical speed for this single-stage power turbine. Figure 8 shows an extreme case of what can happen to the efficiency of a single-stage power turbine due to a thermal uprate. We could solve the problem by going to a two-stage power turbine, but this would need to run slower and would probably change the engine's outside dimensions, both of which would impact our retrofitable options. Also, with the higher firing temperature, the velocities leaving the power turbine will probably be increased, which will go against the total-to-static efficiency of the power turbine and diffuser/collector system. For this example, we will assume that we end up with the same total-to-static efficiency for the power turbine and diffuser/collector system. Making some reasonable assumptions for the amount of additional cooling air required we could expect this thermal uprate option to produce performance improvement of 1100 HP (820 Kw)/(14.1 percent) with a reduction in heatrate of about 2.0 percent plus an increase in exhaust gas temperature of about 85°F (29°C) to aid in heat recovery applications.

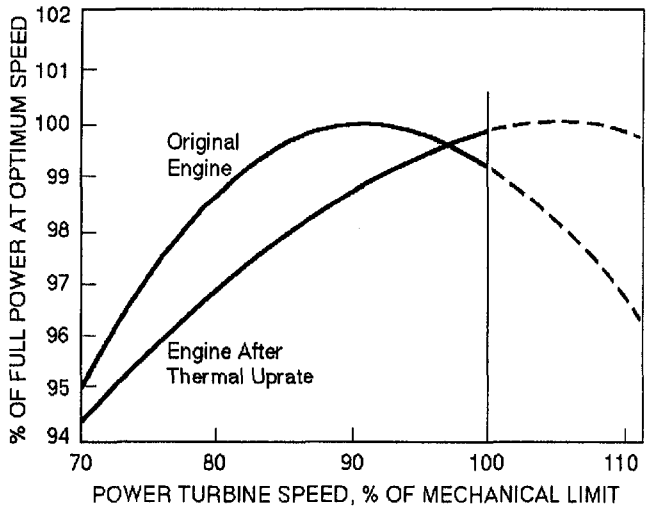

Fig. 8 Comparison of possible full load versus speed curves

Thermal uprates in one form or another have been applied to almost all of Solar Turbines mature engine products. Over the years, probably the most aggressive thermal uprate program at Solar was in uprating the Centaur 40 engine to the Centaur 50 model (Padgett, 1985). In this program, the compressor sections remained relatively unchanged but the combustion and turbine sections were redesigned to allow the TRIT to be raised from 1660°F (904°C) to 1850°F (1010°C). This major redesign job of the combustion and turbine sections required new materials, the addition of a cooled first-stage turbine blade row, and a much more complicated secondary cooling system. The payoff for this effort, however, was a new Centaur 50 engine at almost exactly the same size as the Centaur 40 engine, but with improved power output of almost 1000 Hr (746 Kw)/(21 percent) and a 3.9 percent reduction in heatrate with a 120°F (49°C) increase in exhaust gas temperature.

Adding a Recuperator

Some engines lend themselves to being fitted with a recuperator to increase cycle efficiency. For this to work, the turbine exhaust temperature must be higher than the compressor exit temperature since the recuperator uses the turbine exhaust to pre-heat the compressor exit air before it enters the combustor. In very high-pressure ratio engines, this might not be the case.

If the cycle conditions allow a recuperator to be added, the compressor section and the turbine section can usually be used as is. The major changes happen in the middle of the engine. A collector must be added at the compressor exit, a recuperator must be designed, and piping must be added to get the air from the compressor collector to the recuperator and from the recuperator back to the combustor. The combustor will usually have to be modified or redesigned since the temperature entering the combustion section will be hotter than in the original design. The turbine exhaust system will have to be redesigned to best transport the turbine exhaust gas to the recuperator face and provide a near-uniform profile. One system redesign that is often overlooked when considering adding a recuperator is the secondary flow system. With a recuperator, cooling air can no longer be drawn from the plenum outside the combustor liner without redesigning the cooling system to operate with higher flows and higher temperature cooling air. In most cases it will be easier to route compressor discharge air around the recuperator and combustor through external pipes.

Most simple-cycle engines operate at a pressure ratio that is too high for an optimum recuperator cycle. While many engines can have improved cycle efficiency when a recuperator is added, the efficiency level will usually be far less than the 40 percent + level that is possible with an optimum recuperator cycle design.

Because the recuperator adds pressure losses to the cycle, a simple-cycle engine usually sacrifices some power when a recuperator is added due to the lower pressure ratio available for the turbine section.

The base engine has a turbine exit temperature that is about 320°F (160°C) higher than the compressor exit temperature, so a recuperator should improve the efficiency of this cycle. A 90 percent effective recuperator can be assumed with 2 percent pressure loss on the air side and 4 percent on the gas side. To this, 1 percent loss should be added for piping to and from the recuperator. With these assumptions, the new engine would lose

620 Hp (462 Kw)/(7.9 percent) but the engines cycle efficiency would increase from 31.5 percent to 36.8 percent.

Solar has used this uprate option on versions of the Saturn and Centaur engines. On the Centaur engine, the T3000R version has a recuperator and it gets 14 percent better heatrate than the simple cycle version but it has 11 percent less power.

Increased Cycle Pressure Ratio

If improved cycle efficiency is needed, adding stages to the back end of the compressor may be considered. An increased cycle pressure ratio is one of the best ways to improve the cycle efficiency of a simple cycle engine. Aerodynamically, adding additional stages to the back end of an existing multiple-stage axial compressor is not usually a large risk. As rear stages are added, the flowpath annulus area must decrease leading to smaller airfoil heights. This may cause a compressor efficiency problem if the new airfoil heights get too small to maintain adequate tip clearances.

The engine changes required to increase the cycle pressure ratio by this method can be considerable. When stages are added to the aft end of compressor of an existing engine, the following changes are usually required: (a) the compressor shaft gets longer and may cause shaft dynamic problems; (b) the velocities in the combustor will be reduced due to the higher operating pressures requiring a new or modified combustor; and (c) the gas producer turbine will have to be redesigned or extensively modified to accommodate the higher pressure.

We could consider adding three stages to the aft end of our base engine. For this example we will assume that the compressor pressure ratio will increase from 10:1 to 14:1 and that by redesigning the gas producer turbine all our component efficiencies stay the same. If we also assume that we can keep the cooling flow amounts the same, then we should end up with an engine with 7683 Hp (5729 Kw)/(a drop of 1.5 percent) but with an increase in cycle efficiency from 31.5 percent to 33.8 percent. This means that if we can live with the 1.5 percent drop in maximum power, our heat rate or specific fuel consumption will be reduced by 6.8 percent.

Solar has never used this uprate option except in combination with some other option because of the large amount of engine parts that must be changed. Not only does this get expensive, but any proven durability is usually lost.

Conversion to Single Shaft

While not normally done to improve power or heat rate, converting a two-shaft engine to a single-shaft design could be considered an uprate for some applications.

When this is done, it might also be possible to convert to a cold-end-drive arrangement and eliminate the engine exhaust collector. This can be attractive for generator drives because it simplifies the engine controls and the overall system package.

An ideal engine for this type of conversion would have a one or two-stage gas producer turbine and a single-stage power turbine capable of running at or above the speed of the gas producer. If these conditions are met, it should be relatively easy to lock the power turbine rotor to the gas producer rotor, take the power out through the front of the engine, and design a straight out turbine diffuser without a collector. The performance of the new single-shaft engine, in this case, should be 1 percent to 2 percent better than the original two-shaft engine due to the reduced diffuser/collector losses.

Converting a two-shaft design to a single-shaft design becomes more difficult with an engine that has a high-speed, high-flow gas producer section. With this type of gas producer section, it is usually not possible to design the last turbine stage rotor with enough annulus area to get decent efficiency from that stage and reasonable recovery in the turbine diffuser section. For a high efficiency level in the last turbine stage and minimal total pressure loss in the turbine diffuser section, the axial Mach number leaving the turbine should be in the 0.3 to 0.4 range. With a high-speed, high-flow gas producer section, mechanical limits on the last row of turbine blades restrict the amount of turbine exit area that can be designed for. In some cases, a mechanically sound design could result in turbine exit Mach numbers of 0.7 and higher. Even though the last turbine stage can be designed for these conditions and a longer turbine diffuser can increase the amount of velocity head recovery, the resulting turbine/diffuser section will probably not perform as well as the original turbine/diffuser/collector section on the two-shaft engine. When this happens, the amount of performance loss associated with converting from a two-shaft to a single-shaft design could make the project unattractive.

For our base engine, a conversion to a single-shaft arrangement should be an attractive option. With the power turbine already running at 96 percent of the gas producer speed, it should only require minor design modifications to allow it to be attached directly to the gas producer turbine. Assuming that the shafting and compressor section can take the additional torque of a cold-end-drive arrangement, the turbine exhaust collector can be removed and the engine performance should be about 1 percent better than that of the originating two-shaft design.

Complex Cycle Uprates

As the industrial gas turbine suppliers start producing complex cycle engines, the question of how to best provide uprated versions will need to be addressed. There does not seem to be enough experience in the industry yet to definitely answer this question. Most recuperated engines in the industrial field are being designed with little or no temperature margin in the high pressure turbine section or in the recuperator section. In these cases, a thermal uprate of the gas producer turbine section would require that additional temperature capability be added to the recuperator section or that the compressor pressure ratio be increased in order to keep the temperature entering the gas side of the recuperator at an acceptable level (Ragland, 1995). This in turn could require that additional pressure capability be added to the recuperator.

As these complex cycle engines become more popular, the industry will be challenged to come up with uprate options that help add value to the product. Variations of the popular uprate options for simple-cycle engines will probably emerge. For instance, the high-pressure section of a recuperated engine might be used as the core section for an intercooled and recuperated (ICR) engine.

Comparison of Options

What an uprate program is trying to accomplish and the characteristics of the particular engine being uprated will be the primary factors in deciding what uprate method to choose. There is no

Table 5 Base engine performance improvements from different uprate options

Uprate Option	Output Power	Cycle Efficiency
Base Engine	7800 Hp (5816 Kw)	31.5%
1.5X Dimensional Scaling	+128%, 17,800 Hp (13,273 Kw)	32.0% (+1.5%)
Component Eff. Improvement	+3.7%, 8085 Hp (6029 Kw)	32.5% (+3.2%)
Increased Airflow	+4.4%, 8140 Hp (6070 Kw)	31.7% (+0.5%)
Zero Staging	+17.3%, 9150 Hp (6823 Kw)	32.1% (+2.0%)
Increased Firing Temperature	+14.1%, 8900 Hp (6637 Kw)	32.1% (+2.0%)
Add A Recuperator	-7.9%, 7180 Hp (5354 Kw)	36.8% (+16.8%)
Increased Pressure Ratio	-1.5%, 7683 Hp (5729 Kw)	33.8% (+7.3%)
Single-Shaft Conversion	+1.0%, 7878 Hp (5875 Kw)	31.8% (+1.0%)

one best uprate option that will apply in all cases, but several options should be evaluated before a final selection is made.

Our fictional base engine was used to provide examples of approximate performance improvements that could be obtained with the various uprate options. The performance improvements from the different uprate options that were studied for the base engine are tabulated in Table 5. The quantitative values derived for these examples may not hold up when applied to some other engine, but the trends should be of help when trying to decide what uprate option to select.

While the values in Table 5 are all dependent on the assumptions that we made about what could be done to our fictitious base engine, they can be of some help in understanding the advantages and disadvantages of each option.

Other factors must also be considered when deciding which uprate option to pursue. Table 6 is an attempt to relate the development risk, the development costs, and the increased engine costs of the various uprate options for our base engine. Any attempt to generate a table like this must, by nature, be subjective, and the evaluations might change for engine configurations that are significantly different from that of our base engine.

The dimensional scaling option is probably best suited for expanding a product line. It is dependent on having an existing engine with good durability and acceptance in the market place. Scaling up an existing design saves design time and reduces the amount of development testing required. There should be some reduction in cost per unit of power and the durability of the original engine should be maintained. The scaling factor can be selected to produce a wide range of engine power sizes, but the cycle efficiency will change very little from that of the original design. The scaled engine will usually have no parts in common with the original engine, but since the design of the two engines will be the same, any improvements developed for one engine can usually be applied to the other.

If existing engines have room for component efficiency improvements, this can be an attractive way of improving the performance of an engine without significantly increasing the recurring cost of the engine. For example, if improved aerodynamics can be developed that can be retrofit into the existing flowpath, this will improve both power and heat rate and should not increase recurring costs significantly.

Increasing airflow can be a low risk way of providing additional power by changing a minimal number of engine parts. Usually, there is minimal (if any) improvement in heat rate, but the engines exterior dimensions typically do not change, which makes the new engine interchangeable into existing installations. Some adjustments to thrust bearings, inlet filtering system, and engine accessories may be required.

Zero staging the compressor of an existing engine can produce a significant increase in power and usually some heat rate improvement. This is usually a very predictable and relatively low risk development program. This type of a program can allow a manufacturer to offer two engines at different power levels with more than 80 percent parts commonality. This may be attractive to users with large engine fleets because personnel trained to operate and maintain one engine can easily learn to take care of the other. Also, the number of spare parts required to support two engine types can be reduced. The increased airflow will usually require a larger inlet filtering and exhaust system. The starter, fuel, and lubrication systems may have to be upgraded, and the thrust bearing capacity may have to be increased.

Table 6 Subjective risk and cost evaluations for different uprate options

Uprate Option	Development Risks	Development Costs	Change in Cost Per Power Unit
1.5X Dimensional Scaling	Low	Low	Small Reduction
Component Eff. Improvement	Low/Moderate	Low/Moderate	Reduced
Increased Airflow	Low	Low	Reduced
Zero Staging	Low/Moderate	Low/Moderate	Reduced
Increased Firing Temperature	Moderate/High	Moderate/High	Reduced
Add A Recuperator	Moderate/High	Moderate/High	Increased
Increased Pressure Ratio	Moderate	Moderate/High	Small Increase
Single-Shaft Conversion	Low	Low	Small Reduction

The most popular performance uprate option is through increased firing temperature. This option is popular because it provides additional power and improved heat rate without changing the envelope of the engine. On the negative side, however, increased firing temperature can be a major cost driver, plus the development programs can be risky and costly. The durability of the engine can also be compromised if the cooling system design is not adequate.

On some engines, adding a recuperator can produce a significant improvement in cycle efficiency with some loss in maximum power. The compressor and turbine sections can usually be held the same, but, in addition to the recuperator, the collectors and ducting must be added, and the combustor usually has to be redesigned.

If improved heat rate is the main goal of an uprate program, then increasing the cycle pressure ratio could be considered. This option requires several changes to existing engine hardware, and is usually hard to justify unless combined with other uprate options.

Some two-shaft engines may lend themselves to being converted to a single-shaft arrangement. If the power turbine can run at or near the speed of the gas producer section, this conversion may be relatively easy. If the engine can be converted to a cold end drive configuration at the same time, the controls and overall package can be simplified, and it may be possible to gain 1 percent to 2 percent in performance.

These uprate options have been discussed mainly from a performance and aerodynamic perspective. The implementation of any of these options will require a great deal of structural analysis. Anytime additional power is provided, existing parts must be analyzed under any new loads resulting from new values of mechanical forces, torque, pressure, or temperature. Also, these performance uprates can have an impact on auxiliaries such as the starter, the fuel and lube oil system, enclosures, silencers, inlet filtration, and exhaust systems.

Summary

Providing performance uprates to existing industrial gas turbine engines has been a time-honored method of providing additional value to gas turbine end users. This paper has tried to present some of the implications of the different options available for providing performance uprates.

When possible, there is a significant advantage in keeping the high-pressure section of the engine and the firing temperature unchanged. This greatly reduces the size and cost of an uprate program, and greatly reduces the risk of the uprated engine having less durability than the original design.

In any uprate program, it is easy to get locked into only one method for getting the additional performance. As shown here, there are several options for providing extra performance, all with advantages and disadvantages. Several options should be evaluated before a final program direction is selected to see which one best provides additional value to the user community.

References

Padgett, G. L., and Davis, W. W., 1985, "Development of the Centaur Type H Gas Turbine Engine," ASME Paper 85-GT-214.

Ragland, T. L., 1995, "A High Efficiency Recuperated Cycle, Optimized For Reliable, Low Cost, Industrial Gas Turbine Engines," ASME Paper 95-GT-321.

Van Leuven, V., 1994, "Solar Turbines Incorporated, Taurus 60 Gas Turbine Development," ASME Paper 94-GT-115.

Z. J. Zuo
Thermacore, Inc.,
780 Eden Rd.,
Lancaster, PA 17001

A. Faghri

L. Langston

Department of Mechanical Engineering,
University of Connecticut,
Storrs, CT 06269

Numerical Analysis of Heat Pipe Turbine Vane Cooling

A numerical model was developed to simulate transient performance of a heat pipe turbine vane under typical gas turbine engine conditions. Curvilinear coordinates were used to describe the three-dimensional wall and wick heat conduction coupled with the quasi-one-dimensional vapor flow. A unique numerical procedure including two iterative "estimate-correction" processes was proposed to efficiently solve the governing equations along with the boundary conditions. Comparisons with experimental results validated the numerical model and the solution method. A detailed numerical simulation of the heat pipe vane's transient performance indicated the benefits of incorporating heat pipe vane cooling as well as the areas where precautions should be taken while designing heat pipe vanes.

Introduction

As is well known from turbomachinery theory, a higher gas temperature improves thermal efficiency of a turbine engine. Current high efficiency gas turbine engines usually operate at temperatures greater than allowable metal temperatures of turbine components (Nirmalan and Hylton, 1990). Future technology is targeted at obtaining stoichiometric conditions in gas turbine combustors (Harasgama and Burton, 1992). This trend of increasing heat load to turbine components, especially the first-stage turbine vanes, has generated a strong demand for more sophisticated cooling techniques. Additionally, uniform cooling of turbine components is required to avoid large thermal stresses.

Conventional turbine cooling methods include internal convective and impingement cooling, film cooling, and trailing edge ejection. According to previous studies, a good combination of internal and external cooling can be quite effective, permitting substantial gains in engine output and efficiency that accompany the increase in turbine inlet temperature. However, these techniques require the extraction of a relatively large portion (typically 2.5–4 percent) of compressor discharge air, which presents an adverse effect on turbine efficiency. The internal convective cooling and impingement cooling are usually associated with large thermal stresses because of the large temperature gradient in the metal wall. Ejection of a thin film of cooling air from the blade surface to the main stream may lead to large aerodynamic losses that could reduce the turbine efficiency by as much as 0.5 percent (Silverstein et al., 1994). In many cases, these drawbacks become an obstacle to the improvement of turbine efficiency. Therefore, a more advanced and suitable turbine cooling technique is in demand.

Heat pipes are known to have a much greater thermal conductivity than most known materials (Faghri, 1995). A typical heat pipe consists of a closed container, one or more layers of wick material lining the container inner wall, and a fixed amount of working fluid. When heat is applied at one end (evaporator) of the container, the liquid working fluid in the wick structure turns into vapor that travels to the other end (condenser) of the container. At the condenser, the vapor condenses into liquid and releases the latent heat. The condensed liquid is then returned to the evaporator by capillary forces in the wick structure. This internal phase change circulation makes the heat pipe an extremely efficient heat transfer device.

Other important advantages of the heat pipe include nearly isothermal heat transfer, no need of external pumping power, simple and adaptable structure, low cost, and high reliability. The heat pipe, if configured into a turbine airfoil, becomes very attractive for high temperature gas turbine cooling applications.

The idea of fitting turbine vanes or stators with heat pipes has been considered by gas turbine specialists over the years. In 1967, SNECMA, a French jet engine manufacturer, conducted preliminary liquid sodium heat pipe vane experiments (Faghri and Langston, 1995). Langston proposed the use of heat pipe fitted turbine stators (Langston, 1968). Silverstein et al. (1994) conducted a preliminary design and analysis of heat pipe vane cooling as part of a Phase I investigation in conjunction with the U.S. Air Force and the then Allison Gas Turbine Division of General Motors (presently Allison Engine Company). These preliminary feasibility studies have shown promising results. It was concluded by Faghri and Langston (1995) that the use of heat pipe turbine vane cooling technique promises significant improvements in overall gas turbine durability and performance by (1) isothermalization of the vane, thereby minimizing thermal stresses, (2) reduction of the required amount of cooling air, thereby improving turbine efficiency and increasing the amount of cooling air for NO_x control, and (3) elimination of the cooling air ejection, thereby reducing aerodynamic losses.

However, in order for turbine manufacturers to make use of heat pipe vanes in a production engine, much more detailed analysis and simulation must be conducted. As a logical first step, a numerical analysis of a typical heat pipe vane's transient performance under representative engine conditions would provide a firm foundation for further studies.

In the past ten years, a good understanding of heat pipe operating mechanisms have been developed from a number of studies that conducted numerical modeling of heat pipe operations (Faghri and Parvani, 1988; Chen and Faghri, 1989; Bowman, 1991; Jang, et al., 1991; Cao and Faghri, 1991 and 1993). These previous studies focused on a variety of heat pipe operations ranging from steady-state performance to transient behavior, from continuum transient to frozen startup, from cylindrical heat pipes to nonconventional leading edge heat pipes, and from uniform heating and cooling to discrete heating and radiative cooling.

An extensive literature survey revealed no previous studies dealing with numerical analysis of heat pipe turbine vane cooling. The following are three unique aspects that must be considered in the modeling of the heat pipe vane cooling: (1) special geometric configuration of the heat pipe vane makes it impossible to incorporate Cartesian or Cylindrical coordinates; (2) highly nonuniform heating and cooling conditions makes the heat conduction in the wall and wick generally three dimen-

Contributed by the International Gas Turbine Institute and presented at the 1996 Third Biennial Joint Conference on Engineering Systems Design & Analysis, Montpellier, France, July 1–4, 1996. Manuscript received by the ASME Headquarters August 28, 1997. Associate Technical Editor: T. Okiishi.

sional; and (3) external heating and cooling conditions are coupled with mainstream flows in the heating and cooling sections, respectively.

In this paper, a numerical model is presented for transient analysis of the heat pipe vane. The complicated geometric configuration of a heat pipe vane is modeled with a curvilinear coordinate system. The three-dimensional wall and wick heat conduction is coupled with the quasi-one-dimensional vapor flow. Heat transfer coefficients and temperatures of the turbine flows are determined according to the vane geometry and the turbine conditions.

A unique numerical approach involving two iterative "estimate correction" processes is proposed to efficiently solve the governing equations along with the boundary conditions. The numerical model is first solved for cylindrical heat pipes and compared with experimental results. A detailed simulation of the transient performance of a typical heat pipe vane under representative turbine conditions is conducted using the model.

Numerical Model of Heat Pipe Vane Cooling

Several heat pipe vane designs have been proposed for turbine applications (Faghri and Langston, 1995). Figure 1 illustrates the heat pipe turbine vane that was investigated in this study, as well as the curvilinear coordinate system. The evaporator section of the heat pipe vane is in direct contact with the combustion gas. The condenser section is actually an extension of the turbine vane into a passage that contains a stream of cooler air flow acting as a heat sink. More detailed discussions on the heat sink design can be found in the literature by Silverstein et al. (1994) and Faghri and Langston (1995).

Mathematical Formulation. The following assumptions were made to simplify the mathematical model: (1) the vapor inside the heat pipe vane is a continuum flow and in the saturation state—according to Faghri (1995), vapor quality is approximately equal to unity along the heat pipe; (2) the vapor is a one-dimensional, compressible, ideal gas flow—the one-dimensional assumption is well justified by previous studies (Jang et al., 1991; Cao and Faghri, 1991); (3) the effect of the liquid flow on temperature distribution in the wick structure is negligible; (4) thermophysical properties of the working fluid and the wick and wall materials are constant throughout the transient period—this is done to reduce the computational time and the resulting error would be trivial; (5) the wall and wick thickness, except at the leading and trailing edges, is considerably smaller when compared to the vane cross-sectional dimensions; and (6) viscous dissipation, axial heat conduction, and gravitational effect of the vapor flow are negligible.

Referring to Fig. 1 for the reference coordinates, heat conduction in the wall and wick can be modeled as

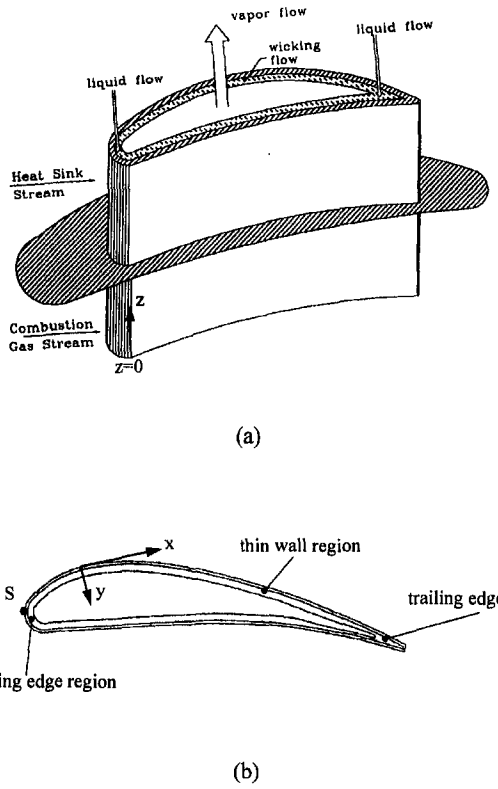

Fig. 1 A sketch of the heat pipe turbine vane: (*a*) heat pipe turbine vane cooling; (*b*) representative vane cross section

$$\rho_w C_{p,w} \frac{\partial T_w}{\partial t} = \frac{\partial}{\partial x}\left(k_w \frac{\partial T_w}{\partial x}\right) + \frac{\partial}{\partial y}\left(k_w \frac{\partial T_w}{\partial y}\right) + \frac{\partial}{\partial z}\left(k_w \frac{\partial T_w}{\partial z}\right). \quad (1)$$

It should be noted that the assumption of thin wall and wick has been incorporated in Eq. (1). However, at the leading and trailing edges, the vane wall is relatively thick, and the heat flux is extremely high. Significant errors could be introduced if Eq. (1) is used directly at the leading and trailing edges. In this model, the leading and trailing edges were treated as two separate regions from the rest of the vane wall and wick. A complete energy balance was applied to control volumes in these two regions to obtain discretization equations.

Nomenclature

A_v = vapor flow cross-sectional area (m^2)
C_f = friction coefficient
c_p = specific heat (J/kg-K)
D_h = hydraulic diameter of the vapor cross section (m)
h = heat transfer coefficient (W/m^2-K)
h_{fg} = latent heat of vaporization (J/kg)
k = thermal conductivity (W/m^2-K)
L = heat pipe length (m)
P = pressure (Pa)
Q = heat transfer rate (W)
q'' = heat flux (W/m^2)
R = gas constant (N-m/kg-K)
Re_v = vapor flow Reynolds number, $Re_v = r_v u_v D_h / m_v$
S = vapor flow channel perimeter (m)
T = temperature (K or °C)
t = time (second)
w = axial (z-) velocity (m/s)
x = circumferential curvilinear coordinate (m)
y = radial coordinate (m)
z = axial coordinate (m)

Greek Symbols

d = total thickness of wall and wick (m)
m = viscosity (N-s/m^2)
r = density (kg/m^3)
t = wick-vapor interfacial shear stress (N/m^2)
w = wick porosity

Subscripts

$\cdot$ = environment
e = evaporator
in = interfacial
ref = reference
sat = saturated
v = vapor
w = wall or wick

Superscripts

$*$ = estimate
c = correction

Thermophysical properties of the liquid-wick mixture were approximated as follows (Faghri, 1995):

$$k_w = \frac{k_{\text{liquid}}[(k_{\text{liquid}} + k_{\text{wall}}) - (1 - \omega)(k_{\text{liquid}} - k_{\text{wall}})]}{[(k_{\text{liquid}} + k_{\text{wall}}) + (1 - \omega)(k_{\text{liquid}} - k_{\text{wall}})]}$$

$$(\rho C_p)_w = \omega(\rho C_p)_{\text{liquid}} + (1 - \omega)(\rho C_p)_{\text{wall}}, \quad (2)$$

where ω is the wick porosity.

Conservation of mass and momentum of the vapor flow gives

$$\frac{\partial}{\partial t}(\rho_v A_v) + \frac{\partial}{\partial z}(\rho_v A_v w_v) = \frac{q'' S}{h_{fg}} \quad (3)$$

$$\frac{\partial}{\partial t}(\rho_v A_v w_v) + \frac{\partial}{\partial z}(\rho_v A_v w_v^2) = -\frac{\partial}{\partial z}(P_v A_v) + \frac{4}{3}\mu_v \frac{\partial}{\partial z}\left(A_v \frac{\partial w_v}{\partial z}\right) - \tau S, \quad (4)$$

where q'' is the wick-vapor interfacial heat flux. The wick-vapor interfacial shear stress was modeled as $\tau = 1/2\rho_v w_v^2 C_f$, where the friction coefficient is

$$C_f = \frac{16}{\text{Re}_v} \quad \text{for } \text{Re}_v \le 2000, \quad C_f = \frac{0.079}{\text{Re}_v^{0.25}} \quad \text{for } \text{Re}_v > 2000. \quad (5)$$

According to previous studies (Bowman and Hitchcock, 1988; Cao and Faghri, 1991), the vapor in the evaporator section is always laminar flow ($\text{Re}_v \le 2000$), and, thus, the first correlation in Eq. (5) should be used. It must be pointed out that the correlations in Eq. (5) are for cylindrical pipe flow. Application of these correlations to the vapor flow in a heat pipe vane whose cross section is highly nonconventional may cause some errors.

Density, temperature and pressure of the vapor flow were correlated by the ideal gas equation

$$P_v = \rho_v R T_v. \quad (6)$$

Since it was assumed that the vapor inside the heat pipe is fully saturated, the energy equation for the vapor becomes unnecessary, and the vapor temperature and pressure can be related by the Clausius-Clapeyron equation

$$\ln \frac{P_v}{P_{v,\text{ref}}} = \frac{h_{fg}}{R}\left(\frac{1}{T_{v,\text{ref}}} - \frac{1}{T_v}\right). \quad (7)$$

Equations (1), (3), (4), (6), and (7) are the governing equations of the numerical model. The corresponding boundary conditions are specified as follows:

$$\text{at any } x, \quad (T_w)_x = (T_w)_{x+S} \quad \left(\frac{\partial T_w}{\partial x}\right)_x = \left(\frac{\partial T_w}{\partial x}\right)_{x+S} \quad (8)$$

$$\text{at } y = 0 \text{ and } y = \delta, \quad h(T_\infty - T_w)_{y=0} = -k_w\left(\frac{\partial T_w}{\partial y}\right)_{y=0}, \quad -k_w\left(\frac{\partial T_w}{\partial y}\right)_{y=\delta} = q'' \quad (9)$$

$$\text{at } z = 0 \text{ and } z = L, \quad \left(\frac{\partial T_w}{\partial z}\right)_{z=0,L} = 0, \quad \left(\frac{\partial T_v}{\partial z}\right)_{z=0,L} = 0, \quad \left(\frac{\partial P_v}{\partial z}\right)_{z=0,L} = 0, \quad (w_v)_{z=0,L} = 0, \quad (10)$$

where h is the heat transfer coefficient in the external main stream (i.e., combustion gas or bypass air). If other types of heating and cooling conditions such as electrical heating and radiative cooling apply, corresponding changes need to be made regarding the boundary conditions at $y = 0$.

Initial conditions of T_w, T_v, P_v, ρ_v, and u_v are discussed in the next section.

Performance Limitations. There are several limitations to the heat transfer capability of a heat pipe vane. Among them, the sonic limit, capillary limit, and boiling limit are often the most critical during the transient startup of the turbine. Various correlations for predicting these performance limitations have been documented by Faghri (1995).

In this study, correlations of sonic, capillary, and boiling limitations were integrated into the numerical procedure. Detailed discussions are presented in the next section.

Numerical Approach. A variety of numerical techniques have been incorporated by previous researchers in the solution of the transient heat pipe problem. Generally, two choices of updating the time level exist: explicit and implicit schemes. Considering that a heat pipe transient can be as long as thousands of seconds (depending on the size of the heat pipe) and the incident heat flux can be extremely large, an implicit scheme was chosen to obtain quicker convergence for all time step sizes.

Discretized governing equations and boundary conditions were obtained by employing the control-volume, finite-difference method. A staggered grid was used for the vapor flow continuity and momentum equations to better represent the relation between the vapor velocity and pressure (Shih, 1984).

Both the alternating-direction implicit (ADI) method, developed by Douglas and Gunn in 1964, and the implicit fractional-step method (Anderson et al., 1984) were incorporated to solve the three-dimensional transient heat conduction in the heat pipe vane wall and wick. Comparisons between the results from these two methods revealed little difference. Since the implicit fractional-step method requires significantly less programming efforts and slightly less computational time, it was chosen as the solution method for the wall and wick heat conduction equations.

Discretized heat conduction equations form tridiagonal matrix equations in both y and z-directions, which were solved using the Thomas algorithm. In the x-direction, however, the periodic boundary conditions in Eq. (8) result in a nontridiagonal matrix equation. A classical Gaussian elimination method was incorporated to obtain solutions in x-direction.

The vapor flow plays a critical role in heat pipe vane operation. In a study by Cao and Faghri (1991), an iterative SIMPLE algorithm was employed to solve the vapor dynamics. Some modifications were made in this study to improve the convergence rate.

The overall numerical sequences are as follows: (i) specify geometric dimensions, thermophysical properties, initial conditions, and external boundary conditions; (ii) reset the timer; (iii) update the time level; (iv) solve the wall and wick heat conduction equation (Eq. (1)) to obtain temperature distribution in the heat pipe vane wall and wick; (v) estimate the vapor temperature based on the wick-vapor interface temperatures; (vi) calculate the vapor density using the ideal gas equation (Eq. (6)); (vii) calculate the wick-vapor interfacial heat fluxes using Eq. (9); (viii) estimate the vapor velocity w_v^* by solving the vapor momentum equation (Eq. (4)); (ix) solve the pressure-correction equation to obtain the corrected vapor velocity w_v; (x) calculate the vapor pressure using the vapor momentum equation (Eq. (4)) based on the corrected vapor velocity w_v; (xi) correct the vapor temperature based on the vapor pressure using the Clausius-Clapeyron equation (Eq. (7)); (xii) repeat steps (iv)–(xi) until converged wall and wick temperatures, vapor temperature, pressure, density, and velocity are obtained; (xiii) check the performance limitations; and (xiv) go to step (iii) until steady-state or a preset time level is reached.

There are two "estimate correction" processes in the above numerical procedure. The one for the vapor pressure involves the iteration between vapor flow continuity and momentum equations, and has been well described in many previous studies (Shih, 1984; Anderson et al., 1984; Patankar, 1988). The estimate-correction process for vapor temperature was proposed for the first time in this work and a detailed discussion follows.

Like the vapor pressure (or velocity) that must satisfy both the continuity and momentum equations, the vapor temperature must satisfy the overall energy balance and the Clausius-Clapeyron equation, according to the assumption of saturated vapor. These two principles are usually united and "hidden" inside the complicated vapor flow energy equation. However, due to the simplifying assumptions, the vapor energy equation is no longer necessary. Therefore, an iterative estimate-correction process should be followed to ensure the vapor temperature satisfies both principles.

Performing an energy balance for the entire vapor provides

$$\frac{\partial}{\partial t}\left[\int_z \rho_v A_v\left(C_{p,v}T_{v,\text{sat}} + \frac{w_v^2}{2}\right)dz\right] = \int_z \frac{q''S}{h_{fg}}\left(C_{p,v}T_{v,\text{sat}} + \frac{P_{w,\text{sat}}}{\rho_{v,\text{sat}}}\right)dz. \quad (11)$$

Substituting the vapor continuity equation (Eq. (3)) into Eq. (11) and dropping the remaining transient term (since this is only an estimate of the vapor temperature) results in

$$\int_z q''dz = \int_z h_{\text{in}}(T_{w,y=\delta} - T_v)dz = 0, \quad (12)$$

where h_{in} is the wick-vapor interfacial heat transfer coefficient. Generally, h_{in} changes along the heat pipe. To further simplify the estimation process, both h_{in} and T_v are assumed to be constant, resulting in

$$T_v = \frac{1}{L}\int_z T_{w,y=\delta}dz. \quad (13)$$

Equation (13) indicates that the vapor temperature can be estimated as the average wick-vapor interface temperature.

It is interesting to note that the transient vapor temperature depends on two different mechanisms: the vapor pressure (vapor dynamics) and the wall temperature (heat conduction). As indicated by Bowman (1991), the vapor transient and the wall transient can have vastly different time scales. The time scale of the wall conduction is related to the thermal capacitance of the heat pipe wall and wick, whereas the time scale of the vapor dynamics is related to the speed of sound in the vapor. These two time scales can be different by several orders of magnitude. It is the vapor temperature that "bridges" these two vastly different transients. The proposed method of iterating the vapor temperature between the wall transient and the vapor dynamics holds both physical sense and numerical advantage.

Another improvement of the present numerical procedure is the correction method for the vapor pressure. Traditionally, the corrected pressure (P_v) is obtained by adding the pressure correction (P^c) to the pressure estimate (P^*). This requires that the absolute value of the pressure correction (P^c) be quite accurate in order to obtain a quicker convergence. However, since the pressure-correction equation contains many simplifications and the boundary conditions for the pressure correction are usually difficult to specify, an accurate estimate of the pressure correction becomes very difficult, if not impossible. A careful inspection of the pressure-correction and velocity-correction equations revealed that it is the gradient instead of the absolute value of the pressure correction that really matters. Therefore, in this model, the pressure correction (P^c) is only used to correct the vapor velocity. The vapor pressure is corrected by using the vapor momentum Eq. (4) based on the corrected vapor velocity. The convergence rate is greatly improved this way.

During the iteration, both the vapor velocity and pressure need to be under-relaxed to prevent numerical over-oscillation or even divergence.

Results and Discussions

The numerical model and the solution method were first validated by comparisons with available experimental results. The model was then used to simulate the performance of a typical heat pipe vane under representative turbine conditions.

According to previous studies (Bowman, 1991; Cao and Faghri, 1991), the numerical results are essentially independent of the grid size. A preliminary simulation of a 1 m long cylindrical heat pipe with an inner diameter of 0.01 m confirmed this observation. A change of grid size from 5 (radial) × 10 (axial) to 10 × 20 resulted in a less than 2 percent difference in the numerical results.

However, the time step size seemed to have a larger influence on the accuracy of the results, especially in the case of strong heating and cooling. A change of time step size from 0.1 to 10 s resulted in an 8 percent difference in the numerical results. It was found that a time step size of approximately 1 s would provide reasonably accurate results with a relative economy of computational time.

Validation of Numerical Model. The numerical calculations were compared with experimental results for two cases of heat pipe operations. The experimental setup and procedure are documented in the corresponding literature.

Table 1 lists geometric dimensions and operating conditions of a cylindrical water-copper heat pipe tested by El-Genk and Huang (1993).

Figure 2 compares steady-state vapor temperatures predicted by the model and the measurement results from El-Genk and Huang (1993). It is obvious that a larger heat input contributes to a higher vapor temperature while other conditions remain unchanged. The deviations of the predicted values from the experimental results are within 3 percent.

Figure 3 illustrates the vapor temperature during a transient period after the evaporator heating power suddenly increases from zero to a specified value. It takes 700 ~ 1100 s for the vapor temperature to reach steady state. Once again, the agreement between the model and the experiment is good.

However, a general trend in both Figs. 2 and 3 shows that the numerical model slightly overpredicts the vapor temperature. This overprediction is because that the numerical calculation does not include heat losses from the heat pipe setup to the environment. The overprediction can be significant for high

Table 1 The water-copper heat pipe tested by El-Genk and Huang

copper tube outer diameter	19.1 mm
copper tube inner diameter	17.3 mm
evaporator length	393 mm
condenser length	170 mm
adiabatic length	47 mm
condenser cooling water jacket inner diameter	22.3 mm
copper wick (150 mesh, two layers) thickness	0.3 mm
working fluid	water
heating condition	uniform electrical heating in the evaporator
cooling condition	convective cooling by the water jacket
initial conditions	room conditions (295 K)

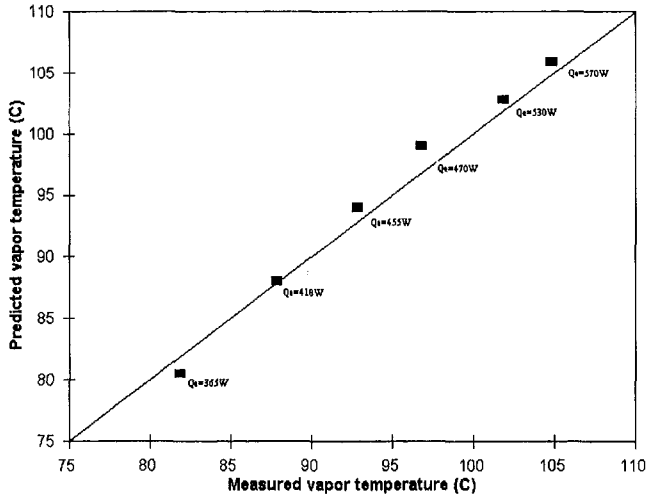

Fig. 2 Comparison of predicted and measured steady-state vapor temperatures of a cylindrical water-copper heat pipe

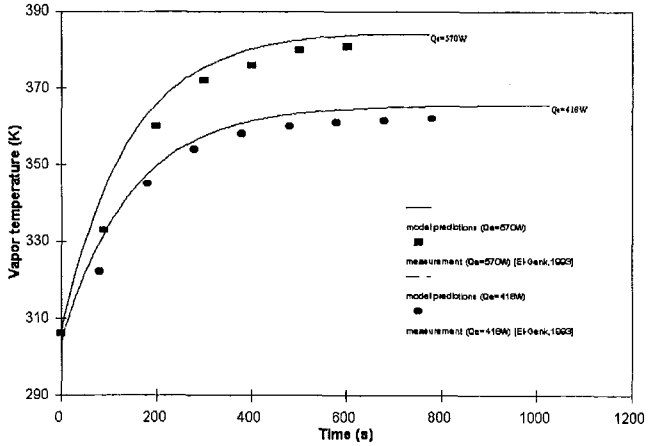

Fig. 3 Comparison of predicted and measured transient vapor temperatures of a cylindrical water-copper heat pipe

temperature heat pipes, as is shown in the following high temperature examples.

A high temperature, sodium stainless-steel heat pipe with multiple heat sources was fabricated and tested in the Heat Transfer Laboratory of Wright State University (Buchko, 1990). A description of the test setup is given in Table 2.

Figure 4 illustrates the comparison of the predicted steady-state vapor and wall temperatures with the experimental results (Buchko, 1990). Heat output from the four heaters was 504, 0, 0, and 507 watts, respectively. It can be seen that at steady state, the vapor is nearly isothermal along the heat pipe. The condenser wall temperature is approximately 8 deg lower than the vapor temperature. The two jumps in the wall temperature occur in regions where the two heaters are supplied with power.

As shown in Fig. 4, the numerical model significantly overpredicts the vapor and wall temperatures since the heat losses were not considered. The deviation between the predictions and the measurements is about 55 degrees in absolute value or 10 percent in relative measure. The reason for this overprediction, as mentioned before, is the neglecting of the heat losses in the numerical model. In the case of high temperature heat pipe, the heat losses can be large in magnitude and may cause errors in model predictions.

In order to assess actual heat losses from the heat pipe to the environment during experimentation, both the evaporator and the adiabatic sections were fitted with water-cooled calorimeters, as was the condenser. The measurements revealed that the heat losses in the evaporator and adiabatic sections were 401 and 55 watts, respectively (Buchko, 1990). In other words, more than 45 percent of the power input was lost to the surroundings instead of transported through the heat pipe.

With the heat losses included in the numerical calculation, the predictions are in good agreement with the experimental results. It should be pointed out that in a practical application such as the heat pipe turbine vane cooling, the "heat loss" should never be a concern since the entire heating and cooling conditions are integrated in the numerical model. Only in laboratory measurements, does the heat loss need to be detailed in order to tell how much heat is really put into the heat pipe.

Figure 5 shows the vapor temperature during a transient period after the power of each heater is suddenly increased from 90 watts to 115 watts. To account for additional heat capacities from the test setup including heaters, radiation shields and supports, etc., a transient heat input $Q = 90 + 25[1 - e^{(-t/480)}]$ was specified at the outer wall surface of the evaporator section (Cao and Faghri, 1991; Faghri et al., 1991). Comparisons with experimental results (Faghri et al., 1991) show good agreement.

The above comparisons between the numerical model and experimental results indicate that the model is capable of predicting the performance of a heat pipe under various heating and cooling conditions with good accuracy.

Table 2 The sodium stainless-steel heat pipe tested by Buchko

evaporator length	520 mm
adiabatic length	188 mm
condenser length	292 mm
heat pipe outer diameter	26.7 mm
vapor channel diameter	21.5 mm
wick (two wraps, stainless steel screen 100 mesh) thickness	0.456 mm
heating condition	4 electrical heating coils of 53 mm long and with 90 mm axial distance between each heater
cooling condition	radiation from the condenser surface to a water-cooled double-wall calorimeter (ε = 0.6 for the condenser surface and 0.9 for the calorimeter surface)

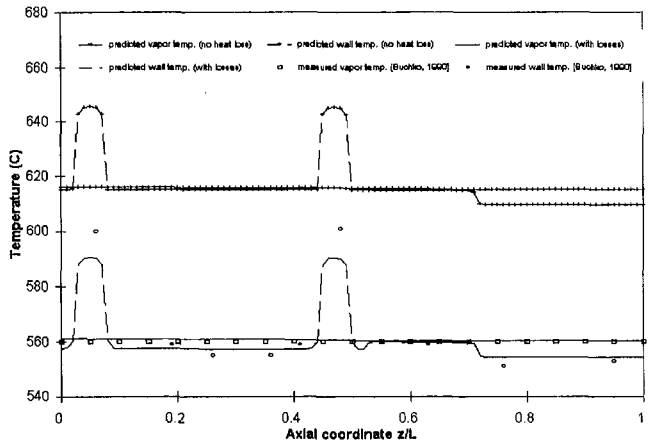

Fig. 4 Comparison of predicted and measured steady-state vapor and wall temperatures of a cylindrical sodium stainless-steel heat pipe with multiple heat sources

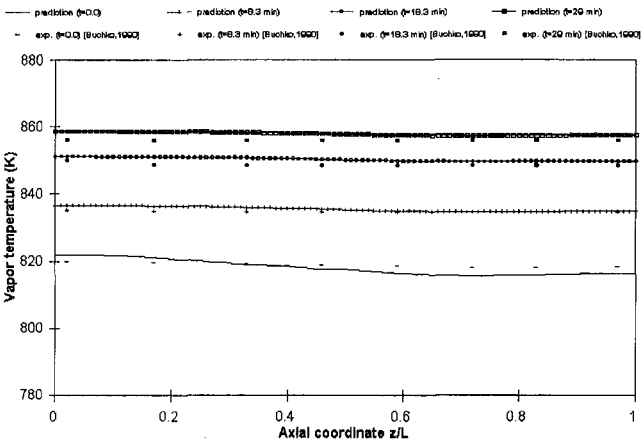

Fig. 5 Comparison of predicted and measured transient vapor temperatures of a cylindrical sodium stainless-steel heat pipe with multiple heat sources

Numerical Simulation of Heat Pipe Vane Performance. With the information based on an advanced military fighter turbine engine and supplied by the Allison Gas Turbine Division, Silverstein et al. (1994) proposed a preliminary heat pipe vane design. To examine the benefits of using heat pipe vanes and to provide insight into heat pipe vane operation, a detailed simulation was conducted using the numerical model developed in this work. To simplify the simulation, it was assumed that the heat pipe vane operates in a 0-g environment.

Dimensions and materials of the heat pipe vane are listed in Table 3 (Silverstein et al. 1994). Temperatures and heat transfer coefficients of the combustion gas, intermediate air, and bypass air depend on the turbine startup schedule. According to Silverstein et al. (1994), the most critical period for the heat pipe vane is from idle to full power when the largest sudden increase in both temperature and heat transfer coefficient is encountered. Temperatures and heat transfer coefficients of the combustion gas, intermediate air, and bypass air at both idle and full power states are listed in Table 4 (Silverstein et al., 1994).

One change has been made to the bypass air temperature at idle state. The original bypass air temperature at idle state is 320 K (Silverstein et al., 1994). However, as indicated by Silverstein et al. (1994) as well as a preliminary run of the present numerical model, continuum vapor flow cannot be established inside the heat pipe vane at the idle state. The purpose of the simulation is to study the transient performance of the heat pipe vane from a steady idle state to a steady full power state. Therefore, the bypass air temperature was changed to 400 K to ensure that a steady-state continuum vapor flow is formed inside the heat pipe vane.

Table 3 Dimension and material specifications of the heat pipe turbine vane designed by Silverstein et al.

span in combustion gas duct	8.26 cm
span in intermediate air duct	4.95 cm
span in bypass air duct	4.95 cm
chord	7.62 cm
area of vane cross-section	6.15 cm^2
surface length around vane cross-section	15.84 cm
wall thickness	0.1 cm
number of arteries	8
artery inner radius	0.05 cm
wick (Haynes 188 400-mesh screen) thickness	0.02 cm
effective pore diameter	20×10^{-4} cm
material of vane wall and endplates	CMSX-4 single crystal alloy*
working fluid	sodium

* Thermophysical properties listed in the report by Silverstein et al. (1994)

Table 4 Heating and cooling conditions of the heat pipe turbine vane designed by Silverstein et al.

	idle	full power
combustion gas temperature	890 K	1650 K
combustion gas heat transfer coefficient	550 (trailing edge) ~ 1200 (leading edge) W/m^2-K	1400 (trailing edge) ~ 3400 (leading edge) W/m^2-K
intermediate air temperature	700 K	700 K
intermediate air heat transfer coefficient	200 (trailing edge) ~ 430 (leading edge) W/m^2-K	355 (trailing edge) ~ 770 (leading edge) W/m^2-K
bypass air temperature	400 K	533 K
bypass air heat transfer coefficient	200 (trailing edge) ~ 430 (leading edge) W/m^2-K	355 (trailing edge) ~ 770 (leading edge) W/m^2-K

In Silverstein's paper (1994), the peak combustion gas temperature is 1978 K. With a layer of thermal barrier coating (TBC) applied to the surface of the vane, the surface temperature was calculated by Silverstein et al. as well below 1400 K. Since the present model does not include the effect of a TBC layer, the combustion gas temperature was assumed to be 1650 K.

Due to the special geometric configuration of the heat pipe vane, heat transfer coefficients of the combustion gas, intermediate air, and bypass air change with location. A comprehensive CFD analysis would be needed to accurately specify these external boundary conditions. To simplify the problem, it was assumed in this study that the heat transfer coefficient does not change with axial coordinate within each section. The circumferential change from the leading edge to the trailing edge is discussed as follows.

Instead of treating the vane as a flat plate to obtain a circumferential profile of the heat transfer coefficient, empirical correlations from a previous study by Zhang and Han (1994) were used in this study. With the circumferential profile of the heat transfer coefficient known from Zhang and Han's paper and the mean heat transfer coefficient known from Silverstein's paper, the local heat transfer coefficient is thus determined.

The mean heat transfer coefficient of the intermediate air flow was not specified by Silverstein et al. (1994). It was assumed in this study that the intermediate air flow has the same heat transfer coefficient as the by-pass air flow. A more precise approach would consider the Reynolds number of the flow.

Figure 6 illustrates the transient vapor temperature and pressure at evaporator exit and the evaporator leading edge wall temperature. While these parameters generally follow the same trend, the largest deviation in trend occurs during the first 20 s. The leading edge wall temperature radically increases due to direct contact with the combustion gas. The increase of vapor temperature is a little slower because of the heat capacitance of the vane wall and wick. The increase of vapor pressure is the slowest, especially for the first 5 s. The following two opposing effects contribute to the relatively slow increase of vapor pressure at the evaporator exit: (1) quick increase of vapor temperature tends to cause the vapor pressure to increase; and (2) a dominantly large vapor pressure drop at the evaporator exit is caused by a quick increase of vapor velocity.

It is seen from Fig. 6 that the heat pipe vane reaches steady state in approximately 100 s, which is about 10 times faster

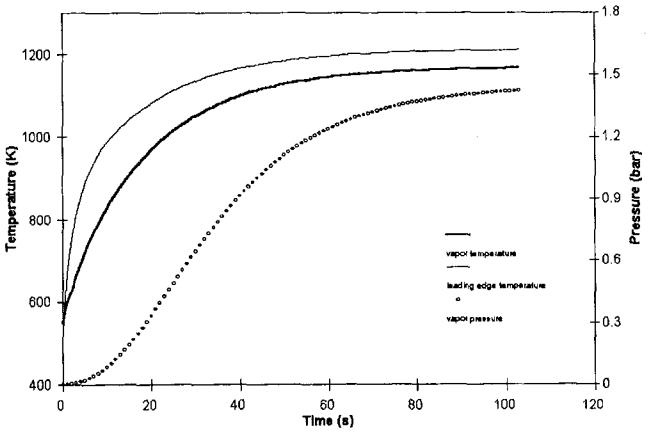

Fig. 6 Transient vapor temperature and pressure, and wall temperature in a heat pipe vane

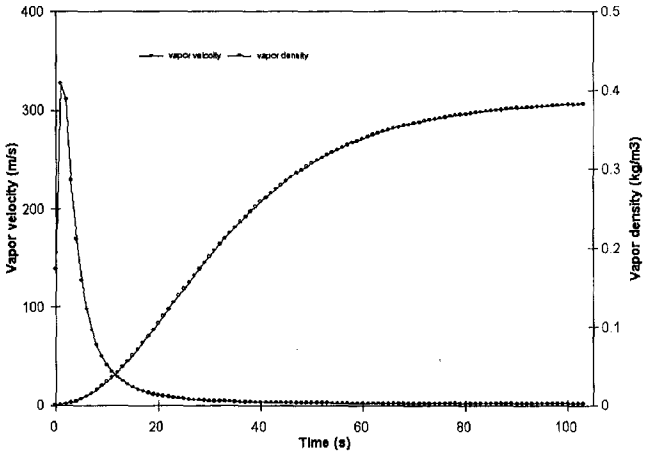

Fig. 8 Transient vapor velocity and density at evaporator exit of a heat pipe vane

than in the previous two cases (Figs. 1 ~ 5). The main reason is that the heat pipe vane is much smaller in size, resulting in a much faster wall and wick transient.

The largest temperature gradient across the leading edge wall is approximately 120°C/mm, corresponding to a heat flux of 2.5×10^6 W/m^2. The vapor pressure increases from 500 Pa to 140,000 Pa within approximately 90 s. This large rate of increase in the magnitude of the vapor pressure can present a serious threat to the vane assembly. In addition, since the turbine vane is in a high pressure environment, the pressure difference across the vane wall can be significant. Structural reinforcement will have to be employed to ensure the structural strength of the vane assembly.

Figure 7 shows the vapor temperature and the vapor pressure variation along the heat pipe vane during the transient period. The vapor flow is nearly isothermal at all times. The pressure drop in the evaporator section and the pressure recovery in the condenser section are observed. The vapor pressure variation lessens with time, which is mainly due to a decreasing vapor velocity profile (smaller frictional loss and vapor acceleration/deceleration). A similar relation between vapor velocity and vapor pressure variation has been indicated by Jang et al. (1991).

Figure 8 shows the transient vapor velocity and density at the evaporator exit. The vapor velocity first jumps to a large value due to the sudden increase of heat flux. After about 2 s, the increase of vapor density dominates, resulting in a decreasing vapor velocity. This phenomenon is particularly prominent for high temperature heat pipes because of the thermophysical properties of the liquid metals. Figure 8 indicates that the short period after suddenly increasing the heating power is the most critical period in terms of the sonic limit and the capillary limit. A steady-state model or even a transient model with a large time step may not be able to catch this velocity peak and thus be unable to accurately predict the heat pipe limitations.

In practice, there are generally two methods to increase the heat transfer rate of a heat pipe: (1) by increasing heat input to the heat pipe; and (2) by increasing cooling rate in the condenser of the heat pipe. Figure 8 indicates an interesting fact that method (2) is more likely to induce the sonic limit. When the condenser cooling rate is increased, the vapor velocity increases not only because of the larger heat transfer rate but also as a result of reduced vapor density due to a lower vapor temperature. Therefore, great care must be taken to avoid reaching sonic limit when increasing the condenser cooling capability. On the other hand, this is the reason that some researchers used method (2) to reach the sonic limit during the experiments (Kemme, 1969).

Figure 9 illustrates the transient energy and temperature of the vapor flow at the evaporator exit. The vapor flow energy is the sum of internal energy ($\rho_v A_v u_v C_{p,v} T_v$) and kinetic energy ($\rho_v A_v u_v (u_v^2/2)$), which can be viewed as the energy carried through the evaporator exit by the vapor flow. During the transient period, the largest change in vapor flow energy occurs in the first 20 s. After that, the vapor flow energy slightly decreases (due to the decreasing vapor velocity) and quickly reaches

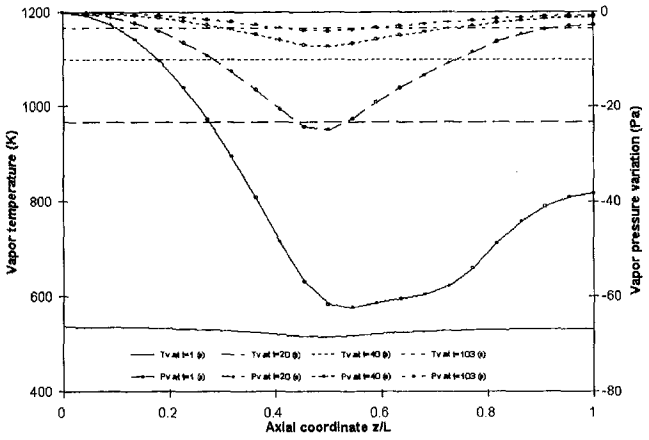

Fig. 7 Transient vapor temperature and pressure variation along a heat pipe vane

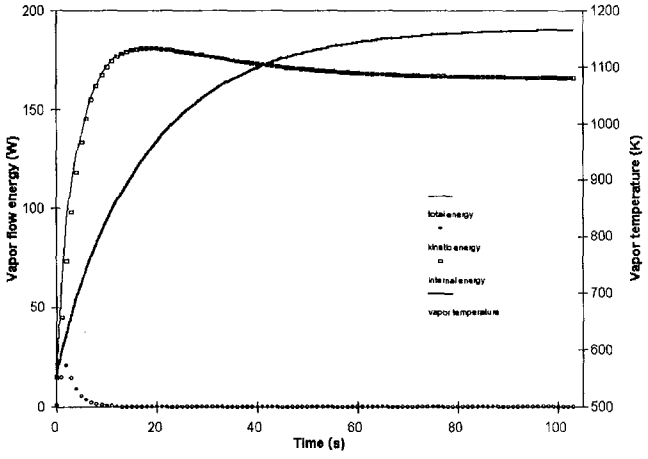

Fig. 9 Transient vapor energy and temperature at evaporator exit of a heat pipe vane

steady state at $t = 70$ s. In some sense, Fig. 9 reveals that the vapor flow energy, an indication of vapor dynamics, finishes its transient faster than the vapor temperature that is affected by a much slower wall and wick transient. Therefore, it might be possible to use a "quasi-steady" vapor model coupled with a transient wall conduction model to study the heat pipe transient, which results in significant savings in computational time. Further investigations are needed to justify this approach. As shown in Fig. 9, the internal energy constitutes most of the vapor flow energy whereas the kinetic energy is very small in magnitude.

Figure 10 shows steady-state outer wall temperatures of heat pipe vanes with different values of vapor channel cross-sectional area and wall thickness. In order to assess the advantage of the heat pipe vane cooling, the vane wall thickness was increased and the vapor channel cross-sectional area was correspondingly reduced. The worst case is, of course, a conventional vane with zero vapor channel cross-sectional area. As shown in Fig. 10, with a larger vapor channel cross-sectional area (correspondingly a larger "heat pipe effect"), the wall temperatures, the wall temperature variations from the leading edge to the trailing edge, and the wall temperature differences between the evaporator and condenser are reduced. This is favorable because (1) reduced wall temperature indicates more potential to increase the combustion gas temperature and thus the turbine efficiency, and (2) reduced wall temperature variations in both axial and circumferential directions lower the thermal stresses in the vane wall and thus prevent thermal fatigue and cracking.

In Fig. 11, the following three ratios are plotted to show performance limitations of the heat pipe vane during the transient: (1) ratio of the total pressure drop in the vapor and liquid to the available capillary pressure in the wick; (2) ratio of the maximum vapor velocity to the speed of sound; and (3) ratio of the maximum temperature gradient in the evaporator wick to the allowable temperature gradient across the wick. Because of the use of composite wicks including arteries, distribution, and pumping layers, the heat pipe vane is well below the capillary limit during the entire transient. The boiling limit is not a threat either, although the leading edge heat flux is quite high. The vapor flow Mach number reaches its maximum value at $t = 2$ s and then decreases due to the increasing vapor density/temperature. It can be concluded that the current design of heat pipe vane is able to complete this specific transient without any difficulty.

Silverstein et al. (1994) proposed an interesting idea that the liquid sodium in the wick might be initially under tension during the transient from idle to full power. To verify this concept, a frozen startup model including the liquid flow momentum equation will be needed. This is a good area for further investigation.

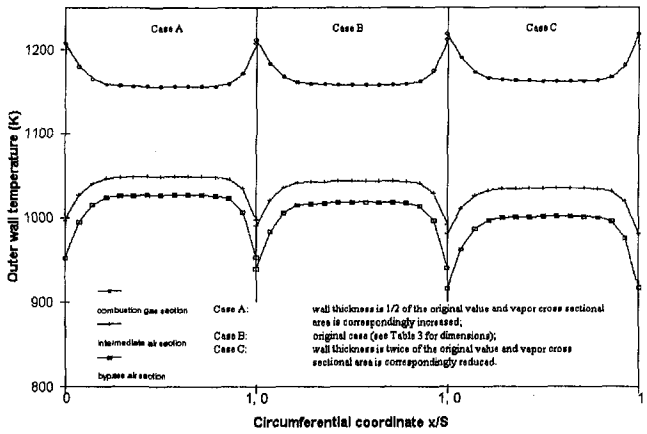

Fig. 10 Steady-state wall temperatures of heat pipe vanes with different wall thickness and vapor cross-sectional area

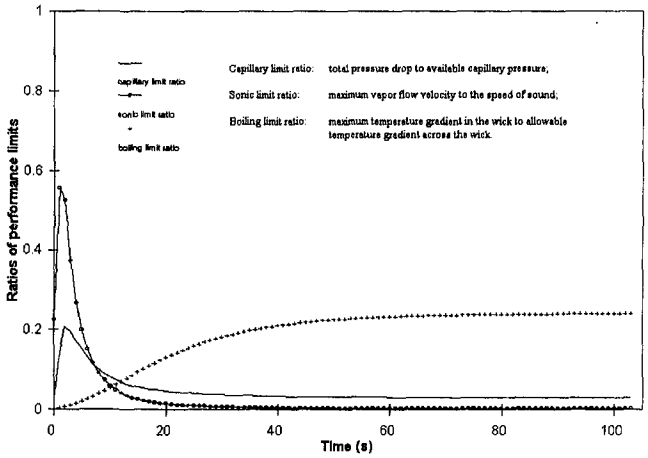

Fig. 11 Performance limitations during a heat pipe vane transient

Conclusions

The heat pipe is a promising candidate for turbine vane cooling. A numerical model has been developed to investigate the transient performance of the heat pipe vane. The coupled three-dimensional wall conduction and quasi-one-dimensional vapor flow model was solved using curvilinear coordinates.

The proposed numerical approach involving two iterative estimate-correction processes was able to efficiently solve the heat pipe vane model and produce reasonably accurate results. Both programming effort and computational time were significantly reduced by incorporating an iterative vapor temperature estimate-correction process instead of solving the complicated vapor flow energy equation. Comparisons with experiments validated the numerical model and the solution approach.

A detailed simulation of the transient behavior of a typical heat pipe vane was presented. Under the specified turbine startup schedule, the current heat pipe vane design can successfully complete the transient from idle to full power without encountering any performance limitation. Wall temperatures and wall temperature gradients can be reduced by using the heat pipe vane. It was shown that great caution must be taken when increasing the condenser cooling rate because of the increased possibility of reaching the heat pipe performance limitations.

This work is a first step in investigating technical feasibility and performance characteristics of the heat pipe vane cooling. Results from this work should provide a basis for further research and design.

References

Anderson, D. A., Tannehill, J. C., and Pletcher, R. H., 1984, *Computational Fluid Mechanics and Heat Transfer,* Hemisphere, Washington, D.C.

Bowman, W. J., 1991, "Numerical Modeling of Heat-Pipe Transients," *Journal of Thermophysics and Heat Transfer,* Vol. 5, No. 3, pp. 374–379.

Bowman, W. J., and Hitchcock, J., 1988, "Transient, Compressible Heat Pipe Vapor Dynamics," *Proc. 25th ASME National Heat Transfer Conference,* Houston, Texas, pp. 329–337.

Buchko, M. T., 1990, Experimental and Numerical Investigation of Low and High Temperature Heat Pipes with Multiple Heat Sources and Sinks, M.S. thesis, Wright State University, Dayton, OH.

Cao, Y., and Faghri, A., 1991, "Transient Multidimensional Analysis of Nonconventional Heat Pipes with Uniform and Nonuniform Heat Distributions," ASME *Journal of Heat Transfer,* Vol. 113, pp. 995–1002.

Cao, Y., and Faghri, A., 1993, "A Numerical Analysis of High-Temperature Heat Pipe Startup from the Frozen State," ASME *Journal of Heat Transfer,* Vol. 115, No. 1, pp. 247.

Chen, M., and Faghri, A., 1989, "An Analysis of the Vapor Flow and the Heat Conduction Through the Liquid-Wick and Pipe Wall in a Heat Pipe With Single and Multiple Heat Sources," *Proc. ASME/AIChE Heat Transfer Conference,* Paper No. 89-HT-12, pp. 1–8.

El-Genk, M. S., and Huang, L., 1993, "An Experimental Investigation of the Transient Response of a Water Heat Pipe," *International Journal of Heat and Mass Transfer,* Vol. 36, No. 15, pp. 3823–3830.

Faghri, A., 1995, *Heat Pipe Science and Technology,* Taylor & Francis, Washington, D.C.

Faghri, A., Buchko, M., and Cao, Y., 1991, "A Study of High Temperature Heat Pipes With Multiple Heat Sources and Sinks: Parts I and II," ASME *Journal of Heat Transfer,* Vol. 113.

Faghri, A., and Langston, L., 1995, Heat Pipe Turbine Vane Cooling, proposal submitted to RFP AGTSR 95-01, Storrs, CN.

Faghri, A., and Parvani, S., 1988, "Numerical Analysis of Laminar Flow in a Double-Walled Annular Heat Pipe," *Journal of Thermophysics and Heat Transfer,* Vol. 2, No. 2, pp. 165.

Harasgama, S. P., and Burton, C. D., 1992, "Film Cooling Research on the Endwall of a Turbine Nozzle Guide Vane in a Short Duration Annular Cascade: Part 2—Analysis and Correlation of Results," ASME *Journal of Turbomachinery,* Vol. 114, pp. 741–746.

Jang, J. H., Faghri, A., and Chang, W. S., 1991, "Analysis of the One-Dimensional Transient Compressible Vapor Flow in Heat Pipes," *International Journal of Heat and Mass Transfer,* Vol. 34, No. 8, pp. 2029–2037.

Kemme, J. E., 1969, "Ultimate Heat-Pipe Performance," *IEEE Transactions on Electronic Devices,* Vol. ED16, No. 8, pp. 717–723.

Langston, L., 1968, Preliminary Study of the Heat Pipe Vane, internal memo to Dr. M. Suo, Pratt & Whitney Aircraft, East Hartford, CN.

Nirmalan, N. V., and Hylton, L. D., 1990, "An Experimental Study of Turbine Vane Heat Transfer With Leading Edge and Downstream Film Cooling," ASME *Journal of Turbomachinery,* Vol. 112, pp. 477–487.

Patankar, S. V., 1988, "Elliptic Systems: Finite-Difference Method I," *Handbook of Numerical Heat Transfer,* Minkowycz et al., eds., Wiley, New York.

Shih, T. M., 1984, *Numerical Heat Transfer,* Hemisphere, Washington, D.C.

Silverstein, C. C., Gottschlich, J., and Meininger, M., 1994, "Feasibility of Heat Pipe Turbine Vane Cooling," ASME Paper 94-GT-306.

Zhang, L., and Han, J. C., 1994, "Influence of Mainstream Turbulence on Heat Transfer Coefficients From a Gas Turbine Blade," ASME *Journal of Heat Transfer,* Vol. 116, pp. 896–903.

Development of a Corrosion Resistant Directionally Solidified Material for Land Based Turbine Blades

N. S. Cheruvu
Southwest Research Institute,
Materials and Structures Division,
P.O. Drawer 28510,
San Antonio, TX 78228-0510

Advanced turbines with improved efficiency require materials that can operate at higher temperatures. Availability of these materials would minimize cooling flow requirements, and, thus, improve the efficiency of a turbine. Advanced processing, such as directional solidification (DS), can improve temperature capability of the majority of Ni based superalloys. However, results of earlier work on IN-738 reveal that the DS process does not significantly improve temperature capability of this alloy. A research program was initiated to develop a corrosion resistant Ni-based DS blade material for land based turbines. In this program, eight heats with varied Cr, Al, Ti, Ta, and W contents were selected for evaluation. Screening tests performed on these heats in the DS condition include tensile, creep, and corrosion. The results of experimental heats were compared with those of IN-738 in the equiaxed condition. From these results, two chemistries offering approximately 100°F temperature advantage at typical row 1 turbine blade operating stress were selected for castability and further mechanical property evaluation. Several row 1 solid and cored turbine blades were successfully cast. The blades were evaluated for grain structure and mechanical properties. Tests were also conducted to evaluate the effects of withdrawal rates on properties. These results are summarized in this paper.

Introduction

There has been a great demand for the most efficient land based turbines. Operation at higher firing temperatures increases efficiency of a gas turbine. All major original equipment manufacturers have been engaged in developing advanced and efficient gas turbines with firing temperatures approaching 1500°C (2732°F) (Farmer et al., 1995; McQuiggan, 1996; Sato et al., 1994). These advanced turbine designs demand new materials and/or technologies that offer higher temperature capability. As a result, there is a great interest in the application of columnar grain (DS) and single crystal (SC) airfoils to these turbines (Carruel et al., 1996; Yamamoto et al., 1995; Sato et al., 1995; Matsuzaki et al., 1992). The DS and SC airfoil technology was initially developed for aero engines in the 1960s. DS blades and SC blades were introduced in the aero engines in mid-1960s and 1970s, respectively. However, this technology was not transferred to the large land based turbine application until recently. The delay in technology transfer from aeroengine to land based gas turbines is partly due to unavailability of cost effective casting processes for large size components.

Recent developments in casting technology has now made it possible to cast large land based turbine blades in the DS (columnar) or SC condition. The DS and SC blades were introduced in the land based gas turbines in 1989 and 1995, respectively (Peterson, 1989; Becker et al., 1995). Westinghouse has introduced DS blades in their 501 G turbine (McQuiggan, 1996). Under ATS funded programs, considerable amount of development work is being performed by all original equipment manufacturers and casting producers on DS and single crystal (CM-247 and CMSX-4 type) alloys. The primary objectives of these programs include (1) optimization of process parameters for large castings to improve casting yield, (2) evaluation of the influence of defects on properties, and (3) assessment of the influence of process parameters, heat treatment, and chemistry on properties.

Initial casting runs for large DS blades for use on land based turbines were performed using IN-738 material (Peterson, 1989; Beck, 1983). For these trials and evaluation, IN-738 material was selected because it has been widely used in the industry for land based turbine blades and vanes (Schneider, 1990). IN-738 exhibits optimum combination of creep strength and hot corrosion resistance. These evaluations revealed that the DS process offered marginal or no improvement in rupture life compared to the rupture of life of equiaxed IN-738. It has been reported by McLean (1983) that the alloys showing a marginal or no improvement tend to have high chromium contents and low volume fraction of γ'. These alloys are normally solution treated at a lower temperature than the alloys (Mar M 200 and Mar M 246) that derive the greatest rupture life improvement from the DS processing. The volume fraction of γ' in an alloy is inversely related to chromium content because chromium increases solubility of γ' formers in the matrix and directly related to solution temperature (Sims et al., 1987). In other words, volume fraction of γ' as well as solidification conditions have significant influence on the rupture life improvement derived by directional solidification.

In 1990, a major program was initiated at Westinghouse to develop a corrosion resistant DS alloy for land based turbine applications. In this program, IN-738 was considered as a base alloy since land base turbine blades traditionally require high chromium levels for corrosion resistance. The elements that contribute to solid solution strengthening, Ta, W, and Cr, and elements that contribute to γ' volume fraction, Al, and Ti contents were selectively varied in IN-738 to enhance rupture life improvement following directional solidification. The requirements set for the new DS alloy were as follows (Pallotta, 1993; Bannister, 1994; Cheruvu, 1995):

Contributed by the International Gas Turbine Institute and presented at the International Gas Turbine and Aeroengine Congress and Exhibition, Orlando, FL, June 2–5, 1997. Manuscript received by the ASME Headquarters July 1, 1997. Paper No. 97-GT-425. Associate Technical Editor: H. A. Kidd.

Table 1 Chemical composition of experimental heats (wt%)

ELEMENT	HEAT IDENTIFICATION								IN
	SAS#1	SAS#2	SAS#3	SAS#4	SAS#5	SAS#6	SAS#7	SAS#8	738
Cr	16	16	14.8	16	17	17	14.75	14	16.0
Co	8.5	8	8	8	8	8	8	8	8.5
Al	3.4	3.4	3.6	4	4	3.4	4	4	3.4
Ti	4.3	4.3	4.3	3.4	3.4	4.3	3	3	3.4
W	2.6	2.6	2.6	2.6	2.6	2.6	4.3	5	2.6
Mo	1.8	0.9	1	0.6	0.4	0.5	0.6	1	1.75
Ta	1.8	2.7	2.7	2.7	1.8	1.8	2.8	3	1.75
Cb	0	0	0.5	0	0	0	0.5	1	0.9
C	0.1	0.1	0.1	0.1	0.1	0.1	0.1	0	0.11

- chromium content greater than or equal to 15 percent
- castable
- temperature advantage of 40 to 55°C (75° to 100°F) at typical row 1 blade operating stress level
- stable with respect to sigma phase precipitation during long-term service
- corrosion and oxidation resistance comparable to IN-738

The results of this program are summarized in this paper.

Directionally Solidified Test Material

The Cr, Al, Ti, Ta, and W were varied in IN-738 and a total of eight chemistries were chosen for evaluation. The nominal aim composition of these eight experimental heats is given in Table 1. Among these heats, chromium and tungsten contents were varied from 14 to 17 percent and 2.6 to 4.5 percent, respectively. Aluminum to titanium ratio was varied from 0.8 to 1.3. The chemistries of test heats were adjusted to maintain Nv value equal to or below 2.4. Directionally solidified test bars (19 mm in diameter × 200 mm long) were cast at Howmet Casting, Hampton, VA. The process parameters, such as mold and pouring metal temperatures, furnace withdrawal rates, etc., used for casting these bars were the same as those used for casting a large, first row turbine blade. The test bars were partially solution treated at 1121°C (2050°F) for two hours and aged at 843°C (1550°F) for 24 hours, along with a set of production blades. Screening tests were performed on these heats in the DS condition to select the best chemistries for further evaluation. Following the selection of optimum chemistries, test slabs and solid and cored blades were cast for further evaluation.

Screening Test Results

The screening test results revealed that alloys containing high chromium and/or tungsten (SAS 5 through 8) did not offer improvement in mechanical properties. Short term rupture properties of these heats were comparable to or slightly lower than that of equiaxed IN-738. The heats, SAS 1 through SAS 4,

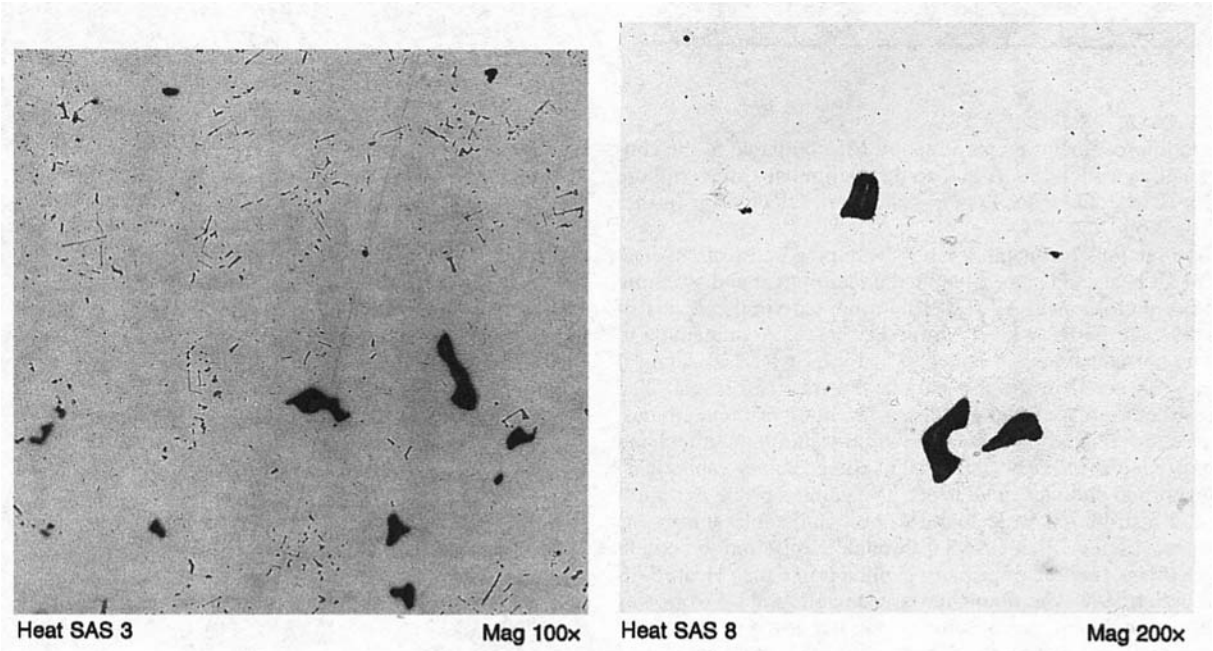

Fig. 1 Typical micro porosity variation in the DS test bars

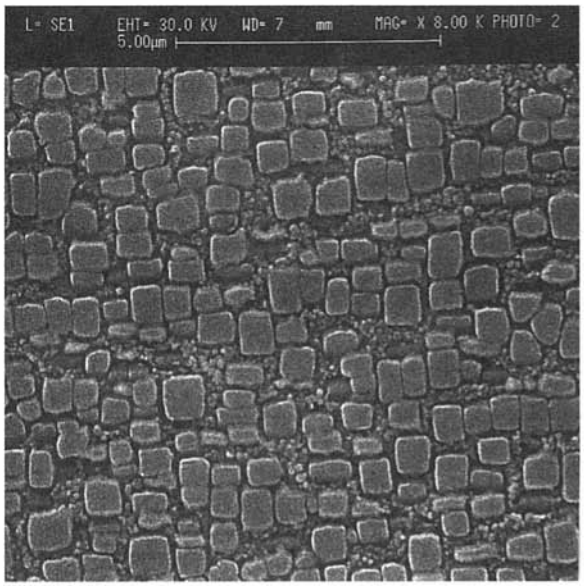

Heat SAS 3 Mag 10000×

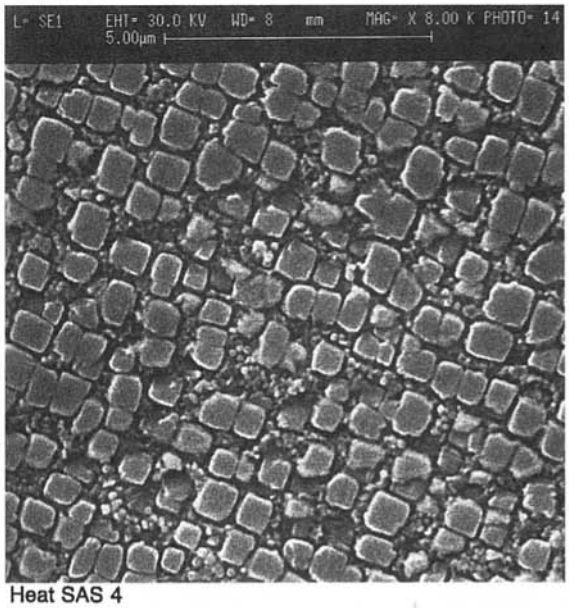

Heat SAS 4

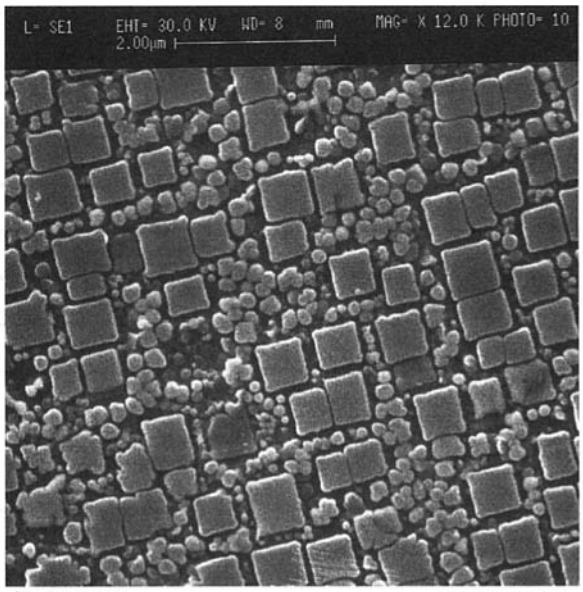

Heat SAS 8 Mag 12000×

Fig. 2 Gamma prime particle and distribution in the test bars

offered improvement in creep rupture life compared to the conventionally cast IN-738. Based on the preliminary creep rupture results, SAS 3 and SAS 4 chemistries were selected for further investigation.

Microsections for metallography were prepared from the test bars of all heats and were examined under optical and scanning electron microscopes. All test bars exhibited similar levels of porosity. The porosity levels in the DS bars are comparable to what is normally seen in conventionally cast IN-738. Typical porosity observed in the test bars is illustrated in Fig. 1. The microstructure of test bars consists of gamma prime, carbides, and eutectic islands. As expected, partial solution treatment and aging produced primary (cuboidal) and secondary (spherical) gamma prime particles in all heats. The gamma prime morphology and distribution were found to be comparable among the test heats (Fig. 2). Heats SAS 5 through 8 appeared to contain lower volume fraction of primary gamma prime than Heats SAS 1 through 4. However, no quantitative metallography work was performed to determine variation of gamma prime volume fraction among the experimental heats. In addition, SAS 7 and SAS 8 alloys containing higher levels of tungsten, exhibited significantly more MC carbides than the other six alloys. Typical distribution and morphology of MC carbides in these heats is shown in Fig. 3. These carbides were found to be rich in

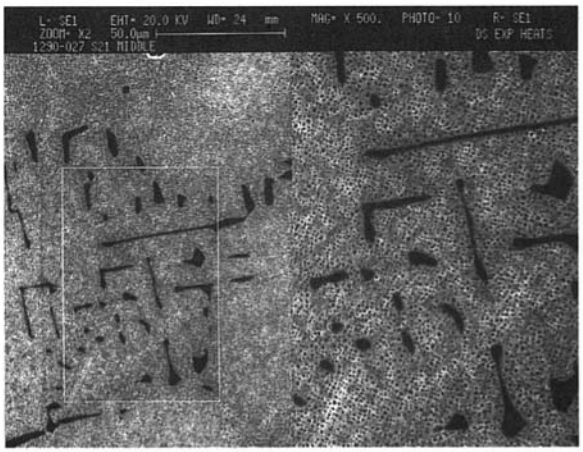

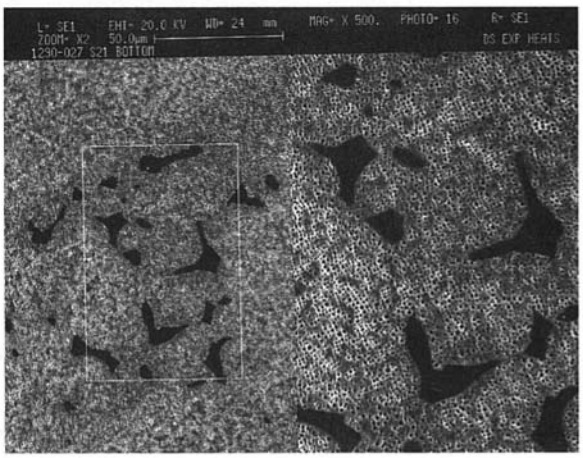

Fig. 3 MC carbides SAS 7 (top) and SAS 8 (bottom)

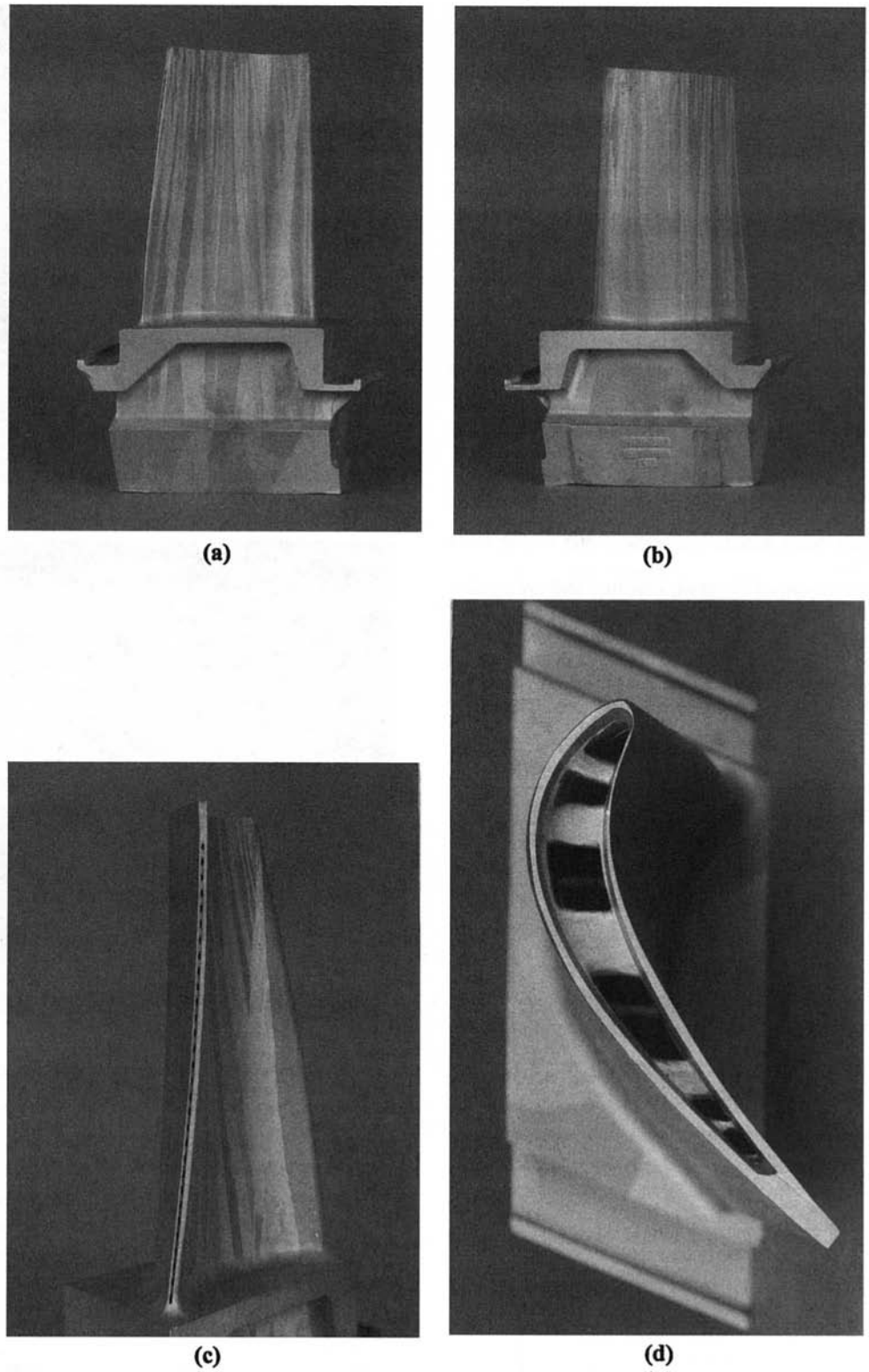

Fig. 4 501 F row 1 directionally solidified blade: (*a*) concave side; (*b*) convex side; (*c*) trailing edge cooling holes; and (*d*) blade tip and internal cooling hole passages

titanium and tungsten (TiC or WC). Tantalum carbides were also seen in the test bars.

Blade Casting Trials

The primary objective of blade casting trials was to establish the castability of these alloys into large complex cooled blades. The secondary goal is to evaluate the mechanical properties of specimens machined from a turbine blade. The W 251 and 501F row 1 blades were chosen for initial casting trials. The W 251 row 1 blade was cast as a solid blade. The 501F blade was cored to cast with conventional serpentine cooling passages and trailing edge cooling holes. For casting these parts, Howmet used their proprietary process parameters developed for large blades. The blades were withdrawn at 305 to 406 mm/h (12 to 16 in/h) and were cast using 100 percent virgin heat. The test

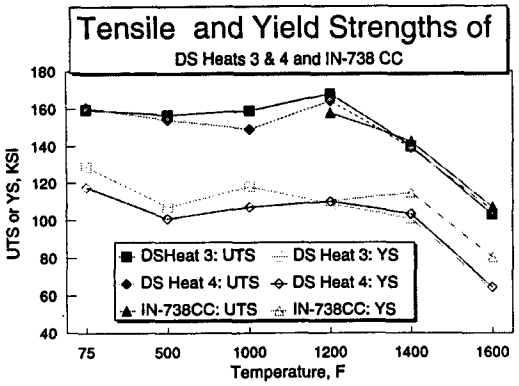

Fig. 5 Comparison of tensile and yield strengths of DS with that of equiaxed IN-738

specimens were machined from the W 251 solid blades for long-term mechanical properties and alloy stability evaluation. To evaluate the effects of withdrawal rates on properties, test slabs were also cast using withdrawal rates of 305 to 406 mm/h (12 and 16 in/h).

The blades were examined for grain structure and orientation with respect to the blade stacking axis, number of grains per unit length across the blade airfoil, freckle chain size and location, and isolated equiaxed grains, etc. Both solid and cored blades exhibited a good grain structure, and the angle between grain was within 15 deg to the blade stacking axis. The blade

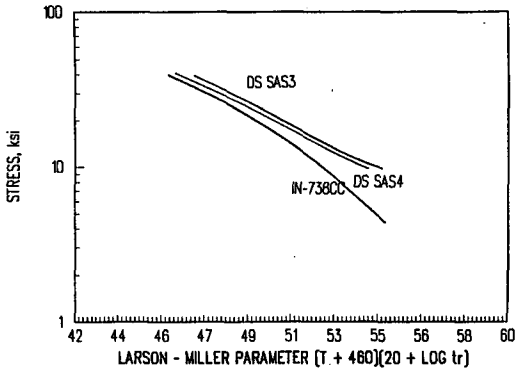

Fig. 6 Comparison of creep rupture of strength of DS alloys and equiaxed IN-738

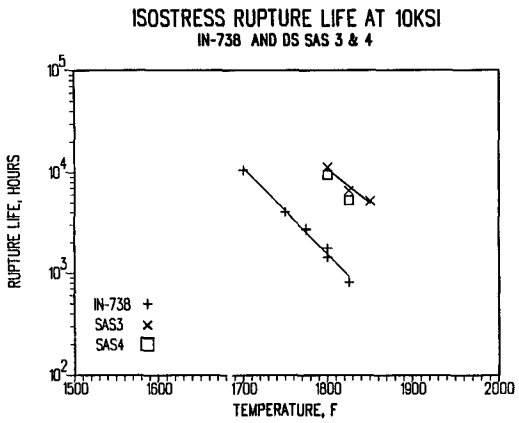

Fig. 7 Creep rupture life and temperature of advantage of DS alloys over equiaxed IN-738

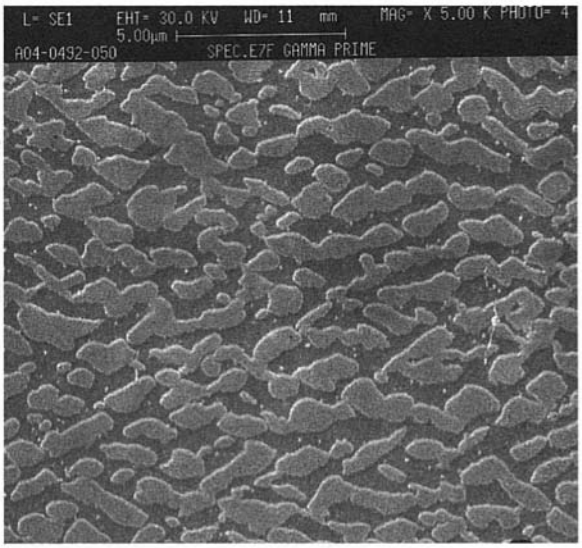

SAS 3

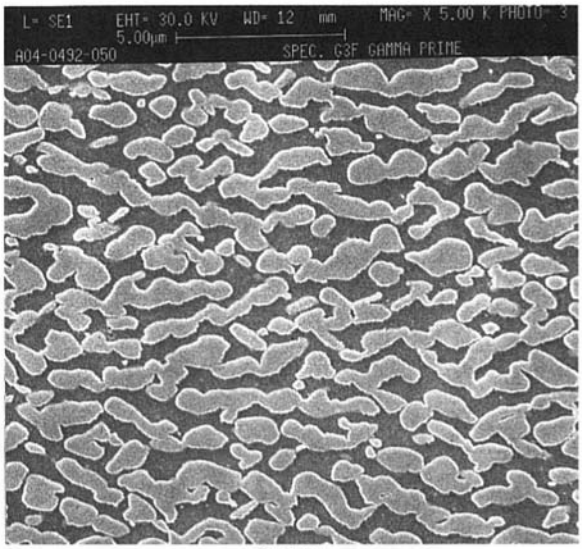

SAS 4

Fig. 8 Micrographs of cross sections from the gage area of broken creep rupture specimens. The creep tests were conducted at 1600°F and 25 ksi. Rupture life was approximately 10,000 hours. No sigma phase was observed.

air foils were free of freckles and equiaxed grains (Fig. 4). A few isolated freckle chains were noted in the shank below the blade platform. Following macro examination, both solid and

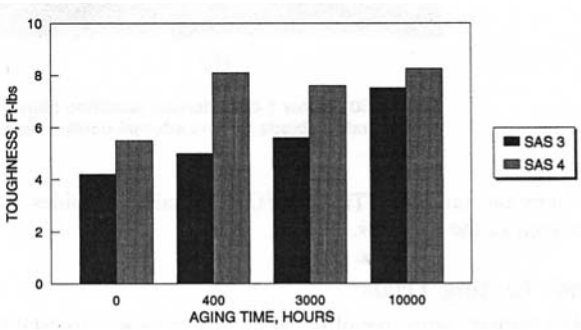

Fig. 9 Room temperature impact toughness of DS heats as a function of aging time at 1600°F

Table 2 Influence of withdrawal rate on tensile properties of DS SAS 4 alloy

Material ID	Rate, in./hr	Test Temp, F	UTS, KSI	YS, KSI	%EL	%RA
SAS 4-1	12	1200	146.4	119.9	12.6	16.0
SAS 4-2	12	1200	148.5	112.8	11.3	17.3
SAS 4-3	12	1600	97.5	66.8	21.9	30.2
SAS 4-4	12	1600	100.8	80.5	15.0	24.3
SAS 4-5	16	1200	144.4	112.9	11.1	16.2
SAS 4-6	16	1200	151.6	111.6	12.6	15.4
SAS 4-7	16	1600	100.1	75.9	17.8	22.9
SAS 4-8	16	1600	102.7	80.6	16.6	24.5

Table 3 Influence of withdrawal rate on creep rupture properties of DS SAS 4 alloy

Withdrawal Rate, in/hr	Stress, ksi	Life, hours	%EL	%RA
12	35	783	15.1	18.2
12	35	832	16.5	26.0
12	40	308	15.6	20.4
12	40	298	14.4	21.7
16	35	824	17.2	20.6
16	35	899	19.0	26.4
16	40	293	15.0	19.5
16	40	302	20.5	21.3

cored blades were sectioned for micro examination. As part of blade qualification, the micro sections prepared from the blades were examined for porosity and intergranular attack. Both solid and cored blades met quality assurance requirements.

Mechanical Properties

Tensile Properties. Tensile tests were performed as a function of temperature on specimens machined from the directionally solidified test bars and slabs of SAS 3 and SAS 4 heats. The bars and slabs were cast from two heats. The specimen length is oriented in the DS growth direction. The yield and tensile strengths of DS SAS 3 and SAS 4 are compared with that of equiaxed IN-738 in Fig. 5. The tensile strength of DS alloys was comparable to that of IN-738. The yield strengths of DS alloys were slightly lower, at 760° and 871°C (1400° and 1600°F), than that of IN-738. This variation in yield strength between DS alloys and IN-738 was not considered significant because cast alloys typically exhibit 34–68 MPa (5–10 ksi) scatter.

Creep Rupture Properties. Creep rupture specimens were machined from the test bars, slabs and blades and tests were conducted at various temperatures and stresses. The creep rupture time among the specimens varied from approximately 200 to 12,000 h. The results of specimens machined from the test bars, slabs, and blades are comparable. The creep rupture results of DS alloys (SAS 3 and SAS 4) are compared with that of IN-738 in Fig. 6. At all stress levels, the rupture strength of both DS alloys is greater than IN-738. In other words, these DS alloys offer temperature advantage over IN-738 at the stress levels investigated. The temperature advantage of DS alloys varied with applied stress level; at lower stress levels it is larger. To determine temperature advantage, creep rupture tests were also performed at applied stress of 10 ksi and at different temperatures. The results of these tests showed that the DS alloys offer approximately 100°F temperature advantage compared to IN-738 (Fig. 7).

Influence of Withdrawal Rate on Properties. In general, slower withdrawal rates affect dendrite arm spacing, the degree of segregation, and MC carbide morphology, etc. The dendrite arm spacing, DS grain size, degree of segregation, and MC carbide size are inversely related to the withdrawal rate. These microstructural variations have a strong effect on mechanical properties of an alloy. The effects of withdrawal rates on tensile and creep rupture properties were evaluated on SAS 4 alloy. The test slabs were cast using withdrawal rates of 305 to 406 mm/h (12 and 16 in/h). The test bars were given a standard solution and aging treatment. The standard heat treatment consists of a partial solution treatment at 2050°F for two hours followed by an aging treatment at 1550°F for 24 hours. Tensile tests were performed at 1200° and 1600°F and the results are presented in Table 2. The results showed that withdrawal rate had no effect on the tensile properties.

Creep rupture tests were performed at 871°C (1600°F) and two stress levels (35 and 40 ksi), and the results are given in Table 3. These results showed that a decrease in withdrawal rate had no effect on creep rupture life and ductility. The effects of withdrawal rate on microstructure have not investigated since the creep properties were found to be independent of withdrawal rates investigated.

Alloy Stability. The long-term stability of the DS alloys with respect to sigma, mu, or eta phase precipitation were evaluated by examining microstructure of creep rupture test specimens tested at 871°C (1600°F) for 10,000 h. Microsections were prepared from the gage and the shoulder section of the test specimens. These sections were examined under an optical microscope. Thin foils were also prepared from the test specimens for transmission electron microscopy. The examination of these samples revealed no acicular sigma, mu, or eta phases (Fig. 8). After 10,000 h exposure at 1600°F, the gamma prime particles in the shoulder and gage section of the specimens have coarsened at the expense of secondary gamma prime particles. The gamma prime particles in the shoulder section were rounded while in the gage section were elongated perpendicular to the loading direction.

It is well known that precipitation of acicular phases (sigma, mu, or eta) in an alloy during long-term service embrittles the alloy. To evaluate the effect of aging on toughness, round impact specimens were machined from the shoulder section of creep rupture specimens tested at room temperature after aging at 871°C (1600°F) for different times ranging from 0 to 10,000 h. In the unaged condition, toughness of DS test bars is comparable to that of IN-738. The impact test results are presented in Fig. 9. Consistent with microstructural observations, the aging at 1600°F did not lower toughness of DS alloys. Toughness of both alloys were slightly increased as a result of aging. These results coupled with the observation of absence of acicular phases in the microstructure suggest that both SAS 3 and SAS 4 heat are stable during long term service.

Corrosion and Oxidation. Cyclic hot corrosion tests were performed at 815° and 871°C (1500° and 1600°F) on DS alloys along with IN-738. For these tests the specimens were sprayed with Na_2SO_4 salt prior exposure to thermal cycles. The thermal cycle consists of 55 min at the test temperature and five min for cooling to the room temperature. The specimens were resprayed every 100 cycles of exposure. Cyclic hot corrosion behavior of alloys was evaluated by weight change measurements and metallography. Both weight change and metallography results indicated that the corrosion resistance of these alloys decreases in the order listed SAS 4, IN-738, and SAS 3. After 400 thermal cycles at 871°C (1600°F), the depth of corrosion attack in SAS 4, IN-738, and SAS 3 was found to be 60, 180, and 400 μm, respectively.

Oxidation tests were conducted at 1850°F (1010°C) for 1200 h. The specimens were cycled three times a day and for a total of 107 cycles. Following testing, metallographic samples were prepared and depth of attack in SAS 4, SAS 3, and IN-738 was found to be 58, 70, and 150 μm, respectively. These results show that the oxidation resistance of DS alloys is comparable to that of IN-738, if not better.

Summary

To develop a corrosion resistant DS alloy for land based turbine application, the solid solution strengthening (Ta, W, and Cr) and γ' forming elements (Al, Ti) contents were selectively varied in IN-738 to enhance rupture life improvement following directional solidification. Following screening tests, two chemistries (SAS 3 and SAS 4) were selected for a systematic study on castability, corrosion resistance, alloy stability, and mechanical properties evaluation. The following conclusions can be drawn from the results of this study.

- SAS 3 and SAS 4 chemistries are castable. Castability of these alloys was demonstrated by casting a complex cooled 501 G row 1 blade.
- These DS alloys offer 55°C (100°F) temperature advantage over equiaxed IN-738.
- Hot corrosion and oxidation resistance of these alloys are comparable to that of IN-738.
- The DS alloys are stable with respect to sigma phase precipitation. No sigma, mu, or eta phases were observed in broken creep rupture specimens which were tested at 871°C (1600°F) and 172 MPa (25 ksi) for 10,000 h.

Acknowledgments

The author was formerly a Fellow Engineer, Westinghouse Electric Corporation, 4400 Alafaya Trail, Orlando, FL 32826. This work was performed at Westinghouse. He wishes to acknowledge Westinghouse Electric corporation for permission to publish this work. The author also wishes to thank Dr. B. B. Seth for his critical review of the paper and his valuable comments.

References

Bannister, R. L., Cheruvu, N. S., Little, D. A., and McQuiggan, G., 1994, "Development of Requirements for an Advanced Gas Turbine System," ASME Paper No. 94-GT-388.

Beck, G., 1983, "Evaluation of DS IN-738 Material," unpublished work, Westinghouse Electric Corporation, Orlando, Florida.

Caruel, F., et al., 1996, "Snecma Experience With Cost Effective DS Airfoil Technology Applied Using CM 186LC® Alloy," ASME Paper No. 96-GT-493.

Cheruvu, N. S., and Roan, D. F., 1995, "Directionally Solidified and Single Crystal Blades For Land Based Turbines," presented at TMS-AIME Fall Meeting/ASM Materials Week, Oct. 29–Nov. 2, 1995, Cleveland, Ohio.

Farmer, R., and Fulton, K., 1995, "Design of 60% Net Efficiency in Frame 7/9H Steam Cooled CCGT," *Gas Turbine World,* May, pp. 12–20.

Matsuzaki, H., et al., 1996, "New Advanced Cooling Technology and Material of the 1500°C Class Gas Turbine," ASME Paper No. 96-GT-16.

McLean, M., 1983, *Directionally Solidified Materials or High Temperature Service,* The Metals Society, 1 Carlton House, London SW1Y 5DB, pp. 153.

McQuiggan, G., 1996, "Design for High Reliability and Availability in Combustion Turbines," ASME Paper No. 96-GT-510.

Pallotta, A. A., and Srinivasan, V., 1993, "Trends in Combustion Turbine Materials and Coatings Westinghouse Perspective," presented at EPRI Workshop, Palo Alto, California, Oct., 1993.

Sato, M., et al., 1994, "High Temperature Demonstration Unit for a 1500°C Class Gas Turbine," ASME Paper No. 94-GT-412.

Sato, M., et al., 1995, "High Temperature Demonstration Unit for a 1500°C Class Gas Turbine," ASME Paper No. 95-GT-365.

Sims, C. T., Stoloff, N. S., and Hagel, W. C., 1987, *Superalloys II,* John Wiley & Sons, New York.

Schneider, K., 1990, "Advanced Blading," *Proceedings of COST 501 and 505 Conference on High Temperature Materials For Power Eng.:* Part II," Kluwer Academic Publishers Group, Boston, MA, pp. 935.

Yamamoto, Y., 1995, "Material Evaluation of Large Single Crystal and Directionally Solidified Bucket Castings for Advanced Land-Based Gas Turbines," ASME Paper No. 95-GT-449.

Steady-State Response of Continuous Nonlinear Rotor-Bearing Systems Using Analytical Approach

J. W. Zu

Z. Y. Ji

Department of Mechanical and Industrial Engineering, University of Toronto, 5 King's College Road, Toronto, Ontario, Canada, M5S 3G8

A continuous modeling of nonlinear rotor-bearing systems is presented in this paper. The shaft is treated as a distributed parameter system using Timoshenko beam theory. A close form, steady-state response of the system is solved analytically for the first time. For cubic nonlinear bearings, the response is composed of three components, synchronous vibration, subsynchronous, and supersynchronous vibration. The harmonic balance method is used to calculate the nonlinear bearing forces. Two examples of nonlinear rotor-bearing systems are shown to illustrate the analysis procedure and the nonlinear characteristics of the system. Solutions from simplified systems are also derived for comparison.

Introduction

Bearings in rotor-shaft systems generally possess nonlinear behavior. For example, the nonlinearity in ball bearings is due to Coulomb friction and the angular clearance between the roller and the ring. Yamamoto (1981) showed that the nonlinear force in single-row deep groove ball bearing is related to the third power of deflections. Ishida (1990) obtained the bearing force for double-row angular contact ball bearings and showed that they are related to the fourth power of deflections.

A simpler model to describe a rotor-bearing system is to treat the whole system as a two degree of freedom rotor. Yamamoto et al. (1979, 1981, 1982) used the harmonic balance method to study the subsynchronous and supersynchronous vibrations of a two degree-of-freedom rotor mounted on nonlinear bearings. Further, Ishida et al. (1990), theoretically and experimentally, discussed nonlinear forced oscillations caused by quartic nonlinearity in angular contact ball bearings. A good agreement was obtained between analytical results and experimental results.

For more accurate modeling of the shaft, discretization methods such as the finite element method are used to approximate the rotor systems as having a finite degree of freedom. Zhao et al. (1994) presented solutions for the imbalance response and stability of squeeze-film-damped nonlinear rotor bearing systems using a collocation method together with a nonlinear least squares regression. Hahn and Chen (1994) analyzed a general squeeze film damped multi-degree-of-freedom rotor systems with motion dependent damper forces.

Harmonic balance analysis was performed to obtain the frequency response of the system. Based on the finite element model of the shaft, Nelson et al. (1982) introduced the method of component mode synthesis to reduce the size of a large order rotor system of equations substantially and solved for forced response of nonlinear bearing systems. Later, in conjunction with the method of component mode synthesis, Nataraj and Nelson (1989) proposed a new quantitative method of estimating steady-state periodic behavior in nonlinear systems, which was developed from the trigonometric collocation method. van de Vorst et al. (1996) analyzed self-excited oscillations of a rotor system supported by oil journal bearings using finite element model and component mode synthesis method. The generalized polynomial expansion method (GPEM), which is another modeling technique, was introduced by Shiau and Jean (1990), Hwang and Shiau (1991), and Shiau et al. (1993) to nonlinear rotor-bearing systems. Compared with the finite element method, the GPEM requires less computing time without reducing accuracy. However, this method is also a numerical approximation by nature.

The most accurate modeling of a rotor-bearing system is the continuous rotor-bearing system modeling using analytical methods. The shaft is treated as a distributed parameter system using beam theory and this results in partial differential equations to describe the motion of the system. While this approach was used to model linear systems such as the work by Eshleman and Eubanks (1969), Zu and Han (1992, 1994), it is rarely used to model nonlinear systems due to the complexity of the analytical approach. Ishida et al. (1996) investigated nonlinear forced oscillations of a vertical continuous rotor with distributed mass. The restoring force of the rotor has geometric stiffening nonlinearity due to the extension of the rotor center line. Shaw (1988) studied transverse vibrations of a slender spinning beam, in which the nonlinear stiffness due to mid-line stretching and nonlinear inertia effects due to the rotation were considered. The only work found so far on nonlinear bearings is by Lee et al. (1993) who applied transfer matrix method, a semi-analytical method, in conjunction with the harmonic balance method to obtain the steady-state response of rotor systems with cubic nonlinear bearings. In their work, the shaft segment is modeled by Timoshenko beam theory. However, the global equations for the transfer matrix cannot be derived and a reformulation is necessary for different systems. In addition, a large number of unknowns are involved in their calculations.

In this work, a continuous shaft-rotor system supported by nonlinear bearings is studied via analytical approach. The shaft is treated as a distributed parameter system described by Timoshenko beam theory and rotor wheels are modeled as rigid disks. In practical machinery, bearings may possess unsymmetrical nonlinearity. However, as a first step to model nonlinear bearings analytically, the bearings are assumed to have cubic stiffness and linear damping characteristics for simplicity. Thus, the bearing force components may be written as

$$F_x = K_1 u_x + K_3 u_x^3 + C\dot{u}_x$$
$$F_y = K_1 u_y + K_3 u_y^3 + C\dot{u}_y, \qquad (1)$$

where K_1 and K_3 are the linear and nonlinear spring force coefficients, and C is the linear damping coefficient. The harmonic

Contributed by the Gas Turbine Division. Manuscript received by ASME Headquarters July 1, 1997. Associate Technical Editor: H. D. Nelson.

balance method is used and a close-form solution for steady-state response of the system is solved for the first time. Two examples of nonlinear rotor-bearing systems are used to illustrate the analysis procedure and system response characteristics.

Analysis of the Shaft

For a continuous shaft depicted in an inertial frame $oxyz$ in Fig. 1, there are four generalized displacements when considering the shear deformation and rotary inertia. u_x and u_y are the two transverse displacements along x and y-direction and ψ_x, ψ_y are the corresponding bending angles. Introducing the complex variables, $u = u_x + iu_y$, $\psi = \psi_x + i\psi_y$ and the nondimensional space variable, $\zeta = z/l$, the equations of motion of the rotating shaft based on Timoshenko beam theory (Zu and Han, 1992) are given by

$$\ddot{u} + \frac{\kappa G}{\rho l^2}(l\psi' - u'') = 0 \tag{2}$$

$$\ddot{\psi} - i\frac{\Omega J_z}{\rho I}\dot{\psi} - \frac{E}{\rho l^2}\psi'' + \frac{\kappa AG}{\rho Il}(l\psi - u') = 0. \tag{3}$$

The relationship between the stress resultants and displacements in a complex form can be written as

$$M(\zeta, t) = M_x(\zeta, t) + iM_y(\zeta, t) = EI\psi'(\zeta, t)/l$$
$$Q(\zeta, t) = Q_x(\zeta, t) + iQ_y(\zeta, t)$$
$$= \kappa AG\left(\frac{1}{l}u'(\zeta, t) - \psi(\zeta, t)\right), \tag{4}$$

where $M(\zeta, t)$ and $Q(\zeta, t)$ are the transverse bending moment and shear force at each cross section along the shaft.

It is well known that the steady-state response of a linear rotor-bearing system due to rotating unbalance is a whirl orbit at the rotating speed, and this is called synchronous vibration. For a nonlinear rotor-bearing system, however, subsynchronous and supersynchronous vibrations also exist in the steady-state response. In the case of cubic nonlinearity, the dominant subsynchronous vibration is at the frequency of $\frac{1}{3}\Omega$ and the dominant supersynchronous vibration is at the frequency of 3Ω. Therefore, the solution to Eqs. (2) and (3) for steady-state response can be assumed as

$$u(\zeta, t) = \sum_p U_p(\zeta)e^{ip\Omega}$$
$$\psi(\zeta, t) = \sum_p \Psi_p(\zeta)e^{ip\Omega} \qquad p = -\tfrac{1}{3}, \tfrac{1}{3}, -1, 1, -3, 3. \tag{5}$$

Note that the solution is the sum of synchronous, subsynchronous, and supersynchronous component of vibration, where p is the harmonic number denoting each of these vibration components. Substituting Eq. (5) into Eqs. (2) and (3), and decoupling U_p and Ψ_p yields the following equations:

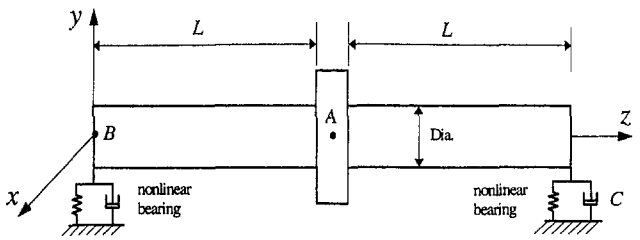

Fig. 1 A shaft-bearing system with an intermediate rotor

$$l_{p2}U_p^{(4)} + l_{p1}U_p'' + l_{p0}U = 0$$
$$l_{p2}\Psi_p^{(4)} + l_{p1}\Psi_p'' + l_{p0}\Psi = 0 \qquad p = -\tfrac{1}{3}, \tfrac{1}{3}, -1, 1, -3, 3, \tag{6}$$

the coefficients l_{p0}, l_{p1}, l_{p2} are dependent on the harmonic number p and the rotating speed Ω; they are given by

$$l_{p0} = \frac{\rho I}{\kappa AG}p^4\Omega^4 - \frac{\Omega J_z}{\kappa AG}p^3\Omega^3 - p^2\Omega^2$$

$$l_{p1} = \frac{I}{l^2A}\left(1 + \frac{E}{\kappa G}\right)p^2\Omega^2 - \frac{\Omega J_z}{l^2\rho A}p\Omega$$

$$l_{p2} = \frac{EI}{\rho Al^4}. \tag{7}$$

Equation (6) represents six sets of differential equations for different p values of the parameter. The solution to Eq. (6), when $\sqrt{l_1^2 - 4l_2l_0} > l_1$ is

$$U_p(\zeta) = A_{p1}\cosh(s_1\zeta) + A_{p2}\sinh(s_1\zeta) + A_{p3}\cos(s_2\zeta) + A_{p4}\sin(s_2\zeta)$$

$$\Psi_p(\zeta) = A'_{p1}\sinh(s_1\zeta) + A'_{p2}\cosh(s_1\zeta) + A'_{p3}\sin(s_2\zeta) + A'_{p4}\cos(s_2\zeta), \tag{8}$$

where

$$s_1 = \sqrt{\frac{-l_1 + \sqrt{l_1^2 - 4l_2l_0}}{2l_2}}, \quad s_2 = \sqrt{\frac{l_1 + \sqrt{l_1^2 - 4l_2l_0}}{2l_2}}.$$

$A_{p1} \sim A_{p4}$ and $A'_{p1} \sim A'_{p4}$ in Eq. (8) are arbitrary complex constants. Of the eight constants, only four are independent. Their relationships can be obtained from Eqs. (3) and (5) as

$$A'_{p1} = c_{p1}A_{p1}, \quad A'_{p3} = c_{p2}A_{p3}$$
$$A'_{p2} = c_{p1}A_{p2}, \quad A'_{p4} = -c_{p2}A_{p4}, \tag{9}$$

Nomenclature

A = cross-sectional area of the shaft
C = linear damping coefficient
E = Young's modules
e = eccentricity of the unbalanced mass of the disk
F_{x3} = cubic term in bearing force along x-direction
F_{y3} = cubic term in bearing force along y-direction
G = shear modules
I = transverse moment of inertia
I_D = total mass of the disk
J_p = polar moment of inertia of the disk
J_z = polar mass moment of inertia
K_1 = linear spring force coefficients
K_3 = nonlinear spring force coefficients
K_b = stiffness of the shaft at the center
l = length of the shaft
M_D = total mass of the disk
u_x, u_y = transverse displacements along x and y-direction
x_1, y_1 = displacements of the bearings along x and y-directions for a Laval-Jeffcott Rotor
x_2, y_2 = displacements of the disk for a Laval-Jeffcott Rotor
κ = shear coefficient
ρ = mass density
Ω = rotating speed of the shaft
ψ_x, ψ_y = bending angles along x and y-direction

where

$$c_{p1} = \frac{1}{s_1}\left(\frac{\rho l}{\kappa G}p^2\Omega^2 + \frac{1}{l}s_1^2\right),$$

$$c_{p2} = \frac{1}{s_2}\left(\frac{\rho l}{\kappa G}p^2\Omega^2 - \frac{1}{l}s_2^2\right).$$

Further determination of the four independent constants must be made from the boundary conditions, which involve nonlinear bearings and will be discussed in the next section.

Substituting Eq. (5) into Eq. (4), the bending moment and the shear force are expressed by

$$M(\zeta, t) = \sum_p M_p(\zeta)e^{ip\Omega t}$$
$$Q(\zeta, t) = \sum_p Q_p(\zeta)e^{ip\Omega t} \qquad p = -\tfrac{1}{3}, \tfrac{1}{3}, -1, 1, -3, 3, \quad (10)$$

where

$$M_p(\zeta) = \frac{EI}{l}(A'_{p1}s_1\cosh(s_1\zeta) + A'_{p2}s_1\sinh(s_1\zeta) + A'_{p3}s_2\cos(s_2\zeta) - A'_{p4}s_2\sin(s_2\zeta))$$

$$Q_p(\zeta) = \kappa AG\left[\left(\frac{s_1}{l}A_{p1} - A'_{p1}\right)\sinh(s_1\zeta) + \left(\frac{s_1}{l}A_{p2} - A'_{p2}\right)\cosh(s_1\zeta) - \left(\frac{s_2}{l}A_{p3} + A'_{p3}\right)\sin(s_2\zeta) + \left(\frac{s_2}{l}A_{p4} - A'_{p4}\right)\cos(s_2\zeta)\right]. \quad (11)$$

The solution to Eq. (6) for the case when $\sqrt{l_1^2 - 4l_2l_0} < l_1$ can be obtained in a similar form and is not provided here.

Nonlinear Bearing Forces

It is necessary to express the nonlinear bearing forces in Eq. (1) in a complex form, compatible with the system equations. While the complex representation of the linear term in Eq. (1) is straight forward, it is not easy to obtain the nonlinear term in a complex form. Therefore, to simplify manipulation, separate the linear part and nonlinear part in Eq. (1) as

$$F_x = F_{xl} + F_{x3}$$
$$F_y = F_{yl} + F_{y3}, \quad (12)$$

where F_{xl} and F_{yl} are components corresponding to the linear term in the bearing force and they can be easily expressed in a complex form by

$$F_l = F_x + iF_y = K_1u + C\dot{u}. \quad (13)$$

F_{x3} and F_{y3} are components corresponding to the cubic term in the bearing force and they are given by

$$F_{x3} = K_3u_x^3$$
$$F_{y3} = K_3u_y^3. \quad (14)$$

Due to the nonlinearity in Eq. (14), it is impossible to directly combine F_{xn} and F_{yn} into a complex form. It is necessary, therefore, to split u back into u_x and u_y through Eq. (5) so that u_x and u_y can be expressed in terms of space and time variables. Separating the forward and the backward whirl components, Eq. (5) can be rewritten as

$$u(z, t) = \sum_{p=1/3,1,3}(U_p(\zeta)e^{ip\Omega t} + U_{-p}(\zeta)e^{-ip\Omega t}). \quad (15)$$

Introducing the following mathematical relationships,

$$e^{ip\Omega t} = \cos(p\Omega t) + i\sin(p\Omega t),$$
$$e^{-ip\Omega t} = \cos(p\Omega t) - i\sin(p\Omega t),$$

Eq. (15) can be rearranged to

$$u(z, t) = \sum_{p=1/3,1,3}[(U_{cpx}(\zeta) + iU_{cpy}(\zeta))\cos(p\Omega t) + (U_{spx}(\zeta) + iU_{spy}(\zeta))\sin(p\Omega t)], \quad (16)$$

where

$$U_{cpx} = \mathrm{Re}(U_p + U_{-p}), \quad U_{cpy} = \mathrm{Im}(U_p + U_{-p})$$
$$U_{spx} = \mathrm{Im}(U_{-p} - U_p), \quad U_{spy} = \mathrm{Re}(U_p - U_{-p}).$$

In Eq. (16), u has been expressed such that the real and imaginary part can be easily determined. Thus, knowing that $u = u_x + iu_y$, the displacement components, u_x and u_y, are obtained as

$$u_x(z, t) = \sum_{p=1/3,1,3}(U_{cpx}(\zeta)\cos(p\Omega t) + U_{spx}(\zeta)\sin(p\Omega t))$$
$$u_y(z, t) = \sum_{p=1/3,1,3}(U_{cpy}(\zeta)\cos(p\Omega t) + U_{spy}(\zeta)\sin(p\Omega t)). \quad (17)$$

Equation (17) can be used to compute the nonlinear term of the bearing forces in Eq. (14). Using the harmonic balance method (Nayfeh and Mook, 1979), which assumes that the harmonic components of the bearing force are the same as those in the displacement response, the nonlinear bearing forces can be calculated as

$$F_{xn} = K_3u_x^3(z, t) \approx \sum_{p=1/3,1,3}(F_{cpx}\cos(p\Omega t) + F_{spx}\sin(p\Omega t))$$
$$F_{yn} = K_3u_y^3(z, t) \approx \sum_{p=1/3,1,3}(F_{cpy}\cos(p\Omega t) + F_{spy}\sin(p\Omega t)), \quad (18)$$

where

$$F_{c1/3x} = K_3[1.5U_{c1x}^2u_{c1/3x} + 0.75U_{c1x}(U_{c1/3x}^2 - U_{s1/3x}^2) + 0.75U_{c1/3x}(U_{c1/3x}^2 + U_{s1/3x}^2 + 2U_{s1/3x}U_{s1x} + 2(U_{c3x}^2 + U_{s3x}^2 + U_{s1x}^2))]$$

$$F_{s1/3x} = K_3[1.5(U_{c1x}^2U_{s1/3x} - U_{c1x}U_{c1/3x}U_{s1/3x}) + 0.75(U_{c1/3x}^2(U_{s1/3x} + U_{s1x}) + U_{s1/3x}(U_{s1/3x}^2 - U_{s1/3x}U_{s1x} + 2(U_{c3x}^2 + U_{s3x}^2 + U_{s1x}^2))]$$

$$F_{c1x} = \frac{K_3}{4}[3U_{c1x}^3 + 3U_{c1x}^2U_{c3x} + 6U_{c1x}(U_{c1/3x}^2 + U_{s1/3x}^2 + U_{c3x}^2 + U_{s3x}^2 + U_{s3x}U_{s1x} + 0.5U_{s1x}^2) + U_{c1/3x}^3 - 3(U_{c1/3x}U_{s1/3x}^2 + U_{c3x}U_{s1/3x}^2)]$$

$$F_{s1x} = \frac{K_3}{4}[3U_{c1x}^2(U_{s3x} + U_{s1x}) - 6U_{c1x}U_{c3x}U_{s1x} + 3U_{c1/3x}^2(U_{s1/3x} + 2U_{s1x}) - U_{s1/3x}^3 + 6U_{s1/3x}^2U_{s1x} + 6U_{s1x}(U_{c3x}^2 + U_{s3x}^2 - 0.5(U_{s3x}U_{s1x} - U_{s1x}^2))]$$

$$F_{c3x} = \frac{K_3}{4}\,[\,U_{c1x}^3 + 6U_{c1x}^2 U_{c3x} - 3U_{c1x}U_{s1x}^2 + 6U_{c3x}(U_{c1/3x}^2 + U_{s1/3x}^2 + U_{s1x}^2 + 0.5(U_{c3x}^2 + U_{s3x}^2))]$$

$$F_{s3x} = \frac{K_3}{4}\,[3U_{c1x}^2(2U_{s3x} + U_{s1x}) + 6U_{s3x}(U_{c1/3x}^2 + U_{s1/3}^2) + 3U_{s3x}(U_{c3x}^2 + U_{s3x}^2) + 6U_{s3x}U_{s1x}^2 - U_{s1x}^2]. \quad (19)$$

Coefficients F_{cpy} and F_{spy} can be obtained as well and they are expressed similar to Eq. (19) by simply changing all x subscripts in Eq. (19) to y subscripts.

With F_{x3} and F_{y3} obtained from Eq. (18), it is easy to combine them into a complex form. Using the following relationships

$$\cos(p\Omega t) = \frac{1}{2}(e^{ip\Omega t} + e^{-ip\Omega t}),$$

$$\sin(p\Omega t) = -\frac{i}{2}(e^{ip\Omega t} - e^{-ip\Omega t}), \quad (20)$$

and substituting Eq. (20) into Eq. (18), the following complex nonlinear bearing force is obtained as

$$F_n = F_{xn} + iF_{yn} = \sum_{p=1/3,1,3} (F_p e^{ip\Omega t} + F_{-p}e^{-ip\Omega t}) \quad (21)$$

in which

$$\begin{aligned} F_p &= \tfrac{1}{2}[(F_{cpx} + F_{spy}) + i(F_{cpy} - F_{spx})] \\ F_{-p} &= \tfrac{1}{2}[(F_{cpx} - F_{spy}) + i(F_{cpy} + F_{spx})] \end{aligned} \quad p = \tfrac{1}{3}, 1, 3. \quad (22)$$

The total complex bearing force is then

$$F = F_l + F_n. \quad (23)$$

With expressions generated to calculate the steady-state response of the system, bearing forces and stress resultants of the shaft, appropriate boundary conditions can then be applied to determine the unknown constants in the expressions. Two example systems are analyzed to illustrate the procedure and typical results.

It should be mentioned that a nonlinear rotor system may exhibit chaotic behavior or multifrequency behavior that is not accounted for in the harmonic balance solution procedure. In addition, harmonic balance method is accurate only for small vibrations. Therefore, the solution method shown above has certain limitations.

Laval-Jeffcott Rotor

The first example is a shaft supported by two ball bearings at the two ends and a central rigid disk, as shown in Fig. 1. Each bearing is assumed to have cubic stiffness and linear damping characteristics expressed by Eq. (1). Considering the symmetry, the system degrees of freedom can be reduced by a factor of two. The boundary conditions can then be written as

$$M(0, t) = 0$$

$$Q(0, t) = F_l(0, t) + F_n(0, t)$$

$$\psi(\tfrac{1}{2}, t) = 0$$

$$Q(\tfrac{1}{2}, t) = -M_D\ddot{u}(\tfrac{1}{2}, t) + M_D e\Omega^2 e^{i\Omega t}). \quad (24)$$

In this example, there is no influence from the gyroscopic moment and the moment of inertia of the disk because the disk is located at the symmetric point of the system. Using Eqs. (5), (10), and (21) and equating the coefficients of the ith terms associated with $e^{ip\Omega t}$ leads to

$$M_p(0) = 0$$

$$Q_p(0) = (K_1 + iCp\Omega)U_p + F_p(0)$$

$$\Psi_p(\tfrac{1}{2}) = 0 \quad p = -\tfrac{1}{3}, \tfrac{1}{3}, -1, 1, -3, 3$$

$$Q_p(\tfrac{1}{2}) = M_D p^2\Omega^2 U_p(\tfrac{1}{2}) + \delta_{1p}M_D e\Omega^2, \quad (25)$$

where

$$\delta_{1p} = \begin{cases} 1 & \text{when } p = 1 \\ 0 & \text{when } p \neq 1 \end{cases}$$

is the Kronecker Delta function. $F_p(0)$ is obtained from Eqs. (22) and (19) by letting $\zeta = 0$. Substituting Eqs. (8) and (11) into Eq. (25), the algebraic equations involving the four unknown complex constants $A_{p1} \sim A_{p4}$ are

$$c_{p1}s_1A_{p1} + c_{p2}s_2A_{p3} = 0$$

$$-(K_1 + iCp\Omega)A_{p1} + KAG\left(\frac{s_1}{l} - c_{p1}\right)A_{p2} - (K_1 + iCp\Omega)A_{p3} + KAG\left(\frac{s_2}{l} + c_{p2}\right)A_{p4} = F_p(0)$$

$$c_{p1}\sinh\left(\frac{s_1}{2}\right)A_{p1} + c_{p1}\cosh\left(\frac{s_1}{2}\right)A_{p2} + c_{p2}\sin\left(\frac{s_2}{2}\right)A_{p3} - c_{p2}\cos\left(\frac{s_2}{2}\right)A_{p4} = 0$$

$$\left[KAG\left(\frac{s_1}{l} - c_{p1}\right)\sinh\left(\frac{s_1}{2}\right) - M_D p^2\Omega^2\cosh\left(\frac{s_1}{2}\right)\right]A_{p1} + \left[KAG\left(\frac{s_1}{l} - c_{p1}\right)\cosh\left(\frac{s_1}{2}\right) - M_D p^2\Omega^2\sinh\left(\frac{s_1}{2}\right)\right]A_{p2} - \left[KAG\left(\frac{s_2}{l} + c_{p2}\right)\sin\left(\frac{s_2}{2}\right) + M_D p^2\Omega^2\cos\left(\frac{s_1}{2}\right)\right]A_{p3} + \left[KAG\left(\frac{s_2}{l} + c_{p2}\right)\cos\left(\frac{s_2}{2}\right) - M_D p^2\Omega^2\sin\left(\frac{s_1}{2}\right)\right]A_{p4} = \delta_{1p}M_D e\Omega^2. \quad (26)$$

Note that due to the complexity of Eq. (19) in which F_p is a function of U_p, $F_p(0)$ is a highly nonlinear function of $A_{p1} \sim A_{p4}$. Since the harmonic number p has six values, $p = -\frac{1}{3}, \frac{1}{3}, -1, 1, -3, 3$, Eq. (26) represents six sets of a system of four nonlinear algebraic equations corresponding to six sets of four unknowns $A_{p1} \sim A_{p4}$ ($p = -\frac{1}{3}, \frac{1}{3}, -1, 1, -3, 3$). Solving Eq. (26) using the quasi-Newton method for each set, all 24 complex constants $A_{p1} \sim A_{p4}$ ($p = -\frac{1}{3}, \frac{1}{3}, -1, 1, -3, 3$) can be determined. Furthermore, substituting these constants back into Eqs. (8) and then Eq. (5), the steady-state response for displacements u and ψ can be obtained.

In order to verify the solutions, a simplified system is analyzed below, in which only the stiffness of the shaft is considered while the mass of the shaft is ignored. The equations of motion for such a system are

$$K_1 x_1 + C\dot{x}_1 + K_3 x_1^3 - \frac{K_b}{2}(x_2 - x_1) = 0$$

$$K_1 y_1 + C\dot{y}_1 + K_3 y_1^3 - \frac{K_b}{2}(y_2 - y_1) = 0$$

$$M_D \ddot{x}_2 + K_b(x_2 - x_1) = eM_D\Omega^2 \cos \Omega t$$

$$M_D \ddot{y}_2 + K_b(y_2 - y_1) = eM_D\Omega^2 \sin \Omega t. \quad (27)$$

For easy and simple solution form of the simplified system, assuming that there is only synchronous whirl, the displacement of the bearing at point A and the displacement of the disk at point B can be obtained explicitly as

$$u_A = \frac{eM_D\Omega^2 + K_b U_B}{K_b - M_D\Omega^2} e^{i\Omega t}$$

$$u_B = U_B e^{i\Omega t}$$

$$U_B = \frac{\frac{3}{4}K_3 A_B^4 + \left(K_1 - \frac{K_b}{2}\frac{r}{1-r}\right)A_B^2}{\frac{K_b}{2}\frac{er}{1-r}} + i\frac{2C\Omega A_B^2(r-1)}{eK_b r} \quad (28)$$

in which $r = \Omega^2/\omega_n^2$ and $\omega_n = \sqrt{K_b/M_D}$. A_B corresponds to the amplitude of the displacement at point B and is determined from the following nonlinear algebraic equation.

$$C^2\Omega^2 A_B^2 + \left[\frac{3}{4}K_3 A_B^3 + \left(K_1 - \frac{K_b}{2}\frac{r}{1-r}\right)A_B\right]^2 = \left(\frac{K_b}{2}\frac{er}{1-r}\right)^2. \quad (29)$$

Numerical simulations are carried out to show the nonlinear effect of the bearings on the dynamic characteristics of the system. The basic parameters used in the simulations are listed in Table 1. Figure 2 shows the frequency response of the system for various values of K_3 which represents different nonlinearity in the bearings. The maximum amplitude on the shaft, which is at the middle where the disk is located, is plotted against the rotating speed Ω. Due to the sharp increase in the amplitude at the resonance, plots are shown only near the synchronous resonance. Results from the simplified analysis are also presented for comparison. It is seen that the agreement is very good for linear bearings when $K_3 = 0$. In the case of nonlinear bearings, where $K_3 = 1.0 \times 10^{11}$ and $K_3 = -1.0 \times 10^{11}$, there are some deviations from the previous full solutions. This

Table 1 Physical parameters of a shaft-bearing system with an intermediate rotor

Shaft	
Young's modules E	2.07e7 N cm^{-2}
Shear modules G	8.1e6 N cm^{-2}
Shear factor κ	0.68
Density ρ	7.75e-3 kg cm^{-3}
Length L	15 cm
Diameter	1.2 cm
Rotor	
Mass M_d	60 kg
Polar moment of inertia	2000 kg cm^2
Transverse moment of inertia I_D	1000 kg cm^2
Eccentricity e	0.006667 cm
Bearing	
Linear stiffness K_1	1.5e4 N/cm^{-1}
Linear damping C	600 N s cm^{-1}

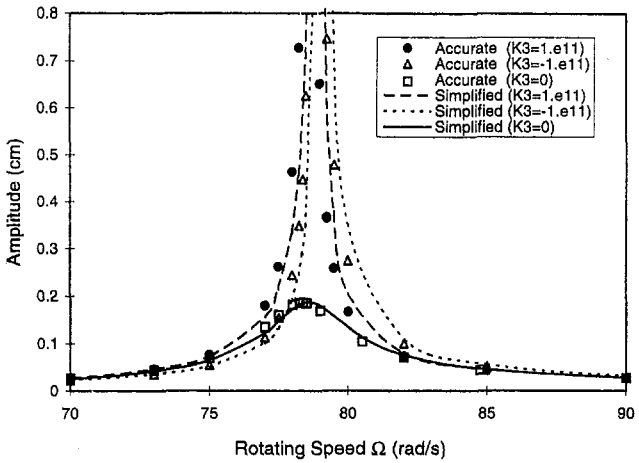

Fig. 2 Frequency response for various K_3

implies that the mass of the shaft has a significant influence on the system dynamic characteristics of the system for nonlinear bearings than for linear bearings. It is observed that having nonlinear bearings in the system increases the maximum displacement substantially. This is because the support from the bearings becomes stiffer with the incorporation of nonlinear bearing effects associated with K_3. Therefore, there is less vibration isolation from the bearings, resulting in larger vibrations at resonance at which vibration reaches its peak value. Similarly, the response curve at resonance becomes sharper for the nonlinear bearings. As the bearing becomes stiffer, the damping effect becomes smaller, causing a sharper peak at resonance. Another phenomenon noticed is that the peak shifts to the right from linear bearings to nonlinear bearings. For linear bearings, the resonant frequency is at $\Omega = 78.4$ rad/s, which is the fundamental natural frequency of the linear system, and for $K_3 = 1.0 \times 10^{11}$, resonance occurs at $\Omega = 78.8$ rad/s.

For nonlinear bearing systems, multiple valued displacements may occur under certain values of K_3. For example, in Fig. 3, the frequency response related to $K_3 = 1.0 \times 10^9$ N/cm^3 displays a jump in the curve. Curve 1–2–3 is generated when the amplitude is computed step by step from a lower rotating speed to a higher speed while curve 4–5–6 is plotted when the calculation is carried out from a higher speed to a lower speed. It is shown that these two calculations result in different amplitude values at the same speed, for example, points 5 and 3 and points 6 and 2. The trend of the missing data is indicated by the arrows on the plot. Results from the simplified solution are also shown in Fig. 3 in dotted

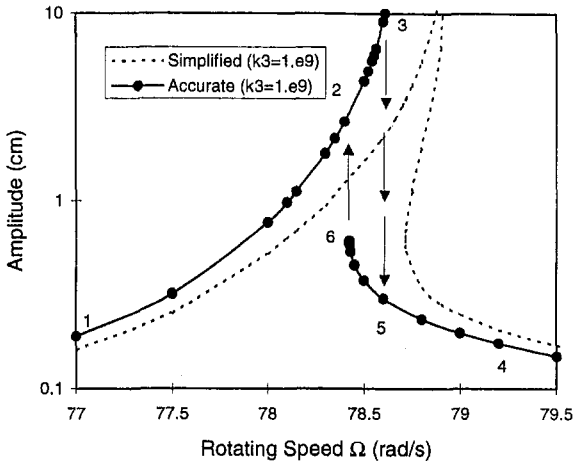

Fig. 3 Frequency response when $K_3 = 1.0 \times 10^9$ N/cm^3

lines, where a similar phenomenon is displayed. This jump phenomenon is due to the unstable solution at the region. A thorough stability analysis was provided by Zhao et al. (1994) for an squeeze-file-damped nonlinear rotor bearing systems, where a multivalued response was also observed.

The whirl orbits at both points A and B are shown in Fig. 4. The orbit at the location of the rotor, point A, is similar to a circle. However, the orbit at the location of the bearing, point B, is much deviated from a circular path, which is attributed to a strong influence from the nonlinearity of the bearing. Recall that the nonlinear response of such a rotor-bearing system is composed of three components, synchronous vibration, subsynchronous vibration, and supersynchronous vibration. Although each of these components at point B projects a circular orbit as shown in Fig. 5, their combination forms a noncircular motion. From the magnitude of each component in Fig. 5, it is clear that the influence from the synchronous motion on the total system response is the strongest while the influence from the subharmonic motion is the smallest.

Overhung Rotor-Bearing System

The second example is a single disk overhung system supported by two end ball bearings and having an end disk, as shown in Fig. 6. The boundary conditions of this system are given by

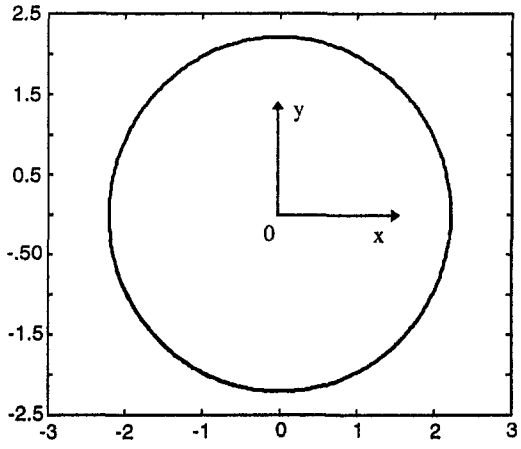

(a) Whirl orbit (cm) with K_J=1.0×10^{11} N cm^{-1} at point A

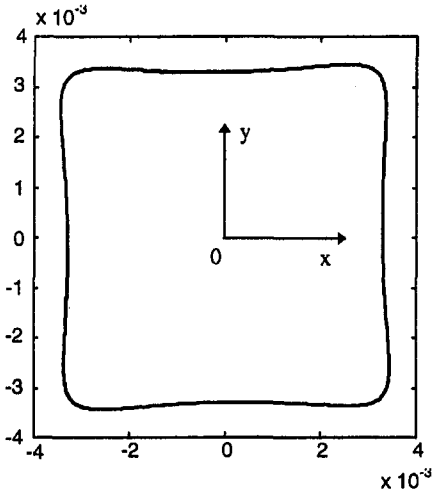

(b) Whirl orbit (cm) with K_J=1.0×10^{11} N cm^{-1} at point B

Fig. 4 Whirling orbits at point *A* and point *B*

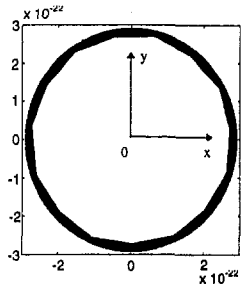

(a) Whirl orbit (cm) of subsynchronous vibration with K_J=1.0×10^{11} N cm^{-1}

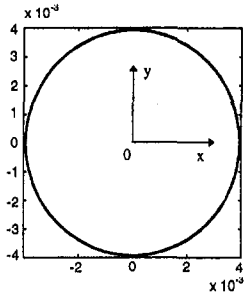

(b) Whirl orbit (cm) of synchronous vibration with K_J=1.0×10^{11} N cm^{-1}

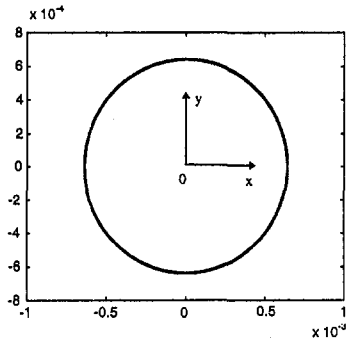

(c) Whirl orbit (cm) of supersynchronous vibration with K_J=1.0×10^{11} N cm^{-1}

Fig. 5 Whirling orbit at point *B* for each harmonic component

$$M(0, t) = 0$$

$$Q(0, t) = F_I(0, t) + F_n(0, t)$$

$$M(1, t) = -I_D\ddot{\psi}(1, t) + i(J_p\Omega)\dot{\psi}(1, t)$$

$$Q(1, t) = eM_D\Omega^2 e^{i\Omega t} - F_I(1, t) - F_n(1, t) - M_D\ddot{u}(1, t). \quad (30)$$

Following the same steps as in the first example, the four nonlinear algebraic equations to solve for $A_{p1} \sim A_{p4}$ ($p = -\frac{1}{3}, \frac{1}{3}, -1, 1, -3, 3$) can be obtained from the boundary conditions, Eq. (30). They are

$$c_{p1}s_1A_{p1} + c_{p2}s_2A_{p3} = 0$$

$$-(K_1 + iCp\Omega)A_{p1} + KAG\left(\frac{s_1}{l} - c_{p1}\right)A_{p2}$$

$$-(K_1 + iCp\Omega)A_{p3} + KAG\left(\frac{s_2}{l} + c_{p2}\right)A_{p4} = F_p(0)$$

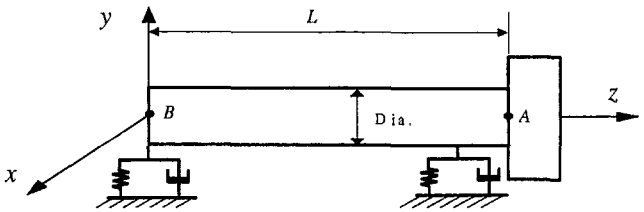

Fig. 6 A shaft-bearing system with an end rotor

$$\left[\frac{EI}{l}c_{p1}s_1\cosh(s_1) - (I_Dp^2\Omega^2 - J_pp\Omega^2)c_{p1}\sinh(s_1)\right]A_{p1}$$

$$+\left[\frac{EI}{l}c_{p1}s_1\sinh(s_1) - (I_Dp^2\Omega^2 - J_pp\Omega^2)c_{p1}\cosh(s_1)\right]$$

$$\times A_{p2} + \left[\frac{EI}{l}c_{p2}s_2\cos(s_2) - (I_Dp^2\Omega^2\right.$$

$$\left. - J_pp\Omega^2)c_{p2}\sin(s_2)\right]A_{p3} + \left[\frac{EI}{l}c_{p2}s_2\sin(s_2)\right.$$

$$\left. + (I_Dp^2\Omega^2 - J_pp\Omega^2)c_{p2}\cos(s_2)\right]A_{p4} = 0$$

$$\left[KAG\left(\frac{s_1}{l} - c_p\right)\sinh(s_1) + (K_1 + iCp\Omega\right.$$

$$\left. - M_Dp^2\Omega^2)\cosh(s_1)\right]A_{p1} + \left[KAG\left(\frac{s_1}{l}c_{p1}\right)\cos h(s_1)\right.$$

$$\left. + (K_1 + iCp\Omega - M_Dp^2\Omega^2)\sinh(s_1)\right]A_{p2}$$

$$-\left[KAG\left(\frac{s_2}{l} + c_{p2}\right)\sin(s_2) - (K_1 + iCp\Omega\right.$$

$$\left. - M_Dp^2\Omega^2)\cos(s_2)\right]A_{p3} + \left[KAG\left(\frac{s_2}{l} + c_{p2}\right)\cos(s_2)\right.$$

$$\left. + (K_1 + iCp\Omega - M_Dp^2\Omega^2)\sin(s_2)\right]A_{p4}$$

$$= \delta_{1p}M_De\Omega^2. \quad (31)$$

Similar to the first example, a simplified model is introduced for comparison, in which the shaft is assumed massless and only the synchronous whirl is taken into account. The maximum amplitude A_A at point A can be obtained from solving the following nonlinear equation.

$$C^2\Omega^2A_A^2 + [\tfrac{3}{4}K_3A_A^3 + K_1A_A - M_D\Omega^2A_A]^2 = e^2M_D^2\Omega^4. \quad (32)$$

The physical parameters used in the simulations are listed in Table 2. The amplitude of maximum displacement versus the rotating speed for linear bearings and nonlinear bearings ($K_3 = 1.0e12$) are shown in Fig. 7 and Fig. 8, respectively. The maximum displacement for this system occurs at the location of the disk. Results from both the general solution and the simplified solution are presented. Opposite to the trend in the first example, the displacement for the nonlinear bearings is smaller than for linear bearings. Note that the disk is mounted right at the location of the right bearing, thus the nonlinear bearing, which increases the stiffness, provides more constraint to the vibration of the disk. In Fig. 8, it is also found that the existence of nonlinear bearings in the system may induce multivalued components in the frequency response. The response will increase monotonously along curve 1–2 when the steady-state responses are calculated from a lower speed. Conversely, when the calculation is performed from a higher to lower speed, curve 3–4 is obtained. Another peculiar phenomenon is that corresponding to the resonant frequency for a linear bearing system, there is no resonance in that frequency range for the system with nonlinear bearings.

The whirl orbits at the disk location are given in Fig. 9 for $K_3 = 1.0 \times 10^{12}$ and $\Omega = 300$ rad/s. There are two displacement values corresponding to this rotating speed. The whirling orbit

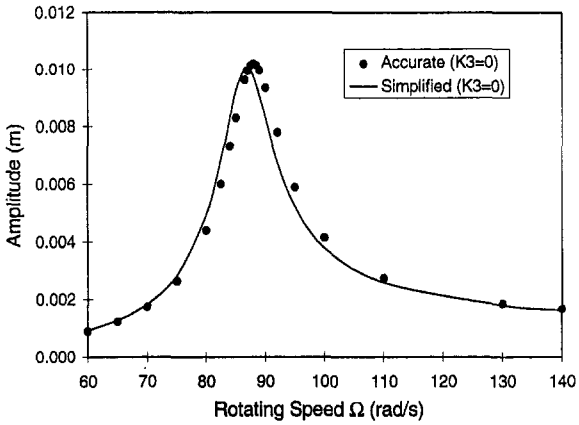

Fig. 7 Frequency response for linear bearing system

Table 2 Physical parameters of a shaft-bearing system with an end rotor

Shaft	
Young's modules E	2.07e11 N m^{-2}
Shear modules G	8.1e10 N m^{-2}
shear factor κ	0.68
Density ρ	7750 kg m^{-3}
Length L	1.0 m
Diameter	0.1 m
Disk	
Disk mass M_d	2.0e3 kg
Polar moment of inertia	200 kg m^2
Transverse moment of inertia I_D	100 kg m^2
Disk eccentricity e	0.001 m
Bearing	
Linear stiffness K_1	1.5e7 N/m^{-1}
Linear damping C	17,200 N s m^{-1}

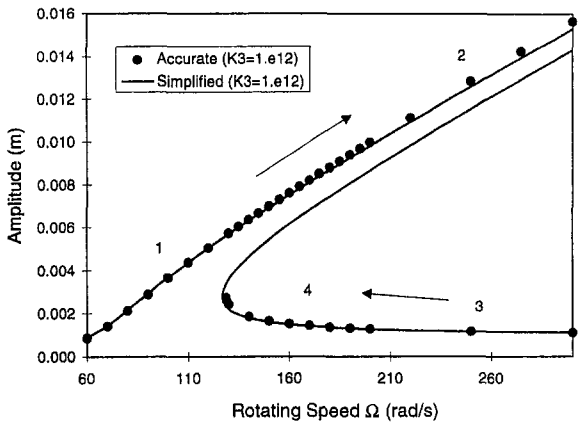

Fig. 8 Frequency response for nonlinear bearing system when $K_3 = 1.0 \times 10^{12}$ N/cm^3

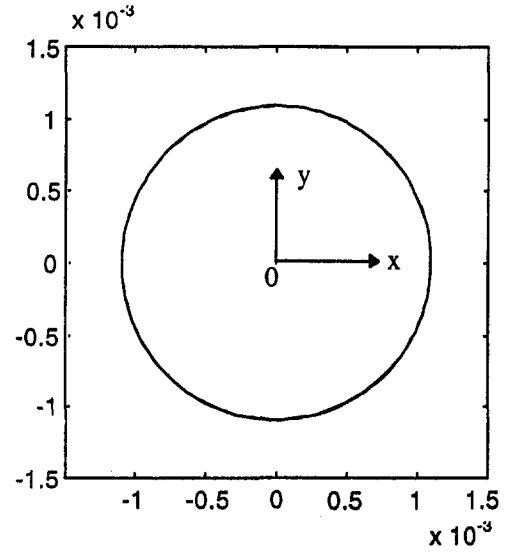

(a)

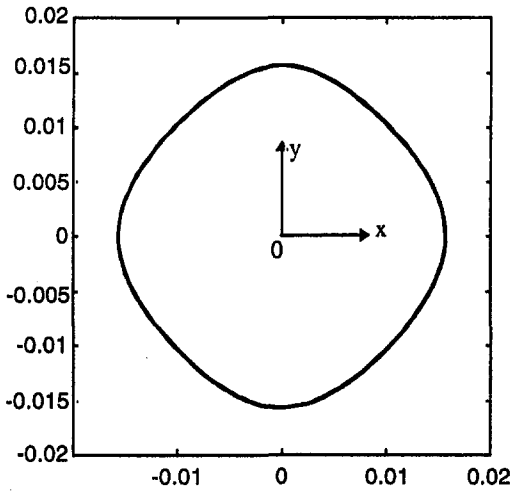

(b)

Fig. 9 Whirling orbits at point *A* for multiple value displacements

obtained from the smaller amplitude value is plotted in Fig. 9(a), where the shape is a circle. The orbit obtained from the larger amplitude value is plotted in Fig. 9(b), where the shape of the orbit is changed to a square orbit. This noncircular orbit is caused by sub and super synchronous vibration for nonlinear bearing systems, as mentioned by Lee et al. (1993) and Zhao et al. (1994).

Summary and Conclusions

The steady-state response of typical shaft-rotor systems with nonlinear bearings is solved analytically in the paper. The shaft is described by a continuous modeling using Timoshenko beam theory and the rotors are considered as rigid disks. Ball bearings with cubic nonlinearity are studied in the analysis. For such nonlinear systems, the steady-state response consists of synchronous vibration, subsynchronous vibration, and supersynchronous vibration. The harmonic balance method is used to obtain the steady-state solution. Two examples of nonlinear rotor-bearing systems are illustrated to show the nonlinear effect. Solutions from simplified systems are also given for comparison. It is found that there may exist multivalued displacements for systems with nonlinear bearings. The displacement of the disk for nonlinear bearings may increase or decrease from that of linear systems depending on the location of the disk. The steady whirl orbits of linear systems are circular while the orbits for nonlinear systems may change to a noncircular shape.

References

Eshleman, R. L., and Eubanks, R. A., 1969, "On the Critical Speeds of a Continuous Rotor," *ASME Journal of Mechanical Design,* Vol. 104, pp. 412–415.

Hahn, E. J., and Chen, P. Y. P., 1994, "Harmonic Balance Analysis of General Squeeze Film Damped Multidegree-of-Freedom Rotor Bearing Systems," *ASME Journal of Tribology,* Vol. 116, pp. 499–507.

Hwang, J. L., and Shiau, T. N., 1991, "An Application of the Generalized Polynomial Expansion Method to Nonlinear Rotor Bearing Systems," *ASME Journal of Vibration and Acoustics,* Vol. 113, pp. 299–308.

Ishida, Y., Ikeda, T., and Yamamoto, T., 1990, "Nonlinear Forced Oscillations Caused by Quartic Nonlinearity in a Rotating Shaft," *ASME Journal Vibration and Acoustics,* Vol. 112, pp. 288–297.

Ishida, Y., Nagasaka, I., Inoue, T., and Lee, S., 1996, "Forced Oscillations of a Vertical Continuous Rotor with Geometric Nonlinearity," *Nonlinear Dynamics,* Vol. 11, pp. 107–120.

Lee, A. C., Kang, Y., and Liu, S. L., 1993, "Steady–State Analysis of a Rotor Mounted on Nonlinear Bearings by the Transfer Matrix Method," *International Journal Mechanical Science,* Vol. 35, pp. 479–490.

Nataraj, C., and Nelson, H. D., 1989, "Periodic Solutions in Rotor Dynamic Systems With Nonlinear Supports: A General Approach," *ASME Journal of Vibration, Acoustics, Stress and Reliability in Design,* Vol. 111, pp. 187–193.

Nelson, H. D., Meacham, W. L., Fleming, D. P., and Kascak, A. F., 1982, "Nonlinear Analysis of Rotor-Bearing Systems Using Component Mode Synthesis," ASME Paper No. 82-GT-303.

Shaw, S., 1988, "Chaotic Dynamics of a Slender Beam Rotating About Its Longitudinal Axis," *Journal of Sound and Vibration,* Vol. 124, pp. 329–343.

Shiau, T. N., Hwang, J. L., and Chang, Y. B., 1993, "A Study on Stability and Response Analysis of a Nonlinear Rotor System With Mass Unbalance and Side Load," *ASME Journal of Engineering for Gas Turbines and Power,* Vol. 115, pp. 218–222.

Shiau, T. N., and Jean, A. N., 1990, "Prediction of Periodic Response of Flexible Mechanical Systems With Nonlinear Characteristics," *ASME Journal of Vibration and Acoustics,* Vol. 112, pp. 501–507.

van de Vorst, E. L. B., Fey, R. H. B., de Kraker, A., and van Campen, D. H., 1996, "Steady–State Behavior of Flexible Rotor Dynamic Systems With Oil Journal Bearings," *Nonlinear Dynamics,* Vol. 11, No. 3, pp. 295–313.

Yamamoto, T., Ishida, Y., and Aizawa, K., 1979, "On the Subharmonic Oscillations at Unsymmetrical Shafts," *Bull. JSME,* Vol. 22, pp. 164–173.

Yamamoto, T., Ishida, Y., Ikedam, T., and Yamada, M., 1981, "Subharmonic and Summed-and-differential Harmonic Oscillations of an Unsymmetrical Rotor," *Bull. JSME,* Vol. 24, pp. 192–199.

Yamamoto, T., Ishida, Y., Ikeda, T., and Yamamoto, M., 1982, "Nonlinear Forced Oscillations of a Rotation Shaft Carrying on Unsymmetrical Rotor at the Major Critical Speed," *Bull. JSME,* Vol. 25, pp. 1969.

Zhao, J., Linnett, I., and Mclean, L., 1994, "Imbalance Response and Stability of Eccentric Squeeze-Film-Damped Nonlinear Rotor Bearing Systems," *JSME International Journal,* Series B, Vol. 37, pp. 886–895.

Zu, J. W., and Han, R. P. S., 1992, "Natural Frequencies and Normal Modes of a Spinning Timoshenko Beam With General Boundary Conditions," *ASME Journal of Applied Mechanics,* Vol. 59, pp. 197–204.

Zu, J. W., and Han, R. P. S., 1994, "Dynamic Response of a Spinning Timoshenko Beam With General Boundary Conditions and Subjected to a Moving Load," *ASME Journal of Applied Mechanics,* Vol. 61, pp. 152–160.

Characterization of Laws of Friction in the Context of Engine Blade Dynamics

A. V. Srinivasan
Worcester Polytechnic Institute,
Department of Mechanical Engineering,
100 Institute Road,
Worcester, MA 01609-2282

D. M. McFarland
Department of Mechanical Engineering,
University of Connecticut,
Storrs, CT 06269-3139

Experience has shown that energy dissipation due to rubbing at interfaces of engine blade shrouds provides damping of bladed disk assemblies. An accurate estimate of such damping has been a subject of study for more than a decade. The most difficult parameter that influences its accurate calculation pertains to an appropriate definition of the laws of friction that relate the rubbing motion with the forces induced. This paper develops an analysis that leads to a mathematical relationship between the forces of friction damping at a vibrating interface and the corresponding relative motion. The analysis permits calculation of forces at the interface if the displacements are known or vice versa. The equations are cast in terms of relative motion between mating shrouds so that degenerate cases of fully locked and freely slipping can be calculated. Examples are given showing simulation results obtained using discrete structural models. Extension of the analysis to the case of a full assembly is discussed.

Introduction

Among the most expensive parts that comprise jet engines are fan, compressor, and turbine blades. In advanced engines, the number of these blades may be as large as a thousand, with a wide variety of aspect ratios. Some of these blades are shrouded either at part span or at the tip. The failure of these blades during development testing continues to be of major concern, and leads to delays in certification and prohibitive development costs. During service, such failures could lead to loss of life and equipment. Thus, the durability of blades is at the heart of structural integrity of the powerplant as well as the aircraft.

While shrouds are designed primarily to provide additional stiffening to avoid resonance and flutter, experience has shown that energy dissipation at these interrupted interfaces has the potential to provide damping. An accurate estimate of such damping has been a subject of study for more than a decade. Among the parameters that influence an accurate calculation, the most difficult parameter has been an appropriate definition of the laws of friction that are needed to relate the displacements with the forces induced at the interrupted interface. The purpose of this paper is to develop a basis for an analytical model that along with high-quality time history data, will help define the laws of friction for use in analytical design systems.

The potentials of dry friction at interfaces of vibrating components leading to damping of vibratory stresses have long been recognized. While rubbing at interfaces leads to energy dissipation, material removal leading to fretting fatigue can also occur. The ideal solution is to coat the interfaces with a material that allows rubbing but prevents surface deterioration. Such a requirement cannot be met unless one is able to design the components taking into account the influence of friction forces at rubbing interfaces.

Friction at interfaces, especially in vibrating components, is a complex mechanism in which a host of parameters control the motion. In addition to the properties of the contacting surfaces, normal loads that hold the surfaces together, frequency of vibration, temperature, etc. can all be influential. The relative importance of these parameters in a vibratory environment needs to be established so that the scope of any analytical effort may be estimated.

Among the multitude of important issues in this field, the primary issue is in regard to the laws of friction, i.e., what is the nature of the relationship between stresses at an interface and the displacement of vibrating components? The emphasis here is to establish functional forms of laws of friction relevant to vibratory rubbing at mating interfaces.

As stated earlier, accurate calculation of resonant frequencies and mode shapes of bladed-disk systems requires proper definition of boundary conditions at shroud interfaces. As discussed by Srinivasan et al. (1978), (*a*) red-line speeds of engines cannot be set with confidence unless the vulnerable frequencies are known a priori and, (*b*) amplitudes at resonance and flutter speeds cannot be determined because accurate mode shapes are required in calculating, for example, work done per cycle of vibration. Research efforts by Srinivasan (1983a, b), Griffin (1991), and Menq (1986a, b) have underlined the need to develop a fundamental understanding of the dynamics of interfaces. Without a proper resolution of the issues alluded to above, designers will have no alternative to guessing damping coefficients for use in an analysis. The forces of friction are not of the viscous type. They are not even a Coulomb type as has been recently established by Menq et al. (1986b). In fact, Coulomb never intended his law to be used in calculating elastic contact.

An excellent review of much of the relevant literature may be found in a paper by Oden and Martins (1985), which also presents some original models and results. A careful reading of this work serves to underscore the difficulty in analyzing friction-related phenomena in "real" systems, stemming largely from the need to decide a priori what parameters are important. In the context of bladed systems, researchers cited in the preceding paragraph have addressed this with experimental and analytical programs (see, for example, the papers by Menq et al.), and the analysis of system response given a friction model appears to be well understood. Attention has largely turned to a careful investigation of when certain effects are important, e.g., is the stick-slip, which can dominate rectilinear response, important when relative motion is expected to be circular or elliptic (Srinivasan, 1984d; Griffin and Menq, 1991).

Contributed by the International Gas Turbine Institute and presented at the 41st International Gas Turbine and Aeroengine Congress and Exhibition, Birmingham, United Kingdom, June 10–13, 1996. Manuscript received by the ASME Headquarters February 6, 1998. Paper No. 96-GT-379. Associate Technical Editor: J. N. Shinn.

Compared to the forward problem of finding response given a friction model, the inverse problem of fitting a model to experimental data is significantly less mature. While the references cited above present some results, there is clearly a need for a direct attack on this problem outside the setting of a particular analytical technique and at a level of rigor and on a scale such that the findings are directly applicable to full-scale bladed disk systems. The friction models identified by such a study should be immediately useful to existing techniques and codes, thus facilitating solution of the response problems arising in design and in life prediction.

Advances in dynamic analysis of structural systems with rubbing interfaces have been hampered because of a lack of knowledge pertaining to the accurate representation of boundary conditions at interfaces. Clearly, the dynamics of substructures (individual components) of a system can be both calculated and measured. Similarly, the dynamics of the entire system can be measured but calculations can be made only on the basis of assumptions in regard to the nature of friction. While the development of analytical friction models based entirely on theory is beyond the scope of current research efforts, developing functional forms based on data appears feasible and useful to fill this important knowledge gap. Thus, our research is aimed at developing dynamic friction models on the basis of examining data from carefully controlled laboratory tests.

Analysis

While the overall research strategy can be broken down into a combined experimental and analytical approach, this paper will address the basics of the analytical aspect. Some numerical results are included to demonstrate its capability for application to bladed-disk assemblies.

The analytical approach discussed here is aimed at deriving a mathematical relationship between the forces of dry friction damping at a vibrating interface and corresponding relative motion. A functional relating them may be allowed for a complete solution of the dynamics of the system. Alternatively, if the displacements are known, the forces can be computed or vice versa. Clearly, measurements of relative motion are much more feasible, in both laboratory testing as well as in rig or engine testing, than the vastly more complex measurement of interface forces. This paper emphasizes that as the preferred option, and serves as a basis for all future experimental programs that may shed some light on the laws of friction. The advantages of such an approach, as will be seen below, are that several laws of friction may be examined for their suitability in the light of experimental data.

This analysis would make direct use of the type of data illustrated in Fig. 1. These traces were obtained using an LED-photodetector device, described in the report by Srinivasan et al. (1984).

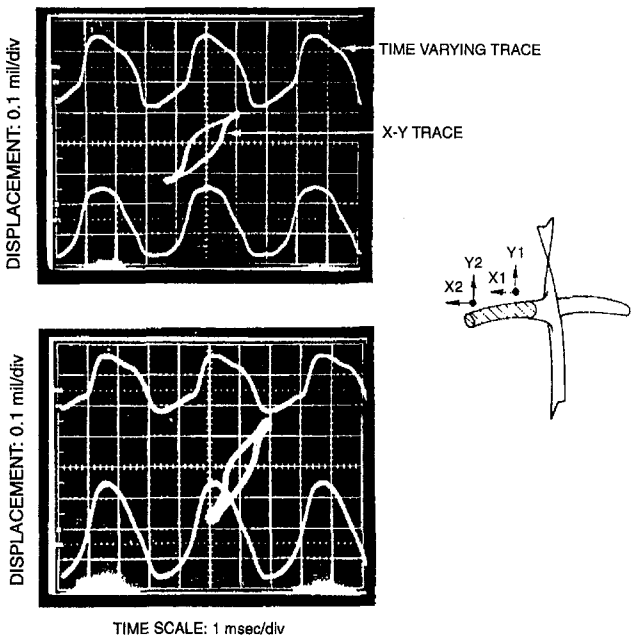

Fig. 1 Measured shroud displacements (Srinivasan et al. 1984)

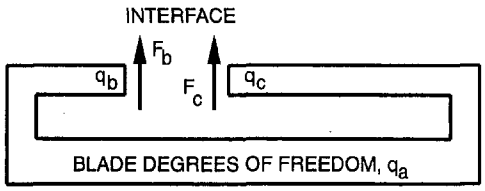

Fig. 2 MDOF system with internal interface

Equations of Motion. For the hypothetical multi-degree-of-freedom system with an internal interface, shown in Fig. 2, assume that, in addition to possible external loads f, there act at the interface equal and opposite damping forces Q and $-Q$, i.e., the net forces are

$$\mathbf{F}_b = -\mathbf{Q} + \mathbf{f}_b \tag{1}$$

and

$$\mathbf{F}_c = +\mathbf{Q} + \mathbf{f}_c, \tag{2}$$

where all such forces have been stacked into vectors, and let $\mathbf{F}_a$ denote the forces associated with the internal degrees of freedom a.

Presuming classical damping everywhere, except at the interface of interest, the equations of motion of this system can be written as

$$\begin{bmatrix} \mathbf{M}_{aa} & \mathbf{0} & \mathbf{0} \\ \mathbf{0} & \mathbf{M}_{bb} & \mathbf{0} \\ \mathbf{0} & \mathbf{0} & \mathbf{M}_{cc} \end{bmatrix} \begin{Bmatrix} \ddot{\mathbf{q}}_a \\ \ddot{\mathbf{q}}_b \\ \ddot{\mathbf{q}}_c \end{Bmatrix} + \begin{bmatrix} \mathbf{C}_{aa} & \mathbf{C}_{ab} & \mathbf{C}_{ac} \\ \mathbf{C}_{ab}^T & \mathbf{C}_{bb} & \mathbf{C}_{bc} \\ \mathbf{C}_{ac}^T & \mathbf{C}_{bc}^T & \mathbf{C}_{cc} \end{bmatrix} \begin{Bmatrix} \dot{\mathbf{q}}_a \\ \dot{\mathbf{q}}_b \\ \dot{\mathbf{q}}_c \end{Bmatrix}$$

$$+ \begin{bmatrix} \mathbf{K}_{aa} & \mathbf{K}_{ab} & \mathbf{K}_{ac} \\ \mathbf{K}_{ab}^T & \mathbf{K}_{bb} & \mathbf{K}_{bc} \\ \mathbf{K}_{ac}^T & \mathbf{K}_{bc}^T & \mathbf{K}_{cc} \end{bmatrix} \begin{Bmatrix} \mathbf{q}_a \\ \mathbf{q}_b \\ \mathbf{q}_c \end{Bmatrix} = \begin{Bmatrix} \mathbf{F}_a \\ -\mathbf{Q} + \mathbf{f}_b \\ \mathbf{Q} + \mathbf{f}_c \end{Bmatrix} \tag{3}$$

or simply

$$\mathbf{M}\ddot{\mathbf{q}} + \mathbf{C}\dot{\mathbf{q}} + \mathbf{K}\mathbf{q} = \mathbf{F}. \tag{4}$$

We desire to consider the relative displacements at the interface,

$$\epsilon = \mathbf{q}_c - \mathbf{q}_b \tag{5}$$

(where $\mathbf{q}_c$ and $\mathbf{q}_b$ represent the two sides of the interface, and these vectors will always be of the same length), and therefore substitute this vector for $\mathbf{q}_b$; this is just a linear transformation with no constraints on the system. Thus,

$$\begin{Bmatrix} \mathbf{q}_a \\ \mathbf{q}_b \\ \mathbf{q}_c \end{Bmatrix} = \begin{bmatrix} \mathbf{I} & \mathbf{0} & \mathbf{0} \\ \mathbf{0} & \mathbf{I} & \mathbf{0} \\ \mathbf{0} & \mathbf{I} & \mathbf{I} \end{bmatrix} \begin{Bmatrix} \mathbf{q}_a \\ \mathbf{q}_b \\ \epsilon \end{Bmatrix} = \mathbf{T}\bar{\mathbf{q}}, \tag{6}$$

where

$$\mathbf{T} = \begin{bmatrix} \mathbf{I} & \mathbf{0} & \mathbf{0} \\ \mathbf{0} & \mathbf{I} & \mathbf{0} \\ \mathbf{0} & \mathbf{I} & \mathbf{I} \end{bmatrix}, \bar{\mathbf{q}} = \begin{Bmatrix} \mathbf{q}_a \\ \mathbf{q}_b \\ \epsilon \end{Bmatrix}. \tag{7}$$

The transformed equations of motion are

$$\mathbf{T}^T\mathbf{M}\mathbf{T}\ddot{\bar{\mathbf{q}}} + \mathbf{T}^T\mathbf{C}\mathbf{T}\dot{\bar{\mathbf{q}}} + \mathbf{T}^T\mathbf{K}\mathbf{T}\bar{\mathbf{q}} = \mathbf{T}^T\mathbf{F}. \tag{8}$$

Performing these operations leads to

$$\left[\begin{array}{cc|c} \mathbf{M}_{aa} & \mathbf{0} & \mathbf{0} \\ \mathbf{0} & \mathbf{M}_{bb} + \mathbf{M}_{cc} & \mathbf{M}_{cc} \\ \hline \mathbf{0} & \mathbf{M}_{cc} & \mathbf{M}_{cc} \end{array}\right] \begin{Bmatrix} \ddot{\mathbf{q}}_a \\ \ddot{\mathbf{q}}_b \\ \hline \ddot{\epsilon} \end{Bmatrix}$$

$$+ \left[\begin{array}{cc|c} \mathbf{C}_{aa} & \mathbf{C}_{ab} + \mathbf{C}_{ac} & \mathbf{C}_{ac} \\ \mathbf{C}_{ab}^T & \mathbf{C}_{bb} + \mathbf{C}_{bc} + \mathbf{C}_{bc}^T + \mathbf{C}_{cc} & \mathbf{C}_{bc} + \mathbf{C}_{cc} \\ \hline \mathbf{C}_{ac}^T & \mathbf{C}_{bc}^T + \mathbf{C}_{cc} & \mathbf{C}_{cc} \end{array}\right] \begin{Bmatrix} \dot{\mathbf{q}}_a \\ \dot{\mathbf{q}}_b \\ \hline \dot{\epsilon} \end{Bmatrix}$$

$$+ \left[\begin{array}{cc|c} \mathbf{K}_{aa} & \mathbf{K}_{ab} + \mathbf{K}_{ac} & \mathbf{K}_{ac} \\ \mathbf{K}_{ab}^T & \mathbf{K}_{bb} + \mathbf{K}_{bc} + \mathbf{K}_{bc}^T + \mathbf{K}_{cc} & \mathbf{K}_{bc} + \mathbf{K}_{cc} \\ \hline \mathbf{K}_{ac}^T & \mathbf{K}_{bc}^T + \mathbf{K}_{cc} & \mathbf{K}_{cc} \end{array}\right] \begin{Bmatrix} \mathbf{q}_a \\ \mathbf{q}_b \\ \hline \epsilon \end{Bmatrix}$$

$$= \left\{\begin{array}{c} \mathbf{F}_a \\ \hline \mathbf{f}_b + \mathbf{f}_c \\ \hline \mathbf{Q} + \mathbf{f}_c \end{array}\right\}. \tag{9}$$

Note that if the structure is continuous, $\epsilon = \mathbf{0}$, and the equations of motion for that case (the first partition) are correct.

If we use the partitioned forms of the equations of motion with the first partition designated by the subscript A and the second by the subscript ϵ,

$$\begin{bmatrix} \mathbf{M}_{AA} & \mathbf{M}_{A\epsilon} \\ \mathbf{M}_{A\epsilon}^T & \mathbf{M}_{\epsilon\epsilon} \end{bmatrix} \begin{Bmatrix} \ddot{\mathbf{q}}_A \\ \ddot{\epsilon} \end{Bmatrix} + \begin{bmatrix} \mathbf{C}_{AA} & \mathbf{C}_{A\epsilon} \\ \mathbf{C}_{A\epsilon}^T & \mathbf{C}_{\epsilon\epsilon} \end{bmatrix} \begin{Bmatrix} \dot{\mathbf{q}}_A \\ \dot{\epsilon} \end{Bmatrix}$$

$$+ \begin{bmatrix} \mathbf{K}_{AA} & \mathbf{K}_{A\epsilon} \\ \mathbf{K}_{A\epsilon}^T & \mathbf{K}_{\epsilon\epsilon} \end{bmatrix} \begin{Bmatrix} \mathbf{q}_A \\ \epsilon \end{Bmatrix} = \begin{Bmatrix} \mathbf{F}_A \\ \mathbf{Q} + \mathbf{f}_c \end{Bmatrix}. \tag{10}$$

Conversion to Modal Coordinates. We desire to work with modal variables rather than the variables $\mathbf{q}_A$. Modal transformations are made by using the eigenvectors obtained by suppressing ϵ, and solving the undamped free vibration problem

$$\mathbf{M}_{AA}\ddot{\mathbf{q}}_A + \mathbf{K}_{AA}\mathbf{q}_A = \mathbf{0}. \tag{11}$$

Using the results of the corresponding eigenproblem, we form the diagonal matrix $[\omega_i^2]$ of eigenvalues and the modal matrix Φ of eigenvectors. The orthogonality of the eigenvectors can then be expressed

$$\Phi^T\mathbf{M}\Phi = [m_i] \tag{12}$$

and

$$\Phi^T\mathbf{K}\Phi = [m_i\omega_i^2], \tag{13}$$

where the matrices $[m_i]$ and $[m_i\omega_i^2]$ are diagonal. Under our original assumption of classical damping, we have also

$$\Phi^T\mathbf{C}\Phi = [2m_i\zeta_i\omega_i]. \tag{14}$$

Note that we are using the eigenvectors of the continuous system, and that the transformation will not be complete unless $\mathbf{M}_{AA}$ is of full rank.

We now introduce the change of coordinates that are

$$\begin{Bmatrix} \mathbf{q}_A \\ \epsilon \end{Bmatrix} = \begin{bmatrix} \Phi & \mathbf{0} \\ \mathbf{0} & \mathbf{I} \end{bmatrix} \begin{Bmatrix} \eta \\ \epsilon \end{Bmatrix}. \tag{15}$$

After the transformation is performed,

$$\begin{bmatrix} [m_i] & \Phi^T\mathbf{M}_{A\epsilon} \\ \mathbf{M}_{A\epsilon}^T\Phi & \mathbf{M}_{\epsilon\epsilon} \end{bmatrix} \begin{Bmatrix} \ddot{\eta} \\ \ddot{\epsilon} \end{Bmatrix} + \begin{bmatrix} [2m_i\zeta_i\omega_i] & \Phi^T\mathbf{C}_{A\epsilon} \\ \mathbf{C}_{A\epsilon}^T\Phi & \mathbf{C}_{\epsilon\epsilon} \end{bmatrix} \begin{Bmatrix} \dot{\eta} \\ \dot{\epsilon} \end{Bmatrix}$$

$$+ \begin{bmatrix} [m_i\omega_i^2] & \Phi^T\mathbf{K}_{A\epsilon} \\ \mathbf{K}_{A\epsilon}^T\Phi & \mathbf{K}_{\epsilon\epsilon} \end{bmatrix} \begin{Bmatrix} \eta \\ \epsilon \end{Bmatrix} = \begin{Bmatrix} \Phi^T\mathbf{F}_A \\ \mathbf{Q} + \mathbf{f}_c \end{Bmatrix}, \tag{16}$$

and expanding these equations we get

$$[m_i]\ddot{\eta} + \Phi^T\mathbf{M}_{A\epsilon}\ddot{\epsilon} + [2m_i\zeta_i\omega_i]\dot{\eta} + \Phi^T\mathbf{C}_{A\epsilon}\dot{\epsilon} + [m_i\omega_i^2]\eta + \Phi^T\mathbf{K}_{A\epsilon}\epsilon = \Phi^T\mathbf{F}_A \tag{17}$$

$$\mathbf{M}_{A\epsilon}^T\Phi\ddot{\eta} + \mathbf{M}_{\epsilon\epsilon}\ddot{\epsilon} + \mathbf{C}_{A\epsilon}^T\Phi\dot{\eta} + \mathbf{C}_{\epsilon\epsilon}\dot{\epsilon} + \mathbf{K}_{A\epsilon}^T\Phi\eta + \mathbf{K}_{\epsilon\epsilon}\epsilon = \mathbf{Q} + \mathbf{f}_c. \tag{18}$$

These equations may be solved if the interface forces $\mathbf{Q}$ are known (or if a function relating them to the other variables is known) or if ϵ is known. Note that a common approach is to assume $\mathbf{Q} = \mathbf{D}\dot{\epsilon}$ and to solve for the damping matrix $\mathbf{D}$. More generally, we may seek a function $\mathbf{Q} = \mathbf{Q}(\epsilon, \dot{\epsilon})$.

A Simplified Problem. We now presume that there is only one interface degree of freedom, $\mathbf{M}_{cc} = \mathbf{0}$, and there is no internal damping in the system. Then, Eqs. (17) and (18) reduce to

$$[m_i]\ddot{\eta} + [m_i\omega_i^2]\eta = \Phi^T\mathbf{F}_A - \Phi^T\mathbf{K}_{A\epsilon}\epsilon \tag{19}$$

$$\mathbf{K}_{A\epsilon}^T\Phi\eta + \mathbf{K}_{\epsilon\epsilon}\epsilon = \mathbf{Q}. \tag{20}$$

We wish to solve these for interface forces $\mathbf{Q}$ for a prescribed ϵ.

We assume the modal external forces are of the form $\Phi^T\mathbf{F}_A e^{i\Omega t}$, where $\Phi^T\mathbf{F}_A$ is real, and, hence,

$$\epsilon = \hat{\epsilon}e^{i(\Omega t + \phi)}, \tag{21}$$

where $\hat{\epsilon}$ is complex (with damping in the system displacements are, in general, not in phase with applied external loads). The solution for η will take the form

$$\eta = \hat{\eta}e^{i\Omega t}, \tag{22}$$

where $\hat{\eta}$ is complex.

Solving (19) leads to

$$\hat{\eta} = [[m_i]([\omega_i^2] - [\Omega^2])]^{-1}(\Phi^T\mathbf{F}_A - \Phi^T\mathbf{K}_{A\epsilon}\hat{\epsilon}). \tag{23}$$

By substituting into (20) it can be shown that

$$\mathbf{Q} = [\mathbf{K}_{A\epsilon}^T\Phi[[m_i]([\omega_i^2] - [\Omega^2])]^{-1}\Phi^T\mathbf{F}_A + (-\mathbf{K}_{A\epsilon}^T\Phi[[m_i]([\omega_i^2] - [\Omega^2])]^{-1}\Phi^T\mathbf{K}_{A\epsilon} + \mathbf{K}_{\epsilon\epsilon})\hat{\epsilon}e^{i\phi}]e^{i\Omega t}. \tag{24}$$

We observe that

$$\Phi[[m_i]([\omega_i^2] - [\Omega^2])]^{-1}\Phi^T = \alpha \tag{25}$$

is the dynamic flexibility matrix for the system, and, hence,

$$\mathbf{Q} = \mathbf{K}_{A\epsilon}^T\alpha\mathbf{F}_A e^{i\Omega t} + (-\mathbf{K}_{A\epsilon}^T\alpha\mathbf{K}_{A\epsilon} + \mathbf{K}_{\epsilon\epsilon})\hat{\epsilon}e^{i(\Omega t + \phi)}. \tag{26}$$

It is clear that a knowledge of vibratory motion at the interface leads to a computation of the damping forces.

State Space Formulation. In an experiment designed to lead to the calculation of $\mathbf{Q} = \mathbf{Q}(\epsilon, \dot{\epsilon})$, one would apply one or more known external loads and measure ϵ, subsequently finding $\mathbf{Q}$ from Eq. (18). With the time history of ϵ and the corresponding $\mathbf{Q}$ in hand, an appropriate functional form can be

sought or candidate forms compared. For simulation purposes, however, no such time history of relative displacements is available. We are left with the choice of explicitly specifying $\epsilon(t)$ or prescribing some kinematic relationship in order to generate realistic input data and calculate $\mathbf{Q}$. Both avenues will be pursued below.

For simplicity, the integration of Eqs. (17) and (18) is carried out in state space. Returning to the general case and solving Eq. (17) for $\ddot{\eta}$ gives

$$\ddot{\eta} = [m_i]^{-1}(\Phi^T\mathbf{F}_A - \Phi^T\mathbf{M}_{A\epsilon}\ddot{\epsilon} - [2m_i\zeta_i\omega_i]\dot{\eta} - \Phi^T\mathbf{C}_{A\epsilon}\dot{\epsilon} - [m_i\omega_i^2]\eta - \Phi^T\mathbf{K}_{A\epsilon}\epsilon). \quad (27)$$

Defining the state vector $\{\eta^T\dot{\eta}^T\}^T$ leads to

$$\begin{Bmatrix}\dot{\eta}\\ \ddot{\eta}\end{Bmatrix} = \begin{bmatrix}\mathbf{0} & \mathbf{I}\\ -[\omega_i^2] & -[2\zeta_i\omega_i]\end{bmatrix}\begin{Bmatrix}\eta\\ \dot{\eta}\end{Bmatrix} + \begin{Bmatrix}\mathbf{0}\\ [m_i]^{-1}\Phi^T\mathbf{F}_A - [m_i]^{-1}\Phi^T(\mathbf{M}_{A\epsilon}\ddot{\epsilon} + \mathbf{C}_{A\epsilon}\dot{\epsilon} + \mathbf{K}_{A\epsilon}\epsilon)\end{Bmatrix}. \quad (28)$$

If we assume some convenient form for $\epsilon(t)$, this equation can be integrated by any of several common techniques. Computations for the examples that follow were made using a Runge-Kutta routine available in the Matlab software package.

As an alternative to simply making up the displacement history normally required as input data, we can specify the ratio of displacements at the interface, i.e., let

$$\mathbf{q}_c = \beta\mathbf{q}_b. \quad (29)$$

We might expect β to be a diagonal matrix or even a scalar on physical grounds, but this is not mathematically necessary. Then,

$$\epsilon = \mathbf{q}_c - \mathbf{q}_b = (\beta - \mathbf{I})\mathbf{q}_b, \quad (30)$$

and noting that

$$\mathbf{q}_b = [\mathbf{0} \quad \mathbf{I}]\Phi\eta, \quad (31)$$

we can write

$$\epsilon = (\beta - \mathbf{I})[\mathbf{0} \quad \mathbf{I}]\Phi\eta. \quad (32)$$

Substituting this into Eq. (28), and using the following definitions:

$$\Gamma_1 = \mathbf{I} + [m_i]^{-1}\Phi^T\mathbf{M}_{A\epsilon}(\beta - \mathbf{I})[\mathbf{0} \quad \mathbf{I}]\Phi \quad (33)$$

$$\Gamma_2 = [2\zeta_i\omega_i] + [m_i]^{-1}\Phi^T\mathbf{C}_{A\epsilon}(\beta - \mathbf{I})[\mathbf{0} \quad \mathbf{I}]\Phi \quad (34)$$

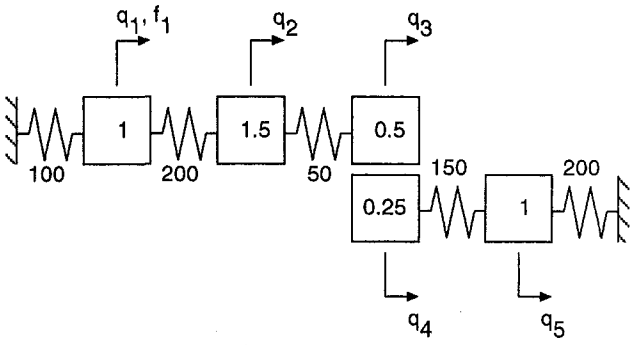

Fig. 3 Five-DOF system of example 1

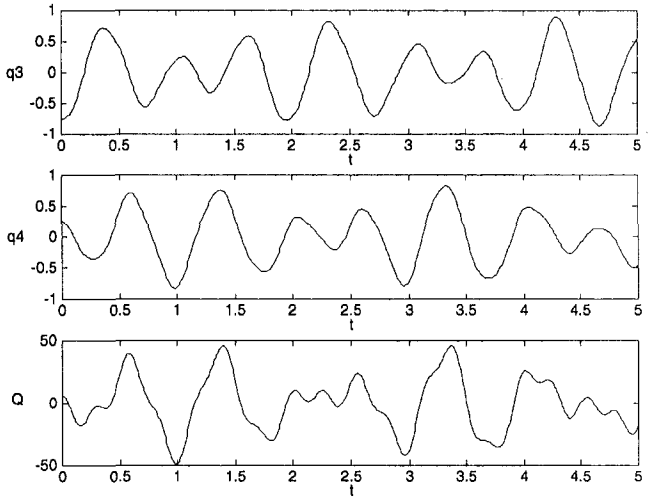

Fig. 4 Response of 5-DOF system to forced relative displacement ϵ

$$\Gamma_3 = [\omega_i^2] + [m_i]^{-1}\Phi^T\mathbf{K}_{A\epsilon}(\beta - \mathbf{I})[\mathbf{0} \quad \mathbf{I}]\Phi \quad (35)$$

we obtain

$$\ddot{\eta} = -\Gamma_1^{-1}\Gamma_2\dot{\eta} - \Gamma_1^{-1}\Gamma_3\eta + \Gamma_1^{-1}[m_i]^{-1}\Phi^T\mathbf{F}_A. \quad (36)$$

Hence, for assumed motion in the form of Eq. (29) we need to integrate

$$\begin{Bmatrix}\dot{\eta}\\ \ddot{\eta}\end{Bmatrix} = \begin{bmatrix}\mathbf{0} & \mathbf{I}\\ -\Gamma_1^{-1}\Gamma_3 & -\Gamma_1^{-1}\Gamma_2\end{bmatrix}\begin{Bmatrix}\eta\\ \dot{\eta}\end{Bmatrix} + \begin{Bmatrix}\mathbf{0}\\ \Gamma_1^{-1}[m_i]^{-1}\Phi^T\mathbf{F}_A\end{Bmatrix}. \quad (37)$$

Examples

Two discrete systems are simulated here, with the interface relative displacement specified in both ways discussed above. The first system is arbitrary in form, intended only to demonstrate the foregoing analysis. The second structure is symmetric about the interface, and, so, more closely resembles a model of two identical blades. In practice, each substructure would likely be represented by a finite element model that would not only capture the structural dynamic behavior of a blade, but, with little additional work, allow the realistic modeling of several interfacial degrees of freedom, and, thereby, permit the determination of the corresponding components of the damping force $\mathbf{Q}$.

Two Dissimilar Discrete Subsystems. As shown in Fig. 3, the system considered here is comprised of two structures, one having 3 degrees of freedom and the other 2. The force $\mathbf{Q}$ acts at the interface between masses 3 and 4, and, so that its effect on the system's response may be clearly seen, we assume the structure to be otherwise undamped. Stiffness and mass values are given in the figure. We identify degrees of freedom 1, 2, and 5 as belonging to set a, and choose DOF 3 as side b of the interface and DOF 4 as side c.

Omitting external loads and specifying the relative displacement,

$$\epsilon(t) = \cos 2\pi f_\epsilon t, \quad (38)$$

where $f_\epsilon = 1.5$ Hz. We easily integrate Eq. (17) to obtain η, and then solve (18) for Q at each time step. Initial conditions were found by solving for the static displacements resulting from imposing $\epsilon(0)$. The displacements of masses 3 and 4 and the force Q are plotted in Fig. 4.

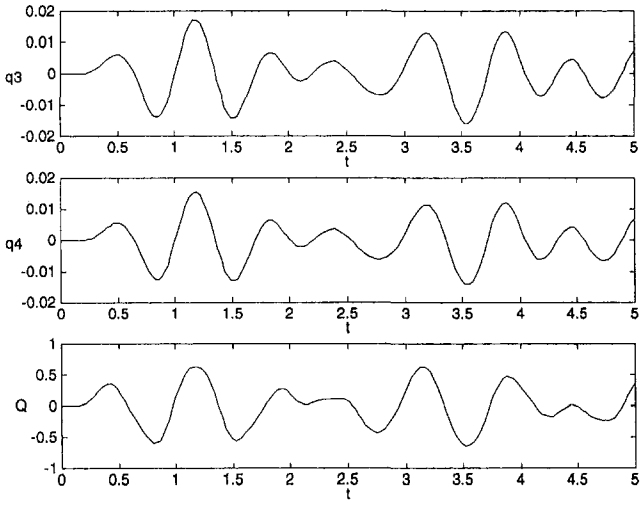

Fig. 5 Response of 5-DOF system to a sinusoidal load with $\beta = 0.9$ and resulting force Q

The same system was next studied by assuming $\beta = 0.9$ and driving mass 1 with the load

$$f_1(t) = \sin 2\pi f_f t, \tag{39}$$

where $f_f = 1.5$ Hz. This value of β was chosen to represent slip between the masses without completely decoupling the substructures, and requires that the motion be such that the displacement of mass 4 is in phase with that of mass 3 but of slightly lesser amplitude. The limiting cases of $\beta = 1$, a "locked" interface, and $\beta = 0$, where the 2-DOF structure does not participate in the response, present no numerical difficulties and were used to test the computer programs. Some choices of β can lead to instabilities, however, as they correspond to negative damping. Nonetheless, this description of the relative motion through a kinematic constraint has proved quite useful in developing these simulations.

Equation (37) was integrated, and Q was recovered as before. Figure 5 shows the displacements of masses 3 and 4, the resulting ϵ, and the calculated Q. In Fig. 6, Q is plotted versus ϵ and $\dot{\epsilon}$. No simple functional form for $Q(\epsilon, \dot{\epsilon})$ suggests itself, but this is not too surprising given the somewhat artificial nature of the assumed motion.

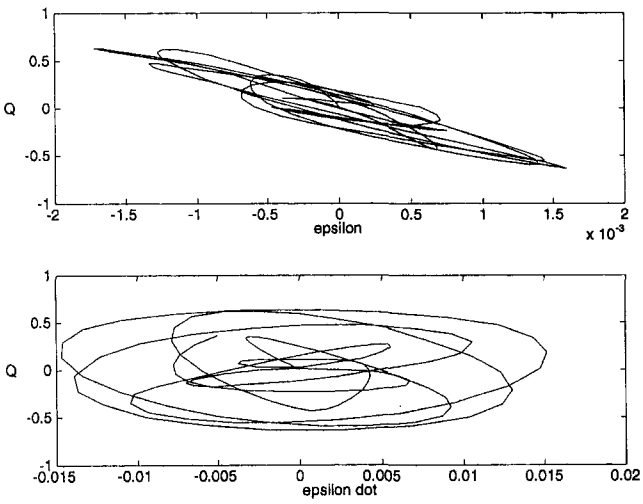

Fig. 6 Force Q plotted versus relative displacement and relative velocity

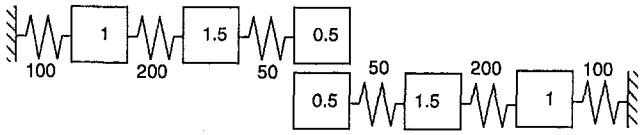

Fig. 7 Symmetric 6-DOF system of example 2

Symmetric Discrete Model. A system consisting of two identical substructures is shown in Fig. 7. The degrees of freedom were grouped as $a = (1, 2, 5, 6)$, $b = 3$, and $c = 4$, and computations similar to those described in the last example were carried out.

Specifying ϵ, as in Eq. (38) but with $f_\epsilon = 2$ Hz, the displacements and the interface force shown in Fig. 8 were computed. As expected, the response of the entire system was found to be symmetric about the interface.

When $\beta \neq 1$ is prescribed instead of ϵ, the symmetry of the system is lost. This is demonstrated by taking $f_1(t)$, as before with $f_f = 2$ Hz, and letting $\beta = 0.95$, leading to the results shown in Fig. 9.

In order to demonstrate the processing of data such as would be obtained from an experiment, the response of this example system to a unit harmonic load $f_1(t)$ of frequency 5 Hz was calculated by direct numerical integration of Eq. (3). For the purpose of this simulation it was necessary to assume a form for the force Q acting at the single interface; the overall effectiveness of the method could then be judged by its ability to identify the parameters of this Q from simulated data. The function

$$Q = -10\dot{\epsilon} - 0.05 \operatorname{sgn} \dot{\epsilon} \tag{40}$$

was selected to represent viscous and Coulomb damping at the interface. (The negative signs of the coefficients follow from the convention used in developing the original equation of motion.) This system was assumed to be otherwise viscously proportionally damped, represented by

$$\mathbf{C} = 0.01\mathbf{K} \tag{41}$$

in Eq. (4). The motion of the structure was simulated for one second, starting from quiescent initial conditions. Time histories of f_1 and of ϵ, $\dot{\epsilon}$, and $\ddot{\epsilon}$ were saved during this calculation and

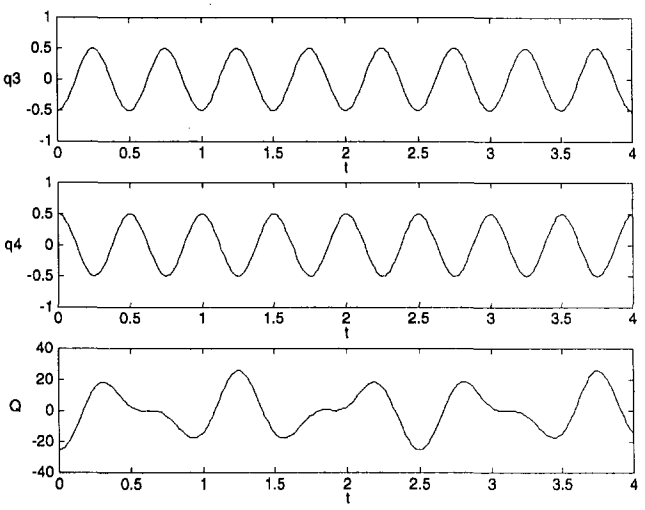

Fig. 8 Response of symmetric system to prescribed relative displacement

used as input in the subsequent calculation, as would be experimentally obtained force and response data.

A record of the interface force was then computed by moving all of the terms in ϵ and its derivatives to the right-hand side of Eq. (17), then integrating it numerically to obtain η, $\dot{\eta}$ and $\ddot{\eta}$. These were substituted into Eq. (18), resulting in a sequence of Q values at the same time steps as the previously simulated ϵ, $\dot{\epsilon}$, and $\ddot{\epsilon}$. This procedure for computing Q is exactly the same as would be done in processing experimentally measured applied load and relative displacement data.

The following three functional forms for Q were then tested:

$$Q_1 = -C\dot{\epsilon} \tag{42}$$

$$Q_2 = -C\dot{\epsilon} - \mu \operatorname{sgn} \dot{\epsilon} \tag{43}$$

$$Q_3 = -C\dot{\epsilon} - \mu \operatorname{sgn} \dot{\epsilon} - k\epsilon \tag{44}$$

The coefficients of these models were determined from the Q and ϵ, $\dot{\epsilon}$ time histories by using Matlab system identification routines to fit an ARX model equation. The results are presented in Table 1, where it may be seen that the best fit was obtained with the "correct" friction model Q_2.

Finally, we should comment on the feasibility of extrapolating from these examples to larger-scale tests and computations. While test rigs designed specifically to produce simple, controlled interfacial motion may actually have only a few degrees of freedom, it is of course desirable to apply the method presented here to more complex, realistic structures. Two points are worthy of note in this regard. First, as the number of degrees of freedom becomes larger, the solution of the matrix eigenproblem that must precede the integration of Eq. (17) will become more expensive, requiring roughly the same type and amount of computation as would a free vibration analysis of the system. Since calculations of the latter type for even complex structural models are today commonly performed at acceptable speeds on workstations and desktop computers, the cost of the eigenproblem solution should not discourage application of the present method. Second, the subsequent numerical integration of uncoupled differential equations that yields η lends itself to efficient computation. The cost of the identification step will depend on the algorithm used and the record lengths processed, but can be expected to be small compared to that of the structural analysis. All computations for the examples of this paper were done on a Macintosh computer using simple, unoptimized algorithms, and ran fast enough that they could be executed interactively.

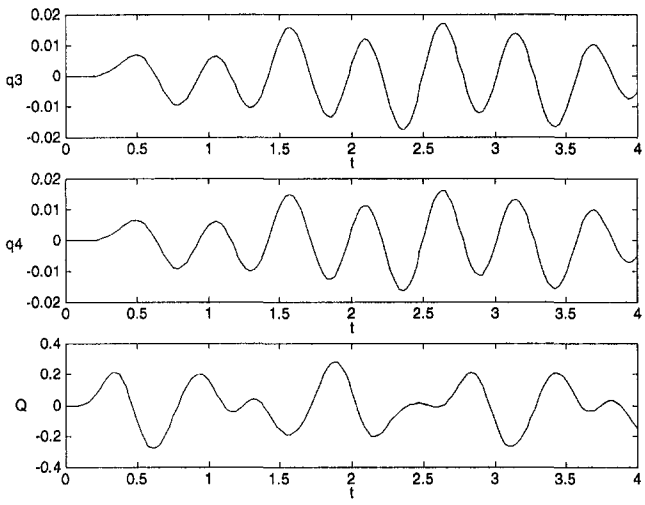

Fig. 9 Forced response of symmetric system with $\beta = 0.95$

Table 1 Identified friction law parameters for example 2

Model	c	μ	k
Q_1	106.85	—	—
Q_2	10.010	0.050	—
Q_3	10.010	0.050	0.025

Conclusion

The main thrust of this paper is to provide an analytical and numerical basis to support the derivation of functional forms of forces at rubbing interfaces in vibrating structures. While the approach developed here is general, the most direct application of the analysis is to the design of bladed disk assemblies with part-span shrouds.

The motivation for this work arises out of largely unsuccessful attempts by several researchers over several decades to characterize dynamic friction forces. Measurement of stresses at interfaces in complex structural interfaces is nearly impossible. This status is understandable if one recognizes that the parameters that govern the dynamics of interfaces include, among others, the normal force that holds the surfaces together, the size and distribution of asperities, and the frequency of vibration. The boundary conditions may vary from a nearly locked joint to a freely slipping condition. It is unlikely that engineers engaged in the design analysis of complex systems such as bladed disk assemblies would accept one or another representation of friction forces that has not been calibrated experimentally.

The analysis presented in this paper can be extended to the analysis of bladed disk assemblies whose basic modes of vibration are available from a computation of the assembly with all shrouds modeled as being locked. The only other data needed is time history of motion at the shrouds. With this hybrid set of information coming from analysis and experimentation, the procedure leads to a description of the interface forces from which functional forms can be obtained. It is hoped that with fairly representative data from laboratory, rig, and engine tests, confidence can be built in the functional forms of dynamic friction forces so that in a new design situation the analyst can make computations on the basis of an assumed, but calibrated, friction law.

References

Griffin, J. H., and Menq, C.-H., 1991, "Friction Damping of Circular Motion and its Implications to Vibration Control," *ASME Journal of Vibration and Acoustics,* Vol. 113, pp. 225–229.

Menq, C.-H., Griffin, J. H., and Bielak, J., 1986a, "The Forced Response of Shrouded Fan Stages," *ASME Journal of Vibration Acoustics, Stress and Reliability in Design,* Vol. 108, pp. 50–55.

Menq, C.-H., Griffin, J. H., and Bielak, J., 1986b, "The Influence of a Variable Normal Load on the Forced Vibration of a Frictionally Damped Structure," ASME JOURNAL OF ENGINEERING FOR GAS TURBINES AND POWER, Vol. 108, pp. 300–305.

Oden, J. T., and Martins, J. A. C., 1985, "Models and Computational Methods for Dynamic Friction Phenomena," *Computer Methods in Applied Mechanics and Engineering,* Vol. 52, pp. 527–634.

Richardson, R. S. H., and Nolle, H., 1976, "Surface Friction Under Time-Dependent Loads," *Wear,* Vol. 37, pp. 87–101.

Srinivasan, A. V., ed., 1976, *Structural Dynamic Aspects of Bladed Disk Assemblies,* bound volume published by ASME at the Winter Annual Meeting, New York, NY.

Srinivasan, A. V., Lionberger, S. R., and Brown, K. W., 1978, "Dynamic Analysis of an Assembly of Shrouded Blades Using Component Modes," *ASME Journal of Mechanical Design,* Vol. 100, No. 3, pp. 520–527.

Srinivasan, A. V., and Cutts, D. G., 1983a, "Dry Friction Damping Mechanisms in Engine Blades," *ASME Journal of Engineering for Power,* Vol. 105, pp. 332–341.

Srinivasan, A. V., ed., 1983b, *Vibrations of Bladed Disk Assemblies,* bound volume published by ASME at the Design Engineering Technical Conference on Mechanical Vibration and Noise.

Srinivasan, A. V., 1984a, "Characteristics of Dry Friction Forces," paper presented at the Vibration Damping Workshop, Long Beach, California.

Srinivasan, A. V., 1984b, "Measurement of Relative Vibratory Motion at the Shroud Interfaces of a Fan," *ASME Journal of Vibration, Acoustics, Stress, and Reliability in Design,*

Srinivasan, A. V., 1984c, "Vibrations of Bladed Disk Assemblies: A Selected Survey," *ASME Journal of Vibration, Acoustics, Stress, and Reliability in Design,* Vol. 106, pp. 165–168.

Srinivasan, A. V., 1984d, unpublished notes, Worcester Polytechnic Institute, Worchester, MA.

Srinivasan, A. V., 1988, "Dynamic Friction" *Large Space Structures and Control,* Springer-Verlag KG, Berlin, Germany, Chapter #.

Srinivasan, A. V., 1994, "Direct Use of Unsteady Aerodynamic Pressures in the Flutter Analysis of Mistuned Blades," *Journal de Physique,* c. October 1995.

Srinivasan, A. V., Cassenti, B. N., and Cutts, D. G., 1984, "Study of Characteristics of Dry Friction Damping," annual report, Technical Report R84-956479-1, United Technologies Research Center, East Hartford, Connecticut.

Srinivasan, A. V., Cassenti, B. N., and Cutts, D. G., 1985, "Study of Characteristics of Dry Friction Damping," final report, Technical Report R85-956479-2, United Technologies Research Center, East Hartford, Connecticut.

Experimental Investigation and Theoretical Prediction of Flutter Behavior of a Plane Cascade in Low Speed Flow

H. Hennings

W. Send

Bunsenstrase 10,
Goettingen, D-37073,
Germany

The Institute of Aeroelasticity operates a test facility which enables aeroelastic investigations of plane cascades in low-speed flow. The test stand serves as a pilot facility to develop tools for analogous investigations in transonic flow. Eleven blades are elastically suspended in a windtunnel with a 1 × 0.2 m^2 cross section. This paper describes the experimental method of determining the flutter boundary by extrapolation of the results measured in subcritical flow. A two-dimensional theoretical model of the 11 blades, including the windtunnel walls, permits the computation of unsteady pressures, forces, and moments in close relation to the experiment. The prediction of flutter is compared with experimental results. In the present investigation, the motion of the blades is constrained to pitch around mid-chord. The vibrating blades are mechanically uncoupled. Any interaction between the blades is effected by the air stream, leading to a sensitive dependence on the aerodynamic forces.

Introduction

Aeroelastic problems in turbomachines are surveyed in several publications covering the research carried out during the past two decades. The AGARD manual on this topic (1987, 1988) provides a comprehensive overview from the beginning. Although Bendiksen's review (1993) attempts to cover this field from the beginning as well, emphasis is placed on recent developments. Försching (1994) concentrates on the formulation of the cascade flutter problem for the three-dimensional case and on parametric studies in subsonic and supersonic flow.

To the authors' knowledge, Lane (1956) is the first to describe the traveling waves in a perfectly tuned rotor as system mode shapes. Assuming linearity in the dynamic system, Crawley (1988) transforms the traveling waves into a formulation on the basis of single blade vibrations. Two different concepts, the plane and the annular cascade, are applied in experimental investigations to approach the fairly complicated geometry of a three-dimensional rotor. The papers cited below are selected from a large variety of publications to exemplify the two concepts.

The plane cascade approximates the coaxial cylindrical section through an annular blade row. Thereby, the infinite number of blades in the circumferential direction is reduced to a finite number enclosed by the windtunnel walls. The experiment described in this paper belongs to this type of modeling the rotor. Carta (1982) forces traveling waves and measures the aerodynamic response. Széchényi et al. (1984) and Buffum and Fleeter (1990) excite one blade and determine the influence coefficients on the other blades.

The annular cascade is the natural model for investigating the flow in turbomachines. However, the realization of inflow conditions is difficult and measurements cause problems in many respects. Knauf (1985) and Körbächer and Bölcs (1994) investigate the behavior of compressor blades.

In contrast to the technique of forced motion in the preceding papers, the free vibrations of three-dimensional elastic blades arranged as an annular blade row are studied by Kurkov (1982), Storey (1984), and Stargardter (1988). With respect to elastic suspension, their arrangements are similar to the setup in the present experiment.

The stabilizing effect of mistuning on the flutter boundary has been discussed in a series of theoretical papers by Bendiksen (1984), Kaza and Kielb (1984), Crawley and Hall (1985), and Bloemhof (1988). In addition to these investigations, the effect of mistuning on the response behavior is described by Kaza and Kielb (1982) and by Dugundji and Bundas (1984). Experimental work has been done by Kaza et al. (1987). Both aspects of mistuning—the stabilizing effect on the flutter boundary and the influence on the response behavior—are also covered by the work outlined in this paper.

This paper addresses four major issues:

1. A full set of all frequency response functions is obtained in the subcritical region of the cascade.
2. The response functions are measured well enough to be decomposable into a complete set of all eigenvectors and eigenvalues of the aeroelastic system.
3. The flutter case is recorded and compared with the subcritical results. A theoretical model is developed in close relation to the experimental setup. The theoretical framework covers the frequency response functions as well as the flutter case.
4. The stabilizing effect of mistuning is demonstrated in the frequency response functions. Flutter velocity increases for a decreasing mass in one selected blade.

Description of the Test Stand

The open-circuit windtunnel is driven by a 75 kW DC motor. The radial compressor delivers a volume flow of 12.5 m^3/s at a total pressure difference of 4.35 kPa. The air velocity reaches 60 m/s in the test section.

Eleven compressor blades made of material reinforced by carbon fiber with constant chord lengths of $l = 0.150$ m and $b = 0.197$ m spans are installed inside. They are fixed on one side by a tapered bolt union at a 50 percent chord length, allowing the angle of incidence to be adjusted. The blade cross section is based on the NACA 65 series with a circular arc camber of 10 deg and a thickness of 6 percent. The stagger angle is 43 deg

Contributed by the International Gas Turbine Institute and presented at the 41st International Gas Turbine and Aeroengine Congress and Exhibition, Birmingham, United Kingdom, June 10–13, 1996. Manuscript received by the ASME Headquarters March 3, 1997. Paper No. 96-GT-417. Associate Technical Editor: J. N. Shinn.

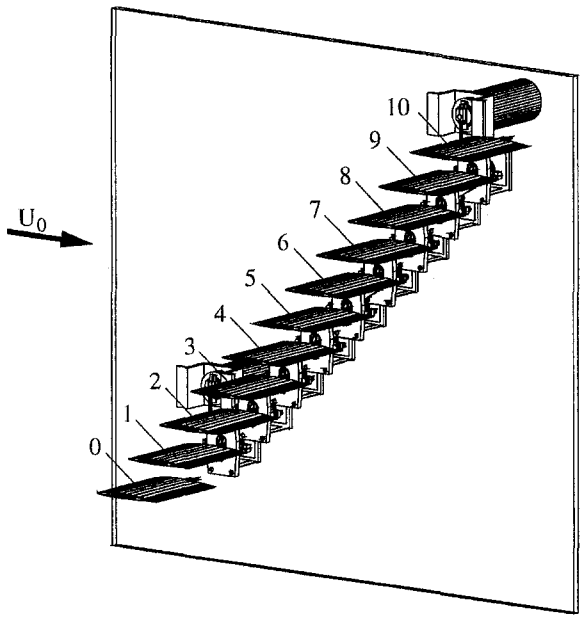

Fig. 1 Test section

and the slant gap is 0.1125 m wide. The blades are numbered from 0 to 10. Figure 1 shows the main features.

Both outer blades are rigidly fixed to the section wall. Despite the one-sided fixture, the remaining blades are supported in such a way that the same motion is achieved at each blade section without any spanwise component. The flexible elements are designed to permit simultaneous plunging and pitching motion. The elastic axis is located at the blade bolt union. The two degrees of freedom can be suppressed individually to investigate pure plunging or pitching motion. The blades can be forced to harmonic motion or they can vibrate freely. The maximum amplitudes are 10 mm for plunging motion and 10 deg for pitching motion.

Stepper motors are used for forced motion, their crank gears driving the individual blades to vibrations with adjustable frequency. The blades are nearly harmonically oscillated with almost equal amplitudes. The phases can be adjusted separately for each blade. In particular, a fixed interblade phase angle can be introduced. Experiments and measurements of this type have been carried out by Sachs (1991). His work also comprises extended pressure measurements.

Present Investigations

In general, the linearized description of an oscillating cascade reads as

$$\mathbf{M}\ddot{\mathbf{q}} + \mathbf{K}\mathbf{q} - \mathbf{L}\mathbf{q} = \mathbf{f}, \quad \mathbf{q} = (q_1, \ldots, q_n)^T. \tag{1}$$

M is the mass matrix, **K** reflects the stiffness of the system, and **L** represents the external fluid forces. **f** is an additional fluid force, which may act on the cascade. The q_i are the degrees of freedom of the mechanical system. The corresponding theoretical model provides the aerodynamic coefficients needed for flutter calculations ($\mathbf{f} = 0$) as well as for the response functions induced by the forced vibration of one of the blades ($\mathbf{f} \neq 0$).

In the present investigation, the motion of the blades is constrained to one type: pitching around mid-chord. Blades 0, 9, and 10 are fixed in all cases. The response of the seven inner blades 2 to 8 due to excitation of blade 1 is considered. In the flutter case, blade 1 is fixed like the blades 0, 9, 10.

Harmonic analysis of Eq. (1) leads to the general solution

$$\mathbf{q}(t) = \sum_{k=1}^{k=n} c_k \phi_k e^{\lambda_k t}, \quad \lambda_k = -\delta_k + j\omega_k, \tag{2}$$

which consists of n complex eigenvalues λ_k together with n eigenvectors ϕ_k. Each eigenvalue represents one frequency together with damping. The corresponding eigenvector describes amplitudes and phases of all degrees of freedom.

Flutter analysis is based on the following two different measurement processes.

Case 1: Subcritical Region. Blade 1 is forced to harmonic pitch motion, thereby exciting the inner seven blades that are free to respond in pitch. The transfer behavior is represented by frequency response functions, leading to the modal parameters. The aim of the measurement is to find all of the expected seven eigenvalues and their eigenvectors, each of the latter ones consisting of seven components.

Case 2: Flutter Case. Blade 1 is fixed. Approaching flutter velocity, all blades start oscillating with almost constant amplitudes in time; however, they differ in magnitude and phase lag from blade to blade. The corresponding individual time histories are evaluated by Fourier analysis, leading to one distinct state of motion.

The following table gives an overview over the various investigations and the applied methods.

All experimental data in this paper are pure kinematic data. They are obtained from measurements using strain gages. No aerodynamic informations like pressure distributions or mo-

Nomenclature

u_0 = windtunnel velocity (m/s)
u_f = flutter velocity (m/s)
l = blade chord (m)
b = span (m)
$S = bl$ = plan form area (m^2)
$\omega = 2\pi f$ = circular frequency (s^{-1})
$\omega^* = \omega l/u_0$ = reduced frequency (−)
ρ = air density (kg m^{-3})
c_M = moment coefficient (−)
i = blade number (−)
j = imaginary unit
α_0 = amplitude of exciting blade 1 (deg)
α_i = amplitude of blade i, i = 2 . . . 8 (deg)
γ_i = phase of blade i, i = 2 . . . 8 (deg)
$\mathbf{M}$ = mass matrix (kg m^2)
$\mathbf{K}$ = stiffness matrix (Nm)
$\mathbf{L}$ = aerodynamic influence matrix (Nm)
$\mathbf{L}^* = \mathbf{L}/\omega^2$ = modified $\mathbf{L}$ (Nms^2)
$\mathbf{q} = (q_i)^T$ = DOF vector and components (−)
$\mathbf{f} = (f_i)^T$ = additional fluid force vector (Nm)
$\phi_k = (\phi_{ki})^T$ = kth eigenvector and components
$\lambda_k = -\delta_k + j\omega_k$ = kth eigenvalue with damping and frequency (s^{-1})
$D_k = \delta_k/\omega_k$ = relative damping (−)
a_k = kth modal participation factor (−)
$r_{i1k} = c_k\phi_{ki}$ = measured ith component of kth eigenvector due to exciting blade 1
$G_{i1}(j\omega) = (\alpha_i(j\omega)/\alpha_0)e^{j\gamma_i(j\omega)}$ = ith complex frequency response function (−)
$G_{i1}(j\omega)_{\text{calc}}$ = reconstructed $G_{i1}(j\omega)$ (−)

Table 1 Experimental and theoretical investigations

	Theory	Experiment
Case 1 Subcritical	Response functions by forced harmonic motion †	Response functions by forced harmonic motion
Case 2 Flutter	Eigenvalue analysis (search for first eigenvalue with zero damping)	Self-excited oscillations with constant amplitude (zero damping)

† This investigation replaces the eigenvalue analysis applied in the previous version of this paper (Hennings and Send, 1996).

ments are needed for evaluating the eigenvalues and eigenvectors. A comprehensive description of the measurement techniques is given by Hennings (1994).

Mechanical Properties

Table 2 shows the elastomechanical properties of the seven inner blades. The m_i are the diagonal elements of matrix **M**, the $m_i\omega_{0i}^2$ are those of **K**. For a pure pitching motion, the "masses" are given as moments of inertia with respect to pitch axis.

The assemblage named "Config. I" with almost identical frequencies is referred to as a "tuned" configuration. The tuning is achieved by adjusting the mass of the blades. The stiffness of the springs cannot be altered. Structural damping needs not to be taken into account. Referring to aperiodic damping as the limiting case, the damping rate is below 0.2 percent. Due to low mass and low structural damping, small aerodynamic forces are sufficient to induce flutter behavior.

Two further configurations named "Config. II" and "Config. III" are considered that are "mistuned." In both cases, blade 5 possesses a higher eigenfrequency. The precise values are listed in Table 3. For the sake of convenience, the resulting mistuned frequency is also noted.

In case 1, the amplitude of the driven blade 1 is $\alpha_0 = 0.4$ deg for all measurements. A particular question as to why the amplitude has not been further diminished to come closer to the flutter point might come up in the course of this paper. The simple answer is that the mechanics of the drive unfortunately does not permit a lower level. During the experiments this level of 0.4 deg turned out to be high enough to identify all modes. Higher amplitudes do not improve the resolution of the modes; they only increase the height of response. Even the low level of α_0, closer to the flutter point than at u_{03} in Table 5, exceeds the desired energy input into the flow field.

Table 2 Mechanical characteristics of "Config. I," $m_{ref} = 3.084 \cdot 10^{-4}$ kgm^2; $\omega_{0i} = \omega_{ref} = 2\pi \cdot 21.0\text{s}^{-1}$

Blade i	$\delta_i = \frac{m_i\omega_{0i}^2}{m_{ref}\omega_{ref}^2} - 1$	$\varepsilon_i = \frac{m_i}{m_{ref}} - 1$	$\frac{\omega_{0i}}{2\pi}$ [Hz]
2	+0.013	+0.013	21.0±0.01
3	-0.009	-0.009	21.0±0.01
4	+0.042	+0.042	21.0±0.01
5	+0.010	+0.010	21.0±0.01
6	-0.012	-0.012	21.0±0.01
7	+0.053	+0.053	21.0±0.01
8	-0.100	-0.100	21.0±0.01

Table 3 Mass parameter and frequency for the three configurations

Config.	*I*	*II*	*III*
ε_5	+0.010	-0.036	-0.096
$\omega_{05}/2\pi$ [s^{-1}]	21.0	21.5	22.2

Theoretical Model

Equation (1) serves as the basic equation for the theoretical computation. The mechanical data in Table 2 are entered into the eigenvalue analysis. The fluid forces **L**—the moments of the pitching motion in this particular experiment—are compiled from the unsteady pressures on the seven blades.

The numerical model is a two-dimensional windtunnel that is set up in the computer exactly as shown in Fig. 1. The mathematical procedure is an higher order panel method, in which the vorticity transport equation is solved for an infinitely thin boundary layer. The method rests on an analytical solution of the three-dimensional wake function (Send, 1984). The method includes the approximate computation of skin friction from the local vorticity vector as well as compressibility effects. In incompressible flow, the steady and the unsteady aerodynamic interference problem between the tunnel walls and the 11 blades, is solved for various reduced frequencies. Thereby, each unsteady solution rests on the knowledge of the steady solution. Recently, a full description of the computational method was accomplished (Send, 1995). However, the code is in use for a longer period without having been fully documented.

Figure 2 illustrates the mathematical formulation of the interference problem. In the case of an infinitely thin boundary layer the relative velocity $\mathbf{v}_{rel}$ has to be tangential to all 13 surfaces (2 windtunnel walls and 11 blades):

$$\sum_{k=1}^{k=13} \mathbf{v}_{rel}(\mathbf{x}_{S,k}, t) \cdot \mathbf{n}_S(\mathbf{x}_{S,k}, t) = 0. \tag{3}$$

$\mathbf{n}_S$ is the vector normal to the respective surface S. The surfaces are discretized into panel elements (50 panels for each wall, 40 for each blade). The relative velocity is the sum of the induced velocity $\mathbf{v}_{ind}$ and the kinematic velocity $\mathbf{v}_{kin}$. The kinematic velocities of all bodies are known. With

$$\mathbf{v}_{ind}(\mathbf{x}_S, t) \cdot \mathbf{n}_S(\mathbf{x}_S, t) = -\mathbf{v}_{kin}(\mathbf{x}_S, t) \cdot \mathbf{n}_S(\mathbf{x}_S, t), \tag{4}$$

Equation (3) leads to an integral equation for the induced velocity, which depends on the unknown vorticity vector **j**:

$$\mathbf{v}_{ind}(\mathbf{x}, t) = \text{rot } \mathbf{A}(\mathbf{x}, t). \tag{5}$$

The vector potential A is given as

$$\mathbf{A}(\mathbf{x}, t) = \frac{1}{4\pi} \iint_{W+S} \frac{\mathbf{j}(\mathbf{x}', t)}{|\mathbf{x} - \mathbf{x}'|} dS', \tag{6}$$

where **j** is a surface function with the dimension m/s. $W + S$ represent the surfaces of all bodies and all wakes downstream.

With **j** given as $\mathbf{j}(\mathbf{x}', t) = \text{grad } \sigma(\mathbf{x}', t) \times \mathbf{n}_S(\mathbf{x}', t)$, the boundary condition (3) leads to an integral equation for one value σ_{22} of the biquadratic scalar function σ in each panel (3 × 3 coefficients). All other coefficients of σ are implicitly defined by continuity conditions and other constraints. The structure of the discretized integral equation is shown in Fig. 2. The matrix on the left-hand side is formed by the influence coefficients of the induced velocities in Eq. (4). Each box in the solution vector represents all unknown σ_{22} for one body; only the shaded inner seven components are needed for the seven blades $i = 2, \ldots 8$.

On the right-hand side, the normal components of the kinematic velocity are given for the eight blades that are in motion. Each column leads to one solution. The first column is the

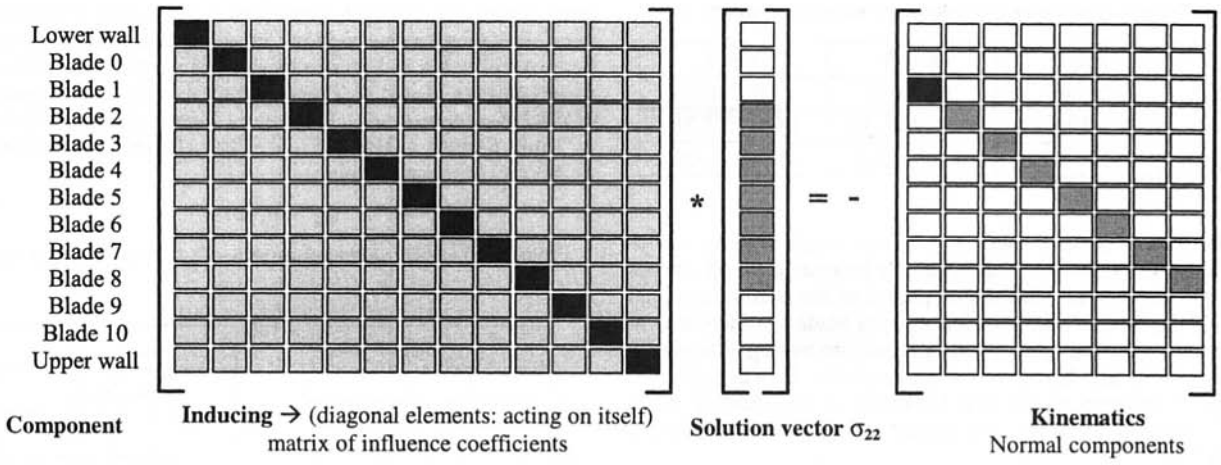

Fig. 2 Illustration of the mathematical formulation of the interference problem

oscillating blade 1 for the response functions. The solution is the additional fluid **f**. The next seven columns lead to a set of seven solutions, which form the influence matrix **L**. Finally, the pressure coefficients are obtained from Bernoulli's equation. The required potential functions $\Phi(\mathbf{x}, t)$ in this equation are related to the vorticity vector **j** via Ampère's theorem, and they are given by

$$\Phi(\mathbf{x}, t) = \frac{1}{4\pi} \iint_{W+S} \sigma(\mathbf{x}', t) \frac{\mathbf{n}(\mathbf{x}', t) \cdot (\mathbf{x} - \mathbf{x}')}{|\mathbf{x} - \mathbf{x}'|^3} dS'. \quad (7)$$

In the case of blade k oscillating, the pressure coefficient reads as follows:

$$c_P(\mathbf{x}, t) = \frac{1}{u_0^2} (\mathbf{v}_{\text{kin},0}^2 - \mathbf{v}_{\text{rel},0}^2) + \frac{2}{u_0^2} \cdot (\mathbf{v}_{\text{kin},0} \cdot \mathbf{v}_{\text{kin},i} - \mathbf{v}_{\text{rel},0} \cdot \mathbf{v}_{\text{rel},i} + j\omega\Phi_i)\alpha_k e^{j\omega t} + [\ldots] \quad (8)$$

All functions depend on **x**. The unsteady vector functions and the potential function (index i) depend also on t.

In the case of harmonic analysis with

$$\mathbf{q} = \mathbf{q}_0 e^{\lambda t}, \quad \ddot{\mathbf{q}} = \lambda^2 \mathbf{q}, \quad (9)$$

Equation (1) reads as

$$(\lambda^2 \mathbf{M} + \mathbf{K} - \mathbf{L})\mathbf{q} = \mathbf{f}. \quad (10)$$

In the fluid force **L**,

$$\mathbf{L} := \omega^2 \mathbf{L}^*(\omega^*), \quad (11)$$

with

$$\mathbf{L}^*(\omega^*) = \tfrac{1}{2}\rho S l^3 \omega^{*-2}[[c_{M,ij}(\omega^*)]], \quad (12)$$

where the $-\omega^2$ is identified with λ^2. The procedure rests on the assumption that fluid forces calculated for a real frequency ω can still by applied in the case of low damping with a complex $\lambda = -\delta + j\omega$.

The additional fluid force vector is given by

$$\mathbf{f} = (L_{i1})^T \alpha_0 e^{j\omega t}, (L_{i1}) = (L_{21}, L_{31}, \ldots, L_{81}). \quad (13)$$

In case 1, the frequency response functions are found by simply solving Eq. (10) for **q**:

$$\mathbf{q} = (\lambda^2 \mathbf{M} + \mathbf{K} - \mathbf{L})^{-1} \cdot \mathbf{f} \quad (14)$$

Dividing both sides by the amplitude α_0, the functions in **q** are the normalized complex response of the seven inner blades to the forced oscillation of blade 1.

In case 2, the additional fluid force vector is zero. Equation (10) is iteratively solved by increasing the flow velocity u_0 until the first eigenvalue shows a real value, i.e., with zero damping. The corresponding velocity is identified as being the flutter velocity of the system. The moment coefficients $c_{M,ij}$ for the seven inner blades are attained in the following way:

- Each column j is extracted from one solution j for the computational model.
- Each row i is constituted from the values for one distinct blade i, $i = 2, \ldots, 8$.
- In solution j, blade $i = j$ is in pitching motion; all other blades remain at rest. For the eigenanalysis, the influence coefficients of the pitching blade on itself and on the other six blades are required, being stored in $c_{M,ij}$.

In fact, this matrix is a 7 by 7 matrix. The nomenclature for the blades in the preceding explanation has been retained only for the consistency of description. For a reduced frequency, $\omega^* = 0.8$, Table 4 illustrates the pattern of **L**. Compared with the corresponding values for a single profile in free stream,

$$c_M = (1.0251, -0.3852),$$

the higher values for both real and imaginary parts reflect the impact from the windtunnel walls and the neighboring profiles on the diagonal elements.

Frequency Response Functions (Case 1)

For "Config. I," the frequency response functions $G_{i1}(j\omega)$ for each blade i due to exciting blade 1 have been measured at three different onset velocities u_{0k} (see Table 5).

Table 4 Complex moment coefficients $c_{M,ij}$ for $\omega^* = 0.8$

REAL	2	3	4	5	6	7	8
2	1.2164	0.0686	0.0150	0.0089	0.0060	0.0041	0.0024
3	-0.5268	1.2186	0.0688	0.0151	0.0090	0.0058	0.0036
4	-0.0291	-0.5275	1.2220	0.0696	0.0155	0.0091	0.0055
5	-0.0071	-0.0267	-0.5271	1.2257	0.0706	0.0162	0.0093
6	-0.0029	-0.0038	-0.0244	-0.5265	1.2299	0.0722	0.0174
7	-0.0026	0.0008	-0.0010	-0.0223	-0.5254	1.2355	0.0750
8	-0.0033	0.0011	0.0037	0.0014	-0.0197	-0.5228	1.2449
IMAG	2	3	4	5	6	7	8
2	-0.4812	0.0118	-0.0139	-0.0117	-0.0086	-0.0062	-0.0043
3	0.2424	-0.4799	0.0133	-0.0124	-0.0106	-0.0079	-0.0057
4	0.0481	0.2426	-0.4791	0.0143	-0.0116	-0.0102	-0.0077
5	0.0229	0.0472	0.2431	-0.4788	0.0145	-0.0116	-0.0104
6	0.0113	0.0208	0.0470	0.2435	-0.4794	0.0137	-0.0127
7	0.0060	0.0086	0.0200	0.0467	0.2432	-0.4815	0.0111
8	0.0033	0.0030	0.0076	0.0195	0.0457	0.2411	-0.4866

Table 5 Parameters for frequency response functions

	$k = 1$	$k = 2$	$k = 3$
u_{0k}	15.8 m/s	16.9 m/s	18.2 m/s
f	19.3-20.5 Hz	18.5-20.5 Hz	18.5-20.5 Hz
ω^*	1.15 -1.22	1.03 -1.14	0.96 - 1.06

The range for the frequency intervals varies slightly due to the maximum response. The frequency increment for all sweeps is $\Delta f = 0.0096$ Hz. During one period of the excitation signal controlling blade 1, the position of each blade i is measured at 32 equidistant time intervals. 64 periods are averaged to obtain the dominant first harmonic of the response. This complex response is referred to the first harmonic of the exciting blade 1. As mentioned already, the higher harmonics are negligibly small.

For the highest velocity u_{03}, the complete set of all response functions is shown in Fig. 3, in which the experimental results are compared with the theoretical computations. Except for the constant shift of about 0.5 Hz in the theoretical values, the functions agree for both amplitudes and phases remarkably well. The shift may be interpreted as an overestimate of the fluid forces by the two-dimensional model. Separating the influence of the fluid forces into a real part, which acts as an additional mass, and into an imaginary part, which produces damping, the wider resonance shapes of the theoretical amplitude functions also give the impression of such a higher damping in the theoretical model.

In Fig. 4 the relative amplitudes for all three velocities are plotted versus frequency. The curves are indexed with k for the respective velocity. The phases of $G_{i1}(j\omega)$ are omitted here.

The results characterize the special nature of the experiment. The light-weight blades are heavily influenced by the fluid forces. In all cases, the maximum response frequency is significantly below the eigenfrequency of the blades. The maxima are shifted towards lower values, and they become larger with increasing flow velocity.

Except in one case, the maxima of the amplitudes $\alpha_i(f)$ are much higher than the amplitude of the exciting blade. The amplifying effect is caused by the aerodynamic influence matrix of a plane cascade (Table 4), in which the influence of a blade on its downstream neighbor is much higher than the influence on its upstream neighbor. The decrease for the last blade 8 is obviously caused by its end-position in the row.

In Fig. 5 the two mistuned configurations *II* and *III* are compared with the tuned one at the largest velocity u_{03}. Although only one blade is mistuned, the maximum amplitudes of all blades decrease with increasing mistuning. This effect leads to the obvious conclusion that mistuning is a very efficient tool for the reduction of undesired excitations. Of course, the very precise tuning of all blades emphasizes the effect in this experiment. Further investigations are necessary for a general proof.

Modal Decomposition (Case 1)

The final destination of the frequency response measurements is their decomposition into a set of modal parameters (i.e. eigenvectors, eigenvalues) forming the solution described in Eq. (2). Vice versa, eigenvectors and eigenvalues may be used to reconstruct the original response functions $G_{i1}(j\omega)$. The decomposition is a sophisticated fitting process designed by Lembregts (1988), in which a least-square method is used to minimize the error between measured and reconstructed response functions $G_{i1}(j\omega)_{\text{calc}}$. These synthesized functions

$$G_{i1}(j\omega)_{\text{calc}} = \sum_{k=1}^{k=N} \left[\frac{r_{i1k}}{j\omega - \lambda_k} + \frac{\bar{r}_{i1k}}{j\omega - \bar{\lambda}_k} \right] \qquad (15)$$

should agree with the original $G_{i1}(j\omega)$. The bars in the second term denote the complex conjugate values. This test leads to very satisfying reconstructions in all of the cases considered here. Amplitudes and phases of Eq. (15) agree with measured values in Figs. 3 and 4. The variables r_{i1k} are the components of the eigenvectors $c_k\phi_k$. The data in Fig. 6 together with those in Table 6 enter in Eq. (15). Relative damping is introduced as the measure for damping:

$$D_k = \delta_k/\omega_k. \qquad (16)$$

Finding all of the expected modes—a complete set of eigen-

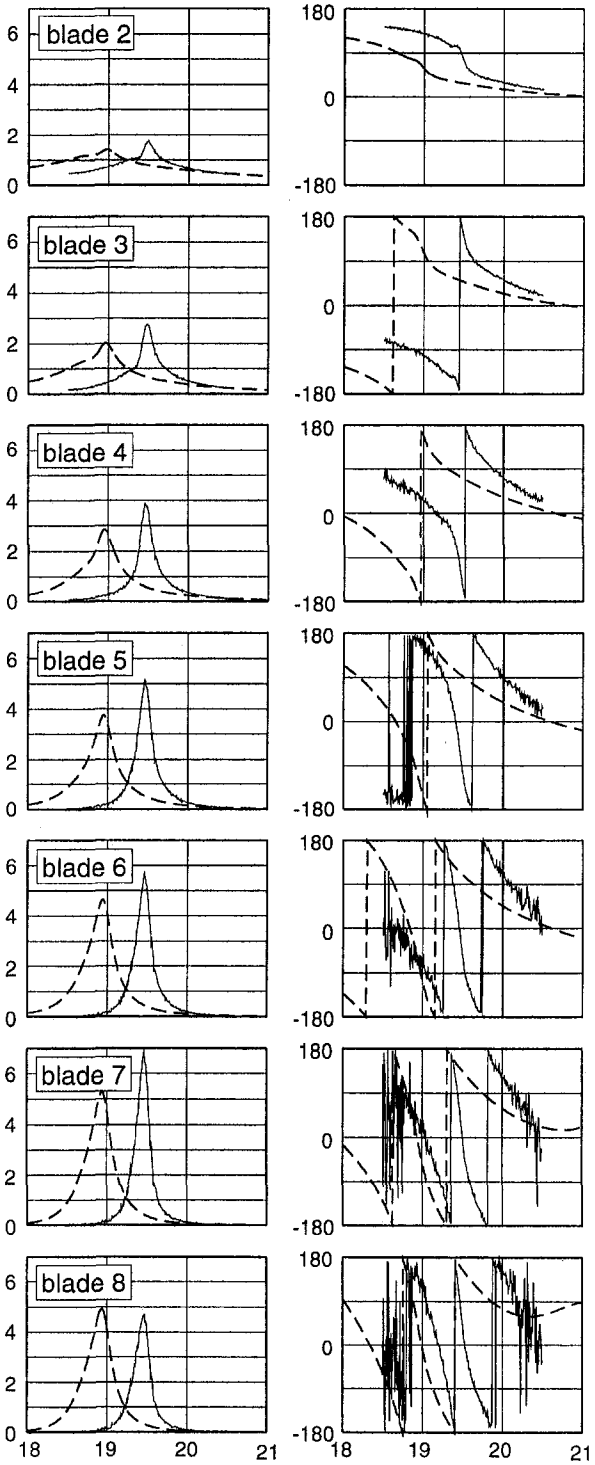

Fig. 3 Amplitudes α_i/α_0 (left) and phases γ_i (right) of frequency response functions versus f[Hz] for "Config. I;" experiment (——) and theory (– – –)

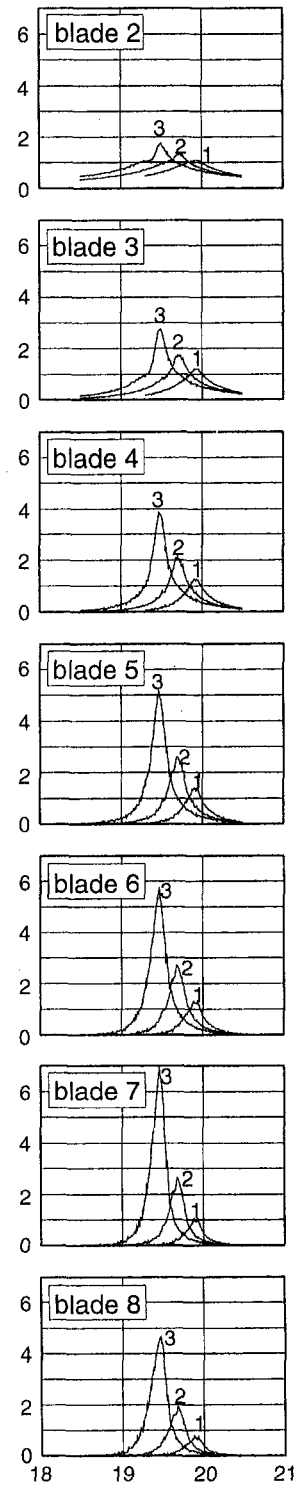

Fig. 4 Amplitudes α_i/α_0 of frequency response functions versus f [Hz], "Config. I"

vectors and eigenvalues—in an aeroelastic configuration is a general problem in itself. When the experiment was planned and set up, it was not clear at that time whether or not additional measures would be required to excite all seven modes.

One obvious reason for the success of this experiment is the position of the exciting blade located upstream of all the other blades. Its aerodynamic influence is most effective in this location. In the opposite position, i.e., situated downstream of blade 8, the same excitation has much less influence. The aerodynamic coefficients in Table 4 show this effect very clearly in the upper (upstream) and lower (downstream) elements along the diagonal.

The other reason is found in the frequency resolution. The extremely small steps of approximately 1/100 Hz at a base frequency of about 20 Hz are needed for proper decomposition. Table 6 shows the main results for "Config. I" at u_{03}. All seven eigenfrequencies range in a frequency band smaller than 1 Hz. It is worthwhile to note that the dying-out transients do not allow such a fine resolution.

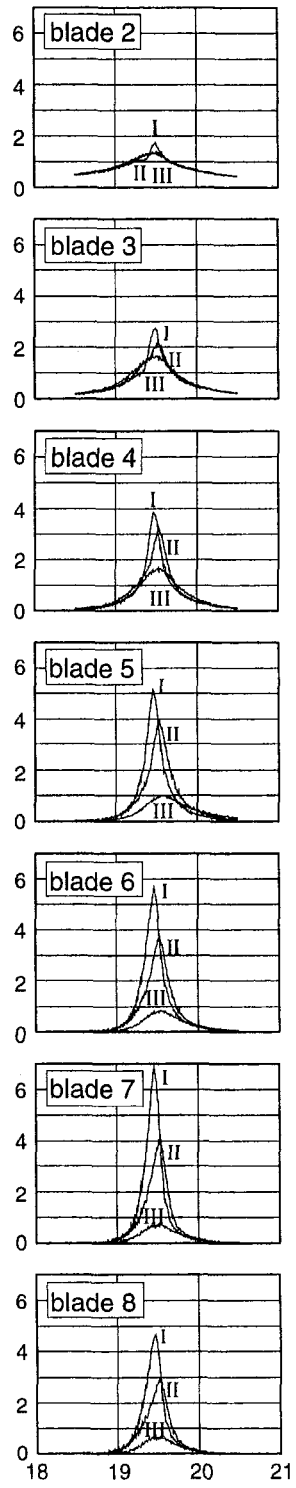

Fig. 5 Amplitudes α_i/α_0 of frequency response functions versus f [Hz], "Config. I, II, and III"

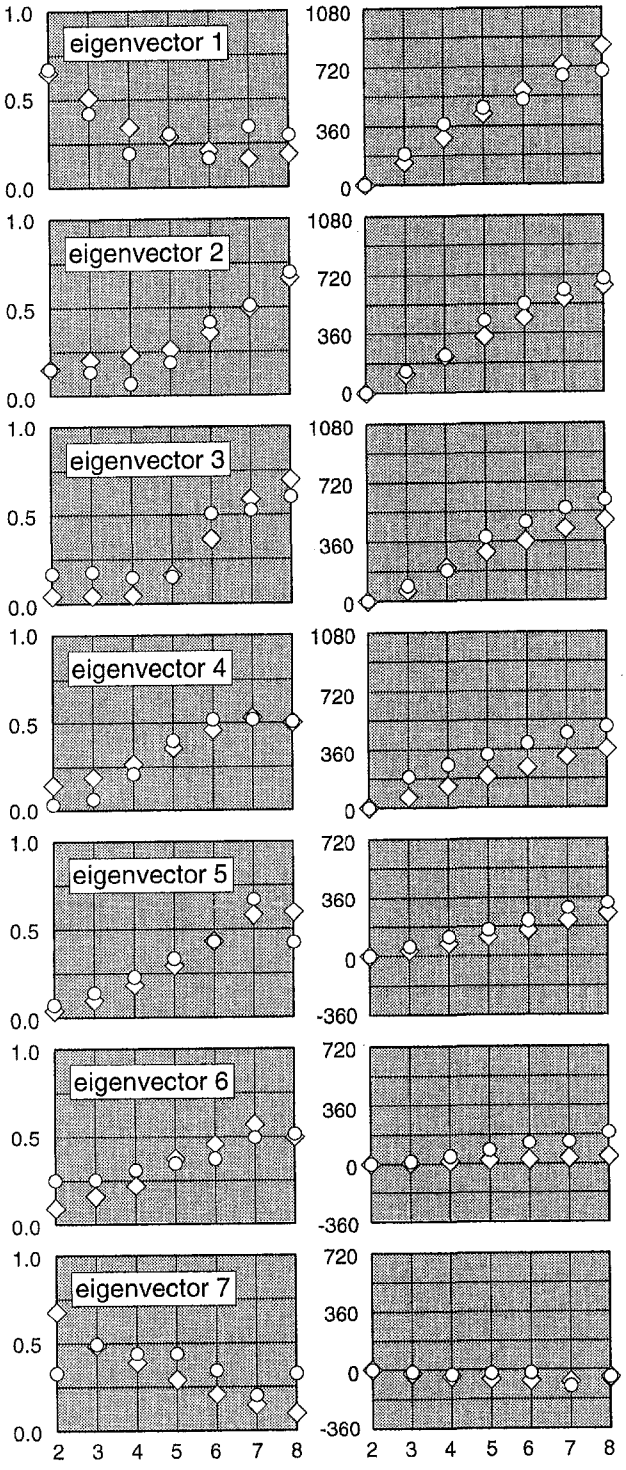

Fig. 6 "Config. I" at u_{03}: experimental (○) and theoretical (◇) amplitudes $|\phi_k|$ [−] (left column) and phases (deg) (right column) of normalized eigenvectors ϕ_k versus blade number i

As already mentioned above, the coefficients r_{i1k} imply the full information for the eigenvectors. Instead of the normal mathematical procedure of normalizing the vectors ϕ_k and calculating the c_k, a slightly different method by computing the modal participation factors a_k is chosen to measure the degree of excitation. Their definition is given by

$$a_k = \frac{\sum_i |r_{i1k}|}{\sum_k \sum_i |r_{i1k}|}. \qquad (17)$$

Table 6 "Config. I" at u_{03}: characteristic model values

Vector k	f_k [Hz]	D_k [%]	a_k [%]
1	18.90	3.07	11.1
2	19.14	0.75	6.9
3	19.33	0.20	1.6
4	19.41	0.42	28.2
5	19.48	0.25	18.6
6	19.54	0.62	22.2
7	19.89	2.54	11.5

Figure 6 shows the measured amplitudes and phases of the normalized complex eigenvectors according to their definition in Eq. (2). The values are compared with the predictions of the theoretical model.

A discussion of the results in Fig. 6 should be preceded by a general comment. Comparing the flutter behavior of an experimental setup with a theoretical model comprises more than merely comparing the flutter velocity, i.e., the dominant eigenvalue. The eigenvectors in the experiment form an overall pattern of dependence on the frequency and, for a cascade, on the interblade phase angle which either basically agrees or disagrees with the theoretical prediction.

In a former comparison between theory and experiment (Hennings and Send, 1996), the authors encountered the strange situation in which most mode shapes agreed quite well, whereas some looked completely different. This obvious discrepancy is now removed.

Different from the computation of the eigenvectors in this earlier paper by solving the eigenvalue Eq. (10), the eigenvectors in Fig. 6 are now obtained from the theoretical response functions in Fig. 3. To get these results, the theoretical response functions are decomposed by exactly the same procedure which is applied to the experimental data.

In particular, the most relevant eigenvector 5 agrees very well with the experimental mode shape. This branch of the solution is the one which becomes the unstable flutter case. So far the present results do not differ from the earlier computations.

Nevertheless, the different results by an eigenvalue analysis and a modal decomposition for one and the same set of theoretical fluid forces leave the question open, to what extent these two procedures differ, and where within the two analyses the results split up into two different branches. The answer, however, exceeds by far the scope of this paper, and, from the authors' point of view, demands a basic and thorough investigation.

Case 2: The Flutter Case

The key result in this paragraph is drawn on the abscissa in Fig. 7(*b*), which is the level of zero damping. By definition, this level is the flutter case. The tuned configuration *I* flutters at the measured flutter velocity

Table 7 Effect of mistuning on flutter velocity

Config.	*I*	*II*	*III*
ε_5 [-]	+0.010	-0.036	-0.096
f_F [Hz]	19.17	19.24	18.88
ω_F^* [-]	0.92	0.91	0.82
u_F [m/s]	19.65	19.99	21.61

$$u_F = (19.6 \pm 0.1) \text{ m/s (experiment)}.$$

The theoretical model predicts flutter of the cascade at

$$u_F = (21.1 \pm 0.3) \text{ m/s (theory)}.$$

Table 7 shows the effect of mistuning, for which the flutter velocity u_F is increased with a diminished mass parameter.

Based on a profile with a sharp trailing edge, the scattering of the theoretical result covers the aerodynamic modeling from low to high density of the computational mesh (panel number). A rounded trailing edge in the manufactured profile causes slight variations in the phases of the theoretical aerodynamic influence matrix. Changes in the phases of the aerodynamic influence matrix (cf. Table 4) of a few degrees easily raise the theoretical value u_F up to 25 m/s. One reason for this sensitivity lies in the smooth approach to the unstable case. Small changes in the moment coefficients cause large effects in the eigenvalue solution. Furthermore, in this comparison one has to keep in mind that the theoretical model does not take into account the effects of the side walls of the windtunnel; it is a purely two-dimensional model.

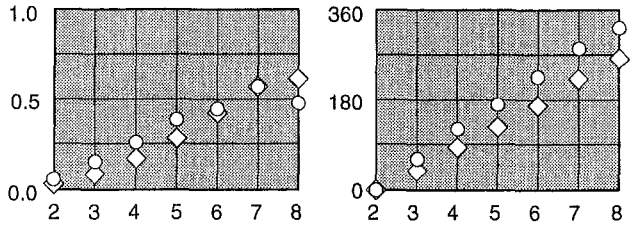

Fig. 8 "Config. I." Mode shape of the flutter case. Experimental (○) and theoretical (◇) amplitudes $|\phi_5|$ [–] (left) and phases (deg) (right) of the normalized eigenvector ϕ_5 versus blade number i

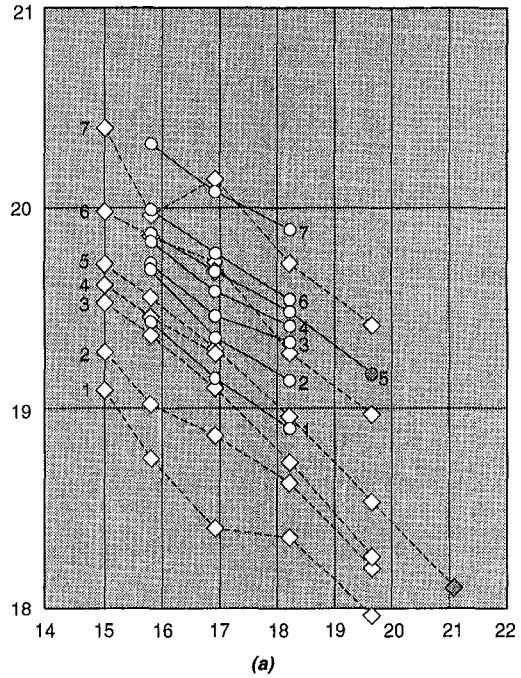

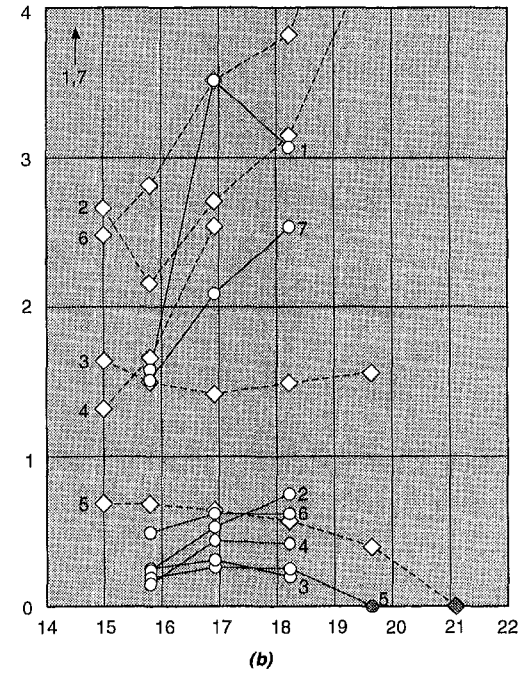

Fig. 7 (a) f_k (Hz) versus u_0 (m/s): experiment (○——○), theory (– – –); (b) D_k (%) versus u_0 (m/s): experiment (○——○), theory (– – –)

The flutter frequency f_F is obtained from Fig. 7(*a*) by finding the respective value for given velocity on the ordinate. The experimental value is 19.2 Hz ($\omega_F^* = 0.92$). The computation yields 18.1 Hz. Though the large scales in Fig. 7 exaggerate the discrepancies between prediction and measurements, the relevant case of eigenvector 5 is fairly well approached.

The decomposition of the response functions into eigenvalues and eigenvectors requires the setting of a frequency range, on which the decomposition is based. Whereas for Fig. 6, the full information in the range (9.7 Hz–29.0 Hz) is used, the theoretical data in Fig. 7 are based on approximately the same interval, which was applied to the experimental data. This interval is about 1 Hz to the left and to the right of the peak in the resonance curve. This is $\frac{1}{10}$ of the above interval. As a consequence of this restriction, the modal participation factor of one of the theoretical eigenvalues drops below a reasonable percentage. Therefore, mode 4 fails to give a result at the highest velocity u_{03}.

Figure 8 shows the shape of the flutter mode which leads back to eigenvector 5 of case 1. Though the build of Fig. 8 looks like the preceding mode shapes, the data are gained in a completely different way. Different from the analysis in the subcritical case 1, the mode is extracted from a time series analysis. The amplitudes are normalized like the values in Fig. 6. The theoretical prediction gives strong support to the diagnosis in case 1. The experimental values hardly permit the prediction, whether eigenvector 3 or 5 leads to the flutter case, whereas the theoretical answer is clearly given.

Finally, the averaged interblade phase angle $\Theta = 43.7$ deg of the theoretical model is reasonably close to the measured value $\Theta = 54.0$ deg.

Concluding Remarks

The main topic of this paper proves the ability for decomposing the measured and calculated response functions of a two-dimensional plane cascade into a complete set of eigenvectors and eigenvalues of the aeroelastic eigenvalue problem. To the authors' knowledge, this goal has been achieved for the first time.

Based on this new experimental technique, measurements in cascades with transonic inflow were planned at the time of this investigation, and they are currently conducted.

Acknowledgments

The authors gratefully acknowledge the work of their colleague Dr. F. Kießling as a helpful consultant during the phase

of designing and assembling the test facility for this experiment. Dr. M. Sinapius prepared the theoretical data to fit into the data acquisition system for the modal decomposition. The authors are grateful for his advice and a very helpful discussion on the results.

References

AGARD, 1987, *Aeroelasticity in Axial-Flow Turbomachines: Vol. 1—Unsteady Turbomachinery Aerodynamics,* M. F. Platzer, and F. O. Carta, eds., AGARDograph 298.

AGARD, 1988, *Aeroelasticity in Axial-Flow Turbomachines: Vol. 2—Structural Dynamics and Aeroelasticity,* M. F. Platzer and F. O. Carta, eds., AGARDograph 298.

Bendiksen, O. O., 1984, "Flutter of Mistuned Turbomachinery Rotors," ASME JOURNAL OF ENGINEERING FOR GAS TURBINES AND POWER, Vol. 106, pp. 25–33.

Bendiksen, O. O., 1993, "Aeroelastic Problems in Turbomachines," *ASME Flight-Vehicle Materials, Structures and Dynamics: Vol. 5—Structural Dynamics and Aeroelasticity,* T. Weisshar, ed., ASME, New York, N.Y., pp. 241–297.

Bloemhof, H., 1988, "Flutter of Blade Rows With Mistuning and Structural Coupling," report, Communication du Laboratoire de Thermique Appliquée et de Turbomachines, EPF Lausanne.

Buffum, D. H., and Fleeter, S., 1990, "Oscillating Cascade Aerodynamics by an Experimental Influence Coefficient Technique," *Journal of Propulsion,* Vol. 6(5), pp. 612–620.

Carta, F. O., 1982, "An Experimental Investigation of Gapwise Periodicity and Unsteady Aerodynamic Response in an Oscillating Cascade: I—Experimental and Theoretical Results," NASA CR-3513, UTRC, East Hartford, CN.

Crawley, E. F., and Hall, K. C., 1985, "Optimization and Mechanisms of Mistuning in Cascades," ASME JOURNAL OF ENGINEERING FOR GAS TURBINES AND POWER, Vol. 107, pp. 418–426.

Crawley, E. F., 1988, "Aeroelastic Formulation for Tuned and Mistuned Rotors," *AGARD—Aeroelasticity in Axial-Flow Turbomachines: Vol. 2—Structural Dynamics and Aeroelasticity,* M. F. Platzer, and F. O. Carta, eds., AGARDograph 298.

Dugundji, J., and Bundas, D. J., 1984, "Flutter and Forced Response of Mistuned Rotors Using Standing Wave Analysis," *AIAA Journal,* Vol. 22 (11), pp. 1652–1661.

Försching, H. W., 1994, "Aeroelastic Stability of Cascades in Turbomachinery," *Prog. Aerospace Sci.,* Vol. 30, pp. 213–266.

Hennings, H., 1994, "Experimentelle Untersuchung des Flatterverhaltens eines ebenen Gitters unter Berücksichtigung gezielter Verstimmung: Messung und Analyse (Experimental Investigation of Flutter Behavior of a Plane Cascade Including Mistuning: Measurement and Analysis)," *German Aerospace Research Establishment (DLR),* Tech. Report IB 232-94J07.

Hennings, H., and Send, W., "Experimental Investigation and Theoretical Prediction of Flutter Behaviour of a Plane Cascade in Low-Speed Flow, ASME Paper 96-GT-417.

Kaza, K. R. V., and Kielb, R. E., 1982, "Flutter and Response of a Mistuned Cascade in Incompressible Flow," *AIAA Journal,* Vol. 20 (8), pp. 1120–1127.

Kaza, K. R. V., and Kielb, R. E., 1984, "Flutter of Turbofan Rotors with Mistuned Blades," *AIAA Journal,* Vol. 22 (11), pp. 1618–1625.

Kaza, K. R. V., Mehmed, O., Williams, M., and Moss, L. A., 1987, "Analytical and Experimental Investigation of Mistuning in Propfan Flutter," ASME Paper 87-0739.

Knauf, W. B., 1985, Experimentelle Untersuchungen zur Ermittlung der aerodynamischen Schaufeldämpfung an einem schwingenden Axialverdichtergitter (Experimental Investigation of the Aerodynamic Blade Damping of an Oscillating Axial Compressor Cascade), Ph.D. thesis, Rhein.-Westf. Techn. Hochschule, Aachen, Germany.

Körbächer, H., and Bölcs, A., 1994, "Experimental Investigation of the Unsteady Behavior of the Compressor Cascade in an Annular Ring Channel," *Proceedings, Symposium on Unsteady Aerodynamics and Aeroelasticity of Turbomachines,* Fukuoka, Japan, pp. 383–400.

Kurkov, A. P., 1982, "Measurements of Self-Excited Rotorblade Vibrations Using Optical Displacements," NASA TM-82953, NASA Lewis Research Center, Cleveland, Ohio.

Lane, F., 1956, "System Mode Shapes in the Flutter of Compressor Blade Rows," *Journal of Aeronautical Sciences,* Vol. 23 (1), pp. 54–66.

Lembregts, F., 1988, Frequency Domain Identification Techniques for Experimental Multiple Input Modal Analysis, Ph.D. thesis, Katholieke Universiteit Leuven, Belgium.

Sachs, W., 1991, Zum Flatterverhalten eines 2-D Verdichtergitters in inkompressibler Strömung (On the Flutter Behavior of a 2D Compressor Cascade in Incompressible Flow), Ph.D. thesis, Rhein.-Westf. Techn. Hochschule, Aachen, Germany.

Send, W., 1984, "Der instationäre Nachlauf hinter schlanken Auftriebskörpern in inkompressibler Strömung (The Unsteady Wake Function of Slender Aerodynamic Bodies in Incompressible Flow," *Zeitschrift für Angewandte Math. und Mech.,* Vol. 64, pp. 7–15.

Send, W., 1995, "Zur Lösung des räumlichen Interferenzproblems in der Instationären Aerodynamik (On the Solution of the Spatial Interference Problem in Unsteady Aerodynamics)," Research Note DLR-FB 95-42. German Aerospace Research Establishment (DLR), Germany.

Stargardter, H., 1988, "Fan Flutter Test," *AGARD—Aeroelasticity in Axial-Flow Turbomachines: Vol. 2—Structural Dynamics and Aeroelasticity,* M. F. Platzer, and F. O. Carta, eds., AGARDograph 298.

Storey, P. A., 1984, "Holographic Vibration Measurement of a Rotating Fluttering Fan," *AIAA Journal,* Vol. 22 (2), pp. 234–241.

Széchényi, E., Cararelli, I., Notin, C., and Girault, J. P., 1984, "A Straight Cascade Wind-tunnel Study of Fan Blade Flutter in Started Supersonic Flow," *Proceedings, Symposium on Unsteady Aerodynamics of Turbomachines and Propellers,* Cambridge, England, pp. 447–458.

Crack Identification in a Cantilever Beam Using Coupled Response Measurements

A. S. Sekhar

P. Balaji Prasad

Indian Institute of Technology,
Department of Mechanical Engineering,
Kharagpur, 721 302, India

Identification of crack location and magnitude through measurement in changes in system characteristics, such as modal measurements, has been studied by various researchers. In the present work based on the new method proposed by Gounaris et al. (1996) for crack detection through coupled response measurements, experiments were carried out on a cracked cantilever beam for eigenfrequencies, bending, and axial response measurements. It has been observed that the rate of change of direct response (bending) is much less at small cracks, while that of the coupled response (axial) changes substantially, which allows for diagnoses of smaller cracks.

1 Introduction

One form of damage that can lead to catastrophic failure if undetected is fatigue cracking of a structure. The dynamic behavior of structures containing cracks is the subject of considerable current interest (Wauer, 1990).

The increasing concern over early crack detection or rotor failures due to the presence of a crack has accelerated the development of nondestructive evaluation techniques based on changes of the modal parameters of the system (Hamidi et al., 1994). Recent publications have proposed the use of one or more of these parameters as a means of identification. As summarized in Hamidi et al. (1994), some researchers (Silva and Gomes, 1990; Rizos et al., 1990; Kim et al., 1991; Pandey et al., 1991; Fox, 1992) have suggested the use of natural frequencies and mode shapes while others (Mannan and Richardson, 1990; Sanman et al., 1991) have recommended the use of frequency response functions. Damage detection can be estimated by comparing the frequency changes obtained from experimental data collected from the structure with sensitivity of the modal parameters obtained from an analytical model of the structure (Silva and Gomes, 1990; Cawley and Adams, 1979). A third group (Dussing and Staker, 1987; Sun and Hardy, 1992) have studied the use of operational deflection forms.

Bamnios and Trochidis (1995) observed that the mechanical impedance changes substantially due to the presence of a crack for case of flexural vibrations. This characteristic can be used as an additional defect information carrier for crack appearance and possible estimation of crack location.

Several investigators have used other techniques for crack detection such as axial impulses (Collins et al., 1991), axial loads (Gomes and Silve, 1992; Krawezuk and Ostachowicz, 1993), periodic or impact force (Iwatsubo and Oks, 1992), and telemetric system (Liao and Gasch, 1992).

Papadoupolos and Dimarogonas (1992), synthesizing their earlier works, presented qualitative and quantitative vibration coupling of a cracked shaft system. They observed coupling apparent in all spectra obtained with a harmonic sweeping excitation thorough the frequency range. This method is very sensitive even for small cracks. The possibility of crack detection through coupling of modes was also demonstrated by Ostachowicz and Krawezuk (1992) for torsional and bending vibration, while Muszynska et al. (1992) used it for coupling of torsional and lateral vibration modes.

Experimental results presented by Papadoupolos and Dimarogonas (1987a, b) confirm the existence of the coupling. Recently, Gounaris et al. (1996) presented a new method of coupled response measurements for the determination of crack depth and location of a transverse surface crack in a beam. Based on this theory, the present study performed some experiments on a cantilever beam of rectangular cross section by introducing a transverse surface crack. The experiments are slightly different from the earlier ones, as the present study aims at finding the rate of change of coupled response with crack.

2 Experimental Setup—Instrumentation

A cantilever beam was selected for the experimental investigations. Its configuration is defined by the following: $L = 39.5$ cm, $B = 3.0$ cm, $h = 0.6$ cm, and crack location = 7.8 cm from the fixed end.

The block diagram of the experimental setup is shown in Fig. 1. The vibrations of the beam were measured by a Triaxial accelerometer placed away from the free end ensuring that the location is not a nodal point. This could measure both axial and bending vibrations. The signals are fed to a vibration meter and the vibration spectra were observed using a real time spectrum analyzer. The signals were generated by a functional generator that were amplified to drive the electromagnetic exciter to excite the beam. The phase changes at resonance were detected using an oscilloscope. One signal from the functional generator and another from the spectrum analyzer were observed on the screen.

With the connections as shown in Fig. 1, the beam was excited by the exciter, and the frequency of excitation was increased in steps from zero. When the excitation frequency matches any one of the natural frequencies of the beam, then a resonance occurs and there will be a rapid change in phase. This phase change corresponds to a rapid rotation of the major axis of the orbit in the oscilloscope. This can be an indication that resonance has occurred.

In addition to the measurements of eigenfrequencies, the bending and axial responses at different frequencies were also recorded. The experiments were repeated for different crack depths that were located at 7.8 cm from the fixed end of the beam. The crack was initiated by a hack-saw blade and depths were measured by using a travelling microscope.

3 Results and Discussion

3.1 Eigenfrequencies. The variation of eigenfrequencies with crack depth are shown in dimensionless form for the first

Contributed by the International Gas Turbine Institute and presented at the ASME Asia '97, Congress and Exhibition September 30–October 2, 1997. Manuscript received by the ASME Headquarters June 19, 1997. Paper No. 97-AA-25. Associate Technical Editor: H. A. Kidd.

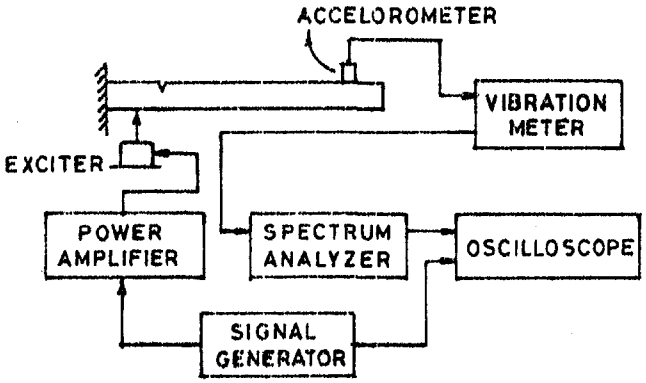

Fig. 1 Block diagram of the experimental set-up

three modes in Figs. 2(*a–c*). It can be observed that all the natural frequencies decrease with an increase in crack depth. The results were compared with results obtained using a FEM (Quin et al., 1990). The experimental results show changes in eigenfrequencies are lower with increase in crack depth. Hence, it will be quite difficult to detect cracks from the changes in eigenfrequencies. Hence, the bending and axial responses were also recorded.

3.2 Response Measurements. Figure 3 shows the variation of bending response amplitude of the beam with excitation frequency for various crack depths. Since the presence of a crack increases the flexibility of the beam, it can be noticed from the Fig. 3 that the bending response increases with increase in crack depth. Also, the shifting of resonance peaks towards lower frequency values can be noticed with an increase in the crack depth. However, the responses are high only for deeper cracks, but the crack has to be identified at a very early state.

3.2.1 Coupled Response Measurements. It has been discussed in Gounaris et al. (1996) that the coupling of different modes due to the presence of crack can be utilized for crack detection. When a cracked beam is excited by a known force or moment there will be response in a direction other than the direction of excitation. In the present study, coupling of bending and axial modes have been used for crack detection.

Figure 4 shows the variation of the axial and bending response with crack depth ($\bar{\alpha}$) for an excitation frequency of 22 Hz. Here, the amplitude ratio is taken with that of cracked to uncracked responses. There exists (possibly due to the beam characteristics) very low axial response, even without a crack. This has been used for the calculation of axial amplitude ratio. The comparison of changes in responses shows clearly that the coupled response (axial) is quite high compared to the bending response even for small crack depths. Thus, the rate of change of axial response is high, as can be seen from the Fig. 4. This fact can be used effectively for crack detection and condition monitoring of beams. The bending response was high for deeper cracks. This is due to the fact that the eigenfrequencies have decreased to values near 22 Hz, which was also the excitation frequency.

The present study confirms qualitatively the findings of Gounaris et al. (1996). However, additional experiments are needed to study the coupling of torsion and bending modes, and also to prepare several nomograms for accurate detection of crack depth and location. However, the rate of change of coupled response could be a very suitable monitoring tool for crack growth. This phenomena of coupled response measurement can also be extended to rotors for crack detection (Papadoupolos and Dimarogonas, 1992).

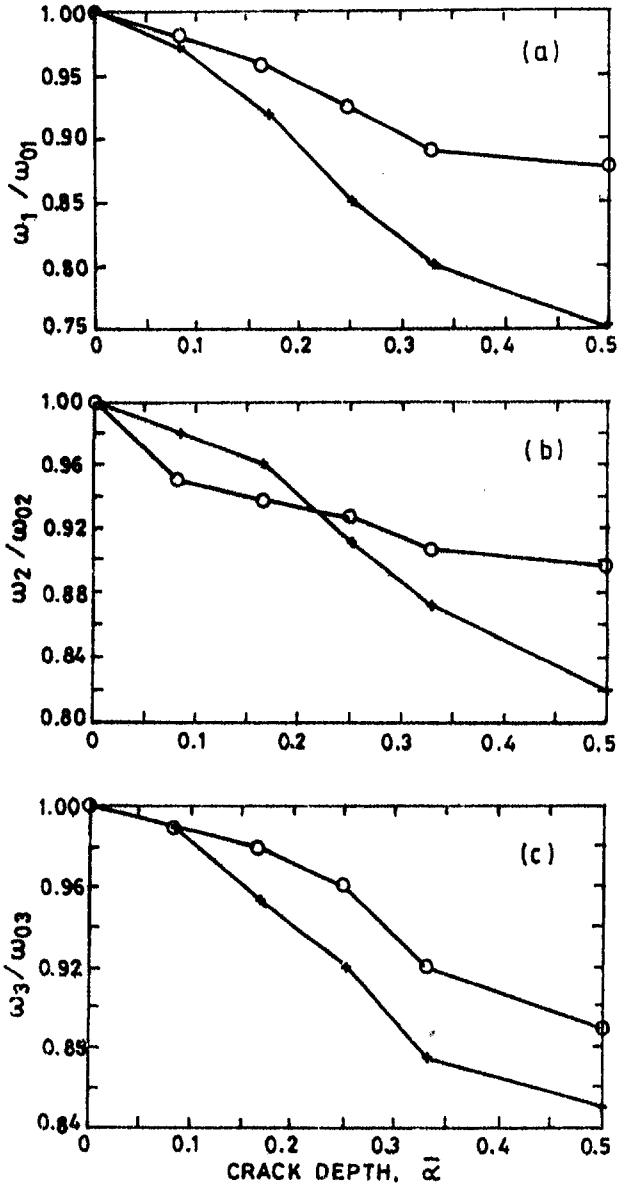

Fig. 2 Variation of eigenfrequencies with crack depth (— + — FEM, — ○ — expt.)

4 Conclusions

Experiments were carried out on a cracked cantilever beam for crack identification purpose. The experiments confirm that the presence of crack in a structural member will cause a local flexibility and will result in a reduction of eigenfrequencies and an increase of response with increase in crack depth. This is well understood in literature.

However, what is less understood is that the rate of change of direct response (bending here) is much less for small cracks while that of the coupled response (axial) changes substantially

Nomenclature

B = beam width
h = beam thickness or depth
L = beam length
α = crack depth
$\bar{\alpha} = \alpha/h$
ω_{oi} = eigenfrequency of uncracked beam for ith mode
ω_i = eigenfrequency of cracked beam for ith mode

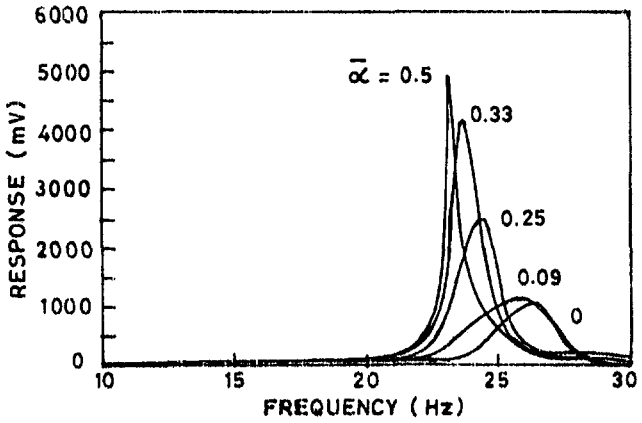

Fig. 3 Variation of bending response with frequency for various crack depths

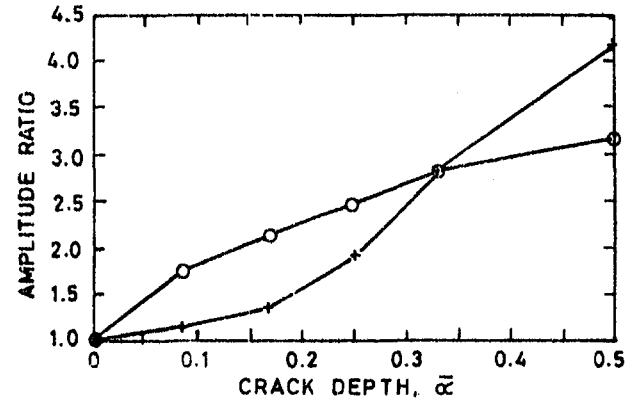

Fig. 4 Variation of response with crack depth (— + — bending, — ○ — axial)

more. This fact can be used for effective identification of small cracks.

References

Bamnios, G., and Trochidis, A., 1995, "Mechanical Impedance of a Cracked Cantilever Beam," *J. Acoust. Soc. Amer.*, Vol. 97, No. 6, pp. 3625–3635.

Cawley, P., and Adams, R. D., 1979, "The Location of Defects in Structures From Measurements of Natural Frequencies," *Journal of Strain Analysis*, Vol. 14, pp. 49–57.

Collins, K. R., Plaut, R. H., and Wauer, J., 1991, "Detection of Cracks in Rotating Timoshenko Shafts Using Axial Impulses," ASME *Journal of Vibration and Acoustics*, Vol. 113, pp. 74–78.

Dussing, O., and Staker, C. H., 1987, "Operational Deflection Shapes: Background, Measurement and Applications," *Proc. of the 5th Int. Modal Analysis Conference*, London, Union College, New York, pp. 1372–1378.

Fox, C. H. J., 1992, "The Location of Defects in Structures: A Comparison of the Use of Natural Frequency and Mode Shape Data," *10th Int. Modal Analysis Conference*, Vol. 1, Spon Union College and SEM, San Diego, CA, pp. 522–528.

Gomes, J. M., and Silve, J. M., 1992, "Dynamic Analysis of Clamped Free Cracked Beams Subjected to Axial Loads," *Proc. 10th Int. Modal Analysis Conference*, Vol. 1, Spon Union College and SEM, San Diego, CA, Feb 3–7, pp. 541–548.

Gounaris, G. D., Papadopoulos, C. A., and Dimarogonas, A. D., 1996, "Crack Identification in Beams by Coupled Response Measurements," *Computers & Structures*, Vol. 58, No. 2, pp. 299–305.

Hamidi, L., Piand, J. B., Pastorel, H., Mansour, W. M., and Massoud, M., 1994, "Modal Parameters for Cracked Rotors—Models and Comparisons," *J. Sound and Vibration*, Vol. 175, pp. 265–278.

Iwatsubo, T., and Oks, A., 1992, "Detection of a Transverse Crack in a Rotor Shaft by Adding External Force," *Proceedings Imech E., Vibrations in Rotating Machinery*, Univ. Bath, United Kingdom, pp. 275–282.

Kim, J. H., Jeon, H. S., and Lee, C. W., 1991, "Applications of the Modal Assurance Criteria for Detecting and Locating Structural Faults," *9th Int. Modal Analysis Conference*, Spon Union College and SEM, Italy, Vol. 11, pp. 536–540.

Krawezuk, M., and Ostachowicz, W. M., 1993, "Transverse Natural Vibrations of a Cracked Beam Loaded With a Constant Axial Force," ASME *Journal of Vibration and Acoustics*, Vol. 115, No. 4, pp. 524–528.

Liao, M., and Gasch, R., 1992, "Crack Detection in Rotating Shafts—An Experimental Study," *Proc. Imech E., Vibrations in Rotating Machinery*, Univ. Bath, United Kingdom, pp. 289–295.

Mannan, M. A., and Richardson, M. H., 1990, "Detection and Location of Structural Cracks Using FRF Measurements," *Proc. 8th Int. Modal Analysis Conference*, Vol. 1, Spon Union College and SEM, Kissimmee, FL, pp. 652–657.

Muszynska, A., Goldman, P., and Bently, D. E., 1992, "Torsional/Lateral Vibration Cross-Coupled Responses Due to Shaft Anistropy: A New Tool in Shaft Crack Detection," *Proc. Imech E., Vibrations in Rotating Machinery*, Univ. Bath, United Kingdom, pp. 257–262.

Ostachowicz, W. M., and Krawezuk, M., 1992, "Coupled Torsional and Bending Vibrations of a Rotor With an Open Crack," *Arch. App. Mech.*, Vol. 62, pp. 191–201.

Pandey, A. K., Biswas, M., and Samman, M. M., 1991, "Damage Detection From Changes in Curvature Mode Shapes," *J. Sound and Vibration*, Vol. 145, pp. 321–332.

Papadopoulos, C. A., Dimarogonas, A. D., 1987a, "Coupled Longitudinal and Bending Vibrations of a Rotating Shaft With an Open Crack," *J. Sound and Vibration*, Vol. 117, pp. 81–93.

Papadopoulos, C. A., and Dimarogonas, A. D., 1987b, "Coupled Longitudinal and Bending Vibrations of a Cracked Shaft," ASME *Journal of Vibrations, Acoustics, Stress and Reliability in Design*, Vol. 110, pp. 1–8.

Papadopoulos, C. A., and Dimarogonas, A. D., 1992, "Coupled Vibration of Cracked Shaft," *ASME Journal of Vibrations and Acoustics*, Vol. 114, pp. 461–467.

Qian, G.-L., Gu, S.-N., and Jiang, J.-S., 1990, "The Dynamic Behaviour and Crack Detection of a Beam With a Crack," *Journal of Sound and Vibration*, Vol. 138, No. 2, pp. 233–243.

Rizos, P. F., Aspragathos, N., and Dimarogonas, A. D., 1990, "Identification of Crack Location and Magnitude in a Cantilever Beam From Vibration Modes," *J. Sound and Vibration*, Vol. 138, pp. 381–388.

Sanman, M. M., Biswas, M., and Pandey, A. K., 1991, "Employing Pattern Recognition for Detecting Cracks in a Bridge Model," *Int. J. Analytical and Experimental Modal Analysis*, Vol. 6, pp. 35–44.

Silva, J. M., and Gomes, A., 1990, "Experimental Dynamic Analysis of Cracked Free-Free Beams," *Exp. Mechanics*, Vol. 30, No. 1, pp. 20–25.

Sun, X. Q., and Hardy, H. R., 1992, "A Study on the Operating Shapes for Nondestructive Evaluation in Geotechnical Engineering," *Proc. 10th Int. Modal Analysis Conference*, Vol. 1, Spon Union College and SEM, San Diego, CA, pp. 1237–1244.

Wauer, J., 1990, "Dynamics of Cracked Rotors: Literature Survey," *ASME Applied Mechanics Reviews*, Vol. 43, pp. 13–17.

A Comparison of Experimental Rotordynamic Coefficients and Leakage Characteristics Between Hole-Pattern Gas Damper Seals and a Honeycomb Seal

Z. Yu

D. W. Childs

Turbomachinery Laboratory,
Texas A&M University,
College Station, TX 77843-3254

Honeycomb annular seals are an attractive design alternative due to their superior static and dynamic performance. However, their implementation in industrial practice has been delayed by the following characteristics: a) manufacturing time can be appreciable, and b) they can seriously damage the shaft if rubbing occurs. To minimize these problems, "hole-pattern" gas damper seals, which are formed by simply drilling holes into an annular smooth seal, were manufactured and tested. The hole-pattern damper seal stator can be made of high-strength plastic materials which are less likely to damage a shaft during rubbing. The experimental results presented demonstrate that, compared to a honeycomb seal, a hole-pattern damper seal with 3.18 mm hole diameters and a high percentage of hole surface has achieved: (a) an average of 12 percent reduction in leakage rate, and (b) considerably higher effective damping, especially under high speeds and low inlet pressure ratio conditions.

Introduction

Annular pressure seals with small clearance are employed in turbomachines such as pumps, compressors, or gas-turbine engines between stationary and rotating elements to limit the leakage of fluid from different pressure stages. However, high pressures and tight clearances within annular seals can produce reaction forces on the rotor that have great impact both on rotordynamic stability and response.

If seal relative motion is small and is about a centered position within an annular seal, the reaction-force model in Eq. (1) applies (Childs, 1993):

$$-\begin{Bmatrix} F_x \\ F_y \end{Bmatrix} = \begin{bmatrix} K & k \\ -k & K \end{bmatrix} \begin{Bmatrix} X \\ Y \end{Bmatrix} + \begin{bmatrix} C & c \\ -c & C \end{bmatrix} \begin{Bmatrix} \dot{X} \\ \dot{Y} \end{Bmatrix} + M \begin{Bmatrix} \ddot{X} \\ \ddot{Y} \end{Bmatrix}. \quad (1)$$

Here, F_x and F_y are the components of reaction forces acting on the rotor; X and Y define the components of the seal-rotor displacements relative to the stator, and the rotordynamic coefficients K, k, C, c, and M are the direct stiffness, cross-coupled stiffness, direct damping, cross-coupled damping, and direct added mass coefficients, respectively.

Figure 1 illustrates the rotordynamic force components acting on a rotor that is whirling synchronously in the direction of rotation at a constant angular frequency ω and amplitude A. In this figure, $(K\text{-}M\omega^2 + c\omega)A$ is the radial force component that acts toward the center of the rotor. This force component is defined by the direct stiffness K, the added mass M, and the cross-coupled damping c. A sufficient change of K can cause a shift of a critical speed. However, the radial force component has generally been considered to be small for gas seals and typically has a negligible influence on rotordynamics.

Returning to Fig. 1, $(k - C\omega)A$ is the tangential force that changes with the cross-coupled stiffness k and direct damping C. This component of force is most responsible for the impact of seals on rotordynamic response and rotordynamic stability. To take both direct damping C and cross-coupled stiffness k into consideration, effective damping $C_{\text{eff}} = C(1 - k/C\omega)$ is a useful parameter to evaluate and compare rotordynamic performance for seals.

Realizing the importance of seal forces, various types of seals have been designed to achieve better rotordynamic and leakage control performance. From a rotordynamic view point, honeycomb seals have shown very promising characteristics. They provide considerably higher effective direct damping, lower cross-coupled stiffness, and better leakage control than see-through labyrinth seals. In practice, honeycomb seals have been used to eliminate a stability problem in the high pressure oxygen turbopump (HPOTP) of the space shuttle main engine (SSME) (Scharrer, 1989). In centrifugal compressors, honeycomb seals have been used to eliminate unwanted vibrations (Zeidan et al., 1993; Sorokes et al., 1994). However, honeycomb seals can have the following disadvantages:

1 On occasions, their comparatively long manufacturing time have prevented their use in retrofits.
2 They can seriously damage the shaft if rubbing occurs.

As an alternative to honeycomb seals, hole-pattern damper seals are considered in this study. Figure 2 illustrates geometric differences between honeycomb and hole-pattern damper seals. Compared to a honeycomb seal, the hole-pattern damper seal has a much simpler surface configuration, which is formed by simply drilling holes into an annular smooth seal stator.

The "damper seal" concept for liquid seals was originated by Von Pragenau (1982), who reasoned that a rough-stator/smooth-rotor combination would yield a lower, asymptotic, circumferential velocity than a smooth rotor (thus yielding lower cross-coupled stiffness values). Childs and Kim (1986b) con-

Contributed by the International Gas Turbine Institute and presented at the International Gas Turbine and Aeroengine Congress and Exhibition, Orlando, FL, June 2–5, 1997. Manuscript received by the ASME Headquarters February 3, 1997. Paper No. 97-GT-9. Associate Technical Editor: H. A. Kidd.

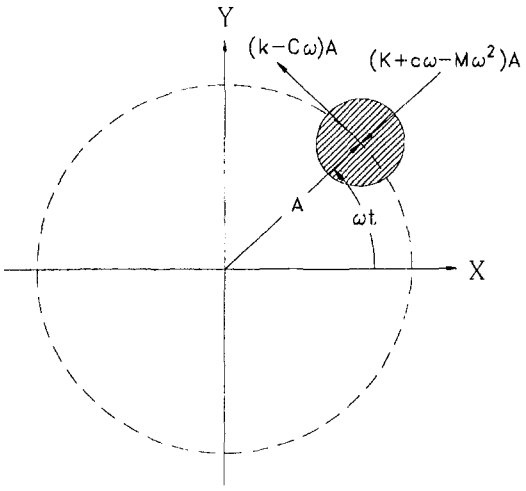

Fig. 1 Forces on a whirling rotor

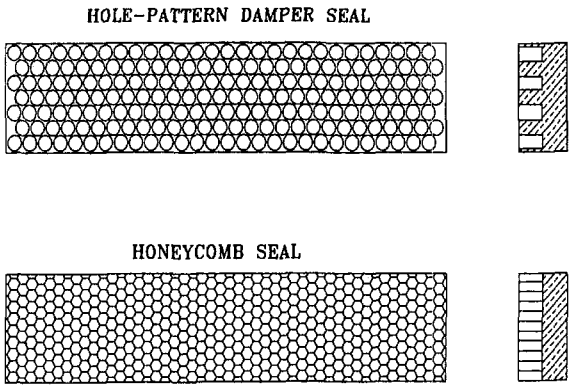

Fig. 2 The surface configuration for hole-pattern damper and honeycomb seal

ducted tests for nine hole-pattern damper liquid seals with various percentage of surface areas in holes. Their tests used roughened stators and a smooth rotor, and showed that an optimum configuration of hole-pattern takes up about 34 percent coverage of holes, and yielded a 37 percent increase of direct damping, while reducing leakage by 46 percent as compared to a smooth seal. A subsequent series of tests were done by Childs et al. (1990) at smaller clearances, and showed approximately the same damping performance for hole-pattern damper seals and smooth seals at the same clearances, about 20 percent lower stiffness values, and one third lower leakage. However, hole-pattern damper gas seals have not been tested before.

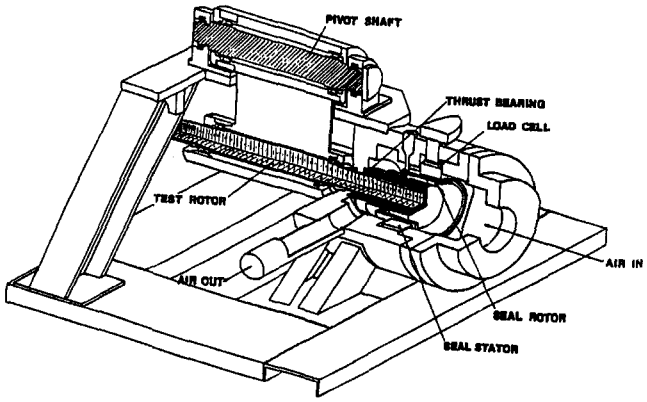

Fig. 3 Test apparatus

Test Apparatus and Experimental Setup

The test apparatus utilizes air as the test fluid and consists of a rotor shaft that is suspended (pendulum fashion) from an upper, rigidly mounted, pivot shaft, as illustrated in Fig. 3. This configuration allows horizontal static and dynamic motion of the rotor, while an eccentric cam within the pivot shaft provides

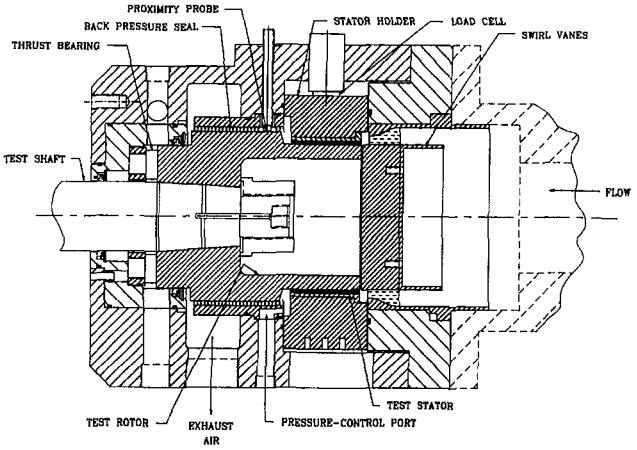

Fig. 4 Cross section of test rig

Nomenclature

A = whirl amplitude (mm)
A_X, A_Y = Fourier transformed absolute acceleration of stator housing (m/s^2)
C, c = direct and cross-coupled damping coefficients (N-s/m)
C_r = seal clearance (mm)
d = hole-pattern damper seal hole diameter (mm)
D = diameter of seal (mm)
D_X, D_Y = Fourier transformed motion of the stator relative to the rotor (m)
f_{SX}, f_{SY} = measured stator housing reaction forces (N)
F_{SX}, F_{SY} = Fourier transformed components of seal reaction forces (N)
H_{XX}, H_{XY} = direct and cross-coupled impedance functions (N/m)
K, k = direct and cross-coupled stiffness (N/m)
M, m = direct and cross-coupled inertia (kg)
$\dot{m}$ = mass flow rate (kg/s)
M_S = mass of stator housing (kg)
P_b = back pressure (bar)
P_r = inlet (reservoir) pressure (bar)
P_{ra} = P_b/P_r, absolute pressure ratio
$\dot{Q}$ = volumetric flow rate (m^3/s)
R = rotor radius (m)
u_0 = $U_{\Theta 0}/R\omega$, inlet circumferential velocity ratio
$U_{\Theta 0}$ = inlet circumferential velocity (m/s)
X, Y = displacement of the stator relative to the rotor (m)
$\ddot{X}_S$, $\ddot{Y}_S$ = absolute acceleration of stator housing (m/s^2)
γ = area fraction factor introduced in Eq. (7)
ω = rotor angular velocity (rad/s)
Ω = rotor precession frequency (rad/s)

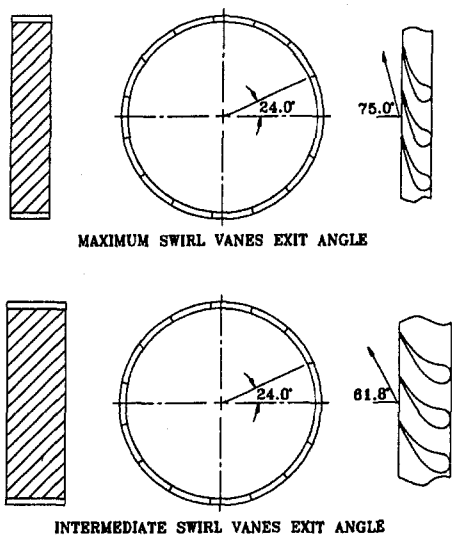

Fig. 5 Swirl vanes exit angles

Table 1 Test points

Rotor Speed ω (rpm)	Inlet Pressure P_r (bar)	Pressure Ratio P_{ra} (-)	Inlet Preswirl in the Direction of Rotor Rotation
4680	7.9	0.65	None
8640	13.1	0.45	Intermediate
16500	18.3	0.3	High

static vertical position capability for the rotor (Childs et al., 1986a; Pelletti, 1990).

The rotor is excited horizontally by a hydraulic shaker head that acts on the rotor shaft housing. The excitation frequency range is from 40 to 70 Hz. The rotor excitation produces seal reaction forces that are measured by three load cells which support the seal stator in a trihedral fashion. Two accelerometers mounted in the *X* and *Y*-directions are used to subtract the forces on the stator housing due to external residual vibrations.

As Fig. 4 illustrates, high pressure air enters the test section from one side of the rig and passes a pre-swirl guide vane before entering the test seal. Inlet pressure is manually regulated by a control valve located upstream of the test section. The seal pressure ratio cross the seal, defined as absolute exit pressure divided by absolute inlet pressure, is controlled by a back-

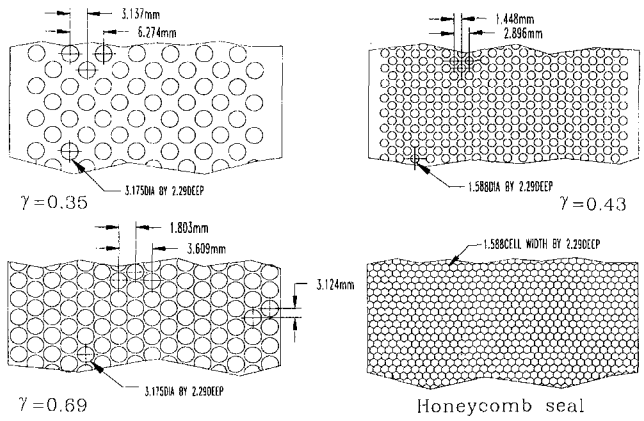

Fig. 6 Surface geometry for test seals

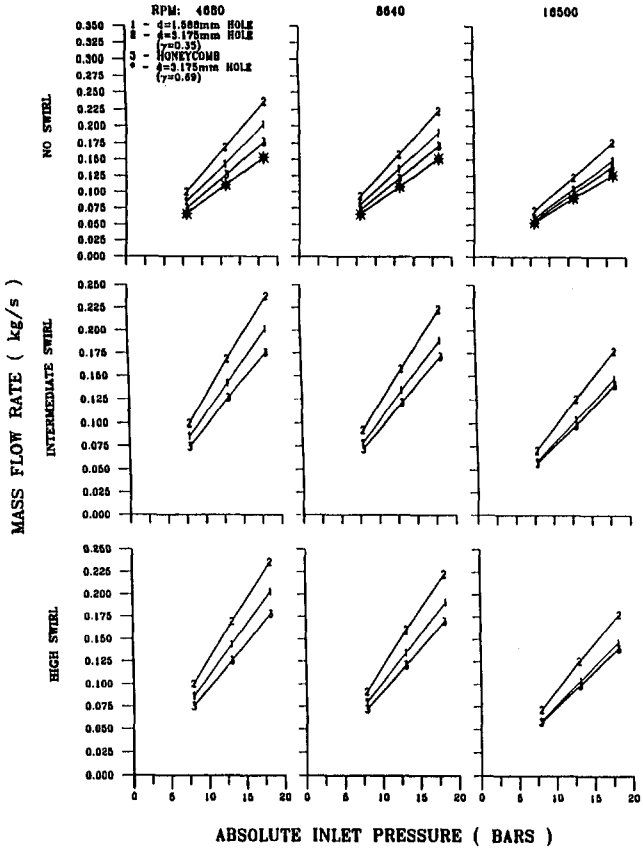

Fig. 7 A comparison of mass flow rate versus inlet pressure for all seals at P_{ra} = 0.45

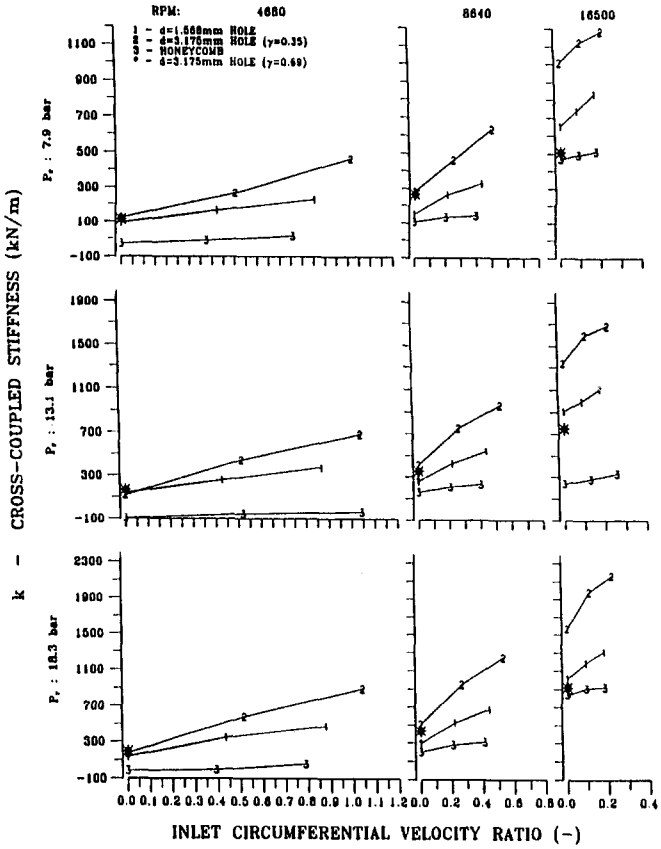

Fig. 8 A comparison of cross-coupled stiffness versus inlet circumferential velocity ratio for all seals at P_{ra} = 0.45

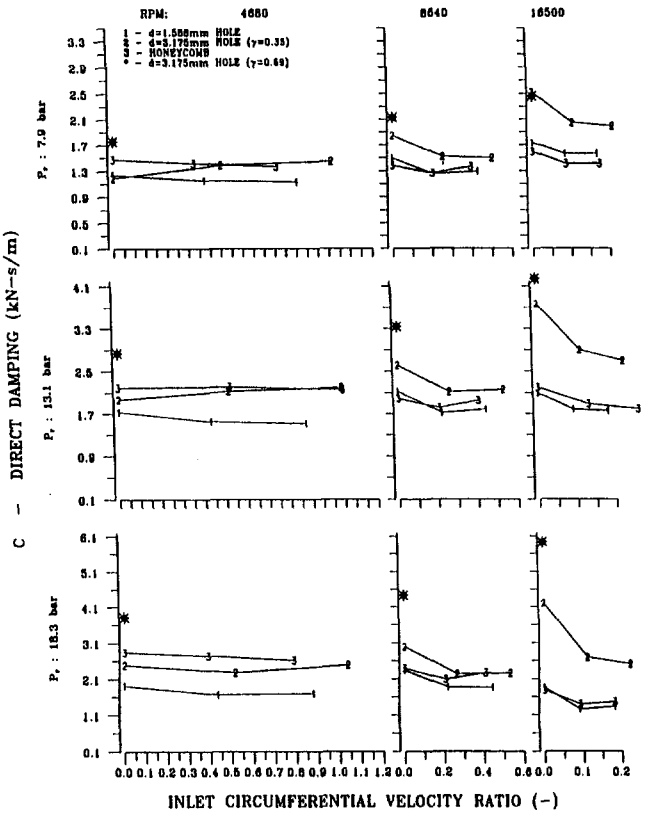

Fig. 9 A comparison of direct damping versus inlet circumferential velocity ratio for all seals at P_{ra} = 0.45

pressure seal with inlet and exhaust ports. Air is injected (or withdrawn) through the ports to decrease (or increase) the pressure drop across the seal.

The test apparatus yields three inlet swirl velocities. Inlet swirl is controlled by the two swirl vanes illustrated in Fig. 5, plus a set of straight vanes. The calculation of inlet circumferential velocity is initiated by dividing the volumetric flow rate $\dot{Q}$ (measured with a turbine flow meter) by the area that is normal to the exit vane angles.

Rotordynamic-Coefficient Identification. The equation of motion for the seal stator housing is

$$\begin{Bmatrix} f_{SX} - M_S\ddot{X}_S \\ f_{SY} - M_S\ddot{Y}_S \end{Bmatrix} = \begin{bmatrix} K & k \\ -k & K \end{bmatrix}\begin{Bmatrix} X \\ Y \end{Bmatrix} + \begin{bmatrix} C & c \\ -c & C \end{bmatrix}\begin{Bmatrix} \dot{X} \\ \dot{Y} \end{Bmatrix} + M\begin{Bmatrix} \dot{X} \\ \dot{Y} \end{Bmatrix}, \quad (2)$$

where M_S is the stator housing mass, and f_{SX} and f_{SY} are the measured reaction forces on the stator housing. The acceleration components of the housing, measured by the accelerometers, are denoted by $\ddot{X}_S$ and $\ddot{Y}_S$.

An analog circuit is used to generate $f_{SX} - M_S\ddot{X}_S$ and $f_{SY} - M_S\ddot{Y}_S$ from measured reaction-forces and acceleration components. The Fourier transform of Eq. (2) is represented by

$$\begin{Bmatrix} F_{SX} - M_SA_X \\ F_{SY} - M_SA_Y \end{Bmatrix} = \begin{bmatrix} H_{XX} & H_{XY} \\ -H_{XY} & H_{XX} \end{bmatrix}\begin{Bmatrix} D_X \\ D_Y \end{Bmatrix}, \quad (3)$$

where

$$H_{XX} = (K - \omega^2 M) + j\omega C$$
$$H_{XY} = k + j\omega c. \quad (4)$$

Rearranging Eq. (3) produces the following relation:

$$\begin{Bmatrix} F_{SX} - M_SA_X \\ F_{SY} - M_SA_Y \end{Bmatrix} = \begin{bmatrix} D_X & D_Y \\ D_Y & -D_X \end{bmatrix}\begin{Bmatrix} H_{XX} \\ H_{XY} \end{Bmatrix} \quad (5)$$

from which H_{XX} and H_{XY} are solved and yield the following impedance relations:

$$H_{XX} = \frac{(F_{SX} - M_SA_X)D_X - (F_{SY} - M_SA_Y)D_Y}{D_X^2 + D_Y^2}$$
$$H_{XY} = \frac{(F_{SX} - M_SA_X)D_Y - (F_{SY} - M_SA_Y)D_X}{D_X^2 + D_Y^2}. \quad (6)$$

Equation (4) shows that the real components of the above impedances, H_{XX} and H_{XY}, contain the stiffness coefficients, while the imaginary component contains the damping coefficients. Thus, the rotordynamic coefficients are calculated via a least-squares curve fit of the real and imaginary components of H_{XX} and H_{XY}.

Test Parameters. The test rig can be used to study the effects of the following six independent test parameters on the rotordynamic and leakage characteristics of a variety of seals:

1 rotor speed
2 seal inlet pressure
3 pressure ratio across the seal
4 inlet fluid rotation
5 seal clearance
6 seal geometry

Test points are measured by varying the first 4 parameters above over the values specified in Table 1. The seal clearance can be controlled by changing the rotors. In this study, each seal has been tested at two clearances 0.30 mm and 0.23 mm.

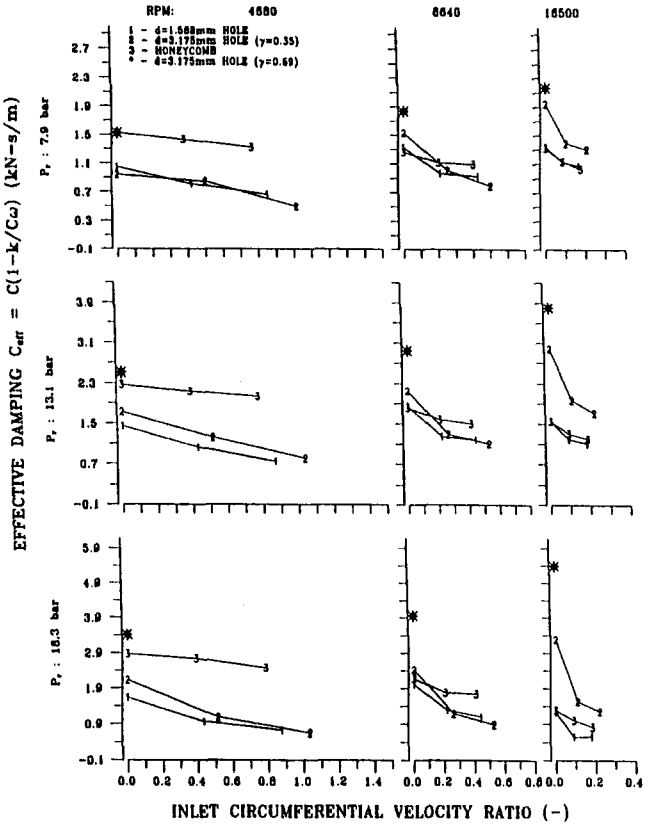

Fig. 10 A comparison of effective damping versus inlet circumferential velocity ratio for all seals at P_{ra} = 0.45

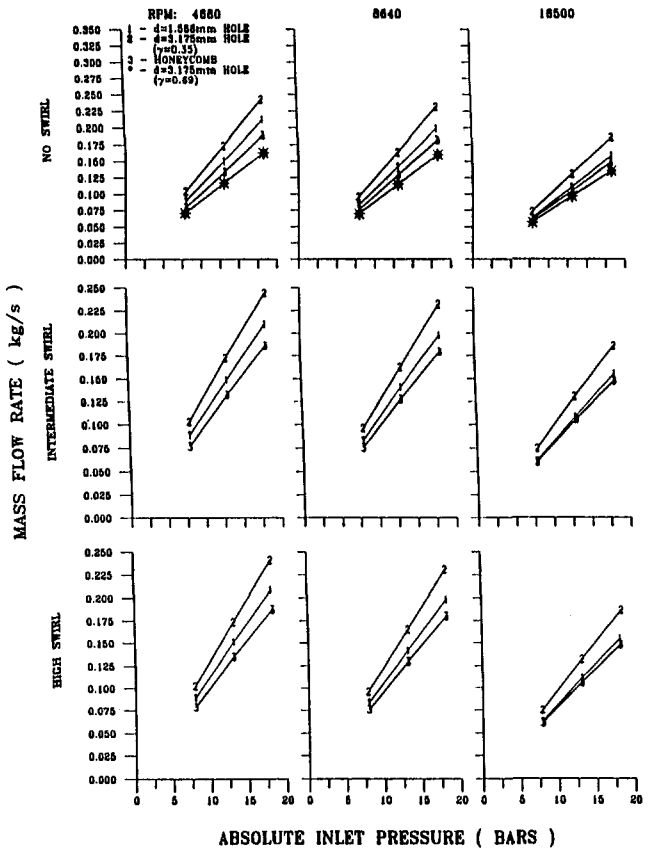

Fig. 11 A comparison of mass flow rate versus inlet pressure for all seals at $P_{ra} = 0.30$

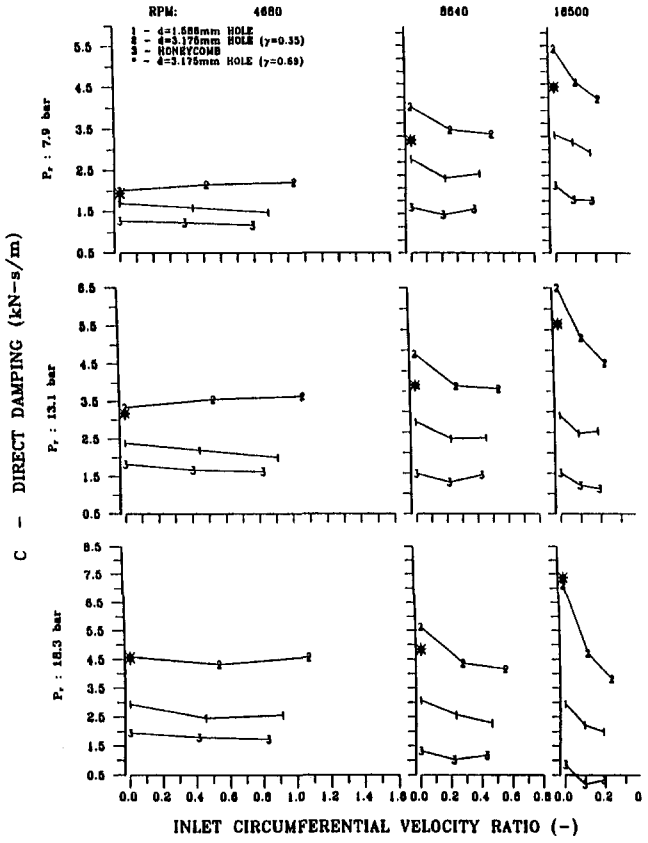

Fig. 13 A comparison of direct damping versus inlet circumferential velocity for all seals at $P_{ra} = 0.30$

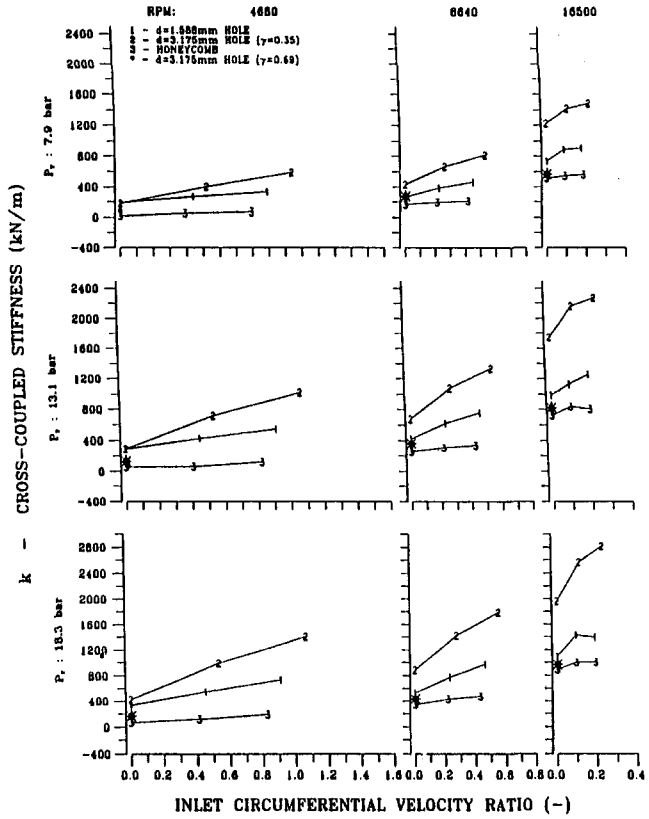

Fig. 12 A comparison of cross-coupled stiffness versus inlet circumferential velocity ratio for all seals at $P_{ra} = 0.30$

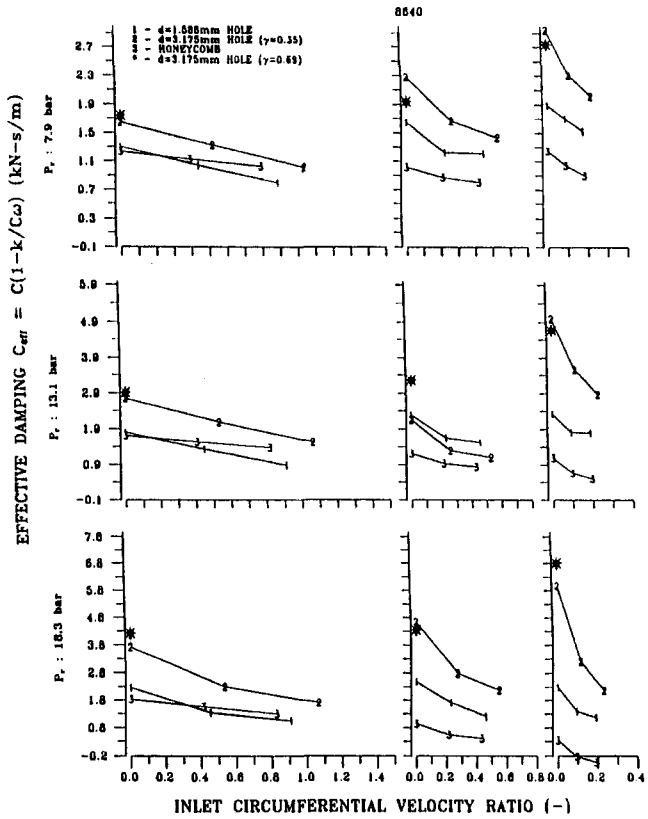

Fig. 14 A comparison of effective damping versus inlet circumferential velocity for all seals at $P_{ra} = 0.30$

Seal Geometries. Three hole-pattern damper seals with different surface configurations and a honeycomb seal were tested. Hole-pattern damper seals were designed using liquid hole-pattern seals experience (Childs et al., 1986b) as reference. All seals have the same diameters (152 mm), lengths (50.8 mm), and hole (or cell) depths (2.29 mm). The surface geometries of hole-pattern damper seals are shown in Fig. 6, where γ is the hole-area fraction, defined as

$$\gamma = \frac{\text{Hole Surface Area}}{\text{Seal Surface Area}} \tag{7}$$

Test Results and Relative Performance

Three hole-pattern damper seals and a honeycomb seal were tested under the same test condition (Table 1) with two radial clearances (0.30 mm and 0.23 mm). Unfortunately, due to an equipment failure that damaged the seal, only one nonswirl condition at one radial clearance (C_r = 0.23 mm) test was completed for the d = 3.175 mm (γ = 0.69) hole-pattern damper seal. Hence, for this seal, the graphical test results are presented by single point. Seals were compared based on leakage-control performance, cross-coupled stiffness k, direct damping C, and effective damping C_{eff}.

As noted, comparisons can not be made between the d = 3.175 mm (γ = 0.69) hole-pattern damper seal and the honeycomb seal at larger clearance since the tests were not completed. For the other two hole-pattern seals, test results are generally poorer than for the honeycomb seal. Therefore, test results at this clearance are not presented.

Figures 7 through 14 illustrate mass flow rate, K, C, and C_{eff} for three hole-pattern damper seals and a honeycomb seal, with pressure ratio P_{ra} = 0.45 and 0.3. An examination of these figures supports the following conclusions:

1 The d = 3.175 mm (γ = 0.69) hole-pattern damper seal has better leakage control performance. There is an average of 12 percent leakage rate reduction when compared to the honeycomb seal. However, the leakage rate for the other two hole-pattern damper seals are normally higher than the honeycomb seal.
2 The magnitudes of cross-coupled stiffness and their sensitivities to increasing inlet circumferential velocity are higher for all hole-pattern damper seals than for the honeycomb seal under all test conditions. Cross-coupled stiffness for all hole-pattern damper seals increases with increasing running speed, absolute inlet pressure, and decreasing inlet pressure ratio.
3 Direct damping for the d = 3.175 mm (γ = 0.69) hole-pattern damper seal is considerably higher than the honeycomb seal under most test conditions. At P_{ra} = 0.30, all hole-pattern damper seals have higher C values than the honeycomb seal. Direct damping for hole-pattern damper seals increases with increasing inlet pressure and decreasing pressure ratio.
4 The effective damping values for the d = 3.175 mm (γ = 0.69) hole-pattern damper seal are generally higher than the honeycomb seal. The magnitudes of effective damping for hole-pattern damper seals increase with increasing inlet pressure, increasing running speed, and decreasing pressure ratio. Note that the effective damping for the d = 3.175 mm (γ = 0.69) hole-pattern damper seal tends to increase with increasing running speed, while those for the honeycomb seal decrease.

Conclusion

Test results have been obtained for three hole-pattern damper seals configuration. According to these results and their comparison with honeycomb seal, the following conclusions hold:

a All hole-pattern seal configurations generally provide higher effective damping than the honeycomb seals.
b At the highest supply pressure and lower pressure ratio (highest pressure drop) the d = 3.175 mm (γ = 0.69) hole-pattern damper seal leaked 12 percent less than the honeycomb seal, and had markedly higher effective damping values. Unforturnately, this seal was damaged during testing and only zero preswirl data are available.
c Based on test results and comparison, hole-pattern damper seals can be attractive alternatives to honeycomb seal.

References

Childs, D. W., Nelson, C. C., Nicks, C., Scharrer, J., Elrod, D., and Hole, K., 1986a, "Theory Versus Experiment for the Rotordynamic Coefficients of Annular Gas Seals: Part 1—Test Facility and Apparatus," *ASME Journal of Tribology*, Vol. 108, pp. 426–432.

Childs, D. W., Kim, C. H., 1986b, "Test Results For Round-Hole-Pattern Damper Seals: Optimum Configurations and Dimensions for Maximum Net Damping," *ASME Journal of Tribology*, Vol. 108, pp. 605–611.

Childs, D. W., Nolan, S. A., and Kilgore, J. J., 1990, "Additional Test Results for Round-Hole-Pattern Damper Seals: Leakage, Friction Factors, and Rotordynamic Force Coefficients," *ASME Journal of Tribology*, Vol. 112, pp. 365–371.

Childs, D. W., 1993, *Turbomachinery Rotordynamics: Phenomena, Modeling, and Analysis*, John Wiley & Sons, Inc., New York, NY, p. 228.

Pelletti, J. M., 1990, "A Comparison of Experiment and Theoretical Predictions for the Rotordynamic Coefficients of Short ($L/D = \frac{1}{6}$) Labyrinth Seals," Master's thesis, Texas A&M University, College Station, TX.

Scharrer, J., 1989, discussion of the paper, "Annular Honeycomb Seals: Test Results for Leakage and Rotordynamic Coefficients; Comparisons to Labyrinth and Smooth Configurations," by Childs, D. W., ASME JOURNAL OF ENGINEERING FOR GAS TURBINES AND POWER, Vol. 106, pp. 927–934.

Sorokes, J., Kuzdzal, M., Sandberg, M., and Colby, G., 1994, "Recent Experiences in Full Load Full Pressure Shop Testing of a High Pressure Gas Injection Centrifugal Compressor," *Proceedings of the Twenty-Third Turbomachinery Symposium*, The Turbomachinery Laboratory, Texas A&M University, College Station, Texas, pp. 3–17.

Von Pragenau, G. L., 1982, "Damping Seals for Turbomachinery," NASA Technical Paper 1987.

Zeidan, F., Perez, R., and Stephenson, E., 1993, "The Use of Honeycomb Seals in Stabilizing Two Centrifugal Compressors," *Proceedings of the Twenty-Second Turbomachinery Symposium*, The Turbomachinery Laboratory, Texas A&M University System, College Station, Texas, pp. 3–15.

A Survey of Blade Tip-Timing Measurement Techniques for Turbomachinery Vibration

S. Heath
Electronics and Measurement Technology Department,
Rolls Royce plc,
P.O. Box 31,
Derby DE24 8BJ, United Kingdom

M. Imregun
Imperial College,
Mechanical Engineering Department,
Exhibition Rd.,
London SW 7 2BX, United Kingdom

This paper aims at providing a comparative survey of current analysis methods for the interpretation of vibration data measured at turbomachinery rotor blade tips using optical laser probes. The methods are classified by the form of the vibration that they attempt to identify, namely, asynchronous and synchronous with respect to rotor speed. The performance of the various techniques is investigated by using both actual assembly measurements and simulated response data. In the latter case, synchronous vibration data are obtained via a multidegree-of-freedom numerical simulator that includes the structural and geometric properties of the bladed-disk assembly, the external forcing terms, and the characteristics of the optical probe. When using experimental data, the results of the tip timing analysis are compared to those obtained from standard strain-gauge tests and the relative merits of the two approaches are discussed with emphasis on the effects of blade mistuning. Existing industry standard, tip-timing analysis techniques are found to exhibit a number of inherent limitations and suggestions were made to address these deficiencies. A detailed tip-timing case study for a steam turbine rotor is presented in some detail, and other potential application areas are explored. Of particular note is the introduction of a new indirect analysis method for identifying the characteristics of synchronous vibration modes using measurements from two probes. Finally, new avenues for future analysis methods and further developments in tip-timing systems are also discussed.

1 Introduction

Vibration measurements on turbomachinery blades form an essential part of the overall engine design process. Contacting vibration measurement techniques, such as strain gauges, are well established, but they rely on complicated telemetry or slip ring systems, they are costly to install, they have a limited operating life, and they often interfere with the aerodynamic and mechanical properties of the assembly. Alternative noncontacting measurement techniques have been developed to minimize such adverse effects, and one particular approach, known as blade tip-timing, measures blade-tip deflection using optical probes mounted in the assembly casing. In the absence of any structural vibration, the time for the tip of a particular blade to reach the optical probe, the so-called blade arrival time, would be dependent on the rotational speed only. However, when the blade is vibrating, blade arrival times will depend on both the amplitude and the frequency of the vibration. In principle, the blade motion can be characterized from knowledge of such data. As with other transducers, such as strain gauges and accelerometers, whether a particular mode can be captured by a given laser probe depends on the measurement location. Typically, measurements are taken near the leading edge of the blade to maintain reasonable sensitivity to the motion of the first few bending and torsion modes.

At constant rotational speed, synchronous vibration can be characterized using velocity or displacement measurements of assembly response from many probes (Endoh et al., 1983) describing such a system with 50 probes. However, given acquisition system costs and required assembly modifications, it is highly desirable to use a small number of probes and substantial research effort in tip-timing is devoted to devising new data processing techniques using a limited number of probes. The determination of synchronous vibration characteristics using a single probe (Zablotsky and Korostelev, 1970) requires measurements to be acquired over a small speed range such that changes in steady-state blade response due to centripetal forces, gas loading, and temperature are assumed to be negligible.

A tip-timing system, shown schematically in Fig. 1, consists of three main elements: (i) the acquisition of raw blade arrival time data by a number of stationary probes placed in the casing, (ii) the derivation of characteristic vibration parameters, such as blade displacement, velocity, and acceleration from the measured data, and (iii) the processing of the characteristic parameters to describe the vibration properties of the bladed-disk assembly. Steps (i) and (ii) are relatively straightforward and the acquisition system technology and parameter derivation methods have reached a mature development point. Step (iii) is crucial to overall system operation as it provides information about the dynamic characteristics of the assembly.

The unsteady components of the blade response are derived from tip-timing measurements of displacement, velocity or acceleration values at fixed points on the blade tip. For asynchronous vibration, the mean value of the measurements over a limited number of samples (or speed range) is used to remove the steady part of the response. For synchronous vibration, the measurement of the unsteady components uses the blade location relative to a nonvibrating rotating datum which can be provided by a reference rotor, a shaft encoder, a once-per-revolution probe, or a blade root probe. McCarty and Thompson (1980) describe a typical displacement measurement system using nonvibrating data derived from a once-per-revolution signal.

The relative merits of using contacting and noncontacting measurement devices have been discussed many times before. It is generally accepted that the former type, such as strain gauges, provide better accuracy while the latter provide more information and, more importantly, do not change the dynamic

Contributed by the International Gas Turbine Institute and presented at the International Gas Turbine and Aeroengine Congress and Exhibition, Orlando, FL, June 2–5, 1997. Manuscript received by the ASME Headquarters March 17, 1997. Paper No. 97-GT-213. Associate Technical Editor: H. A. Kidd.

characteristics of the structure under observation. The importance of such a feature will be illustrated below via an industrial case study. In the case of an industrial turbine, blade failures were observed for extended operation periods. Strain gauge testing of the affected blades failed to indicate critical vibration levels that would result in blade failure. As the blades were only 20 mm high, it was thought that the dynamic properties were significantly affected by the strain gauge attachments. On the other hand, tip-timing measurements, made under identical operating conditions, pinpointed two blades with excessive response levels. A statistical analysis of the tip-timing measurements is shown in Fig. 2 for both the mean and maximum blade responses. Although the mean response of the 101 blades remains relatively unchanged, there is a significant increase in the maximum response, the event being triggered by the opening of a control valve. To capture the same response, not only the strain gauge dimensions would need to be small compared to those of the blade, but also every blade would need to be instrumented, unless the failure position was known to be repeatable.

As existing predictive tools for either synchronous or asynchronous vibration have not yet reached the level of accuracy that is required for design calculations, engine developments rely heavily on rig tests, a feature that necessitates the development of advanced measurement techniques. The main purpose of this paper is to focus on one such technique, blade tip-timing, and to review the principal methods available for the analysis and interpretation of bladed-disk vibration data acquired using optical tip-timing probes. For the purposes of tip-timing data analysis, there are two distinct classes of response, namely, synchronous and asynchronous. Synchronous (or integral order) resonances are assembly modes that are excited at multiples of the rotational speed. Asynchronous resonances are mainly due to aerodynamic instabilities such as rotating stall and flutter.

2 Asynchronous Response Tip-Timing Analysis Methods

Asynchronous response analysis methods aim at identifying the amplitude and frequency of nonintegral order resonances from measurements at the blade tips. The sensors are placed at equally spaced locations around the casing in order to ensure that the response parameters are approximately equally spaced in time. From the sampling theory, the amplitude and frequency components of the assembly response can be identified uniquely up to a frequency:

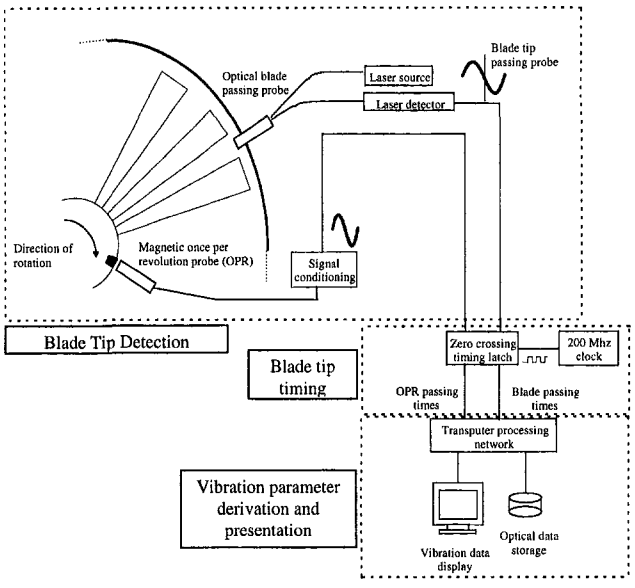

Fig. 1 Typical blade tip-timing system elements

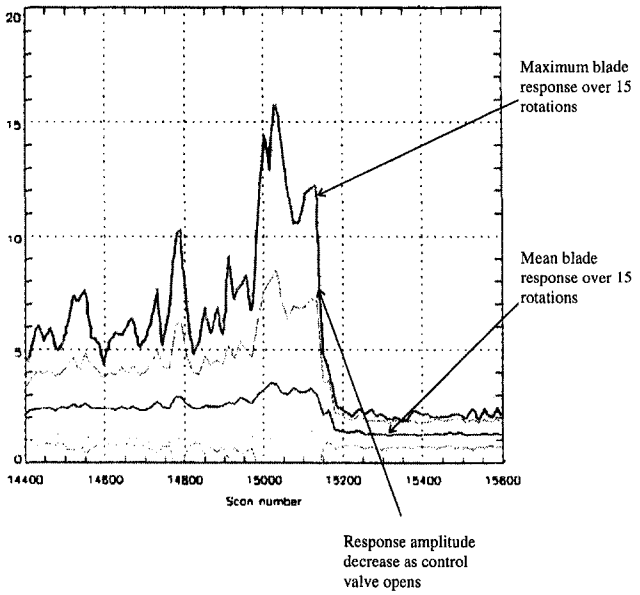

Fig. 2 Statistical analysis of tip-timing asynchronous response measurements

$$\omega_{\max} = \frac{\Omega M}{2}, \tag{1}$$

where M is the number of response measurement points around the periphery, and Ω the assembly rotational speed. McCarty and Thompson (1980) suggested a frequency range of 0–3500 Hz and a maximum rotational speed of 16,600 rpm for a typical axial compressor. Such conditions will require 26 probes to satisfy Eq. (1), a somewhat unrealistic proposition.

In the 1970s and 1980s, NASA and the U.S. Air Force undertook an extensive research program aimed at demonstrating the feasibility of a gas turbine vibration measurement system based on tip timing techniques. The objectives were to obtain accurate information for the amplitude and frequency of the assembly response and to reduce the requirement for contacting vibration measurement techniques. Asynchronous response analysis methods, based on one or two circumferential measurements made at the same axial position, were extensively researched as part of this program. The spectral analysis of the response amplitude at each measurement location was performed in two ways. First, measurements from a single blade on successive assembly rotations were used to compute individual spectra for each blade in the assembly. Second, measurements taken in the blade arrival order at the measurement location were combined to give a single all-blade spectrum. The amplitude of the actual assembly response frequency components can be determined from response amplitude measurements at a single location from either the individual blade spectra (McCarty et al., 1980) or from the all-blade spectrum (Watkins et al., 1985). The individual blade spectra are sensitive to measurement noise and can be affected by multiple frequencies in the response. Both methods are based on a single measurement location and require prior knowledge of the expected assembly resonances. These two methods were extended to two measurement locations by Watkins and Chi (1987), their approach being based on analysis techniques proposed by Kurkov and Dicus (1978) and Kurkov (1983). The NASA and U.S. Air Force research program considered a maximum of two measurement locations and concluded that this approach was adequate for determining the amplitude and frequency components of asynchronous assembly response to a satisfactory level of accuracy for current aerospace measurement requirements. The asynchronous response analysis techniques that are documented in the published literature is summarized in the following diagram:

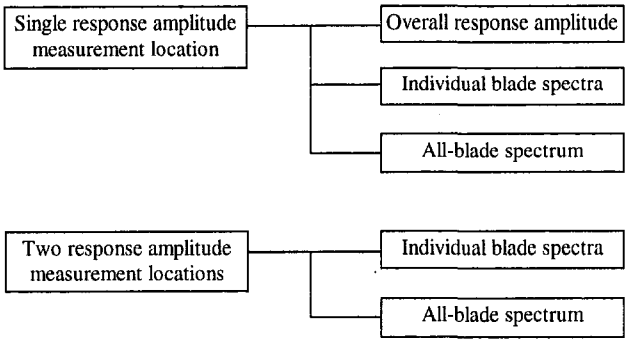

2.1 Overall Response Amplitude. Hohenberg (1967) indicated that the asynchronous response amplitude could be determined from the measurement of a single blade tip response parameter at a single location. The measured maximum-to-minimum amplitude over a finite period is assumed to be equal to the actual maximum-to-minimum amplitude of the assembly response. The method does not provide resonant frequency information, and, hence, the determination of assembly stresses requires prior knowledge of this quantity.

The measurement of the overall response amplitude using a single probe is the simplest tip-timing method and it is widely used for safety monitoring of turbomachines, both during development and in service (Nava et al., 1993; Rozelle et al., 1989). Although the actual overall amplitude has contributions from all assembly response modes, the maximum assembly stress calculated from overall amplitude measurements while traversing a single mode has been shown to be within 10 percent of the value obtained from strain gauge measurements. Given measurement uncertainties in both techniques, tip-timing results can be considered to be acceptable. However, this particular technique is not applicable to close modes and, as mentioned before, cannot identify the resonance frequencies.

2.2 Single Blade Analysis. A number of methods are available for identifying the resonance frequencies from a Fourier analysis of the response parameters, (Kurkov and Dicus 1978; McCarty et al., 1980; Watkins et al., 1985; Watkins and Chi, 1987). All these tip-timing analysis methods have been shown to identify the resonance frequency and the maximum amplitude correctly, as extensive checks have been made against strain gauge data. Broadly speaking, when the assembly vibration is dominated by a single resonance, the frequency of that resonance can be identified with good accuracy. However, if the corresponding maximum amplitude is low, say around 20 μm, which typically corresponds to 1 percent of a 10^7 cycle endurance limit, the quality of the Fourier spectrum is degraded by experimental noise, limiting the application of these methods in such cases. Although the researchers concluded that resonant frequency estimates were reliable, it is the authors' opinion that an accurate interpretation of the spectra was only possible as the resonance values were known from measurements other than tip-timing. The frequency identification using tip-timing analysis methods is particularly difficult because the value is determined indirectly from the single and all-blade spectra. The frequency content of tip-timing response measurements cannot be limited prior to "sampling", and the samples will inevitably contain signals at frequencies above the sampling rate as well as noise. The maximum detection frequency in a single blade spectrum is half the assembly rotation rate, and, hence, most resonances are present only as aliases in the spectrum. Furthermore, the signal to noise ratio is low as noise is aliased into a limited frequency range from a wide frequency range. The true frequency can be derived from

$$f_a = |kf_s - f_r|, \tag{2}$$

where f_a is the frequency in the single blade spectrum, f_s is the sample frequency, f_r is the true resonance frequency, and k is an integer. The application of (2) requires the measurements to be made at approximately constant speed. So, only a limited number of data points can be used in the Fourier analysis which results in a poor spectrum. For typical turbomachinery vibration surveys, where speed changes continuously and contains random variations, single spectra are formed from 256 samples, giving a typical frequency resolution of 0.7 Hz (Watkins et al., 1985). Ensemble averaging of such spectra is not possible as there are significant differences in the acquisition conditions of the individual spectra. In practice, the low frequency resolution, poor signal-to-noise ratio and aliasing of the response frequency components into a limited band do not allow accurate estimates of the spectral peak frequencies. As mentioned earlier, under such conditions, the resonance frequencies cannot be identified reliably using the single-blade spectra technique, unless some guide values are available from some other independent technique.

2.3 All-Blade Spectrum Analysis. All-blade spectrum analysis assumes that the bladed-disk assembly vibrates in nodal diameter modes, that is to say the contour of the stationary points describes a certain number of diameters of the disk. Because of circular symmetry, the nodal diameter modes will occur in orthogonal pairs that will become travelling waves under the effect of rotation. Forward travelling waves correspond to the rotation of the nodal lines in the same direction as assembly rotation and backward ones have their nodal lines rotating in the opposite direction. The amplitude, S_k, and phase, ϕ_k, of the blade response are given by

$$S_k e^{i\phi_k} = \sum_{n=n_{\min}}^{n_{\max}} A_n e^{i(n[2\pi(k-1)/N_b]+\psi_n)}, \tag{3}$$

where N_b is the number of blades on the assembly, k is the blade index $1, 2, \ldots, N_b$, A_n, and ψ_n are the response amplitude and phase for nodal diameter n, where n is positive for forward travelling waves and negative for backward travelling waves. For an even number of blades $n_{\max} = N_b/2$ and $n_{\min} = 1 - N_b/2$, whereas for an odd number of blades $n_{\max} = (N_b - 1)/2$ and $n_{\min} = -(N_b - 1)/2$.

For a single excitation frequency in the rotating reference frame, ω_{rotating}, (3) can be modified to give the blade response time history

$$S_k e^{i\phi_k} e^{i\omega_{\text{rotating}}t} = \Big(\sum_{n=n_{\min}}^{n_{\max}} A_n e^{i(n[2\pi(k-1)/N_b]+\psi_n)}\Big) e^{i\omega_{\text{rotating}}t}. \tag{4}$$

Equation (4) is derived for a rotating reference frame which is fixed relative to the bladed disk assembly. For each nodal diameter, there is a constant phase angle of $n(360(k-1)/N_b)$ degrees between consecutive blades. Assuming that all blades are vibrating at the same frequency, which is implicit in (4), a spatial Fourier transform of the measured response amplitude of successive blades will give the travelling wave response in the stationary (or measurement) reference frame. This approach is referred to as all-blade or travelling-wave analysis. In the stationary reference frame, the blade angular position changes with time due to assembly rotation Ω. In the stationary frame of reference, the right hand side of (4) becomes

$$\Big(\sum_{n=n_{\min}}^{n_{\max}} A_n e^{i(n[\{2\pi(k-1)/N_b\}+\Omega t]+\psi_n)}\Big) e^{i\omega_{\text{rotating}}t}$$

$$= \Big(\sum_{n=n_{\min}}^{n_{\max}} A_n e^{i(n[2\pi(k-1)/N_b]+\psi_n)}\Big) e^{i(\omega_{\text{rotating}}+n\Omega)t}. \tag{5}$$

Using (5), the stationary reference frame resonant frequency, $\omega_{\text{stationary}}$, is given by (6), which is consistent with the form given by Watkins et al. (1985).

$$\omega_{\text{stationary}} = \omega_{\text{rotating}} + n\Omega \quad (6)$$

The sample rate of the all-blade spectrum data is equal to the number of blades times the assembly rotation rate. In general, unlike those obtained from individual blade spectra, the resonant frequencies are not aliased and the problem of resolving true resonant frequencies is thus avoided. The increased spectrum bandwidth also improves the signal-to-noise ratio and enables spectral peaks to be identified more readily. However, a single resonant frequency can produce multiple frequency components in an all-blade spectrum due to the relationship given by (6). The spacing of these frequency components is an integer multiple of the assembly rotation rate, a feature that allows both the calculation of rotating frequencies from a number of components in the all-blade spectrum and a cross-check of the consistency of the results. When performing an all-blade analysis, a limited number of frequency components will be generated for a single resonant frequency as a specific nodal pattern tends to dominate the response.

The objective of analysing an all-blade response spectrum is to identify the nodal diameter modes associated with the frequency components of significant amplitude. When a single response measurement location is used, the interpretation of an all-blade spectrum requires the nodal diameter pattern to be inferred from the values of the expected resonant frequencies, a task which can be difficult in practice. A typical all-blade spectrum, corresponding to tip-timing data acquired by the authors in the case of an industrial compressor, is shown in Fig. 3.

The format used, the so-called Z-plot, is a modified Campbell diagram in which the print density indicates the strength of the vibration amplitude. In this particular case, the phenomenon of interest is rotating stall, the position of which is shown by the rectangular frame. The aim of the analysis is to determine the mode shape (i.e., the number of nodal diameters) associated with this particular rotating stall event. A technique proposed by Watkins and Chi (1987) will be used for this purpose: instead of identifying the nodal diameter number of the mode from the predicted natural frequencies, the all-blade spectra analysis technique can be extended to two measurement probes. In this case, the nodal diameter mode can be identified directly using

$$n = \frac{\Delta\phi}{\Delta\theta}, \quad (7)$$

where $\Delta\phi$ is the true phase difference of the spectral peaks, and $\Delta\theta$ the angular separation of the two probes. Table 1 gives the results of applying the Watkins and Chi technique to the resonance identified in Fig. 3.

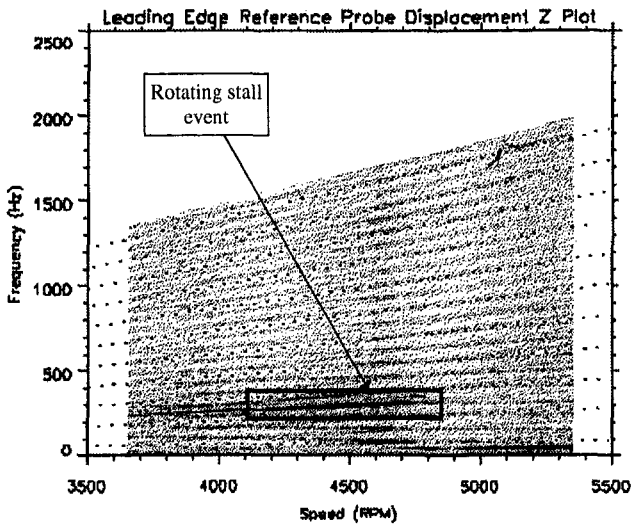

Fig. 3 Z-plot from all-blade spectrum showing rotating stall event

Table 1 All-blade spectrum analysis for identifying the mode of the rotating stall event

Values taken from all-blade spectra				Analysis results			
Rotation speed (RPM)	All blade spectrum peak frequency (Hz)	First location phase (radians)	Second location phase (radians)	Calculated number of nodal diameters	Calculated resonant response frequency (Hz)	Actual number of nodal diameters	Estimated resonant response frequency (Hz)
4564	294.42	-1.216	-0.831	8.149	325.52	8	314.17
4574	294.42	1.026	1.373	7.723	294.37	8	315.50
4594	299.78	0.452	0.795	7.733	292.37	8	312.81
4599	294.42	-1.583	-1.214	7.949	314.89	8	318.83
4614	294.42	1.248	1.603	7.783	304.16	8	320.83
4614	299.78	-2.081	-1.717	7.958	312.28	8	315.48
4629	299.78	2.318	2.701	8.150	329.03	8	317.48
4654	305.13	-0.742	-0.306	8.788	376.58	8	315.46
4664	305.13	1.663	2.047	8.202	332.46	8	316.79
4684	305.13	2.057	2.483	8.659	370.94	8	319.46
4704	310.48	-0.771	-0.373	8.388	347.22	8	316.77
4719	310.48	-3.001	-2.652	7.828	305.27	8	318.77

Table 1 confirms that the shape of vibration, here 8 nodal diameters, can be determined reliably by using two measurement locations. Although it is generally thought that tip-timing techniques cannot provide accurate values of resonant frequencies, measurements at two locations can yield acceptable estimates of asynchronous resonant frequencies and amplitudes. Experience suggests that confident identification of resonances still requires close predictions of their values. Typical industrial development programs use strain gauges for initial vibration measurements on new designs and tip-timing methods during the operation of these designs or their derivatives.

3 Synchronous Response Tip-Timing Analysis Methods

Synchronous response analyses can be divided into direct and indirect methods. Direct analysis methods typically take four response samples on each assembly rotation for approximately constant operating conditions, and identify the resonance characteristics for each sample set. These methods have the potential of identifying maximum vibration amplitudes for single or multiple resonances in real-time. On the other hand, indirect analysis methods typically take one or two response samples at each assembly rotation as a resonance is traversed. Therefore, they can only give a single frequency component, i.e., the resonant frequency. As the resonance is traversed, the excitation and response characteristics change due to changes in the assembly rotation speed. Typically, indirect methods give the engine order of the resonance and a mean value of the associated frequency has to be calculated from the speed range over which resonance occurs.

3.1 Direct Analysis Methods. There is little published information on direct methods, although Robinson and Washburn (1991) indicate that a least-squares sine fit to measurements from four probe locations can give the amplitude and frequency of an integral order vibration. A recent application of curve fitting techniques to determine the response amplitude, phase, and frequency has been mentioned by Jones (1996) without any specific details. However, independent research by the authors revealed that such techniques are very sensitive to measurement noise, a feature that limits their practical application. However, these techniques have the advantage of using a limited of number of probes on a single assembly rotation to give the required vibration characteristics at all operating conditions.

3.2 Indirect Analysis Methods. One indirect method, proposed by Zablotsky and Korostelev (1970), has become a de facto standard method for determining the amplitude of single synchronous resonances, with recent applications being reported by Chi and Jones (1988). The analysis technique is based on measuring a single tip response parameter, such as displacement

(or velocity, or acceleration), using a single probe. The resonance is excited by varying the assembly rotation speed in such a way that the assembly is forced to traverse the resonance of interest. The form of the measured displacement versus rotational speed characteristic depends on the position of the measurement probe, typical plots for different measurement positions being shown in Fig. 4.

The actual resonance amplitude is the peak response amplitude at the measurement location on the blade, this being identical to the measured response amplitude at the 0 deg location. The angular location of the probes refers to a fixed position expressed in terms of the wavelength of the response. Consider a forced response of order n at conditions below the resonance of interest. The origin for angular locations on the assembly casing is chosen to be at a response node and, for the first half cycle of the response, the response amplitude increases as the angular location increases. Therefore, an angular location of α on the resonance corresponds to an angular location of α/n on the casing.

It is usually assumed that the maximum (zero-to-peak) resonant response is given by the maximum-to-minimum values of the measured displacement versus speed characteristic. It is further assumed that this value is independent of the location of the measurement point. It has been shown by Heath and Imregun (1996) that there are inherent errors associated with such assumptions and that the magnitude of the errors depends both on the probe location and the maximum resonance amplitude.

The evaluation of the accuracy of a tip-timing analysis method requires the response to be known accurately. As this is not the case for actual assembly measurements, benchmark response data need to be generated from known system properties. A numerical simulator, capable of calculating accurate blade arrival times from given structural, geometric, data acquisition and excitation parameters, was developed for this purpose and it will also be used here (Heath and Imregun 1996).

A numerical simulation of the assembly response was obtained under known forcing and the corresponding displacement versus speed characteristics were also computed using the same model. The apparent resonance amplitude, $R_{\max}$, was taken as the maximum-to-minimum value in the displacement versus speed plots. The exact value, $A_{\max}$, was obtained directly from the numerical simulation and the percentage discrepancy (or error), ρ, between the exact and apparent values of resonance amplitude was calculated from

$$\rho = \frac{(R_{\max} - A_{\max})}{A_{\max}} \times 100. \tag{8}$$

The relative resonance amplitude, A_{rel}, is defined as

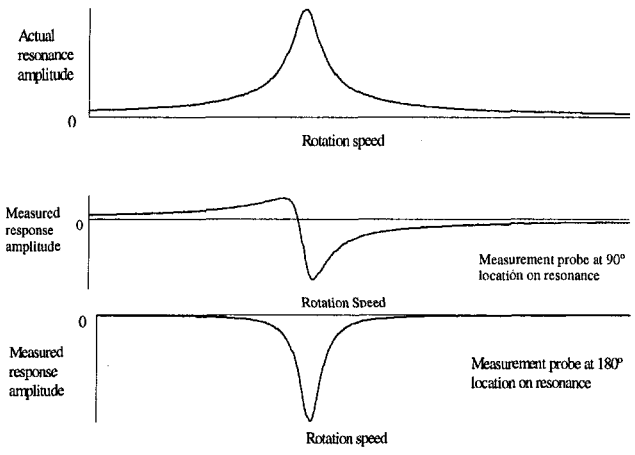

Fig. 4 Comparison of actual and measured response amplitudes for different measurement positions

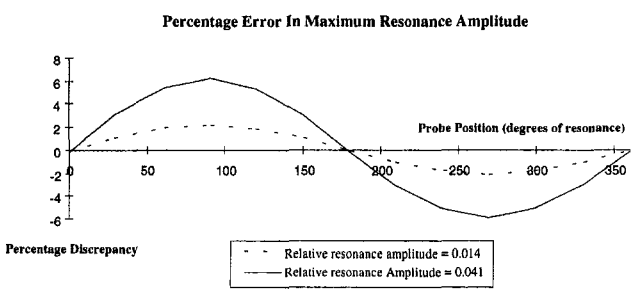

Fig. 5 Maximum resonance amplitude errors for Zablotsky and Korostelev method

$$A_{\text{rel}} = \frac{A_{\max}}{R}, \tag{9}$$

where R is the assembly radius.

The percentage error due to using the Zablotsky–Korostelev method is plotted in Fig. 5 for two different values of the relative resonance amplitude. The x-axis indicates the location of the probes on the resonance, ψ, rather than on the assembly casing.[1]

The errors are caused because of ignoring the dependence of the blade tip arrival time on the actual blade vibration amplitude. For synchronous responses, this assumption means that the detection point on the response is dependent on the vibration amplitude. Given that (in the stationary reference frame) the amplitude of a synchronous response is a function of angular position and of peak response amplitude, the phase of the response with respect to a stationary forcing term will change as the amplitude varies. Therefore, the response amplitude at the stationary measurement point will also change. However, as the arrival time is dependent on the response amplitude, the apparent change in the phase of the response at the measurement point will not be the same as the actual phase change between the forcing term and the response, hence the observed discrepancy in Fig. 5.

For a given measurement location and assembly tip radius, plots of percentage error can be used to calculate the true value $A_{\max}$ from the apparent value $R_{\max}$. It is estimated that a maximum error of about ± 8 percent will be seen for typical operating conditions. However, equivalent strain gauge measurements can produce errors of approximately ± 10 percent, and, hence, corrections may not be necessary for small vibration amplitudes. However, these errors should not be ignored since (i) some modern fan blades are designed to undergo relatively large amplitudes, and (ii) blade mistuning, due to small manufacturing differences, can significantly affect the analysis results. This second point will be discussed further below.

3.3 Mistuning Effects. Mistuning, or small blade-to-blade manufacturing differences, will cause the blades to have dramatically different response levels, and the assembly will exhibit many close modes because of the splitting double modes. Mistuning will also distort the displacement versus speed characteristic, and, hence, adversely affect the results of the analysis. The effects of mistuning were quantified using a numerical simulation of a 12-bladed disk assembly, running in the vicinity of a split 3 nodal-diameter mode,[2] and subject to an engine-order excitation of 3. The finite element model of the assembly was adjusted to give a ± 5 percent variation in the individual blade cantilever frequencies. The true maximum resonance displacement was obtained directly from the finite element model and the corresponding displacement versus speed

[1] For a resonance of order n, the location on the resonance is related to angular position on the casing θ by the relationship: $\psi = n\theta + \gamma$, where γ is an angular offset determined by the angular position of the resonance relative to the casing.

[2] Double modes split into two single ones with close frequencies and similar but not identical mode shapes.

Table 2 Actual and apparent maximum displacements at resonance

Blade number	True maximum blade displacement (mm)	Observed peak-to-peak blade displacement (mm)	Maximum displacement error
1	17.56	16.55	-5.8%
4	19.26	18.55	-3.7%
9	17.20	16.98	+1.3%
11	19.61	19.34	+1.3%

characteristics were computed via the tip-timing numerical simulator. The actual and apparent resonance amplitudes from the Zablotsky and Korostelev method are given in Table 2.

Variations in the maximum displacement error are to be expected, as mistuning results in a different actual maximum displacement for each blade when traversing the resonance. However, Fig. 5 shows that the percentage error has a fixed sign for a fixed probe location. In Table 2, blades 1 and 9 have similar actual maximum displacements, but the percentage errors are of opposite sign. Therefore, mistuning can cause further errors in the results of the Zablotsky and Korostelev analysis method. However, the effects of mistuning can be readily seen in the displacement versus speed plots, and, unless there is a marked mistuning effect, the measured maximum displacement values are probably still as accurate as those provided by strain gauges. However, the Zablostky and Korostelev method is unable to determine the amplitude of vibration in the vicinity of close modes where individual values for maximum-to-minimum displacements cannot be readily discerned. Figure 6 shows a typical displacement versus speed plot for such a situation. The measured displacement in Fig. 6 is relative to a nonvibrating datum, giving a fixed offset of approximately 50 mm. The maximum resonance amplitude measured in Fig. 6 is about 1.5 mm.

3.4 Indirect Analysis Method for Frequency Determination. The authors have developed a new indirect analysis method, the so-called two-parameter plot technique, for identifying the maximum amplitude, the resonant frequency and the excitation order of a vibration mode using measurements from two probes. A detailed discussion is given in the appendix. The method has been successfully applied to industrial cases and the resonant frequency, the maximum amplitude, and the excitation order have been determined with good accuracy. A typical case study will be discussed here for illustrative purposes. The displacements versus speed plots, obtained at two probes while traversing a resonance, are shown in Fig. 7. The objective of the analysis is to determine the engine order of the excitation, which is known to be 2 from other sources.

The information has been analysed for each blade in turn and the order of the excitation has been calculated independently. The results are plotted in Fig. 8, and it is easily seen that the mean value of the predicted engine order excitation is almost 2. It should be noted that no corresponding amplitude plots are given as the objective of the analysis was the determination of the excitation order only.

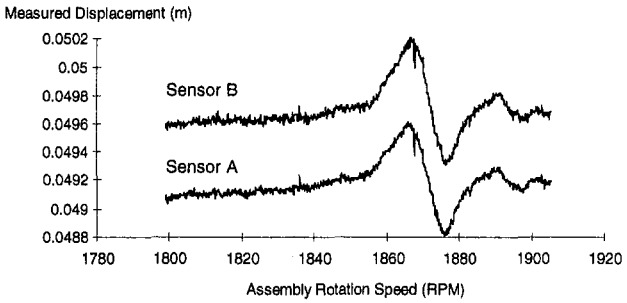

Fig. 7 Measured displacement versus speed characteristic as the resonance of interest is traversed

4 Concluding Remarks

1 A review of tip-timing analysis methods has been carried out and the performance of these methods has been discussed in some detail. Whilst tip-timing measurements inherently contain less information than those provided by strain gauges, methods for their analysis allow the amplitude and frequency of all response types to be identified. However, the interpretation of tip-timing data is far from being trivial and further refinement of the various available methods is necessary for their use by non tip-timing specialists.

2 If it was possible to use a large number of probes so that a standard Fourier analysis could be conducted, there would be no analysis difficulties in identifying the vibration characteristics. However, the use of a large number of probes, say more than 10, is impractical. Therefore, alternative, albeit approximate, methods need to be developed. As the rotor diameter increases, the possibility of increasing the number of probes also increases but at significant additional cost. It is common aerospace practice to install a maximum of four probes per stage of blading.

3 The industry-standard Zablotsky and Korostelev analysis method has a number of inherent limitations. The errors due to measurement sensor location and maximum resonance amplitude may be considered acceptable when comparing the accuracy of the method with that of strain gauge measurements. Also, further work is necessary to understand the effects of mistuning fully.

4 A new indirect analysis method, the so-called two-parameter plot technique, has been developed for identifying the vibration characteristics of synchronous resonances using two probes only. However, further development is necessary to allow its routine application to any measured data, especially when unexpected resonances are encountered. Although the accuracy of the method is affected by relative resonance amplitudes and mistuning, such errors have been quantified and are considered to be acceptable. It is believed that fur-

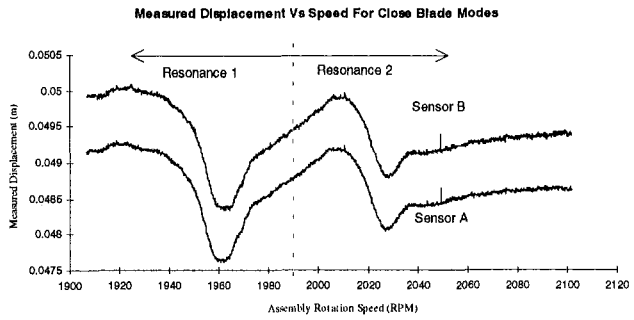

Fig. 6 Measured displacement versus speed characteristic for close modes

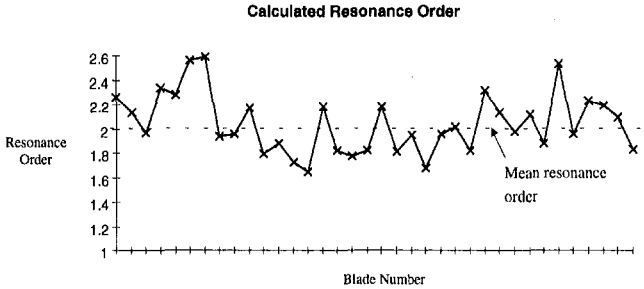

Fig. 8 Identification of the excitation order

ther refinements of the method should virtually eliminate these shortcomings but work has not yet reached this stage. An extension to asynchronous vibration measurements is considered to be possible.

5 Tip-timing has become an accepted vibration measurement technique in the turbomachinery industry. The number of strain-gauge measurements has been reduced significantly, creating substantial savings on development and commissioning costs. However, tip-timing systems described in the open literature have rudimentary presentation and analysis capabilities and there are no equivalent commercial systems. Therefore, improvements to the user interface and further development of validated analysis methods will allow a more widespread use of the tip-timing method.

5 Acknowledgments

The tip-timing measurement technique research program was funded by EPSRC and Rolls-Royce plc, and carried out at Imperial College, London between October 1992 and October 1995. The authors are grateful to Mr. P. Loftus of Rolls-Royce plc for his encouragement and support throughout the research program. Thanks are also due to Mr. T. Slater of Rolls-Royce plc for his suggestions, ideas, and support in applying the proposed measurement techniques to operating turbomachines.

6 References

Chi, R. M., and Jones, H. T., 1988, "Demonstration Testing of a Non-interference Technique for Measuring Turbine Engine Rotor Blade Stresses," presented at the AIAA/SAE/ASME/ASEE 24th Joint Propulsion Conference, Boston, MA, AIAA-88-3143.

Endoh, M., Matsuda, Y., and Matsuki, M., 1983, "Non-contact Measurement of Rotating Blade Vibrations," *International Gas Turbine Congress,* Tokyo, Japan, October 23–29, pp. 953–960.

Heath, S., and Imregun, M., 1996, "An Improved Single-Parameter Tip-Timing Method for Turbomachinery Blade Vibration Measurements Using Optical Laser Probes," *International Journal of Mechanical Science,* Vol. 38, No. 10, pp. 1047–1058.

Hohenberg, R., 1967, "Detection and Study of Compressor Blade Vibration," *Experimental Mechanics,* Vol. 7, No. 2, pp. 19–24.

McCarty, P. E., and Thompson, J. W., 1980, "Performance Evaluation of a Prototype Non-Interference Technique for Measurement of Turbine Compressor Blade Stress," Report AEDC-TR-80-5, Arnold Engineering Centre, Arnold Air Force Station, TN.

McCarty, P. E., Thompson, J. W., and Ballard, R. S., 1980, "Development of a Non-Interference Compressor Blade Stress Measurement System," *Instrument Society of America,* ISBN 87664-473-6, pp. 745–757.

Rozelle, P. F., Evans, D. H., and Seth, B. B., 1989, "Development and Application of a Blade Vibration Monitor," *Latest Advances in Steam Turbine Design, Blading, Repairs, Assessment, and Condenser Interaction,* ASME, New York, pp. 37–45.

Watkins, W. B., Robinson, W. W., and Chi, R. M., 1985, "Noncontact Engine Blade Vibration Measurements and Analysis," presented at the AIAA/SAE/ASME/ASEE 21st Joint Propulsion Conference, Monterey, CA, AIAA-85-1473.

Watkins, W. B., and Chi, R. M., 1987, "A Non-Interference Blade Vibration Measurement System for Gas Turbine Engines," presented at the AIAA/SAE/ASME/ASEE 23rd Joint Propulsion Conference, San Diego, CA, AIAA-87-1758.

Kurkov, A., and Dicus, J., 1978, "Synthesis of Blade Flutter Vibratory Patterns Using Stationary Transducers," presented at the Gas Turbine Conference and Products Show, London, England, 78-GT-160.

Kurkov, A. P., 1983, "Measurements of Self-Excited Rotor-Blade Vibrations Using Optical Displacements," presented at the 28th International Gas Turbine Conference and Exhibit, Phoenix, Arizona. Paper No. 83-GT-132.

Nava, P., Paone, N., Rossi, G. L., Tomansini, E. P., 1993, "Design and Experimental Characterisation of a Non-Intrusive Measurement System of Rotating Blade Vibration," Paper No. 93-GT-16, International Gas Turbine and Aeroengine Congress, Ohio.

Robinson, W. W., and Washburn, R. S., 1991, "A Real Time Non-Interference Stress Measurement System (NSMS) for Determining Aero Engine Blade Stresses," Paper #91-103, *Proceedings 37th International Instrumentation Symposium,* Instrument Society of America, Ann Arbor, MI, pp. 793–797.

Jones, H., 1996, "A Nonintrusive Rotor Blade Vibration Monitoring System," Paper No. 96-GT-84, International Gas Turbine and Aeroengine Congress, Birmingham.

Zablotsky, I. Ye, and Korostelev, Yu. A., 1970, "Measurement of Resonance Vibrations of Turbine Blades with the ELURA Device," *Energomashinostroneniye,* Vol. 2, No. 2, pp. 36–39.

APPENDIX

Two-Parameter Plot Method for Resonance Identification European Patent Application EPA 0826949-A2

Consider a synchronous resonance measured using two sensors, A and B, located on the assembly periphery. Let sensor A be at angular position, θ_A on the assembly periphery and let $\Delta\theta$ be the angular spacing in the direction of rotation between sensors A and B. For a resonance of order n, the response amplitudes measured at sensor A, x_A and sensor B, x_B are given by:

$$x_A = A(\omega)\cos(n\theta_A + \psi(\omega)) + C \qquad \text{(A-1)}$$

$$x_B = A(\omega)\cos(n\theta_A + \psi(\omega) + n\Delta\theta) + C \qquad \text{(A-2)}$$

where $A(\omega)$ and $\psi(\omega)$ are the amplitude and phase of the assembly response and C is a constant offset. If $\Delta\psi$ is the angular separation of the sensors on the resonance, equation (A-2) can be rewritten as:

$$x_B = A(\omega)\cos(n\theta_A + \psi(\omega) + \Delta\psi) + C \qquad \text{(A-3)}$$

When the sensor angular separation $\Delta\psi$ on the resonance is 90°, equation (A-3) becomes:

$$x_B = -A(\omega)\sin(n\theta_A + \psi(\omega)) + C \qquad \text{(A-4)}$$

For a single-degree-of-freedom system, a polar plot of the system's response forms a circle as a resonance is traversed. Such a situation is shown in Fig. A1 by considering the excitation frequency and the response amplitude & phase.

Given the polar plot above and the form of equations (A-1) and (A-4), a plot of x_A against x_B will also describe a circle if the assembly response can be approximated to that of a single-degree-of-freedom system and if the sensors are separated by 90° on the resonance of interest. Let us assume that, in the vicinity of resonance, the synchronous response of a tuned assembly can be approximated to that of a single-degree-of-freedom system. In this case, a plot of x_A against x_B for a 90° angular separation will describe a circle. The location of that circle in the XY plane will be determined by the fixed offset C which may be different for each sensor. The location of the point on the circle corresponding to excitation frequencies significantly away from resonance will be determined by the angular position of the sensors on the resonance $n\theta_A$, n being the order of the excitation.

Equations (A-1) and (A-3) were used to produce plots of x_A versus x_B for various sensor angular separations on the resonance, all with zero offset. Such plots, shown in Fig. A2, will be called "two-parameter" plots and they will defined in terms of ellipse geometry, though they are not true ellipses in the sense that there is no symmetry about the major axis (Fig. A3).

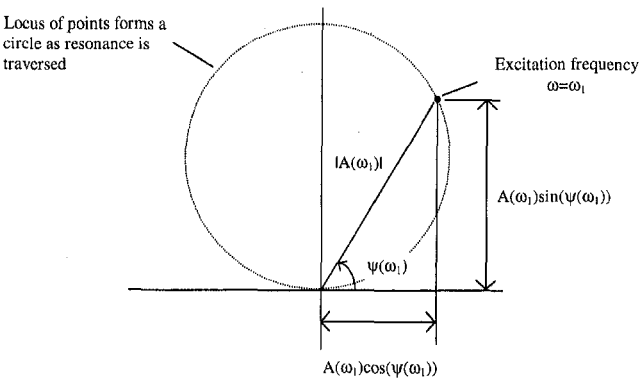

Fig. A1 Polar plot for single-degree-of-freedom-system resonance

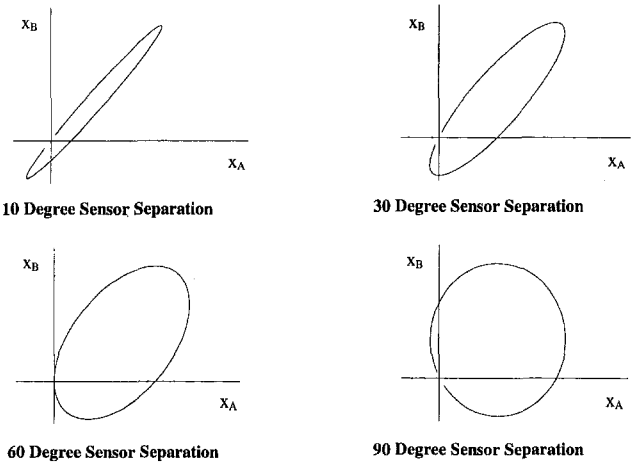

Fig. A2 Plots of x_A versus x_B for various sensor angular separations

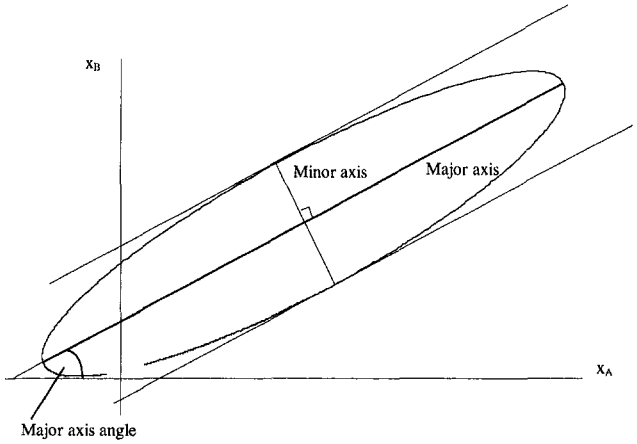

Fig. A3 Definition of two-parameter plot terminology

Major axis: Straight line joining the two points furthest apart on the plot

Minor axis: Maximum length straight line joining two points on the plot normal to the major axis

Major axis angle: Angle between major axis and horizontal plot axis

Axis ratio: $\dfrac{\text{Length of minor axis}}{\text{Length of major axis}}$

A relationship was found between the sensor angular separation, and the two-parameter plot axis ratio & the major axis angle. The relationship is independent of the location of sensor A on the resonance and is illustrated in Fig. A4. The major axis angle is always $\pm 45°$ except for sensor separations of 90° and 270° for which it is undefined as the two-parameter plots are circles at these sensor separations.

The relationship between the sensor separation, the axis ratio and the major axis angle is periodic for intervals of 360°. Four

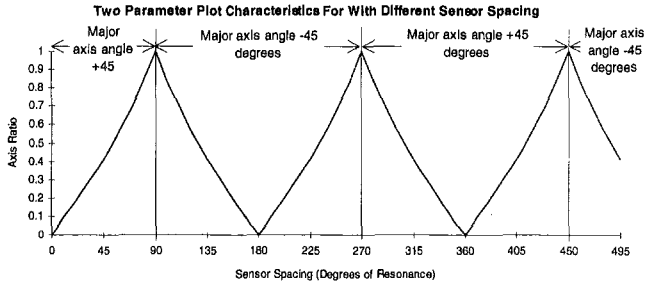

Fig. A4 Relationship between axis ratio, major axis angle and sensor angular separation

Table A1 Sensor separation region definitions

Region	Sensor separation range
1	0° to 90°
2	90° to 180°
3	180° to 270°
4	270° to 360°

Table A2 Polynomial coefficients for each sensor separation region

Region	P	Q	R	S
1	-7.22644	-21.82787	119.08946	-0.16976
2	7.27262	21.84211	-119.16418	180.17559
3	-7.28363	-21.82579	119.15622	179.82559
4	7.21876	21.84879	-119.10273	360.17127

regions can be identified within each 360° interval. Table A1 lists the sensor separation ranges for each region.

Within each region there is an almost linear relationship between the sensor separation and the axis ratio. In practice, the axis ratio and the major axis angle can identified from a two-parameter plot and the sensor separation calculated using Fig. A4. To enable a direct calculation of the sensor separation, a third-order polynomial fit of axis ratio to sensor separation was performed for each region. Equation (A-5) defines the polynomial used and Table A2 gives the polynomial coefficients for each region.

$$\text{Sensor spacing} = P \times (\text{Axis ratio})^3 + Q \times (\text{Axis ratio})^2 + R \times (\text{Axis ratio}) + S \quad \text{(A-5)}$$

Multiple values of sensor separation must be determined using the relationship of Fig. A4. Although sensor separation may be multi valued, the calculated resonance order should be a positive integer. It is possible that a number of sensor separation values will satisfy this condition and, in such cases, a knowledge of the expected or reasonable resonance order may be necessary.

Once the sensor angular separation $\Delta\psi$ is known, the excitation order, n, can be calculated from:

$$n = \frac{\Delta\psi}{\Delta\theta} \quad \text{(A-6)}$$

where $\Delta\theta$ is the physical angular spacing between the sensors.

Crack Initiation in a Coated and an Uncoated Nickel-Base Superalloy Under TMF Conditions

P. K. Johnson

M. Arana

K. M. Ostolaza

J. Bressers

Joint Research Centre,
European Commission,
P.O. Box 2,
1755 ZG, Petten, The Netherlands

A thermomechanical fatigue (TMF) cycle, intended to represent aeroengine blade working conditions, was selected for carrying out tests on uncoated and aluminide coated SRR99 samples until test piece failure. Optical images of the surface of test pieces were collected during testing to monitor surface crack initiation and accompanying transformations. Using these images, surface changes were quantified as a function of time. Post test each sample was taken through an incremental polishing procedure to allow damage in the tested material to be studied as a function of depth, using optical microscope-based quantitative metallography and scanning electron microscopy (SEM). The relationship between the observed surface changes and the damage built-up subsurface was examined. Differences in damage density on the surface and subsurface planes between coated and uncoated samples could accommodate the observed life reductions.

1 Introduction

Nickel-base superalloys are used in aeroengine blades with a protective nickel-aluminide diffusion coating to provide oxidation resistance at the high temperatures that are reached during engine operation (Wood, 1989). The effect of the presence of the coating upon the operational life of single crystal superalloy blades is an issue of concern.

Conflicting results have been reported when comparing the lives of coated and uncoated samples under a range of laboratory fatigue test conditions including TMF (Wright, 1988; Heine et al., 1986; Bain, 1985). Under TMF conditions that mimic the strain-temperature behavior at critical locations in blades at different mechanical strain ranges, the presence of an aluminide coating on SRR99 was reported to result in considerable life reductions at 0.7 percent mechanical strain range (Bressers et al., 1996; Ostolaza et al., 1996). In this paper, the differences between the damage processes operating in uncoated and nickel aluminide coated SRR99 are contrasted in order to rationalize the observed life reducing effect of the presence of the coating.

2 Experimental Procedure

In order to corroborate the observed differences in life between uncoated and Ni aluminide coated samples (Bressers et al., 1996) three further coated tests at 0.7 percent strain range were performed. Cylindrical bars of the single-crystal Ni-based superalloy SRR99, each with the long axis oriented within 10 degrees of the ⟨001⟩ direction, were supplied by Rolls Royce plc. Test bars were manufactured with a rectangular cross section (12 × 3 mm) such that each of the remaining ⟨001⟩ directions lay perpendicular to the flat surfaces of the gauge section. Details about the testing procedure are described elsewhere (Bressers et al., 1996). Nominal TMF testing conditions and life results are summarised in Table 1.

The uncoated sample and one coated sample (life 7846 cycles) were selected in order to examine differences in damage mechanisms. The as-received coating has two major layers. The main outermost coating layer was a polycrystalline B2-NiAl (3–6 μm grain size) + γ'. Between the main coating (23 ± 2.5 μm thick) and the superalloy lies the subcoating diffusion zone (17.5 ± 2.5 μm thick) followed by a narrow continuous layer of γ' (2 to 3 μm thick). One of the wide flat sample surfaces was scanned during TMF testing at specific cycles by a video camera system used with a machine resolution ranging from 2.5 to 4.5 μm per pixel. This procedure supplied a set of digitized light microscope images of the coating surface, traceable to the test cycle number (Bressers et al., 1993).

Use was made of an incremental polishing and image processing procedure designed to allow the characterization of the crack population and the coating, as a function of depth, over large areas (Ostolaza et al., 1996). Fragments of the failed samples were mounted and layers of coating were removed from the scanned surface in a controlled step-by-step procedure. Images of the new surface after each polishing step were digitized for measurement. Both sets of images were processed to obtain crack statistics. Crack density, numbers, and spatial characteristics were calculated. During this polishing procedure, the crack morphology was examined through the sample thickness. Energy dispersive spectroscopy was used to chemically characterise the surface at each polishing step.

3 Results and Discussion

3.1 Crack Initiation and Growth Kinetics. The cracks in the uncoated sample generally initiated at or near the surface following the formation during testing of oxide "spikes" that have been described previously in terms of a discontinuous oxidation-fatigue process (Johnson and Bressers, 1996). Some cracks were seen, during image record reviews, to emanate from the top or base of the spikes as illustrated in Fig. 1. However, the cracking event is generally difficult to detect, and, therefore, the initiation and growth

Contributed by the International Gas Turbine Institute and presented at the International Gas Turbine and Aeroengine Congress and Exhibition, Orlando, FL, June 2–5, 1997. Manuscript received by the ASME Headquarters March 7, 1997. Paper No. 97-GT-236. Associate Technical Editor: H. A. Kidd.

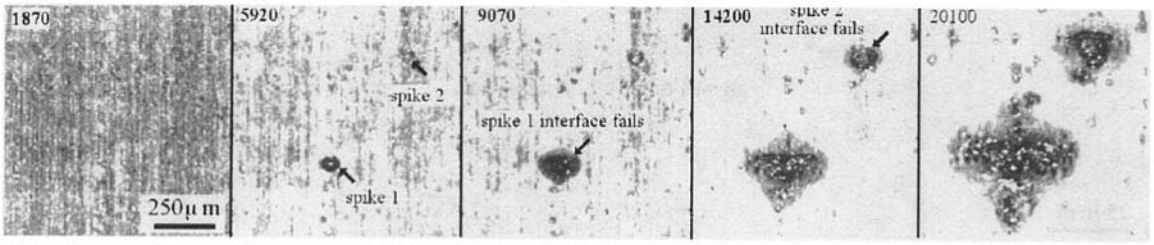

Fig. 1 Crack generation from tensile failure of an oxide spike interface

kinetics reported for the uncoated sample do not distinguish between spikes and cracks. Post test, a large proportion of cracks, that have grown enough to be identified, could be correlated directly with the type of event illustrated in Fig. 1. The proportion of spikes that had produced a crack was estimated, at the centre and at a peripheral gauge position, leading to values of 18 percent and 13 percent respectively. A simplified sequence of events for this crack initiation process is sketched out as follows:

$$\text{(Casting defects)} \xrightarrow{\text{Oxidation} - \text{fatigue}} \text{Oxide spike} \xrightarrow{\text{tensile failure of interface}} \text{cracks}$$

The discontinuously oxidized area fraction was measured as an indicator of the overall damage initiation and growth. It should be taken into account that both oxide spikes and cracks behave as rigid inclusions at the sample surface under compression. Consequently, both features will contribute to discontinuous oxidation, since a strain gradient will be formed between the inclusion and superalloy that will disturb the continuous oxide growth process on the surface (Johnson and Bressers, 1996). Figure 2 shows the experimental data of the initiation rate of "spikes" and the oxidized area fraction covered versus time from an area (4 × 2.6 mm) at the center of the specimen.

As a first step in the analysis of the phenomena contributing to the discontinuous oxidation processes, the oxidized area fraction has been fitted to an Avrami type rate equation, also indicated in Fig. 2,

$$\xi = 1 - \exp(-K \cdot t^n),$$

where $K = 3.27 \cdot 10^{-11}$ cycle^{-n} and $n = 2.6$. The $2 \le n \le 3$ value indicates that the initiation rate is decreasing and that the overall transformation is approximately two dimensional (Christian, 1975). The K value could represent a compact parameter for characterizing mixed-surface damage processes under different load and temperature conditions.

In the coated case, a time sequence of images of the surface is shown in Fig. 3. By 1000 cycles a large number of bright particles are seen that could correspond to the oxidation products of coarsened coating constituents. Very few cracks can be detected by visual inspection before 2000 cycles. Surface crack density and length data were collected as a function of time.

Figure 4 shows accumulated initiation events per unit area of surface features larger than 50 μm corresponding to cracks in the case of the coated sample and to oxidation "spikes" (crack precursor) for the uncoated sample. The initiation rate at the coated sample surface changes drastically between 2000 and 3000 cycles; thereafter, the crack number increases approximately linearly until the end of the test. Spike initiation was recorded from the first cycle; the main initiation process tended to saturate well before the end of the test.

In order to compare the crack growth in both samples the length of the crack with the maximum size out of the surface crack population was selected at each time step. Figure 5 shows the evolution of the length of this crack in both tests. Growth rates are similar until 5000 cycles when the largest crack at the coated sample surface accelerates. This phenomenon could be explained in conventional terms via the contribution of crack coalescence events to rapid extension of the major crack.

3.2 Post Test Examination. The surface oxide in the uncoated sample was removed to expose individual spikes and cracks: Fig. 6(*a*) shows part of the front surface at 80 μm depth. Figure 6(*b*) shows a micrograph of a section through an oxide spike. Spikes often contain a central Ni oxide "peg" and concentric layers of oxidation products. These layers can be classified in four different types showing concentrations of Al, Cr, or Ta oxides or mixed (Al, Cr, Ti, and Ta) oxides interspersed with compact Ni-oxide layers.

In the coated material three main layers with different types of damage and microstructure were identified from 15 polishing steps finishing at 65 μm depth:

- At around 24 μm depth the damage chiefly consists of oxidised cavities in the coating. The microstructure is composed mainly of an Al-rich constituent (A) with an Ni to Al ratio 5:3 (suggesting Ni_5Al_3). A small proportion of a constituent (B) with a Ni to Al ratio of 3:1 and a trace of Ti (suggesting γ') was also detected.
- At 37 μm depth cracking due to failure of A–B boundaries is predominant. Coating regions running parallel to the sample long axis with a locally high volume fraction of constituent B and decorated with a high proportion of Cr and W-rich particles were detected. These areas showed a lower damage level than in the rest of this sample plane. The presence of coarse-grain-boundary particles suggest that these regions of the coating might offer a higher resistance to creep related processes. As the subcoating is entered a proportion of cracks showed an association with substrate solidification defects (shrinkage porosity).

Table 1 Nominal conditions and life results of the TMF tests

	number of tests, n	R	$\Delta\varepsilon_m$	LAG	ΔT (°C)	Life ($\bar{x} \pm \sigma_{n-1}$) in cycles
Uncoated	1	-∞	0.7	-135°	300-1050	21820
Coated	4	-∞	0.7	-135°	300-1050	9469 ± 2367

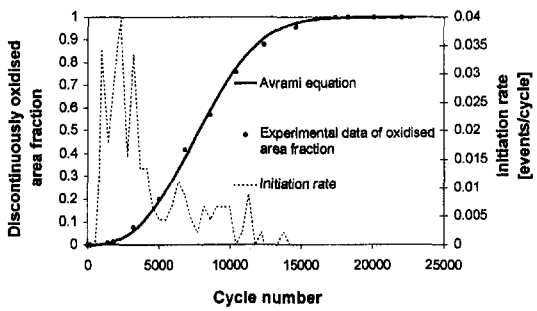

Fig. 2 Discontinuous oxidation kinetics and "spike" initiation rate

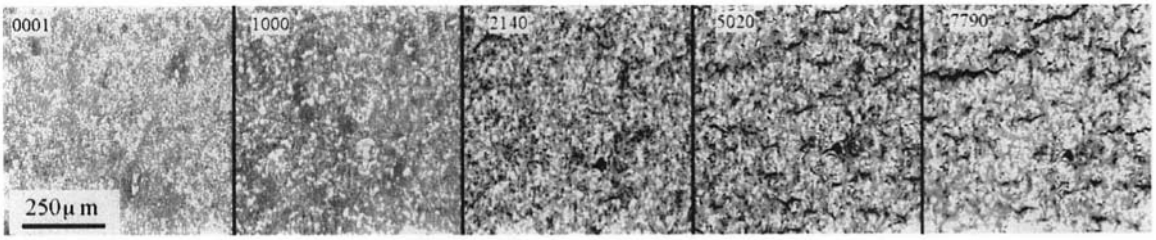

Fig. 3 Details of surface changes in the coated sample

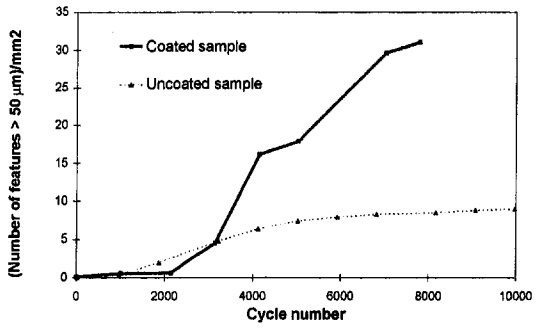

Fig. 4 Surface initiation events

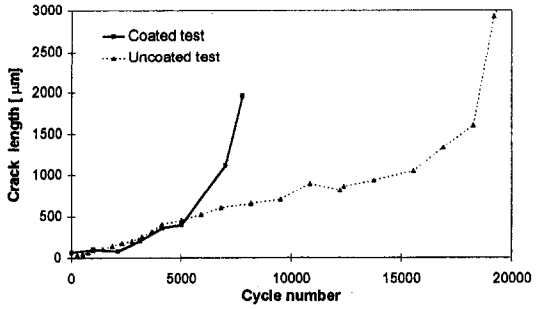

Fig. 5 Maximum crack length during testing

- At 65 μm the continuous γ' layer has been passed, but the microstructure does not yet correspond completely to that of the bulk.

Etching revealed that the constituent B in the main coating and subcoating layer appeared to be heavily twinned, which was not the case for the continuous γ' layer. Figure 7 shows the overall sample surface at different depths on a similar scale to the uncoated micrograph (Fig. 6(a)). Crack density versus depth is plotted in Fig. 7(d) showing that the crack density drops drastically upon reaching the subcoating zone.

A comparison has also been made using crack density values taken from the uncoated sample, and from the coated sample, when the bulk is just reached. The values are shown in Table 2.

4 Summary

From the results discussed above, the following aspects can be highlighted:

1 The uncoated material shows one principal small crack initiation mechanism eventually producing mode I opening cracks in the substrate. The crack population appears to develop via a process involving surface oxidation.
2 The incubation period for massive crack initiation in the coating possibly corresponds to the transformation of B2-NiAl + γ' into constituents A (with a Ni to Al ratio 5:3) and B (with a Ni to Al ratio 3:1), which accompanies interdiffusion and particle coarsening.
3 The maximum crack length and crack growth rate for both tests are very similar up to 5000 cycles, beyond which the maximum crack growth rate in the coated sample accelerates very quickly and produces the failure of the specimen at 7800 cycles. A higher density of cracks is likely to be a major contributor to crack coalescence events.
4 The result of the addition of the coating to the superalloy is a 5 times higher crack density (mm of crack/mm^2) at the end of life of the coated specimen when entering the substrate. This can be summarized by defining a mean substrate crack generation parameter $\bar{p}$ in mm of crack/(mm^2 × cycle) that would define the ability of the coating to deliver cracks into the substrate per unit area and time.

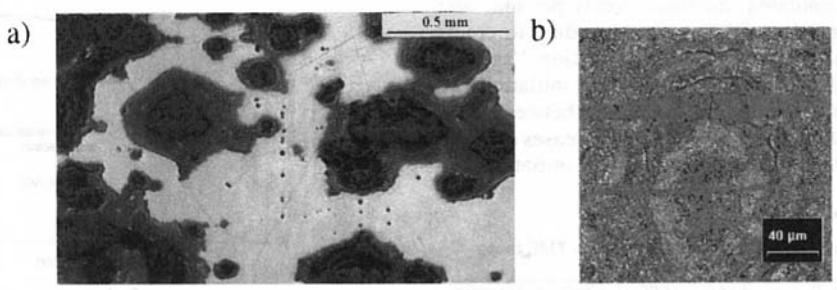

Fig. 6 (a) Light micrograph of the uncoated sample with the oxide layer partially removed; (b) detail of an oxide spike

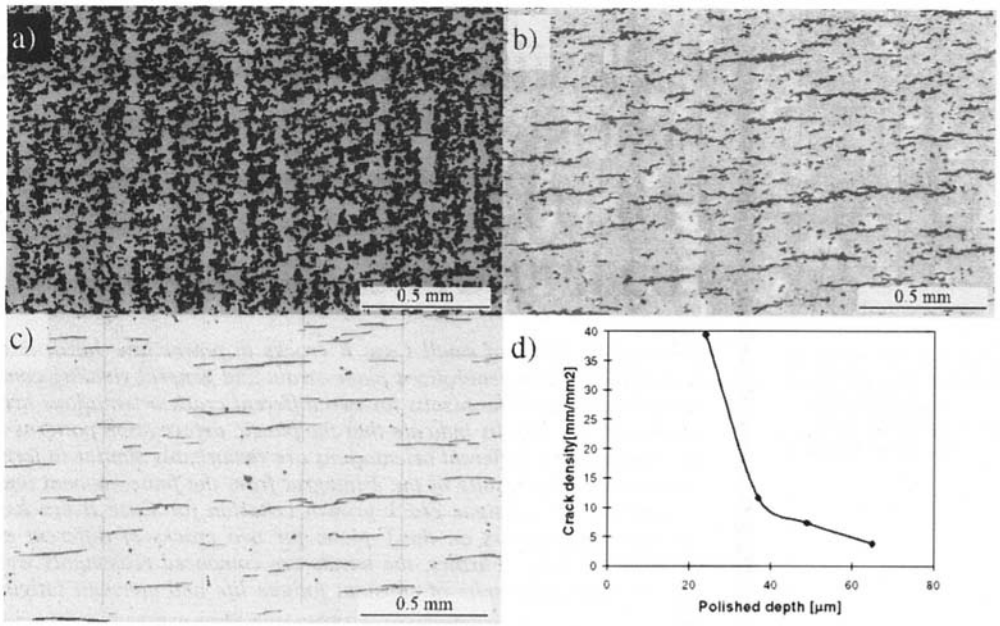

Fig. 7 Coated samples (*a*), (*b*), and (*c*) micrographs at 24 μm, 37 μm and 65 μm depth, respectively, and (*d*) crack density versus polished depth

Table 2 Crack density comparison between coated and uncoated sample

	Coated sample at 60 μm depth	Uncoated sample at surface
N cracks/mm^2	31.4	3 (16.5 spikes/mm^2)
cracks mm/mm^2	3.8	0.79

$$\left.\begin{aligned} N_{f,\text{coated}} \times \overline{\rho}_{\text{coated}} &= 3.8 \\ N_{f,\text{uncoated}} \times \overline{\rho}_{\text{uncoated}} &= 0.79 \end{aligned}\right\} \Rightarrow \frac{\overline{\rho}_{\text{coated}}}{\overline{\rho}_{\text{uncoated}}} = 13$$

In this case, the coating has produced 4.8 times more crack length in nearly a third of the time implying a mean crack generation ratio coated/uncoated of 13. This type of parameter should prove useful for comparing coatings on samples not tested to destruction.

Acknowledgments

The authors thank R. De Cat and F. W. de Haan for their work in test performance and software support. PKJ, MA and KMO thank the European Commission for funding under the Human Capital and Mobility Program. NIH image public domain software was used for image analysis.

References

Bain, K. R., 1985, "*The Effects of Coatings on the Thermal Mechanical Fatigue Life of a Single Crystal Turbine Blade Material,*" American Institute of Aeronautics and Astronautics, paper AIAA-85-1366.

Bressers, J., Estevas-Guilmain, J., De Cat, R., Knight, S., and Ridge, J., 1993, "An Automated Computer Vision System for Monitoring the Initiation and Growth of Microcracks," R. A. Ainsworth and R. P. Skelton, eds., *Behaviour of Defects at High Temperature,* ESIS 15, Mechanical Engineering Publications, London.

Bressers, J., Timm, J., Williams, S., Bennett, A., Affeldt, E., 1996, "Effects of Cycle Type and Coating on the TMF Lives of a Single Crystal Nickel-Based Gas Turbine Alloy," *Thermomechanical Fatigue Behavior of Materials,* M. J. Verrilli and M. J. Castelli, eds., ASME STP 1263, American Society for Testing and Materials, Philadelphia, pp. 82–95.

Christian, J. W., 1975, *The Theory of Transformation in Metals and Alloys,* Part I, second edition, Pergamon Press, Ltd, Oxford, England, p. 20.

Heine, J. E., Warren, J. R., and Cowles, B. A., 1986, "Thermal Mechanical Fatigue of Coated Blade Materials," Report WRDC-TR-89-4027, Wright Research Development Centre, Wright-Patterson Air Force Base, OH.

Johnson, P. K., and Bressers, J., 1996, "Characteristics of a Population of Naturally Initiated Cracks That Evolves During the Thermomechanical Fatigue Testing of SRR99," *Proceedings International Symposium on Fatigue Under Thermal and Mechanical Loading,* J. Bressers, L. Rémy, M. Steen, and J. L. Vallés, eds., Kluwer Academic Publisher, Boston, MA, pp. 315–320.

Ostolaza, K., Johnson, P. K., Arana, M., and Bressers, J., 1996, "Effect of the Cycle Type on the Damage of a Diffusion Aluminide Coating on a Ni-Based Monocrystalline Superalloy Tested Under TMF Conditions," *Proceedings of the III Iberical workshop in Fracture,* Luso (Portugal), Anales de la Mecánica de la Fractura, Vol. 13, pp. 297–292.

Wood, M. I., 1989, "Mechanical Interactions Between Coatings and Superalloys Under Conditions of Fatigue," *Surface and Coatings Technology,* Vol. 39/40, pp. 29–42.

Wright, P. K., 1988, "Oxidation-Fatigue Interactions in Single-Crystal Superalloy," *Low Cycle Fatigue,* ASTM STP 942, H. D. Solomon, G. R. Halford, L. B. Kaisan, and B. N. Leis, eds., American Society for Testing and Materials, Philadelphia, PA, pp. 558–575.

A Plastic Fracture Mechanics Analysis of Small Case B Fatigue Cracks Under Multiaxial Loading Conditions

Y. Wang

J. Pan

Center for Structural Durability Simulation,
Mechanical Engineering and
Applied Mechanics,
The University of Michigan,
Ann Arbor, MI 48109

The near-tip fields of small Case B cracks in power law, hardening materials are investigated under generalized plane-strain and general yielding conditions by finite element analyses. The results for two different crack orientations are examined and compared. The results indicate that the plastic deformation patterns near the tips of the cracks of two different orientations are remarkably similar in terms of the global coordinates. The results of the J-integral from the finite element analyses are used to correlate to a fatigue crack growth criterion for Case B cracks. The trends of constant ΔJ-contours on the Γ-plane for two cracks of different orientations are virtually the same. Further, the trends are compared reasonably well with those of the experimental results of constant fatigue life and constant fatigue crack growth rate.

Introduction

Based on the linear elastic fracture mechanics (LEFM), the stress intensity factor K has been extensively used to characterize fatigue crack growth. However, when small fatigue cracks are subject to general yielding conditions, the use of LEFM to model the fatigue processes becomes questionable. Therefore, nonlinear or elastic-plastic fracture mechanics concept based on the cyclic J-integral, ΔJ, has been used to correlate fatigue crack growth under general yielding conditions (Dowling and Begley, 1976; Dowling, 1977). The results of these correlations indicate that the crack growth rate can be characterized by ΔJ under general yielding conditions.

Brown and Miller (1973) proposed a multiaxial fatigue theory based on the physical interpretation of the mechanisms of fatigue crack growth. Their theory can be represented graphically by contours of constant fatigue life on the Γ-plane where the maximum shear strain $1/2\gamma^*$ is the abscissa and the normal strain ϵ_n^* on the maximum shear strain plane is the ordinate. The following two types of stage I fatigue cracks are proposed: Case A for cracks propagating along the surface and Case B for cracks propagating away from the surface.

Investigations of Case A cracks and Case B cracks at 45 deg inclined to the largest principal strain direction have been carried out by Wang and Pan (1996a, b). The results of Case A fatigue cracks suggest that the growth in the maximum shear strain direction is possibly the consequence of a crack growth criterion controlled by the maximum effective plastic strain of the near-tip strain fields. Also, the trend of constant J-contours on the Γ-plane is quite similar to that of the constant fatigue life contours for 1 percent Cr-Mo-V steel (Brown and Miller, 1979) and that of constant crack growth rate for Type 304 stainless steel at 550°C (Ogata et al., 1993). However, for Case B fatigue cracks, the results of the near-tip strain fields suggest that the crack should propagate into the specimen at about 30 deg inclined to the largest principal strain direction based on the Case A crack growth criterion. Nevertheless, for cracks at 45 deg inclined to the largest principal strain direction, the trend of constant J-contours on the Γ-plane is quite similar to those of the constant fatigue life contours for QT 35 steel and RR 58 aluminum alloy (Brown and Miller, 1973).

In this paper, we examine the near-tip fields of Case B cracks at 90 deg to the largest principal strain direction under generalized plane-strain and general yielding conditions, and compare the results with those for 45 deg cracks. We attempt to correlate the near-tip fields of the cracks to a criterion of fatigue crack growth under multiaxial loading conditions. Based on the concept of the characterization of fatigue crack growth by ΔJ we correlate the results of constant ΔJ for 90 deg cracks under different strain ratios to the experimental results of constant fatigue life for Case B cracks under multiaxial loading conditions.

Governing Equations

To examine the applicability of plastic fracture mechanics to low-cycle multiaxial fatigue theories, we here present an analysis based on a simple nonlinear material model. We consider a power-law hardening material with a uniaxial tensile stress-strain relation as

$$\frac{\epsilon}{\epsilon_0} = \alpha\left(\frac{\sigma}{\sigma_0}\right)^n, \tag{1}$$

where ϵ is the tensile strain, σ is the tensile stress, ϵ_0 and σ_0 are the reference strain and stress, respectively, α is a material constant, and n is the hardening exponent. When n is equal to 1, Eq. (1) represents a linear elastic material. When n approaches infinity, Eq. (1) gives a rigid-perfectly plastic behavior. However, the Ramberg–Osgood law is usually used to describe the nonlinear stress-strain behavior in uniaxial tension:

$$\frac{\epsilon}{\epsilon_0} = \frac{\sigma}{\sigma_0} + \alpha\left(\frac{\sigma}{\sigma_0}\right)^n. \tag{2}$$

The Ramberg–Osgood law can be generalized to multiaxial stress states. Within the context of the small-strain theory, the strains ϵ_{ij} can be written as the sum of an elastic part ϵ_{ij}^e and a plastic part ϵ_{ij}^p:

Contributed by the International Gas Turbine Institute and presented at the International Gas Turbine and Aeroengine Congress and Exhibition, Orlando, FL, June 2–5, 1997. Manuscript received by the ASME Headquarters March 7, 1997. Paper No. 97-GT-237. Associate Technical Editor: H. A. Kidd.

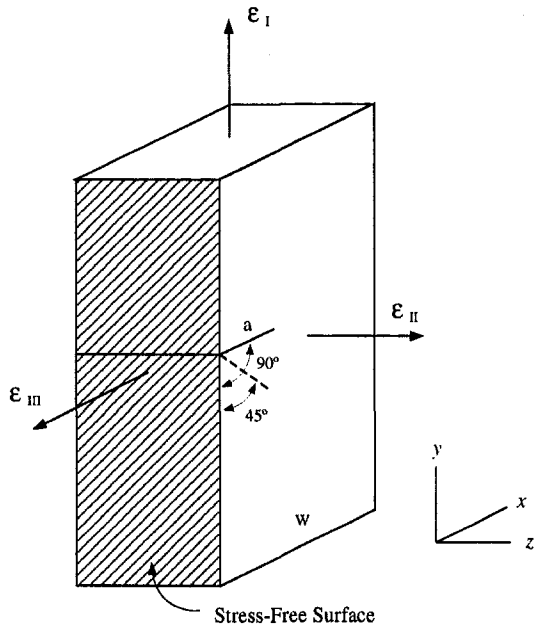

Fig. 1 An edge-cracked panel with a 90 deg crack subject to biaxial strains. The dashed line indicates a 45 deg crack considered by Wang and Pan (1996b).

$$\epsilon_{ij} = \epsilon^e_{ij} + \epsilon^p_{ij} \tag{3}$$

with

$$\epsilon^e_{ij} = \frac{1+\nu}{E} s_{ij} + \frac{1-2\nu}{3E} \sigma_{kk}\delta_{ij} \tag{4}$$

and

$$\epsilon^p_{ij} = \frac{3}{2} \alpha \left(\frac{\sigma_e}{\sigma_0}\right)^{n-1} \frac{s_{ij}}{\sigma_0}, \tag{5}$$

where ν is Poisson's ratio, E is Young's modulus, s_{ij} are the deviatoric stresses which are defined as $s_{ij} = \sigma_{ij} - 1/3\sigma_{kk}\delta_{ij}$, and $\sigma_e (= (3/2 s_{ij} s_{ij})^{1/2})$ is the effective stress. Here, i and j have a range of 1 to 3 and the summation convention is adopted for repeated indices. Also, the effective plastic strain ϵ_e is defined as $\epsilon_e = (2/3 \epsilon^p_{ij} \epsilon^p_{ij})^{1/2}$.

Finite Element Model

Metallographic observations of Parsons and Pascoe (Parsons and Pascoe, 1976) indicate that small fatigue cracks were initiated and propagated in the direction of maximum shear strain into the specimen at 45 deg away from the specimen surface under low cycle, plane-strain conditions. However, under other biaxial stressing conditions, small fatigue cracks were initiated in the direction of maximum shear strain into the specimen to the size of several grains (stage I crack propagation (Forsyth, 1961)). Then, the cracks were propagated normal to the largest principal strain direction (stage II crack propagation (Forsyth, 1961)). Based on the observations, we consider an edge-cracked panel under generalized plane strain conditions in the out-of-plane direction as shown in Fig. 1. We select a coordinate system such that the x and y-axes are the in-plane coordinates, and the z-axis is the out-of-plane coordinate. As shown in Fig. 1, the edge-cracked panel is subjected to biaxial strains in the y and z-directions. As shown in the figure, ϵ_I represents the largest principal strain, ϵ_{II} represents the second largest principal strain, and ϵ_{III} represents the third principal strain. The crack is assumed to be perpendicular to the largest principal strain direction as stage II Case B cracks. In the figure, a represents the crack length, and w represents the width of the panel. The strains ϵ_I and ϵ_{II} are applied by displacing the top surface and the lateral surface uniformly in the y and z-directions.

Figure 2 shows a finite element model of the generalized plane-strain crack problem. Here, eight-node quadrilateral elements are used. In the immediate crack-tip region, we have a ring of 32 wedge-shaped elements. Collapsed nodes are used for these wedge-shaped elements. The entire finite element model consists of 766 elements and 3955 nodes. In this study, we are interested in the near-tip fields of small cracks under general yielding conditions. Therefore, the ratio a/w is taken as small and practical as possible to ensure that the effect of the crack tip plasticity on the remote boundary is minimum. Here, the ratio a/w is taken as 0.02.

All our computations are performed using the finite element code ABAQUS (Version 5.4). We choose the Ramberg–Osgood material behavior to describe the material deformation plasticity behavior. We select $n = 3$ to represent high-hardening materials, $n = 10$ to represent low-hardening materials, and $n = 20$ to approximate perfectly plastic materials. Also, we select the material constants such that the elastic contribution becomes negligible when compared with the plastic contribution. Therefore, our solutions can be used to approximate those for pure power-law hardening materials.

Computational Results

For various combinations of the applied strains along the boundary, the near-tip stress and strain fields are investigated. To link our results with the existing multiaxial fatigue theories, we define a strain ratio ξ as the ratio of the out-of-plane constraint strain ϵ_{II} in the z-direction to the largest applied strain ϵ_I in the y-direction,

$$\xi = \frac{\epsilon_{II}}{\epsilon_I}. \tag{6}$$

In order to make connections to the existing multiaxial fatigue theories, we will present our results on the Γ-plane in terms of the normal strain on the maximum shear strain plane and the maximum shear strain, although we recognize that the crack planes do not coincide with the maximum shear strain planes for 90 deg cracks. We defined the slope s on the Γ-plane as the

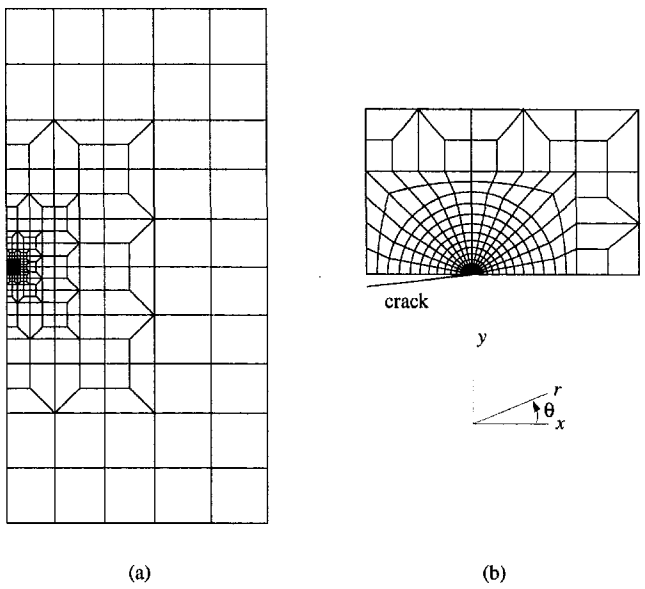

Fig. 2 (*a*) Finite element model for an edge-cracked panel; (*b*) finite element model of the near-tip region

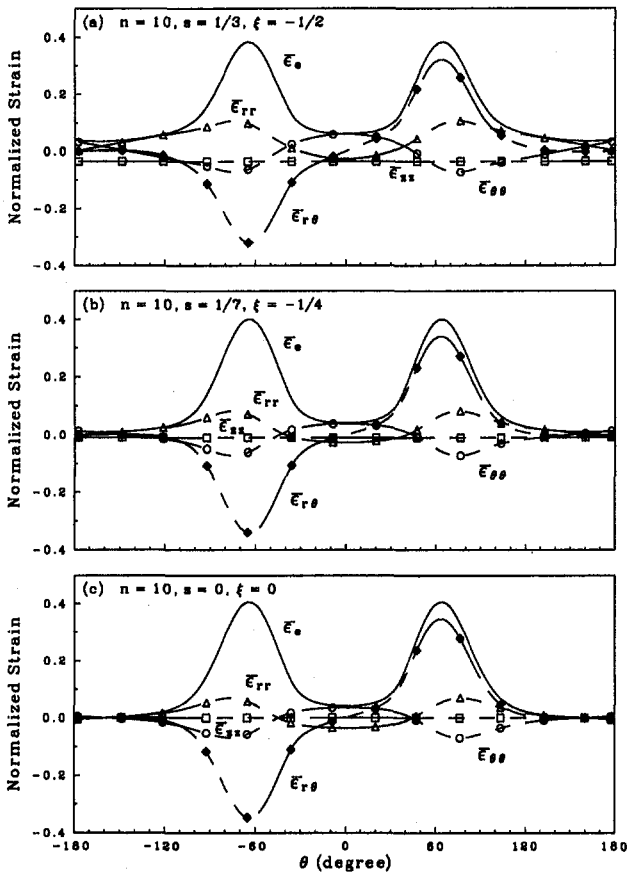

Fig. 3 The angular variations of the near-tip strains normalized by $\alpha\epsilon_0(J/\alpha\sigma_0\epsilon_0 r)^{n/(n+1)}$ at $r = 2J/\sigma_0$ for $n = 10$: (a) $\xi = -1/2$; (b) $\xi = -1/4$; and (c) $\xi = 0$

ratio of the normal strain ϵ_n^* on the maximum shear strain plane to the maximum shear strain $1/2\gamma^*$

$$s = \frac{\epsilon_n^*}{1/2\,\gamma^*}. \tag{7}$$

Note that the maximum shear strain occurs at the direction 45 deg from the ϵ_I direction toward the ϵ_{III} direction. Here, ϵ_{III} represents the normal strain in the direction perpendicular to the stress-free surface. Note that $\epsilon_I \geq \epsilon_{II} \geq \epsilon_{III}$ for Case B cracks. Therefore, $\epsilon_n^* = 1/2(\epsilon_I + \epsilon_{III})$ and $1/2\gamma^* = 1/2(\epsilon_I - \epsilon_{III})$. For example, if incompressibility is assumed, the ratio ξ is equal to $-1/2$, and the slope s is equal to $1/3$ under uniaxial tension. Under plane-strain conditions ($\epsilon_{II} = 0$), ξ and s are both equal to 0. Consequently, the range of ξ is between $-1/2$ (uniaxial tension) and 0 (plane strain) and s is between $1/3$ (uniaxial tension) and 0 (plane strain) for Case B cracks when incompressibility is assumed.

In our finite element computations, we set $\nu = 0.4999$, $\alpha = 1$, and $E/\sigma_0 = 1.0 \times 10^4$ in the Ramberg–Osgood constitutive law to approximate the behavior of pure power-law hardening materials. We consider three materials with the hardening exponent n equal to 3, 10, and 20. We also select three applied strain ratios corresponding to $\xi = -1/2$, $-1/4$, and 0 (or $s = 1/3$, $1/7$, and 0). A complete set of the near-tip stress and strain fields is presented in Wang (1997). Selected results will be shown here.

Figure 3 shows the angular variations of the near-tip strains normalized by $\alpha\epsilon_0(J/\alpha\sigma_0\epsilon_0 r)^{n/(n+1)}$ at the radial distance of $r = 2J/\sigma_0$ for $n = 10$ and $\xi = -1/2$, $-1/4$, and 0 (or $s = 1/3$, $1/7$, and 0). Here, the polar coordinates r and θ are centered at the crack tip, and $\theta = 0$ deg represents the crack line direction. Note again that for incompressible materials, $\xi = -1/2$ represents a uniaxial tension under generalized plane-strain conditions, $\xi = 0$ represents a plane-strain loading, and $\xi = -1/4$ represents an intermediate case. The common characteristic of the near-tip strain fields for different ξ's and different n's is that the maximum value of $\bar{\epsilon}_e$ is located at $\theta \approx \pm 60$ deg.

With the selection of $a/w = 0.02$ for the edge-cracked panel, the effect of the crack tip plasticity on the stress field of the remote boundary is shown to be minimum (Wang, 1997). Therefore, our computational results can be used to approximate the results for a/w approaching zero. In this case, the J-integral for pure power-law hardening materials, based on the Il'yushin theory (1946), can be expressed as

$$J = \alpha\epsilon_0\sigma_0 a H_I(\xi, n)\left(\frac{\epsilon_I}{\epsilon_0}\right)^{(n+1)/n} \tag{8}$$

or

$$J = \alpha\epsilon_0\sigma_0 a H_{II}(\xi, n)\left(\frac{\epsilon_{II}}{\epsilon_0}\right)^{(n+1)/n} \tag{9}$$

where H_I and H_{II} are dimensionless functions of the hardening exponent n and the strain ratio ξ. The above equations show that J is simply expressed as a function of the hardening exponent n, one of the remote applied strains, and the strain ratio ξ. The values of H_I and H_{II} as functions of ξ and n are listed in Wang (1997). Equations (8) and (9) are used later in this paper to develop the constant J-contours on the Γ-plane for characterization of Case B crack growth and fatigue life under multiaxial loading conditions.

Characterization of Low-Cycle Multiaxial Fatigue

When we consider the modeling of cracks in the length scale of a few grains, the microstructure of the material, such as the grain orientation, inclusions, voids, and precipitates along the grain boundary should be considered. Other factors such as the elastic and plastic anisotropy of the grains, the residual stresses due to manufacturing processes, and prior plastic deformation due to cyclic loading conditions should also be considered. In addition, crack closure under cyclic loading conditions should be considered, as indicated in Newman (1995). When the crack length and the size of plastic deformation associated with the tip become much larger than a few grain sizes, a continuum plasticity theory such the J_2 plasticity theory can be used to investigate the near-tip fields of these cracks.

Here, we make a few assumptions so that the crack-tip field obtained here can be used to correlate the fatigue life for Case B cracks. First, we assume that Case B cracks observed in experiments such as those in Parsons and Pascoe (1976) are noninteracting to each other. Then our small crack model can be applicable. When the interaction of multiple cracks needs to be considered, the boundary condition of the edge-cracked panel and the ratio a/w can be modified to reflect the interaction of the plasticity from the multiple crack tips.

Zheng and Liu (1986) argued that under low-cycle fatigue conditions stabilized stress-strain hysteresis loops occur due to the high cyclic strains experienced by the material elements near the propagating crack tip. Therefore, it is justified to use the cyclic stress-strain relation to calculate the crack-tip stress and strain fields. They further argued that under completely reversed cyclic loads the tensile half of the hysteresis loop (ABC), as shown in Fig. 4, causes the crack to open and grow. It is then justified to make a monotonic loading calculation for the cyclic crack-tip stress and strain fields.

It is well known that surface fatigue cracks are initiated by extrusion and intrusion processes under cyclic loading conditions. The slip processes occur on the most favorable crystallographic planes where the magnitudes of the resolved shear

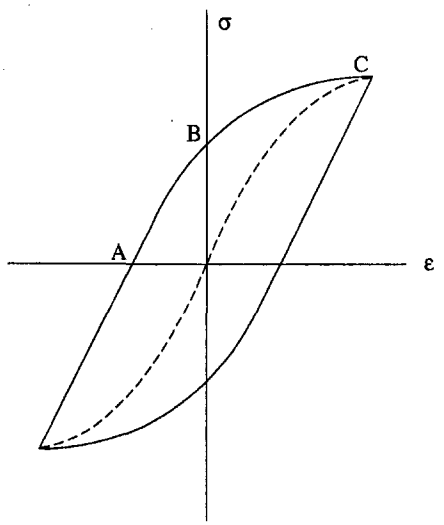

Fig. 4 A stabilized cyclic stress-strain curve

stresses are possibly the largest. From the viewpoint of a two-dimensional crystal model, the orientation of the fatigue cracks should be 45 deg inclined to the largest principal stress direction. However, due to the discreteness nature of available slip planes and directions in each grain, the surface fatigue crack planes maybe more or less appear to be 45 deg inclined to the largest principal stress direction in those grains with favorable slip planes and directions for extrusion and intrusion processes. Therefore, fatigue cracks with crack planes 45 deg inclined to the largest principal stress direction seem to be a good starting point for studying stage I Case B fatigue cracks as in Wang and Pan (1996b). However, after the stage I cracks grow into the material to the size of several grains, they change to stage II cracks with crack planes perpendicular to the largest principal strain direction.

If a crack propagates in the same direction under a quite large number of cyclic loads under low-cycle fatigue conditions, certain self-similar condition or steady-state condition may prevail near the tip. If stabilized stress-strain hysteresis loops of the material elements occur near the propagating crack tip, the near-tip fields that we obtained for the deformation plasticity materials should shed some light on the mechanics of fatigue

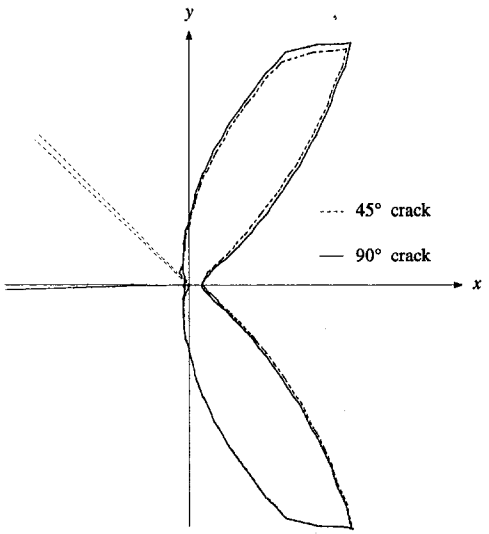

Fig. 5 The effective plastic strain contours at $\epsilon_e = 0.125$ for $n = 20$ under $\epsilon_I = 0.012$ and $\epsilon_{II} = 0$. The solid line represents the results for the 90 deg crack and the dashed line represents the results for the 45 deg crack.

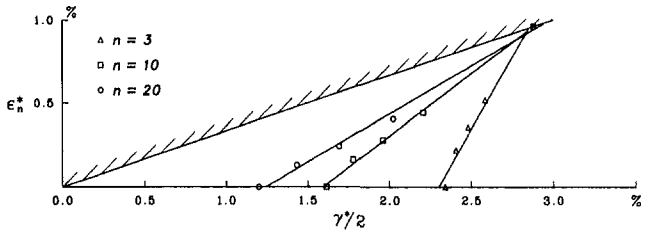

Fig. 6 The constant J contours on the Γ-plane. The solid straight lines represent the fitted results based on Eq. (10).

crack propagation. As shown in Fig. 3, the maximum value of the normalized near-tip effective plastic strain $\bar{\epsilon}_e$ is located near $\theta = \pm 60$ deg for different ξ's. If we argue that the crack growth direction is controlled by the maximum value of the effective plastic strain ϵ_e as for Case A cracks, then Case B cracks should be oriented at 30 deg inclined to the largest principal strain direction and this leads to a conflict with the experimental observations of both stage I and stage II Case B cracks (Brown and Miller, 1973; parsons and Pascoe, 1976). At this point, we may argue that stage I cracks and their orientations must depend on the local material properties which cannot be characterized well by the J_2 plasticity theory that we use here.

We have examined the results for the cracks oriented at 45 deg and 90 deg inclined to the largest principal strain direction in Wang and Pan (1996b) and in this investigation. We have found that the maximum effective plastic strain directions in terms of the global coordinates (x, y, and z) are almost independent of the crack orientation for both 45 deg and 90 deg cracks. Figure 5 shows the effective plastic strain contours at $\epsilon_e = 0.125$ for a 45 deg and a 90 deg crack under $\epsilon_I = 0.012$ and $\epsilon_{II} = 0$. The effective plastic strain contours for the two cracks are remarkably similar.

In order to correlate the J-integral and the fatigue life under multiaxial loading conditions, we plot constant J-contours, marked by symbols, for $n = 3$, 10, and 20 on the Γ-plane in Fig. 6. Note that the constant fatigue life contours for several metals were plotted on the Γ-plane in Brown and Miller (1973). Since we are working with pure power-law hardening materials, the constant J-curves on the Γ-plane are self-similar. Our results can be fitted by a linear equation

$$\frac{1/2\gamma^*}{A} - \frac{\epsilon_n^*}{B} = 1, \tag{10}$$

where A and B are constants. Table 1 lists the values of A and B for $n = 3$, 10, and 20. The fitted results based on Eq. (10) are also shown as the solid straight lines in Fig. 6. The trends of these straight lines in Fig. 6 are similar to those of constant fatigue life obtained from experiments for QT 35 steel and RR 58 aluminum alloy (Brown and Miller, 1973). As listed in Table 1, as n increases, the ratio B/A (i.e., the slope of the fitted curve) decreases, and, consequently, the effect of ϵ_n^* on fatigue life increases. We have also compared the results for 90 deg cracks with those for 45 deg cracks in Wang and Pan (1996b) under the same loading conditions. We have found that the J-values for the 90 deg cracks are larger than those for 45 deg cracks by about 40 percent. This suggests that after small Case B cracks are initiated at 45 deg inclined to the

Table 1 Values of A and B for $n = 3$, 10, and 20 for the constant J contours shown in Fig. 6

n	A	B	B/A
3	0.02301	0.03975	1.728
10	0.01593	0.01187	0.7449
20	0.01241	0.007125	0.5739

largest principal strain direction due to extrusion and intrusion processes, the Case B cracks should change their orientations to that perpendicular to the largest principal strain directions. Also, we have found that the constant ΔJ-contours for cracks of different orientations have the same trend for each n.

Conclusions

A small crack model is proposed to investigate low-cycle fatigue under multiaxial loading conditions. We first present some representative results of the near-tip strain fields for cracks in power-law hardening materials under generalized plane-strain and general yielding conditions. The results for cracks of two different orientations show that the maximum effective plastic strain contours are almost independent of the crack orientation for Case B fatigue cracks. Also, constant ΔJ-contours on the Γ-plane have the same trends for cracks of different orientations. In addition, the trends of constant ΔJ-contours on the Γ-plane for cracks of different orientations are quite similar to those of the constant fatigue life contours for QT 35 steel and RR 58 aluminum alloy (Brown and Miller, 1973).

References

Brown, M. W., and Miller, K. J., 1973, "A Theory for Fatigue Failure Under Multiaxial Stress-Strain Conditions," *Proceedings of Institution of Mechanical Engineers,* Vol. 187, pp. 745–755.

Brown, M. W., and Miller, K. J., 1979, "High Temperature Low Cycle Biaxial Fatigue of Two Steels," *Fatigue of Engineering Materials and Structures,* Vol. 1, pp. 217–229.

Dowling, N. E., and Begley, J. A., 1976, "Fatigue Crack Growth During Gross Plasticity and the *J*-Integral," *Mechanics of Crack Growth,* ASTM STP 590, pp. 82–103.

Dowling, N. E., 1977, "Crack Growth During Low-Cycle Fatigue of Smooth Axial Specimens," *Mechanics of Crack Growth,* ASTM STP 637, pp. 97–121.

Forsyth, P. J. E., 1961, "A Two Stage Process of Fatigue Crack Growth," *Proceedings of Crack Propagation Symposium,* Cranfield, pp. 76–94.

Il'yushin, A. A., 1946, "The Theory of Small Elastic-Plastic Deformations," *Prikadnaia Matematika i Mekhanika,* PMM, Vol. 10, pp. 347–356.

Newman, J. C., Jr., 1995, "Fatigue-Life Prediction Methodology Using a Crack-Closure Model," *Journal of Engineering Materials and Technology,* Vol. 117, pp. 433–439.

Ogata, T., Nitta, A., and Blass, J. J., 1993, "Propagation Behavior of Small Cracks in 304 Stainless Steel Under Biaxial Low-Cycle Fatigue at Elevated Temperature," *Advances in Multiaxial Fatigue,* ASTM STP 1191, pp. 313–325.

Parsons, M. W., and Pascoe, K. J., 1976, "Observations of the Surface Deformation, Crack Initiation and Crack Growth in Low-Cycle Fatigue under Biaxial Stress," *Materials Science and Engineering,* Vol. 22, pp. 31–50.

Wang, Y., and Pan, J., 1996a, "Characterization of Low-Cycle Multiaxial Fatigue by a Plastic Fracture Mechanics Model," *Fatigue and Fracture—1996, Volume 1,* PVP-Vol. 323, ASME, New York, pp. 317–322.

Wang, Y., and Pan, J., 1996b, "Mixed-Mode Crack-Tip Fields Under General Yielding Conditions and Implications to Low-Cycle Multiaxial Fatigue Theory," *1996 International Mechanical Engineering Congress and Exposition,* J. C. I. Chang, et al., eds., ASME, New York, pp. 269–279.

Wang, Y., 1997, "Mixed-Mode Fracture in Ductile Materials and Low-Cycle Multiaxial Fatigue Theory, Ph.D. thesis, The University of Michigan, Ann Arbor, MI.

Zheng, M., and Liu, H. W., 1986, "Fatigue Crack Growth under General-Yielding Cyclic-Loading," *Journal of Engineering Materials and Technology,* Vol. 108, pp. 201–205.

Theory and Methodology of Optimally Measuring Vibratory Strains in Closely Spaced Modes

M.-T. Yang

J. H. Griffin

Carnegie Mellon University,
Department of Mechanical Engineering,
Pittsburgh, PA 15213

Stress ratios are traditionally used to infer maximum stresses in blades from strain measurements. This method may not be applicable to all the modes of modern low aspect ratio (LAR) blades since LAR blades often have high frequency "tip" modes that are so closely spaced that slight changes in structural properties can cause significant mode shape changes. In this paper, it is first shown that the actual tip modes of a LAR blade can be well approximated as linear combinations of the "nominal" modes. The stress field of the blade can then be estimated by calculating the modal content from multiple strain measurements. However, since placement and gage inaccuracies can introduce significant errors in the calculation, it is necessary to find the optimal gage placement that minimizes the error in estimated stresses. An error estimate using "norms" and an efficient optimization method are developed for this purpose.

1 Introduction

Stress ratios and strain gage measurements are frequently used to infer the maximum stress in a vibrating blade. The "stress ratio" for a mode of vibration is usually defined as the ratio of the maximum vibratory stress in the blade to the strain measured at the gage location, multiplied by Young's modulus. The stress ratio is determined from either a finite element analysis of the nominal blade geometry or from laboratory tests and, once determined, is often assumed to be a property that is the same for all blades on the disk. This is a valid assumption if the natural frequency of the mode is well isolated from those of neighboring modes. Modern, low aspect ratio fan and compressor blades behave more like plates than beams, and usually have pairs of chordwise, "tip" modes with nearly identical frequencies. When a blade has two modes with nearly the same natural frequencies, the corresponding modes can interact (Yang and Griffin, 1996), and the actual mode shapes can be highly sensitive to small geometric variations that occur during the manufacturing process. As a result, the "stress ratio" for these modes can vary significantly from blade to blade, and a single stress ratio no longer provides an accurate method for estimating the maximum stress.

A familiar example of closely spaced modes that illustrates the physics associated with the problem is when the frequency of a primarily bending mode is slightly higher than the frequency of a torsional mode. If a parametric study is conducted in which the chord of the blade is increased, it is found that the torsional frequency will tend to increase and, under casual examination, appear to cross the frequency of the bending mode. In fact, under closer inspection one finds that, because the blade is asymmetric (Kim and Griffin, 1994), the frequencies do not cross but veer away from each other. In the veering region, both modes will contain different combinations of the original bending and torsional mode shapes. As the chord of the blade is increased even further, the frequencies emerge from the veering region and the mode shapes have completely switched. This paper focuses on identifying the modal content of modes in the veering region since in this case small changes in the blade's geometry due to manufacturing variations can significantly affect their mode shapes.

This paper is organized so as to explain the five concepts that are needed in order to develop a methodology for optimally determining the maximum stress in the case of closely spaced modes. The first is that "nominal" mode shapes from any blade with a representative geometry can be used as a basis for representing the mode shapes in the actual blades. As a result, more than one strain gage measurement must be made on a blade and the resulting information is used to determine the proportions of the "nominal modes" that constitute the modal response in the actual blade. The second concept is associated with establishing how many modes can interact in this manner. LAR blades have such high modal density that three or even four nominal modes might be needed as a basis. These two concepts are presented in section 2.

A problem that arises in implementing this approach is in choosing where to place the strain gages since the actual mode shape can be any combination of two or more nominal modes. The approach presented here is to choose the gage locations so as to minimize the error in the estimate of the maximum stress. Thus, the three remaining concepts are associated with the formulation and development of the optimization problem. In section 3, expressions are developed for the error in the stress caused by placement or gage errors. In section 4, the development of an efficient optimization problem is presented. The approach is illustrated in section 5 using an example from a representative compressor blade. It was found that the standard optimization algorithms for obtaining the optimum gage locations were relatively slow, thus the last concept involves the introduction of a simple, relatively efficient optimization scheme that makes the approach easier to implement.

2 Representing the Response in Terms of Nominal Modes

This section deals with the first two concepts developed in this paper. Namely, that the mode shapes in actual blades can be represented as a sum of nominal modes from a representative geometry, and that the number of modes that can interact can be determined from the spacing of the nominal frequencies and the amount of variation in the modal properties of the blade.

2.1 Blade Modes Can be Represented as a Sum of Nominal Modes. In order to motivate this section, consider the following example of the differences in closely spaced tip

Contributed by the International Gas Turbine Institute and presented at the International Gas Turbine and Aeroengine Congress and Exhibition, Orlando, FL, June 2–5, 1997. Manuscript received by the ASME Headquarters March 7, 1997. Paper No. 97-GT-238. Associate Technical Editor: H. A. Kidd.

modes as seen in two nominally identical blades. Figure 1 shows the mode shapes for the two blades that were computed using slightly different finite element models based on their carefully measured geometries. The modes are quite close together, the frequency difference being about 1 percent. It is clear that the modes for the two blades individually look very different. However, it is clear from even casual observation that each of the modes of blade B has some of the attributes of both of the modes of blade A. In fact, the modes of either blade could be used as a basis to represent the modes of the other blade. The mathematical reason for this result is explained by the following perturbation analysis.

Assume that the "nominal modes" satisfy the structural eigenvalue problem:

$$\mathbf{K}\vec{\phi}_j = \lambda_j \mathbf{M}\vec{\phi}_j \quad j = 1, 2, \ldots, n, \tag{1}$$

where $\mathbf{K}$ and $\mathbf{M}$ are the stiffness and mass matrices of a blade of the nominal geometry[1]. λ_j and $\vec{\phi}_j$ are the eigenvalue and eigenvector associated with the jth mode, and n is the number of degrees of freedom of the system. Similarly, for a manufactured blade, the governing equation can be written as

$$\mathbf{K}'\vec{\phi}_j' = \lambda_j' \mathbf{M}'\vec{\phi}_j' \quad j = 1, 2, \ldots, n, \tag{2}$$

where $\mathbf{K}'$ and $\mathbf{M}'$ are the slightly perturbed stiffness and mass matrices for the actual blade, and λ_j' and $\vec{\phi}_j'$ are the eigenvalue and eigenvector associated with the jth perturbed mode. Assuming perturbations of order δ, where δ is small, the perturbed quantities can be written as

$$\mathbf{K}' = \mathbf{K} + \delta\mathbf{K}^{(1)} + \delta^2\mathbf{K}^{(2)} + \ldots \tag{3}$$

$$\mathbf{M}' = \mathbf{M} + \delta\mathbf{M}^{(1)} + \delta^2\mathbf{M}^{(2)} + \ldots \tag{4}$$

$$\lambda_j' = \lambda_j + \delta\lambda_j^{(1)} + \delta^2\lambda_j^{(2)} + \ldots \quad j = 1, 2, \ldots, n \tag{5}$$

$$\vec{\phi}_j' = \vec{\phi}_j + \delta\vec{\phi}_j^{(1)} + \delta^2\vec{\phi}_j^{(2)} + \ldots \quad j = 1, 2, \ldots, n \tag{6}$$

Substituting (3) through (6) into (2), and equating terms of the same order give the standard results (Meirovitch, 1980)

$$\lambda_j^{(1)} = \frac{\vec{\phi}_j^T(\mathbf{K}^{(1)} - \lambda_j\mathbf{M}^{(1)})\vec{\phi}_j}{\vec{\phi}_j^T\mathbf{M}\vec{\phi}_j} \tag{7}$$

$$\vec{\phi}_j^{(1)} = \sum_{i\neq j} \alpha_{ji}^{(1)}\vec{\phi}_i, \tag{8}$$

where

$$\alpha_{ji}^{(1)} = \frac{\vec{\phi}_i^T(\mathbf{K}^{(1)} - \lambda_j\mathbf{M}^{(1)})\vec{\phi}_j}{(\lambda_j - \lambda_i)\vec{\phi}_i^T\mathbf{M}\vec{\phi}_i} \quad i \neq j. \tag{9}$$

Equations (8) and (9) imply that, when the unperturbed eigenvalues λ_i and λ_j are well separated, $\vec{\phi}_j^{(1)}$ is of order 1, and the change in the mode shape is small if δ is small. However, when the separation between the eigenvalues is also small (i.e., of order δ), then (9) suggests that $\vec{\phi}_j^{(1)}$ becomes of order $1/\delta$, and the overall change in the mode shape is of order 1. To be more precise, suppose all of the eigenvalues of the unperturbed system are separated by order 1 except for the q clustered eigenvalues $\lambda_{r+1}, \lambda_{r+2}, \ldots$, and λ_{r+q} that are separated by order δ. Then it can be shown (Wu et al., 1995) that $\vec{\phi}_j'$ have the form

$$\vec{\phi}_j' = \begin{cases} \vec{\phi}_j^{(0)} + \delta\vec{\phi}_j^{(1)} + \delta^2\vec{\phi}_j^{(2)} + \ldots \\ \qquad\qquad \text{for } j = r+1, \ldots, r+q \\ \vec{\phi}_j + \delta\vec{\phi}_j^{(1)} + \delta^2\vec{\phi}_j^{(2)} + \ldots \quad \text{otherwise,} \end{cases} \tag{10}$$

where

[1] Typically, the nominal geometry is either taken from the designer's drawings or may represent the average geometry as measured on a set of manufactured blades.

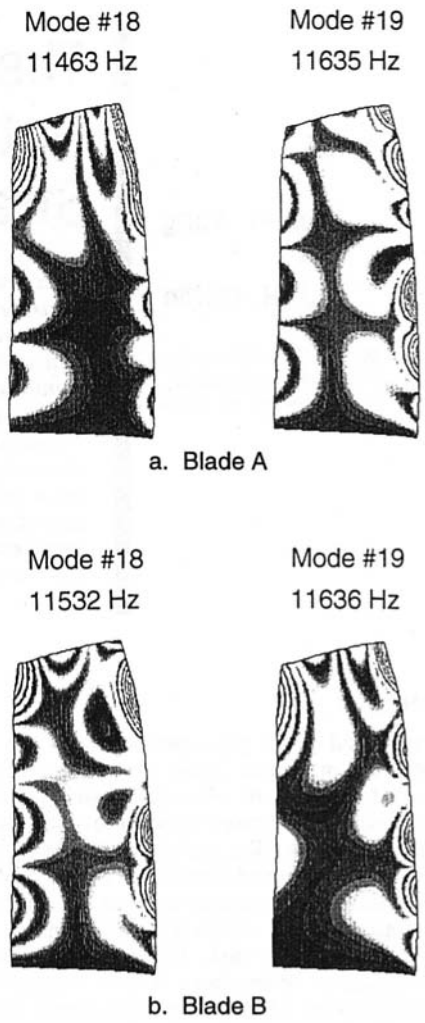

Fig. 1 Tip modes of two blades with slightly different geometries

$$\vec{\phi}_j^{(0)} = \sum_{i=r+1}^{r+q} \alpha_{ji}^{(0)}\vec{\phi}_i \quad j = r+1, \ldots, r+q. \tag{11}$$

The $\alpha_{ji}^{(0)}$ are quantities of order 1 that can be determined for specific cases using standard perturbation methods, for example, Yang and Griffin (1996). In summary then, (10) and (11) confirm that when the geometry is slightly perturbed there can be significant mode shape changes (order 1) if the modes are closely spaced and that in this case the perturbed modes can be approximated as a linear combination of the unperturbed closely spaced modes. In terms of modal strains (10) and (11) imply

$$\epsilon_i'(\vec{y}) = \begin{cases} c_{ii}\epsilon_i(\vec{y}) + O(\delta) & \text{for distinct modes} \\ \sum_{j=r+1}^{r+q} c_{ij}\epsilon_j(\vec{y}) + O(\delta) & \text{for closely spaced modes,} \end{cases} \tag{12}$$

where $\vec{y}$ denotes the location and orientation, ϵ_i' is the strain of the ith perturbed mode, c_{ij} is a coefficient that specifies the amount of the jth unperturbed mode in the ith perturbed mode, and ϵ_j is the strain associated with the jth unperturbed mode. Dropping the i subscript for simplicity, the second equation can be written

$$\epsilon'(\vec{y}) = \sum_{j=r+1}^{r+q} c_j\epsilon_j(\vec{y}) + O(\delta) \text{ for closely spaced modes.} \tag{13}$$

2.2 The Number of Modes Required for a Basis. The number of nominal modes required for a basis is the number of closely spaced modes that can interact. This number depends on the closeness of the frequencies and the statistical variation that occurs in the modal properties. This problem was investigated in an earlier paper by the authors (Yang and Griffin, 1996). This subsection briefly summarizes the key results from that earlier paper.

It was found that determining whether modes would interact could be established by considering two modes at a time. Two modes would not interact if the fractional frequency difference of the nominal modes was sufficiently large. Specifically, two modes would not interact if

$$\frac{\Delta f}{\bar{f}} > \frac{\sigma(k_{ij} - m_{ij})}{2\sigma(\alpha_{ij})_{\text{allowable}}},$$

where $\sigma(\cdot)$ denotes a standard deviation, Δf is the frequency difference, $\bar{f}$ is the mean frequency, and k_{ij} and m_{ij} are parameters associated with ith and jth modes in the normalized modal stiffness and mass matrices. The term α_{ij} is the modal contribution from ith unperturbed mode to jth perturbed mode.

The standard deviation in the modal parameters can be calculated using a finite element program, and the method described in the referenced paper if the variations in the geometries of manufactured blades are carefully measured for a particular blade design. For example, it was found by the authors that, for a representative LAR compressor blade, all values of $\sigma(k_{ij} - m_{ij})$ for the first thirty modes were less than 0.005. If the allowable standard deviation of modal interaction

$$\sigma(\alpha_{ij})_{\text{allowable}}$$

is 5 percent, then two modes would not significantly interact if their frequency difference is greater than 5 percent. Consequently, for this blade, a mode calculated from the nominal geometry with a frequency that is separated from its neighbors by more than 5 percent can be treated as an isolated mode and a single stress ratio can be used to interpret strain gage data. Alternatively, if a mode is not isolated then all nominal modes within 5 percent of its frequency must be used as a basis in determining its behavior.

3 Determining the Error in the Estimate of Maximum Stress

In the case of closely spaced modes, the mode shape in the actual blade is unknown except for the fact that it is some linear combination of the closely spaced nominal modes. The goal of the measurements is to determine the amount of each constitutive mode present, and use the information to calculate the maximum stress in the blade. Consequently, the objective of the optimization process is to place the strain gages so that any errors in the strain measurements have a minimal effect on the calculation of the maximum stress.

First, a procedure will be described for calculating the maximum stress in the blade under the assumption that there are no strain gage errors. The resulting equations will then be used to establish expressions for the error in the maximum stress that results when measurement errors are introduced.

3.1 Expressions for the Maximum Stress. From (13), it is clear that strain measurements at multiple points on the actual (perturbed) blade have to be taken in order to resolve the modal content of the perturbed mode, i.e., determine c_j by solving the equations,

$$\epsilon'(\vec{x}_i) = \sum_{j=r+1}^{r+q} c_j \epsilon_j(\vec{x}_i) \quad i = 1, 2, \ldots, m, \tag{14}$$

where $\vec{x}_i$ represents the location and orientation of the ith gage, and m is the number of gages. Terms of Order δ are small and have been dropped. (They could be treated in a manner similar to gage errors as described in the following sections.) Alternatively, (14) can be recast in a matrix form

$$\vec{\epsilon}'(\vec{x}) = \mathbf{E}(\vec{x})\vec{c}, \tag{15}$$

where

$$\vec{x} = [\vec{x}_1^T, \vec{x}_2^T, \ldots, \vec{x}_m^T]^T \tag{16}$$

$$\vec{\epsilon}'(\vec{x}) = [\epsilon'(\vec{x}_1), \epsilon'(\vec{x}_2), \ldots, \epsilon'(\vec{x}_m)]^T \tag{17}$$

$$\mathbf{E}(\vec{x}) = \begin{bmatrix} \epsilon_{r+1}(\vec{x}_1) & \cdots & \epsilon_{r+q}(\vec{x}_1) \\ \vdots & \ddots & \vdots \\ \epsilon_{r+1}(\vec{x}_m) & \cdots & \epsilon_{r+q}(\vec{x}_m) \end{bmatrix} \tag{18}$$

$$\vec{c} = [c_{r+1}, c_{r+2}, \ldots, c_{r+q}]^T. \tag{19}$$

From (15), the least square fit solution for $\vec{c}$ is

$$\vec{c} = \mathbf{E}^+(\vec{x})\vec{\epsilon}'(\vec{x}), \tag{20}$$

where $m \geq q$ and $\mathbf{E}^+$ is the generalized inverse of $\mathbf{E}$ (Ben-Israel and Greville, 1974) with the following expression:

$$\mathbf{E}^+ = (\mathbf{E}^T\mathbf{E})^{-1}\mathbf{E}^T. \tag{21}$$

For the ideal case in which there are no measurement errors, (20) simply provides an exact solution. Notice that, when $m = q$, $\mathbf{E}^+$ will simply become $\mathbf{E}^{-1}$.

Now, once the modal content $\vec{c}$ is known, the stress at any location and orientation $\vec{y}$ can be readily calculated:

$$\sigma'(\vec{y}) = \sum_{j=r+1}^{r+q} c_j \sigma_j(\vec{y}), \tag{22}$$

where σ' is the stress of the perturbed mode, and σ_j is the modal stress associated with the jth unperturbed mode. Writing (22) in a matrix form,

$$\sigma'(\vec{y}) = \vec{\sigma}^T(\vec{y})\vec{c}, \tag{23}$$

where

$$\vec{\sigma}(\vec{y}) = [\sigma_{r+1}(\vec{y}), \sigma_{r+2}(\vec{y}), \ldots, \sigma_{r+q}(\vec{y})]^T. \tag{24}$$

Substituting (20) into (23), the stress of the perturbed mode for a given location and orientation $\vec{y}$ is

$$\sigma'(\vec{y}) = \vec{\sigma}^T(\vec{y})\mathbf{E}^+(\vec{x})\vec{\epsilon}'(\vec{x}). \tag{25}$$

Thus, given strain measurements of the perturbed mode from m gages ($\vec{\epsilon}'$) and the strains of the q unperturbed modes corresponding to the gage locations and orientations ($\mathbf{E}$), (25) calculates the modal stress of the perturbed mode. However, if the gage placements are poorly chosen, the inaccuracies in placements and gages can be significantly magnified. In the following sections, an error estimate will be developed from (25) so that the optimal placements for gages can be found by minimizing the error in the modal stresses.

3.2 Stress Errors Caused by Measurement Errors. The errors in strain measurements $\Delta\vec{\epsilon}'$ are caused by gage placement errors $\Delta\vec{x}$ and gage errors $\Delta\vec{g}$. According to (15), they have the following relation:

$$\vec{\epsilon}'(\vec{x}) + \Delta\vec{\epsilon}' = \mathbf{E}(\vec{x} + \Delta\vec{x})\vec{c} + \Delta\vec{g}. \tag{26}$$

However, since $\Delta\vec{x}$ and $\Delta\vec{g}$ are not known when the strains are measured, (15) is used to infer the modal content under the assumption that there are no measurement errors. As a result, all of the measurement errors generate an error in the modal content $\Delta\vec{c}$ where

$$\vec{\epsilon}'(\vec{x}) + \Delta\vec{\epsilon}' = \mathbf{E}(\vec{x})(\vec{c} + \Delta\vec{c}). \quad (27)$$

By equating the right-hand side of (26) and (27) and solving for $\Delta\vec{c}$,

$$\Delta\vec{c} = \mathbf{E}^{+}(\vec{x})\{[\mathbf{E}(\vec{x} + \Delta\vec{x}) - \mathbf{E}(\vec{x})]\vec{c} + \Delta\vec{g}\}. \quad (28)$$

Equation (28) provides an error estimate for the modal content. Now, since (23) with errors can be written as

$$\sigma'(\vec{y}) + \Delta\sigma' = \vec{\sigma}^{T}(\vec{y})(\vec{c} + \Delta\vec{c}), \quad (29)$$

where $\Delta\sigma'$ is the error in the stress of the perturbed mode. Subtracting (23) from (29) implies

$$\Delta\sigma' = \vec{\sigma}^{T}(\vec{y})\Delta\vec{c}. \quad (30)$$

Substituting (28) into (30) implies

$$\Delta\sigma' = \vec{\sigma}^{T}(\vec{y})\mathbf{E}^{+}(\vec{x})\{[\mathbf{E}(\vec{x} + \Delta\vec{x}) - \mathbf{E}(\vec{x})]\vec{c} + \Delta\vec{g}\}. \quad (31)$$

Equation (31) is the error estimate for the calculated stress of the perturbed mode in terms of gage placement error and gage error.

4 Optimization Problem

4.1 Statement of the Problem. An initial statement of the optimization problem would be to choose the placement of the gages $\vec{x}$ so as to minimize the error in the maximum stress as determined by Eq. (31). The optimization process would have to consider all possible values of $\vec{c}$, $\vec{x}$, $\Delta\vec{x}$, and $\Delta\vec{g}$. Further complications are that the maximum stress location $\vec{y}_{\max}$ would change with the modal content $\vec{c}$ and that the gage error could be a nonlinear function of strain, which in turn is a function of the gage location and the modal content. Consequently, this initial statement of the optimization problem is too complex and would result in prohibitive computational costs. Thus, a number of simplifications are introduced to make the problem tractable and provide a practical engineering solution.

4.2 Linearized Strain Gage Error. Strain gage error is, in general, a nonlinear function of strain. One reason for this is that there is a threshold value of strain below which it is difficult to measure. In addition, there will be an error in the calibration constant of the gage that results in an error proportional to the strain. Thus, the gage error might be approximated by a bi-linear curve as depicted in Fig. 2(a). The nonlinear nature of the error makes the optimization process far more costly. From a practical point of view, the threshold error means that gages should not be placed in areas of low stress since the percentage error in the measurements would be large. The approach used in this paper is to assume that the strain gage error is linear (Fig. 2(b)) and to have a separate optimization criterion that the strain gages will not be placed in low strain areas, i.e., candidate strain gage locations must satisfy the condition that

$$\frac{\text{modal strain}}{\text{maximum modal strain}} > \beta \quad (32)$$

for all constituent modes, where β, the cutoff ratio, is less than 1, and is specified by the user. Assume $\Delta\vec{g}$ is linear in $\vec{\epsilon}'$ over the range of interest, then

$$\Delta\vec{g} \equiv \Delta\mathbf{G}\vec{\epsilon}', \quad (33)$$

where $\Delta\mathbf{G} = \text{diag}\ (\Delta G_1, \Delta G_2, \ldots, \Delta G_m)$, and ΔG_i is the ratio of the gage error to the actual strain at the ith gage. Then, by substituting (15) in (33) and including the placement error $\Delta\vec{x}$, the following relationship is obtained:

$$\Delta\vec{g} = \Delta\mathbf{G}\mathbf{E}(\vec{x} + \Delta\vec{x})\vec{\mathbf{c}}. \quad (34)$$

Substituting (34) in (31), implies

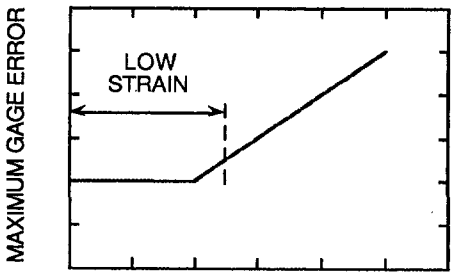

a. Approximated by a bilinear curve

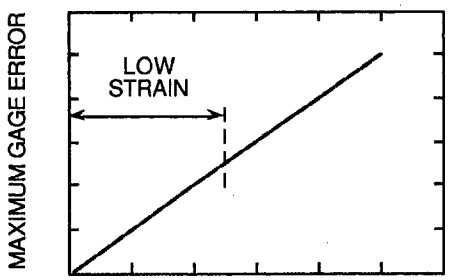

b. Approximated by a straight line

Fig. 2 Maximum gage error as a function of measured strain

$$\Delta\sigma' = \vec{\sigma}^{T}(\vec{y})\mathbf{E}^{+}(\vec{x})[\mathbf{E}(\vec{x} + \Delta\vec{x}) - \mathbf{E}(\vec{x}) + \Delta\mathbf{G}\mathbf{E}(\vec{x} + \Delta\vec{x})]\vec{c}. \quad (35)$$

The advantage of using (35) instead of (31) is that the magnitude of $\vec{c}$ can be eliminated from the simulation and only the "orientation" of $\vec{c}$ needs to be considered.

4.3 Use a Matrix Norm to Minimize $\Delta\vec{c}$ Instead of $\Delta\sigma'(\vec{y}_{\max})$. Substituting (34) in (28), results in

$$\Delta\vec{c} = \mathbf{E}^{+}(\vec{x})[\mathbf{E}(\vec{x} + \Delta\vec{x}) - \mathbf{E}(\vec{x}) + \Delta\mathbf{G}\mathbf{E}(\vec{x} + \Delta\vec{x})]\vec{c}. \quad (36)$$

Using "norms," (36) implies that the fractional error in the modal content has an upper bound, i.e.,

$$\frac{\|\Delta\vec{c}\|}{\|\vec{c}\|} \le \|\mathbf{M}\|, \quad (37)$$

where

$$\mathbf{M} = \mathbf{E}^{+}(\vec{x})[\mathbf{E}(\vec{x} + \Delta\vec{x}) - \mathbf{E}(\vec{x}) + \Delta\mathbf{G}\mathbf{E}(\vec{x} + \Delta\vec{x})]. \quad (38)$$

Thus, the upper bound on the fractional error in the modal content can be optimized by minimizing the norm of $\mathbf{M}$ for all $\Delta\vec{x}$ and $\Delta\mathbf{G}$ within certain prescribed physical limits. The advantage of using (37) to minimize $\|\Delta\vec{c}\|/\|\vec{c}\|$ instead of using (35) to minimize $\Delta\vec{\sigma}$ at $\vec{y}_{\max}$ is that the search of $\vec{y}_{\max}$ for each orientation of $\vec{c}$ is eliminated as well as simulating the orientation of $\vec{c}$ from the optimization process.

The potential difficulty in using norms is that it may provide a highly conservative bound on the error and may not result in an optimal choice of gage placements. This issue is explored in the following one-dimensional, two mode case study. The

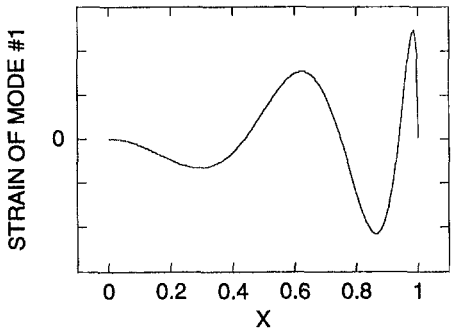

a. Mode #1

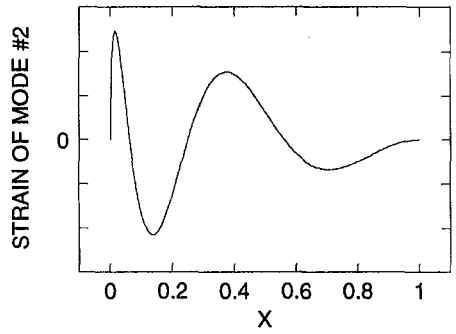

b. Mode #2

Fig. 3 Strains of one-dimensional localized "tip modes"

nominal mode shapes shown in Fig. 3 were chosen to have the characteristics of typical tip modes, i.e., the high strain regions are highly localized (Balaji and Griffin, 1995). First, an exhaustive parametric study was conducted for specific placement and gage errors in which the error in the maximum stress was calculated as a function of the two strain gage locations x_1 and x_2 for all possible ratios of c_2 to c_1. The maximum error is plotted as a function of gage position in Fig. 4(a). Then $\|\mathbf{M}\|$ is plotted as a function of gage location in Fig. 4(b)[2]. From the figures, it is clear that both quantities exhibit similar trends and, consequently, a minimum of one quantity is approximately a minimum of the other. In fact, a minimization of the error in the stress resulted in an optimum gage location $\vec{x} = (0.37, 0.86)$, a maximum stress error of 12.7 percent, and a value of $\|\mathbf{M}\|$ equal to 22.9 percent. A minimization of $\|\mathbf{M}\|$ resulted in an optimum gage location $\vec{x} = (0.14, 0.87)$, a value of $\|\mathbf{M}\|$ equal to 20.7 percent, and a maximum stress error of 13.2 percent. From an expense point of view, minimizing $\|\mathbf{M}\|$ was a factor of 30 more efficient while producing satisfactory results. The improvement in efficiency would be even larger for more realistic applications.

4.4 Linearize $\|\mathbf{M}\|$. Computational efficiency can be further improved by linearizing the expressions for $\mathbf{M}$. For small $\Delta\mathbf{G}$ and $\Delta\vec{x}$, (38) implies the first order approximation of $\mathbf{M}$ is

$$\mathbf{M}(\vec{x}, \Delta\mathbf{G}, \Delta\vec{x}) \cong \mathbf{M}_g(\vec{x}, \Delta\mathbf{G}) + \mathbf{M}_x(\vec{x}, \Delta\vec{x}), \quad (39)$$

where

$$\mathbf{M}_g(\vec{x}, \Delta\mathbf{G}) = \mathbf{E}^+(\vec{x})\Delta\mathbf{G}\mathbf{E}(\vec{x}) \quad (40)$$

$$\mathbf{M}_x(\vec{x}, \Delta\vec{x}) = \mathbf{E}^+(\vec{x})\mathbf{E}(\vec{x} + \Delta\vec{x}) - \mathbf{I}. \quad (41)$$

(39) implies that

[2] The infinity norm is used in this research.

$$\|\mathbf{M}(\vec{x}, \Delta\mathbf{G}, \Delta\vec{x})\| \leq \|\mathbf{M}_g(\vec{x}, \Delta\mathbf{G})\| + \|\mathbf{M}_x(\vec{x}, \Delta\vec{x})\|. \quad (42)$$

Substituting (42) in (37), we have

$$\frac{\|\Delta\vec{c}\|}{\|\vec{c}\|} \leq \|\mathbf{M}\| \leq \|\mathbf{M}_g\| + \|\mathbf{M}_x\|. \quad (43)$$

The advantage of using (43) is that it decouples $\Delta\mathbf{G}$ and $\Delta\vec{x}$ effects, thus reducing the number of combinations that need to be considered in the simulations. In addition, since the extremes of linear functions are at the "end points," only the errors associated with the "end points" have to be calculated.

5 Case Study and Optimization Methods

The two modes depicted in Fig. 1 were calculated from a two-dimensional finite element model of a representative modern compressor blade. Because their frequencies are quite close, they interact significantly, and, consequently, provide an interesting example of the optimization process.

A 40 by 40 mesh was used to model the airfoil (Fig. 5). To further simplify the calculations, the gages were assumed to be located at the centers of elements. Thus, 1600 possible gage locations had to be considered for each of the two strain gages. In addition, the orientation of the gages also had to be specified for each location. Orientations of 0 deg to 180 deg at intervals of 15 deg were simulated. A gage orientation error of plus or minus 5 deg and gage error of 5 percent were assumed.

5.1 Alternating Optimization and Simulated Annealing Compared With Benchmark. As indicated in Fig. 4, the gage placement optimization problem exhibits a number of local minima in terms of multiple variables[3]. An optimization procedure based on simulated annealing was utilized to find the optimum gage locations since simulated annealing has a well estab-

[3] As a result, linear programming methods are not appropriate for this problem.

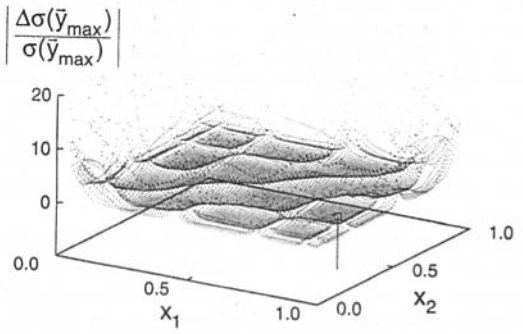

a. Percentage error of maximum stress

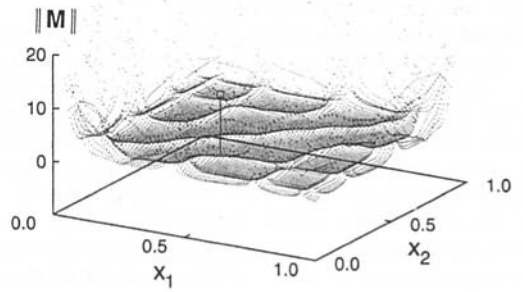

b. Upper board of percentage error of modal content (eq. (37))

Fig. 4 Comparison of two different optimization indices. The squares indicate the global minimums.

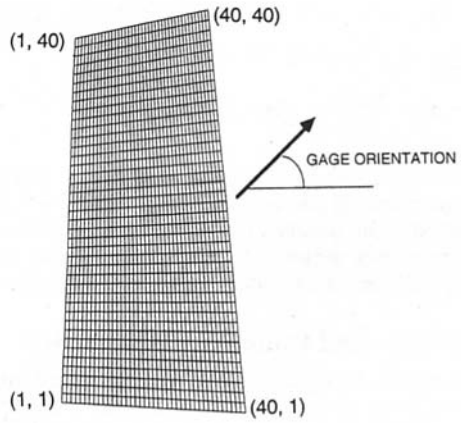

Fig. 5 Finite element model of a two-dimensional simplified blade

lished reputation for efficiently solving problems of this type (Press et al., 1992). In order to first validate the optimization program, the simulated annealing solution was compared with results from an "exact solution" of a simplified test problem. The exact solution was found using an exhaustive search of the parameter space. To make the problem more tractable for the exhaustive search, only gage orientation errors and gage error were simulated. The cutoff ratio β (section 4.2) was assumed to be zero.

The simulated annealing procedure gave the same global minimum as the exhaustive search, i.e., if the gages were optimally placed, then one gage should be located at (12, 27, 75 deg) and the second gage at (37, 5, 60 deg), where the first two numbers specify the location of the element (column and row) and the third the orientation of the gage. For the optimum gage arrangement, $\gamma_M = 7.4$ percent, where γ_M denotes $\|\mathbf{M}_g\| + \|\mathbf{M}_x\|$ as in Eq. (43).

The exhaustive search computer program ran for 11 hours on an IBM RISC 6000 workstation. The simulated annealing algorithm took an order of magnitude less time (1 hour) to find the same global minimum. Even though the simulated annealing program was much faster than an exhaustive search, it was still a relatively slow procedure—especially if gage location errors were included in addition to gage orientation errors[4]. In order to make the optimization procedure efficient a new simple optimization procedure was developed that seems to work quite well for the gage optimization problem.

Upon examination of the data it was found that the optimum gage locations could usually be found by optimizing one strain gage location at a time. More specifically, first arbitrarily fix the location of the first gage and minimize γ_M by an exhaustive search on the orientation and location of gage 2 and the orientation of gage 1. Then, repeat the process with the location of the second gage fixed at its optimized location. Continue to alternate until the procedure converges.

It should be noted that this procedure sometimes results in local minima. Therefore, several runs using different guesses of gage one's initial location should be made and the one with the lowest local minimum is taken as an approximation of global optimum. When this "alternating optimization" approach was used to solve the benchmark problem, it took approximately 12 seconds per initial guess to find a converged solution. In the majority of cases the procedure, in fact, converged to the global optimum. Consequently, even with multiple initial guesses the alternating optimization procedure was an order of magnitude faster than simulated annealing.

[4] Because of its two-dimensional nature, four extreme location errors have to be considered in the simulation. Location errors of one gage combined with those of the other gage will increase the computation costs by a factor of sixteen.

5.2 Full Simulation: Effect of β on Error and Computation Time. A complete simulation that included gage location errors as well as orientation and gage errors was performed using alternating optimization. The resolution for gage orientation was 15 deg and for gage location was one element. The maximum error in the orientation and location of the gages was also set at 5 deg and one element and the gage error at 5 percent. The initial position of gage one was varied using nine different values corresponding to 3×3 grid in the airfoil. The algorithm converged to the same optimum in every case. Once the optimum strain gage placements were determined that would minimize the norm of $\mathbf{M}$ as established by equation (43), then the maximum error in modal content and in the maximum stress were calculated, i.e.,

$$\gamma_c \equiv \operatorname*{Max}_{\|\vec{c}\|=1} \frac{\|\Delta\vec{c}\|}{\|\vec{c}\|} \tag{44}$$

$$\gamma_\sigma \equiv \operatorname*{Max}_{\|\vec{c}\|=1} \left| \frac{\Delta\sigma'(\vec{y}_{\max})}{\sigma'(\vec{y}_{\max})} \right|, \tag{45}$$

where $\vec{y}_{\max}$, determined by modal content $\vec{c}$, is the location and orientation where the maximum stress occurs. The values of γ_c and γ_σ were evaluated by checking 36 uniformly distributed $\vec{c}$'s on the unit circle $\|\vec{c}\| = 1$.

The results of simulations for various cut-off ratios β are shown in the first three columns of Table 1. Recall that the purpose of the cut-off ratio is that it prevents placing strain gages in locations where the strains in the nominal modes are too small. An examination of Table 1 reveals several interesting results. The first is that the amount of computing time decreases as β increases since fewer strain gage locations need to be considered in the optimization. Although it appears that the errors will be larger for larger values of β, in fact, the simulations do not include the effect of the larger percentage gage error that occurs for low strain measurements. Thus, the placement of the strain gages that result from a larger value of β may well correspond to a lower actual error. The second result is the degree to which the value of γ_M provides a reasonable estimate of γ_c and γ_σ (the maximum error in the modal content and in the maximum stress). The fact that γ_M is smaller than γ_c in two of the cases is surprising since the norm of $\mathbf{M}$ should provide an upper bound on γ_c. Recall that the norm of $\mathbf{M}$ did provide an upper bound on γ_c in the case study discussed in section 4.3. However, the γ_M used in this section utilizes the approach given in section 4.4 and is only a linearized approximation of the norm of $\mathbf{M}$. The use of a linearized estimate of the norm significantly increases computational efficiency at the expense of losing the strict results that $\gamma_c \leq \gamma_M$. However, it is clear from the results that γ_M still provides a reasonable estimate of the maximum errors in the modal content and the maximum stress.

The last column of Table 1 shows a representative result that would occur if the gages were placed arbitrarily. For this case,

Table 1 Comparison of optimized gage placements derived from different β and an arbitrary gage placement

Cutoff Ratio β	0%	25%	35%	—
CPU Time (mins.)	25.2	14.6	9.3	—
Gage 1 Location	(13, 40)	(13, 40)	(11, 39)	(37, 1)
Gage 1 Orientation	150°	150°	150°	45°
Gage 2 Location	(40, 1)	(40, 1)	(40, 1)	(6, 5)
Gage 2 Orientation	45°	45°	45°	75°
γ_M	14.5%	14.5%	20.1%	30.6%
γ_c	14.7%	14.7%	18.9%	29.3%
γ_σ	13.7%	13.7%	15.7%	28.3%

the error that could occur in the maximum stress is almost twice as large as for the optimal case. In fact, by maximizing γ_M, it is possible to find gage locations that would result in much larger errors. Consequently, the optimization of gage placement and orientation can significantly reduce the amount of error that can occur in determining the maximum stress in closely spaced modes.

6 Conclusions

Modern, low aspect ratio blades often have closely spaced, high frequency "tip" modes that are sensitive to the slight changes in the geometry of the blade that can occur during the manufacturing process. From perturbation analyses, it is known that the modes that occur in the actual blades can be approximated as a linear combination of the unperturbed modes, i.e., the modes that occur in a blade with a nominal geometry. This suggests that stresses in the actual blades can be estimated by making multiple strain measurements and inferring the modal content of the constituent modes. If this effect is not taken into account, then the mode may be incorrectly identified—a mistake that could result in extremely large errors in the estimated stresses.

A current procedure that may be used is to perform a complete experimental stress survey on closely spaced modes and establish different stress ratios for every instrumented blade. A problem with this approach is that it is quite expensive and may not work since these modes are very sensitive to small changes in the structural properties, and the properties are changed by the speed of the engine. As a result, the process of rotating the blade may cause closely spaced frequencies to change and even switch in order. Thus, the results of the stress survey may not be applicable under engine operating conditions.

Once it is understood that the modal content of the actual response needs to be determined by multiple strain measurements, then the location and orientation of the gages have to be carefully selected since a poor choice can significantly amplify any gage or placement errors. The procedure for optimizing the location of the strain gages is made significantly more complicated by the fact that the actual mode shape is known only to the extent that it is a linear combination of the nominal modes. A procedure was discussed for determining how many nominal modes are required as a basis. Then, mathematical expressions were developed for the error in the maximum stress as a function of the gage and placement errors. The formulation was then simplified through the use of matrix norms and various linearizations in order to make the problem more computationally tractable.

Several test problems were solved in order to validate and illustrate the approach and a new optimization procedure was introduced that significantly reduced computation times. It was shown that the optimal selection of gage locations could reduce the error in the estimate of the maximum stress by at least a factor of two. Thus, a theory and methodology have been developed and demonstrated for optimally measuring the maximum stress that occurs in closely spaced modes.

References

Balaji, G. N., and Griffin, J. H., 1997, "Resonant Response of a Tapered Beam and Its Implications to Blade Vibration," ASME JOURNAL OF ENGINEERING FOR GAS TURBINES AND POWER, Vol. 119, pp. 147–152.

Ben-Israel, A., and Greville, T. N. E., 1974, *Generalized Inverses: Theory and Applications,* Wiley, New York.

Kim, N., and Griffin, J. H., 1994, "Sensitivity of Bonded and Composite Beams," *Journal of Sound and Vibration,* Vol. 177, pp. 71–92.

Meirovitch, L., 1980, *Computational Methods in Structural Dynamics,* Alphen aan den Rijn, The Netherlands.

Press, W. H., Teukolsky, S. A., Vetterling, W. T., and Flannery, B. P., 1992, *Numerical Recipes in C, The Art of Scientific Computing,* 2nd ed., Cambridge University Press, New York.

Wu, W.-T., Griffin, J. H., and Wickert, J. A., 1995, "Perturbation Method for the Floquet Eigenvalues and Stability Boundary of Periodic Linear Systems," *Journal of Sound and Vibration,* Vol. 182, pp. 245–257.

Yang, M.-T., and Griffin, J. H., 1997, "A Normalized Modal Eigenvalue Approach for Resolving Modal Interaction," ASME JOURNAL OF ENGINEERING FOR GAS TURBINES AND POWER, Vol. 119, pp. 647–650.

Time-Dependent Crack Initiation and Growth in Ceramic Matrix Composites

M. R. Begley
University of Connecticut
Storrs, CT 06268

B. N. Cox
Rockwell International,
Thousand Oaks, CA 93017

R. M. McMeeking
University of California, Santa Barbara
Santa Barbara, CA 93107

Matrix cracking in ceramic matrix composites with fine grained fibers at high temperatures will be governed by fiber creep, as relaxation of the fibers eliminates crack tip shielding. Using a time dependent bridging law that describes the effect of creeping fibers bridging a crack in an elastic matrix, crack growth initiation and history have been modeled. For a stationary crack, crack tip stress intensity factors as a function of time are presented to predict incubation times before subcritical crack growth. Two crack growth studies are reviewed: a constant velocity approximation for small-scale bridging, and a complete velocity history analysis which can be used to predict crack length as a function of time. The predictions are summarized and discussed in terms of identifying various regimes of crack growth initiation, subcritical growth, and catastrophic matrix cracking.

1 Introduction

High strength ceramic fibers can be achieved by decreasing fiber grain size, which limits the flaw size in the fibers. Ceramic matrix composites (CMCs) are made by combining these fibers with relatively coarse-grained matrices. Since the role of the matrix is generally to provide ductility to the composite, the decrease in matrix strength due to large flaw sizes is not considered detrimental. The low temperature behavior of such composites has been studied extensively both experimentally and analytically, and is generally well understood (Evans and Zok, 1994).

The primary motivation for using such composites, however, is the high temperature capabilities of the ceramic constituents. At high temperatures, predicting composite performance becomes more complicated due to oxidation and creep (Heredia et al., 1995; Lamouroux et al., 1994). The fine-grained fibers are particularly susceptible to creep, as small grain sizes increase avenues for grain boundary diffusion. (The coarser grained matrix can be considered to behave elastically, as creep rates are significantly lower.) Crack bridging by intact fibers becomes time-dependent at high temperatures, as fiber creep causes crack closure forces to decay over time (Begley, 1997; Begley et al., 1997; Begley et al., 1995a; Begley et al., 1995b; El-Azab and Ghoniem, 1995; Henager and Jones, 1994; Henager and Jones, 1993; Nair and Gwo, 1993). Furthermore, cracks that can be considered benign at low temperatures may cause significant problems at high temperatures, as they may provide pathways for oxidation to occur in the interior of the composite or degrade the components ability to contain gases (Evans et al., 1996). The question of crack stability at room temperature thus changes at elevated temperatures to questions about when and how fast cracks grow.

This paper is intended to provide a summary of some recent work on predicting time dependent crack growth in CMCs caused by fiber creep at high temperatures. A time dependent bridging law has been developed to describe the effect of creeping fibers bridging a matrix crack in a composite whose matrix can be considered elastic (Begley et al., 1995a). This bridging law has been used to estimate the time needed to initiate crack growth from both fully bridged and partially bridged stationary cracks (Begley, 1997). The issue of crack growth rate has been addressed in both the small-scale and large-scale bridging regimes (Begley et al., 1997; Begley 1995b). Representative results are presented and used to discuss the issues raised by time dependent crack growth in both unidirectional and laminated CMCs.

In the crack behavior studied in this work, a finite crack tip stress intensity factor is assumed to exist. For analysis of initiation times, it is assumed that the crack geometry and loading is such that the crack tip stress intensity factor, K_{tip}, is less than the toughness of the matrix, K_c (adjusted for matrix volume fraction). For crack growth studies, it is assumed that crack growth occurs under the condition that $K_{\text{tip}} = K_c$. The analyses and results are often similar to a cohesive zone approach in different materials (Knauss, 1993; Fager et al., 1991); however, it should be emphasized that the assumption of a finite stress intensity factor at the crack tip (based on the fact that the matrix remains elastic) leads to significant differences.

2 Time Dependent Bridging

The crack tip shielding provided by creeping fibers bridging a matrix crack can be analyzed by determining the relationship between the crack opening rate and bridging traction for a representative bridged section of the crack. Such cell models can then be integrated with traditional fracture mechanic relations to develop an integral equation which is solved for the closure forces in the bridged section of the crack. These closure forces are then used in the usual manner to predict the reduction in crack tip stress intensity factor.

A full derivation for a creeping fiber embedded in an elastic matrix results in the following bridging law, which incorporates the effects of frictional slip between the fiber and the matrix (Begley et al., 1995a):

$$\dot{\delta}(t) = \frac{(1-f)^2 E_m^2 D}{2f^2 \tau E_f}\left\{\frac{\sigma(t)}{E_L} + \frac{fBE_f^2}{E_L^2}\int_{-\infty}^{t}\sigma(\bar{t})e^{-(t-\bar{t})/T}d\bar{t}\right\}$$

$$\times\left\{\frac{\dot{\sigma}(t)}{E_L} + \frac{BE_f\sigma(t)}{2(1-f)E_m}\left[1 + \frac{fE_f(fE_f-(1-f)E_m)}{E_L^2}\right.\right.$$

$$\left.\left.\times\left\{\int_{-\infty}^{t}\frac{\sigma(\bar{t})}{T\sigma(t)}e^{-(t-\bar{t})/T}d\bar{t}\right\}\right]\right\}. \quad (1)$$

Contributed by the International Gas Turbine Institute and presented at the International Gas Turbine and Aeroengine Congress and Exhibition, Orlando, FL, June 2–5, 1997. Manuscript received by the ASME Headquarters March 15, 1997. Paper No. 97-GT-275. Associate Technical Editor: H. A. Kidd.

D is the diameter of the fibers; f is the fiber volume fraction; B is the creep coefficient of the fibers; τ is the shear sliding stress between the fibers an the matrix; E_f, E_m, and E_L are the elastic moduli of the fiber, matrix and composite, respectively; and T is the characteristic relaxation time for the intact composite, given by $E_L/B(1-f)E_mE_f$.

For a growing crack, the convolution integrals in (1) (which reflect the history dependence of the bridging stress) complicate things, and the following simplified bridging law has been used in crack growth studies (Begley et al., 1997; Begley et al., 1995b):

$$\dot{\delta}(t) = 2\lambda\sigma(t)[\dot{\sigma}(t) + \beta\sigma(t)], \qquad (2)$$

where λ is the rate-independent bridging coefficient, and β is a modified creep coefficient. The assumptions that justify simplifying Eq. (1) to Eq. (2) are based on comparing the relative magnitudes of terms in the full bridging law and neglecting smaller terms. In summary, Eq. (2) neglects creep of the fibers in the intact portion of the composite, which is acceptable during crack growth studies since creep in the slip region adjacent to the matrix crack, and the short time ($t \ll T$) response of Eq. (1), dominate the shielding effect of the fibers. Further details of these assumptions and their validity is discussed fully by Begley (1997), Begley et al. (1997), and Begley et al. (1995b).

3 Time to Initiate Crack Growth

For a given crack geometry and load level, the crack tip stress intensity factor may be beneath the critical stress intensity factor of the matrix, implying that some time is required to relax the shielding effect of the fibers to the point that crack growth occurs. Such a situation would arise when a matrix flaw exists that spans multiple fibers, provided the load is beneath the critical stress to propagate the bridged matrix crack. Another example is the case of an overload, where the applied load on the composite decreases; during the peak loading, the matrix crack is driven to the length where $K_{tip} = K_c$ for the peak load. If the load is subsequently decreased, K_{tip} falls beneath K_c and some time is required to decay the bridging tractions until crack growth occurs.

In the following calculations, the crack is assumed to be stationary; thus, the problem is simply to calculate the evolution of the bridging stress over time. The bridging stress profile at a given instant in time was then used to predict the instantaneous value of the crack tip intensity factor. The geometry is a fully bridged center crack of length $2a$ in an infinite panel. The crack tip stress intensity factor as a function of time is shown in Fig. 1 for several different cases.

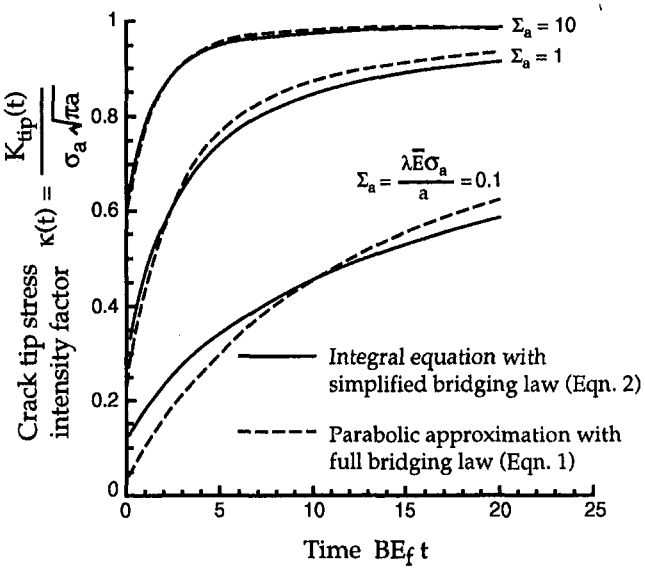

Fig. 1 Two calculations for the crack tip stress intensity factor as a function of time for three different loads and $f = 0.3$, $E_f = E_m = E_L = \bar{E}$

The curves compare the effects on the crack tip stress intensity factor of two different simplifications, for three different load levels. The solid lines were generated using the bridging stress profile generated by the solution of an integral equation derived using Eq. (2), the simplified bridging law. The dashed lines were calculated using the full bridging law and imposing a parabolic approximation for crack opening. (At high loads or for short cracks, the crack opening will be nearly parabolic; assuming the form of the profile allows the differential form of the integral equation to be reduced to a simple one-degree-of-freedom differential equation.) It can be seen that at high loads the effect of the convolution integrals is negligible. As discussed by Begley (1997), even at lower loads the neglect of the convolutions is usually not significant. The discrepancy in Fig. 1 between the two calculations for the lowest load is mostly a

Nomenclature

a, $\dot{a}$ = crack half length, crack tip velocity
$a_m = \pi/4\ (\lambda\bar{E}K_c)^{2/3}$ = characteristic length scale for the composite
B = creep coefficient of the fibers ($\dot{\epsilon}_f = (\dot{\sigma}_f/E_f) + B\sigma_f$)
D = fiber diameter
E_f, E_m = Young's modulus of the fibers and matrix
$E_L = fE_f + (1-f)E_m$ = rule of mixtures composite Young's modulus
$\bar{E}$ = composite modulus which accounts for orthotropy
$\bar{\epsilon} = \lambda\bar{E}^2\epsilon/l$ = normalized total fiber strain at the crack plane
$\bar{\epsilon}_{cr}$ = normalized critical total strain to fiber failure
f = fiber volume fraction
K_c = critical stress intensity factor for matrix crack extension
K_∞ = far-field applied stress intensity factor
$\bar{K}_\infty = \lambda\bar{E}K_\infty/l = K_\infty/K_c$ = normalized applied stress intensity factor
$(K_\infty)_{asym}$ = asymptotic applied stress intensity factor at low crack speeds
$l = (\lambda\bar{E}K_c)^{2/3} = \lambda\bar{E}\sigma_{mc}$ = characteristic length scale for the composite
$T = E_L/(1-f)BE_fE_m$ = characteristic relaxation time of intact composite
$v_{ss} = \dot{a}/\beta l$ = normalized steady-state crack velocity
α_{asym} = asymptotic bridge length at low crack speeds
$\beta = BE_fE_L/2(1-f)E_m$ = modified creep coefficient of the fibers
δ, $\dot{\delta}$ = total crack opening, total crack opening rate
$\delta_{mc} = \lambda\sigma_{mc}^2$ = total crack opening at steady-state matrix cracking stress (for the rate-independent case)
$\Delta_{cr} = \lambda\bar{E}^2\delta_{cr}/l^2 = \delta_{cr}/\delta_{mc}$ = normalized critical total crack opening governing fiber failure
$\lambda = D(1-f)^2E_m^2/4f^2\tau E_fE_L^2$ = rate-independent bridging coefficient ($\delta = \lambda\sigma^2$)
σ, $\dot{\sigma}$ = bridging stress, bridging stress rate
$\sigma_{mc} = [12f^2\tau E_fE_L^2K_c^2/D(1-f)E_m^3]^{1/3}$ = steady-state matrix cracking stress
τ = shear sliding stress at the fiber-matrix interface

result of the inaccuracy of the parabolic form used to reduce the integral equation.

4 Constant Velocity Crack Growth: Small-Scale Bridging

In situations where the length of the bridging zone is much smaller than the crack length, small-scale bridging is said to apply and the governing equations can be simplified from the general case. An example of such a scenario may occur in laminated CMCs, where cracks first appear in the 90 deg layers with fibers perpendicular to the loading direction. These cracks will advance into the adjacent 0 deg plies and arrest at room temperature; at loads much smaller than the matrix cracking stress, the bridging zone is much smaller than the total crack length.

The case being modeled here is a semi-infinite crack loaded with a far-field applied stress intensity factor, K_∞, growing at a constant speed, v_{ss} (Begley et al., 1997). The bridging law dictating material behavior in the bridged zone is given as Eq. (2). Fibers fail in the wake of the crack and the bridging zone size remains constant. The solution represents a steady-state configuration, as the zone of creeping fibers bridging the crack propagates with the crack tip.

The length of the bridging zone depends on the crack growth rate, and is determined by a fiber failure criterion. Two failure criteria are presented here: a critical crack opening, Δ_{cr}, and a critical total strain in the fiber, $\bar{\varepsilon}_{cr}$.

Figure 2 illustrates how crack velocity varies as a function of applied stress intensity factor K_∞ for the two cases. For both cases, there is a rapid increase in crack velocity as the applied stress intensity factor is raised above the matrix toughness. The figure demonstrates the existence of upper and lower bounds on the applied loading. The assumption of a finite crack tip stress intensity factor dictates that a minimum K_∞ exists, below which no crack growth will occur; this minimum is merely the matrix toughness. For applied loads above this value, fiber creep will decrease bridging tractions to drive crack growth, though perhaps at very small velocities.

Since the simplified bridging law (given as Eq. 2) reduces to the appropriate rate independent bridging law in the limit of no creep, an upper limit exists. As the applied load increases towards the level at which bridging (without creep) is no longer effective enough to maintain $K_{tip} = K_c$, crack velocities tend toward infinity. Thus, the upper limit corresponds to load levels at which instantaneous matrix crack occurs.

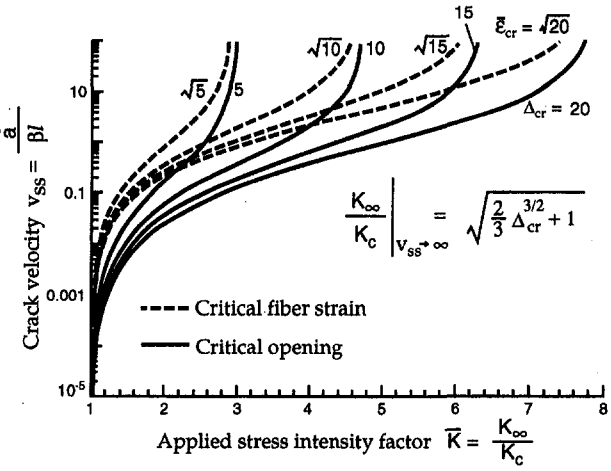

Fig. 2 Steady-state crack velocity as a function of far-field applied stress intensity factor for two fiber failure criteria and $f = 0.3$, $E_f = E_m = E_L = E$

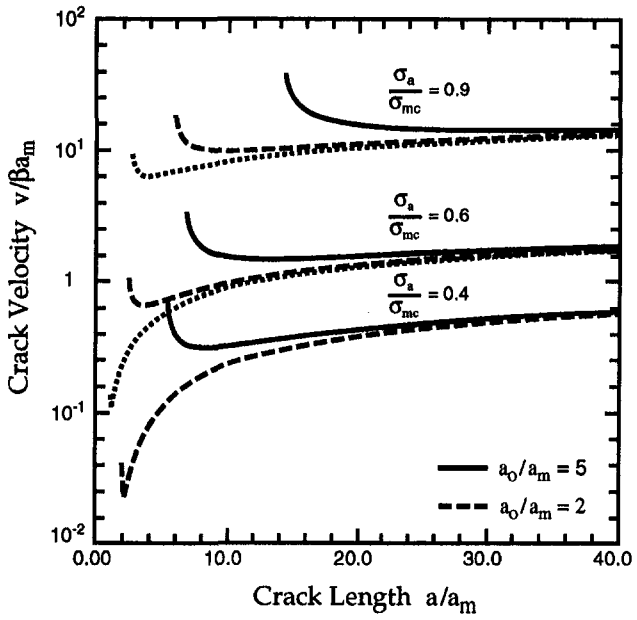

Fig. 3 Crack velocity as a function of crack length for several values of applied load and notch sizes using the simplified bridging law

One of the attractive results of the simplifying assumptions used in this analysis is that they allow closed-form asymptotic solutions when crack speeds are low. The asymptotic dependence of the bridging zone length and crack velocity on the applied stress intensity factor are summarized below for the case where fiber failure is governed by a critical strain criterion (Begley et al., 1997):

$$\left(\frac{K_\infty}{K_c}\right)_{asym} = 1 + \frac{4}{\pi^{1/4}}\left(\frac{3E_fE_L}{4(1-f)E_m}\right)^{1/3}(\bar{\varepsilon}_{cr})^{1/3}(v_{ss})^{2/3}; \quad (v_{ss}\to 0) \quad (3)$$

$$\left(\frac{\alpha}{l}\right)_{asym} = \frac{1}{4}\left(\frac{3E_L}{4(1-f)E_m}\right)^{4/3}(\bar{\varepsilon}_{cr})^{4/3}(v_{ss})^{2/3}. \quad (4)$$

These closed form solutions reveal a simple power law relationship between applied stress intensity factor and crack velocities that may be useful in comparing with experiments with very small bridging zones.

5 General Time Dependent Crack Growth: Large-Scale Bridging

Obviously, cracks may not grow at constant velocity, and the bridging length may be comparable to specimen dimensions. For such cases, full large-scale bridging have been performed to predict crack length and velocity as a function in time (Begley et al., 1995b). Fiber failure was not incorporated into the analysis. The geometry being considered is a center crack of length $2a$ in an infinite panel with a 'notch', or unbridged portion of matrix crack of lengths $2a_o$. Crack growth is assumed to occur with the condition that the crack tip stress intensity factor equals the matrix toughness. The numerical procedure is summarized by Begley et al. (1995b); one attractive aspect of the technique used is that the bridging law has exactly the correct form in the limit of small time increments. Hence, the bridging behavior near the crack tip, where fibers are responding nearly elastically, is captured accurately. The results of these analyses are summarized in Figs. 3 and 4.

Crack velocities as a function of crack length are shown in Fig. 3 for several different values of applied nodes and several

different notch sizes. The curves start at different initial values of crack length, corresponding to the case where $K_{tip} = K_c$ for the rate independent case. Thus, for these cases the initiation time discussed in section 3 is zero. All cases show that the crack will initially decelerate as the rate of decay of bridging tractions decreases. After the initial transient has finished, the crack accelerates monotonically, eventually becoming asymptotically independent of initial notch size.

The crack velocity as a function of crack length can be integrated to predict crack length as a function of time. Such results are shown in Fig. 4 for one of the notch sizes in Fig. 3 and the same load levels. The curves illustrate the large effect the deceleration transient will have on the overall crack growth; the larger the dip in the crack velocity curve, the larger the dwell time in Fig. 4. For laminates, critical crack lengths at which catastrophic cracks cross the specimen may be short, i.e., equal to the ply thickness, emphasizing the importance of solutions in the transient regime.

6 Predicting Time Dependent Crack Growth in CMCs

6.1 Crack Growth Initiation. For a given loading scenario, the first question to answer is whether or not crack growth starts immediately, or whether some time is required to decrease the shielding in bridged cracks. The answers lie in the rate-independent behavior of CMCs, which has been extensively studied; provided the loading rate is high enough, the composite constituents will initially respond elastically. The upper limit on the applied loading, such that crack growth studies are applicable, is the steady-state matrix cracking stress, which represents the load level at which matrix cracks will propagate across the composite catastrophically in a rate-independent manner.

For cracks created by load histories where the specimen or component is loaded monotonically beneath the matrix cracking stress, the transition to subcritical crack growth will be instantaneous. Both cracks grown from a notch in a unidirectional composite and cracks tunneling into 0 deg plies in a laminate will arrest at the crack length at which $K_{tip} = K_c$. Therefore, any amount of fiber creep will decrease crack tip shielding and cause crack growth; initiation times for these cases are zero. The crack length at which $K_{tip} = K_c$ with rate-independent behavior will be the initial condition used in the time dependent study. The rate independent behavior of both unidirectional CMCs and laminates is summarized by Cox and Marshall (1997), which can be used to identify relevant starting geometries for time dependent studies.

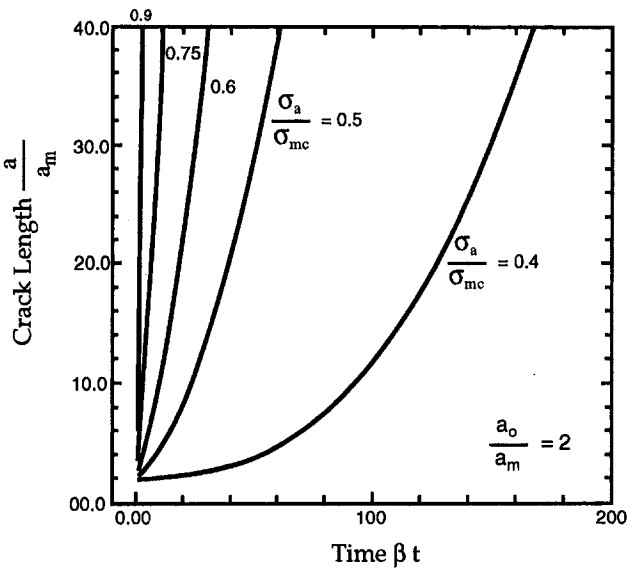

Fig. 4 Crack length as a function of time calculated by integrating the curves in Fig. 3

Initiation times will not be zero for cracks created by an overload, where the load applied to the composite decreases after some maximum. For these cases, the starting crack length is the length created by the maximum load, where $K_{tip}(\sigma_{max}) = K_c$. If the load drops, K_{tip} will fall below K_c, and the crack will remain stationary until fiber creep degrades shielding enough to cause crack growth. Obviously, such histories affect subsequent crack growth as fiber strains will accumulate. Further modeling and experiments are needed to discover the effect of creep prior to crack growth.

6.2 Regime of Subcritical Crack Growth. Once crack growth has started, the relevant question to answer is when the cracks reach lengths that are undesirable. This is most likely the length at which the crack crosses the specimen, resulting in two halves of intact composite held together by creeping fibers. For laminates, the critical length at which cracks propagate unstably may be the 0 deg ply width, depending on the ratio of 0 deg/90 deg widths (Cox and Marshall, 1997).

Once the critical crack length has been identified, the models described in sections 4 and 5 can be used to estimate the amount of time required to reach this length. Noting that a_m in Fig. 3 is on the order of a tenth of a millimeter for most CMCs, it can be seen that most (if not all) of the relevant crack growth for typical laminates occurs during the transient period of crack growth. Thus, the pertinent regions in Figs. 3 and 4 are the ones where the normalized crack length a/a_m is less than 10 or so. For loads above 60 percent of the matrix crack stress, the time to reach a critical crack length is quite small, as the transient region becomes less and less pronounced. For such cases, matrix cracks quickly cross the specimen and composite rupture is governed by the rupture behavior of the fibers loaded uniformly.

For loads significantly below the matrix cracking stress, velocities will may be quite small, implying that fibers have significant time to creep. Naturally, the fibers will exhibit a finite amount of creep ductility and for slower velocities, will fail during the subcritical crack growth. A transition exists then, between subcritical crack growth characterized by fiber failure in the wake of the crack (Begley et al., 1997) and fiber failure after the crack has reached critical dimensions (Begley et al., 1995b). Experiments are needed to confirm this transition and evaluate the validity of the predictions presented here.

6.3 Appropriateness of the Bridging Law and Single Crack Model. In general, bridging laws developed from cell models fail to capture certain aspects of bridging behavior. Notably, the equation presented here does not account for the possibility of "reverse" slip, where the direction of relative sliding between the fiber and the matrix changes sign. This is most likely to happen in regions of the bridging zone that are unloading. For stationary cracks, this is most likely to be the case, and further calculations are warranted. For growing cracks, however, it has been shown that growth is dominated by the near-tip behavior of the bridging region (Begley et al., 1997; Begley et al., 1995b). Near the crack tip, bridging fibers will be loaded rapidly and will respond nearly elastically, or with the "short time" response of the bridging law. In this regime, both the possibility of "reverse" slip and the convolution integrals in Eq. (1) can be reasonably neglected.

It should be pointed out that a single crack model does not account for the stress redistribution that will occur if multiple matrix cracks occur near a stress concentration. Multiple matrix cracks are common, and a more realistic bridging law which incorporates the effect of overlapping slip zones would be more useful. Additionally, different weight functions used in developing the integral equations could be used, to account for arrays of multiple cracks.

Despite the limitations on the bridging law outlined above, the results will be qualitatively consistent with more detailed analyses incorporating reverse slip and crack interaction. The essential features of the constitutive law for the bridging zone will not be changed by considering slip zone reversal or overlap; namely, that the bridging stress increases with opening and decays with time. Most importantly, the details of appropriate bridging laws always require empirical calibration, preferably with crack-growth data rather than micromechanical tests (Cox, 1995). Regardless of the exact form of the bridging law, accurate predictions over a wide range of stress levels should be possible once the model is calibrated against experiments.

Acknowledgments

MRB and RMM were supported by the University Research Initiative, ONR Contract No. N-0014-92-J-1808. BNC was supported by AFOSR Contract No. F49620-94-C-0030.

References

Begley, M. R., 1997, "Time Dependent Cracks in Ceramic Matrix Composites: Crack Growth Initiation," *International Journal of Solids and Structures,* Vol. 34, p. 1035.

Begley, M. R., Cox, B. N., and McMeeking, R. M., 1997, "Creep Crack Growth With Small-Scale Bridging in Ceramic Matrix Composites," *Acta Metallurgica et Materiala,* Vol. 45, p. 2897.

Begley, M. R., Evans, A. G., and McMeeking, R. M., 1995a, "Creep Rupture in Ceramic Matrix Composites With Creeping Fibers," *Journal of the Mechanics and Physics of Solids,* Vol. 43, p. 727.

Begley, M. R., Cox, B. N., and McMeeking, R. M., 1995b, "Time Dependent Crack Growth in Ceramic Matrix Composites With Creeping Fibers," *Acta Metallurgica et Materiala,* Vol. 43, p. 3927.

Cox, B. N., 1995, "Life Prediction for Bridged Cracks," *Life Prediction for Titanium Matrix Composites,* W. S. Johnson, J. Larsen, and B. N. Cox, eds., ASTM STP, ASTM, Philadelphia, PA.

Cox, B. N., and Marshall, D. B., 1997, "Crack Initiation in Brittle Fiber Reinforced Laminates," *Journal of the American Ceramic Society,* in press.

El-Azab, A., and Ghoniem, N. M., 1995, "Investigation of Incubation Time for Subcritical Crack Propagation in SiC-SiC Composites," *Journal of Nuclear Materials,* Vol. 219, p. 101.

Evans, A. G., and Zok, F. W., 1994, "The Physics and Mechanics of Fibre-Reinforced Brittle Matrix Composites," *Journal of Material Science,* Vol. 29, p. 3857.

Evans, A. G., Zok, F. W., McMeeking, R. M., and Du, Z. Z., 1996, "Embrittlement in Ceramic Matrix Composites," *Journal of the American Ceramic Society,* Vol. 79, p. 2345.

Fager, L.-O., Bassani, J. L., Hui, C.-Y., and Xu, D.-B., 1991, "Aspects of Cohesive Zone Models and Crack Growth in Rate-Dependent Materials," *International Journal of Fracture,* Vol. 52, p. 119.

Henager, C. H., and Jones, R. H., 1993, "High Temperature Plasticity Effects in Bridged Cracks and Subcritical Crack Growth in Ceramic Matrix Composites," *Materials Science and Engineering A,* Vol. 166, p. 211.

Henager, C. H., and Jones, R. H., 1994, "Subcritical Crack Growth in CVI Silicon Carbide Reinforced With Nicalon Fibers: Experiment and Model," *Journal of the American Ceramic Society,* Vol. 77, p. 2381.

Heredia, F. E., McNulty, J. C., Zok, F. W., and Evans, A. G., 1995, "Oxidation Embrittlement Probe for Ceramic Matrix Composites," *Journal of the American Ceramic Society,* Vol. 78, p. 2097.

Knauss, W. G., 1993, "Time Dependent Fracture and Cohesive Zones," *Journal of Engineering Materials and Technology,* Vol. 115, p. 262.

Lamouroux, F., Steen, M., and Valles, J. L., 1994, "Uniaxial Tensile and Creep Behavior in an Alumina Fiber-Reinforced Ceramic Matrix Composite: I—Experimental Study," *Journal of the European Ceramic Society,* Vol. 14, p. 529.

Nair, S. V., and Gwo, T. J., 1993, "Role of Crack Wake Toughening on Elevated Temperature Crack Growth in a Fiber Reinforced Ceramic Matrix Composite," *Journal of Engineering Materials and Technology,* Vol. 115, p. 273.

Analysis of Interfacial Cracks in a TBC/Superalloy System Under Thermomechanical Loading

S. Q. Nusier

G. M. Newaz

Wayne State University,
Mechanical Engineering,
5050 Anthony Wayne Drive,
Detroit, MI 48202

In thermal barrier coatings (TBC) residual stresses develop during cool down from processing temperature due to the thermal expansion mismatch between the different layers (substrate, bond coat, and TBC). These residual stresses can initiate microcracks at the bond coat/TBC interface and can lead to debonding at the bond coat/TBC interface. The effect of voids or crack-like flaws at the interface can be responsible for initiating debonding and accelerating the oxidation process. Effect of oxide layer growth between bond coat and ceramic layer (TBC) can be modeled as volume increase. In this work we represent this change in volume as an induced pressure across the interface. Mixed-mode fracture analysis of a thin circular delamination in an-axisymmetrically multi-layer circular plate is developed. Geometrical nonlinearity is included in the analysis, since we have a large deflection case. The elastic deformation problem of a circular plate subjected to a clamped boundary condition at the edge of the delamination, an out of plane pressure load, and a compressive stress due to thermal mismatch between different layers, was solved numerically using a Rayleigh–Ritz method. The strain energy release rate was evaluated by means of the path-independent M-integral. The numerical results of this problem based on the energy method were verified using finite element method. Both methods correlate well in predicting the energy release rate for Mode I and Mode II, deflection, and postbuckling solutions. The energy release rates G, for both Mode I and Mode II using virtual crack extension method, were evaluated. The specimen was cooled down from processing temperature of 1000°C to 0°C. The variation of the properties as a function of temperature was used for analysis. It was found that the use of temperature dependent properties in contrast to constant properties provides significantly different values of J-integral and G.

Introduction

Thermal barrier coatings (TBCs) provide thermal insulation, and the bond coat provides oxidation resistance at high temperature to high temperature alloy substrates. Plasma-sprayed zirconia-yttria ceramic layer with a nickel-chromium-aluminum-yttrium bond coat on a substrate made of nickel-based superalloy (Chang et al., 1987) is a common superalloy/TBC system. Application of these superalloy/TBC systems can be found in both aerospace and land-based gas turbine engines. In automotive applications, the piston head for diesel engine is coated to achieve a longer lifetime and a higher performance in terms of fuel reduction and power. However, these coatings have durability problems, due to the material and thermal mismatch between the coating and the metallic substrate. Thermal residual stresses develop during cool down from processing temperatures in TBC/metallic substrate. Environmental effects (specifically, oxidation) create additional residual stresses due to the growth of an oxide layer causing additional material mismatch between the oxide surface and the TBC. These residual stresses may initiate microcracks such as debonding and radial cracks, and can have profound effect on the response of the TBC and interfacial damage accumulation and failure. Their understanding is essential to predict the behavior of the coatings and their performance. The processing technique itself may produce voids or elongated flaws such as air bubble along the interfaces, which may initiate debonding.

Contributed by the International Gas Turbine Institute and presented at the International Gas Turbine and Aeroengine Congress and Exhibition, Orlando, FL, June 2–5, 1997. Manuscript received by the ASME Headquarters March 20, 1997. Paper No. 97-GT-391. Associate Technical Editor: H. A. Kidd.

Thermal fracture of multilayer ceramic thermal barrier coatings was studied by Takeuchi and Kokini (1994). The effect of a transient thermal load on a coating which is bonded to a cylindrical substrate was studied by Hornack and Kokini (1988). Finite element method was used to obtain a solution for a circumferential edge crack normal to the coating. The finite element method has been used in conjunction with a numerical interface fracture mechanics model to investigate the structural response of coated brittle materials subjected to normal and shear loads (Oneil and Wayne, 1994). A finite element model to calculate the Mode II stress-intensity factors was developed by van der Zande and Grootenboer (1986). The optimum size for a so-called singular element has been determined. Ahmad (1993) provides micromechanics based fracture analysis and correlation of experimental data for metal ceramic and other interfaces. Suo (1995) studied wrinkles that induce interfacial stress and cause voiding. The strain energy release rate components G_I and G_{II} in Mode I and Mode II at the tip of an interface crack in a bimaterial plate under tension in a direction normal to the interface were evaluated using finite element analysis and modified crack closure integral (MCCI) technique by Dattaguru et al. (1994). An elastoplastic solution for the interface crack with contact zones was studied by Aravas and Sharma (1991). Singular thermal stress fields in bonded viscoelastic quarter planes are studied by Blanchard and Ghoniem (1989). Singular stress and heat flux fields at the tip of the crack in a general nonhomogeneous material are studied by Jin and Noda (1994). New domain integrals for axisymmetric interface crack problems are derived by Nahta and Moran (1993). The effect of crack front curvature is shown to play an important role in the derivation of the integrals.

Descriptions of residual stresses and their influence on mechanical failure of coatings were studied by Evans et al. (1983).

The mechanics of the delamination and spalling of compressed films or coatings has been analyzed using a combination of fracture mechanics and post-buckling theory by Evans and Hutchinson (1984). The phenomenon of delamination buckling and growth in a time dependent radial compressive load is analyzed by Boltega and Maewal (1983). An iterative procedure based on the fourth-order Runge–Kutta integration formula is used to generate a family of nondimensionalized post-buckling solutions of von Karman's nonlinear plate theory by Yin (1985). A mixed-mode fracture analysis combining nonlinear thin-plate stress solutions with crack-tip elasticity results has been developed to account for local variations of G_I, G_{II}, and G_{III} in thin film debond problems associated with large film deformations by Chai (1990). A shaft-loaded blister test has been developed by Wan and Mai (1995) to measure the interfacial energy of a thin flexible polymeric film adhered to a rigid substrate. Expressions have been derived that describe the critical stress and pressure necessary to rupture oxide blisters that form on aluminum during growth of corrosion pits by Ryan and McCafferty (1995).

Although numerous efforts have been made to understand the effect of cracks on the life of TBC coated specimens, evolution and growth of the cracks still require special attention. It is now determined that in some TBC systems, such as electron beam-plasma vapor deposition (EB-PVD), there is microcrack initiation. Microcracks coalesce to form major delamination cracks as reported by Newaz et al. (1996). Interfacial crack in a layered disk specimen is shown in Fig. 1. An important consideration is the nature of crack growth characteristics at the TBC/bond coat interface. In a previous study by Nusier and Newaz (1996), it was shown that a central delamination under pure thermal loading has no stress intensification at the crack tip unless the delamination is large enough to promote buckling. By investigating the issue of interfacial crack growth, we will be able to evaluate the condition necessary for their growth under thermomechanical loading. This button specimen under consideration is amenable to axisymmetric modeling due to geometry. The importance of this problem is due to the fact that in order to achieve realistic prediction of TBC spallation performance, one needs to study the interaction of various layers and interfacial cracks at high temperature.

Theoretical and Computational Analysis

The TBC coating in a button specimen, as studied by Nusier and Newaz (1995), is in a state of biaxial compression. Residual compression stresses has been observed in TBC coating that was applied using electron beam–plasma vapor deposition (EB-PVD) technique. This residual compression stress arises because of thermal expansion mismatch. Buckling failure mode has been observed by Newaz et al. (1996) in the EB-PVD system. Oxidation growth between bond coat and ceramic layer (TBC) can be modeled as volume increase which can be represented as an induced pressure across the interface (TBC/Oxide). Mixed-mode fracture analysis of a thin circular delamination in an-axisymmetrically, multi layer circular plate is given in the following sections.

Theoretical Analysis. Let a circular plate of radius a be clamped at the edge of the delamination and subject to a uniformly distributed pressure p. The clamped edge has a radial displacement $a\epsilon_0$ due to the applied compressive load (Fig. 1(a)). The deflection and slope at the clamped edge is zero, also the radial displacement at the center of the plate is zero. For a large deflection, the strain in the radial and the tangential direction are

$$\epsilon_r = \frac{du}{dr} + \frac{1}{2}\left(\frac{dw}{dr}\right)^2, \quad \text{and} \quad \epsilon_\theta = \frac{u}{r}; \tag{1}$$

where u and w are the radial and vertical components of the displacement vector, respectively. Let N_r and N_θ be the corresponding tensile forces per unit length and applying Hooke's law and we obtain

$$N_r = \frac{Eh}{1-\nu^2}(\epsilon_r + \nu\epsilon_\theta), \quad \text{and} \quad N_\theta = \frac{Eh}{1-\nu^2}(\epsilon_\theta + \nu\epsilon_r), \tag{2}$$

where h is the TBC thickness, E is the TBC Young's modulus, and ν is the TBC Poisson's ratio. The strain energy due to bending is given by

$$V = \frac{D}{2}\int_0^{2\pi}\int_0^a \left[\left(\frac{\partial^2 w}{\partial r^2}\right)^2 + \frac{1}{r^2}\left(\frac{\partial w}{\partial r}\right)^2 + \frac{2\nu}{r}\frac{\partial w}{\partial r}\frac{\partial^2 w}{\partial r^2}\right] r dr d\theta, \tag{3}$$

where D is the flexural rigidity of the plate, and is given by

$$D = \frac{Eh^3}{12(1-\nu^2)}. \tag{4}$$

The strain energy due to stretching of the middle plane is

$$V_1 = 2\pi\int_0^a \left(\frac{N_r\epsilon_r}{2} + \frac{N_\theta\epsilon_\theta}{2}\right) r dr. \tag{5}$$

The elastic deformation problem for a circular plate subjected to the boundary conditions indicated earlier was solved using a Rayleigh–Ritz method (an energy method) based on the following polynomial series solution:

$$w = \sum_{i=1}^{n} c_i\left(1 - \frac{r^2}{a^2}\right)^{i+1}, \quad \text{and}$$

$$u = r(a^2 - r^2)\left(\sum_{i=1}^{n} b_i r^{2i-2}\right) - \epsilon_0 r, \tag{6}$$

where c_i and b_i are constants to be evaluated from the condition that the total energy of the plate for a position of equilibrium is a minimum. Hence,

$$\frac{\partial V_1}{\partial b_i} = 0, \quad \text{and} \quad \frac{\partial(V + V_1)}{\partial c_i}\delta c_i = 2\pi\int_0^a p\delta w r dr. \tag{7}$$

The first part of Eq. 7 gives us an n-linear equation for the constants b_i, and these equations are solved in symbolic form. The second part of Eq. 7 gives us an n-nonlinear equation for the constants c_i; the solution of the constants b_i were used. All

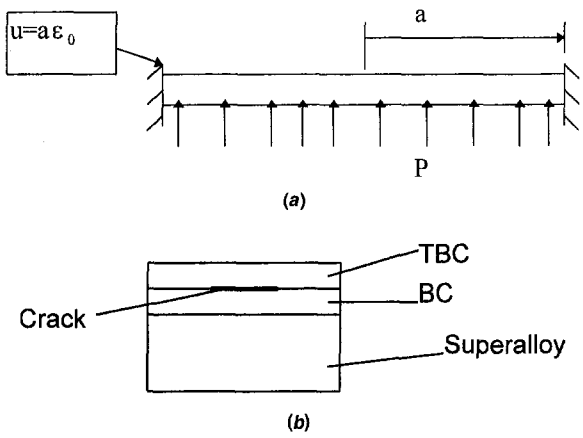

Fig. 1 (a) Circular plate under uniform pressure and edge displacement of $a\epsilon_0$ and (b) circumferential crack between the ceramic layer and the bond coat layer in a stepped-disk specimen

of this symbolic calculation is carried out by using *Mathematica* (1996). The set of nonlinear equations have been solved by IMSL (1989) library subroutine NEQNJ based on Levenberg–Marquardt algorithm with a user-supplied jacobian obtained by *Mathematica* also. The solution converged after 6 terms ($n = 6$) for the case considered.

The compressive strain in the TBC layer can be obtained by applying the equilibrium radial force equation for the three layers. This solution is valid only for thick substrate. The radial stress in each layer is written in the following form:

$$\sigma^c = \frac{E^c}{1-\nu^c}[\epsilon - \alpha^c(T - T_r)],$$

$$\sigma^b = \frac{E^b}{1-\nu^b}[\epsilon - \alpha^b(T - T_r)]$$

$$\sigma^s = \frac{E^s}{1-\nu^s}[\epsilon - \alpha^s(T - T_r)], \tag{8}$$

where σ is the radial stress, α is the thermal expansion coefficient, and T_r is the stress-free temperature, and the superscripts c, b, and s refer to TBC, bond coat, and substrate, respectively. The equilibrium radial force equation for the three layers is

$$\sum F = \sigma^c A^c + \sigma^b A^b + \sigma^s A^s = 0. \tag{9}$$

Substituting Eq. 8 into Eq. 9, and solving for ϵ gives

$$\epsilon = \frac{\left(\frac{E^c}{1-\nu^c}\alpha^c A^c + \frac{E^b}{1-\nu^b}\alpha^b A^b + \frac{E^s}{1-\nu^s}\alpha^s A^s\right)(T - T_r)}{\frac{E^c}{1-\nu^c}A^c + \frac{E^b}{1-\nu^b}A^b + \frac{E^s}{1-\nu^s}A^s}. \tag{10}$$

Now, the compressive strain in TBC is

$$\epsilon_0 = \epsilon - \alpha^c(T - T_r). \tag{11}$$

In case of temperature dependent properties, the previous Eqs. 8–11 will be written in incremental form for each dT, then they will add up to get the right value of ϵ. For example, the variation of ϵ due to dT change in temperature will be given as

$$d\epsilon = \alpha|_T(T - T_0) - \alpha|_{T-dT}(T - dT - T_0), \tag{12}$$

where T_0 is the reference temperature and is equal to zero.

Computational Fracture Analysis. Linear elastic fracture mechanics can be used to assess the conditions for crack growth of bimaterial interfaces. The mechanics of interface fracture can be traced back to the earlier works of Griffith (1921) and Irwin (1960) on the general theory of fracture, of Williams (1959) on the elastic stress distribution around an interface crack, and of England (1965), Erodogan (1965), and Rice and Sih (1965) on explicit solutions for interface cracks. The classical fracture mechanics concepts enable us to predict, without a detailed description of the crack tip processes, crack growth behavior in a fracture specimen. In recent years, complexity of obtaining closed-form solutions have been circumvented through computational fracture analysis to determine conditions for crack growth at bimaterial interfaces. However, the analytical basis is essential to studying the critical parameters that characterize interface fracture.

Another approach to characterize fracture at bimaterial interface is via the J-integral. Originally developed by Eshelby (1956), the basic concept of J-integral is a path-independent evaluation of the energy release rate. In other words, it is a measure of decrease in potential energy of the system with increase in crack length. In linear elastic fracture mechanics

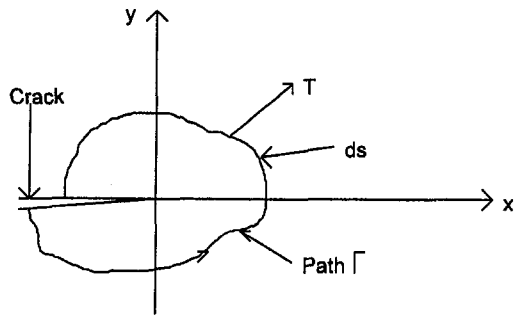

Fig. 2 Notation and parameters used for *J*-integral

"J" is equivalent to G. The J-integral can be written as (Rice, 1968)

$$J = \int_\Gamma W dy - \int_\Gamma T\frac{\partial u}{\partial x}\,ds, \tag{13}$$

where W is the strain energy density. Figure 2 shows the notation and parameters for J-integral for a homogeneous medium. The analysis can be easily extended for a line crack between two materials assuming crack growth along the interface. The essence of J definition and its meaning remains unaltered for a crack at the bimaterial interface.

Following the work done by Yin (1985), the energy release rate associated with uniform-expansion growth of a circular delamination in a compressively loaded plate is obtained by means of the M-integral. The strain energy-release rate per unit increment of the area of delimination is given by

$$G = \frac{1-\nu^2}{2Eh}\left\{\left[\frac{Eh}{1-\nu}\epsilon_0 - N_r(a)\right]^2 + 12\left[\frac{M_r(a)}{h}\right]^2\right\}, \tag{14}$$

where $M_r(r)$ is given by

$$M_r(r) = D(w'' + \nu w'/r), \tag{15}$$

where the prime denote differentiation with respect to r.

For arbitrary combinations of N and M the stress field at the crack tip is governed by both K_I and K_{II} (Thouless et al., 1987). Dimensional considerations require that the stress intensity factors be related to the load quantities by

$$K_I = d_1 N h^{-0.5} + d_2 M h^{-1.5}, \quad K_{II} = d_3 N h^{-0.5} + d_4 M h^{-1.5}, \tag{16}$$

where the d_i are constants. The energy release rate is given by

$$G = \frac{(1-\upsilon^2)}{E}(K_I^2 + K_{II}^2). \tag{17}$$

Solving the crack problem for one loading combination and comparison of Eqs. 16 and 17 gives (Thouless et al., 1987)

$$d_1 = 0.434, \quad d_2 = 1.934, \quad d_3 = 0.558, \quad d_4 = -1.503. \tag{18}$$

There is one idealized condition that we explored related to the specimen geometry. The presence of circumferential crack between the ceramic layer and the bond coat layer is as shown in Fig. 1, which was analyzed using finite element method. The general code ABAQUS (1995) was used for these analyses. The energy release rate G can be estimated by using the virtual crack extension method. The J-integral value can be found directly from ABAQUS.

Within linear elastic fracture mechanics, two parameters are generally used to describe the conditions at the crack tip, normally the stress intensity factor(s), and the energy release rate. Evaluation of the stress intensity factor requires a through understanding of the state of stress at the crack tip. Energy release

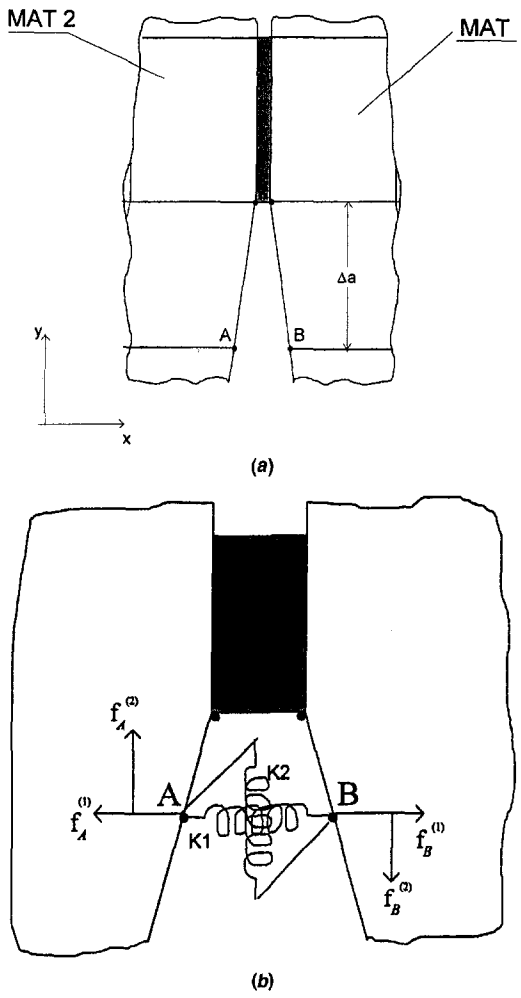

Fig. 3 (*a*) Interfacial crack between bond coat and TBC and (*b*) forces and displacement illustrations for a crack

rate evaluation, on the other hand, is based more on an energy criteria, and, hence, is more popular.

A procedure for calculating the energy release rate, G, that has gained increasing acceptance over the past decade is the virtual crack extension method (VCEM). This was originally developed by Hellen and Parks (1975), who subsequently extended the method to cover material nonlinearities, and the evaluation of the J-integral. The strain energy release rate components G_I and G_{II} are calculated at the crack tip based on the Irwin's crack closure integral, which primarily states that, while considering a virtual crack extension method, the strain energy released is equal to the work done to close the crack back to the original size. The total strain energy release rate G_t could be evaluated through this integral by considering two problems with crack lengths of a and $a + da$, and finding the difference between their levels of strain energy. It can be seen that this method is very convenient to evaluate the individual strain energy release rate components, G_I and G_{II}, in a mixed mode situation. Dattaguru et al. (1994) used this method to evaluate the strain energy release rate components, G_I and G_{II}, at bimaterial interface. Three models were used in their study; namely, the bare interface model, the resin layer model, and the subinterface crack model. The oscillatory singularity is not present in the resin layer model and in the subinterface crack model. For the case were the resin layer thickness and the distance between the subinterface crack and the interface are progressively decreased to an infinitesimally small value, they follow the trends of the bare interface model.

The method of VCE used to evaluate G is explained in the following few steps. The energy release rates in mode I and II are given by

$$G_I = \frac{1}{2A} f_x \Delta u_x, \quad G_{II} = \frac{1}{2A} f_y \Delta u_y, \tag{19}$$

where f_x and f_y are the reaction forces, A is the crack surface area corresponding to Δa, and similarly Δu_x and Δu_y are the difference in the displacements of nodes A and B in the x and y-directions respectively (Figs. 3(a) and 3(b)).

The reaction forces and the displacements were obtained via two runs. For the first run, we assume a very weak spring, so the opening displacement and sliding displacement can be determined from springs deflection. In the second run, the spring stiffness is assumed to be very high compared to the material stiffness, so the reaction forces can be determined. In this study, an eight node isoparametric element is used. The energy release rates in mode I and mode II are given by

$$G_I = \frac{1}{2A} [f_{x1} \Delta u_{x1} + f_{x2} \Delta u_{x2}],$$

$$G_{II} = \frac{1}{2A} [f_{y1} \Delta u_{y1} + f_{y2} \Delta u_{y2}]. \tag{20}$$

Hence,

$$G_{\text{total}} = G_I + G_{II}. \tag{21}$$

Results and Discussion

The presence of circumferential crack between the ceramic layer and the bond coat layer as shown in Fig. 1 was analyzed using a Rayleigh–Ritz method and finite element method. The general code ABAQUS was used for finite element analysis. The energy release rate G was estimated by using the virtual crack extension method.

Finite element method was used in order to determine the J-integral value and the energy release rate. Virtual crack extension method was used to evaluate the energy release rate for both Mode I and Mode II crack growth. For layered disk specimen, the disk radius is 12.7 mm, the bond coat layer thickness is 0.04826 mm, the TBC thickness is 0.127 mm, and the uncoated Nickel-based superalloy had a thickness of 3.175 mm. These dimensions are shown in Fig. 4. The properties of these three layers are given in Table 1. We analyzed a model case where the specimen was plasma sprayed in air with a thin zirconia–yttria ($ZrO_2 - 8$ wt% Y_2O_3) layer on a nickel-chromium-aluminum-zirconium bond coat, as in Chang et al. (1987). The speci-

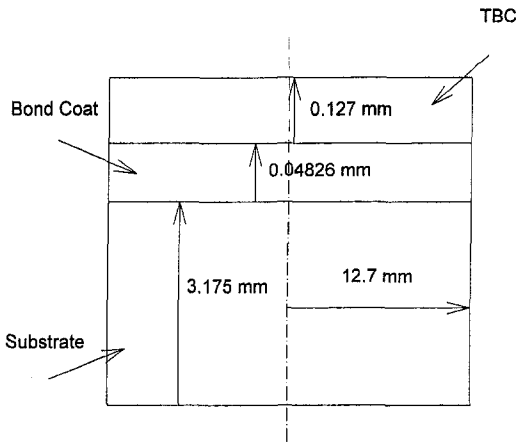

Fig. 4 Dimension of TBC layer in relation to bond coat and superalloy substrate

Table 1 Material properties at 22, 566 and 1149°C

Material	Young's modulus (GPa)	Poisson's ratio	Coefficient of thermal expansion ($^0C^{-1}$)
Substrate	175.8 150.4 94.1	0.25 0.2566 0.3224	13.91×10^{-6} 15.36×10^{-6} 19.52×10^{-6}
Bond coat	137.9 121.4 93.8	0.27 0.27 0.27	15.16×10^{-6} 15.37×10^{-6} 17.48×10^{-6}
TBC	27.6 6.9 1.84	0.25 0.25 0.25	10.01×10^{-6} 11.01×10^{-6} 12.41×10^{-6}

men was cooled down from a processing temperature of 1000°C to a temperature of 0°C. A half model for stepped-disk specimen was used since the specimen is axisymmetric. An eight node isoparametric element type was used; the total number of elements was 1380. Along the longitudinal axis, the nodes can move in the axial direction only. The mesh was very fine close to the crack tip, and to make sure that the mesh is fine enough, another model with the same number of element but has one tenth of element size near to the crack tip; the difference in the results was less than 1 percent. Details of the finite element mesh near the crack tip is shown in Fig. 5.

Figure 6 shows the variation of maximum deflection versus pressure ratio for a delamination radius of 20 times the TBC thickness. For zero pressure load, the deflection has a value greater than zero due to early stage of buckling. At this stage, the total energy release rate at crack tip may not be high enough for crack propagation. However, as the coating deflection increases to gradual buckling and induced crack surface pressure, G_t may exceed the critical value that can cause crack growth. It is clear that the use of temperature-dependent properties in contrast to constant properties provide significantly different values of maximum deflection. The finite element results compare to numerical results correlate very well. The variation of the maximum deflection versus pressure ratio is nonlinear compare to linear variation, as in the case of no geometrical nonlinearity. Using temperature dependent properties gives a 20–30 percent higher maximum deflection and energy release rate, as seen in Figs. 6 and 7. The variation of J and G_t versus pressure ratio from finite element method and virtual crack extension method (VCEM) are shown in Fig. 7. Comparison between the energy release rate evaluated by energy method and by finite element method (J-integral) is shown in Fig. 8. The finite element method and numerical method are in very good agreement.

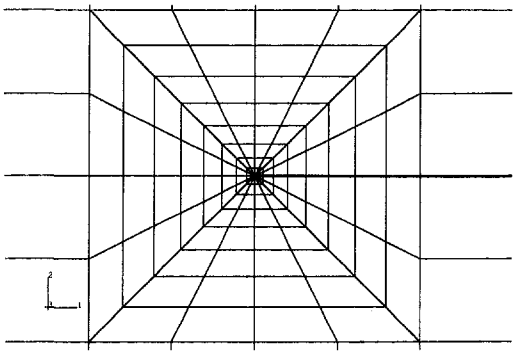

Fig. 5 Detailes of near crack-tip finite element mesh

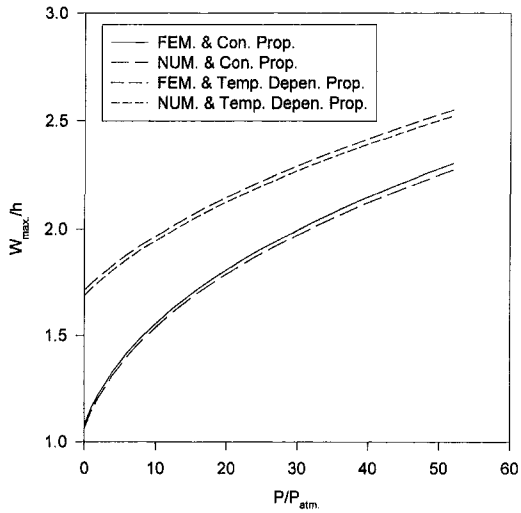

Fig. 6 Variation of maximum deflection versus pressure ratio, for both constant (Con.) and temperature (Temp.) dependent properties (Prop.), $a = 20h$

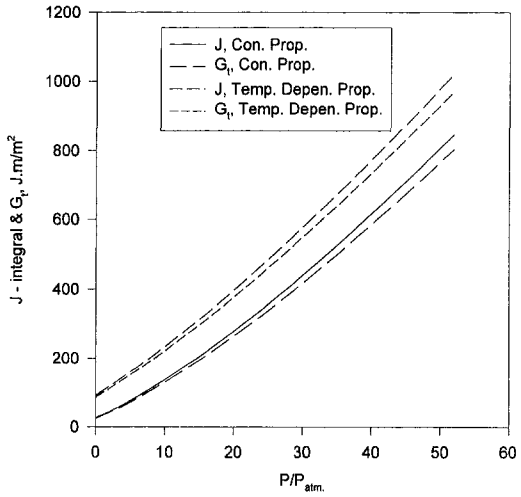

Fig. 7 Variation of the J & G versus pressure ratio, for both constant and temperature dependent properties, $a = 20h$

Figure 9 shows the variation of G_I and G_{II} versus pressure ratio for a delamination radius of twenty times the TBC thickness. This figure shows good agreement between finite element method results based on VCEM and numerical results. Mode I is dominant in this case. Figure 10 is same as Fig. 9, but temperature dependent properties were used. In Fig. 10, we observe that Mode II energy release rate component is much smaller compared with the mode I component for both numerical and VCEM analyses. In either case, results match well. Figure 11 shows the variation of J-integral delamination radius from numerical analysis. From this figure, one can obtain the conditions when the crack will propagate. From literature the critical energy release rate is varied between 100–300 J · m/m^2 for this system configuration. For a value of 300 J · m/m^2, and a delamination radius of four times the TBC thickness, the crack will propagate at induced pressure value equivalent to 500 atmosphere ($\approx$50 MPa). This value is easy to develop due to volume increase because of oxide layer growth. Also, based on finite element analysis conducted by the authors for this system with a wavy interface, the results shows that an axial stress of 250 MPa can be developed for a sine wave interface with amplitude

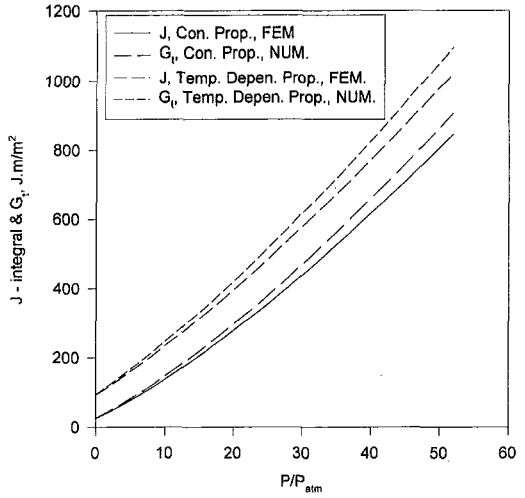

Fig. 8 Variation of J & G versus pressure ratio, numerical, and finite element method are used, for both constant and temperature dependent properties, $a = 20h$

of 2.4 μm and wave length of 127 μm. These values are practical for this system (Newaz et al., 1996).

Conclusions

The effect of interfacial microcracks was investigated using a fracture mechanics approach under thermomechanical loading. Thermal load was used in conjunction with internal surface induced pressure for interfacial cracks. The use of temperature-dependent properties in contrast to constant properties provide significantly different values of J-integral and G values. A layered disk-type specimen with a central crack has mixed mode conditions under thermomechanical loading. The total energy release rate evaluated by the virtual crack extension method and the J-integral value, evaluated directly by ABAQUS, agree quite well. The maximum deflection and total energy release rate evaluated by finite element method and energy method are in very good agreement.

For a TBC toughness value of 300 J · m/m^2 and a delamination radius of four times the TBC thickness, the crack will propagate at induced pressure value equivalent to 500 atmosphere ($\approx$50 MPa). The results clearly indicate that small internal pressure due to oxidation-induced volume change may create the necessary conditions for crack growth during thermal

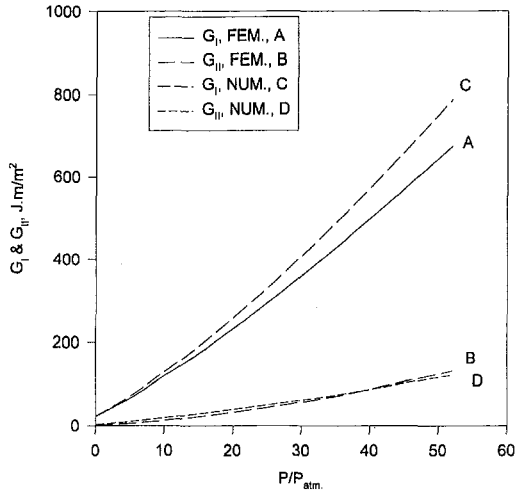

Fig. 9 Variation of G_I & G_{II} versus pressure ratio, numerical, and finite element methods are used, constant properties, $a = 20h$

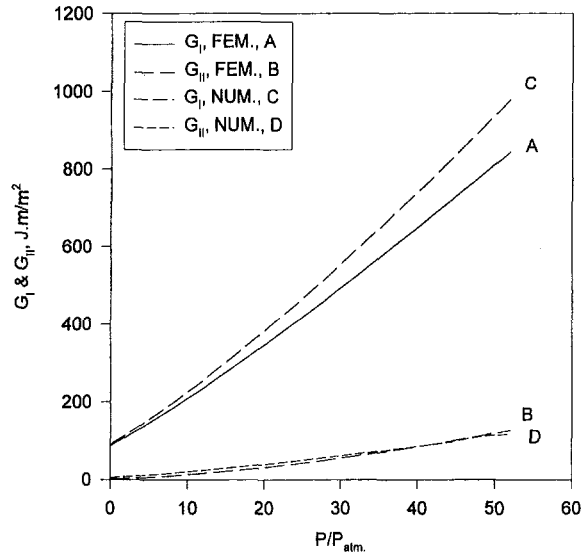

Fig. 10 Variation of G_I & G_{II} versus pressure ratio, numerical, and finite element method are used, temperature dependent properties, $a = 20h$

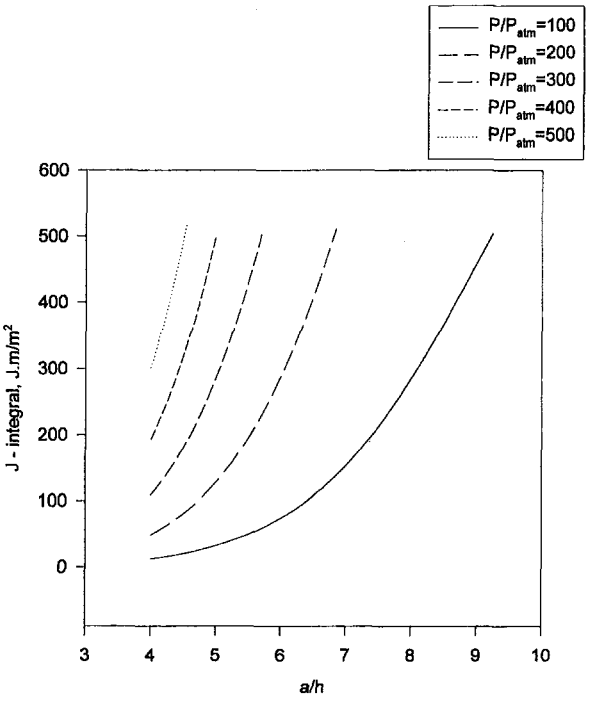

Fig. 11 Variation of G versus delimination radius at different pressure ratio, numerical, and temperature dependent properties are used, $a = 20h$

cycling. This value may easily develop due to volume increase because of oxide layer growth or due to the presence of a wavy interface.

Acknowledgment

Funding for this research was provided through a grant (#F49620-95-1-0201) from the Air Force Office of Scientific Research (AFOSR). Dr. Walter Jones is the program monitor. Discussion and interaction with Dr. P. K. Wright of GEAE is gratefully acknowledged.

References

Ahmad, J., 1993, "A Micromechanics Based Representation of Combined Mode I and Mode II Toughness of Brittle Materials and Interfaces," *ASME Journal of Engineering Materials and Technology,* Vol. 115, pp. 101–105.

ABAQUS, 1995, Hibbitt, Karlsson and Sorensen, Inc., 1080 Main Street, Pawtucket, RI 02860-4847.

Aravas, N., and Sharma, S. M., 1991, "An Elastoplastic Analysis of the Interface Crack with Contact Zones," *J. Mech. Phys. Solids,* Vol. 39, No. 3, pp. 311–344.

Blanchard, J. P., and Ghoniem, N. M., 1989, "Relaxation of Thermal Stress Singularities in Bonded Viscoelastic Quarter Planes," *ASME Journal of Applied Mechanics,* Vol. 56, pp. 756–762.

Bottega, W. J., and Maewal, A., 1983, "Delamination Buckling and Growth in Laminates," *Transactions of the ASME,* Vol. 50, 184–189.

Bottega, W. J., and Maewal, A., 1983, "Dynamics of Delamination Buckling," *Int. J. Non-Linear Mechanics,* Vol. 18, No. 6, pp. 449–463.

Chai, H., 1990, "Three-Dimensional Fracture Analysis of Thin-Film Debonding," *Int. J. Fracture,* Vol. 46, pp. 237–256.

Chang, G. C., and Phucharoen, W., and Miller, R. A., 1987, "Finite Element Thermal Stress Solutions for Thermal Barrier Coatings," *Surface and Coatings Technology,* Vol. 32, pp. 307–325.

Dattaguru, B., Venkatesha, K. S., Ramamurthy, T. S., and Buchholz, F. G., 1994, "Finite Element Estimates of Strain Energy Release Rate Components at the Tip of an Interface Crack Under Mode I Loading," *Engineering Fracture Mechanics,* Vol. 49, No. 3, pp. 451–463.

Dundurs, J., 1969, discussion, *ASME Journal of Applied Mechanics,* Vol. 36, p. 650.

England, A. H., 1965, "A Crack Between Dissimilar Media," *ASME Journal of Applied Mechanics,* Vol. 32, pp. 400–402.

Erdogan, F., 1965, "Stress Distribution in Bonded Dissimilar Materials With Cracks," *ASME Journal of Applied Mechanics,* Vol. 32, pp. 403–410.

Eshelby, J. D., 1956, "The Continuum Theory of Lattice Defects in Solid State Physics," Vol. 3, pp. 79–141.

Evans, A. G., Crumely, G. B., and Demaray, R. E., 1983, "On the Mechanical Behavior of Brittle Coatings and Layers," *Oxidation of Metals,* Vol. 20, No. 5/6.

Evans, A. G., and Hutchinson, J. W., 1984, "On the Mechanics of Delamination and Spalling in Compressed Films," *Int. J. Solids Structures,* Vol. 20, No. 5, pp. 455–466.

Griffith, A. A., 1921, *Phil. Trans. Roy. Soc. Lond.,* Vol. A221, pp. 163–197.

Hellen, T. K., 1975, "On the Method of Virtual Crack Extensions," *Int. J. Num. Meth.,* Vol. 9, pp. 187–207.

IMSL, 1989, User's Manual, version 1.0, Visual Numerics, Inc., Houston, TX.

Irwin, G. R., 1960, *Structural Mechanics,* J. N. Goodier and N. J. Hoff, eds., Pergamon Press, Oxford, pp. 557–591.

Jin, Z., and Noda, N., 1994, "Crack-Tip Singular Fields in Nonhomogeneous Materials," *ASME Journal of Applied Mechanics,* Vol. 61, pp. 738–740.

Kokini, K., and Hornack, T. R., 1988, "Transient Thermal Load Effects on Coatings Bonded to Cylindrical Substrates and Containing Circumferential Cracks," *J. of Eng. Mat. and Tech.,* Vol. 110, pp. 35–40.

Mathematica, 1996, version 3, Wolfram Media, Inc., Champaign, IL.

Nahta, R., and Moran, B., 1993, "Domain Integrals For Axisymmetric Interface Crack Problems," *Int. J. Solids Structures,* Vol. 30, No. 15, pp. 2027–2040.

Newaz, G. M., Nusier, S. Q., Chaudhury, Z. A., and Wright, K. P., 1996, "Damage Accumulation Mechanisms in Thermal Barrier Coatings," presented at IMECE'96, Atlanta, GA.

Nusier, S. Q., and Newaz, G. M., 1996, "Analysis of Interfacial Cracks in a TBC/Superalloy System Under Thermal Loading," submitted to J. of Engineering Fracture Mechanics.

Oneil, D. A., and Wayne, S. F., 1994, "Numerical Simulation of Fracture in Coated Brittle Materials Subjected to Tribo-Contact," *J. of Eng. Mat. and Tech.,* Vol. 116, pp. 471–478.

Rice, J. R., 1988, "Elastic Fracture Mechanics Concepts of Interfacial Cracks," *ASME Journal of Applied Mechanics,* Vol. 55, pp. 98–103.

Rice, J. R., 1968, "Mathematical Analysis in the Mechanics of Fracture, in Fracture," treatise, H. Leibowitz, ed., Vol. 2, Academic Press, New York, pp. 191–311.

Rice, J. R., and Sih, G. C., 1965, "Plane Problems of Cracks in Dissimilar Media," *ASME Journal of Applied Mechanics,* Vol. 32, pp. 418–423.

Ryan, R. L., and McCafferty, E., 1995, "Rupture of an Oxide Blister," *J. Electrochem. Soc.,* Vol. 142, No. 8, pp. 2594–2597.

Suo, Z., 1995, "Wrinkles of the Oxide Scale on an Aluminum–Containing Alloy at High Temperature," *J. of Mechanics of Physics and Solids,* Vol. 43, No. 6, pp. 829–846.

Takeuchi, Y. R., and Kokini, K., 1994, "Thermal Fracture of Multilayer Ceramic Thermal Barrier Coatings," ASME JOURNAL OF ENGINEERING FOR GAS TURBINES AND POWER, Vol. 116, pp. 266–271.

Thouless, M. D., Evans, A. G., Ashby, M. F., and Hutchinson, J. W., 1987, "The Edge Cracking and Spalling of Brittle Plates," *Acta Metall.,* Vol. 35, No. 6, pp. 1333–1341.

van der Zande, H. D., and Grootenboer, H. J., 1986, "A Finite Element Approach to Interface Cracks," *ASME Journal of Applied Mechanics,* Vol. 53, pp. 573–578.

Wan, K., and Mai, Y., 1995, "Fracture Mechanics of a Shaft-Loaded Blister of Thin Flexible Membrane on Rigid Substrate," *Int. J. Fracture,* Vol. 74, pp. 181–197.

Williams, M. L., 1959, "The Stresses Around a Fault or Crack in Dissimilar Media," *Bull. Seismol. Soc. Am.,* Vol. 49, pp. 199–204.

Yin, W., 1985, "Axisymmetric Buckling and Growth of a Circular Delamination in a Compresses Laminate," *Int. J. Solids Structures,* Vol. 21, No. 5, pp. 503–514.

Ceramic Coating Edge Failure Due to Thermal Expansion Interference

H. A. Nied
Advanced Manufacturing Technology Associates, 13 Shadow Wood Way, Ballston Lake, NY 12019

An investigation of thermal barrier coatings on a metal substrate was conducted when the assembly was subjected to both thermal heating and mechanical edge loads generated by interference in adjoining expansion gaps. Both finite element and closed form solution models were developed and compared. The results of the analyses predict that the application of both thermal and mechanical edge loads on the edge of ceramic/metal composites can produce severe local edge spallation in the ceramic coating when an inadequate expansion gap is provided.

Introduction

Ceramic thermal barrier coatings on metal substrates provide a reduced temperature in the metal due to the low thermal conductivity of the ceramics that enhances the capability of the ceramic/metal structure. Many fabrication methods are currently being used to produce ceramic coatings on metal substrates. Schwartz (1990) describes the various methods currently used to either join or apply ceramics to other materials. The fabrication of a ceramic coating onto a metal substrate has always been a challenge because of the extreme mismatch in the material properties such as the thermal expansion and elastic modulus. A common coating process is the thermal plasma spray technique that is currently widely used for coating many types of metal components in the aircraft engine industry.

In the thermal spray process, the metal substrate is first prepared by applying a thin coat of material called the bondcoat acting as a graded transition between the metal and ceramic coating. Then ceramic layers are applied to the bondcoat by the solidification of droplets of molten ceramic particles in the form of stacked platelets. A molten spherical droplet of ceramic impinges first onto the bondcoat and metal substrate. Then, successive layers are deposited over previously deposited ceramic with each pass of the torch. Each ceramic particle releases its heat energy into the bulk material and, thereby, rapidly solidifies. The exchange of heat energy increases the temperature of the previously deposited ceramic and metal substrate considerably above the ambient during the spraying process. This thermal plasma spray process producing successive layers with each pass of the torch fabricates, essentially, a multilayered composite. Verbeek (1992) describes in detail the production, characterization, and testing of thermal barrier coatings manufactured by the spray process. His research was focused on the formation mechanism and the microstructure of the coating.

This fabrication process of coating produced at elevated temperature by incremental spray layering generates residual stresses in the assembly when it is cooled to room temperature. Generally, the uniformity and thickness of the thermal barrier coating on the metal substrate can be controlled to design requirements. However, it is difficult to control the amount of overspray at the edges of the component, which can lead to subsequent manufacturing problems. Edge overspray requires an additional grinding operation to square the ends, and provides the necessary uniformity of the coated structure when mounted adjacent to other components in gas turbine engines. Expansion gaps must be established between components to prevent large mechanical loads being applied against the ceramic coating leading to cracking and spallation.

A variety of ceramic coated assemblies have been incorporated into aircraft engine hot gas path components for thermal protection such as shrouds, turbine blades, and elements in combustors. When an assembly of ceramic coated components are used in arrays, design engineering must provide an adequate expansion gap between assemblies to prevent the edge loading of the ceramic coated assembly. Figure 1 shows the type of expansion gap interference that can occur.

If too large an expansion gap is used, the structure is thermally inefficient and unwanted excessive interior heating of the metal substrate can cause damage. If not enough clearance between components is provided, the thermal expansion of the ceramic/metal structure can produce very high edge loads on the ceramic coated assembly leading to subsequent spallation, delamination, and failure of the ceramic coating, as shown in Fig. 2. The situation of gap closure is particularly damaging if the ceramic extends beyond the edge of the metal substrate.

This paper investigates ceramic/metal assemblies subjected to both thermal stress and mechanical edge loads when there is an inadequate thermal expansion gap between the adjacent components. The severe edge loading produced, even though it is compressive, usually leads to edge cracking, delamination, or a spallation failure. This problem was investigated using a finite element computer program to determine the severity of various edge loads on ceramic systems when subjected to simulated engine heating.

Since cracks and spallation have been observed during both manufacturing and application, analyses were conducted with and without cracks in the vicinity of the interface between the coating, bondcoat, and metal substrate. Edge loading on the ceramic coatings creates both a combined opening and shear fracture mode that produces a spallation of the material in the region where the expansion interference occurs.

In addition, as a part of this study a closed form solution to determine the stress intensity factor for an edge loaded single material was also derived that could provide design engineering with a simple approximate solution to prevent excessive edge loading on ceramic coated assemblies before constructing a refined FE model.

Background

Many published studies have focused on the state of stress at the free edge of the thermal mismatched assembly. These investigations have revealed the existence of a stress singularity at the free edge that is generated by both the geometry and the difference in the material properties at the interface. This

Contributed by the International Gas Turbine Institute and presented at the International Gas Turbine and Aeroengine Congress and Exhibition, Orlando, FL, June 2–5, 1997. Manuscript received by the ASME Headquarters March 20, 1997. Paper No. 97-GT-410. Associate Technical Editor: H. A. Kidd.

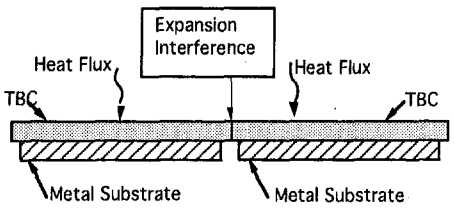

Fig. 1 Ceramic coated shroud subjected to edge interference

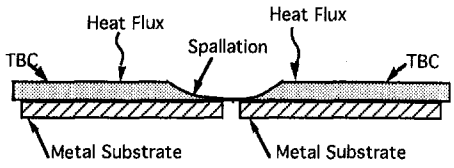

Fig. 2 Ceramic coated shroud edge spallation

localized stress field was found to have a pronounced effect on the stress intensity factors of edge interfacial cracks.

Raju and Crews (1981) developed a quasi-three-dimensional analysis to analyze the edge stress problem for a four-layer composite using a finite element formulation. Their results clearly show a free edge stress concentration that is due to both a geometric singularity and the material mismatch in properties. Kokini (1984) determined the thermal stresses at the free edge of finite cylinders made of dissimilar materials using the finite element method. His results indicated a singularity on the free edge at the dissimilar material interface. Parks (1988) reported the results of his experiments conducted to determine the interfacial stress behavior of bonded bimaterial specimens. His results confirm the existence of edge stress concentrations. Kuo (1989), using a structural mechanics formulation, investigated a semi-infinite, bimetallic thermostat model subjected to uniform heating or cooling. He discusses in detail the free edge boundary layer effect; namely, the existence of a free edge stress singularity that gives rise to high local stress concentration at the interface. Nied (1991a) developed a simple one-dimensional ceramic coated metal substrate model to determine the shear stress distribution at the interface of dissimilar materials due to the thermal mismatch of expansion properties of the components during elevated temperature processing that was applied to a representative thermal barrier coating on a metal substrate.

All of the above investigations were directed to determining the state of stress at the dissimilar material interface and the free edge of composite. Their results revealed that the localized free stress concentration played an important role in the structural integrity of the composite and its propensity for delamination.

These investigations were complemented by the modeling and analyses of dissimilar material composites from the fracture mechanic's viewpoint. Experimental research and analytic studies were conducted to determine the stress intensity factors generated when there is an edge crack at the interface, near the interface, and at the free edge of a composite by using linear elastic fracture mechanics theory.

In general, the focus in the literature has been to investigate the structural behavior of bonded dissimilar materials using a fracture mechanic's formulation. Several of these references are cited for completeness. Rice and Sih (1965) determined the stress intensity factors for cracks at the common interface of dissimilar materials using the complex potential approach of Muskhelishvili. Lu and Erdogan (1983a, b) determined the stress intensity factors of cracks on or approaching the interface of dissimilar materials by using integral equation formulations. One of the cases studied by Lu and Erdogan (1983b) provided the solution for the stress intensity factors at the intersection of the free end for thermal mismatch by equivalent edge load conditions. Cannon et al. (1986) studied the decohesion of ceramic-metal interfaces by using a fracture energy concept. Thouless et al. (1987) investigated the cracking and spalling due to edge loading by analysis and test.

Kokini (1987) investigated the effect of changing thermal expansion coefficients on the deformation and the edge interfacial crack between a ceramic-to-metal bond subjected to a transient thermal load when the state of stress at the free edge plays an important role on bond integrity. Rice (1988) reexamines the fracture mechanics concepts applied to a crack at the common interface in a dissimilar material. Kokini (1988) continues his investigation of interfacial cracking of dissimilar materials when subjected to transient thermal loading. Here again, it is shown that the state of stress at the free edge plays an important role on bond integrity. Thouless et al. (1989) studied the delamination of ceramic coatings using a strain energy release rate method applied to a simple model. Nied (1991b) investigated the stress intensity factors for an edge crack originating at the interface of a ceramic-metal composite for the thermal mismatch residual stresses produced by a plasma spray process using both a closed form mathematical solution for the edge stress concentration and a finite element model. It is obvious that an understanding of the fracture behavior at dissimilar material interfaces are of great interest for the application of thermal barrier coated assemblies.

Modeling Description

Finite Element Model Description. An updated version of a two-dimensional FE computer code developed by Gifford (1979), which had the capability for both thermal stress and fracture mechanics analyses, was used for investigating edge load behavior of thermal barrier coated (TBC) assemblies. A 455 node half model was constructed with a refined mesh at the free edge and along the bondcoat between the metal substrate and the ceramic coating. This FE model was used to investigate the structural behavior due to cool down from manufacturing as well as determining the thermal stresses and mechanical loads generated during simulated engine application. Figure 3 shows the general mesh features of this model.

The cool down analysis from the processing temperature revealed that very high residual stresses were generated in the ceramic at the free edge along the bondcoat interface. The magnitude of these stresses were found to be sufficient for crack nucleation for some designs and processing variables. Therefore, computer runs were made with and without a crack at the free end to examine this condition.

Nomenclature

E = modulus of elasticity, Pa
K_I = opening mode stress intensity factor, Pa $\sqrt{m}$
K_{II} = shear mode stress intensity factor, Pa $\sqrt{m}$
M = edge moment, N-m
P = edge axial compressive load, N
a = substrate edge distance to crack tip, m
c_i = load coefficients with index i = 1, 2, 3, 4
c = ceramic edge distance to crack tip, m
h = ceramic coating thickness, m
e = exponent
δ = edge displacement, m

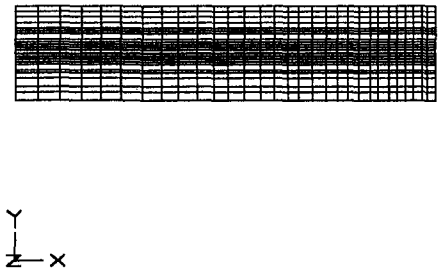

Fig. 3 Finite element mesh model of ceramic/bondcoat/metal substratecomposite

The FE program uses a 12-node isoparametric cubic element that provided the potential for evaluating the free edge distortion and stress concentration to a much higher degree than the usual four-noded quad elements commonly used in FE codes. In addition, the FE code has the feature for inserting enriched crack tip elements that contain the necessary fracture mechanics singularity that can be conveniently applied to the edge and interior crack geometries. Therefore, a FE analysis would directly provide both the K_I and the K_{II} stress intensity factors for the opening mode I and shear mode II, respectively. In addition, the FE program provided the mixed mode equivalent stress intensity factor and the direction of crack propagation based on the maximum normal stress across the crack.

The finite element models constructed were used for investigating various cases such as complicated composite geometries subjected to nonlinear temperature fields and mechanical loads induced by edge interference. In addition, some of these results were compared to the simple approximate analytic model derived for design purposes. For comparison to the closed form solution, the 455 node multi-material FE model was simplified to an isothermal condition and equivalent material properties with the same basic edge geometry used in the simple closed form solution.

Mathematical Model Description. Figure 4 shows the model used by Thouless et al. (1987) for determining a closed form solution of an edge loaded corner of a single brittle material subjected to both a force and a moment by combining asymptotic solutions for short and long cracks. Their solutions for both the opening and shear mode stress intensity factors were found to be

$$K_I = c_1 \frac{P}{\sqrt{h}} + c_2 \frac{M}{h^{3/2}}$$

$$K_{II} = c_3 \frac{P}{\sqrt{h}} + c_4 \frac{M}{h^{3/2}}, \tag{1}$$

where the associated coefficients for the K-factor expressions are given by

$$c_1 = 0.434,$$

$$c_2 = 1.934,$$

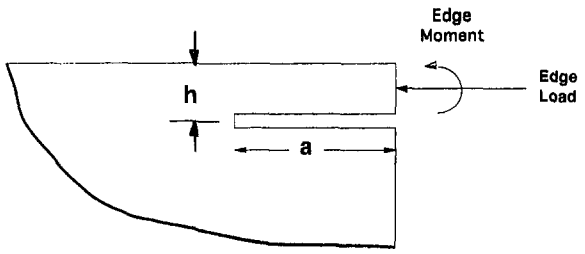

Fig. 4 Thouless model for edge load

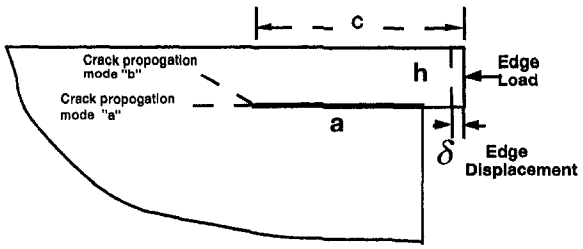

Fig. 5 Fracture mechanics model for edge load

$$c_3 = 0.558,$$

$$c_4 = -1.503. \tag{2}$$

Following the method used by Thouless et al. (1987), a similar model, Fig. 5, was constructed having a layer thickness **h** subjected to an ceramic edge displacement δ with a crack length **a**. This single brittle material model is used as a first-order approximation of coating on a substrate. Following the method used by Thouless et al. (1987), an approximate solution for the stress intensity factors of a ceramic coated substrate subjected to edge displacement can be derived by combining the asymptotic solutions for short and long cracks.

The linear relationship for edge force and displacement is given by

$$P = (Eh)\left(\frac{\delta}{c}\right). \tag{3}$$

When the linear relationship for edge force and displacement is substituted into the derivation, the following simple expressions were determined:

$$K_I = 0.453E\sqrt{h}(1 - e^{-\sqrt{a/h}})\frac{\delta}{c},$$

$$K_{II} = 0.582E\sqrt{h}(1 - e^{-\sqrt{a/h}})\frac{\delta}{c}. \tag{4}$$

These simple approximate solutions based on a single material model can be effectively used by designers for sizing adequate expansion gaps before constructing a complex finite element model.

Results

Various FE models were used to simulate the mechanical interference and heat loading conditions of a first stage engine shroud. The expansion interference investigated was in the range of interference from 0.00 cm up to 0.0254 cm (0.010 in.) at an edge. Due to the symmetry of the structure, only the half length geometry 2.54 cm (1 in.) of the TBC shroud assembly was necessary to be modeled. This assembly consisted of NiCrAlY bondcoat 0.0381 cm (0.015 in.) thickness between the metal substrate of IN718 0.1575 cm (0.062 in.) in thickness and a ZrO_2 ceramic coating 0.132 cm (0.052 in.) in thickness. The design of the shroud is such that it is restrained in bending, but allowed to expand in the horizontal direction.

During manufacture, the ends of the TBC shrouds typically had an overspray extension beyond the end of the metal substrate of 0.0254 to 0.0381 cm (0.010 to 0.015 in.). After the edge grinding operation, the ceramic edge was held to (0.0254 cm (0.010 in.) overhang. An FE model of this geometry was constructed with a 0.0254 cm (0.010 in.) TBC overhang. Several cases of edge interference were investigated from zero to a maximum edge interference of 0.0254 cm (0.010 in.) edge interference corresponding to the ceramic overhang in the expansion gap. The edge interference was applied to the model

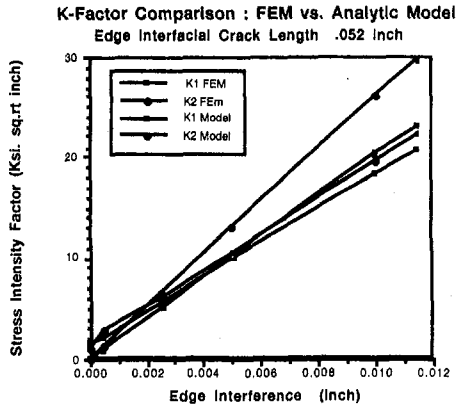

Fig. 6 Comparison of K factors obtained by FEM and analytic model

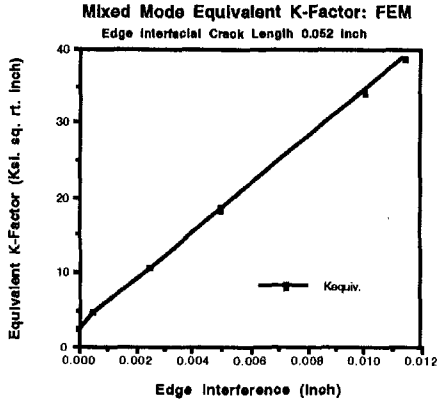

Fig. 8 Equivalent K-factor as a function of edge interference

while subjected to a through-the-thickness temperature gradient for this study of spallation and delamination propensity.

When a flux boundary condition, representative of a simulated engine application, was applied to the outer surface of the TBC in the FE model, a nonlinear temperature distribution was produced. The flux value was varied until the bottom surface of the metal substrate corresponded to temperature test measurements made during tests. The analyses determined that the temperature on the outer surface of the TBC was 1208°C (2207°F), 1065°C (1950°F) at the bondline, and 1052°C (1925°F) at the lower surface of the substrate. This temperature distribution was then used to conduct the mechanical interference analyses.

The localized edge distortion was primarily confined to the ceramic TBC and the localized shear stress concentration at the interface between the ceramic and metal substrate attained 1310 MPa (190 Ksi). To study the spallation behavior, a 0.132 cm (0.052 in.) crack was embedded in the model in the bondcoat interlayer between the ceramic and the metalsubstrate.

For pure thermal expansion interference, various interference cases were investigated and compared using both the mathematical model and the FE models.

Figure 6 compares both the K_I and K_{II} stress intensity factors for various edge interference applied to the edge of the TBC. Values of stress intensity factors for edge interferences from 0.0127 cm (0.005 in.) or higher could lead to spallation in the TBC. Reasonable agreement exists between the FE and analytic models for the K_I opening mode stress intensity factors. The disagreement for the K_{II} shear mode stress intensity factors between the FE and the analytic models is principally due to the analytic model being only valid for a homogeneous, single material without accounting for the shear deformation mechanism provided by the bondcoat.

Figure 7 shows the tendency for crack propagation in a 52 deg direction measured from the crack plane that is independent of the edge deformation over a broad range of edge interferences. This nearly constant angular direction is primarily due to the edge geometry and manner in which the edge load is applied. In this case, only a horizontal load without an edge moment was applied to the model.

Figure 8 shows a plot of the mixed mode equivalent stress intensity factor as a function of the edge interference that is essentially linear. The value of the equivalent stress intensity factor was provided directly as output from the FE program. Broek (1991) defines and describes the equivalent stress intensity factor relationship based on the mixed mode K_I and K_{II} stress intensity factors and the crack angle. When the equivalent stress intensity magnitude is equal to the fracture thoughness, spallation, and delamination would be predicted to occur.

As an aid to the designer, the approximate solution given by the Eq. (4) was nondimensionalized. That result is shown in Fig. 9 for determining either the K_I and K_{II} stress intensity factors generated by edge interference of the model shown in Fig. 5. It should be noted that this model tends to over predict the K_{II} shear mode stress intensity factors since the simplified model is composed of a single material and does not include the bondcoat transition interlayer. The grading effect provided by the bondcoat between the TBC and the metal substrate acts to reduce the interfacial shear stress and the shear deformation in the ceramic. Nevertheless, this solution was found to be convenient for obtaining approximate stress intensity values during component design or as an aid to construct a FE model.

Conclusions

Edge loads whether produced by mechanical or thermal interference are particularly damaging to a ceramic/metal composite.

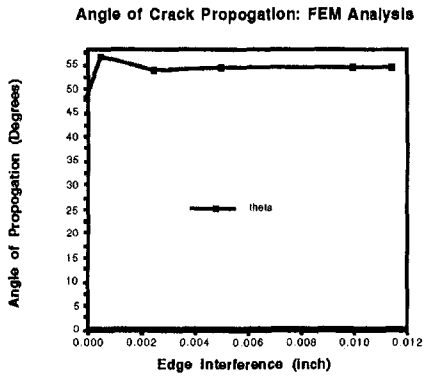

Fig. 7 Crack propagation angle as a function of edge interference

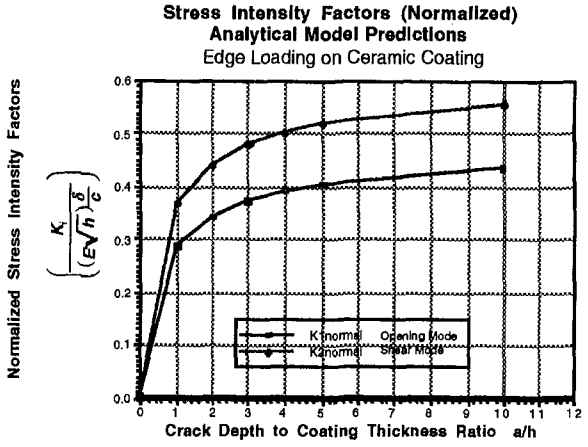

Fig. 9 Normalized stress intensity factors

If the edge load is applied to the ceramic, spallation of the ceramic locally at the edge is a typical failure mode well recognized in thermostructural designs. It was shown by both FE and mathematical modeling that the state of stress and the fracture mechanics stress intensity factors can be reasonably predicted. In the case of TBC coated thermal shrouds used in aircraft engines, careful consideration of the design must be made by thoroughly investigating the elevated temperature behavior.

References

Broek, D., 1991, *Elementary Engineering Fracture Mechanics,* 4th ed., Kluwer Academic Publishers, Boston, MA.

Cannon, R. M., Jayaram, V., Dalgleish, B. J., and Fisher, R. M., 1986, "Fracture Energies of Ceramic-Metal Interfaces," *Ceramic Microstructures '86—Role of Interfaces,* J. A. Pask and A. G. Evans, eds., Plenum Press, New York, pp. 959–968.

Gifford, L. N., 1979, "APES—Finite Element Fracture Mechanics Analysis," Report DTNSRDC-79/023, David W. Taylor Ship Research and Development Center.

Kokini, K., and Perkins, R. W., 1984, "Free Edge Thermal Stress Singularities in Finite Concentric Cylinders," *Computers and Structures,* Vol. 19, No. 4, pp. 531–534.

Kokini, K., 1987, "Interfacial Cracks in Ceramic-to-Metal Bonds Under Transient Thermal Loads," *J. Amer. Ceramic Soc.,* Vol. 70, No. 12, pp. 855–859.

Kokini, K., 1988, "Material Compatibility in Interfacial Transient Thermal Fracture of Ceramic-to-Metal Bonds," *ASME Journal of Applied Mechanics,* Vol. 55, pp. 767–771.

Kuo, An-Yu, 1989, "Thermal Stresses at the Edge of a Bimetallic Thermostat," *ASME Journal of Applied Mechanics,* Vol. 56, pp. 585–589.

Lu, Ming-Che, and Erdogan, F., 1983a, "Stress Intensity Facors in Two Bonded Elastic Layers Containing Cracks Perpendicular to and on the Interface—I," *Eng. Frac. Mech.,* Vol. 18, No. 3, pp. 491–506.

Lu, Ming-Che, and Erdogan, F., 1983b, "Stress Intensity Facors in Two Bonded Elastic Layers Containing Cracks Perpendicular to and on the Interface—II," *Eng. Frac. Mech.,* Vol. 18, No. 3, pp. 507–528.

Nied, H. A., 1991a, "Edge Stress Concentrations in Layered Ceramic–Metal Composites Due to Thermal Mismatch," *Proc. 4th National Thermal Spray Conference,* ASM, Metal Park, OH.

Nied, H. A., 1991b, "Edge Stress Intensity Factors in Layered Ceramic–Metal Composites Due to Thermal Mismatch," *Proc. 1991 Intl. Conf. on Failure Analysis,* ASM, Metal Park, OH.

Parks, V. J., 1988, "Stresses in a Bonded Wafer," *Experimental Mechanics,* Vol. 28, No. 1.

Raju, I. S., and Crews, J. H., Jr., 1981, "Interlaminar Stress Singularities at a Straight Free Edge in Composite Laminates," *Computers and Structures,* Vol. 14, No. 1–2, pp. 21–28.

Rice, J. R., and Sih, G. C., 1965, "Plane Problems of Cracks in Dissimilar Media," *ASME Journal of Applied Mechanics,* pp. 418–423.

Rice, J. R., 1988, "Elastic Fracture Mechanics Concepts for Interfacial Cracks," *ASME Journal of Applied Mechanics,* Vol. 55, pp. 98–103.

Schwartz, M. M., 1990, *CERAMIC JOINING,* ASM International, Metal Park, OH.

Thouless, M. D., Evans, A. G., Ashby, M. F., and Hutchinson, J. W., 1987, "The Edge Cracking and Spalling of Brittle Plates," *Acta Metall.,* Vol. 35, No. 6, pp. 1333–1341.

Thouless, M. D., Cao, H. C., and Mataga, P. A., 1989, "Delamination From Surface Cracks in Composite Materials," *Jour. Material Sci.,* Vol. 24, pp. 1406–1412.

Verbeek, A. T. J., 1992, "Plasma Sprayed Thermal Barrier Coatings: Production, Characterization and Testing," Thesis Eindhoven, ISBN 90 3860082 8, Drukkerij van Deursen bv, Nederweert.

J. Ahmad

U. Santhosh

Research Applications Inc.,
11772 Sorrento Valley Road, Suite 145,
San Diego, CA 92121-1085

S. Hoff

Aviation Applied Technology Directorate,
U. S. Army Troop and Aviation Command,
Bldg. 401, Lee Boulevard,
Fort Eustis, VA 23604

A Metal Matrix Composite Damage and Life Prediction Model

A simple analytical model is derived for the prediction of time-dependent deformation and damage response of metal matrix composites under fiber direction loading. The model can be used in conjunction with a number of viscoplastic constitutive models to describe the matrix material behavior. Damage in the form of progressive fiber fractures is incorporated using a mechanistic approach. The criterion for fiber fractures can be based on statistical information on fiber strength. When used in conjunction with a prescribed failure condition for a composite, the model provides a means for predicting composite life under general thermomechanical load conditions. Based on comparison of results with detailed finite element analyses and with laboratory test data, it appears that the simple model provides reasonably accurate predictions.

Introduction

Global deformation response of metal matrix composites (MMCs) to applied mechanical and thermally induced stresses depends upon (a) the mechanical and thermal properties of the constituent materials, (b) residual stresses in the constituents induced by the composite consolidation process, and (c) the nature and extent of micromechanical defects and damage that may occur and accumulate over time.

Considerable progress has been achieved by a number of investigators toward developing predictive global deformation response models applicable to unidirectional, continuous fiber reinforced titanium matrix composites (TMCs) with ceramic fibers subjected to fiber-direction (0 deg) and transverse (90 deg) applied loads. The so called "unit cell" based micromechanics approach has been successfully employed using both detailed finite element models as well as simpler strength of materials based models to predict global deformation response of a number of TMCs subjected to a variety of thermal and mechanical load conditions (for example, see references [1–4]). In the context of damage modeling, the effect of fiber-matrix debond damage (observed under 90 deg loading) on global MMC deformation response has been successfully predicted by a number of investigators using the micromechanics approach (for example, see [2–5]). However, modeling of the effect of defects and other observed damage modes, such as discrete fiber fractures and discrete matrix cracks, has received considerably less attention. This is despite reported experimental observations and nondestructive evaluation (NDE) results [6] that indicate, for example, that discrete broken fibers exist in as fabricated MMC panels and that progressive fiber fracture is a dominant damage mechanism leading to failure under in-phase thermomechanical fatigue (TMF) conditions. A model that can accurately predict the effect of discrete broken fibers and progressive fiber damage on global MMC deformation response can enhance current life prediction capabilities and provide residual strength prediction capability by quantifying the effect of cumulative damage.

A reason for the lack of sufficient progress in developing models to accurately predict the effect of fiber fractures is that fiber fractures are often discrete. Therefore, approaches based on stress analysis of a single unit cell cannot be used because the assumption in such approaches is that the composite is an assemblage of a large number of identical unit cells. Thus, the approach can be used only if none or all the fibers are fractured. To model discrete defects and progressive fiber damage by the unit cell approach, one needs a method that allows some of the cells to have fractured fibers. Choosing to use the finite element method to accomplish this leads to unmanageably large computational resource requirements. Choosing the simpler strength of materials approach, the challenge has been to derive a set of equations which reflect the actual physical phenomena associated with fiber fractures in a reasonably realistic fashion, and without making the equations intractable by simple and efficient numerical solution techniques.

The present paper contains the description of a relatively simple, yet mechanistic, model for the analysis of unidirectional composites with discrete fiber fractures under fiber direction loading. Equations are presented that can be used to assess the effect as well as predict the occurrence of discrete and progressive fiber damage. It is assumed that the fiber material is isotropic and linear elastic at all temperatures. The matrix material is modeled as elastic-viscoplastic. For the special case of a composite with all fibers intact and the inelastic strain rate of the matrix material expressed in a simple power-law form, a closed form expression for composite strain is presented. Reasonableness of key assumptions made in deriving the simple model is verified by comparing solutions with detailed finite element analysis results of special cases. Finally, predictions made by using the model are compared with available test data.

The modeling approach adopted in the present work is fundamentally different than that of Curtin [7]. In reference [7], the effect of broken fibers on composite deformation response is incorporated by artificially reducing the effective fiber modulus. The present approach involves a more mechanistic, albeit simple, modeling of fiber fracture. The statistical nature of fiber fractures is addressed by prescribing a criterion based on statistical distribution of fiber strength. The present model can be readily adopted in a probabilistic analysis framework.

Model Derivation

Consider a unidirectional composite ply with some fractured fibers schematically shown in Fig. 1. Imagine the composite to be an assemblage of the following two types of cells: (a) those with the fiber intact and, (b) those with the fiber fractured at mid-length of the cell. The ratio of the volume occupied by type (b) cells to the volume occupied by the composite is η, and the fiber volume fraction is V_f. Assume that the fiber material is

Contributed by the International Gas Turbine Institute and presented at the International Gas Turbine and Aeroengine Congress and Exhibition, Orlando, FL, June 2–5, 1997. Manuscript received by the ASME Headquarters March 15, 1997. Paper No. 97-GT-445. Associate Technical Editor: H. A. Kidd.

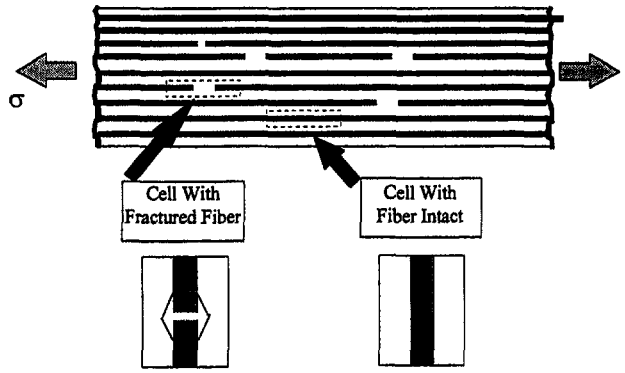

Fig. 1 Conceptual view of composite with discrete fractured fibers

isotropic and linearly elastic at all temperatures. It has Young's Modulus $E_f(T)$ and (tangent) coefficient of thermal expansion (CTE), $\alpha_f(T)$, where T is the temperature. Assume that the matrix material is isotropic and elastic-viscoplastic at all temperatures. It has Young's Modulus $E_m(T)$, its CTE is $\alpha_m(T)$, and its inelastic strain rate is of the following form (in tensor notation):

$$\dot{\epsilon}^i_{kl(m)} = \lambda S_{kl(m)}. \tag{1}$$

In Eq. (1), S_{kl} is the deviatoric stress tensor, subscript (m) designates matrix material, the left hand side is inelastic (i) strain rate tensor, and $(\dot{\cdot})$ denotes differentiation with respect to time. The parameter λ can be a function of matrix stress, strain, temperature and state variables. Under the action of average applied stress σ acting on the composite in the fiber direction, it is assumed that compared to the fiber direction fiber and matrix stress component, the other stress components are much smaller. Thus, the stress state is essentially one-dimensional and, therefore, Eq. (1) can be written as follows:

$$\dot{\epsilon}^i_m = \tfrac{2}{3}\lambda\sigma_m. \tag{2}$$

First consider a cell of length $2l$ with the fiber intact and displaced at each end by amount δ under the action of average axial stress σ. The displacement rate continuity at the fiber matrix interface requires that

$$\dot{\delta} = \dot{\delta}_f = \dot{\delta}_m. \tag{3}$$

Dividing through by l, and defining the resulting quantities as strain averages over the cell length, we get

$$\dot{\epsilon} = \dot{\epsilon}_f = \dot{\epsilon}_m. \tag{4}$$

The fiber being elastic, the total strain is composed of elastic and thermal strains, i.e.,

$$\dot{\epsilon}_f = \frac{\dot{\sigma}_f}{E_f} - \frac{\sigma_f \dot{E}_f}{E_f^2} + \dot{\alpha}_f(T - T_r) + \alpha_f \dot{T}, \tag{5}$$

$$\text{in which, } \dot{E}_f = E_f' \dot{T} \text{ and } \dot{\alpha}_f = \alpha_f' \dot{T}, \tag{6}$$

and $(')$ denotes differentiation with respect to temperature (T).

Enforcing force equilibrium, we get

$$\sigma = v_f \sigma_f + (1 - v_f)\sigma_m \tag{7}$$

and

$$\dot{\sigma} = v_f \dot{\sigma}_f + (1 - v_f)\dot{\sigma}_m. \tag{8}$$

Combining Eqs. (4) to (8), we have

$$\dot{\epsilon} = \frac{1}{E_f}\left[\frac{\dot{\sigma} - (1 - v_f)\dot{\sigma}_m}{v_f}\right] - \frac{\dot{E}_f}{v_f E_f^2}[\sigma - (1 - v_f)\sigma_m] + [\alpha_f'(T - T_r) + \alpha_f]\dot{T}. \tag{9}$$

Now, strain in the matrix is composed of elastic, inelastic, and thermal strains, i.e.,

$$\dot{\epsilon}_m = \frac{\dot{\sigma}_m}{E_m} - \frac{\sigma_m \dot{E}_m}{E_m^2} + \frac{2}{3}\lambda\sigma_m + [\alpha_m'(T - T_r) + \alpha_m]\dot{T}, \tag{10}$$

$$\text{in which, } \dot{E}_m = E_m' \dot{T},\ \dot{\alpha}_m = \alpha_m' \dot{T} \text{ and } \alpha_m' = \frac{d\alpha_m}{dT}. \tag{11}$$

$$\text{Therefore, } \dot{\sigma}_m = \left[\dot{\epsilon}_m + \frac{\sigma_m \dot{E}_m}{E_m^2} - \frac{2}{3}\lambda\sigma_m - [\alpha_m'(T - T_r) + \alpha_m]\dot{T}\right]E_m. \tag{12}$$

Substituting Eq. (12) into (9), using Eq. (4), and simplifying, we get:

$$\dot{\epsilon} = \frac{\dot{\sigma}}{E} + \frac{2}{3}\frac{(1 - v_f)E_m\lambda\sigma_m}{E} + (1 - v_f)[\alpha_m'(T - T_r) + \alpha_m]\dot{T} - \left[\frac{(1 - v_f)\sigma_m E_m'}{E_m} + \frac{[\sigma - (1 - v_f)\sigma_m]E_f'}{E_f}\right]\frac{\dot{T}}{E}. \tag{13}$$

In Eq. (13), prime $(')$ denotes differentiation with respect to temperature (T) and E represents effective modulus of the composite given by

$$E(T) = v_f E_f + (1 - v_f)E_m. \tag{14}$$

Stress in the matrix (σ_m) is the sum of matrix stress due to applied stress σ and the consolidation process induced residual stress (σ_m^T) at the reference temperature. Thus,

$$\sigma_m = \frac{\sigma}{(1 - v_f)}\left(1 - \frac{v_f E_f}{\sigma}\bar{\epsilon}\right) + \sigma_m^T. \tag{15}$$

Substituting Eq. (15) into (13), the strain rate for the composite can be expressed as follows:

$$\dot{\epsilon} = \frac{\dot{\sigma}}{E} + \frac{2}{3}\frac{(1 - v_f)E_m\lambda}{E}\left[\frac{\sigma}{1 - v_f}\left(1 - \frac{v_f E_f \bar{\epsilon}}{\sigma}\right) + \sigma_m^T\right] + (1 - v_f)[\alpha_m'(T - T_r) + \alpha_m]\dot{T} - \frac{\dot{T}}{E}\left[\frac{(1 - v_f)E_m'}{E_m}\left\{\frac{\sigma}{(1 - v_f)}\left(1 - \frac{v_f E_f \bar{\epsilon}}{\sigma}\right) + \sigma_m^T\right\} + \frac{\sigma}{E_f} - \frac{(1 - v_f)}{E_f}\left\{\frac{\sigma}{1 - v_f}\left(1 - \frac{v_f E_f \bar{\epsilon}}{\sigma}\right) + \sigma_m^T\right\}\right], \tag{16}$$

in which $\bar{\epsilon} = \epsilon - \alpha_f(T - T_r)$. A reasonably accurate estimate of σ_m^T is as follows:

$$\sigma_m^T(T) = \frac{E_m(T)E_f(T)v_f}{E(T)}(\bar{\alpha}_f - \bar{\alpha}_m)(T - T_p), \tag{17}$$

where T_p is the (stress free) highest temperature during composite consolidation, and $\bar{\alpha}_f$ and $\bar{\alpha}_m$ are temperature averaged CTE values of the fiber and the matrix given by

$$\bar{\alpha}_{f,m} = \frac{1}{T_p - T}\int_T^{T_p} \alpha_{f,m} dT. \quad (18)$$

Alternatively, a more precise estimate of σ_m^T can be obtained by integrating Eq. (16) over the temperature range T_p to T_r, with the initial condition that at $T = T_p$, $\sigma_m^T = 0$. Note that if this alternative method is used for the subsequent integration of Eq. (16), the total strain ϵ should be redefined such that at the reference temperature (T_r), $\epsilon = 0$.

Special Case of Composite Without Fiber Fractures, Under Sustained Load, Constant Temperature, and Power-Law Matrix Material Constitutive Behavior. Under these special conditions, $\dot{T} = 0$ and $\dot{\sigma} = 0$. If the inelastic strain rate of the matrix material can be expressed by the following simple function involving material characteristic constants A and n:

$$\dot{\epsilon}_m^i = A\sigma_m^n, \quad (19)$$

$$\text{then, comparing it with Eq. (2), } \lambda = \tfrac{3}{2} A\sigma_m^{n-1}. \quad (20)$$

With these substitutions in Eq. (16), and using the following initial condition:

$$\epsilon(t = 0) = \frac{\sigma}{E}, \quad (21)$$

the solution of Eq. (16) gives the following time-dependent composite strain:

$$\epsilon(t) = \frac{1 - v_f}{C_1 E_f v_f}\left[C_1\left\{\frac{\sigma}{1 - v_f} + \sigma_m^T\right\} - \left\{\frac{(n-1)E_f v_f C_1}{1 - v_f} t + C_2\right\}^{-1/n}\right]. \quad (22)$$

In the above solution,

$$C_1 = \left[\frac{(1 - v_f)AE_m}{E}\right]^{1/n} \quad \text{and}$$

$$C_2 = \left[C_1\left\{\frac{\sigma}{1 - v_f} + \sigma_m^T\right\} - \left\{\frac{\sigma E_f v_f C_1}{E(1 - v_f)}\right\}\right]^{1-n}.$$

In more general cases of varying applied stress and temperature, and for more complicated constitutive models for the matrix materials, the solution of Eq. (16) together with the initial condition given by Eq. (21) can be obtained by numerical integration.

Composite With Discrete Fractured Fibers. Consider a cell that contains a fractured fiber as shown in Fig. 2. On either side of the fiber crack is a region of length a over which the fiber and matrix are debonded under the action of (theoretical) stress singularity at the front of a fiber crack intersecting the fiber-matrix interface. The length a is the distance over which the stress normal to the interface associated with the fiber crack tip is larger than or equal to the interface "strength." Most titanium-based matrix composites with silicon carbide fibers have "weak" interface. Thus, the interface "strength" is the compressive residual stress on the interface induced by the composite consolidation process.

The region of length s ahead of each debond terminus in Fig. 2 is shear-lag distance. Over this distance, stress along the interface has both shear and normal components. Shear stress becomes zero at $x = \pm(a + s)$ and only normal stress component prevails beyond the shear-lag distance. It is shown later through detailed finite element analyses that $s \ll a$. As shown in Fig. 2, the combined distance $(a + s)$ is denoted by d, and

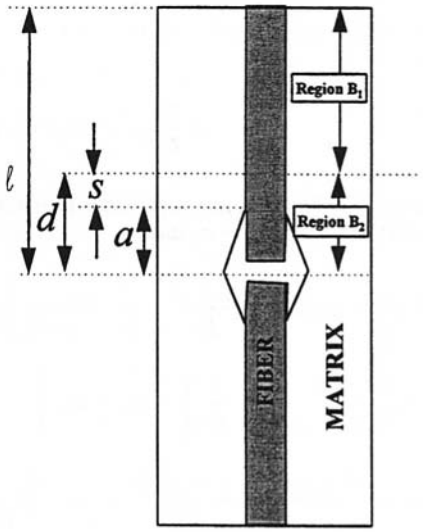

Fig. 2 Cross-section of a cell containing a fractured fiber

the ratio d/l by ρ. The cell is subdivided into regions B_1 and B_2.

We now return to the conceptual view of a composite with discrete fractured fibers. Let U denote the total cross-section normal to σ with no fractured fibers and let B denote the total cross-section with fractured fibers. For simplicity, assume that each fractured fiber cell has a single fracture. This assumption is only to simplify the forthcoming derivation, and can be readily removed if a situation so requires.

The applied average stress σ is shared by U and B in the following manner:

$$\sigma = (1 - \eta)\sigma_U + \eta\sigma_B. \quad (23)$$

Recall that η is the ratio of volume with fractured fibers to the total composite volume. With the present assumptions, η is the fraction of fractured fibers. The modulus and CTE values corresponding to U, B, and B_1 and B_2 regions of Fig. 2 are as follows:

$$E_{B_2} = (1 - v_f)E_m,\ E_{B_1} = E_U,\ E_U = v_f E_f + (1 - v_f)E_m,\ E_B = \frac{(1 - v_f)E_{B_1}E_m}{\rho E_{B_1} + (1 - \rho)(1 - v_f)E_m},$$

$$\alpha_U = \alpha_{B_1} = [(1 - v_f)E_m\alpha_m + E_f\alpha_f v_f]/E_U,$$

$$\alpha_{B_2} = \alpha_m,\ \alpha_B = \frac{\alpha_{B_1}\alpha_{B_2}E_{B_1}E_{B_2}}{(\rho\alpha_{B_1}E_{B_1} + (1 - \rho)\alpha_{B_2}E_{B_2})E_B}, \quad (24)$$

and for the composite containing the regions U, B_1, and B_2,

$$\alpha = [(1 - \eta)E_U\alpha_U + \eta E_B\alpha_B]/E.$$

Because displacements of U and B must be the same,

$$\delta = \delta_U = \delta_B \quad (25)$$

and

$$\delta_B = \delta_{B_1} + \delta_{B_2}. \quad (26)$$

Decomposing into their elastic (superscript e), inelastic (superscript i) and thermal (superscript T) parts,

$$\delta_B = \delta_{B_1}^e + \delta_{B_1}^i + \delta_{B_1}^T + \delta_{B_2}^e + \delta_{B_2}^i + \delta_{B_2}^T. \quad (27)$$

Now, using Eq. (25) and defining average strains in regions B_1 and B_2 to be ϵ_{B_1} and ϵ_{B_2},

$$\epsilon = \frac{\sigma_{B_1}}{E_{B_1}}(1-\rho) + \epsilon^i_{B_1}(1-\rho) + \epsilon^T_{B_1}(1-\rho) + \frac{\sigma_{B_2}}{E_{B_2}}\rho + \epsilon^i_{B_2}\rho + \epsilon^T_{B_1}\rho. \quad (28)$$

Differentiating Eq. (28) with respect to time, utilizing Eq. (24), and using the facts that $\sigma_{B_1} = \sigma_B$ and $\alpha_{B_2} = \alpha_m$, we get

$$\dot{\epsilon} = \rho\dot{\epsilon}^i_{B_2} + (1-\rho)\dot{\epsilon}^i_{B_1} + \left[\frac{1-\rho}{E_U} + \frac{\rho}{(1-v_f)E_m}\right]\dot{\sigma}_B + \dot{\rho}\left[\sigma_B\left\{\frac{1}{(1-v_f)E_m} - \frac{1}{E_U}\right\} + \epsilon^i_{B_2} - \epsilon^i_{B_1}\right] - \frac{[\sigma-(1-\eta)\sigma_U]}{\eta}\left[\frac{(1-\rho)\dot{E}_U}{E_U^2} + \frac{\rho\dot{E}_m}{(1-v_f)E_m^2} + \dot{\rho}\left(\frac{1}{E_U} - \frac{1}{(1-v_f)E_m}\right)\right] + [\dot{\alpha}_{B_1}(T-T_r) + \alpha_{B_1}\dot{T}](1-\rho) - [\alpha_{B_1}\dot{\rho} - \dot{\alpha}_m\rho](T-T_r) + \alpha_m[\rho\dot{T} + (T-T_r)\dot{\rho}]. \quad (29)$$

Differentiating Eq. (23) with respect to time and rearranging terms,

$$\dot{\sigma}_B = [\dot{\sigma} - (1-\eta)\dot{\sigma}_U + \dot{\eta}(\sigma_U - \sigma_B)]/\eta. \quad (30)$$

Also, from Eq. (23),

$$\sigma_B = [\sigma - (1-\eta)\sigma_U]/\eta. \quad (31)$$

Decomposing ϵ_U into its elastic, thermal, and inelastic parts, and differentiating with respect to time,

$$\dot{\epsilon}_U = \frac{\dot{\sigma}_U}{E_U} + \dot{\epsilon}^i_U - \frac{\sigma_U\dot{E}_U}{E_U^2} + \dot{\alpha}_U(T-T_r) + \alpha_U\dot{T}. \quad (32)$$

Solving for $\dot{\sigma}_U$ in Eq. (32), substituting into Eq. (30), and then substituting the result together with Eq. (31) into Eq. (29) we get

$$\dot{\epsilon}[1 + F(1-\eta)E_U] = \frac{F}{\eta}\left[\dot{\sigma} + E_U(1-\eta)\dot{\epsilon}^i_U - \frac{(1-\eta)\sigma_U\dot{E}_U}{E_U} + \frac{\dot{\eta}(\sigma_U - \sigma)}{\eta} + (1-\eta)E_U[\dot{\alpha}_U(T-T_r) + \alpha_U\dot{T}]\right] + \frac{\dot{\rho}H}{\eta}[\sigma - (1-\eta)\sigma_U] + \dot{\rho}[\epsilon^i_{B_2} - \epsilon^i_{B_1}] + (1-\rho)\dot{\epsilon}^i_{B_1} + \rho\dot{\epsilon}^i_{B_2} - \frac{\sigma-(1-\eta)\sigma_U}{\eta}\left[\frac{(1-\rho)\dot{E}_U}{E_U^2} + \frac{\rho\dot{E}_m}{(1-v_f)E_m}\right] + [\dot{\alpha}_{B_1}(T-T_r) + \alpha_{B_1}\dot{T}](1-\rho) - [\alpha_{B_1}\dot{\rho} - \dot{\alpha}_m\rho](T-T_r) + \alpha_m[\rho\dot{T} + (T-T_r)\dot{\rho}], \quad (33)$$

in which

$$F = \frac{1-\rho}{E_U} + \frac{\rho}{(1-v_f)E_m} \quad \text{and}$$

$$H = \frac{E_U - (1-v_f)E_m}{E_mE_U(1-v_f)}. \quad (34)$$

Also, in accordance with Eqs. (2),

$$\dot{\epsilon}^i_U = \tfrac{2}{3}\lambda_1\sigma_{mU}, \quad (35)$$

$$\dot{\epsilon}^i_{B_1} = \tfrac{2}{3}\lambda_2\sigma_{mB_1}, \text{ and} \quad (36)$$

$$\dot{\epsilon}^i_{B_2} = \tfrac{2}{3}\lambda_3\sigma_{mB_2}. \quad (37)$$

In the above equations,

$$\lambda_1 = \lambda_2 = \frac{E_m(1-v_f)}{E_U}\lambda \text{ and} \quad (38)$$

$$\lambda_3 = \lambda. \quad (39)$$

Also, the stresses in the matrix material in regions U, B_1, and B_2 can be expressed as

$$\sigma_{mU} = \frac{\sigma_U - \bar{\epsilon}E_fv_f}{1-v_f} + \sigma^T_m, \quad (40)$$

$$\sigma_{mB_1} = \frac{\sigma - (1-\eta)\sigma_U}{\eta(1-v_f)} - \frac{E_fv_f(\epsilon - (1-\rho)\alpha_f(T-T_r) - \rho\epsilon_{B_2})}{(1-v_f)(1-\rho)} + \sigma^T_m, \text{ and} \quad (41)$$

$$\sigma_{mB_2} = \frac{\sigma_B}{1-v_f}. \quad (42)$$

Given an expression for λ (i.e., given a constitutive model for the matrix material), the differential Equation (33), together with the expressions given by Eqs. (34)–(42), can be numerically solved for composite strain $\epsilon(t)$ with the following initial conditions:

$$\sigma(0) = \sigma_0, \quad \epsilon(0) = (\sigma_0/E) + \alpha(T-T_r),$$

$$\eta(0) = \eta_0, \ \sigma_U(0) = \frac{\sigma_0E_{U^0}}{E^0} + \frac{\eta_0E_{B_0}}{1-\eta_0}(\alpha_{B_0} - \alpha_{C_0}),$$

$$\rho(0) = \rho_0, \quad \epsilon^i_{B_1}(0) = \epsilon^i_{B_2}(0) = 0,$$

$$\epsilon_{B_1}(0) = \frac{\sigma_0 - (1-\eta_0)\sigma_U(0)}{\eta_0E_{U_0}} + \alpha_{U_0}(T_0 - T_r), \text{ and}$$

$$\epsilon_{B_2}(0) = \frac{\sigma_0 - (1-\eta_0)\sigma_U(0)}{(1-V_f)E_{m_0}\eta_0} + \alpha_m(T_0 - T_r). \quad (43)$$

In the present work, numerical solutions were obtained by the Fourth Order Runge Kutta method. Two different matrix material constitutive models, which were used in the analysis of verification and validation example cases whose results, are discussed next.

Constitutive Models. One of the expressions for λ employed in the present work is that given by Eqs. (19) and (20). Another analogous expression employed for (time independent) elastic-plastic analysis of composites is as follows:

$$\lambda = 0.0 \quad \text{for} \quad \sigma_m < \sigma_{Ym} \quad \text{and} \quad \lambda = \tfrac{3}{2}Q\sigma_m^{p-2}\dot{\sigma} \quad \text{for} \quad \sigma_m \geq \sigma_{Ym}, \quad (44)$$

where Q and p are constants obtained by fitting the equation $\epsilon_m^i = Q/p\sigma_m^p$ to the uniaxial stress-inelastic strain curve of the matrix material at the temperatures of interest, and σ_{Ym} is the corresponding yield strength. It is noted that when $p = 1$, Eqs. (44) represent λ for a bilinear stress-strain behavior with constant tangent modulus ($d\sigma/d\epsilon$) equal to $1/Q$.

The third constitutive model employed in the present work is based on the unified viscoplastic theory of Bodner and Partom [8], as used by Neu [9] for TIMETAL® 21S[1] and by Forringer et al. [10] for Ti-15-3 matrix materials. Detailed discussion of the model can be found in references [9] and [10].

Progressive Fiber Damage. Equation (33) for strain rate of a composite with discrete fractured fibers includes η, $\dot{\eta}$, ρ, and $\dot{\rho}$ terms that represent fraction of broken fibers, rate of additional fiber fractures with time, debond length associated with each fiber fracture, and growth rate of debond length, respectively. To model progressive fiber damage, η and ρ (or their rates) can be prescribed using appropriate criteria consistent with the governing physical phenomena. For example, the growth rate of ρ can be prescribed as a function of remote fiber stress and instantaneous debond length ρ in the manner of fracture mechanics models commonly used in the analyses of fatigue and creep crack growth. However, as discussed again later, detailed finite element analysis results have indicated that the global composite deformation is only mildly dependent on ρ and strongly dependent on η for values of η in the range of practical interest.

The value η can be prescribed using a fiber fracture criterion based on instantaneous stress in a fiber and statistical distribution of fiber strength. Using the analysis of Majumdar [11] based on Weibull statistics, the probability of failure (P_f) of a fiber of length L, is given by

$$P_f = 1 - \exp\{-(L/L_o)\cdot(\sigma/\sigma_o)^m\}, \qquad (45)$$

where m and σ_o are the Weibull modulus and strength, respectively, and L_o is the gage length on which the Weibull strength, σ_o, is based. Thus, the expected number of breaks in a fiber of length L is simply $\{(L/L_o)\cdot(\sigma/\sigma_o)^m\}$. Based on this in conjunction with SCS-6[2] fiber strength distribution, η can be expressed as follows:

$$\eta = 1.9525\left(\frac{\sigma_f}{4266}\right)^{5.5} \qquad (46)$$

for all values of σ_f, where σ_f is stress in the fiber in MPa. For $\sigma_f < 2300$ MPa, a reasonably good approximation of η is as follows:

$$\eta = 0.1904\left(\frac{\sigma_f}{1700} - 1.0\right) \qquad (47)$$

Verification and Validation Examples

Two problems whose solution by the present model could be readily verified by elastic-plastic finite element analyses are of predicting tensile response of a composite with no fiber damage, and of a composite with all its fibers fractured. These problems were solved using a unit cell model and assuming the inelastic strain of the matrix material to be given by Eq. (44), with $p = 1$ and tangent modulus ($=1/Q$) equal to 6.4 GPa. These values correspond to TIMETAL® 21S uniaxial tensile stress-strain curve at 482°C. The other needed elastic properties for the fiber (SCS-6) and the matrix materials were obtained from reference [2]. Detailed micromechanics analysis results by the finite element method for the problems with and without broken fibers have been reported in reference [13]. These finite element solutions were obtained for $v_f = 0.33$ and without the consideration of consolidation process induced residual stresses. The finite element analysis of the case with broken fibers involved the use of a nonlinear contact algorithm to model possible closure of the fiber-matrix debond associated with the fiber fracture location. The reference [13] analyses were performed with a fine mesh in the fiber fracture region, with the smallest element size equal to 10^{-6} times the fiber radius. Thus, these finite element results can be used as highly accurate reference solutions for verifying the present model results.

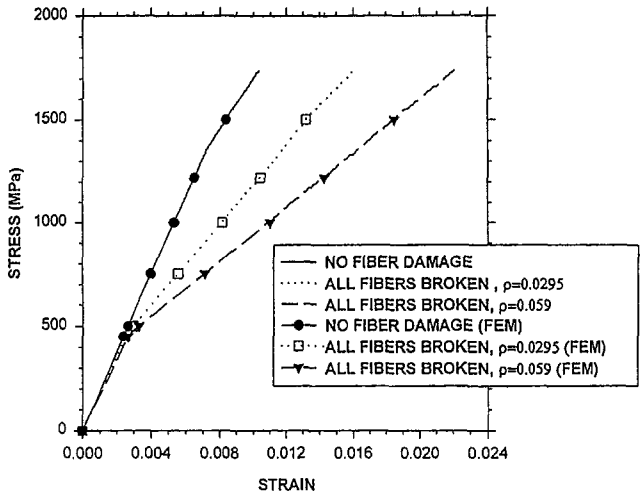

Fig. 3 Comparison of finite element reference solutions and present results

Figure 3 shows the present results and the corresponding finite element solutions from reference [13] for three different cases. The first case is of the composite without any fractured fibers. The other two cases correspond to two different debond length to gauge length ratios (ρ) for the composite with all fibers broken. It is seen that in all three cases, the present results are in close agreement with the reference finite element solutions.

Figure 4 shows the results of analyses performed to assess the effect of the parameters η (representing number of broken fibers) and ρ (representing fiber-matrix debond length) on global composite deformation response. These results were obtained using the Bodner model to represent the elastic-viscoplastic response of the matrix material according to the data provided in reference [10], and correspond to a SCS-6/Ti-15-3 composite with $v_f = 0.41$ at room temperature. The effect of consolidation process induced residual stresses was taken into account in these analyses. It is seen that for η values in the practical range of interest (say, less than 0.2 or so), the value of ρ has very little influence on the global composite response. The effect of ρ does become significant if η is large, as shown in Fig. 3 for $\eta = 1.0$.

Another prediction of the model that could be readily verified by finite element analysis is of time dependent deformation of a composite without broken fibers and the matrix material represented as an elastic-creeping solid with creep strain rate given by the power-law (see Eq. 20). We consider a unidirectional SCS-6/TIMETAL®21S composite with fiber volume fraction of 0.35 subjected to a constant axial stress of 690 MPa at 650°C. For the conditions selected, the exact solution given by Eq. (16) is applicable. Figure 5 shows the model prediction together with inelastic finite element micromechanics analysis results. Agreement between total strain predictions made using the model and by finite element analysis is reasonably close. Figure 6 shows the predicted average stress values in the fiber and the matrix as they vary with time. Note that soon after

[1] TIMETAL® 21S is a trademark of the Timet Corporation, Henderson, NV.
[2] Silicon carbide fiber is produced by Textron Specialty Materials.

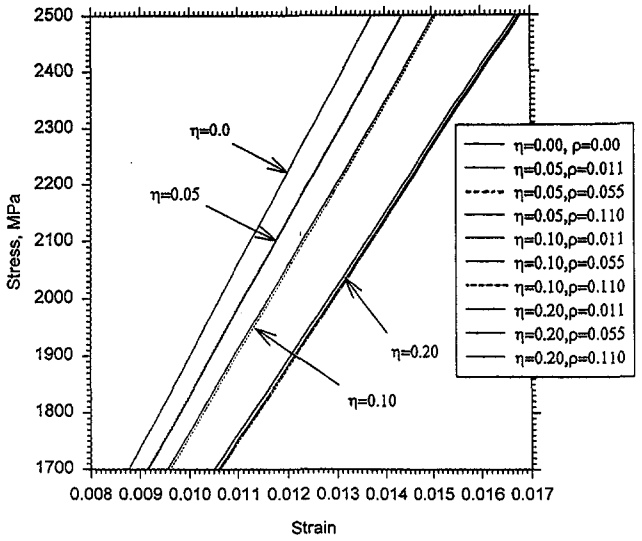

Fig. 4 Parametric results showing effect of η on composite strain

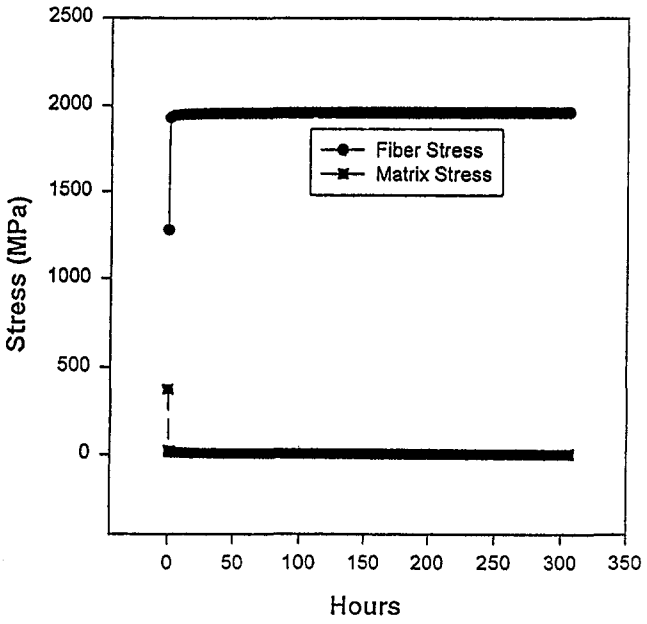

Fig. 6 Average stress in fibers with no broken fibers and matrix inelastic strain rate represented by power law $\dot{\epsilon}^I = 1.019 \times 10^{-14}(\sigma)^{4.8937}$ per second, with σ in MPa

loading, there is a relatively rapid change in stresses followed by a plateau. Matrix stress in the plateau region is close to zero. Consequently, no time dependent composite deformation is seen during the corresponding time interval in Fig. 5. Fiber stress is approximately 2.0 GPa, which, for SCS-6 fibers, may result in some fiber breaks. This aspect is discussed next.

The test data for the material system and temperature and load conditions just considered were obtained from Ashbaugh [14]. In the tests, the samples were loaded in the fiber direction to maximum load, then the load was held constant. The specimens were tested with cold grips. That is, only the gage section was heated to the test temperature. Displacement measurements were made using clip gages mounted at specimen edges. Average composite strains were calculated by dividing the measured displacements by the gauge length. Using the acoustic emission technique, it was estimated that approximately 0.03 percent of the total number of fibers in the test specimen fractured prior to reaching the 690 MPa maximum applied stress.

For the power-law expression (Eq. (19)) describing inelastic strain rate of the matrix material, the constants A and n at 650°C were obtained from reference [14], and are shown in Fig. 5. Matrix and fiber material elastic constants at 650°C and temperature dependent CTE values were also obtained from the same source.

Figure 7 shows the predictions made using the present model together with the test results corresponding to 690 MPa applied average stress. The agreement between predicted strain when 3 percent of the fibers were considered to be fractured and the test data is reasonably close and consistent with acoustic emission information cited earlier. The source of the abrupt variations in the test data is not known. The predicted strains when no fibers

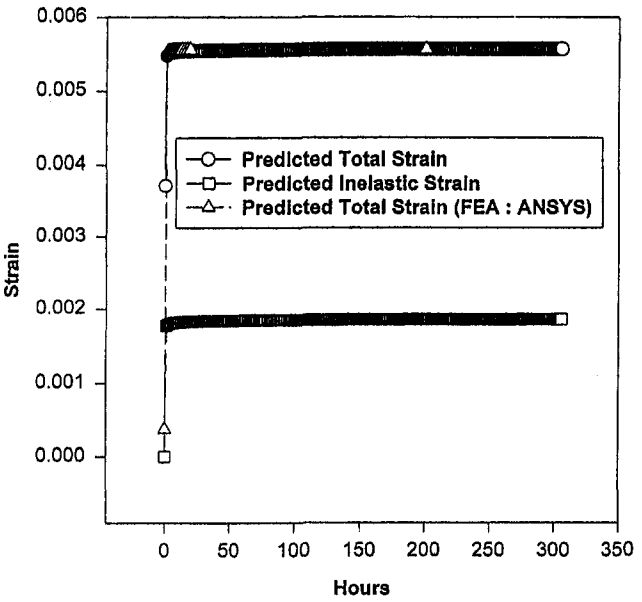

Fig. 5 Comparison of model predictions and finite element analysis results with no broken fibers and matrix inelastic strain rate represented by the power law $\dot{\epsilon}^I = 1.019 \times 10^{-14}(\sigma)^{4.8937}$ per second, with σ in MPa

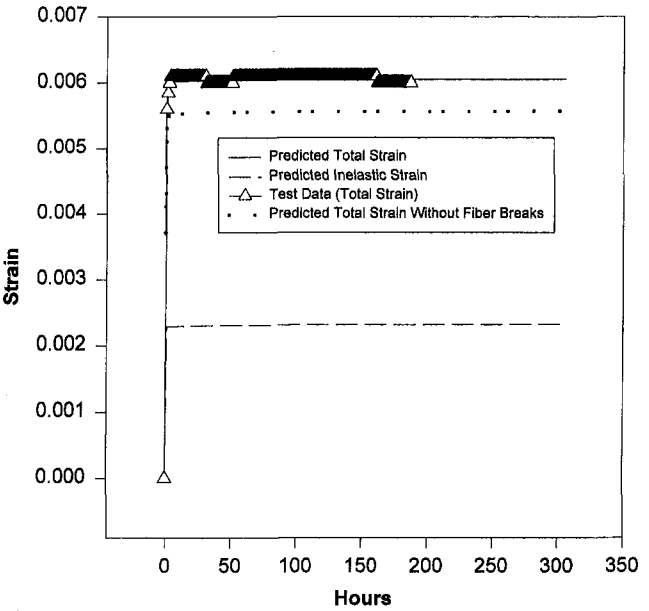

Fig. 7 Comparison of model predictions and test data broken fibers and matrix inelastic strain rate represented by the power law $\dot{\epsilon}^I = 1.019 \times 10^{-14}(\sigma)^{4.8937}$ per second, with σ in MPa

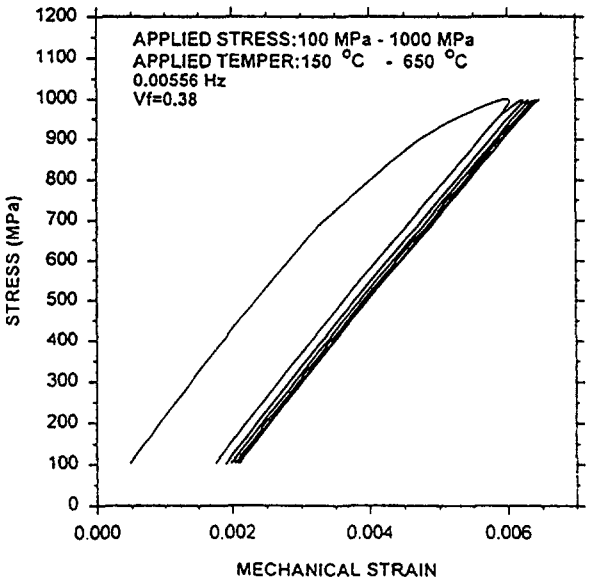

Fig. 8 Predicted deformation response of TIMETAL 21S/SCS-6 composite subjected to in-phase thermomechanical cyclic loading

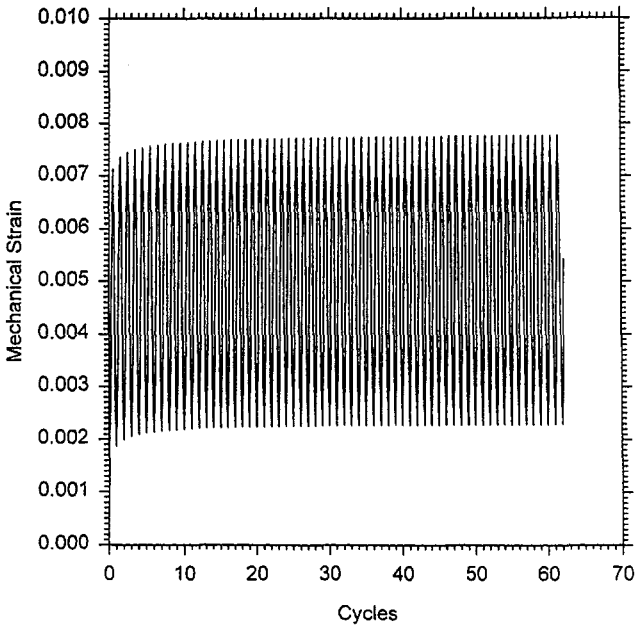

Fig. 9 Predicted deformation response of Ti-15-3/SCS-6 composite subjected to in-phase thermomechanical cyclic loading

were considered to be fractured are somewhat lower than that measured values.

Prediction Of Time-Dependent Deformation Of Composite Subjected To Thermomechanical Load Cycles. This verification problem involved the analysis of a unidirectional SCS-6, TIMETAL®21S composite with fiber volume fraction of 0.38 subjected to thermomechanical fatigue (TMF) conditions. Specifically, the composite was subjected to thermal cycles in the range of 150°C to 650°C, with in-phase stress cycles in the range of 100 MPa to 1000 MPa at 0.00556 Hz frequency. Using the Bodner model to describe the matrix material response, finite element results for this case have been reported in [2]. Figure 8 shows the stress-mechanical strain response computed using the present model. These results are in close agreement with the finite element analysis results of reference [2]. Neither the present simple model nor the finite element computations involved consideration of fiber fractures.

Figure 9 shows the results of another analysis performed using the present model to predict the response of a unidirectional SCS-6/Ti-15-3 composite with $v_f = 0.41$ under in-phase TMF conditions. The temperature and stress ranges for this case were 300°C to 538°C and 111 MPa to 1114 MPa, respectively, at 0.011 Hz frequency. Majumdar and Newaz [11] have reported results of four tests performed under these conditions. There is considerable discrepancy among the reported test results. Therefore, the test data do not provide a good basis for validating model predictions. Nevertheless, the model predictions of mechanical strain plotted against number of TMF cycles are shown in Fig. 9, corresponding to the fiber fracture criterion given by equation (47). As indicated in reference [11] test data, the results do shows strain "ratcheting" with increasing number of cycles. This ratcheting is the result of progressive fiber fractures occurring in the composite. The predicted fiber stress is shown in Fig. 10. It is seen that at 63 cycles, the fiber stress is predicted to be approximately 2700 MPa. In this range, it may be more appropriate to use Eq. (46) rather than equation (47) as the fiber fracture criterion. Figure 11 shows a comparison of strains predicted using the two criteria.

Conclusions

Based on the results that could be validated by detailed finite element analyses and test data, it appears that the relatively simple modeling approach for predicting time dependent damage and deformation response of unidirectional MMCs is reasonably accurate. The method is easily implemented on a personal computer for cycle by cycle analyses of complex thermomechanical load patterns. Also, the method can be easily extended to other composite lay-ups through judicious use of simple lamination theory.

In life prediction applications, the method can be useful if a failure criterion for the composite is prescribed in terms of a failure stress or failure strain of the fiber. For example, one can prescribe the failure stress to be the fiber 'bundle' strength. Then, the simple analysis method can be used to predict number of cycles needed for the fiber stress to reach the bundle strength. For the SCS-6 fiber, bundle strength is approximately 3700 MPa

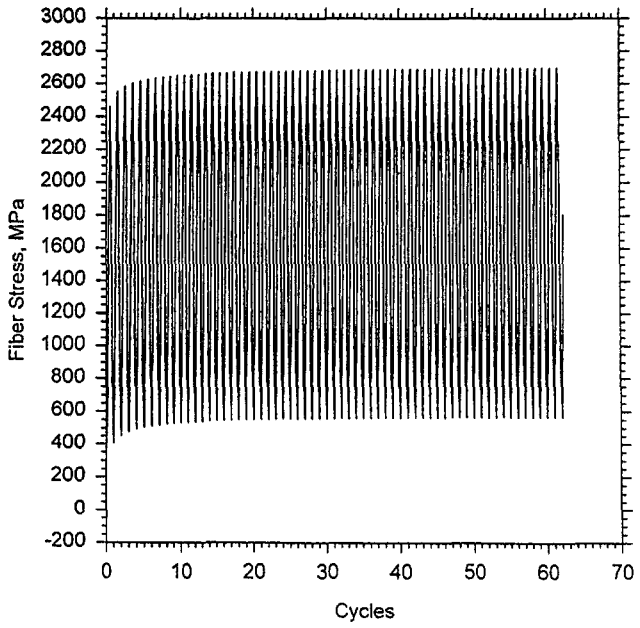

Fig. 10 Predicted average stress in the fibers of Ti-15-3/SCS-6 composite subjected to in-phase thermomechanical cyclic loading

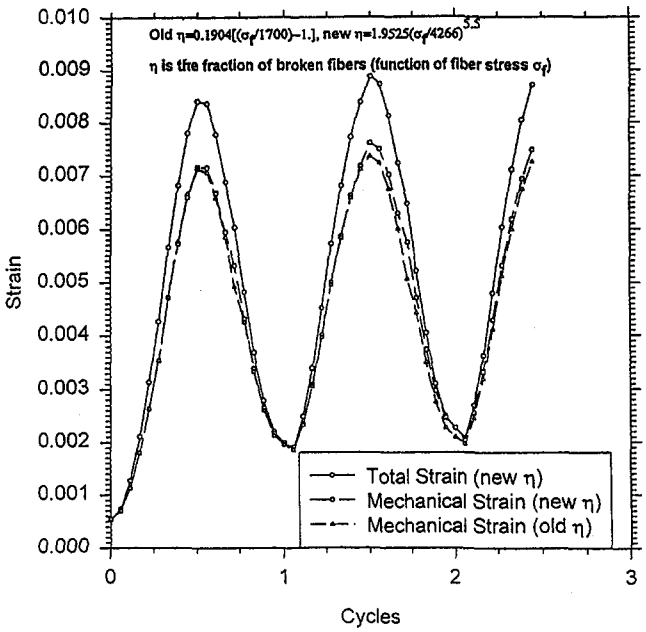

Fig. 11 Comparison of predicted deformation response of Ti-15-3/SCS-6 composite subjected to in-phase thermomechanical cyclic loading using two different fiber fracture criteria

and corresponds to approximately 0.1 percent strain. Alternatively, one can prescribe composite failure criterion in terms of a certain critical percent of broken fibers (i.e., a critical value of η).

References

1 Santhosh, U., and Ahmad, J., 1992, "Metal Matrix Composites Under Biaxial Loading," *Constitutive Behavior of Metal Matrix Composites,* B. S. Majumdar, G. M. Newaz, and S. Mall, eds., MD-Vol. 40, ASME, New York, pp. 53–66.

2 Kroupa, J. L., and Neu, R. W., 1994, "The Non-Isothermal Viscoplastic Behavior of a Titanium-Matrix Composite," *Composite Engineering,* Vol. 4, No. 9, pp. 965–977.

3 Sherwood, J. A., Quimby, H. M., and Doore, R. J., 1992, "Damage Modeling in Fiber Reinforced Composites," *Fracture and Damage,* A. Nagar, ed., AD-Vol. 27, ASME, New York, pp. 59–63.

4 Ahmad, J., Santhosh, U., and Haq, I.-U., 1993, "An Analysis of Time Dependent Deformation of Metal Matrix Composites," *Proc. of The American Society for Composites-Eighth Technical Conference,* Technomic Publishing Co., Lancaster, PA, pp. 715–723.

5 Santhosh, U., and Ahmad, J., 1992, "Nonlinear Micromechanics Analysis Prediction of the Behavior of Titanium Alloy Matrix Composites," *Fracture and Damage,* A. Nagar, ed., AD-Vol. 27, ASME, New York, pp. 65–76.

6 Neu, R. W., and Roman, I., 1994, "Acoustic Emission Monitoring of Damage in Metal Matrix Composites Subjected to Thermomechanical Fatigue," *Composite Science and Technology,* Vol. 52, pp. 1–8.

7 Curtin, W. A., 1991, "Theory Of Mechanical Properties of Ceramic Matrix Composites," *J. American Ceramic Society,* Vol. 74, p. 2837.

8 Bodner, S. R., and Partom, Y., 1975, "Constitutive Equations for Elastic-Viscoplastic Strain Hardening Materials," *ASME Journal of Applied Mechanics,* Vol. 42, pp. 385–389.

9 Neu, R. W., 1993, "Non-Isothermal Parameters for the Bodner-Partom Model," *Material Parameter Estimation for Modern Constitutive Equations,* L. A. Bertram, S. B. Brown, and A. D. Freed, eds., MD-Vol. 43/AMD-Vol. 168, ASME, New York, pp. 211–226.

10 Forringer, M. A., Robertson, D. D., and Mall, S., 1997, "A Micromechanical Based Approach to Fatigue Life Modeling of Titanium Matrix Composites," *Composites,* Part B, Vol. 28, No. 5–6, pp. 507–521.

11 Majumdar, B. S., and Newaz, G. M., 1995, "In-Phase TMF of SCS-6/Ti-15-3 MMC," *1995 HITEMP Proceedings,* Vol. 2, NASA Report No. 10178, pp. 22.1–22.12.

12 Santhosh, U., and Ahmad, J., 1992, "Metal Matrix Composite Response Under Biaxial Loading," *Constitutive Behavior of High Temperature Composites,* B. S. Majumdar, G. M. Newaz, and S. Mall, eds., MD-Vol. 40, ASME, New York.

13 Nicholas, T., and Ahmad, J., 1994, "Modeling Fiber Breakage in Metal Matrix Composites," *Composite Science and Technology Journal,* Vol. 52, pp. 29–38.

14 Ashbaugh, N. E., 1994, "Mechanical Behavior of High Temperature Structural Materials," WL-TR-95-4003, Materials Directorate, Wright Laboratory, Air Force Material Command, Wright-Patterson AFB, OH 45433-7734.

An Experimental Determination of Losses in a Three-Port Wave Rotor

J. Wilson
Dynacs Engineering Company, Inc.,
2001 Aerospace Parkway,
Brook Park, OH 44142

Wave rotors, used in a gas turbine topping cycle, offer a potential route to higher specific power and lower specific fuel consumption. In order to calculate this potential realistically, a knowledge of the loss mechanisms is required. The experiment reported here was designed as a statistical experiment to identify the losses due to finite passage opening time, friction, and leakage, using a three-port, flow divider, wave rotor cycle. Incidence loss was also found to be important. Rotors of 12 in. diameter were used, with two different lengths, 9 in. and 18 in., and two different passage widths, 0.25 in. and 0.54 in., in order to vary friction and opening time. To vary leakage, moveable end walls were provided so that the rotor to end wall gap could be adjusted. The experiment is described, and the results are presented, together with a parametric fit to the data.

Introduction

The performance of gas turbine engines can be improved if the combustion temperature can be raised. This is difficult to do because the turbine inlet temperature is limited by material considerations (Peacock and Sadler, 1992). Increased performance can be achieved if the pressure entering the turbine can be increased, while maintaining the rate of heat addition. Thus, the combustion step should be configured so as to result in a pressure gain, rather than a pressure loss. Two techniques for achieving this are unsteady combustion (Kentfield, 1995), and use of a wave rotor topping cycle (Meyer, 1947; Zauner et al., 1993; Kentfield, 1995). Because unsteady combustion currently shows only modest pressure gains, the wave rotor approach seems preferable. Calculations show that increases of 20 percent in specific power, and reductions in specific fuel consumption of 18 percent are possible by using a four-port wave rotor topping cycle (Wilson and Paxson, 1996).

Wave rotors are devices which use unsteady waves to produce steady streams of gas which are at either higher or lower stagnation pressure than the input stream. The rotor itself has a set of passages on its periphery. In the present experiment, which was designed for no exchange of shaft work, the passages are straight, and aligned axially. As the rotor rotates, these passages are alternately exposed to ports at differing pressures. Typically, at the exhaust, or low pressure, port, the passage contains gas at some higher pressure just before the passage rotates into juxtaposition with the port. Exposure to the low port pressure causes an expansion wave to propagate into the passage. Later in the cycle, the passage, now at lower pressure, will be opened to the inlet port, where the gas is at higher pressure, thereby causing a shock wave to be propagated into the passage, and increasing the stagnation pressure of the gas. The exact sequence of waves will depend on the cycle employed. Several different cycles are possible, each serving a different function. Examples are three-port cycles, used as flow dividers or equalizers (Kentfield, 1969), four-port cycles, used for superchargers (Jenny and Zumstein, 1982), topping cycles for gas turbine engines (Meyer, 1947; Zauner et al., 1993) and a wave superheater wind-tunnel (Weatherston et al., 1959), and five and nine-port cycles, again intended for use as topping cycles (Thayer et al., 1981). In addition, wave engines for generating shaft work have been developed (Pearson, 1985; Weber, 1995). However, all the cycles have common features, and a study of one should produce results applicable to all cycles, at least in a general sense. For example, two common features are that all cycles employ an expansion wave, and expanding through too large a pressure ratio leads to losses for any cycle. Obviously, for maximum output, whatever the application, the efficiency of the wave rotor should be as high as possible, i.e., the losses should be minimized. In order to do this, it is necessary to know the source of the losses and their dependence on controlling parameters. This study is aimed at assessing experimentally the magnitude of various wave rotor losses as a function of the parameters which affect them. This is achieved by measuring the performance of a wave rotor as various geometrical parameters (passage width, rotor length, and rotor-casing clearance) are varied. In addition to providing insight into how the parameters effect performance, this scheme also furnishes a useful data base for theoretical modeling (Paxson, 1995). The losses are not specific to one cycle, and so any convenient cycle can be used for this study. To be sure, the results obtained with one cycle will not be directly applicable to another cycle quantitatively, but will be qualitatively. For example, there will always be a trade-off between opening time and friction because increasing the passage width increases opening time, but decreases the total friction. Leakage depends on a nondenominational parameter which should be low for good efficiency. How low will depend on the exact cycle, but probably should be no larger than the value proposed as a result of these studies. For simplicity, the three-port flow divider cycle was chosen for these experiments. In the flow divider, a single inlet flow is split into two outlet flows, one at higher stagnation pressure than the inlet flow, and the other at lower stagnation pressure than the inlet flow. No heat is added, so the apparatus is relatively simple (Fig. 1). However, this cycle can not be used as a topping stage.

In order to make an experimental study of losses, a wave rotor has been built at NASA Lewis Research Center, that operates on the three-port flow divider cycle. This paper contains a brief statement of the philosophy of the experiment, a description of the experiment, and a summary of the measurements made. Finally, results are presented showing that reduction of the rotor-to-wall clearance gap leads to a large improvement in performance and that friction and opening-time effects, as well as incidence losses, also play an important role in the performance.

Contributed by the International Gas Turbine Institute and presented at the International Gas Turbine and Aeroengine Congress and Exhibition, Birmingham, United Kingdom, June 10–13, 1996. Manuscript received by the ASME Headquarters September 3, 1997. Paper No. 96-GT-117. Associate Technical Editor: J. N. Shinn.

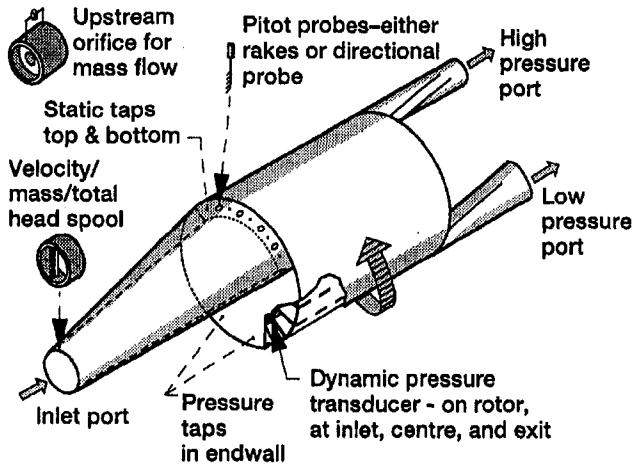

Fig. 1 Schematic diagram of the apparatus with the diagnostics used

The Flow Divider Cycle

The performance of a flow divider is conveniently indicated on a plot of the ratio of high pressure port stagnation pressure to inlet stagnation pressure versus the ratio of low pressure port stagnation pressure to inlet stagnation pressure, with the mass flow ratio β as a parameter (Kentfield, 1969). An upper limit to the performance of the flow divider can be calculated very simply, using what is called the acoustic approximation. In this approximation, the following assumptions are made about the flow:

1 Flow conditions are constant within each region; regions are separated by waves.
2 Waves are not reflected at ports.
3 Waves travel at a single speed, which is the average of the wave propagation speeds on either side of the wave, and, hence, do not spread.
4 No change in entropy occurs across the waves.

The results of this calculation are shown in Fig. 2(a). This performance, which is called the isentropic performance, is significantly higher than anything that can be achieved in practice, but it does illustrate the features of flow divider performance, i.e., that a large ratio of high pressure to inlet pressure is only achieved at a low value of β. The dotted line terminating the curves of constant mass ratio β at the upper left, corresponds to an inlet Mach number of unity. In this approximation, the curves of constant β are concave upwards, and maximum performance (i.e., largest high pressure ratio) will be achieved at an inlet Mach number of unity.

A more accurate calculation can be made by using characteristics to evaluate the expansion out of the passages into the low pressure port and by including shock waves in the compression portion of the calculation. This will be called the ideal cycle. The resulting flow divider performance is shown in Fig. 2(b). Now the curves of constant β are concave downwards, and the maximum performance (whether defined as pressure rise or efficiency) occurs for an inlet Mach number less than unity. A further, important difference is where choking occurs. For the isentropic cycle, the inlet Mach number is greater than either of the outlet Mach numbers, and choking would occur at the inlet. In the ideal cycle, for values of β of 0.5 and less, reducing the low pressure leads to a Mach number of unity in the low pressure port while the inlet port is still subsonic. In other words, choking occurs at the low pressure port, not the inlet port. Although the ideal performance contains wave losses that are inherent in any real cycle, and so is a better approximation than the isentropic calculation, it can not be achieved in practice since instantaneous opening time and no friction are assumed; conditions which are obviously not attainable.

Nomenclature

a = speed of sound
B = width of a passage on the rotor
b_o, b_i, b_{ii} = constants defined in Eq. (25)
C_p = specific heat at constant pressure
D_h = hydraulic diameter of passages
$\mathcal{D}(x)$ = drag on a plate of length x
F = dimensionless friction parameter, defined in Eq. (5)
f = loss factor defined in Eq. (15)
G, G_p, G_w = leakage parameters, defined in Eqs. (22) to (24)
H = height of a passage on the rotor
i = angle of incidence of entering air in the rotor reference frame
K = coefficient of incidence loss
L = length of the rotor
M_j = Mach number in region j
n = $2\pi/\theta_{\text{cycle}}$
P_j = absolute stagnation pressure in region j
It_j = relative stagnation pressure in region j
R = radius of the rounding on the leading edge of the inlet port
T_j = absolute stagnation temperature in region j
Tr_j = relative stagnation temperature in region j
t = time
U = circumferential velocity of the rotor at the average radius of the passages
V_j = absolute velocity in region j
W_j = relative velocity in region j
α = angle of flow in inlet duct
β = ratio of mass flow in high pressure port to total mass flow
γ = ratio of specific heats
δ = end wall to rotor gap spacing
δ_p = end wall to rotor gap spacing at a port
δ_w = end wall to rotor gap spacing away from a port
$\delta_2(x)$ = boundary layer momentum thickness
ϵ = expansion ratio—ratio of the pressure in the low pressure port to the pressure in a passage just before reaching the low pressure port
η = efficiency
θ_{cycle} = angular extent of one cycle of waves
θ_p = angular extent of low pressure port
$\theta_{w_{\text{in}}}$ = angular extent of low pressure region at inlet endwall
$\theta_{w_{\text{out}}}$ = angular extent of low pressure region at exit endwall
θ_w = $\theta_{w_{\text{in}}} + \theta_{w_{\text{out}}}$
ν = kinematic viscosity
ρ = gas density
τ = dimensionless opening time, defined in Eq. (2)
ω = rate of rotation of the rotor

Subscripts

cav = cavity surrounding the rotor into and from which leakage occurs
j = general subscript for any of the three subscripts below
in = inlet port
hi = high pressure port
lo = low pressure port
pas = passage immediately before opening to the low pressure port

Superscript

l = lossless

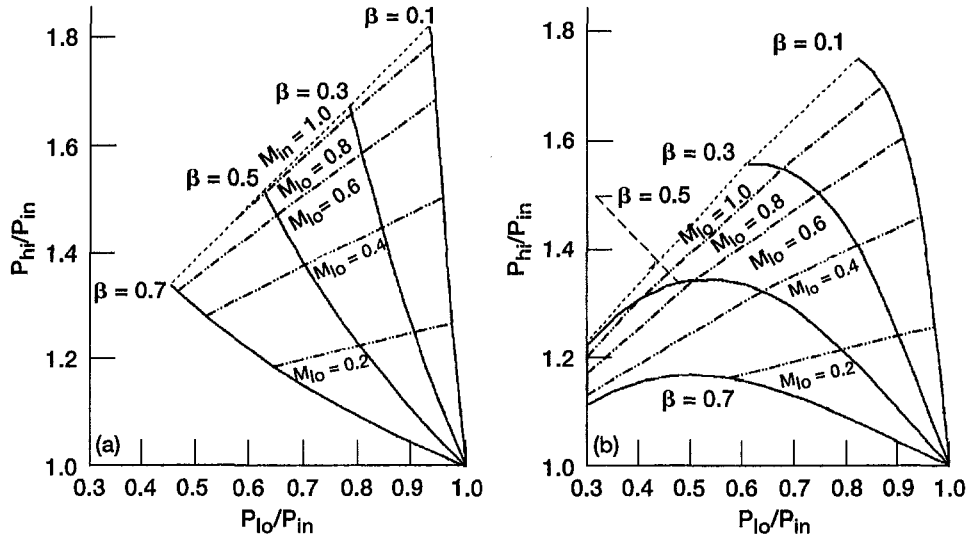

Fig. 2 Performance of a three-port flow divider calculated for (*a*) the isentropic cycle (left) and (*b*) the ideal cycle

The isentropic assumption is only valid for weak waves, which is the case for the lower right hand region of Fig. 2, where pressure ratios are close to unity. Comparison of Figs. 2(*a*) and (*b*) shows that the isentropic calculation works reasonably well for outlet Mach numbers M_{lo} less than about 0.3. The experiments of Kentfield (1969) were entirely within this range, and his curves did not display a pressure ratio maximum. For topping-cycle application, the pressure ratio should be as large as possible; therefore, one consideration in the present experiment was to operate the wave rotor under conditions for which the acoustic approximation would not be valid and to observe whether there is indeed a maximum in the performance. Consequently, a design expansion ratio of 0.33 was chosen, corresponding to a Mach number of the expanded flow of 0.85. The expansion ratio, ϵ, is the ratio of the pressure in the low pressure port to the pressure in a rotor passage just before it is opened to the low pressure port. This ratio determines the Mach number of the flow in the low pressure port. For an expansion ratio of 0.33, the expansion wave exhibits significant spreading, as can be seen in the wave diagram of the cycle shown in Fig. 3. The efficiency of a flow divider has been defined by Kentfield (1969) as the product of compression and expansion efficiencies.

$$\eta = \frac{\beta}{(1-\beta)}\left[\frac{(P_{hi}/P_{in})^{(\gamma-1)/\gamma} - 1}{1 - (P_{lo}/P_{in})^{(\gamma-1)/\gamma}}\right] \qquad (1)$$

The isentropic performance can be derived from this formula by inserting $\eta = 1$.

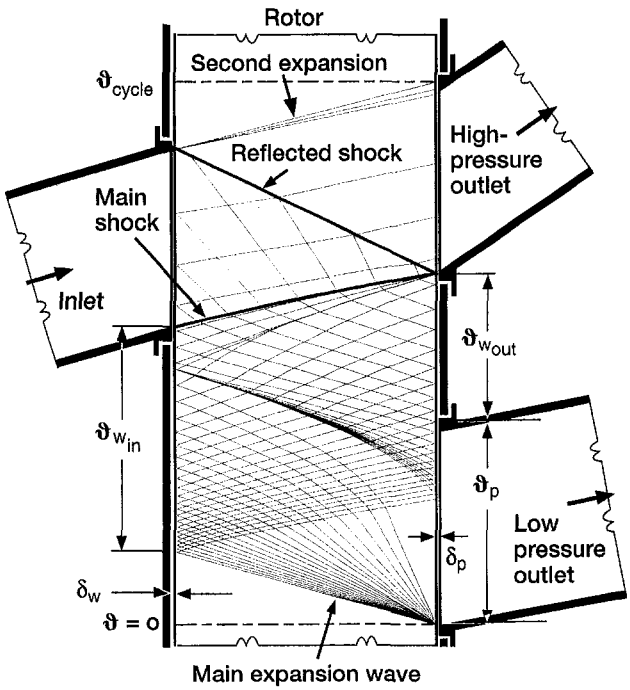

Fig. 3 Characteristics calculation of the flow divider cycle for ϵ = 0.33. The leakage gaps δ_p and δ_w are shown for illustrative purposes (not to scale)

Loss Mechanisms

Although several wave rotors have been built in the past, only two studies of losses appear to have been reported. These are for the theoretical estimates of losses by Hoerler (1969) for the Comprex®, and for the flow divider by Kentfield (1969). Kentfield gives the following losses as being in order of decreasing importance:

1 basic wave effects
2 cell width, i.e., opening time effects
3 wall friction, passage entry, and exit losses
4 leakage

Hoerler calculated losses for the rotor itself as percentage losses in efficiency for an experimental Comprex, and also for a hypothetical optimized Comprex. The results are given in Table 1. In addition, there are losses for ducts and stators external to the rotor. Hoerler states that leakage can dominate all other rotor losses, particularly for small machines, which is just the opposite of the conclusions by Kentfield. This disagreement reflects the different geometries of the two machines considered, as will be explained below.

It will be assumed that the friction, opening time, and leakage losses, will scale with one predominant parameter for each loss. The derivation of the parameter for each of these losses, the evaluated losses, is outlined below. In addition, there are other losses that are estimated and used to correct the data.

Evaluated Loss Mechanisms

Basic Wave Effects. Basic wave effects are the losses due to shock waves and spreading of expansion waves, which cause

Table 1 Loss of efficiency in a comprex®

Source of loss	Loss in experimental COMPREX	Loss in optimized COMPREX
Shocks and Fans	4.5%	3.3%
Passage opening/closing	4.1%	4.2%
Friction (turbulent)	7.2%	2.1%
Heat transfer	3.3%	2.1%
Rotational velocity	4.2%	2.0%
Leakage	10.1%	1.1%
Mechanical	2.3%	0.1%
Interface mixing	0	0
Total	35.7%	14.9%

the difference in performance between the ideal cycle and the isentropic cycle. A real cycle can have shock waves instead of compression waves. There is a loss of stagnation pressure across a shock wave, leading to a reduction in performance. Expansion waves spread in space as they propagate, resulting in nonuniform velocities in the exit ports. Mixing of the nonuniform velocity distribution to form a uniform distribution causes a stagnation pressure loss. These losses are unavoidable in a real device. Moreover, they are quite large for low values of expansion ratio, as can be seen by the differences between the performance in Fig. 2(*a*) and that in Fig. 2(*b*). the losses due to these effects depend on β and ϵ, and are readily calculable if the timing is correct, i.e., if the ports open and close at the appropriate times as determined by the arrival, or launching, of waves. For maximum performance, the timing will be different for each value of β and ϵ considered. An actual device will usually have timing fixed for one set of conditions, and operation off design will create extra waves, causing additional losses. This can be handled computationally using a one-dimensional CFD code for wave rotor cycles (Paxson, 1995). The ideal cycle performance can not be measured directly in an experiment. It can be determined from experimental results by measuring performance as a function of the other losses, and by extrapolating them to zero.

Finite Passage Opening Time. Since the passages have a finite width, there is a finite time taken for a passage to rotate past the leading or trailing edge of a port, and to become fully open or closed. In the case of an inlet port, for which instantaneous opening of the passage would cause a shock wave to propagate down the passage, a finite opening time will result in a compression wave, which will steepen into a shock wave as it travels down the passage. The degree to which it steepens depends on the ratio of the opening time to the time taken by the wave to travel the length of the passage. Thus the relevant nondimensional parameter is

$$\tau = \frac{\text{Passage Opening Time}}{\text{Wave Travel Time}} = \left(\frac{B}{U}\right)\left(\frac{a}{L}\right). \quad (2)$$

The speed of sound, a, will vary depending on which region of the cycle is being considered. For simplicity of definition, the inlet stagnation value will be used. Note that for any particular cycle, the rotor velocity U will be inversely proportional to the axial length of the passage L, and, hence, τ is determined mainly by the value of the passage width, B. In addition to the effect on wave steepening, which may be advantageous, finite opening time will result in deleterious throttling losses when the passage is partially open. Further, finite opening time will create a gradual rise in velocity at the outlet ports, and finite closing time will create a gradual reduction in velocity at the outlet ports. The resulting nonuniform velocity distribution will result in a drop in stagnation pressure when it is mixed out to a uniform value downstream. Clearly this loss will increase as τ increases.

Friction. Although the rotor passages are long and slender, their maximum length-to-width ratio is less than the entrance length for pipes. Thus, the flow can be considered to have a boundary layer. This is confirmed by measurements of the radial velocity distribution in the high pressure port, which shows a uniform velocity over the central 70 percent of the passage, and in the two-dimensional calculations of the flow in the entrance and high pressure ports of the experimental geometry (Welch and Chima, 1993), also showing a relatively small boundary layer. The flow in a passage open to the low pressure port can be thought of as flow over a flat plate, with the leading edge of the "plate" being the location of the leading edge of the expansion wave. A friction parameter can then be defined as the ratio of the drag force due to the flat plate to the product of dynamic pressure and flow area, i.e.,

$$F = \mathcal{D}(x)/\tfrac{1}{2}\rho W^2 BH. \quad (3)$$

The drag is related to the boundary layer momentum thickness at the end of the passage (Schlichting, 1979). For reasons explained below, the boundary layer was assumed laminar. With this assumption, the boundary layer momentum thickness is given by (Schlichting, 1979)

$$\delta_2(x) = 0.67x(Wx/\nu)^{-0.5}. \quad (4)$$

The length of the boundary layer varies linearly with time as the expansion moves into the passage. By averaging over the time that the port is open, the friction parameter becomes

$$F = 7.2\,\frac{L}{D_h}\left[\frac{LW}{\nu}\right]^{-0.5}. \quad (5)$$

This parameter will be taken as representative of the effect of friction on the cycle as a whole. The dominant factor in the friction parameter is L/D_h.

Leakage. Leakage can take place radially from the passage to the casing if the passage is at high pressure, or from the casing to the passage if the passage is at low pressure. The result will be a "short-circuiting" from high pressure to low, leading to reduced performance. In addition, circumferential leakage is possible, from passage to passage. The pressure difference driving circumferential leakage is small except when a wave has reached the end of a passage. Thus circumferential leakage is likely to be small. For radial leakage, the rate of mass leakage will be proportional to the area available for leakage, which is $2\delta B$ at each end of a passage. The leakage will be into the passage while it is in a region of low pressure. From Fig. 3, the low pressure region on the inlet side extends over an angle $\theta_{w_{\text{in}}}$, where the leakage gap is δ_w, and on the outlet side, the low pressure region is the low pressure port, of extent θ_p, and gap δ_p, and the region between the low pressure port and the high pressure port, of extent $\theta_{w_{\text{out}}}$ and gap δ_w. Thus, the time spent at low pressure on the inlet side of the wave rotor is

$$t = \theta_{w_{\text{in}}}/\omega \quad (6)$$

and

$$t = \theta_p/\omega + \theta_{w_{\text{out}}}/\omega \quad (7)$$

on the outlet side. The amount of mass leaking into a passage will be

$$\text{mass} \sim \rho_{\text{cav}} 2B(\delta_w\theta_{w_{\text{in}}} + \delta_p\theta_p + \delta_w\theta_{w_{\text{out}}})/\omega. \quad (8)$$

The leakage parameter is defined as the ratio of the mass leakage to the mass in a passage before it reaches the low pressure

port, i.e., $\rho_{pas}BHL$. If ρ_{pas} is assumed equal to ρ_{cav}, the leakage parameter becomes

$$G \sim 2(\delta_p\theta_p + \delta_w\theta_w)/\omega HL. \quad (9)$$

For operation of a specific wave rotor, ωL is a constant. For convenience, relative values of $\theta_p = 0.71$ and $\theta_w = 1.29$, were used, and the proportionality constant was chosen so that the leakage parameter is defined as

$$G = (\delta_p\theta_p + \delta_w\theta_w)/H. \quad (10)$$

Then, if the leakage gaps are equal, i.e., $\delta_p = \delta_w = \delta$, this reduces to

$$G = 2\delta/H. \quad (11)$$

Based on this derivation, one would expect that the leakage in the Comprex studied by Hoerler (1969) would be similar to that in the experiments of Kentfield (1969) since the ratio $2\delta/H$ was virtually the same for both devices), but Hoerler claimed leakage was important, whereas Kentfield said that it was not. However, the two devices operated on quite different cycles, and whereas the experiment of Kentfield used a cycle similar to that of the present experiment, the Comprex cycle was different. In the Comprex, which used a four-port cycle, the inlet port and exhaust port were at approximately the same pressure, which was significantly lower than the two high pressure ports. The cavity was therefore likely to be at some intermediate pressure. This means that the assumption that $\rho_{cav} = \rho_{pas}$ is probably not correct for the Comprex, and, also, there would be leakage into the inlet port. Both of these effects would lead to more leakage. An additional difference was the relative extent of the low pressure regions, with more of it in a port region for the Comprex. It thus seemed important to ascertain in the present experiment whether leakage at a wall is more, or less, important than leakage at a port. In order to do this, the wall gap and port gap were varied independently. Thus, separate port and wall leakage parameters were defined, i.e.,

$$G_p = \delta_p\theta_p/H \quad (12)$$

and

$$G_w = \delta_w\theta_w/H. \quad (13)$$

Corrected Loss Mechanisms

There are additional sources of pressure change within the wave rotor deriving from flow in rotating machinery. These are the changes in total pressure between the relative and absolute reference frames, to compression or expansion on entering the rotor (depending on the angle of incidence with which the flow meets the passage side walls), and to entry and exit losses (resulting from the blunt-edge passage walls). These effects are described below. The resulting pressure changes were estimated in order to correct the observed absolute frame pressure measurements appropriately.

Rotational Velocity Loss. The wave action takes place entirely within the rotor, producing changes of pressure in the relative frame. However, the actual performance of a device is measured in the absolute frame, and will be affected by the rotor rotational speed (Wilson and Paxson, 1996). The experiments were run at three different rotational speeds, and, so, should be compared in the relative frame to remove the effect of the differing rotational speeds. Also, the ideal performance, as given above, is in the relative frame (since no correction for rotation was made, which is equivalent to assuming that the rotational velocity is zero). Thus, it is necessary to correct the observed absolute results to the relative frame. If no work is done on the gas, and for axial passages, the relative total temperatures will be related to the absolute total temperatures by (Glassman, 1994)

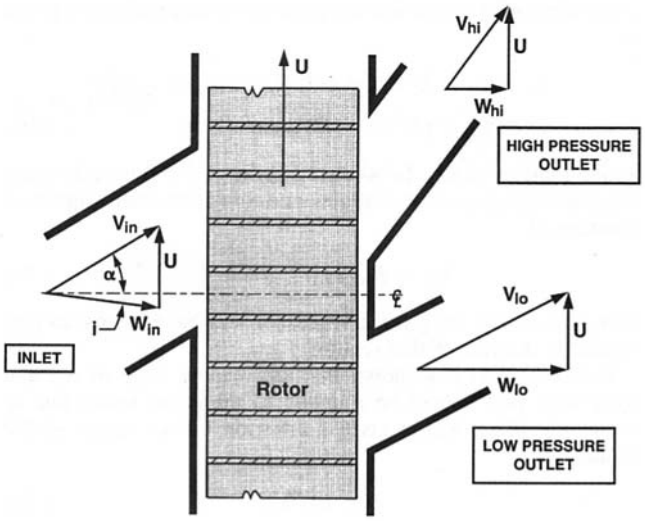

Fig. 4 Inlet and outlet velocity diagrams for the wave rotor

$$Tr_j = T_j - U^2/2C_p, \quad (14)$$

and the ratio of relative to absolute stagnation pressure will be

$$\frac{Pr_j}{P_j} = \left[\frac{Tr_j}{T_j}\right]^{\gamma/(\gamma-1)}. \quad (15)$$

The absolute efficiency, calculated by inserting absolute values of stagnation pressure into Eq. (1), will be less than the relative efficiency, calculated by using relative stagnation pressures in Eq. (1). Thus, this effect is equivalent to a loss. However for the flow divider (though not necessarily for other cycles), this effect is small. Even at the highest rotational speed, the drop in efficiency is only 1 percent.

Flat Plate Compressor Effect. If the inlet duct is at the correct angle, and if the flow angle α is equal to the duct angle everywhere in the port, then the inlet flow will enter the passages smoothly at zero angle of incidence in the relative frame, $i = 0$ (Fig. 4). For this to be the case, the flow angle must satisfy the relation

$$\sin(\alpha) = U/V_{in}. \quad (16)$$

This will only occur at design conditions, and even then, only if the design is correct! Off design the flow will be at a finite angle of incidence, i, to the passage side walls. Work will be done on the air if i is negative or it will be extracted from it if i is positive.

This is equivalent to a flat plate compressor. The work done on the gas will result in a stagnation temperature rise ΔT,

$$\Delta T = \beta T_{hi} + (1 - \beta)T_{lo} - T_{in}, \quad (17)$$

which can be calculated from the Euler equation for turbomachinery;

$$C_p\Delta T = U(U - V_{in}\sin(\alpha)). \quad (18)$$

Measurements of motor power in some runs showed that the temperature rise could be as high as 20°R, corresponding to a motor power of about 10 HP. Both the velocity V_{in} and the flow angle α vary across the inlet port, and the work done must be evaluated by integration.

Such a calculation provides the work put into the gas by the motor, but does not give values for pressure. With work input,

the relative inlet stagnation temperature (at any station) is given by

$$T_{in} = T_{in} - U^2/2Cp + U(U - V_{in}\sin\alpha)/Cp$$
$$= T_{in} + (U^2/2 - UV_{in}\sin\alpha)/Cp, \quad (19)$$

which reduces to Eq. 14 when $V_{in}\sin\alpha = U$. Thus, a lossless flat plate compressor would generate a relative inlet stagnation pressure of

$$It'_{in} = P_{in}(Tr_{in}/T_{in})^{\gamma/(\gamma-1)}. \quad (20)$$

However, a real flat plate compressor will have losses, as discussed in the rest of this section.

Keller (1984) has shown that the leading edge of a wave rotor inlet port should be rounded to minimize losses due to vortex shedding. Keller gives a criterion for the radius of the rounding;

$$R \geq BU/V_{in}. \quad (21)$$

In order to ensure that this criterion was well satisfied in the present experiment, a large radius (1.6 in.) was chosen, but the circle was truncated so the flow angle at the leading edge of the port was −32 deg. Unfortunately, this rounding was too large, as it affected the inlet flow field, causing a large fraction of the flow to enter the rotor at an angle less than that for zero relative incidence angle, resulting in work being done on the air by the rotor. Air hitting a row of airfoils at an angle of incidence will suffer a loss of stagnation pressure, called incidence loss. The loss of stagnation pressure due to incidence loss can be defined as

$$\Delta P = K\tfrac{1}{2}\rho W^2_{in}. \quad (22)$$

Data on loss of kinetic energy due to incidence has been given by Emmert (1950) for both sharp-edged blades and round-nosed blades (without defining what constitutes sharp and round). The data of Emmert can be fitted quite well with an expression of the form

$$K = f|\sin^3(i)|. \quad (23)$$

Using $f = 0.6$ provides a good fit to the round-nose blade data, and $f = 1.5$ gives a reasonable fit to the sharp-nose blade data. The loss coefficient is dependent on Mach number, as well as on incidence angle. Data on loss coefficients for cascades of four different airfoils, at a variety of Mach numbers, has been given by Lieblein (1965). The data of Fig. 130(d) of Lieblein, which is for a sharp-edged airfoil, shows that f increases with Mach number. In addition to varying with Mach number, values of loss coefficient can depend on Reynolds number and solidity. In the present experiment, the Mach number varies between about 0.2 and 0.9. Thus, the value of f could be larger than the values which fitted the data of Emmert. A priori, there is no obvious value of f to use. Instead, values of f were chosen, the data were corrected with this value, and then extrapolated to obtain an experimental value for the efficiency with no friction, zero opening time, and no leakage, i.e., the ideal efficiency. Strictly speaking, this is only the ideal efficiency at the design condition, $\epsilon = 0.33$. The true ideal efficiency requires the port timing to be changed for each value of ϵ. Nevertheless, the term ideal efficiency will be used here to mean the efficiency with $\tau = F = G_p = G_w = 0$, but with the fixed experimental timing. The value of f was altered until the experimental value of ideal efficiency agreed with the ideal efficiency calculated using the one-dimensional CFD Code of Paxson (1995). In other words, the experiment, together with the one-dimensional code, was used to determine a value of f.

With a value of f assumed, the relative stagnation pressure produced by the flat plate compressor is

$$It_{in} = It'_{in} - \tfrac{1}{2}\rho_{in}W^2_{in}f|\sin^3(i)|. \quad (24)$$

Depending on the flow angle and velocity, the resulting stagnation pressure could be greater or less than the relative stagnation pressure when no work is done. Since the flow angle and velocity vary across the inlet port, the relative stagnation pressure will also vary across the inlet port. A single value is required for input into the efficiency equation, and is obtained by averaging the relative stagnation pressures calculated at various positions within the port.

Entrance and Exit Losses. The wall between the passages has a finite thickness. Consequently, there is an area change between the flow in the ducts and the flow in the passages. The squared ends of the walls will present an obstruction to the flow on entering, and a drag on leaving, leading to stagnation pressure losses. This effect was calculated by assuming the leading edge is at the entering stagnation pressure, and the trailing edge is at the downstream static pressure. The resulting force on the flow is included in the momentum equation, which is then solved with the continuity and energy equations to give the downstream stagnation pressure. The calculated losses in stagnation pressure are less than 2 percent for the narrow passages and less than 1 percent for the wide passages.

Experimental Design

In order to be able to obtain experimental values of the losses due to opening time, friction, and port and wall leakage, the parameters τ, F, G_p, and G_w must be varied. An efficient way to formulate an experiment to obtain empirical fits to data when there are three or more variable parameters is the Box-Behnken scheme (Box and Behnken, 1960). This is a three-level scheme, i.e., measurements are made at three values of each parameter. It is then possible to fit the results with a second-degree polynomial. Thus, in the present wave rotor experiment, the measured variable (or response) is the efficiency η; the four independant variables are τ, F, G_p, and G_w; and the fit will be of the form

$$\eta = b_o + b_1\tau + b_2F + b_3G_p + b_4G_w + b_{11}\tau^2 + b_{22}F^2 + b_{33}G_p^2 + b_{44}G_w^2 + b_{12}\tau F + b_{13}\tau G_p + b_{14}\tau G_w + b_{23}FG_p + b_{24}FG_w + b_{34}G_pG_w, \quad (25)$$

where the constants b_o, b_i, and b_{ii} are determined from the experimental measurements. Replication of the center point provides an estimate of the experimental error. The set of runs that must be made in order to evaluate the constants was determined using commercial software (Seshadri and Deming, 1990), and is listed in Table 2. RS/Explore was used to determine the constants from the experimental data.

In designing the experiment, the actual rotor dimensions had to be determined. A review of the literature showed that the geometry had differed significantly for rotors built in the past, sometimes with no indication of the value of the end-wall to rotor gaps. The details of several past rotors are given in Table 3. The nondimensional opening time τ has varied over a range of 0.1 to 0.35. The major component of the friction parameter, namely the ratio L/D_h, has varied between 3.7 and 84. Finally, the leakage parameter G (previous workers have not differentiated between G_p and G_w) has varied from 0.005 to 0.017. The objective in designing this experiment was to cover as much of this range as possible. In order to do this, the actual experiment consisted of two different rotors 12 in. in diameter with one 18 in. long and the other 9 in. long. Both were built with passages 0.25 in. wide and 0.4 in. high, with 120 passages per rotor. After a series of runs at 0.25 in. passage width, every other wall was removed, and another series of runs was made at approximately twice the passage width. The ducts were designed so that one cycle of waves took up less than the whole circumference of the rotor, i.e., $\theta_{cycle} < 2\pi$. Only one cycle of

Table 2 Set of runs for the statistical experiment

Run number	Rotor length, in.	Passage width, in.	n	RPM	Port gap, in.	Wall gap, in.	P_{in}
1	18	0.25	1.5	3700	0.010	0.010	30
2	18	0.025	3.0	1850	0.005	0.010	30
3	↓	↓	↓	↓	0.015	0.010	↓
4	↓	↓	↓	↓	0.010	0.005	↓
5	↓	↓	↓	↓	0.010	0.015	↓
6	9	0.25	1.5	7400	0.010	0.010	38
7	↓	↓	↓	↓	0.010	0.005	30
8	↓	↓	↓	↓	0.010	0.015	↓
9	↓	↓	↓	↓	0.005	0.010	↓
10	↓	↓	↓	↓	0.015	0.010	↓
11	18	0.54	1.5	3700	0.010	0.010	30
12	↓	↓	↓	↓	0.005	0.005	↓
13	↓	↓	↓	↓	0.015	0.005	↓
14	↓	↓	↓	↓	0.015	0.015	↓
15	↓	↓	↓	↓	0.005	0.015	↓
16	↓	↓	↓	↓	0.010	0.010	↓
17	18	0.54	3.0	1850	0.010	0.005	30
18	↓	↓	↓	↓	0.010	0.015	↓
19	↓	↓	↓	↓	0.005	0.010	↓
20	↓	↓	↓	↓	0.015	↓	↓
21	↓	↓	↓	↓	0.010	↓	15
22	↓	↓	↓	↓	0.010	↓	53
23	18	0.54	1.5	3700	0.010	0.010	30
24	9	0.54	1.5	7400	0.005	0.010	30
25	↓	↓	↓	↓	0.015	0.010	↓
26	↓	↓	↓	↓	0.010	0.005	↓
27	↓	↓	↓	↓	0.010	0.015	↓

Note that runs 11, 16, 23 are replicates.

waves was used, and, thus, there was a long, nominally wave-free region between the closing of the high pressure port and the opening of the low pressure port. This was to allow any waves remaining from the high pressure port closing to die out, thereby giving the uniformity prior to opening the low pressure port that was assumed in calculating the cycle. One set of ducts was designed for operation at $n = 1.5$ for both the 9 in. and 18 in. long rotors. Adding a different set of ducts for operation at $n = 3$ with the 18 in. rotor provided a combination giving three values of τ and L/D_h covering the range 20 to 58, and, hence, three values of F. In order to vary the port leakage gaps, the ports were built as inserts supported on a flange. Placing shims under the flange permitted variation of the rotor to port gaps. The rotor to wall gap was varied by providing moveable end walls at each end, consisting of disks that could move axially. Springs at three locations pushed the disks away from the rotor, and three screws forced the disks towards the rotor. Adjustment of the screws gave the desired gap spacing. The minimum spacing that could be used safely was 0.005 in.; larger than had been hoped for. This gave a value of $G = 0.025$, which was greater than the values used by other workers due to the small passage height of the present experiment.

The port geometries for all the runs are given in Table 4. What is given in Table 4 is the circumferential angle at which each port opens and closes measured in the direction of rotation from the opening of the low pressure port. Also given are the duct angles, which are the angles made by the centerlines of the ducts to the rotor axis.

Control of the wave rotor flows was by a butterfly valve in each leg. The supply pressure was around 55 psia. The inlet valve was adjusted to throttle this supply pressure down to the desired inlet stagnation pressure, usually 30 psia. The expansion ratio was set by the low pressure valve (based on a low pressure port static pressure reading) and a pressure tap in the endwall (giving the passage pressure just before opening to the low pressure port). The high pressure valve controlled the mass ratio β, based on the input and high pressure orifice mass flow readings. The rotor was turned by a variable speed electric motor with a constant speed control. An independent measurement of the rotor speed was also made.

Experimental Measurements

The efficiency of the flow divider (Eq. 1) is determined by the ratios of P_{hi}/P_{in} and P_{lo}/P_{in} at a particular value of β. Higher values of both ratios correspond to higher efficiency. The necessary measurements are, therefore, the mass flows in each port and the stagnation pressures of the inlet, high pressure, and low pressure flows. The mass flows were measured with standard orifice meters. The ports are obviously sections of an annulus. A transition piece in front of the inlet port took the flow in the inlet pipe, and converted it to the port shape, which accelerated the flow in the process and brought it onto the rotor at the correct angle. Immediately upstream of the transition piece, but downstream from the orifice, was a diagnostic spool with three wall static taps, five pitot tubes, and a thermocouple. The inlet stagnation pressure and temperature were determined by measurements at this spool. Similarly, the outlet ports had transition pieces to take the flow from the port shape back to round, and which also acted as diffusers. The downstream area of these diffusers was fixed by the exhaust pipe diameter. With the diffuser area ratio determined, the length was chosen to give maximum diffuser efficiency, using the diffuser performance curves of Mattingly et al. (1987). A diagnostic spool was placed immediately at the exit of each diffuser, with the intention of using the measurements to evaluate exit stagnation pressures. However, the velocity distribution was found to very nonuniform, and it was not clear whether the resulting stagnation pressure would be reliable. Instead, measurements made at the ports were used to calculate a stagnation pressure. There were 5 static pressure taps on the top and bottom of each port and four pitot tube installations. The pitot installations carried either a rake of 5 pitot tubes to determine radial velocity distribution, or a tube-type combination probe (Glawe and Krause, 1974) to determine center-line velocity and direction. In the high pressure port, velocities are low and relatively uniform, and an average of the individual port stagnation pressure measurements was taken as the port stagnation pressure. In the low pressure port, the veloc-

Table 3 Comparison of different wave rotors

Machine type	Thayer Pressure exchanger	Weatherston Pressure exchanger	Pearson Wave turbine	Hoerler Pressure exchanger	Kentfield Flow divider	This work Flow divider
Length L″	15.8	66	3.5	4.25	11	9.18
Diameter D″	14.4	60	9	3.23	8	12
Passage width B″	0.4	0.55	0.7	0.19	0.66	0.25, 0.54
Passage height H″	1.5	1.43	1.5	1.1	2.2	0.4
Hydraulic dia D_h″	0.63	0.79	0.95	0.32	1.05	0.31, 0.46
RPM	1 960	2 700	18 000	11 200	5500	1850-7400
Cycles/revolution n	2.5	1	1	2	3	1.5, 3
Leakage gap δ″	0.004-0.013			0.004	0.007	0.005, 0.01, 0.015
Ratio L/D_h	25	84	3.7	13	10.5	20-58
Ratio 2δ/H	0.005-0.017			0.007	0.006	0.025-0.075
Opening time τ	0.2	0.1	0.3	0.33	0.35	0.08-0.35

Table 4 Port timing and duct angles

Run	Inlet port			High pressure port			Low pressure port		
	Opening angle	Closing angle	Duct angle	Opening angle	Closing angle	Duct angle	Opening angle	Closing angle	Duct angle
1	108°	172°	22°	129°	194°	47°	0°	70°	13°
2-5	55°	86°	11°	66°	96.5°	28°	0°	35°	6.5°
6-10	108°	172°	36°	129°	194°	65°	0°	70°	27°
11-16,23	108°	169°	22°	129°	190°	47°	0°	70°	13°
17-22	55°	84°	11°	67°	93°	28°	0°	35°	6.5°
24-27	108°	172°	36°	129°	190°	65°	0°	70°	27°

ity distribution is very nonuniform, both radially and circumferentially. The measurements were used to create a circumferential velocity distribution and, by using a rake probe, a radial velocity distribution. These distributions were used to create mass, momentum, and energy integrals for a mixing calculation (Foa, 1960) from which the stagnation pressure for a uniform downstream velocity was evaluated and used as the low pressure port stagnation pressure. The pressure measurements were steady state. For some runs, a dynamic pressure transducer was installed 4 in. downstream of the low pressure port. The signal from this transducer was a sine wave at the passage passing frequency, with a peak to peak value of 0.5 percent of the steady-state pressure. Thus, the pressures were essentially steady state. All steady state pressure measurements were recorded through an electronically scanned pressure (ESP) measurement system (Fronek et al., 1987). The pressure measuring system automatically self-calibrates every 20 minutes to maintain a 0.1 percent accuracy.

Results

For the statistical experiment, runs were made at a nominally constant value of $\beta = 0.37$, mostly at an input stagnation pressure of 30 psia, varying ϵ from 0.33 to 0.8, unless the full range was not accessible. Because it was not possible to achieve $\beta = 0.37$ exactly on every run, runs were also made at a nominal $\beta = 0.36$ and $\beta = 0.38$. From these extra runs, a local value of the derivatives of P_{hi}/P_{in} and P_{lo}/P_{in} with respect to β, could be calculated. They were used to correct the runs at nominal $\beta = 0.37$ to values corresponding to exactly $\beta = 0.37$. Each run was duplicated, and then the average of the corrected values of P_{hi}/P_{in} and P_{lo}/P_{in} for the two runs was taken as the final result.

The results were plotted as P_{hi}/P_{in} versus P_{lo}/P_{in}. A sample of the results showing the observed, absolute frame performance changes for the different rotors with both port and wall gaps set equal to 0.010 in. is given in Fig. 5. All these runs were made at an inlet stagnation pressure of 30 psia. The runs made with the 18 in. rotor at $n = 3$ have a larger opening time than the runs with $n = 1.5$, but the same value of friction factor. Thus, it is seen that increasing the opening time reduces performance. Runs with the wider passages are superior in performance to runs made with the narrow passages. The runs with the wider passages have a larger opening time but a lower friction factor than the runs with the narrow passages. For these runs, reduction in friction is more beneficial than the increase in opening time is deleterious. This is more evident for the runs with the 18 in. rotor than it is for the runs with the 9 in. rotor, indicating that friction is becoming less important for the shorter rotor. With the 9 in. rotor, the maximum value of P_{hi}/P_{in} occurs at an expansion ratio of 0.55, at a value of $P_{lo}/P_{in} = 0.553$, the maximum efficiency, calculated with P_{hi}/P_{in} and P_{lo}/P_{in}, is at an expansion ratio of 0.65. The performance curves have the same shape as the curves of Fig. 2(*b*), but are lower than the (interpolated) curve for $\beta = 0.37$, indicating that there are indeed additional losses.

Results obtained with the 18 in. rotor at three different gap spacings are shown in Fig. 6. The three runs at a gap spacing of 0.010 in. are the replicated runs at the center point, giving an idea of the experimental error due to lack of reproducibility of gap setting. It is clearly much less than the change in performance caused by a gap change of 0.005 in., so the observed effect is real. The variation at a fixed gap setting is of the order of 0.003, much less than the error due to gap setting, showing that irreproducibility of gap setting is the major source of experimental error. There is a significant increase in performance as the gap spacing is reduced.

Additional tests were made in which the inlet stagnation pressure was varied. These tests showed that performance increased as pressure was raised from 10 to 30 psi, but stayed constant with further increases in pressure. A reasonable explanation is

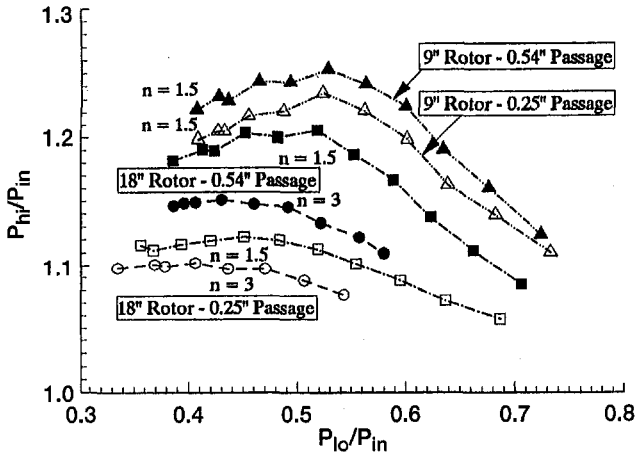

Fig. 5 A summary of the experimental results, showing the variation in performance with changes in opening time and passage length

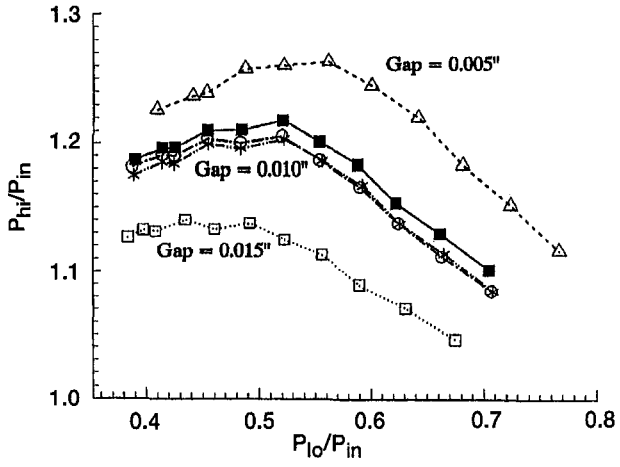

Fig. 6 A summary of the experimental results obtained while varying the leakage gap. Results for a gap of 0.010 in. represent the center point, which was run three times.

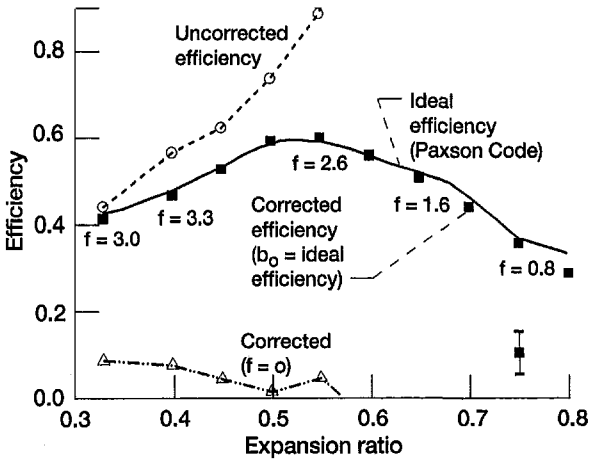

Fig. 7 Values of b_o versus expansion ratio obtained assuming a laminar friction factor. The ideal efficiency (——) was calculated with the CFD code of Paxson (1995).

that the low pressure runs were laminar, but that raising the pressure, and, hence, Reynolds number, caused the flow to become turbulent.

Evaluation of the Results

Statistical Experiment. At each value of expansion ratio, values of P_{hi}/P_{in} and P_{lo}/P_{in} were used to calculate an efficiency for each run, which was entered into the statistical program RS/Explore as the response. Values of τ, F, G_p, and G_w for each run were entered as the variables. In principle, this should have been done for all 27 runs. However, as explained in the discussion of the tests in which inlet pressure was varied, there was reason to suspect that the two high pressure runs (runs 6 and 22) were turbulent, whereas the other runs were laminar. Consequently, these two high pressure runs were omitted from the evaluation with a laminar friction factor. Using the remaining runs, the program calculated those values of the coefficients b_o, b_i, and b_{ii} that gave the best fit of Eq. (25) to the data, with confidence limits as to whether the term should be in the model. Terms with confidence less than 90 percent were dropped. The value of b_o is obviously the efficiency with $\tau = F = G_p = G_w = 0$, i.e., the ideal efficiency. What value is obtained for b_o depends on what values of P_{hi}/P_{in}, P_{lo}/P_{in}, and f were used. Results are shown in Fig. 7. A calculation of the ideal efficiency as a function of expansion ratio made with the CFD code of Paxson (1995) is also included in Fig. 7. There are three different values of b_o. The first, denoted "uncorrected efficiency", was obtained by inserting the measured absolute values of P_{in}, P_{hi}, and P_{lo} in Eq. (1) to calculate efficiency. Since this efficiency will contain a pressure change from the flat plate compression, it should not agree with the calculated efficiency that has only a wave rotor contribution except at design conditions ($\epsilon = 0.33$) where the work input is relatively low. In fact, this is seen. It is concluded that the uncorrected efficiency is not appropriate for determining wave rotor performance. The second efficiency denoted "corrected efficiency, $f = 0$ in. was obtained by using It_{in}, It_{hi}, and It_{lo} calculated as described in the section on loss mechanisms, but with the entry less subtracted from It_{in}, the exit loss added to It_{hi} and It_{lo}, and with $f = 0$. This is an even worse fit to the calculated efficiency, showing that this description of the losses is not valid. Finally, the efficiency denoted "corrected efficiency" again used It_{in}, It_{hi}, and It_{lo} corrected for entry and exit loss, but with the value of f adjusted so that the value of b_o agreed with the calculated ideal efficiency. In effect then, the experiment has been used to determine the value of f. For the 9 in. rotor, the maximum corrected efficiency occurs at an expansion ratio of 0.55, as does the ideal efficiency. The fact that the uncorrected efficiency has a maximum at an expansion ratio of 0.65 is undoubtedly a consequence of the work contribution to the uncorrected efficiency.

At each value of expansion ratio, the model best fitting the data, corrected with the adjusted value of f, is given in Table 5 (assuming a laminar friction factor). If no value is given for a coefficient, then that term has been dropped from the model. The values of f are also given in Table 5 and are in reasonable agreement with the values that fit Emmert's data. It will be seen that, for expansion ratios between 0.33 and 0.6, a single model can be fitted to the data, namely,

$$\eta = b_o + b_1\tau + b_2F + b_3G_p + b_4G_w + b_{11}\tau^2 + b_{12}\tau F. \quad (26)$$

The values of the coefficients b_i and b_{ii} at each expansion ratio are not very different from the averages over the six expansion ratios, which are also listed in Table 5 with their standard deviation. The fact that the coefficients do not change much with expansion ratio suggests that this formulation is reasonably correct. The model is slightly different for the higher expansion ratios, but the results, particularly for b_1 and b_2, are less reliable since the runs with $n = 3$ could not be made for $\epsilon = 0.75$ and 0.8 (and only partially for $\epsilon = 0.7$). However, higher pressure ratios are generated for expansion ratios below 0.6, so this is the region of greater interest.

Table 5 Values of the constants in Eq. (25)

Parameter	ε	0.33	0.4	0.45	0.5	0.55	0.6	0.65	0.7	0.75	0.8	Average, ε = 0.33–0.6	
												b_i	Standard deviation
	b_o	0.413	0.467	0.527	0.591	0.598	0.557	0.504	0.436	0.352	0.283	----	---
τ	b_1	–0.802	–0.892	–0.944	–1.123	–1.036	–0.811	–0.620	–0.402	–1.417	–1.856	–0.935	0.13
F	b_2	–1.132	–1.299	–1.456	–1.638	–1.639	–1.100	–1.167	–0.795	–1.067	–0.972	–1.377	0.24
G_p	b_3	–2.286	–2.985	–3.563	–4.278	–4.848	–5.262	–5.017	–8.026	–4.533	–4.290	–4.034	1.12
G_w	b_4	–0.914	–1.130	–1.271	–1.409	–1.282	–1.794	–1.656	–1.711	–1.785	–1.532	–1.351	0.30
τF	b_{12}	2.94	3.513	3.796	4.434	4.610	2.205	3.079	2.204	11.327	13.377	3.859	0.68
τ^2	b_{11}	0.545	0.543	0.502	0.610	0.317	0.578	----	----	----	----	0.516	0.10
G_p^2	b_{33}	----	----	----	----	----	----	----	5.235	----	----	----	---
	f	3.0	2.92	3.23	3.24	2.64	2.4	1.6	1.32	0.84	0.8	----	---

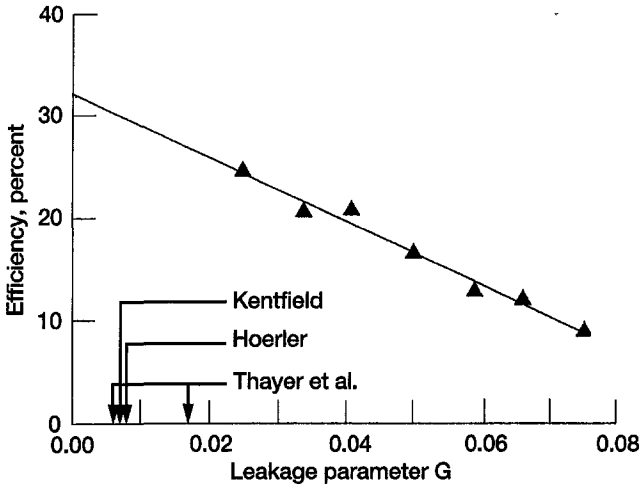

Fig. 8 Experimentally observed relative flow divider efficiency versus leakage parameter for the 9 in. rotor at an expansion ratio of 0.6

The model for expansion ratios less than 0.6, i.e., Eq. (26), is surprisingly simple. It shows that the efficiency decreases linearly with the end wall to rotor gap spacing. The linear relationship between relative efficiency and leakage parameter is confirmed in Fig. 8 showing relative efficiency versus leakage parameter for the 9 in. rotor. This result indicates that values of leakage parameter of 0.005 or less are desirable for good efficiency. From the values of b_3 and b_4, it is concluded that leakage is more sensitive to the port gap than to the wall gap. The model also shows that the smallest possible values of τ and F should be used. However, τ and F should not be minimized independently; in a more complete description of this work (Wilson, 1996) it has been shown that for optimum efficiency τ and F should be related via

$$F = 0.7\tau. \tag{27}$$

Conclusions

Operation of a three-port wave rotor has shown that at a constant value of $\beta = 0.37$ the maximum observed pressure ratio occurs at an expansion ratio of 0.55. The maximum corrected efficiency also occurs at an expansion ratio of 0.55. This expansion ratio is significantly higher than the lowest possible expansion ratio. The loss of efficiency in a wave rotor due to leakage has been demonstrated experimentally to be linear in the end wall to rotor gap spacing. Values of the leakage parameter $G = 2\delta/H$ less than 0.005 are required for good efficiency.

Analysis of the data has indicated that in addition to losses due to finite opening time, friction, and leakage, there are stagnation pressure losses dependent on angle of incidence of the entry flow, and also stagnation pressure gains caused by work input to the gas from the rotor. A simple empirical model was found to fit the dependence of the relative efficiency on opening time, friction, and leakage, from which it was predicted that maximum efficiency will be obtained by designing such that friction and opening time are minimized. A model of the incidence losses gave losses in reasonable agreement with limited prior data. The experiment showed that the incidence losses increase with the inlet Mach number. Incidence losses can be significant and must be taken into account in designing inlet ports.

Acknowledgments

The author is grateful to D. Paxson and G. Welch for many fruitful discussions. Special thanks go to C. Horn III, T. J. Doerberling, L. J. Bellisario, and P. Adams whose careful work in the laboratory made this work possible, to D. Fronek for taking care of all the details of instrumentation, and to H. Weaver for operational support.

References

Box, G. E. P., and Behnken, D. W., 1960, "Some New Three-Level Designs for the Study of Quantitative Variables," *Technometrics,* Vol. 2, pp. 455–75.

Emmert, H. D., 1950, "Current Design Practices for Gas-Turbine Power Elements," *Transactions of the ASME,* Vol. 72, pp. 189–200.

Foa, J. V., 1960, *Elements of Flight Propulsion,* John Wiley and Sons, New York, NY, pp. 161–166.

Fronek, D. L., Setter, R. N., Smalley, R. R., and Blumenthal, P. Z., 1987, "A Distributed Data Acquisition System for Aeronautics Test Facilities," NASA TM-88961.

Glassman, A. J., 1994, "Basic Turbine Concepts," chap. 2 of "*Turbine Design and Application,*" Glassman A. J., ed., NASA SP-290.

Glawe, G. E., and Krause, L. N., 1974, "Miniature Probes for Use in Gas Turbine Testing," NASA TM X-71638.

Hoerler, H. U., 1969, "Abschaetzung der Verluste in instationaer-gasdynamischen Kanaltrommel-Drucktauschern," Doctoral Dissertation Number 4402, Eidgenoessische Technische Hochschule, Zurich, Switzerland.

Jenny, E., and Zumstein, B., 1982, "Pressure Wave Supercharging of Passenger Car Diesel Engines," *CP C44/82,* The Institution of Mechanical Engineers, London, England, pp. 129–141.

Keller, J. J., 1984, "Some Fundamentals of the Supercharger Comprex®," in *Machinery for Direct Fluid-Fluid Energy Exchangers,* J. F. Sladky Jr., ed., ASME AD-07, pp. 47–54.

Kentfield, J. A. C., 1969, "The Performance of Pressure Exchange Dividers and Equalisers," *Journal of Basic Engineering,* pp. 361–370.

Kentfield, J. A. C., 1995, "On the Feasibility of Gas-Turbine Pressure-Gain Combustors," *International Journal of Turbo and Jet Engines,* Vol. 12, pp. 29–36.

Lieblein, S., 1965, "Experimental Flow in Two-Dimensional Cascades," chap. VI in *Aerodynamic Design of Axial-Flow Compressors,* I. A. Johnson, and R. O. Bullock, eds., NASA SP-36.

Mattingly, J. D., Heiser, W. H., and Daley, D. H., 1987, *Aircraft Engine Design,* AIAA Education Series, American Institute of Aeronautics and Astronautics, Washington, DC.

Meyer, A., 1947, "Recent Developments in Gas Turbines," *Mechanical Engineering,* Vol. 69, pp. 273–277.

Paxson, D. E., 1995, "Comparison Between Numerically Modeled and Experimentally Measured Wave-Rotor Loss Mechanisms," *Journal of Propulsion and Power,* Vol. 11, No. 5, pp. 908–914.

Peacock, N. J., and Sadler, J. H. R., 1992, "Advanced Propulsion Systems for Large Subsonic Transports," *Journal of Propulsion and Power,* Vol. 8, No. 3, pp. 703–708.

Pearson, R. D., 1985, "A Gas Wave-Turbine Engine Which developed 35 H.P. and Performed Over a 6:1 Speed Range," *Proceedings of the 1985 ONR/NAVAIR Wave Rotor Research and Technology Workshop,* R. P. Shreeve, and A. Mathur, eds., report NPS-67-85-008, Naval Postgraduate School, Monterey, CA, pp. 125–170.

Schlichting, H., 1979, *Boundary-Layer Theory,* McGraw-Hill Book Company, New York, NY, p. 637.

Seshadri, S., and Deming, S. N., 1990, *Interactive Computer Programs for Using Three- and Four-Factor Box-Behnken Designs in Research, Development, and Manufacturing,* Statistical Programs, Houston, TX.

Thayer, W. J., III, Taussig, R. T., Zumdieck, J. F., Vaidyanathan, T. S., and Christiansen, W. C., 1981, "Energy Exchanger Performance and Power Cycle Evaluation: Experiments and Analysis," final report by MSNW to DOE under Contract AC06-78ER01084.

Weatherston, R. C., Smith, W. E., Russo, A. L., and Marrone, P. V., 1959, "Gasdynamics of a Wave Superheater Facility for Hypersonic Research and Development," CAL Report No. AD-118-A-1.

Weber, H. E., 1995, *Shock Wave Engine Design,* John Wiley and Sons, Inc, New York, NY.

Welch, G. E., and Chima, R. V., 1993, "Two-Dimensional CFD Modeling of Wave Rotor Flow Dynamics," NASA TM-106261.

Wilson, J., and Paxson, D. E., 1996, "Optimization of Wave Rotors for Use as Gas Turbine Engine Topping Cycles," *Journal of Propulsion and Power,* Vol. 12, No. 4, July/Aug., pp. 778–785.

Wilson, J., 1996, "An Experiment on Losses in a 3-Port Wave Rotor," NASA CR-198508.

Zauner, E., Chyou, Y.-P., Walraven, F., and Althaus, R., 1993, "Gas Turbine Topping Stage based on Energy Exchangers: Process and Performance," ASME Paper ASME 93-GT-58.

Modeling Piston-Ring Dynamics, Blowby, and Ring-Twist Effects

T. Tian

L. B. Noordzij

V. W. Wong

J. B. Heywood

Sloan Automotive Laboratory,
Massachusetts Institute of Technology,
60 Vassar St.,
Bldg. 31-166,
Cambridge, MA 02139

A ring-dynamics and gas-flow model has been developed to study ring/groove contact, blowby, and the influence of ring static twist, keystone ring/groove configurations, and other piston and ring parameters. The model is developed for a ring pack with three rings. The dynamics of the top two rings and the gas pressures in the regions above the oil control ring are simulated. Distributions of oil film thickness and surface roughness on the groove and ring surfaces are assumed in the model to calculate the forces generated by the ring/groove contact. Ring static and dynamic twists are considered, as well as different keystone ring/groove configurations. Ring dynamics and gas flows are coupled in the formulation and an implicit scheme is implemented, enabling the model to resolve detailed events such as ring flutter. Studies on a spark ignition engine found that static twist or, more generally speaking, the relative angle between rings and their grooves, has great influence on ring/groove contact characteristics, ring stability, and blowby. Ring flutter is found to occur for the second ring with a negative static twist under normal operating conditions and for the top ring with a negative static twist under high-speed/low-load operating conditions. Studies on a diesel engine show that different keystone ring/groove configurations result in different twist behaviors of the ring that may affect the wear pattern of the keystone ring running surfaces.

Introduction

Engineers strive for better understanding of ring dynamics and gas flow to optimize the piston ring-pack in controlling engine oil consumption, oil degradation, engine blowby, piston/ring/liner wear, hydrocarbon emissions (HC), and friction. The trend of reducing the height of the crown land and the top ring width for reducing HC emissions increases the temperature in the top ring region. Thus, piston and ring engineers are greatly concerned with the adverse effects on oil stability and ring performance. Although increasing the tension of the oil control ring probably is the most effective way to control oil consumption (Jackson, 1996), unfortunately friction and wear are increased by doing so. Thus, a great deal of attention is focused on improving the design of the top two rings and neighboring parts on the piston to reduce oil consumption without sacrificing engine efficiency.

Various forces acting on the rings inevitably generates ring dynamic twist. Creating different static ring-twists is one of the major ways to control blowby, oil consumption, and wear (Rabute, 1995). The net force on the ring and the contact between the ring and the ring groove are altered greatly with different ring twist angles. As a result, ring stability, land gas pressure, and the wear of ring/groove and ring/liner may be changed.

There have been a number of ring dynamics and gas flow models developed for different purposes. In their work on the influence of ring twist on ring/liner lubrication, Ruddy et al. (1979a, b) addressed the importance of the contact point between rings and their grooves and found some interesting phenomena related to ring twist such as possible ring flutter if the contact point of the ring and its groove is at outside edge. However, in their work, gas flow was not included and a reacting force from the groove was calculated by assuming quasi-steady axial ring motion after the ring makes contact with the groove. For their HC emissions and blowby studies, Namazian and Heywood (1982) developed a ring-dynamics and gas-flow model with consideration of the gas flow through ring grooves. The ring twist effect was neglected in their work. Keribar et al. (1991) developed an integrated ring pack model. Physically based models for the forces between the rings and their grooves were used. The flow through the ring grooves was, however, simplified as an orifice flow. Of all the published theoretical work, ring flutter and the effects of ring/groove configurations on ring flutter have not been well documented.

The purpose of this work is to model the dynamics of the top two rings, gas flows, and the influence of the ring and piston design parameters such as ring static twist, piston tilt, inner and outer sealing types of keystone top rings and grooves, the chamfer and cutout of the piston and rings, and ring materials. Pressures generated by the squeezing of oil and asperity contact between the rings and their grooves are incorporated into the dynamic equations governing the axial and angular motion of the rings. Gas flows through the clearances between the rings and their grooves are modeled as a low-Reynolds-number flow in an inclined channel, along with the orifice flow through ring gaps. To preserve gas mass conservation, the mass of the gas stored between the rings and the grooves are also considered by using a simple displacement model developed in this work. With these considerations and the coupling of ring dynamics and gas flows, the model is able to resolve detailed events such as ring flutter when the inertia force is comparable to the gas pressure. The model output includes the following

- ring axial and angular positions
- gas pressures in different regions
- gas flow rates between adjacent regions and blowby
- asperity contact forces and moments
- centers and average pressures of the asperity contacts
- oil film thickness changes on the upper and lower surfaces of ring grooves
- hydrocarbon emissions from the piston crevice

By further incorporating the oil transport model on the piston lands, the present model can be used to study oil transport in the piston ring-pack.

Contributed by the Internal Combustion Engine Division and presented at the Fall Technical Conference of the ASME Internal Combustion Engine Division, Springfield, OH, October 20–23, 1996. Manuscript received by the ASME Headquarters December 2, 1997. Associate Technical Editor: D. Assanis.

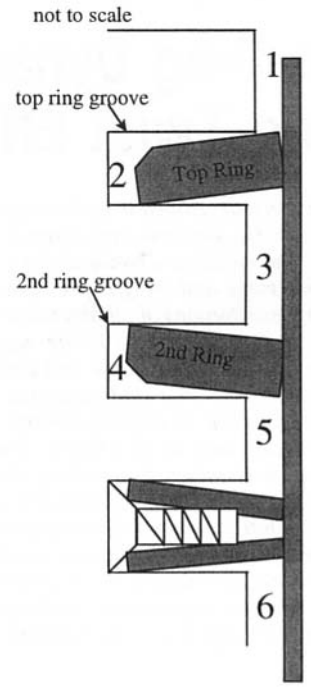

Fig. 1 Definition of different regions

Model Formulation

As shown in Fig. 1, regions 1–5 are used to denote different cavity regions. The gas pressures in these regions are assumed uniform. Gas pressure in region 1 is the given cylinder pressure. The gas pressures in regions 2–5 are modeled along with the twist angles and the axial positions of the centers of the gravity of the top two rings. The upper and lower surfaces of rings and grooves are all assumed to be flat with in the radial direction. The moment mentioned in this paper is the moment relative to the center of the gravity of a section of the ring.

For ring dynamics, forces, and moments on the rings from the following sources are considered:

- oil squeezing pressure between a ring and its groove
- asperity contact pressure between a ring and its groove
- gas pressure
- inertia due to piston acceleration/deceleration
- friction force on the ring running surfaces
- moment generated from the radial pressure on the ring running surfaces

The last two sources are obtained by using a ring-pack lubrication model (Tian et al., 1996).

Gas flows via the following paths are included in the model:

- ring gaps
- clearances between the rings and their grooves
- displacement of the gas stored between the rings and their grooves

Finally, ring motion and gas pressure are interrelated and they have to be solved simultaneously.

Oil Film Squeezing Between a Ring and Its Groove. As shown in Fig. 2, it is currently assumed that there is a uniformly distributed oil layer on the upper and lower surfaces of the piston grooves. It is intended that later with incorporation of an oil transport model in different ring-pack regions, this assumption will be relaxed as we will keep track of the distribution and quantities of the oil in different regions.

Reynolds equation is used to model the oil pressure between rings and their grooves:

Nomenclature

A_{gap} = downstream gap area
B = engine bore size
C_D = flow coefficient
$D_{O,i}$ = outer diameter of the ith ring, i = 1, 2
$D_{I,i}$ = inner diameter of the ith ring, i = 1, 2
E_i = elastic modulus of the ith ring, i = 1, 2
$F_{iner,i}$ = inertia force of the ith ring due to piston acceleration/deceleration, i = 1, 2
$F_{rl,i}$ = friction on the ith ring running surface between ring and liner
$I_{r,i}$ = moment of inertia of the ith ring, i = 1, 2
$M_{rl,i}$ = moment on ith ring from the radial pressure on the ring running surface, i = 1, 2
R = the gas constant
T = temperature
T_i = average temperature of region i, i = 1, 5
$T_{r,i}$ = torsional resistance of the ith ring, i = 1, 2
V_i = volume of region i, i = 1, 5
b_i = width of the ith ring, i = 1, 2
h = clearance between a ring and its groove
$h_0(t)$ = ring/groove clearance at ring CG
h_{oil} = oil film thickness on the grooves
$h_{r,i}$ = lift of the ith ring's center of gravity, i = 1, 2
$\dot{m}_{D,i,(i+1),i}$ = mass flow rate into the ring/groove clearance between region i and (i + 1) from region i, i = 1, 4
$\dot{m}_{D,i,(i+1),(i+1)}$ = mass flow rate into the ring/groove clearance between region i and (i + 1) from region (i + 1), i = 1, 4
$\dot{m}_{ij}$ = mass flow rate from region i to region j, i = 1, 5,
j = 2, 6
$m_{r,i}$ = mass of the ith ring, i = 1, 2
p_D = gas pressure of downstream
p_U = gas pressure of upstream
p_c = asperity contact pressure
p_i = gas pressure of region i, i = 1, 5
p_{oil} = pressure generated in the oil between a ring and its groove
$p^l_{gas,i}$ = gas pressure acting on the bottom (lower surface) of the ith ring, i = 1, 2
$p^l_{oil,i}$ = oil pressure acting on the bottom of the ith ring, i = 1, 2
$p^l_{asp,i}$ = asperity contact pressure acting on the bottom of the ith ring, i = 1, 2
$p^u_{gas,i}$ = gas pressure acting on the top (upper surface) of the ith ring, i = 1, 2
$p^u_{oil,i}$ = oil pressure acting on the top of the ith ring, i = 1, 2
$p^u_{asp,i}$ = asperity contact pressure acting on the top of the ith ring, i = 1, 2
α = ring and groove relative angle
$\alpha_{r,i}$ = twist angle of the ith ring, i = 1, 2
$\alpha_{0,j}$ = static twist angle of the ith ring, i = 1, 2
γ = ratio of specific heats
μ_{oil} = oil dynamic viscosity
μ_{gas} = gas dynamic viscosity
ρ_{gas} = gas density

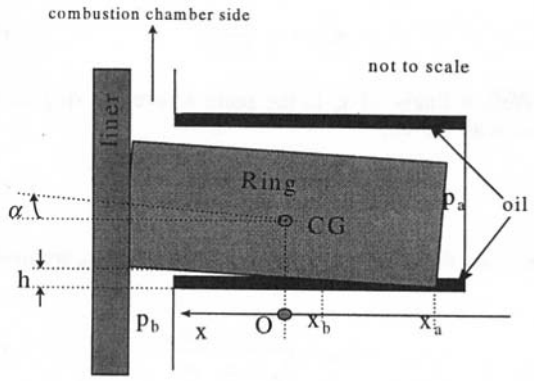

Fig. 2 Schematic of ring/oil contact

$$\frac{1}{12\mu_{\text{oil}}}\frac{d}{dx}\left(h^3\frac{dp_{\text{oil}}}{dx}\right)=\frac{\partial h}{\partial t} \tag{1}$$

with boundary condition

$$\begin{cases} p_{\text{oil}}(x_a)=p_a \\ p_{\text{oil}}(x_b)=p_b, \end{cases} \tag{2}$$

where x_a and x_b are the boundaries of the region where oil is filled between the ring and its groove, and the ring is approaching to the groove such that

$$\max\,[h(x_a,t),h(x_b,t)]\le h_{\text{oil}} \tag{3a}$$

and

$$\frac{\partial h}{\partial t}(x,t)\le 0 \quad \text{for} \quad x_a\le x\le x_b. \tag{3b}$$

For generality, notation p_a and p_b are used to represent the gas pressures of the regions defined in Fig. 1.

For the flat surfaces of the rings and the grooves considered in this model,

$$h(x,t)=h_0(t)+\alpha x \tag{4a}$$

and

$$\frac{\partial h}{\partial t}=\frac{\partial h_0}{dt}+x\frac{d\alpha}{dt}. \tag{4b}$$

Integrating (1) gives

$$\frac{dp_{\text{oil}}}{dx}=\frac{1}{h^3}\left\{12\mu_{\text{oil}}\left[\frac{dh_0}{dt}(x-x_a)+\frac{1}{2}\frac{d\alpha}{dt}(x^2-x_a^2)\right]+c_1\right\}, \tag{5}$$

c_1 is determined by integrating (5) and combining (2), as follows:

$$c_1=\frac{p_b-p_a-12\mu_{\text{oil}}\left(J_1\frac{dh_0}{dt}+\frac{1}{2}J_2\frac{d\alpha}{dt}\right)}{J_0}, \tag{6}$$

where

$$J_0=\int_{x_a}^{x_b}\frac{dx}{h^3}$$

$$J_1=\int_{x_a}^{x_b}\frac{(x-x_a)}{h^3}dx$$

$$J_2=\int_{x_a}^{x_b}\frac{(x^2-x_a^2)}{h^3}dx. \tag{7}$$

Integrating by parts, one obtains the axial force and the moment generated by the pressure from the oil:

$$F_{\text{oil}}=\int_{x_a}^{x_b}p_{\text{oil}}dx=p_b(x_b-x_a)-\int_{x_a}^{x_b}(x-x_a)\frac{dp_{\text{oil}}}{dx}dx \tag{8a}$$

$$M_{\text{oil}}=\int_{x_1}^{x_2}p_{\text{oil}}\,xdx \tag{8b}$$

$$=\frac{p_b(x_b^2-x_a^2)}{2}-\frac{1}{2}\int_{x_a}^{x_b}(x^2-x_a^2)\frac{dp_{\text{oil}}}{dx}dx.$$

In any other part of the region between a ring and its groove where either the ring is not in contact with the oil or the ring is moving away from the groove, the gas pressure is assumed to be the same as the gas pressure of the region (one of regions 1–5) that is connected to this part and the axial force and the moment can be easily estimated.

Asperity Contact Between Ring and Groove. Pressure generated from asperity contact between the rings and their grooves is modeled by using Greenwood and Tripp's theory (1971). For computation convenience, the fitting formula of Hu et al. (1993) is used for rough surfaces with Gaussian distribution assumed:

$$p_c=\begin{cases} 0 & h/\sigma>4 \\ K_c\left(4-\dfrac{h}{\sigma}\right)^z & h/\sigma<4, \end{cases} \tag{9}$$

where σ is the combined surface roughness, h is the nominal clearance between a ring and its groove, K_c is a parameter dependent on asperity and material properties of the rings and the piston, and z is a correlation constant as described by Hu et al. (1993).

Gas Flow Through the Clearance Between a Ring and its Groove. When the clearance between a ring and its groove is greater than the given oil film thickness, gas passes through the ring groove. Gas flow is approximated as locally parallel because of the small clearance (~100 μm), small Reynolds number (<1000), and small slope of the inclined channel between the rings and their grooves (~1°). Using the standard procedure in deriving Reynolds equation, we obtain the volume flow rate per unit length along the circumferential direction from region a to region b (Fig. 3):

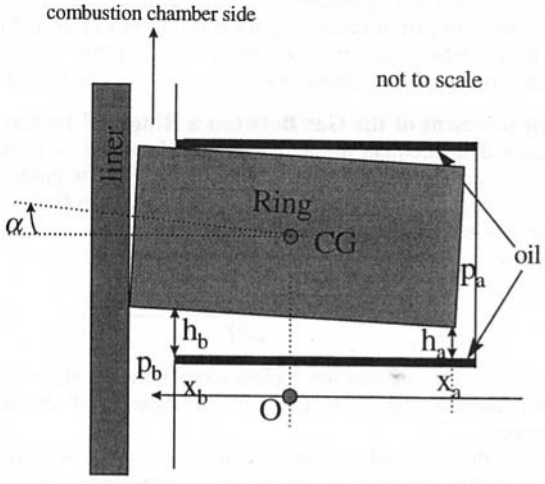

Fig. 3 Gas and gas flow between a ring and its groove

$$\dot{V}_{\text{gas}} = (p_a - p_b) \Big/ \left[12\mu_{\text{gas}} \int_{x_a}^{x_b} \frac{dx}{(h - h_{\text{oil}})^3} \right]. \quad (10)$$

Approximating the gas density as

$$\rho_{\text{gas}} = \frac{(p_a + p_b)}{2RT}, \quad (11)$$

we obtain the mass flow rate per unit length along the circumferential direction:

$$\dot{m}_{\text{gas}} = (p_a^2 - p_b^2) \Big/ \left[24\mu_{\text{gas}} RT \int_{x_a}^{x_b} \frac{dx}{(h - h_{\text{oil}})^3} \right], \quad (12)$$

where T is the piston temperature in the region considered, and gas viscosity is obtained by using $\mu_{\text{gas}} = 3.3 \times 10^{-7} \times T^{0.7}$. The units of temperature and viscosity are Kelvin and Pa-s, respectively.

Equation (12) is degenerated into Equation (9*b*) in the work of Namazian et al. (1982), if there is no angle between the ring and its groove.

Gas Flow Through a Ring Gap. Results of isentropic orifice flow are used for estimating the gas flow through ring gaps between adjacent piston land regions:

$$\dot{m}_{\text{gap}} = \frac{C_D A_{\text{gap}} p_U}{\sqrt{RT_U}} f_m, \quad (13a)$$

where

$$f_m = \begin{cases} \gamma^{1/2} \left(\dfrac{2}{\gamma + 1} \right)^{(\gamma+1)/2(\gamma-1)} & \text{if } \dfrac{p_D}{p_U} \le \left(\dfrac{2}{\gamma + 1} \right)^{\gamma/(\gamma-1)} \\ \left(\dfrac{p_D}{p_U} \right)^{1/\gamma} \left\{ \dfrac{2\gamma}{\gamma - 1} \left[1 - \left(\dfrac{p_D}{p_U} \right)^{(\gamma-1)/\gamma} \right] \right\}^{1/2} & \\ & \text{if } \dfrac{p_D}{p_U} > \left(\dfrac{2}{\gamma + 1} \right)^{\gamma/(\gamma-1)} \end{cases} \quad (13b)$$

and

$$C_D = 0.85 - 0.25 \left(\frac{p_D}{p_U} \right)^2. \quad (13c)$$

Equation (13*c*) is obtained by fitting the experimentally measured data (Shapiro, 1953).

Downstream and upstream may have different gap areas because different piston lands may have different radius and there may be chamfer and cutout on the piston. In this model, the gap area of the downstream side is used as A_{gap} in Eq. (13*a*).

Displacement of the Gas Between a Ring and Its Groove. A simple displacement model is developed to take into account the mass variation of the gas between a ring and its groove. As shown in Fig. 3, if h_a and h_b are both greater than 0, the mass of the gas stored between the ring and its groove is approximated as

$$m_{rg} = \frac{(p_a h_a + p_b h_b)(x_b - x_a)}{2RT}, \quad (14a)$$

where h_a and h_b are the local clearances between the ring and the oil layer on the groove at the boundaries of the region concerned.

If x_b is the point where the ring starts to contact with the oil, α is negative and this region is only connected to region a. Thus m_{rg} is represented as

$$m_{rg} = -\frac{p_a h_a^2}{2\alpha RT}. \quad (14b)$$

Correspondingly, if x_a is the point where the ring starts to contact with the oil,

$$m_{rg} = \frac{p_b h_b^2}{2\alpha RT}. \quad (14c)$$

The mass flow rates into this region at x_a and x_b are modeled as

$$\dot{m}_{Da} = \frac{h_a}{h_a + h_b} \frac{dm_{rg}}{dt} \quad (15a)$$

$$\dot{m}_{Db} = \frac{h_b}{h_a + h_b} \frac{dm_{rg}}{dt}, \quad (15b)$$

respectively.

Keystone Top Ring/Groove Configurations. Keystone type of top ring/groove configurations are considered in the model by making coordinate transformation. The angles of upper and lower surfaces of the top ring and its groove are all taken as independent variables so that various keystone ring/groove configurations can be studied. For keystone rings, there exists relative sliding between the ring and its groove when the ring is moving axially relative to its groove. Friction is thus generated. The contribution of this friction to ring dynamics is much smaller than the corresponding normal forces and thus is neglected in the current model.

Other Considerations. When the engine is in operation, the clearances between the piston lands and the liner may differ from those at cold condition due to thermal stress and the deformation from gas pressure. In addition, oil and oil deposit may be present in different regions. As a result, the volumes of different regions (1–5), ring gap areas, and the clearance between rings and their grooves may vary from the cold geometry. In addition, rings may not perfectly conform to the cylinder bore, and this may introduce another path for gas leakage. Provisions are made to include these in the model.

Gas flow rates into and out of the piston crevice are calculated. The hydrocarbon emissions from the piston crevice are then estimated according to the work of Cheng et al. (1993) and Hamrin et al. (1995).

Governing Equations. Based on mass conservation and Newton's second law, equations are formulated for p_2, p_3, p_4, p_5, $h_{r,1}$, $\alpha_{r,1}$, $h_{r,2}$, and $\alpha_{r,2}$:

$$\frac{V_2}{\pi BRT_2} \frac{dp_2}{dt} = \dot{m}_{12} - \dot{m}_{23} - \dot{m}_{D12,2} - \dot{m}_{D23,2} \quad (16a)$$

$$\frac{V_3}{\pi BRT_3} \frac{dp_3}{dt} = \dot{m}_{13} + \dot{m}_{23} - \dot{m}_{35} - \dot{m}_{34} - \dot{m}_{D23,3} - \dot{m}_{D34,3} \quad (16b)$$

$$\frac{V_4}{\pi BRT_4} \frac{dp_4}{dt} = \dot{m}_{34} - \dot{m}_{45} - \dot{m}_{D34,4} - \dot{m}_{D45,4} \quad (16c)$$

$$\frac{V_5}{\pi BRT_5} \frac{dp_5}{dt} = \dot{m}_{35} + \dot{m}_{45} - \dot{m}_{56} - \dot{m}_{D45,5} \quad (16d)$$

and

$$\frac{m_{r,i}}{\pi B} \frac{d^2 h_{r,i}}{dt^2} = \int p^l_{\text{gas},i} dx + \int p^l_{\text{oil},i} dx + \int p^l_{\text{asp},i} dx + F_{rl,i} - \int p^u_{\text{gas},i} dx - \int p^u_{\text{oil},i} dx - \int p^u_{\text{asp},i} dx + F_{\text{iner},i} \quad (16e)$$

$$\frac{I_{r,i}}{\pi B}\frac{d^2\alpha_{r,i}}{dt^2} = \int xp^{l}_{\text{gas},i}dx + \int xp^{l}_{\text{oil},i}dx + \int xp^{l}_{\text{asp},i}dx + \int xp^{u}_{\text{gas},i}dx + \int xp^{u}_{\text{oil},i}dx + \int xp^{u}_{\text{asp},i}dx + F_{rl,i}\,d_i + M_{rl,i} - T_{r,i}(\alpha_{r,i} - \alpha_{0,i}) \quad (16f)$$

for $i = 1, 2$, representing the top and second rings, respectively. The bounds of the integrals in Eqs. (16*e*) and (16*f*) are determined by the instantaneous positions and the moving directions of the rings. The torsional stiffness of a complete ring is used for $T_{r,i}$ (Ruddy et al., 1979*a*).

$$T_{r,i} = E_i b_i^3 \ln\left(\frac{D_{O,i}}{D_{I,i}}\right) \Big/ 3(D_{O,i} + D_{I,i}). \quad (17)$$

Computation Algorithm. New variables $\dot{h}_{r,i}$ and $\dot{\alpha}_{r,j}$ are introduced such that all equations are first order in time:

$$\dot{h}_{r,i} = \frac{dh_{r,j}}{dt}$$

$$\dot{\alpha}_{r,i} = \frac{d\alpha_{r,i}}{dt}. \quad (18)$$

The final set of 12 equations are highly stiff. Thus, first-order implicit scheme is adapted. Newton's iteration with a globally convergent algorithm (Press et al., 1992) is used. All the Jacobians are derived analytically to improve computation efficiency. The time step is 0.1 deg of crank angle. A relaxation scheme is used if the clearance between a ring and its groove at certain location becomes negative during the iteration. Typically, the running time is 1–2 minutes for one engine cycle on a Pentium 90 PC.

Sample Results for a Spark Ignition Engine

The model is applied to a production 2.0 liter four-cylinder gasoline engine. Extensive measurements of land pressures and oil film thickness have been conducted (Noordzij, 1996). Here, static twists of the top two rings are varied to study their effects on ring dynamics, gas flow, and the contact of the rings and their grooves for two engine operating conditions:

- case 1: 2000 rpm/WOT
- case 2: 4000 rpm/0 load

The value of 0.5 μm is used as the combined surface roughness of the rings and their grooves.

Case 1 (2000 rpm/WOT).

General Features of the Predictions of Positive Static-Twists on Top Two Rings. Figure 4 shows the predicted land pressures, relative lift of the centers of the gravity (CG), and the twist angles of the top two rings. Relatively large positive static-twist is used for the top two rings to illustrate the characteristics of the ring dynamics under positive static-twist. On the upper edge of the piston third land, there exists a cutout that increases the effective second-ring gap area. As a result, the second land pressure is relatively low. Calibration has been made by introducing thermal expansion on the piston land and ring gaps to match the measured land pressures and blowby.

The relative lift is defined as the ring axial lift normalized by the ring groove clearance. As seen in Fig. 4(*b*), the top ring (first ring in the graphs) lift and twist have different behaviors at different parts of the cycle. To better understand the behavior of the top ring lift, the forces and the moments on the top ring are plotted in Fig. 5, and the lifts at the outside and inside edges of the top ring are plotted in Fig. 6.

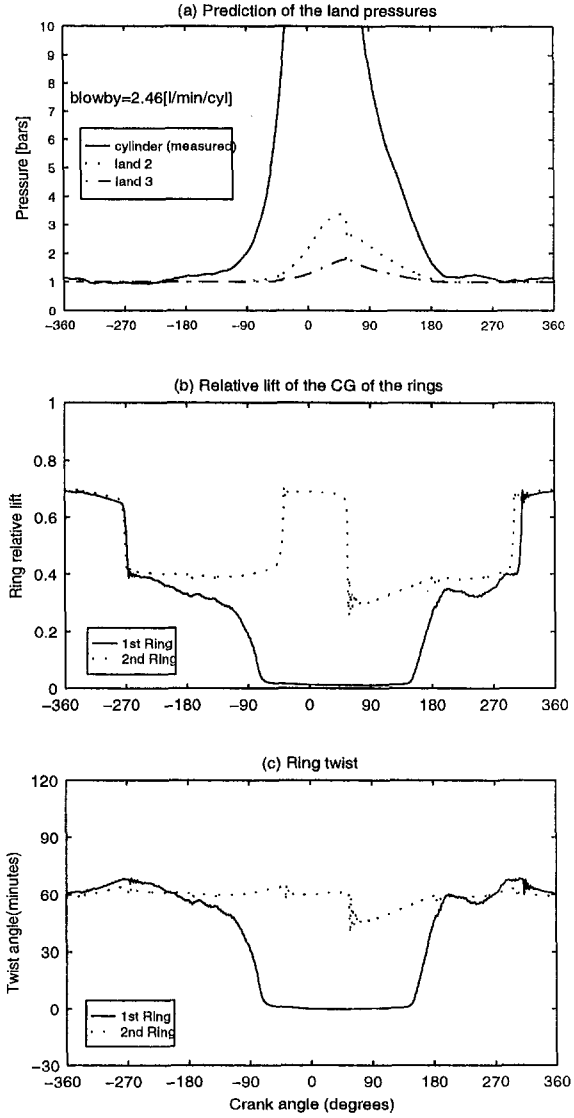

Fig. 4 Prediction of land pressures, ring lift, and twist angles; static twist: first ring 0.02 rad, second ring 0.02 rad

- At the first half of the intake stroke (−360 deg to approximately −270 deg) and late exhaust stroke (approximately 300 deg to 360 deg), the top ring is lifted primarily due to the upward inertia force. Because of the positive twist, the top ring and the upper groove have smallest clearance at the outside edge (Fig. 6(*a*)). The moments acting on the ring are not sufficient to twist the ring significantly during this period. Therefore, the CG of the top ring hangs in the middle of the groove.
- As the inertia switches direction at the middle of the intake stroke, the top ring moves to the bottom of the groove (−270 deg to −180 deg). Again, because of the positive twist, the inside edge of the top ring makes contact with the rough surface and the oil on the bottom of the groove.
- Then starting from around −180 deg, as the cylinder pressure increases, negative moment (anticlockwise in Fig. 2) is gradually generated from the forces on the bottom inside edge of the top ring (Fig. 5(*b*)). The top ring is thus bent anticlockwise and the twist angle is decreasing (Fig. 4(*c*)). Therefore, the CG of the top ring gets closer to the bottom of the groove (Fig. 4(*b*)). Then as the cylinder pressure keeps rising, the inside edge of the top ring is moving away from the bottom of the groove (Fig. 6(*a*). As a result, the

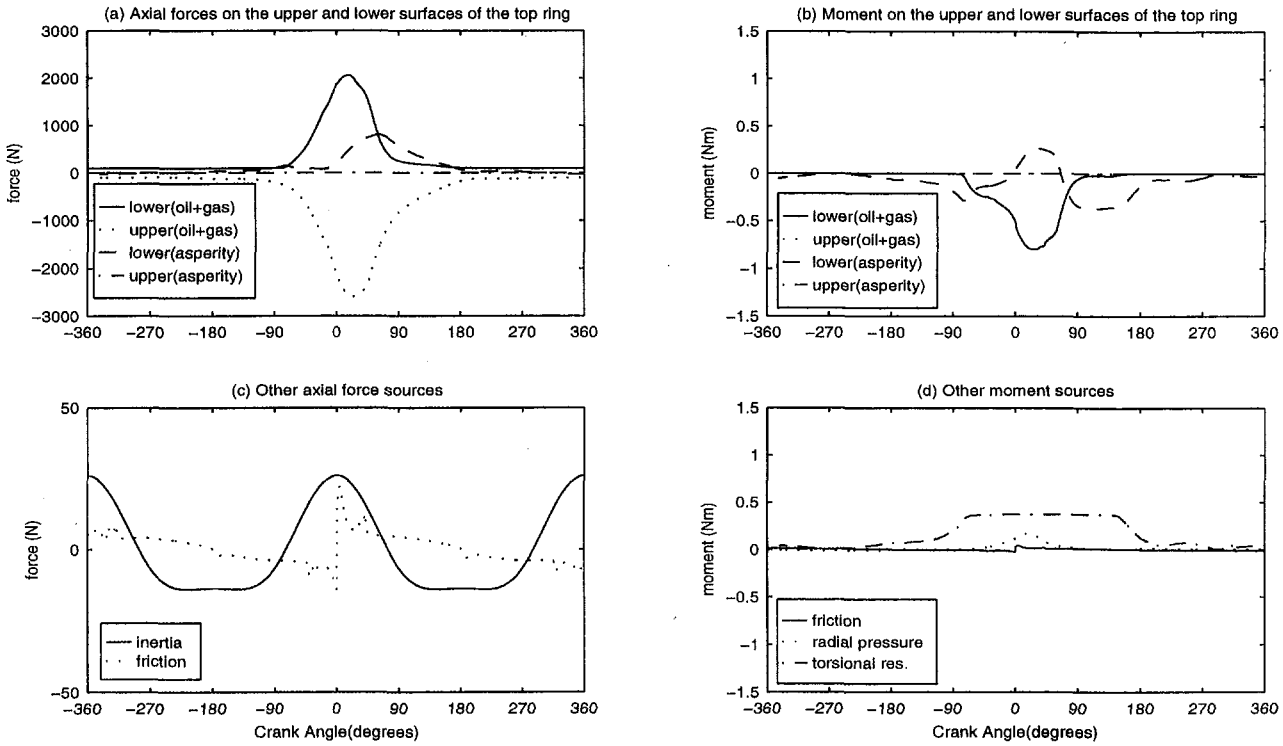

Fig. 5 Predicted force and moment on the top ring

gas with high pressure penetrates into the bottom of the ring and generates a negative moment (Fig. 5(*b*)). The ring twist angle continues to decrease until the cylinder pressure reaches its maximum. Then because of the rapid drop of the cylinder pressure and rise of the second land pressure, the total negative moment on the ring starts to decrease. As a result, the twist angle of the top ring increases due to the torsional resistance of the ring. The force and moment from the asperity contact reaches a maximum around 70 deg ATDC due to the reduction of the ring and groove clearance at the inside edge (Figs. 5(*a*) and 5(*b*)). Starting from around 300 deg ATDC, the top ring is lifted by the inertia force.

Figure 7 visually summarizes three typical positions of the top ring.

The behavior of the second ring is relatively simple for this static-twist value because the gas pressure is much less in the surrounding regions of the second ring.

The mass flow rates through different paths are plotted in Fig. 8. The mass flow rates through the top ring groove and into the piston crevice are basically related to the derivative of the cylinder pressure, and thus show some wiggles because the measured cylinder pressure is not perfectly smooth. The sharp peaks in Fig. 8(*b*) occurs when the second ring is in transition (Fig. 4(*b*)).

Effects of the Top Ring Static Twist on the Top Ring/Groove Contact. The top ring static twist is then varied to examine the twist effects. Top ring static twist is found to have negligible effects on gas flows under this operating condition, primarily because the inertia force is too small compared to the force from the gas pressure to affect the sealing function of the ring. However, the characteristics of the asperity contact between the top ring and its groove are significantly affected by the static twist. Figure 9 shows the center of the asperity contact and the average contact pressure on the bottom surface of the top ring

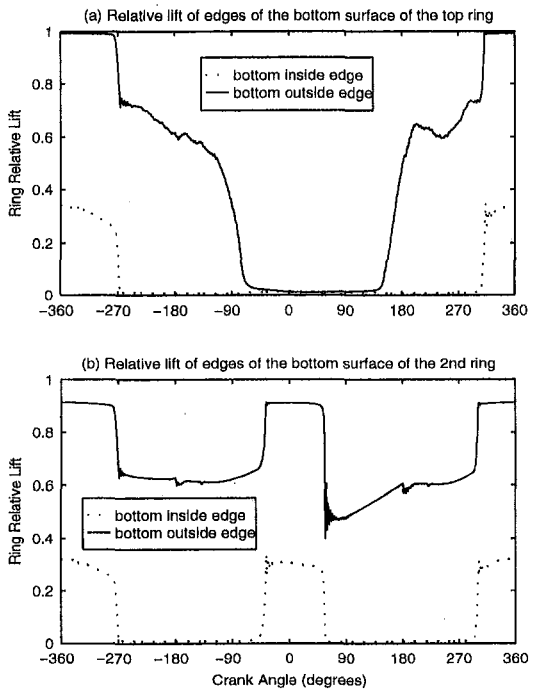

Fig. 6 The lift of the edges of the top two rings

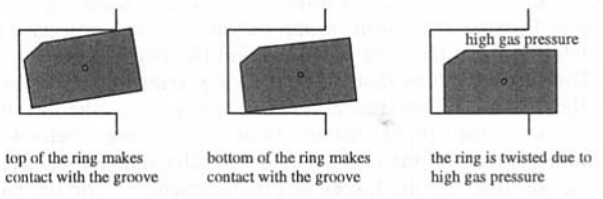

Fig. 7 Illustration of three typical positions of the top ring with a positive static twist

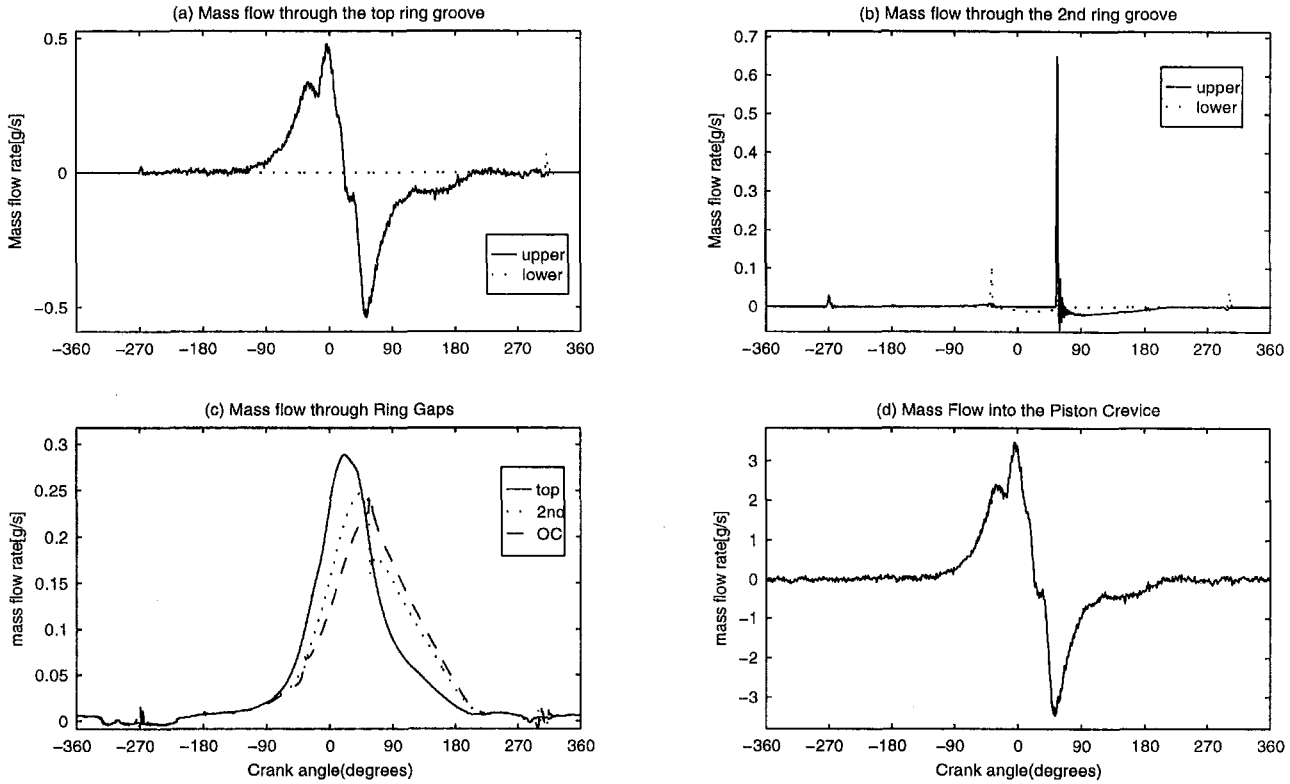

Fig. 8 Gas mass flow rate through different paths

for different static twists. The asperity contact center is defined as the ratio of the integrated moment from the asperity contact and the integrated axial force from the asperity contact. On the vertical axis of Fig. 9(*a*), zero corresponds to the location of the CG, and positive direction points to the outside edge and negative the inside edge. The contact center location is normalized by the ring radial depth. During certain periods, the center location has constant value 0, which means no asperity contact. The maximum static twist used is 0.03 rad. Under this static twist, the top ring can block the whole groove. Therefore, there is always asperity contact on the lower surface of the top ring. One can see that when the static twist is positive, the peak contact pressure increases with the increase of the static twist angle and the center of the contact location moves further to the outside edge with the decrease of the static twist during compression/expansion strokes. On the other hand, for zero or negative static twist, the center of the contact is always around the outside edge during the high cylinder-pressure period. Negative static twist results in more concentrated contact at the bottom outside edge of the top ring/groove, giving a peak average contact pressure greater than small positive static twist. The variation of the asperity contact behavior under different static ring twist may have indications on the ring/groove wear. Large ring static twist may cause more wear on the inside of the bottom surfaces and outside of the upper surfaces of the ring and its groove. As a result of the wear, the angle difference of the ring and its groove may be reduced. Ultimately, due to the nonuniformity of the static twist along the circumferential direction, some parts of the ring may behave like a negatively twisted ring, even for a ring initially having a positive static twist.

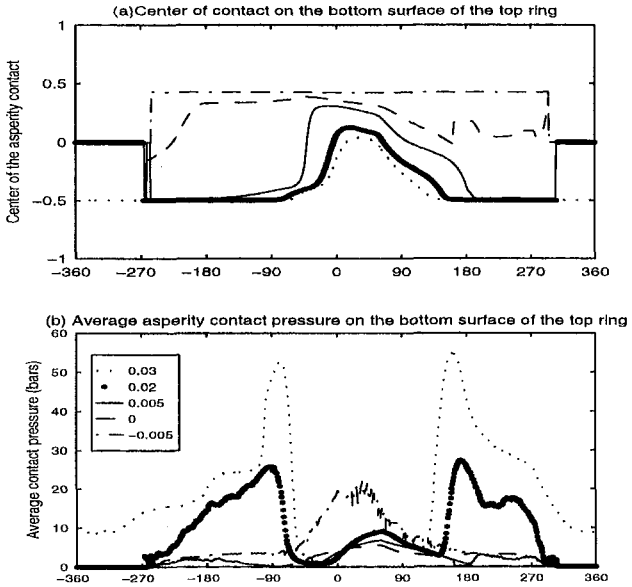

Fig. 9 Asperity contact center and average asperity contact pressure on the bottom surface of the top ring for different top ring twist. Numbers in the legend represent the values of the top ring static twists in radian.

Effects of the Second Ring Static Twist on Second Ring Stability and Blowby. Under this running condition, different static twists can dramatically change the stability of the second ring and the gas flows in the region related to the second ring.

If the second ring has a negative static twist, it flutters during the late compression and early expansion strokes as shown in Fig. 10. This flutter phenomenon for the ring with a negative static twist can be explained as follows:

- When the second ring is lifted, the ring makes contact with the upper groove surface at the inside edge. Therefore, most of the ring upper surface is exposed to the second land. The second land pressure is able to overcome the upward inertia force and pushes the ring downwards.
- As the ring moves downwards, the gas, driven by the pressure difference, penetrates into the region behind the second

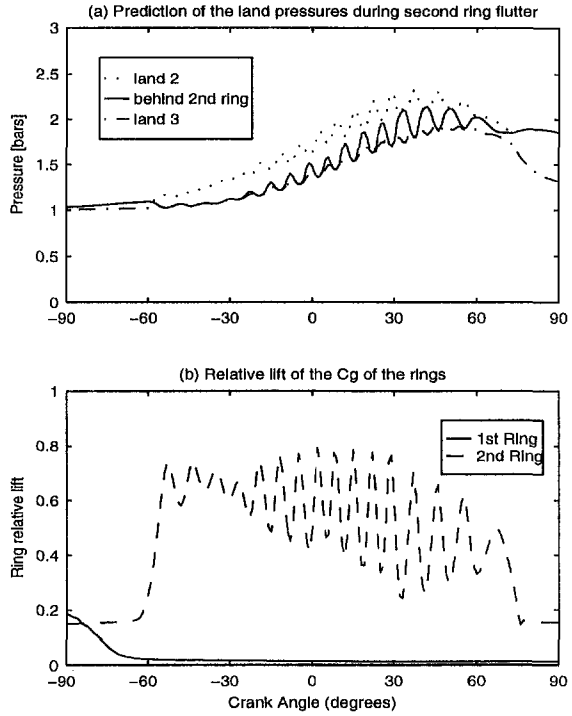

Fig. 10 Predicted second ring flutter for a negative static twist on the second ring (−0.01 rad)

ring and part of the gas goes further into the third land. As a result, the second land pressure is reduced and the pressures of the region behind the second ring and third land are increased. Because of the negative twist angle, most part of the bottom of the second ring is exposed to the raised gas pressure in the region behind the second ring. Thus, the net downward force from the gas pressure is reduced significantly and the inertia force regains the dominance. The ring is again lifted.

- The above sequence repeats until the upward inertia force reverses direction.

During second ring flutter, there is gas passing through the clearance between the second ring and its groove, which can be seen from the sharp peaks in Fig. 11. This second ring flutter may be beneficial for oil consumption, because the oil inside the second ring groove may be blown down to the third land during ring flutter. Furthermore, the blowby is not increased by the flutter under this operating condition, because for most of the period when there is high cylinder pressure, the gas flow through the top ring gap is choked flow. For choked flow, the flow rate through the top ring gap doesn't depend on the second land pressure. In addition, there is almost no reverse flow through the top ring gap, and, therefore, all the gas flowing into the second land goes to the crankcase blowby.

Studies also show that the second ring flutters even when the second ring has no static twist. This is because the increased second land pressure is able to create a negative twist on the second ring. On the other hand, if the static twist is great enough to block the whole groove, the flutter is no longer present because the second land pressure is not sufficiently high to bend the ring and to give a clearance allowing significant gas to pass through the ring groove.

The second ring flutter phenomenon was also observed from the experiment (Furuhama et al., 1979) for various operating conditions. Ring flutter can only occur when there is a right match between the inertia force and the gas pressure for the rings with nonpositive static twist or for the ring/groove configuration with a greater groove tilt angle than the static twist angle. The top ring never flutters under this operating condition, even if a negative twist is used because the force from the cylinder pressure is overwhelmingly higher than the inertia force. Nonetheless, positive static twist always stabilizes the ring when the upper land gas pressure is high, and the opposite applies to negative static twist, as shown in Fig. 12.

Case 2 (4000 rpm and 0 load)—Effects of Static Twists and Relative Ring/Groove Angles of the Top Two Rings on Ring Stability and Blowby. Engine tests show that under high-speed/low-load operating conditions, the blowby of spark ignition engines has a sudden rise at some point (Rabute, 1995) and achieves a value much greater than the full load conditions. The only possible explanation may be the presence of top ring flutter under these high-speed/low-load conditions. The model is applied to 4000 rpm/0 load condition with the cylinder pressure obtained from the measurement. Small top ring static twists are used in this case to demonstrate the sensitivity of the top ring stability.

A negative static twist is used for the top ring and the results are plotted in Fig. 13. The top ring flutters when the cylinder pressure is rising during the late compression and early expansion strokes. The blowby is much higher than the previous case with full load. The pressure behind the top ring is also shown in Fig. 13(*a*). The mass flow rates through the top and bottom clearances of the top ring groove between 90 deg BTDC and 90 deg ATDC are plotted in Fig. 14 to illustrate the failure of the top ring sealing during flutter. The mechanism for this top ring flutter is the same as the second ring flutter explained in the previous case. Compared to the previous case, the inertia force is four times higher and the cylinder pressure is much

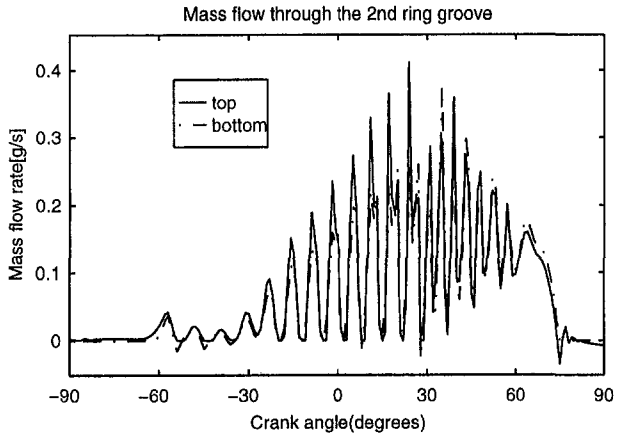

Fig. 11 Mass flow rates through the second ring groove during second ring flutter

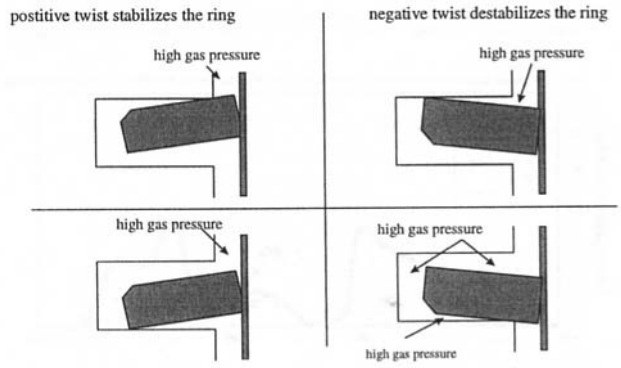

Fig. 12 Illustration of the influence of positive and negative twists on ring stability

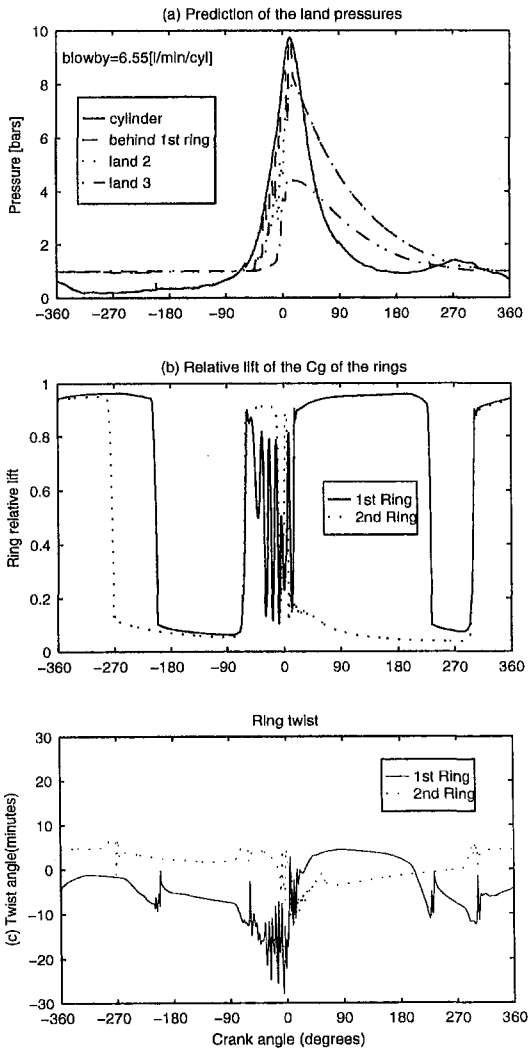

Fig. 13 Top ring flutter; top ring static twist: −0.003 rad, second ring static twist: 0.003 rad.

lower—resulting in top ring flutter. As can be clearly seen, during top ring flutter, gas passes through the clearance of the ring groove and the pressure behind the top ring is first brought up to the same value as the cylinder pressure when the ring is being pushed down. Then the bottom surface of the top ring is exposed to this raised pressure in the region behind the top ring

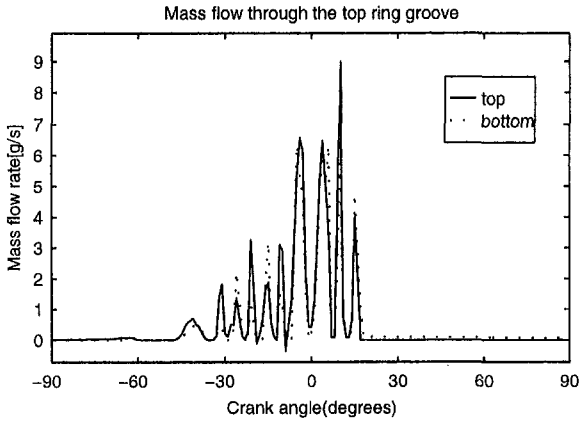

Fig. 14 Mass flow rates through the top ring groove during top ring flutter

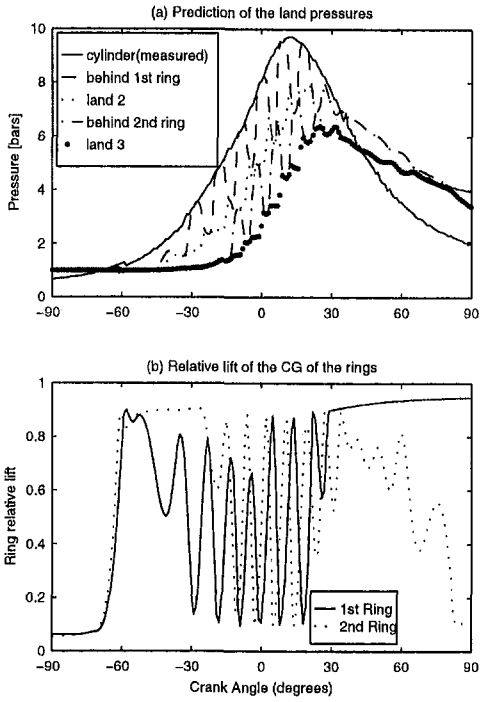

Fig. 15 Both top two rings flutter; static twist −0.003 rad is used for both top two rings. Blowby = 7.17 l/min/cyl.

because of the negative twist. As a result, the net downward force by gas pressure is reduced and the upward inertia lifts the ring. Meanwhile, high pressure gas is driven to the second land through the clearance between the top ring and its bottom groove, and further raises the second land pressure. This sequence goes on for several rounds until the cylinder pressure starts to drop.

Figure 15 shows the results of negative static twist on both the top and second rings. The second ring also flutters and the blowby is greater than if negative twist is only on the top ring. The top ring, however, can be stabilized with a small positive twist as shown in Fig. 16.

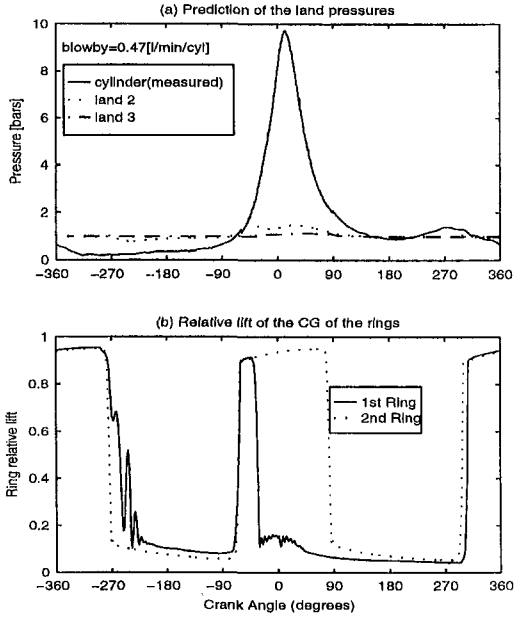

Fig. 16 No flutter for positive static twist; top ring static twist: 0.003 rad, second ring static twist: 0.003 rad.

As discussed in case 1, due to the nonuniformity of the ring static twist and the wear between the rings and the grooves under high-load conditions, the relative angle between the ring and its groove may make the ring behave as a negatively twisted ring at some part of the ring, and, thus, results in top ring flutter under high speed/low load operating conditions. In addition, the deformation from thermal and pressure stress can change the groove shape significantly (Ruddy et al., 1979b). The stability of the ring is essentially determined by the relative angle between the ring and its groove. To see this, a study is made by using a top ring with a positive static twist and the top ring groove tilted, simulating a worn groove shape. As seen in Fig. 17, the groove tilt angle is greater than the ring twist angle and this results in the same flutter behavior of the top ring as the one with a negatively twisted top ring.

Top ring flutter under high-speed/low-load operating conditions was also observed from experimental measurements (Furuhama et al., 1979). The land pressure measurement of the engine studied in the present work also implied top ring flutter under high-speed/low-load operating conditions. Several pressure transducers are installed on the cylinder bore at different liner locations (Noordzij, 1996). Snap shots of the land pressures are captured when the specific land passes by the location of the pressure transducers. Figure 18 shows the results of the measurement and the model prediction. A sudden rise of the second land pressure can be clearly seen from the measurement and the model prediction is able to match the measured land pressures from different probes.

Sample Results for a Diesel Engine—Effects of Different Keystone Top Ring/Groove Configurations

Keystone top ring/groove configurations are widely used in heavy duty diesel engines. Different angles between keystone rings and grooves may result in different wear patterns on the ring running surface and have significant impact on oil consumption (Mihara et al., 1995). Here, a simple study is made by using three different types of keystone ring/groove configurations, namely, inner sealing (16 deg groove angle/15 deg ring angle), flushed (both angles are 15 deg), and outer sealing (15 deg groove angle/16 deg ring angle). Symmetric ring and groove are assumed. The model is applied to a 2.2 liter single-cylinder diesel engine, and the running condition is 1200 rpm/full load. The predicted land pressures have negligible difference among these three configurations and thus only the results of inner sealing are shown in Fig. 19(a). However, the top ring twist behavior has significant differences among these configurations, as shown in Fig. 19(b). The inner sealing results in much greater twist than the other two configurations during the compression and expansion strokes. This twist behavior of the inner sealing configuration is because the ring and groove always make contact at the inside edge of the ring. When the cylinder pressure is higher, force generated at the bottom inside edge of the ring creates a negative moment, and the ring is thus twisted in the negative direction. When the second land pressure surpasses the cylinder pressure around 60 deg ATDC, the top ring is lifted and the force generated at the top outside edge of the ring creates a positive moment and the ring is thus twisted in the positive direction. For the other two configurations, the top ring has very small twist even when the gas pressures are high, because the contact between the ring and its groove is always at the outside edges when pressure differences among different regions are high. As a result, much less net force on the ring from the gas pressure is generated, as explained previously for the SI engine.

The twist behavior of the inner sealing configuration may result in more even wear on the ring running surface than the other two configurations and less oil transport to the top of the liner as indicated in (Mihara et al., 1995).

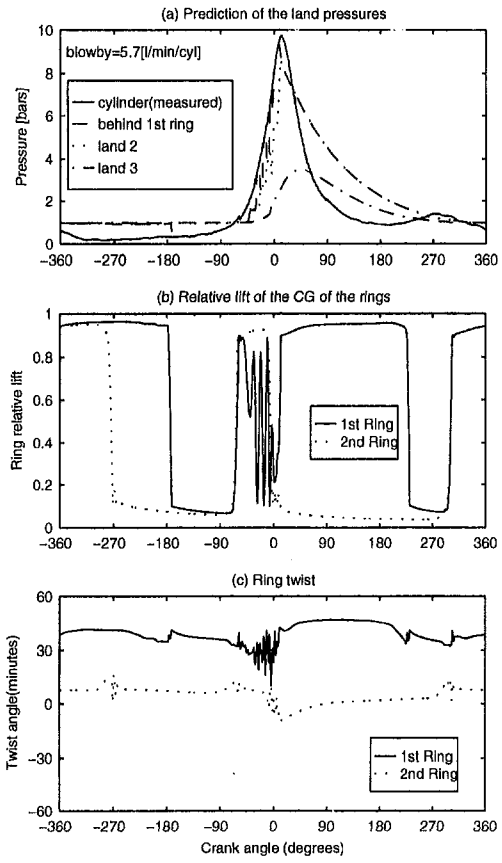

Fig. 17 Top ring flutter with groove tilt angle 0.012 rad and ring static twist 0.01 rad

Conclusions

A ring dynamics and gas flow model is developed, that includes the consideration of ring twist, keystone ring/groove configurations, and other typical ring/piston design parameters. The force between the rings and their grooves are simulated by assuming certain roughness and oil distribution on the rings and grooves. An implicit scheme is successfully implemented for the set of highly stiff system equations. The effects of the static twist are studied by applying the model to an SI engine and a simple study is conducted for different types of keystone ring/groove configurations.

Generally speaking, positive static twist stabilizes a ring when the land immediately above the ring has a higher gas pressure. However, severe asperity contact and wear may thus be generated. In reality, thermal stress and gas pressure inevitably deforms the ring groove, and the static twist is not uniform along the circumferential direction. As a result of all these effects, for some part of the ring, its groove may have greater angle than the static twist of the ring, and the stabilizing effects of the positive static twist may thus be erased.

Negative twist can generate ring flutter if the gas pressure and the inertia force are comparable in magnitude. A second ring with a negative static twist may always flutter during the late compression and early expansion strokes for typical SI engines. This second ring flutter does not increase blowby noticeably for the operating condition studied mainly because the flow though the top ring gap is choked flow when the cylinder pressure is high. The model predicts that the top ring with a negative static twist flutters under high-speed and low-load operating conditions and the blowby thus increases dramatically. Equivalently, it is also found that the top ring also flutters under high-speed/low-load operating conditions if the top ring groove has a greater angle than the top ring twist angle. In

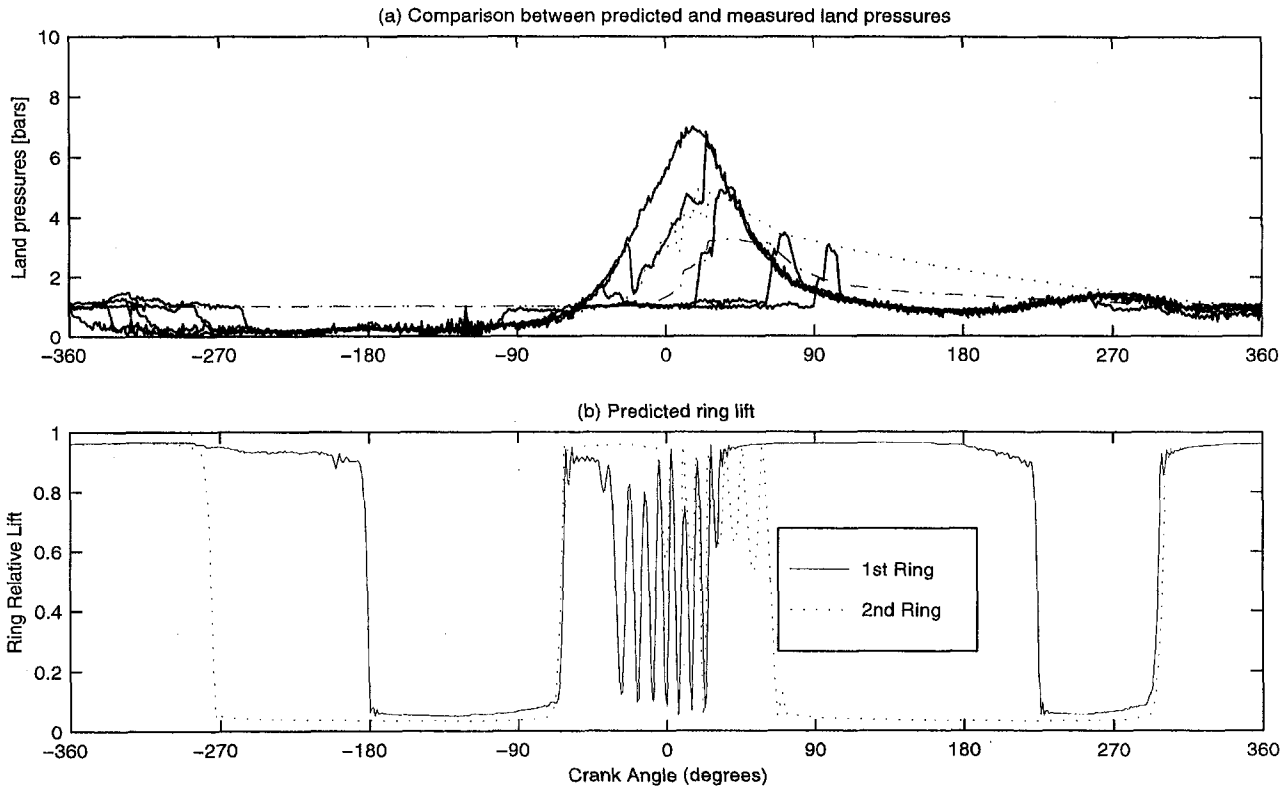

Fig. 18 Comparison with experiment measurement (4000 rpm). For (a) solid lines are measured cylinder pressure and pressures of 4 probes, dotted line is the predicted second land pressure and dot dashed line is the predicted third land pressure.

reality, the groove and ring surfaces may not be perfectly flat. However, the underlying physics of the effects of the ring twist, or more generally, the relative angle between the ring and its groove, is well demonstrated in the current model. Further studies combining the wear pattern of the rings and grooves can generate more insight into the characteristics of the contact and relative motion of the ring and its groove, and their influence on blowby and oil consumption.

The inner-sealing keystone ring/groove configuration can result in significant positive and negative ring twists depending the magnitudes of the cylinder and second land pressures. Because of this dynamic twist, different portions of the ring slide along the liner. As a result, the ring running surface may be more evenly worn than either the flushed or outer-sealing ring/groove configuration. Further investigations will be made for nonsymmetric ring/groove configurations in conjunction with engine tests.

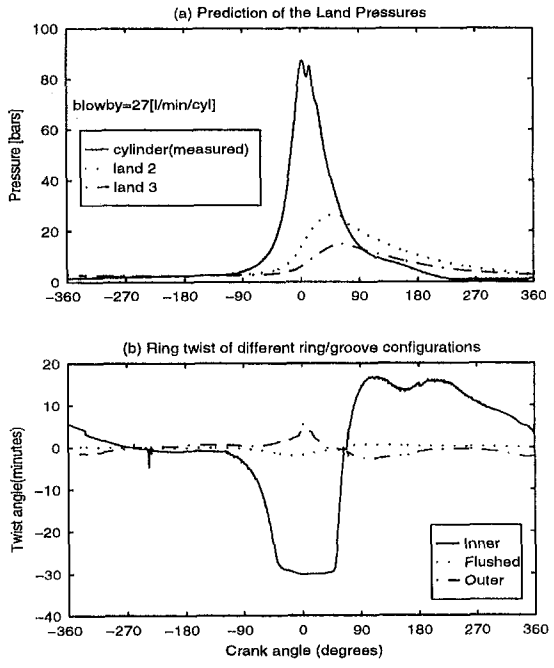

Fig. 19 Predicted land pressures and top ring twist for different keystone ring/groove configurations

Acknowledgments

This work is sponsored by the MIT Consortium on Lubrication in IC Engines. Current members include Dana Corporation, Shell, Renault SA, and Peugeot SA. The authors would like to thank Mr. Remi Rabute of Dana Perfect Circle Europe for his many suggestions throughout this work. The authors would also like to thank Dr. Ian Taylor of Shell for supplying the engine and pressure data for the keystone ring/groove study. The authors also appreciate the technical support and sponsorship from Mr. G. Desplanches and Dr. M. Maamouri of Renault in many related areas.

References

Cheng, W. K., Hamrin, D., Heywood, J. B., Hichgreb, S., Min, K., and Norris, M., 1993, "An Overview of Hydrocarbon Emissions Mechanisms in Spark-Ignition Engines," SAE Paper 932708.

Furuhama, S., Hiruma, M., and Tsuzita, M., 1979, "Piston Ring Motion and Its Influence on Engine Tribology," SAE Paper 790860.

Greenwood, J. A., and Tripp, J. H., 1971, "The Contact of Two Nominally Flat Surfaces," *Proc. Inst. Mech. Engrs.*, Vol. 185, p. 625.

Hamrin, D., and Heywood, J. B., 1995, "Modeling of Engine-Out Hydrocarbon Emissions for Prototype Production Engines," SAE Paper 950984.

Hu, Y., Cheng, H. S., Arai, T., Kobayashi, Y., and Aoyama, S., 1993, "Numerical Simulation of Piston Ring in Mixed Lubrication—A Nonaxisymmetrical Analysis," *ASME Journal of Tribology*, Vol. 116, pp. 470–478.

Jackson, M. A., 1996, "Assessment of a Sulfur Dioxide Based Diagnostic System in Characterizing Real Time Oil Consumption in a Diesel Engine," MS thesis, Department of Mechanical Engineering, MIT, Cambridge, MA.

Keribar, R., Dursunkaya, Z., and Flemming, M. F., 1991, "An Integrated Model of Ring Pack Performance," ASME JOURNAL OF ENGINEERING FOR GAS TURBINES AND POWER, Vol. 113, pp. 382–389.

Mihara, K., and Inoue, H., 1995, "Effect of Piston Top Ring Design on Oil Consumption," SAE 950937.

Namazian, M., and Heywood, J. B., 1982, "Flow in the Piston-Cylinder-Ring Crevices of a Spark-Ignition Engine: Effect on Hydrocarbon Emissions, Efficiency and Power," SAE 820088.

Noordzij, L. B., 1996, "Measurement and Analysis of Piston Inter-Ring Pressures and Oil Film Thickness and their Effects on Engine Oil Consumption," MS thesis, Department of Mechanical Engineering, MIT, Cambridge, MA.

Press, W. H., et al., 1992, *Numerical Recipe,* 2nd ed., Cambridge University Press, London and New York.

Rabute, R., 1995, "Ring Manufacturers' Perspective: Technical Issues of Interest and Comparison of Gas Flow, Oil Consumption model Results with Engine Measurements," internal report, Dana Perfect Circle Europe, 53, Boulevard Robespierre-BP1231 78301 Poissy Cedex, France.

Ruddy, B. L., Dowson, D., Economou, P. N., and Baker, A. J. S., 1979a, "Piston Ring Lubrication—Part III, The Influence of Ring Dynamics and Ring Twist," *Energy Conservation Through Fluid Film Lubrication Technology: Frontiers in Research and Design,* ASME Winter Meeting, ASME, NY, pp. 191–215.

Ruddy, B. L., Parsons, B., Dowson, D., and Economou, P. N., 1979b, "The Influence of Thermal Distortion and Wear of Piston Ring Grooves Upon the Lubrication of Piston Rings in Diesel Engines," *Proceedings of the 6th Leeds-Lyon Symposium on Tribology,* ASME, NY.

Shapiro, A. H., 1953, *The Dynamics and Thermodynamics of Compressible Fluid Flow, Vol. I,* The Ronald Press Company, New York.

Tian, T., Wong, V. W., and Heywood, J. B., 1996, "A Piston Ring-Pack Film Thickness and Friction Model for Multigrade Oils and Rough Surfaces," SAE Paper 962032.

Influence of the Exhaust System on Performance of a 4-Cylinder Supercharged Engine

F. Trenc

F. Bizjan

Department of Mechanical Engineering,
University of Ljubljana,
Ljubljana, Slovenia

A. Hribernik

Department of Mechanical Engineering,
University of Maribor,
Maribor, Slovenia

Twin entry radial turbines are mostly used to drive compressors of small and medium size 6-cylinder diesel engines where the available energy of the undisturbed exhaust pulses can be efficiently used to drive the turbine of a turbocharger. Three selected cylinders feed two separated manifold branches and two turbine inlets and prevent negative interaction of pressure waves and its influence on the scavenging process of the individual cylinders. In the case of a four-stroke, 4-cylinder engine, two selected cylinders, directed by the firing order, can be connected to one (of the two) separated manifold branches that feeds one turbine entry. Good utilization of the pressure pulse energy, together with typically longer periods of reduced exhaust flow can lead to good overall efficiency of the "two-pulse" system. Sometimes this system can be superior to the single manifold system with four cylinders connected to one single-entry turbine. The paper describes advantages and disadvantages of the above described exhaust systems applied to a turbocharged and aftercooled 4-cylinder Diesel engine. Comparisons supported by the analyses of the numerical and experimental results are also given in the presented paper.

Introduction

Two different systems are generally applied when turbocharging a 4-cylinder engine where the exhaust driven turbine and compressor is concerned. Exhaust gases can feed the turbine at nearly constant pressure; they are mixed in one common manifold before entering the turbine inlet scroll. Relatively constant mass-flow ensures good efficiency of the turbine. Mixing of the exhaust flow is unfortunately accompanied by substantial friction losses that in turn decrease the available kinetic energy of the exhaust pulses. As the result of the flow friction heat is generated, the exhaust temperature increases and less kinetic energy is available to raise the pressure.

Better utilization (conservation) of the kinetic energy of an exhaust pulse can be assured by a short and narrow exhaust pipe system where two pairs of engine cylinders, called a "two-pulse system," having particular exhaust periods shifted by 360 deg CA, are connected to two particular manifold branches and feed two separated turbine inlets. Negative interaction of the exhaust pulses of the neighbor cylinders is therefore minimized, and a better gas exchange process can be expected. Besides, a higher level of the pulse energy increases the overall efficiency of the turbocharger (TC). On the other hand, longer periods of lower exhaust mass flow in the separate turbine inlets (periods between the two consecutive pulses) reduce the above mentioned gain.

Watson et al. (1984) and Zinner (1980) described mechanisms that govern constant and mostly three-pulse systems (applied to 6-cylinder engines). A two-pulse system can be attractive for turbocharging of a 4-cylinder automotive or industrial diesel engine. The design of its exhaust manifold is more sophisticated, and has been less used in the past. Hribernik (1997) explained numerically and supported by experimental work the differences and features of constant and two-pulse assisted turbocharging with a 4-cylinder diesel engine. The results encouraged the authors of this paper to extend their research work and compare both exhaust systems throughout the engine operating range.

Boundary Conditions and the Results

Boundary Conditions and Experimental Set-up. A 4-cylinder, four-stroke, air-cooled, turbocharged and aftercooled 7.11 litre diesel engine was experimentally investigated. The engine was developed from an in-line, 6-cylinder turbocharged (TC) engine, optimized (combustion process, valve timing, etc.) for the industrial application; the best performance was expected at the engine peak torque running conditions. Original valve timing of the baseline 6-cylinder engine was applied also for the 4-cylinder engine. The 6-cylinder engine was equipped with a twin-entry turbine, and a three-pulse exhaust system (3 + 3 cylinders are feeding two separate exhaust manifold branches) was consequently applied for the turbocharger as the option generally used, according to Watson et al. (1984) and Zinner (1980). However, in the case of the 4-cylinder engine, the application of a single and twin-entry turbine was examined for better comparisons.

A one-dimensional computer program developed by Hribernik (1995) was used to determine and to explain flow and thermodynamic phenomena, especially during the gas exchange period of the engine. Two-pulse (applying a twin-entry turbine) as well as "constant pressure" (applying a single entry turbine) exhaust systems were compared, and are schematically presented in Fig. 1(*A*, *B*). The dividing wall between two separate manifold branches was removed for the "constant pressure" system, and four exhaust pulses could therefore be mixed before entering the turbine. The same compressor and turbine wheel and different size turbine housings were used for both systems to enhance better comparisons of the results. The turbine inlet scroll flow area is much larger for the two-pulse system application, since the turbine is partially admitted. The exhaust duration is 250 deg CA and is shifted by 360 deg CA for each cylinder connected to the same particular cylinder group (manifold branch): 1 + 4 and 2 + 3, respectively (Fig. 1(*A*)). No admission to the particular turbine entry takes place for approximately 110 deg CA, and the turbine swallowing capacity is not exploited in whole. Mass-flow of the exhaust gases is, on the other

Contributed by the Internal Combustion Engine Division and presented at the 19th Fall Technical Conference of the ASME Internal Combustion Engine Division. Manuscript received by the ASME Headquarters October 7, 1997. Associate Technical Editor: D. Assanis.

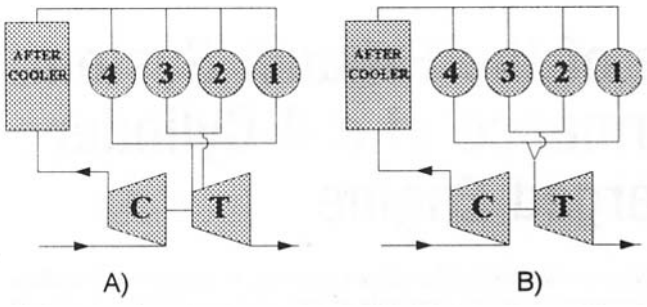

Fig. 1 Outline of two-pulse (*A*) and constant pressure (*B*) exhaust system

hand, equally distributed to the (single) turbine entry in the case of the "constant pressure" system with the common exhaust manifold, and the turbine swallowing capacity is fully exploited. Smaller capacity turbine housing is therefore required for the "constant pressure" system.

It must be pointed out that both charging systems were not individually optimized for the best engine performance due to the lack of suitable turbo equipment; the next step in the research work should be based on the comparisons between the two observed exhaust systems optimized individually for the best engine performance.

Numerical simulations and preliminary experiments have shown, that almost 68 percent larger turbine scroll capacity is required for the two-pulse system to transform the same amount of energy into the useful work of the compressor at the same engine rated output (Hribernik, 1997). Two available twin-entry turbine housings: one 30 cm^2 for the two-pulse and another 22 cm^2 for the "constant pressure" system were used for experimental comparisons to achieve the same boost-pressure rise in the compressor wheel at the same engine running conditions.

Figure 2 shows schematically a twin-inlet radial turbine of a TC. Unfortunately, boost-pressure rise is not affected only by the size of the turbine inlet system, but it is also influenced by the efficiency of the TC. Slightly higher compressor pressure ratios and, therefore, larger air mass-flows were obtained with the two-pulse system, and are a consequence of the higher overall efficiency of the TC with the larger turbine housing. Pressure-time histories in the cylinder, in the exhaust port, and at the turbine inlet section were measured and statistically analyzed by a fast computerized PI Meter. The PI meter is a digital measuring system, introduced by the COM A.G. (1987) for the real-time computation of the indicated mean pressure in the cylinder of an ICE, as well as for measurement and evaluation of a large sample of pressure diagrams at different locations of an engine. Over 500 measurements were taken into the account for better statistical representation of the particular measured results. Sev-

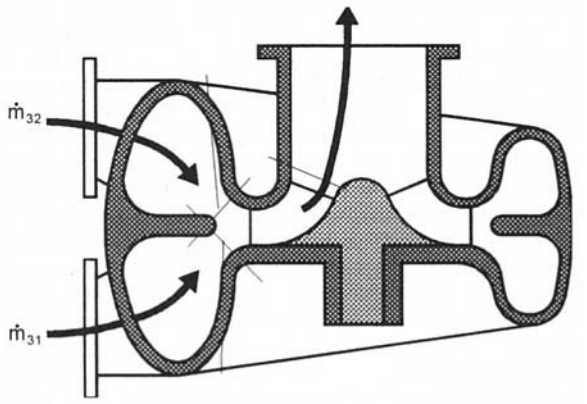

Fig. 2 Outline of a twin-entry radial turbine

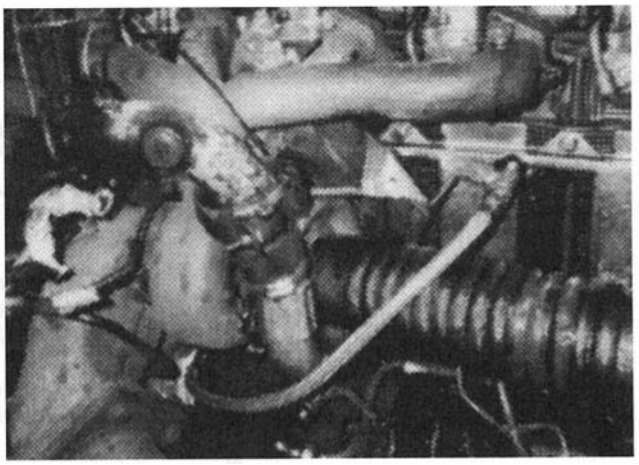

Fig. 3 Photograph of the engine with two-pulse exhaust manifold

eral static (wall) pressure probes and *K*-type thermocouples were used to determine inlet and outlet conditions in the cylinder, TC, and in the aftercooler. Mean indicated pressure of the total engine cycle and of the gas exchange period were simultaneously measured and analyzed. Very accurate laminar flow-meters were used to determine air mass-flow through the engine. The layout of the two-pulse exhaust manifold together with the TC and the engine can be seen on the photograph in Fig. 3.

Results of Numerical and Experimental Work and Discussion. As mentioned above, two different size turbine housings were applied to two different exhaust systems. The main aim was to obtain similar boost-pressures for both systems at the same engine running conditions. Figure 4 shows *A/F* ratio for the described systems: good agreement was obtained at lower

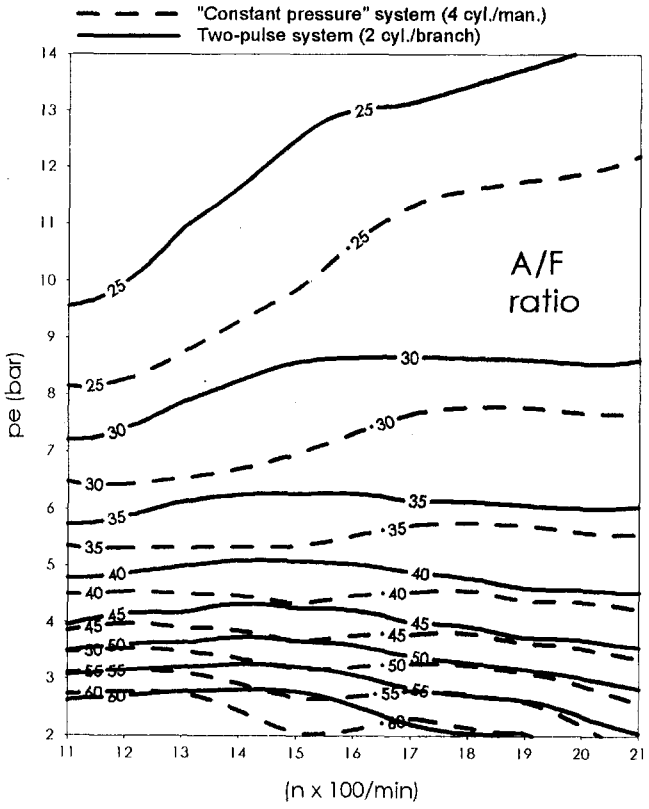

Fig. 4 Comparison of the *A/F* ratios for both exhaust systems

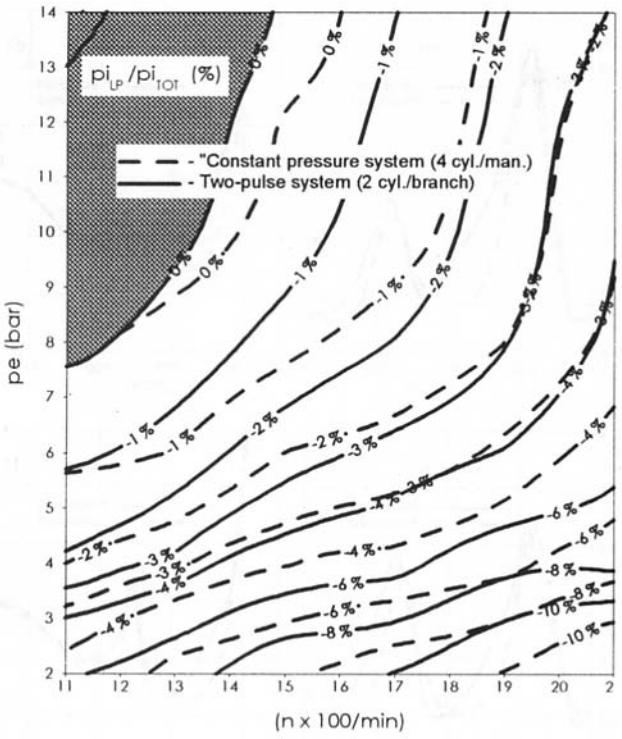

Fig. 5 Relative pumping losses for both exhaust systems

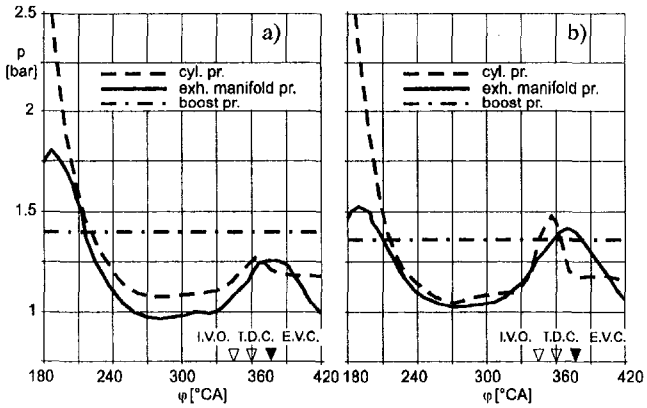

Fig. 6 Pressure history during the valve overlap period for (*a*) two-pulse and (*b*) "constant pressure" system (measurement)

engine loads; however, at higher engine loads the A/F ratio of the two-pulse system exceeded the value of the common manifold ("constant pressure") system by more than 10 percent.

The scavenging process of an engine is mostly affected by the interaction of the exhaust pulses from the exhaust system of the neighboring cylinders. The ratio of the mean indicated pressure (work), used to perform mass exchange within the cylinder ($p_{i,LP}$), versus mean indicated pressure of the total engine cycle ($p_{i,TOT}$) can be used to determine quantitatively the energy consumption for the gas exchange process in an engine. Work used by the mass exchange is generally negative; however, positive values can be expected by very efficient turbocharged engines. Comparison of the above mentioned ratio ($p_{i,LP}/p_{i,TOT}$) used for the evaluation of the gas exchange loop for both exhaust systems is given in Fig. 5. Positive values correspond to the indicated shaded area, and were obtained at lower engine speeds and higher loads for both exhaust systems. A more favorable gas exchange situation regarding pumping losses is generally obtained by the "constant pressure" system. The main reason for this is generally a better utilization of the turbine swallowing capacity, and, consequently, lower in-cylinder pressures (see curves – –, Fig. 6(*a*, *b*) during the exhaust interval with the "constant pressure" system. Therefore, the indicated negative pumping work is lower. On the other hand, the boost pressure is higher (see curves · –pd– · in Fig. 6(*a*, *b*) and the in-cylinder pressure during the exhaust interval is higher as well, when the two-pulse system is used. Higher amplitudes of the pressure pulses lead to better efficiency of the TC, especially at higher loads and lower engine speeds. As the result, relatively higher boost pressures (and in-cylinder pressures during the intake stroke) are obtained that reduce the pumping losses of the two-pulse system. These losses are therefore relatively low and comparable to those of the "constant pressure" system. Relative amplitudes of the pressure pulses are reduced at lower engine loads; TC efficiency is reduced as well, and the relative pumping work (losses) of the two-pulse system increases. At lower engine speeds, the total gain in better pumping capability of the engine with the "constant pressure" system is partially offset due to the reflected pressure waves during the valve overlap period.

We can learn more about the quality of the scavenging process from the in-cylinder measured pressure diagrams during the valve overlap period (from I.V.O. to E.V.C., Fig. 6). Results of measurements for both systems at peak torque conditions (upper left part of Fig. 5 are shown in Fig. 6(*a*) for the two-pulse system and (*b*) for the "constant pressure"—single manifold system. One big pressure pulse (from cylinder 1) is typical for the system (*a*) as well as the second and much lower pulse (displaced by 180 deg CA) that is generated by the exhaust of the cylinder 3 and is reflected from the turbine scroll; transmission of the pressure waves between two separated exhaust manifold branches is performed through the narrow gap of the dividing tongue in the twin-entry turbine housing (see also Fig. 2). The intensity of the reflected (transmitted) pressure pulse and its amplitude is therefore substantially reduced. Reverse flow of the exhaust gases back into the cylinder during the valve overlap period is governed by the pressure difference in the exhaust manifold and in the cylinder (Fig. 6(*a*)), curves ——, and ---), and is very low. There is no back-flow of the residual gases into the intake manifold. The scavenging process of the system (*b*) is affected by a much stronger reflected pressure wave. In this case all cylinders feed one single exhaust manifold, and the interferences between the neighbour cylinders are more intensive, as can be noticed from Fig. 6(*b*). Scavenging of the residual gases from the cylinder 1 is omitted during one third of the disposed time. Moreover, there is a reverse-flow of the exhaust gases into the intake manifold during the first part of the intake stroke. This negative interaction of the neighbor cylinders influences the engine operation especially at lower engine speeds, reported Hribernik (1997). The performance of the "constant pressure" scavenging system could be improved by (1) the change of the valve timing—reduction of the valve overlap period by shifting of the closure time of the exhaust valve and/or (2) by the change of the exhaust manifold geometry; longer manifold branches would delay the arrival of the pressure waves into the exhaust port during the valve overlap period, and (3) by the introduction of a pulse converter in the exhaust manifold.

The scavenging process can be observed quantitatively by comparing the air-delivery ratio Ψ of the engine with both exhaust systems. Ψ is defined by the ratio

$$\Psi = \frac{\dot{m}_{\text{air}}}{\dot{m}_{\text{air,th}}} = \frac{\dot{m}_{\text{air}}}{V_{sv,1} \cdot \rho_2' i_{\text{cyl}} \cdot \dfrac{n_{\text{eng}}}{120}} \qquad (1)$$

and, therefore,

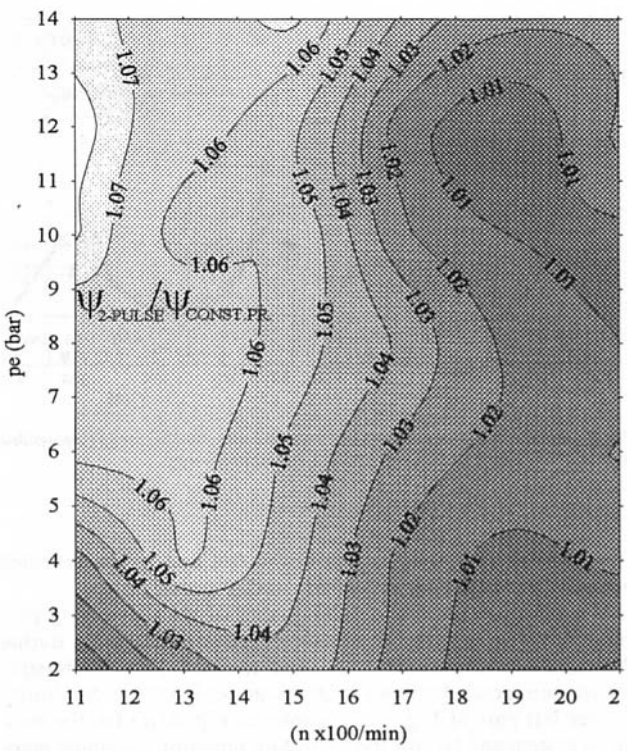

Fig. 7 Relative change of the air-delivery ratio for both exhaust systems

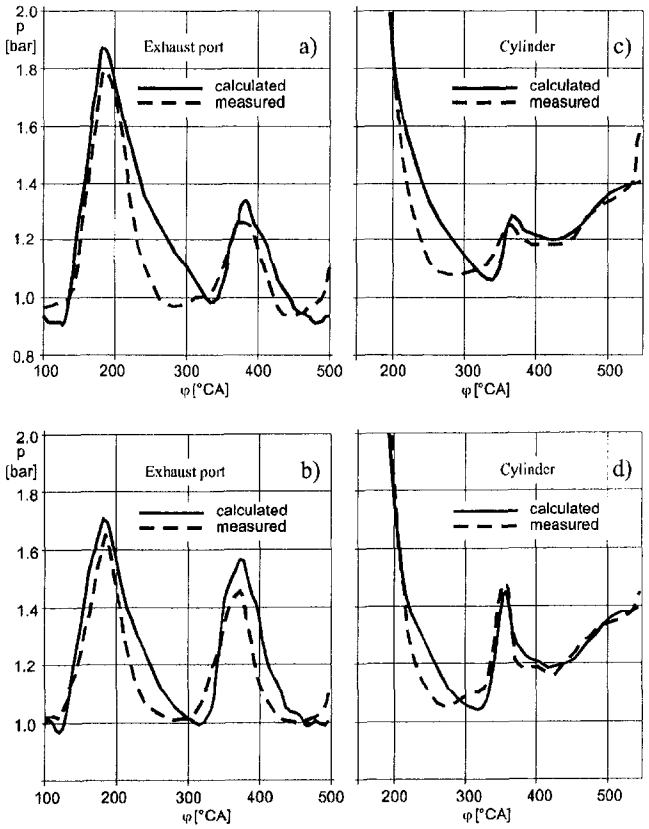

Fig. 8 Pressure diagrams for the following: (*a*) two-pulse system, exhaust port; (*b*) constant pressure system, exhaust port; (*c*) two-pulse system, cylinder; and (*d*) constant pressure system, cylinder

$$\frac{\Psi_{2\text{-pulse}}}{\Psi_{\text{const.pr}}} = \frac{\left(\frac{\dot{m}_{\text{air}}}{\rho_2'}\right)_{2\text{-pulse}}}{\left(\frac{\dot{m}_{\text{air}}}{\rho_2'}\right)_{\text{const.pr}}} = \frac{\dot{m}_{\text{air,2-pulse}}\rho'_{2\text{const.pr}}}{\dot{m}_{\text{airconst.pr}} \cdot \rho_{2,2\text{-pulse}}}, \qquad (2)$$

where $-\dot{m}_{\text{air}}$ is the total mass-flow of the air supplied from the compressor to the engine including the portion that escapes into the exhaust during the valve overlap, $-\dot{m}_{\text{air},th}$ is the theoretical mass-flow that would fill up the swept volume of the engine with the boost-air density at the aftercooler outlet conditions, n_{eng} is the engine speed (1/min), $-V_{sw,1}$ is the swept volume of particular engine cylinders, $-i_{\text{cyl}}$ number of the engine cylinders, $-\rho_2'$ is the boost air density at the aftercooler outlet conditions). The differences in the air-flow of the two systems (caused by a more efficient TC of the two-pulse system) are compensated in the Eq. (2) by the inversely proportioned densities of the boost air. The ratio $\Psi_{2\text{-pulse}}/\Psi_{\text{const.pr.}}$ therefore represents a quantitative measure of the gas exchange process, and may also be used for comparison and evaluation of the engine overall A/F ratio for both TC systems operating under similar conditions. It is not affected by the effectiveness of the turbocharging system as can be noticed from the Eq. (2). Particular Ψ values and their ratios were calculated from the measured engine data. Comparisons of different Ψ ratios indicate a certain excess of the air by the two-pulse system, Fig. 7. Excess air is pronounced at higher loads and lower engine speeds. Unfortunately, it is impossible to determine quantitatively the relative portions of the trapped combustion air and the escaped scavenging air, neither from the air-delivery ratio Ψ (Eq. 1), nor from the Ψ ratios (Eq. 2). More about the details of the scavenging process, especially during the valve overlap period, can be obtained by the analyses of the computed data. Measured and calculated pressure history data during the gas exchange process for both exhaust systems are presented in Fig. 8(*a*) for the two-pulse system in the exhaust port, 8(*b*) for the single manifold "constant pressure" system in the exhaust port, 8(*c*) for the two-pulse system in the cylinder, and 8(*d*) for the "constant pressure" system in the cylinder. Calculated flow velocity distribution in the intake and exhaust port during the valve overlap period for (*a*) two-pulse system, (*b*) "constant pressure" system and for the same engine operating conditions (as for Figs. 6, 7, and 8) are presented in Fig. 9. The two-pulse system is characterized by its good scavenging capability; only a short period of the reverse-gas flow (negative velocity towards the cylinder during the last sequence of the exhaust period) can be noticed, Fig. 9(*a*) (curve ---). The results of numerical investigations showed that 1 percent of the total air-flow through the engine escaped through the exhaust valve during the valve overlap period. On the other hand, there is no fresh charge from the intake manifold to the cylinder during the first half of the valve overlap period (Fig. 9(*b*)) (curve – – –) and a strong

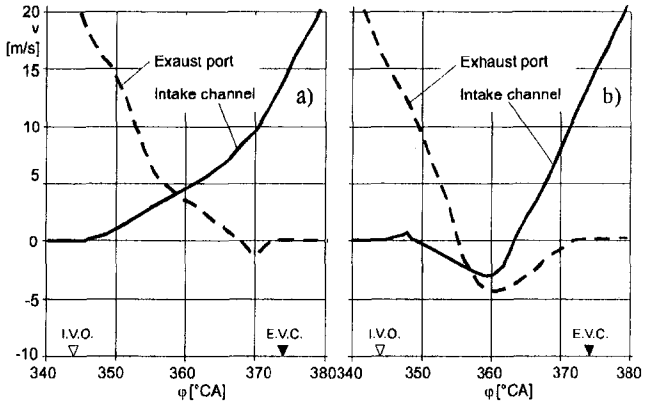

Fig. 9 Calculated pressure distribution in the exhaust and intake port

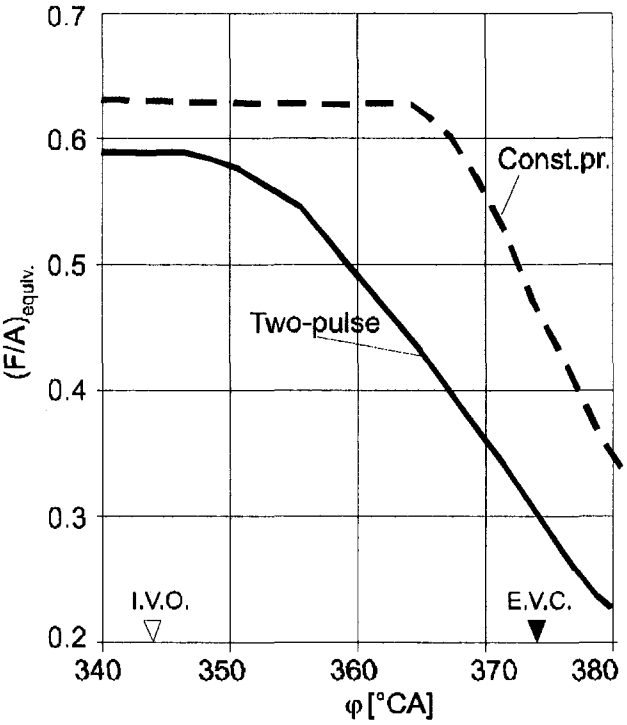

Fig. 10 Comparison of equivalent *F/A* ratio during valve overlap period (computed)

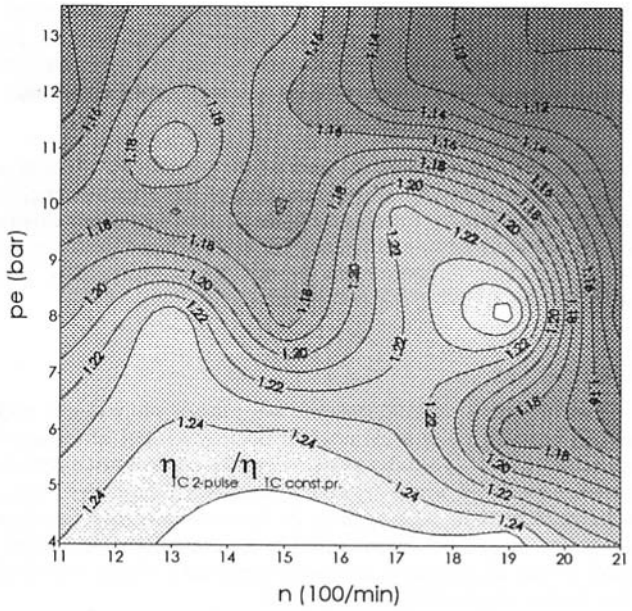

Fig. 11 Ratio of the overall; TC efficiencies for both exhaust systems (measurement)

reverse flow of the exhaust gases from the exhaust manifold can be observed during the valve overlap period, Fig. 9(*b*) (curve ---) for the "constant pressure" system. The difference in the effectiveness of these two scavenging processes can be characterized by the comparison of the equivalent fuel to air ratio during the valve overlap period and is presented in Fig. 10. Equivalent *F/A* ratio starts to decrease immediately after the intake valve opens and reaches the value 0.3 at the closure time of the exhaust valve in the case of the two-pulse system. Due to the reverse flow from the cylinder into the intake port no change of the *F/A* ratio occurs during almost $\frac{2}{3}$ of the valve overlap period when the "constant pressure" system is used. The equivalent *F/A* ratio is as high as 0.45 when the exhaust valve closes. The mass of the residual gases in the cylinder is 50 percent higher in the case of the "constant pressure" system in comparison with the two-pulse system. The already lower excess of fresh air is consequently reduced again, and this is reflected also through higher temperatures of the exhaust gases.

As mentioned at the beginning of this paragraph, the overall efficiency of the TC is higher in the case of the two-pulse system. Absolute values are 7 points higher in comparison with those of the "constant pressure" exhaust system. Figure 11 represents the comparison of the measured overall TC efficiencies for both observed exhaust systems. Relative advantage of the pulse system decreases with the increased boost pressure ratios (higher engine speed and load). Since the advantage (TC efficiency) of the two-pulse system is considerable (the ratio $\eta_{TC,2\text{-pulse}}/\eta_{TC,const.pr.} > 1.2$) some further explanations are necessary. The value 1.2 of the efficiency ratio from the Fig. 11 corresponds (assuming a realistic value of the $\eta_{TC} = 0.58$) to the reduction of the overall TC efficiency by 9 to 10 percent when the "constant pressure" system is observed. This reduction of the total TC efficiency is the consequence of the following:

1 Reduction of the turbine efficiency due to the application of a smaller capacity turbine housing for the "constant pressure" exhaust system. If a 30 cm^2 turbine housing is replaced by the 22 cm^2 housing (by the same exhaust configuration and the same engine running conditions) the turbine relative efficiency is reduced approximately by 5 to 10 percentage points for the same turbine rotor profile (P11 turbine performance data, 1985).

2 Due to lower boost compression ratios obtained by the "constant pressure" system, the engine full load swallowing characteristic was shifted out of the compressor best efficiency zone; 2 percent lower isentropic efficiencies were obtained in the case of the "constant pressure" system during the experiments.

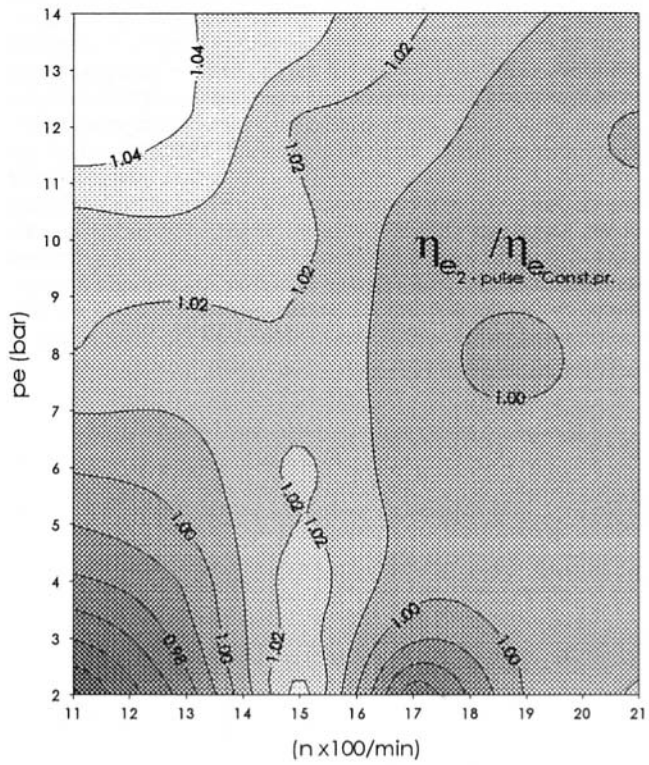

Fig. 12 Ratio of the effective engine efficiencies for both exhaust systems

3 The kinetic pulse energy of the exhaust gases is better preserved and more successfully converted into pressure in the case of the 3 and two-pulse exhaust systems, and an additional improvement of the turbine efficiency can be expected (Zinner, 1980; Watson et al. 1984).

Watson also reports, that the gain of the overall TC efficiency of 3–4 percent results in the reduction of the effective engine fuel consumption by 1 percent. Figure 12 represents comparison of the effective engine efficiency for both exhaust systems: up to a 4 percent improvement in the fuel consumption was achieved by applying the two-pulse system.

Conclusions

Two different exhaust systems were tested numerically and experimentally on a 4-cylinder turbocharged and aftercooled diesel engine. A two-pulse system consists of a split two branch exhaust manifold where two pairs of selected cylinders feed a relative large twin entry turbine. A "constant pressure" system is, on the other hand, represented by a common exhaust manifold, where all cylinders are connected into a single manifold and feed a single entry turbine scroll.

The two-pulse system is characterized, owing to its better utilization of the exhaust kinetic energy, by its remarkable overall efficiency of the turbocharger. Partial admission (periods of windage) does not affect too much the efficiency of the turbine. As the result of higher turbine efficiency (at almost the same compressor efficiency), the following advantages were noticed (especially at the engine peak torque operating conditions) (1) higher boost pressures and air-flows are obtained; (2) higher air to the exhaust gas pressure differences, determined through the turbo power balance (Zinner, 1980) ensure acceptable (low) pumping losses of the engine also for the two-pulse system; (3) lower exhaust temperatures (through higher A/F ratios); and (4) better engine fuel consumption can be noticed (especially at the engine peak torque operating conditions).

The smaller turbine housing of the constant pressure system is basically connected with lower turbine efficiency that in turn reduces the overall efficiency of the turbocharger. An improvement of the engine scavenging capability (higher volumetric efficiency and lower fraction of the trapped residual gases) and overall engine efficiency could be expected also at lower engine speeds, if the valve timing were changed and if longer cylinder-to-cylinder manifold pipes were applied. Disturbances of the reflected pressure waves and their negative effect on the cylinder scavenging could thus be reduced. It was stated at the beginning of the paper that neither the turbocharger components nor the exhaust systems used and presented in this study were optimized for the best engine performance. Therefore, there might be some limitations in the performed comparisons and conclusions. Further research work will be concentrated on the comparison of the performance data of the optimized engine with both exhaust systems. Nevertheless, we can already conclude that the two-pulse system, with its larger and more efficient turbine, leads to a better scavenging capability of a 4-cylinder engine (especially at lower engine speeds and larger loads). The advantage of the two-pulse system, i.e., a better utilization of the exhaust energy diminishes as the engine speed and the boost pressure increase since it is offset by a larger pumping work required for the gas exchange. Advantage of different types of the pulse systems (better utilization of the pulse energy in the turbine) also decreases as the boost pressure ratios increase since the relative size of the pressure amplitude (its dynamic component) decreases.

The results have shown some of the following additional advantages and disadvantages of both exhaust systems and the way they influence characteristics of a 4-cylinder diesel engine:

Two pulse system	Constant pressure system
Very good overall TC efficiency	Good overall TC efficiency
Moderate engine pumping losses	Lower engine pumping losses
Lower negative interaction between neighboring cylinders	Moderate negative interaction between neighboring cylinders
Very good scavenging during the valve overlap period at lower engine speeds and higher loads	Good scavenging during the valve overlap period—better at higher engine speeds and lower loads
Higher combustion A/F ratio, lower exhaust temperatures, higher air delivery ratio and engine efficiency especially at lower speeds and higher engine loads	Lower combustion A/F ratio, higher exhaust temperatures, more residual gases, lower engine efficiency (especially at lower speeds and higher engine loads)
More sophisticated design of the exhaust manifold	Simple design of the exhaust manifold
Larger, more efficient turbine—better base for the variable geometry (VG) turbocharger	Smaller TC—better engine acceleration capability

References

Hribernik, A., 1995, "Comparison of Zero and One-Dimensional Methods for Simulation of the Process in Turbocharged Diesel Engines," *SV-Journal of Mechanical Engineering,* Vol. 41, No. 7–8, Ljubljana, Slovenia, ISSN 0039-2480, pp. 229–238.

Hribernik, A., 1997, "Comparison of Performances of a 4-Cylinder Supercharged Diesel Engine with Single or Twin Entry Turbine," *SV-Journal of Mechanical Engineering,* Vol. 43, No. 9–10, Ljubljana, Slovenia, ISSN 0039-2480, pp. 373–382.

PII turbine performance data, 1985, HOLSET, Engineering Co., Ltd., Huddersfield, UK.

PI Meter, User Manual, COM G.m.b.H., Graz, Austria.

Watson, N., Janota, M. S., 1984, *Turbocharging the Internal Combustion Engine,* Macmillan Publishers Ltd., London.

Zinner, K., 1980, *Aufladung von Verbrennungsmotoren,* Springer-Verlag, Berlin, ISBN 3-540-10088-1.

Use of an Expert System to Study the Effect of Steam Parameters on the Size and Configuration of Circulating Fluidized Bed Boilers

L. LaFanechere
Electricité de France,
D.E./S.E.P.T.E.N.,
Villeurbanne, France

P. Basu
Technical University of Nova Scotia,[1]
Halifax, Nova Scotia
Canada

L. Jestin
Electricité de France,
D.E./S.E.P.T.E.N.,
Villeurbanne, France

CFBCAD©, an Expert system developed jointly by the authors, is used to investigate into the effect of steam parameters on the size and configuration of circulating fluidized bed (CFB) boilers. Resulting data would assist designers and users to appreciate the influence of steam cycle parameters on the overall design of CFB boilers. The paper studies the effect of different steam cycles ranging from small capacity, low pressure boilers without reheat, to large capacity, high pressure reheat boilers. The drum pressure exerts an important influence on the area as well as the configuration of heating surfaces. The temperature difference between the flue gas and the feed water inlet temperature has an optimum value for minimum heat transfer surface requirement.

Introduction

Several hundred circulating fluidized bed (CFB) boilers are in use world wide. The fuel flexibility and environment-friendly features make such boilers very attractive to users, especially those faced with rigid environmental regulations and/or a low-grade fuel. The technology is relatively new, and the number of years of operating experience logged is limited. Yet, most companies consider this technology at least once during the process of selection of the appropriate combustion technology for their specific plants.

In conventional pulverized fuel fired boilers, the arrangement of different heating elements (economizers, evaporators, etc.) of a boiler depends on steam as well as on heat transfer conditions. This dependence is well documented (Stultz and Kitto, 1992). However, none of the above information is available for fluidized bed boilers.

Conventional procedure-based design methods cannot handle design issues involved in the emerging technology of CFB boilers. A great deal of manual intervention is required to address the design issues. An expert system, based on both rules and procedures, can perform this task efficiently. So, a detailed research into design methodologies of different components and critical studies into the performance of commercially operating CFB boilers was carried out, and an Expert system, CFBCAD©, was developed through a cooperative effort of the Electricite d de France, Greenfield Research Inc., and the Technical University of Nova Scotia. A full discussion of the expert system, CFBCAD©, is beyond the scope of the present paper. While the full details may be available from Greenfield Research Inc. (CFBCAD—An Expert System, 1996), a limited discussion of the design constraints will be included here.

Design of CFB Boilers

The disposition of heating surfaces of a boiler is carefully thought out to make the most economic use of heating surfaces. For example, a counter flow heat exchanger maximizes the temperature difference between steam (or water) and flue gas; thereby minimizing the heat transfer surface requirement. However, in some cases the strength constraints of tube metals may override the boiler configuration arrived at from surface minimization. When water or slightly superheated steam flows through the tube, its metal temperature is closer to that of the fluid, but when the tube carries a highly superheated steam, its metal temperature would be closer to that of the flue gas. The metal temperature, much in excess of an already sufficiently hot steam, requires the use of expensive alloys. To offset the cost of special alloys, which are several times more expensive than conventional metals, designers locate the final stage of superheaters in a relatively cooler zone at the top of the back-pass, while accepting a lower temperature difference, and, consequently, a larger surface area. Thus, arrangements of heating elements are governed by local temperature and heat transfer conditions as well as economic considerations. The present work attempts to find optimum surface dispositions for different steam parameters in CFB boilers. It will analyze influence of steam parameters on the surface configuration and try to identify any trend if it exists.

The thermal design of a CFB boiler is very complex, due to several areas of uncertainty and steps involving decisions. This makes the use of conventional algorithm types of computer code difficult. Also, owing to the innovative nature of the human, a designer finds it very difficult to apply his decision making skill and experience consistently in identical ways to a large number of designs. For the present research, it is very important to apply design judgments uniformly because our attempt is to study the effect of individual parameters while keeping everything else constant. Situations like this can be best handled by an artificial intelligence based tool like an expert system. This powerful tool allows the application of decision making logic and experience of old plants and handling of conflicting design considerations in an uniform and consistent manner.

In view of the above requirement, a commercial expert system like CFBCAD© for thermal design of CFB boilers was used. For a given feed stock specification steam parameter and environmental stipulation, CFBCAD© develops the optimum size and configuration of a CFB boiler following a default or

Contributed by the Power Division and presented at the 13th International Conference on Fluidized Bed Combustion, May 7–10, 1995, Orlando, FL. Manuscript received by the ASME Headquarters October 30, 1997. Associate Technical Editor: D. Lou.

[1] Name changed to Dalhousie University.

designers prescribed choice and methodology. Although the expert system carries out the entire design, the designer can control any step while the design is in progress. The main architecture of the program is shown in Fig. 1.

The main elements of the design method are described next.

Input Parameters. In a typical design process, input parameters would include the following: fuel and sorbent composition, steam cycle, emission, and ambient parameters.

Designer Choice. Each company and its design office has its own design preference or schemes. In the case of CFB boilers, they may include wing walls, omega tubes, external heat exchangers (EHE), full division walls, etc.

Stoichiometric Calculations. It uses design and sulfur capture equations from Basu and Fraser (1991).

Steam Enthalpy Calculations. Enthalpies of water and steam are calculated at different points of the water/steam circuit using a computerized steam table.

Efficiency. Flow rate of coal, limestone and flue gas. A detail heat balance calculation gives the boiler efficiency and the flow rates of coal, limestone, and flue gas.

Design Constraints. The next step of the design of the boiler considers, as far as possible, a list of constraints given by the user. As these constraints are often contradictory, the expert system tries to take into account (totally or partly) most of them and strike a compromise for contradictory constraints according to a preference table defined in the program (giving the percentage of importance for each constraint). The main constraints dealing with heat duty distribution and furnace, backpass, and cyclone design are described in Lafanechère et al. (1995a).

Heat Duty Distribution. An initial allocation of heat duty in the backpass is carried out, abiding by the list of constraints given by the user. The process begins with the air heater, continuing with the economizer, and finishing with the division of the heat duty available in the backpass between the reheater and the superheater. The heat duty in the furnace or the external heat exchangers is computed next. These duties will be modified, if necessary, following design calculations for the cyclones and the furnace. A detail analysis of the heat transfer and the hydrodynamic calculations in the CFB furnace is carried out on the basis of a practice-based model of Lafanechère and Jestin (1995b).

Design of Cyclones. The cyclones are designed with respect to the constraints described in Lafanechère et al. (1995a), and by following the approach outlined by Lewnard et al. (1993). Also, a pressure balance calculation is carried out from the cyclone inlet to the loop seal and to the furnace bottom to assure a good circulation of solids around the CFB loop.

Design of the Furnace. The furnace is designed according to the constraints described in Lafanechère et al. (1995a), as well as an experience table of operating CFB boilers (Greenfield (CFBCAD—An Expert System, 1996).

Design of the Backpass. The design of the backpass is carried out to determine the size and the physical arrangement of the different heat exchanger elements.

Matching of the Different Components. In this final step, the program checks if the different components (furnace, cyclone, backpass) are matching together in respect of operating conditions and geometry, and modifies them if necessary (Isaka et al., 1989).

Validation of the Model

The complex rule and procedure-based design system developed is similar to a mathematical model whose accuracy is not accepted till its predictions are found in reasonable agreement with field results. Similarly, the present system predicts a series of performance data and geometrical dimensions. So for validation, these were compared against those of large commercially operating CFB boiler plants. Two plants representing the state of the art of two types of designs (with and without external heat exchanger) were chosen for validation. The first one is the Point Aconi unit (Canada), a 165 MWe reheat boiler with wing walls and omega tubes and without EHE (Fraser et al., 1991). The second one is the E. Huchet unit (France), a 125 MWe reheat boiler with EHE (Lucas et al., 1993). The designs produced by CFBCAD© have been compared with the actual plant designs and the operating results with measurements from these boilers. Table 1 shows the comparison for these two utility boilers. Values represent percentage variation between the operating unit and the results of the expert system.

For both E. Huchet and Point Aconi units, values given by the expert system are close to those for the actual plant. Some differences appear. Reasons for these differences are explained next.

Furnace. The shape of the furnace, which depends to some extent on the preferences of the designer varied (width-depth ratio). However, the furnace cross section is very similar due to the choice of similar fluidization velocity.

Back-pass. In order to optimize the boiler configuration, CFBCAD© shapes the backpass—conforming to the number of cyclones and the shape of the bed cross section. This leads to a different width-depth ratio of the backpass. For example, the expert system shapes the furnace to fit the cyclones between the furnace and the backpass. That is not the case the for E. Huchet boiler as built. Here, the cyclones are on each side of the furnace. The CFBCAD© uses a lower flue gas velocity in the back-pass than the Point Aconi and a higher one than the E. Huchet unit. This factor accounts for 3.2 percent larger cross

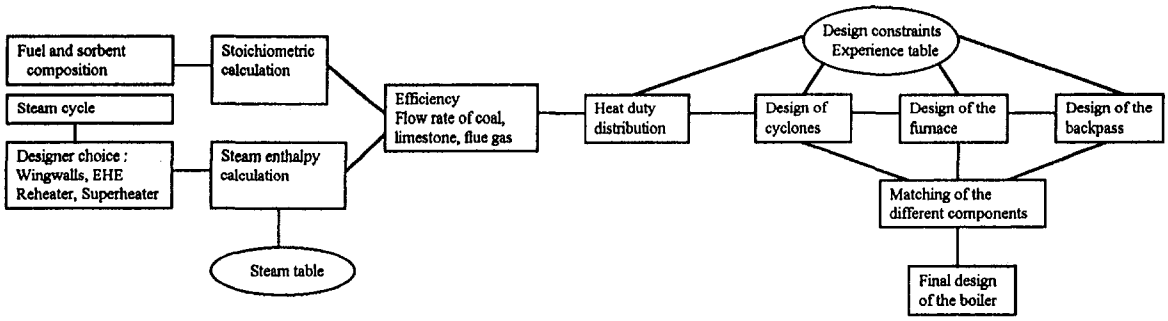

Fig. 1 Main architecture of the expert system

Table 1 Comparison between results of CFCAD and the values from actual commercial boiler

Difference = (CFBCAD - Actual) / Actual (%)		Point Aconi	E. Huchet
Parameters		165MWe	125MWe
Boiler	efficiency (LHV basis)	-0.07	-0.11
	fuel feed rate	0.42	0.06
	limestone feed rate	0.41	0.13
	flue gas flow rate	-0.20	1.59
	sulfur capture efficiency	8.89	-
Heat duty	superheater back pass	0.00	0.56
	reheater back pass	0.65	-3.96
	economizer back pass	-3.66	-0.02
	super heater furnace or EHE	0.11	1.69
	reheater furnace or EHE	-	1.05
	evaporative water wall and wingwall or backpass evaporator	0.36	-0.66
Steam temperatur	final super heater inlet temp.	3.80	0.04
EHE temp.	outlet temp. of particles	-	1.10
Furnace	width	7.61	52.02
	depth	-6.67	-34.54
	cross section	-0.01	-0.50
	height	0.03	7.67
	height of water wall	0.00	9.37
Back pass	width	46.76	35.74
	depth	-14.86	-19.70
	cross section	3.24	-12.16
Cyclone	number	0.00	0.00
	diameter	-2.78	-5.31
Heat transfer surface area	superheater backpass	-2.94	1.42
	reheater backpass	-45.41	-2.38
	economizer backpass	-0.95	-0.97
	superheater furnace or EHE	0.82	-4.44
	reheater furnace or EHE	-	-9.72
	evaporative water wall and wingwall or backpass evaporator	1.69	-18.62

section of the back-pass for the Point Aconi unit and 12 percent smaller for the E. Huchet unit. The back-pass walls and roof are used in the E. Huchet boiler as an evaporative heat transfer surface, whereas the Expert system keeps the excess surfaces as a margin for the superheat circuit. This leads to a 18 percent smaller evaporative heat transfer area.

Heat Transfer Surface. The reheater heat transfer area is much different for Point Aconi unit (−45 percent) due to a different technological choice for the reheat temperature control. The Point Aconi unit uses a bypass in the reheater (Gounder et al., 1993), and CFBCAD© uses attemperation water spray. The bypass system modifies the steam velocity in order to control the heat transfer coefficient, and leads to a lower temperature difference in the last two stages of the reheater. This requires a higher heat transfer area, which is not taken in account in CFBCAD©.

Influence of Steam Cycle Parameters on the Boiler Design

A major objective of a boiler designer is to arrange heat transfer surfaces to optimize the thermal efficiency and the economic investment. Heat transfer surfaces including waterwalls, superheaters, and reheaters absorb heat from the furnace gas heating water to the saturation point, evaporating it, and superheating and reheating the resulting steam. The air heater and economizer recover heat from the furnace exit gases to preheat combustion air and to increase the temperature of incoming feed water, respectively. The boiler designer must proportion heat absorbing and heat-recovery surfaces to make best use of the heat released by the fuel. This arrangement is fuel dependent (Lafanechère et al., 1995a) and also closely linked to the steam cycle parameters.

All designs were prepared for one specific coal. It is a Sub bituminous a coal with the following composition: ash = 7 percent; moisture = 14 percent; carbon = 64 percent; hydrogen = 4 percent; oxygen = 9.6 percent; nitrogen = 1 percent; and sulfur = 0.4 percent. The different steam cycle parameters used are given in Table 2.

Division of Heat Duties Between Back-Pass and CFB Loop. The distribution of heat duty between economizer, evaporator, superheater, and reheater depends on the drum pressure and steam temperature. The combustion technology employed does not affect it. However, the distribution of heat duties within individual heat exchangers (superheaters, reheaters, or evaporators) may be combustion-technology specific. These are split between two separate zones of heat absorption: the circulation loop (furnace and EHE (if any)) and the convective pass. However, Lafanechère et al. (1995a) showed that the distribution of total heat duty between the circulating loop and the back-pass is independent of the steam parameters. It only depends on the coal quality.

To split the heat duty of individual heat transfer elements, the following practical considerations have to be taken into account:

1 The metal tube temperature of the superheater should not be so high as to require too expensive material. For that purpose, the last stage of superheater is often located at the top of the back-pass, where the heat flux is lower than in the furnace or the EHE.
2 Split the superheater and reheater in order to maximize the log mean temperature difference so that a smaller heat transfer area is needed.
3 In the case of EHE, allocate as much reheater duty as possible in one of them (usually the last stage of the reheater, to optimize the temperature difference). This will allow a better control of the reheat outlet temperature. The other EHE will be used for superheater, and will allow a better furnace temperature control.

Effect of Steam Temperature. The design exercise was carried out for two steam temperatures 510°C and 540°C, while keeping all others parameters constant (set 2 and 3 from Table

Table 2 Different steam cycles used for the study

Cases	Drum pressure	Outlet superheater temperature	Reheater pressure	Reheater inlet temperature	Reheater outlet temperature	Feed water temperature
Set	MPa	°C	MPa	°C	°C	°C
1	8.5	510	without	without	without	240
2	12.5	510	4.0	355	540	
3	12.5	540				
4	14.5					
5	16.5					
6	18.5					
7	20.5					
8	22.0					

2). A higher steam temperature calls for higher superheater heat duty. This reduces the flue gas temperature exiting the back-pass superheater. Furthermore, the overall heat flux is lower for higher steam and, consequently, for the wall temperature, so, a higher steam temperature would require a higher surface area per unit thermal output.

Effect of Drum Pressure on Heat Duty Distribution. Figure 2 shows, for the set 3 to 8 from Table 2, how, following the above considerations, one would split heat duties of superheaters and reheaters between the back-pass and the furnace for boilers without external heat exchangers. Similarly, Fig. 3 shows the same for boilers with external heat exchangers.

When the drum pressure increases, the latent heat for evaporation decreases, and the economizer heat duty increases. Above 17 MPa for drum pressure (cases 6, 7, and 8) the heat duty available in the back-pass is lower than the reheater heat duty. So, it becomes necessary to use a reheater in the furnace. For a given furnace temperature, a higher drum pressure lowers the amount of heat available in the back-pass for the reheater and superheaters, because of the increasing heat duty of the economizer and the constant stack temperature. The choice of the part of the reheater and the superheater to be put in the back-pass and in the furnace, for boilers without external heat exchangers, is made mainly on cost considerations. This choice optimizes the intermediate steam temperatures to allow the use of a less expensive metal tube for the first stage of reheater.

In case of boilers with external heat exchangers, the heat duty distribution depends primarily upon the operating and cost considerations. As shown in Fig. 3, the external heat exchangers try to maintain a sufficient amount of reheater surface in them to allow an easy control of the final reheat temperature, and to keep enough superheater surfaces to allow a good furnace temperature control. For a low pressure boiler, the increased evaporative heat duty will need to increase the height of the waterwall, and, therefore, the height of the furnace. Alternatively (as it is the case in Fig. 3, for 12.5 MPa), it is possible to use an evaporator in external heat exchangers to maintain the height of the furnace within a reasonable value.

In the case studied here (Table 2), we consider a drum pressure up to 20 MPa. However, such a high pressure is relevant only for supercritical steam cycle (above 22 MPa).

Effect on Heat Transfer Surface. Heat transfer surfaces have an important bearing on the overall cost of the boiler. Using the Expert system method described earlier, the total heat transfer surface has been calculated for all eight sets of steam parameters of Table 2. The heating surfaces required (per thermal megawatt produced by the boiler) are shown in Fig. 4.

The total heat transfer surface reported in Fig. 4 includes the economizer, the evaporator, the superheater, and the reheater, but it does not include the air heater.

We first compare the design of a low pressure (8.5 MPa) boiler without a reheater with that of a high pressure (12.5 MPa) boiler with reheater at the same steam temperature and

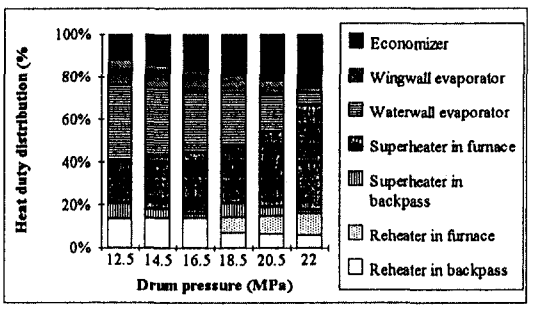

Fig. 2 Variations in heat duty distribution with drum pressure for boilers without external heat exchanger

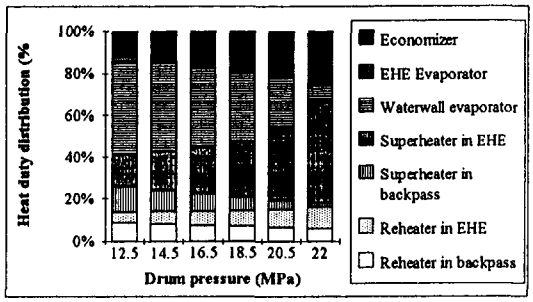

Fig. 3 Variations in heat duty distribution with drum pressure for boilers with external heat exchangers

flow rate (set 1 and 2 from Table 2). Higher pressure implies more heat duty in preheating than in evaporation. So the evaporator heat duty in the 12.5 MPa boiler is smaller than that in the 8.5 MPa boiler, while the heat duty of the economizer is much higher in the 12.5 MPa boiler than in the 8.5 MPa unit. The overall heat transfer coefficient is not very sensitive to the boiler pressure, but for a given stack temperature, the flue gas needs to enter the economizer at a higher temperature. This drives up the temperature differential in the economizer, and, therefore, a smaller surface area per unit thermal output is required. We notice this trend in both designs with and without EHE.

For the set 3 to 8 from table 2, the heat duty of the economizer increases with the drum pressure as shown in Figs. 2 and 3. This allows it to recover the constant heat duty available in the back-pass with a higher temperature difference, and, therefore, decreases the heat transfer surface requirement in both designs with and without EHE.

In spite of a higher heat transfer coefficient in the EHE than in the furnace, there is almost no difference in the total heat transfer surface per megawatt produced between the design with or without EHE. The lower heat transfer coefficient in the furnace is compensated by a higher gas side temperature.

Effect on the Furnace Height. The waterwalls heat duty calculation must be carried out to determine the necessary height of waterwalls. If the calculated height is too high, the use of evaporative wing walls or EHE will be needed.

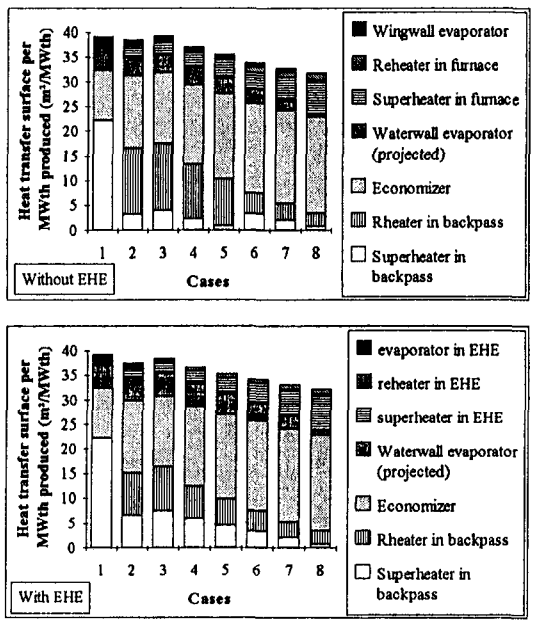

Fig. 4 Variations in the total heat transfer surface area (without air heaters) per thermal megawatt produced for different steam cycles (cf. Table 2), for a boiler with and without external heat exchangers

CFB combustors are not so influenced by the slagging and fouling as other kind of boilers (especially pulverized-coal-fired boilers). Also, the residence time of the coal particles is longer in a CFB boiler due to the recirculation process. So, it is possible to decrease substantially the height of a CFB furnace depending on the heat duty and the heat transfer surface required to perform the evaporation. The use of wing walls also modifies the waterwall surface requirement and allows one to decrease the furnace height. Figure 5 presents calculated height of the furnace (waterwall height plus refractory height) for the steam cycles given in Table 2. These calculations have been undertaken for 145 kg/s steam flow rate boilers. The design without external heat exchangers leads to a shorter furnace due to the use of wing wall evaporators. The height of the boiler has been limited to 42 m for overall cost considerations. For a very high drum pressure (over 20 MPa) the minimum cyclone height, calculated to have a sufficient collection efficiency and to allow an adequate circulation of particles through the loop seal, dictates the height of the furnace. However, the decrease in the furnace height implies a lower gas residence in the furnace, and, therefore, a lower sulfur capture efficiency. In the same way, the unburned carbon will increase. A compromise has to be found, depending on the emission level requirement and the limestone to sulfur molar ratio to be used.

Effect of Temperature Off-Set in Economizer Water Outlet. Usually the final steam temperature and pressure are dictated by the steam turbine to be used. The feed water temperature depends on the feed water heater arrangement and efficiency. To prevent the possibility of boiling in the economizer, the water temperature at the outlet of the economizer is set a certain amount below the saturation temperature of the water. This temperature off-set affects the economizer design. In general, this off-set of temperature is rather small but higher than 10°C (Gottung and Darling, 1989) to prevent steam generation in the economizer. However, some boilers use evaporative economizer, and others use an off-set of temperature in the economizer up to 70°C. This parameter, that modifies the economizer heat duty, leads to a different back-pass heat duty distribution.

Figure 6 presents the variation of the total heat transfer surface (including air heater) per thermal megawatt produced as a function of the off-set of temperature in economizer for the steam cycle 4 from Table 2. An increasing off-set of temperature in the economizer decreases the heat duty of the economizer, leaving more heat to be recovered by other heat exchangers in the back-pass (superheater and reheater) and increasing the heat duty of the waterwalls (and wing walls or evaporative EHE). The heat duty, available in the back-pass, that is not performed by the economizer will be performed by the superheater and the reheater, but with a lower temperature difference. This will increase the heat transfer surface to be installed in the back-pass. For the steam parameter set 4 of Table 2, these variations of the total heat transfer surface are not significant while the off-set of temperature in economizer stays beneath 30°C.

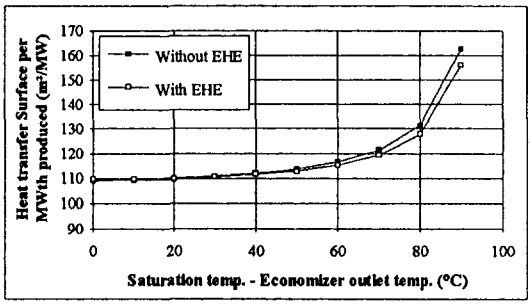

Fig. 6 Variations of the total heat transfer surface (including air heater) per megawatt produced with the off-set of temperature from saturation at economizer outlet

Effect of Temperature Off-Set in Economizer Water Inlet. Another parameter to be chosen in the CFB boiler design is the temperature difference between the flue gas and the feed water at the economizer inlet. We consider a counter-flow economizer here. This parameter determines the division of heat duty between the economizer and the air heater. For a given stack temperature and off-set of temperature at economizer outlet, it will also define the temperature difference in both economizer and air heater. The variations in the total heat transfer surface (including air heater) per megawatt produced are presented in Fig. 7 as a function of the temperature difference at economizer inlet. The figure presents an optimum value. Increasing this parameter increases the temperature difference in the economizer and decreases the economizer heat transfer surface, but this also increases the heat duty of the air heater where the heat transfer coefficient is much lower than the economizer. A decrease in this parameter decreases the temperature difference in the economizer and consequently increases the heat transfer surface of the economizer. This also decreases the heat duty of the air heater and its heat transfer surface. The optimum value shown in Fig. 7 (around 35°C) is also influenced by the heat transfer coefficients and the steam parameters used in the calculation.

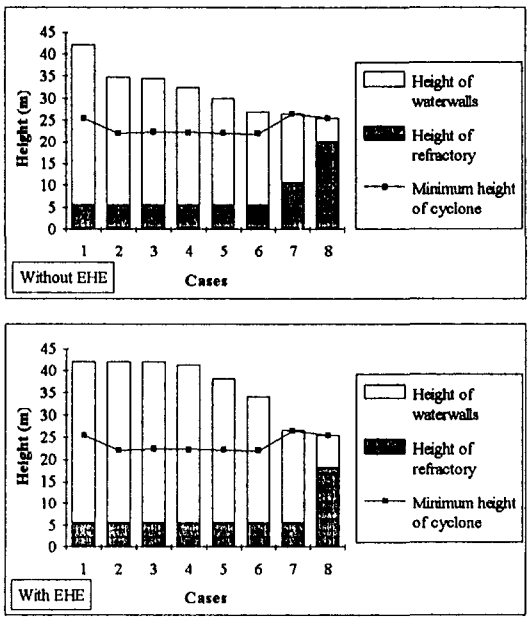

Fig. 5 Variations of the height of waterwalls and refractory for different steam cycle (cf. Table 2), for boilers with and without external heat exchangers

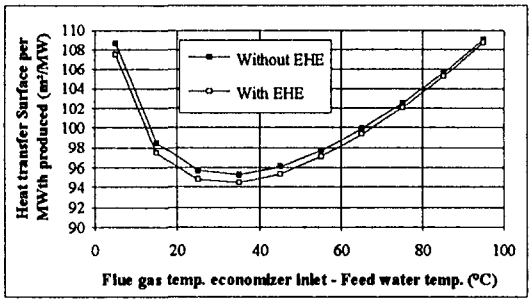

Fig. 7 Variations of the total heat transfer surface including air heater) per megawatt produced with the exit temperature difference in economizer

Conclusion

A rule and procedure based expert system (CFBCAD©) is developed through a synthesis of operating experiences of CFB boilers and knowledge of processes occurring in individual components of CFB boilers. Performances and geometric parameters predicted by the expert system were verified with those of two commercially operating CFB boilers manufactured by two major companies. The design and performance predicted by CFBCAD is in good agreement with those of the two plants. A preliminary study into the effect of steam parameters, carried out using the CFBCAD© as a predictive tool, led to the following major observations:

1 The steam cycle parameters and especially the drum pressure lead to different distribution of the heat duty in both the circulating loop and the back-pass. These configurations will give significant difference in the total heat transfer surface installed for the same heat recovered by the boiler.
2 The drum pressure also affects the heat exchanger distribution within the furnace. For a high drum pressure, the evaporative heat duty will be low (the heat duty of superheater and reheater in furnace or EHE will increase in the same proportions), and the height of the furnace will be low.
3 The difference of temperatures between the flue gas and the feed water in the economizer as well as the off-set of temperature at the economizer outlet modify the heat transfer requirement of economizer and air heater. Considering the different costs involved in the building of the economizer and the air heater, an optimum of these parameters can be found.

Acknowledgment

The project is financially supported by Electricité de France (S.E.P.T.E.N.) Lyon, and Greenfield Research Inc., Halifax.

Literature Cited

Fraser, S., Schaller, B., and Darguzas, J., 1991, "Design of a 165 MWe Reheat Coal Fired CFB Boiler," *Proc. 11th Int. Conf. on Fluidized Bed Combustion,* Vol. 1, E. J. Anthony, ed., ASME, New York, pp. 41–50.

Gottung, E. G., and Darling, S. L., 1989, "Design Considerations for Circulating Fluidized Bed Steam Generation," *Proc. 11th Int. Conf. on Fluidized Bed Combustion,* A. Manaker, ed., ASME, New York, pp. 617–624.

Gounder, P. K., Antonio, F., and Pyykkonen, A., 1993, "Ahlstrom Pyropower's Reheat Experience," preprint from 4th Int. Conf. On Circulating Fluidized Bed Technology, Somerset, PA, USA, American Institute of Chemical Engineers, p. 205.

CFBCAD—An Expert System, 1996, Greenfield Research Inc., Box 25018, Halifax, Canada, B3M 4H4.

Isaka, H., Hyvarinen, K. H., Morita, A., Yano, K., and Ooide, M., 1989, "Design Considerations for Circulating Fluidized Bed Steam Generation," *Proc. 10th Int. Conf. on Fluidized Bed Combustion,* Vol. 2, K. J. Heinschel, ed., ASME, New York, pp. 783–791.

Lafanechère, L., Basu, P., and Jestin, L., 1995a, "Effects of the Fuel Parameters on the Size and Configuration of Circulating Fluidized Bed Boilers," *Journal of Institute of Energy,* Dec., Vol. 68, pp. 184–192.

Lafanechère, L., and Jestin, L., 1995b, "Study of a Circulating Fluidized Bed Furnace Behavior in Order to Scale it up to 600 MWe," *Proc. 13th Int. Conf. on Fluidized Bed Combustion,* Vol. 2, K. J. Heinschel, ed., ASME, New York, pp. 971–980.

Lewnard, L., Herb, B. E., Tsao, T. R., and Zenz, J. A., 1993, "Effect of Design and Operating Parameters on Cyclone Performance for Circulating Fluidized Bed Boilers," *Circulating Fluidized Bed IV,* A. A. Avidan, ed., American Institute of Chemical Engineers, pp. 525–531.

Lucas, Morin, Semedard, Jaud, Joos, Masniere, 1993, *Utility-Type CFB boilers: 250 MWe and beyond,* Proc. 12th Int. Conf. on Fluidized Bed Combustion, Vol. 1, L. N. Rubow, ed., ASME, New York, pp. 9–15.

Stultz, S. C., and Kilto, J. B., eds., 1992, *Steam: its Generation and Use,* 40th ed., Babcock Wilcox, Barberton, OH, p. 1–5.

N. N. Wang

J. M. Wei

X. S. Cai

Z. W. Zhang

G. Zheng

X. H. Yu

College of Power Engineering,
University of Shanghai for Science
and Technology,
516 Jun Gong Road,
Shanghai 200093, P. R. China

Optical Measurement of Wet Steam in Turbines

The wetness fraction of steam causes dangerous erosion of turbine blades and other components, and decreases efficiency of stages. The instrumentation of wet steam has, therefore, attracted growing interest from the point of safety and economical operation of power stations. Based on the light scattering technique, a method is presented that is capable of measuring the wetness fraction of steam, the mean water droplet diameter as well as their full size distribution. An optical probe has been constructed that can be used in the turbines in operation. Its main characteristic and features are discussed in this paper. Experimental results in a 200 MW condensing steam turbine are also given.

Introduction

The presence of moisture in the form of fine water droplets in the steam of steam turbines causes dangerous blade erosion damage and decreases its thermal efficiency. In conventional fossil fuel power stations, wet steam occurs at some point in the low pressure turbine. Its negative effects are thus restricted only to blades in the final stages. Nevertheless, these problems are particularly serious for turbines in nuclear power stations supplied with dry saturated steam from the light water-cooled reators since almost the whole turbine stages are working in the wet steam region. The drive for higher efficiency forces the manufacturers to build turbines of superior performance, and detailed information on individual stage efficiencies is required. Particular areas of interest are in the wet steam stages. Owing to the complex phenomenon of steam condensation and aerodynamic process of vapor-liquid, two-phase flow in these stages, difficulties in computational methods for modeling and predicting the aerothermodynamic performance are especially prevalent. Very little has been published in the open literature about these problems. On the other hand, whereas the HP and IP cylinder efficiencies may be derived to satisfactory accuracy from the standard heat rate tests, the LP cylinder efficiency cannot be accessed accurately from the heat rate data. This problem stems from the fact that it is impossible to determine the wetness fraction and/or enthalpy of the exhaust saturated steam from pressure and temperature measurements. Therefore, the growing need to develop techniques and methods for direct measurement of the wetness friction of steam in turbines has thus become urgent.

Various methods for measuring the wetness fraction and then the enthalpy of the partially condensed steam at the turbine exhaust have been under development over many years. Since the 1960s, several calorimetry probes have been developed (Roegener, 1960; Kasprzyk, 1964). Calorimetry probes are based on the thermodynamic principle. Only a small amount of the wet steam is extracted from the main flow and analyzed. In order to collect a representative sample for accurate analysis, the sampling procedure should be iso-kinematical. Iso-kinematical sampling in the running turbines is extremely difficult due to the unsteady and three-dimensional character of flow in these stages, and the local thermodynamic and aerodynamic parameters of the flow are also disturbed. The probe must be well heat insulated in order to achieve accurate results. This complicates the construction of the probe. Calorimetry probes measure only the wetness fraction of the steam. No information about the water droplet size is obtained, which is very desirable to know in order to reveal the mechanism of additional wetness losses in these stages, because wet steam of the same wetness fraction but with different water droplet diameter causes different negative effects. By the thermodynamic methods, every measurement takes several hours since full thermal equilibrium of the whole probe body should be established from one operating condition to another. In most cases, calorimetry probes have a relatively large dimension. They are thus used mostly to make the measurements beyond the last stage, but not between the blade rows of stages. Owing to the reasons mentioned above, calorimetry probes are now seldom used in the instrumentation of wet steam in turbines.

Recently, optical methods, based on the light scattering technique, have shown to give accurate and repeatable data (Moore and Sieverding, 1987). The most important advantages may be cited as follows:

1 Not only the wetness fraction of the steam, but also the size of water droplets contained can be obtained from the measurements.
2 Optical probes are of nonintrusive type due to the transparency of the light. Measurements are performed directly in the turbines. No sampling is needed. The local aerothermodynamic parameters are not disturbed.
3 The measurement is fast, usually within 1–2 minutes.
4 Optical probes can be constructed in a long tubular form with a minor outer diameter. They can thus be used to make the measurements not only beyond the last stage, but also between the blade rows of the turbine stages.

Owing to the reasons mentioned above, the light scattering methods have dominated the wet steam instrumentation since the 1970s. Several optical probes have also been developed and used to make the measurement in the model and operating turbines (Walters, 1985; Barbucci, 1988; Kleitz, 1991). For a number of years, the instrumentation of wet steam has also been investigated based on the total light scattering technique (Wang, 1982; Cai et al., 1994). This will be discussed in the following sections.

Contributed by the Power Division. Manuscript received by the ASME Headquarters March 3, 1997. Associate Technical Editor: D. Lou.

Basic Principle

In the literature, the total light scattering method is sometimes named the extinction or turbidity method. When a beam of light of intensity I_0 passes through the wet steam containing water droplets, there will be an attenuation in light intensity or an extinction of the incident light. The transmitted light intensity I can be expressed by the following equation:

$$I = I_0 \exp(-\tau L), \tag{1}$$

where L is the path length of the light beam in wet steam, and τ is the turbidity of the medium. For a monodisperse system with water droplets of diameter D, and in the absence of multiple and dependent scattering, the turbidity τ is given by the following equation:

$$\tau = \frac{\pi}{4} D^2 N E(D, \lambda, m), \tag{2}$$

where N is the number concentration of water droplets, and $E(D, \lambda, m)$ is the total scattering coefficient or extinction coefficient that is the ratio of total energy scattered by a droplet to the energy geometrically incident on the droplet. Coefficient $E(D, \lambda, m)$ is a function of the droplet diameter D, the wavelength of the light λ, and the refractive index of water droplet m, and can be exactly calculated from rigorous classical Mie's Theory. In real conditions, the water droplets formed in wet steam flows may be polydispersed. If a polydispersion with the number concentration distribution function $N(D)$ is discussed, the turbidity of the system is the sum of all the contributions over the whole droplet size range.

$$\tau = \frac{\pi}{4} \int_0^\infty D^2 N(D) E(D, \lambda, m) dD \tag{3}$$

Substituting Eq. (3) into Eq. (1), the extinction (I/I_0) can be obtained.

$$\ln (I_0/I) = \frac{\pi}{4} L \int_0^\infty D^2 N(D) E(D, \lambda, m) dD \tag{4}$$

The volume concentration of water droplets and wetness fraction are

$$C = \frac{\pi}{6} \int_0^\infty N(D) D^3 dD \tag{5}$$

$$Y = \frac{C\rho_f}{\rho_g + C\rho_f}, \tag{6}$$

where ρ_g and ρ_f are the local specific weight of liquid and vapor phase of the saturated steam. In the method proposed by the authors of the present paper, a number of monochromatic light of different wavelengths $\lambda_1, \lambda_2, \ldots \lambda_n$ are used to make the extinction measurements. A set of equations can be then written.

$$\ln (I_0/I)_i = \frac{\pi}{4} L \int_0^\infty D^2 N(D) E(D, \lambda_i, m) dD$$

$$i = 1, 2, \ldots n \tag{7}$$

Theoretically, it is possible to extract the size distribution function $N(D)$ from the above equations, if corresponding extinction readings at these wavelengths $(I_0/I)_1, (I_0/I)_2, \ldots (I_0/I)_n$ are measured. Once the water droplet size distribution function $N(D)$ is found, the wetness fraction Y can be then determined from Eq. (5) and (6). In fact, Eq. (7) is a set of the Fredholm integral equations of the first kind, which is difficult to be solved. In the literature, a number of methods dealing with the ill-conditional nature of the inversion problem have been presented, but only a few can give satisfactory result for our case—the extinction or the total light scattering technique. Based on the NNLS and Powell method, an inversion algorithm for this purpose has been developed by authors (Cai, 1991). Comprehensive computer simulations and experimental studies have proven its ability and resolution to recover the size distribution function $N(D)$ from the measured extinction values (Wang et al., 1994).

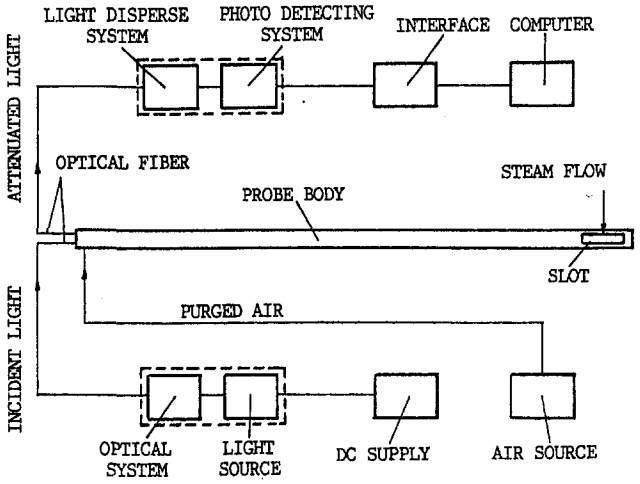

Fig. 1 General arrangement of the optical probe

The Configuration of Optical Probe

Based on the total light scattering or extinction method stated above, a new optical probe has been constructed in the authors' laboratory, which has some advantages and features if compared with other probes. Figure 1 shows the general arrangement of the optical probe. It is essentially composed of five main subsystems: the probe body, the light source, the light disperse and photodetecting system, the air system, and the data acquisition and processing system. The probe body is from 10 mm to 40 mm in diameter and several meters in length in accordance with different applications. At one end of the probe body there is a slot served as the measuring volume through which the wet steam passes. A white light from halogen lamp is used as the light source, which is conducted to the probe body by an optical fiber. When passing through the measuring volume, the light interacts with fine water droplets contained in the wet steam flow and is attenuated. The attenuated light is reflected by a mirror installed just behind the slot and passes the slot again. The transmitted light, which is attenuated twice by water drop-

Nomenclature

C = volume concentration of water droplets
D = water droplet diameter, μm
E = extinction coefficient
I = transmitted light intensity, W/m^2
I_0 = incident light intensity, W/m^2
L = path length of light, m
m = refractive index
N = number concentration of water droplets, 1/m^3
$N(D)$ = number concentration distribution function of water droplets
Y = wetness fraction
λ = wavelength, μm
ρ_f = specific weight of liquid phase, kg/m^3
ρ_g = specific weight of vapour phase, kg/m^3
τ = turbidity

lets is then directed by another optical fiber to the light disperse and photodetecting system. Such configuration simplifies the whole measuring system as well as the probe body itself and permits the probe to be used in higher temperature atmosphere.

The transmitted white light from the probe is dispersed by a specially designed optical grating system to form a continuous spectrum. The light intensity signals at several wavelengths are then picked out and their magnitudes are detected by the succeeding photodetecting array system. This ensures that all the intensity signals at different wavelengths are simultaneously measured at one moment. The accuracy of the final results is thus improved. Experimental time needed to make the extinction measurements is also minimized to a great extent. This system is simple in construction and reliable in use, because no rotating or moving parts are needed. Extinction readings picked out from the spectrum are in the visible range from 0.45–0.80 μm; therefore, usual optical and photodetecting components can be used. No problems occur that might be associated with the use of ultraviolet and/or infrared light. As much as 15 light intensity signals at corresponding wavelengths are picked out from the spectrum. If necessary, this system can be easily reconstructed to change the number of those picked out light signals to meet different needs. In order to achieve accurate results, light intensity signals at every wavelength are repeatedly measured 256 times to get an average value for the data processing. The total data collecting time to scan all wavelengths is less than 1 second, while the time for data processing is within 1–2 minutes by a personal computer.

By the construction of the probe, it is very important to protect all optical components submerged in the wet steam flow from direct contact with it, as the steam tends to condensate on their surfaces. Obviously, this will lead to abnormal operation of the instrumentation and cause wrong results. This is done by special admission of a small amount of purged air, which is continuously and slightly blowing onto the surfaces of these components. On the other hand, when the signal I_0 is measured, a large amount of air should be admitted into the measuring volume to expel the wet steam from it. I_0 denotes the collected light intensity when there is no wet steam in the measuring volume.

Experimental Studies in Laboratory

Before the optical probe was used to measure the wet steam in operating turbines, several experiments were carried out in the laboratory to test its availability and performance. First of all, saturated steam of 0.1 Mpa and 100°C generated by an electric generator was measured. Its maximum capacity was 100 Kw. Figure 2 shows the diagram of the experimental setup. The optical probe was inserted into the outlet of the generator. Table 1 gives the results of measurements made at different heating power. The following main points can be concluded from these figures:

1 The constructed optical probe, particularly the light disperse and photodetecting system as well as the air system work reliably.
2 The probe is proven to be normally worked at 100°C atmosphere, which is much higher than that at the low pressure end of turbines. Also, it is reasonably expected that the configuration of the new designed probe permits it to be used in much higher temperature mediums.
3 Owing to the limitations of the experimental setup, the minimum and maximum wetness fraction measured in these experiments are 0.029 percent and 11.1 percent, respectively, which cover almost the whole possible range of wetness fraction practically met in modern steam turbines.
4 The mean droplet diameters are in the order of several micrometers, which are larger than those occurred in the operating turbines, because in these experiments the droplets are carried over from the surface of the boiling water by the steam flow rather than formed by the spontaneous condensation of rapidly expanded steam flow.

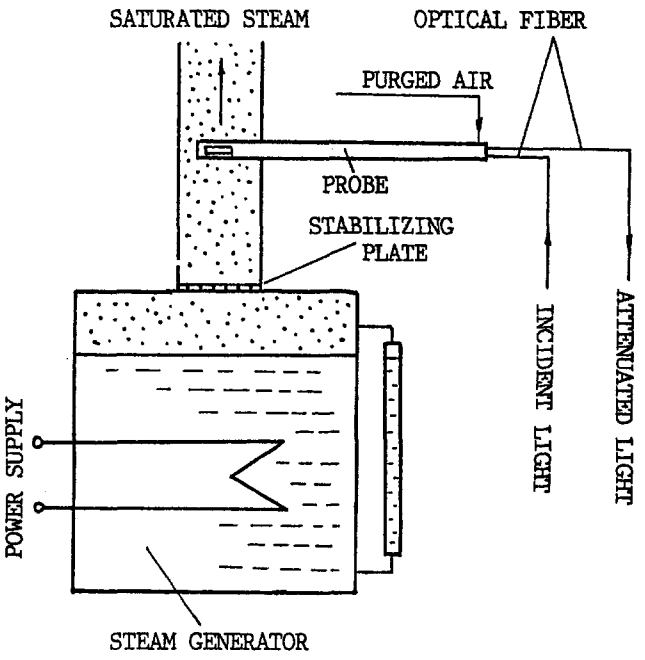

Fig. 2 General arrangement of the experimental setup

Measurements were also carried out in high speed steam flow. In cooperation with The University of Stuttgart, Germany, experiments were performed in a steam tunnel of ITSM (Renner et al., 1994). The optical probe was inserted into the exit of a slotted nozzle where the steam is wet after expansion and its speed ranges from subsonic to supersonic in accordance with various testing conditions. Figure 3 shows one of the measurement results when the Mach number is $M = 0.90$ and the distance from the nozzle exit is 20 mm. Figure 3(a) and (b) give the distribution of wetness fraction and mean droplet diameter along the upper half nozzle height; Figure 3(c) shows the full size distribution of droplets near the central position of the nozzle. The droplets formed by spontaneous condensation in the high speed steam flow are nearly monodispersed, as expected. The measured mean droplet size is about 1.5 μm, which matches the theoretically predicted value quite well.

Measurements in Operating Steam Turbines

Measurements were performed in three operating steam turbines of capacity 12 MW, 200 MW, and 300 MW, respectively. In all the cases, the probe was inserted into the LP cylinder and located at the down stream of the last rotating blade row to measure the wetness fraction of exhausted steam. A probe handling device was fixed to the turbine casing, which is used to longitudinally control the position of the probe, and rotate it around its axis to align the direction of the flowing steam. It is so arranged that during the measurements, the probe body can be easily inserted into or drawn out from the casing without

Table 1 Results of measurements at different heating power

No.	1	2	3
Power, *Kw*	4.5	13.5	40.5
Wetness fraction, %	0.029	1.93	10.8
Droplet dia., μm	1.66	3.05	6.35

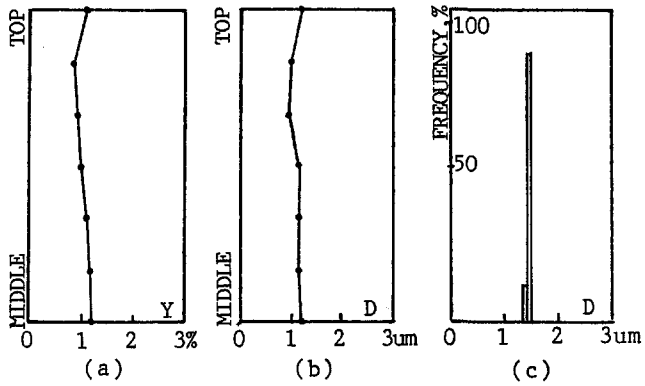

Fig. 3 Results of measurements at the exit of a slotted nozzle (M = 0.9): (*a*) distribution of wetness fraction; (*b*) distribution of mean droplet diameter; and (*c*) droplet size distribution at the nozzle center position

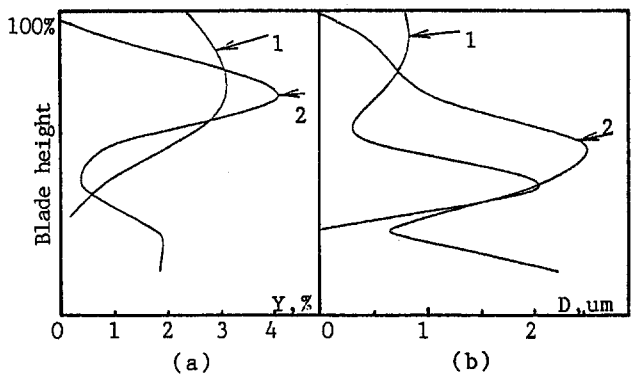

Fig. 5 Results of measurement at 170 MW turbine load (condenser pressure: 1-0.0118 MPa, 2-0.0256 MPa): (*a*) wetness fraction Y; (*b*) mean droplet diameter D

stopping the normal turbine operation. This simplifies the whole testing procedure and reduces the experimental time.

In the following, the results of measurements performed in a 200 MW reheat turbine with Heller air cooling system are given and discussed. The power station is located in Inner Mongolia, in the northern borden area of China. For Heller, air cooling system the pressure in the condenser is influenced to a great extent by the surrounding atmosphere and changes with the climate conditions. Owing to the hard climate condition of the power station (not far from the desert and the dust-laden atmosphere), the air cooling system was polluted, and this led to much higher condenser pressures than the normal values.

Experiments were performed at five different turbine loads, i.e., 200 MW, 170 MW, 150 MW, 130 MW, and 110 MW, and at different condenser pressures. For every operating condition, measurements were made at seven different positions along the blade height, which is of 710 mm long. In order to achieve reliable results, data were acquired once every minute and repeated five times. The total data collecting time was approximately five minutes for every blade height and half an hour for every operating condition. As an example, Fig. 4 shows the distribution of wetness fraction Y and mean water droplet diameter D along the blade height at 200 MW load when the condenser pressure is 0.0147 MPa, and Fig. 5 shows the same parameters at 170 MW load for both lower (0.0118 MPa) and higher (0.0256 MPa) condenser pressure, respectively. By the data processing the influence of coarse water has been taken into account with the indications stated in the literature (Williams and Lord, 1976). Table 2 gives the results of six repeated measurements made at the blade tip when the load is 200 MW. The average values of wetness fraction and droplet diameter

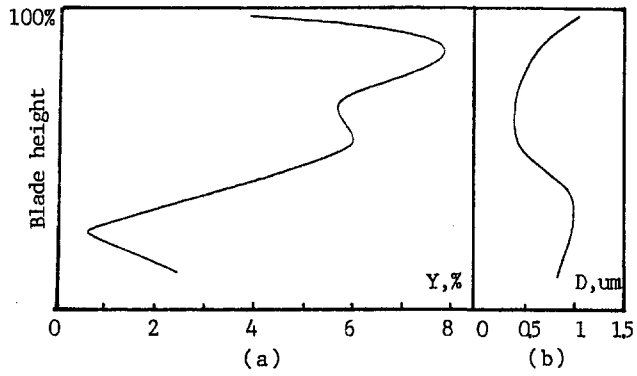

Fig. 4 Results of measurements at 200 MW turbine load (condenser pressure: 0.0147 MPa): (*a*) wetness fraction Y; (*b*) mean droplet diameter D

are 3.69 percent and 1.03 μm, respectively. As can be seen from these figures, the steam flow in low pressure stages of modern turbines is characterized by three-dimension and high turbulence, the optical probe gives repeatable measurements. The relative standard deviations of Y and D in Table 2 are 6.89 percent and 10.7 percent, respectively. Obviously, the values of wetness fraction measured in our experiments are much smaller than those in the conventional power station due to the higher condenser pressure.

It should be pointed out that there is, up to now, no common idea in the literature about the distribution of both wetness fraction and water droplet size along the blade height in the LP turbine stages. In our measurements, the wetness fraction has a maximal value near the middle part of the blade and decreases rapidly toward the blade tip and root. This may be effected by the stubs on the moving blades placed at about 60 percent of the blade height. This trend is similar to that published in the literature (Accornero, 1987). The wetness fraction Y decreases with decreasing turbine load and increases with lowering condenser pressure, as expected.

The distribution of water droplet size is not even along the blade height either. No regularity can be drawn from these measurements. Only one thing is clear, i.e., the diameters of water droplet formed by the spontaneous condensation in the operating turbines are generally less than 2 μm. This is in good agreement with other experiments. Using the developed inversion algorithm, Table 3 gives detailed information about the full size distribution of water droplets at the blade tip (operating condition No. 1 in Table 2). Clearly, water droplets formed in the turbine stages due to the spontaneous condensation are of narrow distribution and nearly monodispersed, as noted in most literature.

It is worthy of note that in modern steam turbines a dry saturation or superheated region may appear in the last stage with decreasing turbine load and increasing condenser pressure. In the turbines with Heller air cooling system where the pressure in the condenser is sufficiently high, it is possible for this phenomenon to appear at much higher loads. For example, even at 170 MW (85 percent turbine capacity), a dry saturation or superheated region begins to establish at the blade tip and root, when the condenser pressure is 0.0256 MPa (Fig. 5). This has been confirmed by the parallel thermodynamic measurements. In our experiments, the superheated region has a wider extent in the root part (about $\frac{2}{7}$ blade height) than in the tip. The

Table 2 Repeated measurements of Y and D

No.	1	2	3	4	5	6	(Average)
Y, %	3.89	3.40	3.67	3.34	4.05	3.78	(3.69)
D, μm	1.15	0.91	0.95	0.93	1.17	1.05	(1.03)

Table 3 Water droplet size distribution

Size class, μm	Wt in band, %	Cum. Wt(under), %
0.15-0.30	0.00	0.00
0.30-0.50	0.00	0.00
0.50-0.80	6.81	6.81
0.80-1.20	93.19	100.00
1.20-1.70	0.00	100.00
1.70-2.30	0.00	100.00
Wetness fraction Y=3.89%		
Mean water droplet diameter D=1.15 μm		

measured wetness fraction is thus equal to zero. When the condenser pressure decreases to 0.0118 MPa, the superheated region disappears.

Conclusion

Based on the total light scattering technique, a method is presented to measure simultaneously the wetness fraction, the mean water droplet diameter, and their full size distribution. A number of monochromatic light of different wavelengths are used in the measurement. The corresponding extinction caused by fine water droplets contained in the steam flow is collected. Inversion algorithm is developed and used to extract the desirable information from the measured extinction readings. An optical probe has also been constructed. Experimental studies performed in the laboratory to measure the wetness fraction and droplet diameter at the outlet of an electrical steam generator and at the exit of a slotted nozzle have proven the availability and reliability of the constructed probe. The optical probe has also been satisfactorily used to make the wet steam measurements in several running turbines. The detailed data obtained in a 200 MW reheat condensing turbine with Heller air cooling system are given. Measurements were carried out behind the blade of the last stage. No regularity can be drawn about the distribution of wetness fraction and water droplet diameter along the blade height. In some operating conditions a dry saturation or super heated region may appear in the last stage. The water droplet size measured in the operating turbine is generally less than 2 μm.

Reference

Accornero, A., and Maretto, L., 1987, "Field Measurements in LP Cylinder of a 320 MW Turbine," "Aerothermodynamic of Low Pressure Steam Turbines and Condensers," M. J. Moore et al., eds., Hemisphere, Bristol, PA, pp. 185–195.

Barbacci, P., 1991, "Steam Quality Measurements by an Optical Probe Using a Light Scattering Method," Proceedings of the International Conference on Multiphase Flow, Tsukuba, Giappone, Settembre, pp 132–138.

Cai, X. S., 1991, "Total Light Scattering Techniques and its Application in Wet Steam Measurement," Ph.D. thesis, University of Shanghai for Science and Technology, Shanghai, China.

Cai, X. S., Wang, N. N., and Wei, J. M., 1994, "The Development of Optical Measurement Technique for Wet Steam in Turbines," Proceedings of the 3rd Int. Symposium on Multiphase Flow and Heat Transfer, Xian, China, pp. 432–430.

Kasprzyk, S., 1964, "Ein Selbstansaugendes Kalorimeter zur Bestimmung der Dampffeucht," *Brennstuff-Wärme-Kraftwerk (BWK)*, Vol. 16, pp. 350–355.

Kleitz, A., 1991, "Three Probes for Water Droplet Sizing in Wet Steam Turbines," Proceedings of the European Conference on Turbomachinery, Londen, pp. 176–183.

Moore, M. J., and Sieverding, C. H., 1987, "Aerothermodynamic of Low Pressure Steam Turbines and Condensers," Hemisphere, Bristol, PA.

Renner, M., Stetter, H., and Cai, X. S., 1994, "Flow and Wetness Measurements at a Transonic Wind Tunnel with a Slotted Nozzle," Proceedings of the 12th Symposium on Measuring Technique for Transonic and Supersonic Flow in Cascades and Turbomachines, Prague, Czech, pp. 171–177.

Roegener, H., 1960, "Bestimmung der Abdampfnaesse bei Kondensationsturbinen," BWK, Vol. 12, pp. 220–225.

Walter, P. T., et al., 1985, "Wetness and Efficiency Measurement in LP Turbine with an Optical Probe as a Aid to Improving Performance," Joint ASME/AEEE power Generation Conference, Paper No. 85-JPGC-GT-9.

Wang, N. N., 1982, "Naessemessung in Niederdruckturbine mit Lichtsonde," Ph.D. thesis, University of Stuttgart, Germany.

Wang, N. N., and Zheng, G., 1994, "A Theoretical and Experimental Study of the Total Light Scattering Technique for Particle Size Analysis," *Particle and Particle System Characterization*, Vol. 11, pp. 309–314.

Williams, G. H., and Lord, M. J., 1978, "Measurement of Coarse Water Distribution in the LP Cylinder of Operating Steam Turbine," *Proc. Inst of Mechanical Engineers*, Vol. 190, No. 4.

Analysis of Failure Modes Resulting in Stress Corrosion Cracking of 304N Tubing in a High Pressure Heater Desuperheater

D. C. Karg

L. M. E. Svensen

A. W. Ford

Santee Cooper,
1 Riverwood Drive,
Moncks Corner, SC 29461

M. C. Catapano

Powerfect, Inc.,
9 Great Meadow Lane,
E. Hanover, NJ 07936

Santee Cooper (South Carolina Public Service Authority) experienced twenty-three tube failures in a high pressure feedwater heater that was in service less than three years. The tube failures were located at baffles adjacent to both exits of the dual flow desuperheater. Metallurgical analysis of the failed tubes indicated that stress corrosion cracking of the 304N stainless steel was the primary failure mode (Rudin, 1994; Shifler, 1994). The investigation to determine the factors leading to the onset of stress corrosion cracking included analysis of heater acceptance tests, the heater manufacturer's proposal and manufacturing procedures, operational data, eddy current reports, metallurgical reports, and a heater design review for vibration and wet wall potential (formation of condensation on the outside diameter (OD) of the tube prior to the desuperheater exit).

Background

In 1991, Santee Cooper implemented a program to replace seven of the eight original high pressure heaters on their four 290 megawatt generating units at their Winyah Station in Georgetown, South Carolina. The original heater tubes were 70/30 copper nickel. One of the original heaters was replaced in 1980. It is tubed with 304 stainless steel tubing and has not had any failures.

Detailed specification requirements were developed, proposals reviewed and heaters ordered and replaced. The replacement program has been ongoing over the last five years, with the heater replacements prioritized based on the condition of the original heater.

Each unit turbine cycle has six feedwater heaters. For reference, the first high pressure heater after the deaerator is no. 5 and the final heater prior to the boiler is no. 6. The final heater receives cold reheat steam (high pressure turbine exhaust). In this position in the cycle, the inlet steam temperature and available superheat to the no. 6 heater are directly affected by the main steam conditions to the high pressure turbine.

Generating units no. 1 and no. 2 are cooled by a cooling pond, while units no. 3 and no. 4 are cooled by cooling towers. Both cooling systems receive fresh river water for makeup. The subject heater is the no. 6 heater on unit no. 2. It was replaced in November 1991 with 304N stainless steel tubing. The original heater was significantly plugged and frequently failed causing both high pressure heaters to be isolated for repairs. The new heater was to be designed for full load operation with complete bypass of the upstream no. 5 heater since it was also significantly plugged and would not be replaced for 19 months.

At the time of the replacement of the no. 6 heater, the upstream no. 5 heater had 30 percent of its tubes plugged and a 3.5 inch bypass hole cut in the pass partition plate to reduce the tubeside velocity. During the acceptance test of the no. 6 heater, the inlet feedwater temperature was 15°F below design, due to the deteriorated condition of the no. 5 heater. This raised the steam flow in the new heater to 206,081 lbs/hr, or 29 percent over normal design steam flow. The heater manufacturer stated that the heater was designed for a steam overload flow of 269,770 lbs/hr or 68 percent above the normal operating design flow of 160,292 lbm/hr. Overload steam flow is defined as the additional steam loading above normal design flow. The additional loading is caused by a reduction in inlet feedwater temperature generally from a full or partial bypass of an upstream heater.

The heater did not meet the design terminal temperature difference (TTD) of 0.0°F and the design drain cooler approach (DCA) of 10.0°F. Due to the higher steam flow, the heater manufacturer recommended setting the heater water level to 17.2 degrees DCA to meet the design TTD. At this heater level, the heater met the design TTD.

The no. 6 heater was subject to overload steam loading for the first 19 months of service due to the condition of the upstream no. 5 feedwater heater. The no. 5 heater was replaced in June 1993. The number of plugged tubes and size of the bypass hole in the pass partition plate at the time the heater was removed is not available to predict the extent of the overload condition on the no. 6 heater. As stated earlier the no. 6 heater was to be designed for the steam overload associated with complete bypass of the no. 5 heater.

Analysis of Failure and Damage Patterns

The no. 6 heater developed 23 tube failures in August 1994 after less than three years of service. Seven of the failed tubes were pulled for metallurgical analysis, and eddy current analysis (Murdock, 1994) was performed on the remaining tubes.

The tube failures and the majority of tubes indicating outside diameter wall loss by eddy current were located at baffles adjacent to both of the outlets of the dual flow desuperheater. Failed tubes and those indicating greater than 50 percent wall loss by eddy current were plugged. The total tubes plugged were 175 or 17.3 percent.

The single segmental dual flow desuperheater design admits steam into the center of the desuperheater. The steam flow is

Contributed by the Power Division and presented at the 1995 International Joint Power Generation Conference, Minneapolis, MN, October 8–October 12, 1997. Manuscript received by the ASME Headquarters December 20, 1997. Associate Technical Editor: D. Lou.

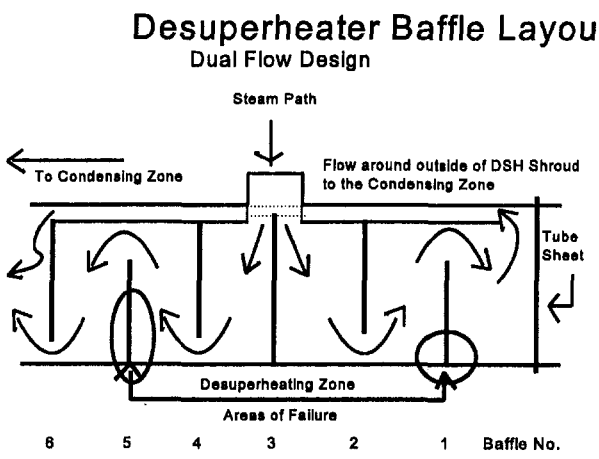

Fig. 1 Layout of desuperheater baffle

divided approximately 50 percent in the direction of the condensing zone and 50 percent in the direction of the tubesheet then into a duct around the desuperheater shroud into the condensing zone (refer to Fig. 1).

The characteristics of the failure pattern, and eddy current indications were as follows (for baffle numbering see Fig. 1):

- All known failure locations, except one, were located at the last desuperheater baffle in the direction of steam flow toward the tubesheet (the second baffle from the center of the desuperheater, and closest baffle to the tubesheet; baffle no. 1).
- The other known failure location was at the second baffle from the center of the desuperheater in the direction of steam flow toward the condensing zone (baffle no. 5).
- The majority of the tube failures were located in the 6 inner rows. The tubes pass through an open window in the second desuperheater (baffle no. 2), therefore having the longest unsupported length (31 inches). This damage pattern is a possible indication of vibration from inadequate design or manufacture (i.e., excessive baffle tube hole sizing).
- Eddy current indicated that approximately 130 of the 1011 tubes had 50 percent or greater OD wall defects at the second baffle from the center of the desuperheater in both directions of flow (baffles no. 1 and 5).
- 92 of the indications were at baffle no. 1. Of these indications, 82 percent were on the tubes with the longest unsupported length in the direction of the tube sheet.
- 37 of the indications were at baffle no. 5. Of these indications, 35 percent were on the tubes with the longest unsupported length in the direction of the condensing zone.
- A portion of the failures and eddy current damage is likely to be a result of collateral damage caused by leaking heater tubes.
- The failures were circumferential cracks at or near the baffles. Pitting was evident on the tube OD, approximately the width of the supporting baffle. Metallurgical analysis found chlorides present in some of the pits (Shifler, 1994).

Failure Mode and Analysis Methods

Metallurgical analysis of the failed tubes indicated stress corrosion cracking as the mode of failure. The analysis revealed evidence of cyclic stress on the tube exterior. The inner surface of the fracture exhibited dimple type rupture indicative of stress overload. The conclusion was that cyclic stress from vibration or rapid thermal cycling assisted by a corrodant such as chlorides propagated crack growth. The combination of elevated temperature, residual stresses, and a corrodant such as chlorides are required for stress corrosion cracking to occur.

Elevated temperature is inherent in the operating environment of the heater. The potential for residual stresses and chloride contamination to occur can result from the manufacture and operation of the heater. Residual stresses can be increased in the manufacturing process of the tubing, depending on the methods of tube straightening and U-bend stress relief. In operation the stresses can be induced by excessive vibration.

Chlorides may exist on the tube OD from the manufacturing process from lubricants, cleaning fluids, and/or the water used during the shell side hydrostatic test. In operation, chlorides can enter the feedwater from condenser tube leaks. The method of chlorides entering the steam side of the heater is unknown, as they should be reduced to insignificant levels in the steam drum. Possibilities are a heater tube leak or carryover with feedwater from the superheat attemperator sprays.

The available information supported vibration in the desuperheater as a major contributor to the tube failures. Santee Cooper contracted a consultant, Powerfect Inc., to assist with vibration analysis, determine the wet wall potential, and provide their opinion on the heater failure modes. The following data was supplied:

1 Heater proposal of the Manufacturer
2 Design drawings of the Manufacturer
3 Failed tube metallurgical reports
4 PEPSE (Minner et al., 1993) simplified design heater performance predictions
5 Heater acceptance tests and low load heater test data
6 Eddy current reports

The PEPSE simplified design data consisted of computer heat balance models to evaluate the potential for wet tube wall at 50 percent unit load from operating test data and predict the vibration potential at normal full load feedwater flow with the upstream no. 5 heater bypassed. The consultant concluded that the tube failures were caused by a combination of contributing factors, including the combined effect of vibration and corrosion from the wet wall condition (Catapano, 1995).

Vibration Analysis. In order to determine the potential for vibration in the desuperheater, the design was checked against industry accepted standards for conservative design. The data

Table 1 Analysis of PEPSE data

No. 6 Feedwater Heater Study	Units	PEPSE prediction Full load @ 290 MWg with No. 5 FWH bypassed	Heater Design @ Full load with No. 5 FWH in service
FW Flow	lbs/hr	1,976,600	1,888,157
FW in Temp.	°F	350.7	404.7
FW out Temp	°F	473.9	476.9
Steam Flow	lbs/hr	271,651	160,292
Steam press.	psia	542.5	549.6
Steam Temp.	°F	626.1	630.0
Saturation Temp	°F	475.5	476.9
Degrees of Superheat	°F	150.6	153.1
Drain Temp.	°F	382.5	391.1
TTD	°F	1.6	0.0
DCA	°F	31.8	10.0

Table 2 Analysis of test data at 50 percent load compared to turbin heat balance at 69 MWg

No. 6 Feedwater Heater Study	Units	Turbine Heat Balance @ 69 MWg	Test Data @ 50% load 143 MWg
FW Flow	lbs/hr	460,000	1,116,297
FW in Temp.	°F	301.7	361.3
FW out Temp	°F	352.9	420.3
Steam Flow	lbs/hr	24,150	78,111
Steam press.	psia	139.7	320.3
Steam Temp.	°F	509.7	455.8
Saturation Temp	°F	352.9	423.4
Degrees of Superheat	°F	156.8	32.4
Drain Temp.	°F	311.7	366.2
TTD	°F	0.0	3.1
DCA	°F	10.0	4.9

utilized for the analysis was at normal full load feedwater flow with the upstream no. 5 heater fully bypassed.

Analysis of the PEPSE data from Table 1 "Full load @ 290 MWg with no. 5 FWH bypassed", indicated that the heater design exceeded safe conservative design limits for vibration at full load feedwater flow with the no. 5 heater fully bypassed. The consultant concluded that the vibration could have increased the stress level in the tubes and contributed to stress corrosion cracking.

Wet Tube Wall Analysis. A second contributing factor to the tube failures was a potential for wet tube wall in the desuperheater at low load with low superheat temperatures. The heater receives cold reheat steam. During low load operation, the boiler is not always capable of achieving 1000°F main steam temperatures typically indicated on the turbine design heat balances. The feedwater heater manufacturer utilized turbine cycle heat balance data at low load (69 MWg) for their wet wall design margin (Table 2).

It is common for utility boilers to occasionally operate well below 1000°F, especially at low load. As the main steam temperature is reduced, the cold reheat temperature and available superheat is also reduced to the no. 6 heater. This increases the potential for condensation to form prior to desuperheater exit.

Analysis of actual test data at 50 percent load, Table 2 "Test Data @ 50 percent load 143 MWg", indicated that wet tube wall condition would occur prior to the exit of the desuperheater at this condition with abnormally low superheat temperature. An additional concern identified by the consultant was a "dead zone" in the desuperheater near baffle no. 1. The area could allow condensation to accumulate during start-up or low load and contribute to the concentration of chlorides as the condensation boils off as load is increased.

Condensation can form on the outer tube wall at low load and alternately dry as load increases, increasing the potential for very low levels of chlorides to reach higher concentrates. This condition increases the potential for crevice corrosion in the tube to baffle interface, leading to pitting and the concentration of chlorides to accumulate in the pits.

Some of the possible sources of chlorides on the steam side of the heater were discussed earlier. Santee Cooper is continuing to investigate the possibility that the chlorides could have contaminated the steam side of the heater from the shell side hydrostatic test during manufacture of the heater. The removal and inspection of tube samples at least the length of the desuperheater would be required. This would verify if the pitting is widespread rather than isolated to baffles at both exits of the desuperheater, consistent with the wet tube wall condition and suggested by eddy current indications. If the pitting is widespread, the possibility of chloride contamination from water utilized for the hydrostatic test would be further investigated.

Conclusion

A combination of vibration at full load with the upstream heater bypassed (increasing tube stress levels), coupled with the potential for pitting corrosion due to wet tube wall at low load, contributed to the potential for tube failures. Additionally, an investigation is in progress to determine if manufacturing methods contributed to the failures. Chloride contamination from the shell side hydrostatic test or oversized tube holes contributing to vibration are possibilities.

In future heater design reviews, consideration should be given to having the vibration and wet wall analysis of the manufacturer checked by a consultant. Utilities should include potential operating conditions such as operation below design steam temperatures in the heater bid specifications. Manufacturing quality control in regard to tube hole manufacturing tolerances, water quality used for hydrostatic tests, and overall quality of work should also be monitored closely.

The future reliability and design of the no. 6 heater are a concern. As well, two other heaters of the same design and manufacturer were purchased prior to the problems with this heater. One of the heaters was installed on unit 3 in May 1994. The second was purchased for unit 4 and has not yet been installed. A detailed inspection of the shell side of the existing unit 2 no. 6 heater could determine if a design or operating modification is required on these heaters.

With the potential for overload steam conditions reduced with the installation of the new no. 5 heater, Santee Cooper is considering replacing the unit 2 no. 6 heater with the heater purchased for unit 4.

If the existing no. 6 heater is replaced, a "post mortem" inspection will be conducted to determine if the heaters of this design require modification. The inspection will also allow Santee Cooper to evaluate the potential modes of failure that have been discussed in this document.

References

Catapano, M. C., 1995, "Winyah Generating Station Unit No. 2 Feedwater Heater No. 6," technical report, Powerfect Power Plant Heat Transfer Consultants Inc., East Hanover, NJ.

Minner, G. L., et al., 1993, PEPSE—Performance Evaluation of Power Systems Efficiencies, Software Version 61, Scientech, Idaho Falls, ID.

Murdock, K., 1994, "Unit #2 Feedwater Heater #6," Eddy Current Inspection Report No. 455-40178-03, Law Engineering Industrial Services, Charlotte, NC.

Rudin, S. B., 1994, "Metallurgical Analysis of Feedwater Heater Tube Failures," Metallurgical Reports No. 94-91395 and 94-91899, Midstates Analytical Laboratories, Inc., Tulsa, OK.

Shifler, D. A., 1994, "Winyah Generating Station Unit No. 2–No. 6 High Pressure Heater Tube," Metallurgical Report M-2821, Powell Laboratories LTD, Baltimore, MD.

D. R. Hounslow

W. Grindley

Aero & Industrial Technology Ltd.,
Burnley, United Kingdom

R. M. Loughlin

J. Daly

Dresser Rand,
Wellsville, NY 14895

The Development of a Combustion System for a 110 MW CAES Plant

The use of stored energy systems is receiving increased attention for power generation. Alabama Electric Co-operative (AEC) have installed a 110 MW Compressed Air Energy Storage (CAES) plant at McIntosh, Alabama. The plant employs tandem high and low-pressure fired expanders with the high-pressure combustors operating at 44 atm and the low-pressure units at 15 atm. Both are designed to operate with natural gas, or on No. 2 fuel oil, as a standby fuel. This paper describes the development of both the high and low-pressure combustors for this unique application, the testing of prototypes at simulated conditions at up to 8 atm using customized test rigs, and the definition of a design for application to the plant. Problems encountered during the first three years of operation are described and the solutions to overcome these are also presented.

Introduction

Early power generation load management systems such as consumer incentives for the use of off-peak power and the use of contract clauses with customers to disconnect part or all of the load during peak hours, proved in the long run to be inadequate.

Subsequent solutions included the use of fast response combustion turbines, and for load leveling, the use of pumped hydro power stations, where these were practical.

In geographically flat regions and those with limited water and real estate resources, the Compressed Air Energy Storage (CAES) system offers a further potential solution for load leveling.

The first CAES plant in the United States is now in operation for AEC in McIntosh, Alabama. The plant uses relatively inexpensive off-peak energy to drive a motor to compress air, which is stored in a solution mined underground cavity in the McIntosh salt dome. When peaking or intermediate power is needed, the stored air is withdrawn, preheated in a recuperator, heated further by burning fuel, and expanded through high and low-pressure expansion turbines, which drive a generator.

AEC contracted with the joint venture of Gibbs and Hill and Harbert International for the design and construction of the McIntosh CAES plant. Dresser Rand, Wellsville, was selected as the supplier of the turbomachinery, with AIT, Burnley, providing the high and low-pressure combustion systems.

Plant Description

Details of the plant and its form of operation are given in [1–3]. The overall plant is shown schematically in Fig. 1.

The nominal utilization of the plant was specified at some 26 weeks each year in two major periods covering the peaks caused by the winter heating and summer air conditioning requirements. A typical weekly plant operating cycle would involve five days of power generation in one or two daily periods for up to 10 hours/day with overnight compression cycles of some 10 hours/day. On the remaining days the plant would be operated in compression for up to 30 hours to return the cavern to full pressure (some 74 atm). At full load some 75 percent of the power is developed in the LP expander with the HP contributing the remaining 25 percent.

The turbomachinery includes a three-body compressor train, a motor/generator, and two expanders. The expanders and compressors are connected to the motor/generator by clutches.

During off-peak periods the high-pressure combustors on the HP expander are fired to bring the motor/generator to synchronous speed to initiate the compression cycle and air is then pumped into the cavern. When peaking power is required, the expanders and generator are brought to synchronous speed by firing the HP combustors. The LP combustors are subsequently fired and both expanders are used at all power conditions from 10 MW up to the plant maximum of 110 MW. During periods of inactivity, when the plant is neither in the compression or power generating modes, the turbomachinery is maintained at readiness through the use of a low-level hot airflow at some 370°C produced by a small standby combustor. This is fired automatically when the HP expander casing temperature falls below 260°C and remains operative until the casing reaches 370°C or the plant is restarted.

The plant incorporates a recuperator, which recovers waste heat from the LP expander exhaust to preheat cavern air. This heat recovery achieves a 25 percent reduction in plant fuel consumption and heat rate relative to operation without a recuperator.

The expander train incorporates a steam turbine derivative high-pressure expander with a combustion firing temperature of 811 K and a newly developed LP expander with a nominal firing temperature of 1144 K.

Two high-pressure combustors feed directly into the inlet casing of the HP expander. On the LP expander eight combustors fed in a reverse flow configuration discharge through eight cast transition ducts to feed directly into the first-stage nozzles of the LP expander.

Combustor Operating Conditions

To maximize reliability and to use proven components with minimum modification, conservative limits were chosen for the expander section. With respect to the combustors, the target NO_x levels allowed for the use of conventional technology. The resultant HP and LP combustor conditions are detailed in Table 1 for operation with the recuperator operative and bypassed.

Contributed by the International Gas Turbine Institute and presented at the 40th International Gas Turbine and Aeroengine Congress and Exhibition, Houston, Texas, June 5–8, 1995. Manuscript received by the International Gas Turbine Institute February 27, 1995. Paper No. 95-GT-312. Associate Technical Editor: C. J. Russo.

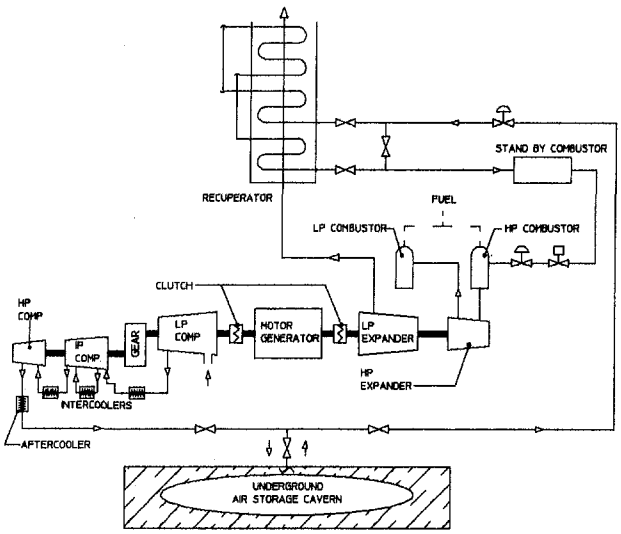

Fig. 1 CAES plant schematic

Fuels. The CAES plant was designed to operate as a dual fuel unit with operation on natural gas as the prime fuel and No. 2 fuel oil as a stand-by fuel. Excluding commissioning and proving trials, operation for power generation has almost exclusively involved the use of natural gas. The specified plant natural gas properties are compared in Table 2 with those of the typical analysis of the natural gas used during the combustor development programme on the shop tests at the Combustion Technology Centre (CTC, Burnley). Gas oil was used in the shop tests with similar properties to the specified No. 2 fuel oil.

Table 1 Nominal operating conditions specified for the CAES combustors—natural gas

	RECUPERATOR		RECUPERATOR BY-PASSED	
	110 MW	10 MW	95 MW	10 MW
HP COMBUSTION SYSTEM				
Air Mass Flow kg/s	154.6	36.2	170.0	40.6
Inlet Temp. K	558	626	308	308
Outlet Temp. K	811	811	563	563
Inlet Pressure atm	43.9	10.2	40.2	9.6
AFR	160.8	219.1	158.7	159.8
LP COMBUSTION SYSTEM				
Gas Mass Flow kg/s	155.6	36.4	171.1	40.9
Inlet Temp. K	654	632	463	459
Oulet Temp. K	114.4	852	954	898
Inlet Pressure atm	15.44	3.06	15.5	3.54
AFR	79.9	192.6	79.9	92.4

Table 2 Gaseous fuel properties

	CUSTOMER SPECIF.	A I T NATURAL GAS
CONSTITUENTS % BY VOLUME:		
Methane	90.00	94.36
Ethane	5.00	4.22
Propane	0	0.31
Butane	0	0.03
Pentane	0	0.01
Carbon Dioxide	0	0.46
Nitrogen	5.00	0.61
ULTIMATE % BY WEIGHT:		
Hydrogen	22.68	24.12
Carbon	69.26	73.92
Nitrogen	8.06	1.09
Oxygen	0	0.87
Specific Gravity (rel to air)	0.600	0.584
Density at 60°F and 30 in Hg (lb/ft^3)	0.046	0.0447
NET CALORIFIC VALUES:		
Btu/cu ft at 60°F and 30 in Hg	902.5	936.5
Btu/lb	19684	20952
Equivalent Formula	$C_1H_{3.9}$	$C_1H_{3.9}$
Mean Molecular Wt	17.34	16.94
Gas Constant	160.3	164.2
Stoichiometric Air Fuel Ratio	15.69/1	16.76/1

Shop Test Rig Operating Conditions. The mass flow available in the test laboratories of CTC, Burnley, is 10.9 kg/s at a pressure of about 8 atm. All shop development tests on both the HP and LP combustors were carried out at the plant values of air inlet and outlet temperatures, with the air mass flow to the combustors reduced in proportion to the maximum inlet pressure attainable on the test rig. In this way the combustors were operated on the shop tests at the design value of the outer casing Mach number and the design combustion liner percentage pressure loss. This method of engine simulation has been proven over many years and is widely accepted in the gas turbine industry for the prediction of most aspects of combustor performance. A comparison of the engine and test rig nominal conditions is given in Table 3 for Natural Gas Operation.

Combustor Test Rig. The test rig arrangement is shown in Fig. 2. This shows a plan view, the air inlet feed pipe being situated on top of the air inlet casing on the shop test site.

The air inlet casing was fitted with a perforated distribution liner to provide uniform flow conditions to the combustor/casing rear annulus.

At its upstream end the combustor was located co-axially with the casing via four suspension pins attached to a flow shield, which in turn was mounted to the casing using three suspension pins. The downstream end of the combustor was located in a split seal ring fitted to the transition duct upstream support and a closure plate was fitted to the casing upstream flange onto which the fuel injector was mounted.

From the combustor discharge a circular to 45 deg sector transition duct directed the exhaust gas to the water-cooled exhaust drum. This was fitted with a five-point thermocouple rake and traverse mechanism to measure the exhaust gas temperature distribution. Downstream of the exhaust drum the water-cooled ducting incorporated an exhaust gas sampler.

Table 3 Rig and plant operating conditions—gaseous fuel

		BASE RECUPERATOR				BY-PASS RECUPERATOR			
		110 MW		10 MW		95 MW		10 MW	
		RIG	PLANT	RIG	PLANT	RIG	PLANT	RIG	PLANT
HP COMBUSTOR									
AIR FLOW	kg/s	10.9	77.3	10.9	18.1	10.9	85	10.9	20.3
INLET TEMPERATURE	K	558	558	626	626	308	308	308	308
EXIT TEMPERATURE	K	811	811	811	811	563	563	563	563
INLET PRESSURE	atm	6.19	43.9	6.12	10.2	5.17	40.2	5.17	9.6
LP COMBUSTOR									
AIR FLOW	kg/s	10.2	19.4	4.5	4.5	10.9	21.3	5.1	5.1
INLET TEMPERATURE	K	654	654	632	632	463	463	459	459
EXIT TEMPERATURE	K	1144	1144	852	852	954	954	898	898
INLET PRESSURE	atm	8.16	15.44	3.06	3.06	7.96	15.5	3.54	3.54

Thus, in the case of the LP combustor, the development test rig arrangement simulated the engine configuration, in terms of aerodynamics, location, and support.

In order to use the same test rig for the HP combustor development, minor compromises were accepted. None of these were expected to influence the measured performance. The differences from the engine were as follows:

- Air entry on the plant is via the casing side and the HP combustor exit flow discharges directly into the HP expander, not via a transition duct.
- The HP combustor discharge diameter on the plant is 12 in. in diameter, compared with 10 in. on the shop test rig and the rear location is different in detail to the engine.

For tests on the HP combustors the air supply was unvitiated. In the case of the LP, an in-line rig standard preheater was included to simulate the vitiation from the HP.

Shop Test Rig Instrumentation. The combustor exhaust gas composition was determined from gas samples taken from hot water cooled multipoint gas sampling rakes sited in the rig exhaust pipework. The gas sample was transferred to analytical equipment via electrically heated lines, the sample temperature being maintained in accordance with EPA requirements. The composition of the gas was determined by means of on-line infrared analyzers for carbon monoxide and carbon dioxide, a flame ionization detector for unburned hydrocarbons and a chemiluminescence analyzer for NO_x. Smoke levels were determined by the SAE filtration technique. Humidity was determined using a Dew Point meter.

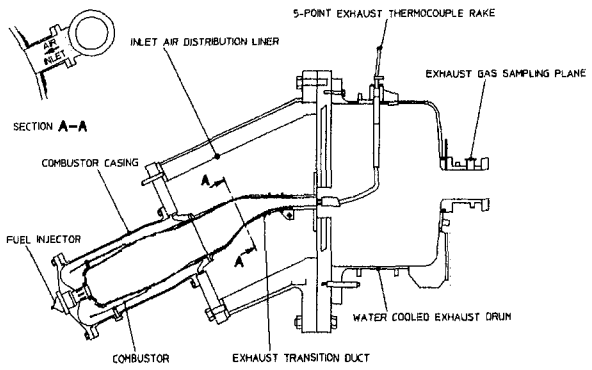

Fig. 2 Test rig arrangement

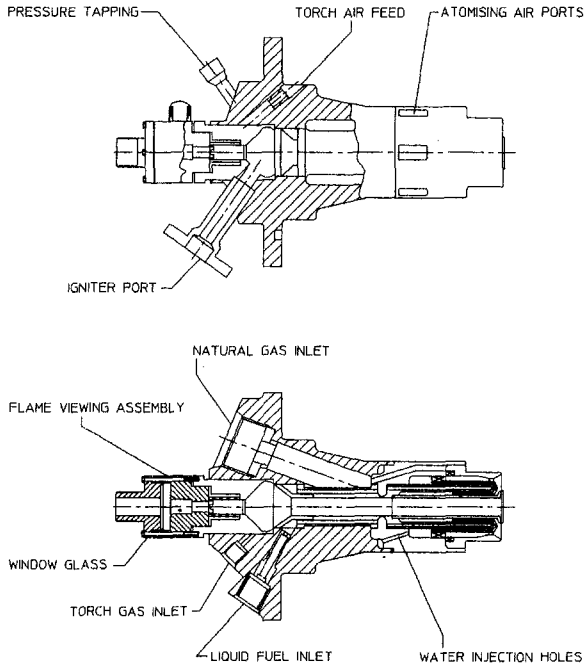

Fig. 3 Fuel injector

For the measurement of exhaust gas temperature, an exhaust thermocouple rake comprised of five chromel/alumel thermocouples positioned on centers of equal area within the 45 deg sector of the transition duct exit plane was used. The thermocouple tips incorporated double radiation shields to prevent heat loss to surrounding cold surfaces. Exhaust traverses were effected by moving the rake by remote control through 16 angular stations of equal pitch.

Combustor wall temperatures were determined by coating the external surfaces with temperature-sensitive paint (Thermindex OG6).

Combustor pressure loss measurements were obtained by recording levels of inlet and exit static pressure. Loss in total pressure was then derived using calculated mean values for inlet and exit kinetic pressures based upon recorded inlet and exit temperatures and metered air and fuel flows. Inlet static pressure was measured at tappings on the combustor casing wall and exhaust static pressure from a tapping in the upstream flange of the water cooled exhaust traverse drum.

Combustor gas pressure oscillations were monitored from a pressure tapping in the fuel injector pilot zone (Fig. 3). This tapping was connected by a short length (approximately 230 mm) of 2.4 mm internal diameter tube to a piezo-electric transducer. The transducer output was fed via an amplifier to a wave form analyzer, which processed the signal to provide measurements of the dominant frequency and amplitude, together with a frequency/amplitude spectrum analysis.

Design Philosophy

The types of combustor that can be considered for the CAES application are silo, annular, or individual pipe chambers. In this application for the LP combustor eight individual pipe chambers were chosen, to be equispaced around the expander, to give a greater control of the outlet temperature distribution, to give reduced weight for easy maintenance, and to allow for comprehensive rig testing before delivery. Two combustors were selected for the HP expander for similar reasons. As the HP combustors operate at three times the pressure of the LP with four times the mass flow per combustor, the diameters of the two units were therefore similar, permitting the use of a common test rig.

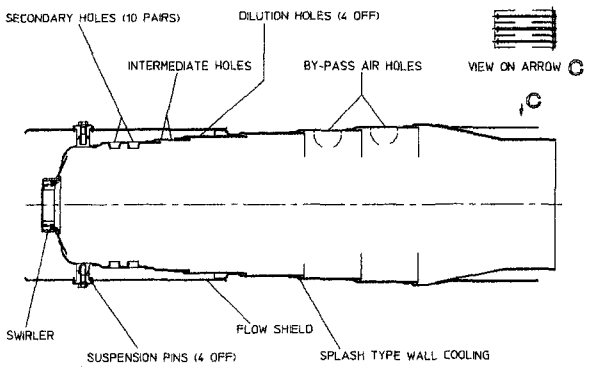

Fig. 4 HP combustor

Fuel Injectors. A common design of dual fuel injector was selected for both the HP and LP combustors. The principal difference was that the HP fuel injector had a smaller tip diameter to match the smaller diameter of the HP combustor head. Each combustor had one fuel injector.

The fuel injector design was such that it combined the functions of liquid and gaseous main fuel injection, a gas-only torch igniter, flame viewing, and water injection. Figure 3 illustrates the internal geometry and main features. Little development was required on the fuel injectors and the only change made during the rig test program was to increase the torch pilot zone volume and provide a swirl component to the air feed.

Combustors. The designs of the HP and LP combustors are shown in Figs. 4 and 5.

The air feed to the HP unit was by way of a flanged connection on the side of the air casing. The feed to each of the eight LP units was fully reversed with a common feed on the LP expander. The hot exhaust gas from each of the eight LP combustor liners was fed into eight circular to sector nozzle transition ducts ahead of the LP expander first-stage nozzles. The lower mean outlet temperature of the HP combustors allowed the outlet gases to discharge directly into the expander plenum casing ahead of the first-stage nozzles without the need for transition ducts. Each LP combustor liner features a detachable flow shield for air flow management and the discharge from the combustion liner fits into the appropriate nozzle transition by means of a combined gripper and piston ring, which gives centralization, sealing, and accommodation for differential expansion. The nozzle transition duct is suspended from the air casing by a centralizing pin and two pins on a chordal axis to allow for the differential expansion. The flow shield and combustion liner arrangement ensures that virtually all the airflow for combustion passes around the dome profile with minimal pressure loss and presents an unbiased flow to the combustion liner holing.

Both the HP and LP combustor liners were manufactured from 2.00-mm-thick Hastalloy X.

In the evolved version of the HP combustion liner, the primary zone was of a conventional design with an axial swirler, midflare cooling, and ten pairs of plunged secondary holes positioned in-line and equispaced. Additional flow entered the liner head through two rows of 40 plain intermediate holes and a row of four plain dilution holes. Since the HP unit was to operate at relatively weak air fuel ratios through its operational range (Table 1) only about one third of the total combustor airflow entered the head. The remaining two thirds was admitted downstream through twelve plunged holes and in the form of cooling air.

The LP combustion liner also had an axial swirler/secondary hole primary zone, with further air added downstream through plain intermediate and dilution holes. Approximately 75 percent of the total air was admitted upstream of the flow shield location and the remaining 25 percent was used to cool the rear sections.

The LP combustion liner head differed in detail from that of the HP unit in that there was a miniflare skirt immediately outboard of the swirler, no midflare cooling, and an array of external cooling fins to reduce local metal temperatures.

Shop Test Results and Discussions

The early combustion testing of the initial design of both HP and LP combustors demonstrated a generally satisfactory level of performance with regard to most items, including exhaust emissions and exhaust temperature distribution. Metal temperatures when operating on natural gas were also acceptable. However, the following three specific problems were identified:

- When operating with liquid fuel, difficulties were experienced on both the HP and LP combustors with ignition of the main fuel by the torch flame.
- Metal temperatures of the HP combustor operating on liquid fuel were above the target level.
- Combustion generated pressure pulsations, of potentially damaging levels, were experienced on the LP combustor when operating on natural gas with vitiated inlet air, operation with unvitiated air being satisfactory.

The ignition problem was readily resolved by increasing the torch pilot zone volume and adding a swirl component to the torch air flow to produce a strong flame extending more than 250 mm beyond the torch tube exit.

The metal temperature and pressure pulsation problems, however, proved more persistent and required development to achieve a performance level suitable for the production of plant standard hardware.

The basic philosophy of the development was to achieve a more positive primary zone flow pattern by incorporating an axial swirler and plunged hole secondary air admission, to produce a strong toroidal recirculation. Variations in the ratio of swirler/secondary hole air were investigated to produce the optimum performance. In the case of the LP combustor, detailed changes were made to the method of cooling air admission, in the combustor head region, in order to achieve acceptable metal temperatures together with freedom from pressure pulsations.

Emissions. The emissions levels from the HP combustor, with unvitiated inlet air, were readily and directly measurable. However, in the case of the LP combustor the emissions were, to an extent, governed by the emissions from the in-line combustion air preheater used to simulate the efflux from the HP expander. This preheater was significantly less efficient than the developed HP and LP combustors. Table 4 shows the CO, UHC, and NO_x emission levels from both HP and LP combustors. These results show that the LP combustor was very efficient and able to burn out most of the CO and UHC from the

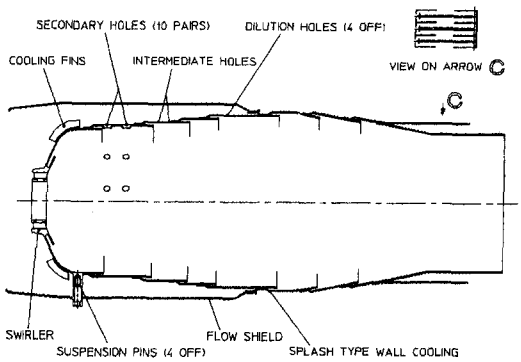

Fig. 5 LP combustor

Table 4 Combustion emissions at rig simulated 110 MW base recuperator conditions

	NATURAL GAS				LIQUID FUEL			
	COMBUSTION EFFICIENCY (1) %	CO ppmv	UHC ppmv	NO_x (2) ppmv	COMBUSTION EFFICIENCY (1) %	CO	UHC	NO_x (2) ppmv
HP	99.95	5.8	3.0	65.5	99.93	15.7	1.2	78.6
RIG PREHEATER	99.41	117	18	-	99.55	97	17	-
LP	99.96	12.2	2.4	35.5	99.97	13.4	0.7	73.3
VALUES ESTIMATED FOR PLANT OPERATION	-	12.2	2.4	101	-	13.4	0.7	152

(1) BY GAS ANALYSIS

(2) NET VALUES CALCULATED FOR PLANT OPERATION

rig preheater. Thus, when operating on the plant, CO and UHC levels less than those measured on the rig could be expected, as:

- The HP combustor produced less CO and UHC's than the rig preheater.
- The additional pressure on the plant compared to that for the shop tests would provide a more amicable combustion environment.

The NO_x values quoted are those measured on the test rig and in the case of the LP combustor, the net value obtained after subtracting the contribution from the rig preheater. The values corrected to plant operating pressures have been obtained by scaling, using the plant to rig pressure ratio to the exponent 0.5 as generally accepted in the industry. Estimated plant emission levels of NO_x have been obtained by summing the contribution from both the HP and LP combustors since, unlike CO and UHC's the NO_x once formed in the HP combustor is likely to pass through the LP combustor unchanged, without significantly influencing NO_x generation in the LP combustor itself. Additionally, the performance at the minimum load conditions of 10 MW was good, with the combustion efficiency of the HP unit in excess of 99.94 percent on both fuels.

Tests with water addition at a rate equivalent to 50 percent of the fuel flow showed that a 50 percent reduction in NO_x could be expected on the plant and the emissions of CO and UHC would also be within the specified limits for liquid fuel operation (Table 5). When using natural gas (Table 6), the water injection rate on the LP combustor was limited to 25 percent of the fuel flow due to pressure pulsations.

Exhaust smoke at the rig operating conditions is given in Table 7. The increase in pressure to the true plant 110 MW

Table 5 Effect of water injection on emissions simulated 110 MW base recuperator condition—liquid fuel

		COMBUSTION EFFICIENCY (1) %	CO ppmv	HC ppmv	NO_x ppmv	NO_x (NET) ppmv	NET NO_x CORRECTED TO PLANT PRESSURE ppmv
HP	NO WATER	99.93	15.7	1.2	28.3	-	78.6
	WATER ADDED (50% FUEL FLOW)	99.95	11.8	0	16.0	-	44.9
LP	NO WATER	99.97	13.4	0.7	66.5	52.5	73.3
	WATER ADDED (50% FUEL FLOW)	99.94	25.1	4.1	34.0	20.0	27.9
ESTIMATED PLANT VALUES	NO WATER	-	13.4	0.7	-	-	151.9
	WATER ADDED (AS ABOVE)	-	25.1	4.1	-	-	72.8
TARGET VALUES WITH WATER (50%)	HP	-	13.8	1.6	-	-	-
	LP	-	31.4	3.4			
SPECIFIED PLANT VALUES WITH WATER (50%)		-	50	-	-	-	90.5

(1) BY GAS ANALYSIS

Table 6 Effect of water injection on emissions simulated 110 MW base recuperator condition—natural gas

		COMBUSTION EFFICIENCY (1) %	CO ppmv	HC ppmv	NO_x ppmv	NO_x (NET) ppmv	NET NO_x CORRECTED TO PLANT PRESSURE ppmv
HP	NO WATER	99.95	5.8	3.0	24.0	-	65.5
	WATER ADDED (50% FUEL FLOW)	99.64	57.3	16.5	10.0	-	27.3
LP	NO WATER	99.96	12.2	2.4	39.5	25.5	35.5
	WATER ADDED (25% FUEL FLOW)	99.97	13.0	1.5	34.0	20.0	27.8
ESTIMATED PLANT VALUES	NO WATER	-	12.2	2.4	-	-	101.0
	WATER ADDED (AS ABOVE)	-	13.0	1.5	-	-	55.1
TARGET VALUES WITH WATER (50%)	HP	-	13.8	1.6	-	-	-
	LP	-	31.5	3.6			
SPECIFIED PLANT VALUES WITH WATER (50%)		-	50	-	-	-	64

(1) BY GAS ANALYSIS

Table 7 Shop test smoke S.A.E. numbers at simulated 110 MW base recuperator conditions

	NATURAL GAS	LIQUID FUEL
HP	4	14
LP	5	24
RIG PREHEATER	18	18

operating pressures was not expected to result in visible smoke when using natural gas. With liquid fuel the situation was considered borderline and needed to be evaluated on the plant.

Metal Temperatures. With natural gas the HP combustor was cool over its entire length with peak temperatures of between 695°C and 814°C recorded in the primary zone, using thermal paint, as shown in Fig. 6. Operation on gas oil fuel showed an increase up to 860°C.

The final development standard of the LP combustor did not include the midflare cooling used on the head of the HP unit since there was evidence that air admission in this region tended to provoke dynamic pressure pulsations when operating on natural gas. The omission of the midflare cooling led to higher metal temperature on the head, which was successfully reduced by the use of cooling fins to improve the external heat transfer. With natural gas local peak temperatures in the range 814°C–860°C occurred on the primary zone walls. With liquid fuel the increase was confined to only local regions exceeding 860°C.

Shop Development Rig Performance Summary

The shop test program (some 100 test hours) showed that:

- CO, UHC, and NO_x emissions levels would be within the specified targets and that NO_x could be reduced by 50 percent by water addition.
- The co-axial torch within the injectors gave a satisfactory ignition performance and the system weak extinction limits for natural gas operation of some 1001/1 and 800/1 for the HP and LP units exceeded requirements more than fourfold. The HP on liquid fuel gave a weak extinction of 2700/1.
- The exhaust temperature distributions from both the HP and LP combustors were within the targets specified.
- The metal temperatures on natural gas were generally within the target requirements and when using liquid fuel

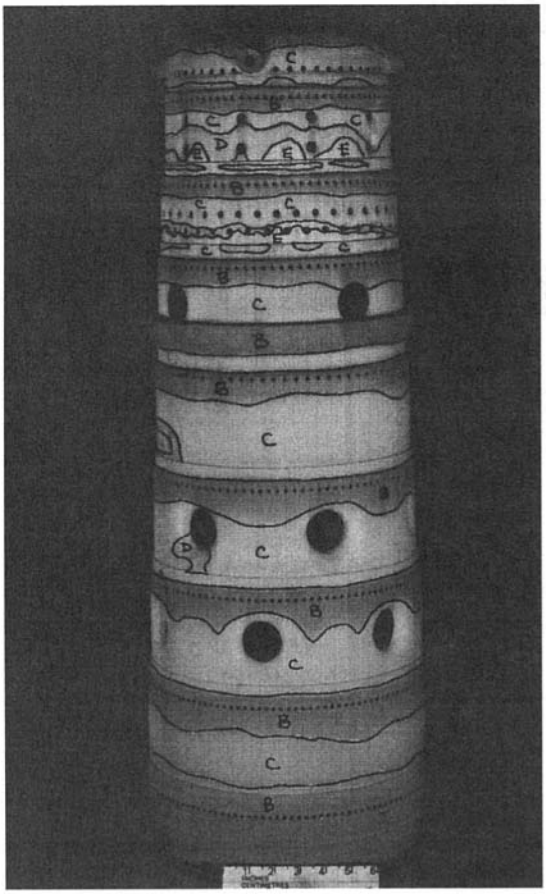

KEY °C

A	BELOW	-	441
B	441	-	515
C	515	-	542
D	542	-	695
E	695	-	814
F	814	-	860
G	ABOVE	-	860

Fig. 6 HP combustor paint test

the increase in metal temperatures would allow for standby use.

Plant Operating Experience

As the Alabama CAES plant is the first of its type in the USA and the cycle and mode of operation is different to conventional gas turbines, there was an initial period of trials, in addition to the normal periods of power generation into the grid. During the first year of operation the combustors logged over 1000 hours of operation but more importantly were subject to over 1000 start/stop cycles, equivalent to over 2 years duty. On occasions the combustors were subject to up to 10 cycles in one day and the need to provide data and generate power limited access to the combustors for routine inspection.

At that stage of evolution of the plant there were three areas of concern. The first was a recurring blockage of the liquid fuel passages on both the HP and LP fuel injectors, the second was a higher than expected smoke footprint, as measured using the Ringelmann technique, when operating on liquid fuel and the third was a mechanical failure of the HP combustors after some 800 cycles.

The fuel injector blockage highlights a problem specific to CAES plants. As the turbine is not coupled to the compressor, the ability to forward purge the liquid fuel after shutdown or during fuel transfer is limited. Initially only a low-pressure purge can be used in order to minimise the drainage of fuel into the combustor, thus limiting over temperature excursions. This is exacerbated during trip shutdown when the motive airflow has to be rapidly removed to prevent overspeeding the expander. Additionally the thermal mass of the plant can result in high soak temperatures in the fuel galleries causing fuel degradation and consequently blockage. The initial purge system for both HP and LP fuel injectors was obtained from potentially high temperature sources between the recuperator outflow and the HP combustor for the HP injector, and from the HP combustor discharge for the LP injectors. The purge system was subsequently upgraded to:

(*a*) Provide a cool source of air, directly from the cavern.
(*b*) Introduce a two-stage purge to allow for an initially low flow rate to limit temperature excursions, with a higher flow rate after flame extinction.

These modifications to the purge procedure have substantially eliminated the earlier blockage problems.

With regard to exhaust smoke, the initial plant combustors, as anticipated and as predicted from the shop tests, gave a clean exhaust on natural gas. On liquid fuel, however, the increase from the shop test pressure of 6.12 atm to the 110 MW plant pressure of 43.9 atm gave a much higher increase in exhaust smoke levels than expected, with opacity levels well in excess of 40 percent (target levels 20 percent).

Some benefit was seen by introducing an air feed to the HP injectors. This did not totally solve the problem and a decision was taken to carry out shop development to improve the HP combustor smoke footprint. By significantly weakening the primary zone, the exhaust smoke of the HP was found to be virtually eliminated, as can be seen from the plant test data, Table 8. On these tests the plant emissions were checked for full load smoke, with both HP and LP combustors fired by natural gas, with both fired by liquid fuel and finally with both options of HP gas/LP liquid and HP liquid/LP gas.

As the results show relatively smoke-free operation on natural gas and a similar level with the HP on liquid fuel and the LP on natural gas, it was concluded that the LP combustor was now the main contributor. However, the target levels had not yet been met for liquid fuel operation.

In the light of shop tests on the LP combustor under vitiated conditions, where pressure pulsations could easily be a problem, it was decided that combustor modifications to the LP in line with those carried out on the HP should not be tried. The plant exhaust was finally cleared by the introduction of a manganese fuel additive. Current manganese concentrations are set at some 50–65 ppm by weight in the fuel. The results with the manganese additive are given in Table 9.

The failure of the original HP combustors occurred at the junction of the flare and primary zone wall, in the region of the

Table 8 Plant exhaust smoke emissions with differing fueling (values quoted are exhaust stack percent opacity readings)

		HP COMBUSTOR	
		LIQUID FUEL	NATURAL GAS
LP COMBUSTOR	LIQUID FUEL	40	35
	NATURAL GAS	5 - 10	CLEAR

Table 9 Plant exhaust smoke emission with manganese-based fuel additive (values quoted are exhaust stack percent opacity readings) (liquid fuel to both HP and LP)

POWER RATING	ADDITIVE TO:-		
	HP/LP	LP ONLY	HP ONLY
100 MW	10 → 15	≤ 20	N.A.
75 MW	10	15	45 - 50
50 MW	10	15	30 - 35
30 MW	10 → 15	10 → 15	15 - 20

NOTE: SMOKE EMISSIONS WITHOUT ADDITIVES ARE SIMILAR TO "HP ONLY"

support pins, when most of the operation had been using natural gas as fuel. The metal temperatures in the region of failure were low, as indicated by both shop and plant thermal paint tests. Finite element stress and thermal analysis indicated that the problem may have been caused by the method of restraint of the combustion liner within the flow shield, thermal bending stress concentrations around the row of holes at the flare edge, and the need to use thicker than normal material for the flares and liner walls for operation at the full-load pressures of 43.9 atm.

The HP combustors were redesigned to reduce the restraint and rigidity of the head, eliminate the flare edge holes, and further reduce metal temperatures. Finite element stress plots of the original and redesigned combustors are shown in Fig. 7. With the redesigned units re-installed, the plant showed initially satisfactory operation but subsequently indicated a propensity for distress in the same region.

Further modifications to improve cooling in the head region by the introduction of a machined flow shield with a narrower annulus to give increased annulus velocities and external heat transfer was predicted to give ultralow temperatures. These were reproduced on the shop test rig. This philosophy was also incorporated into the LP combustors.

On re-build into the plant a modified HP and two modified LP combustors were fully instrumented with thermocouples to measure metal temperature at strategic points. Figures 8 and 9 give the thermocouple locations for the HP and LP, respectively. These have provided the insight into the basic cause for the HP combustor failure.

The metal temperatures of the HP combustor are now very low during steady-state running, Table 10, but exhibit temperature excursions during trips and occasionally on normal plant shut down on both fuels. The metal temperatures for the LP are higher, in keeping with the higher gas inlet and firing temperatures but are well within the target levels at steady state, Table 11.

Again, they occasionally exhibit temperature excursions during trips and normal shut downs. A typical example of an early temperature excursion during trip from 27 MW indicated that cooling skirt temperatures could rise from a steady static level of less than 427°C to 685°C on the LP within 20 seconds of the trip, with an even greater rise on the HP from some 427°C to 724°C.

The cooling skirt, sited at the junction between the combustor head and the combustor liner barrel, provides the starting film for cooling the liner wall and is in the region of the failure on the HP. The rapid rise in temperature of the skirt indicates posttrip combustion localized within the primary zone during a period when the cooling air film is shut down. Distortion of

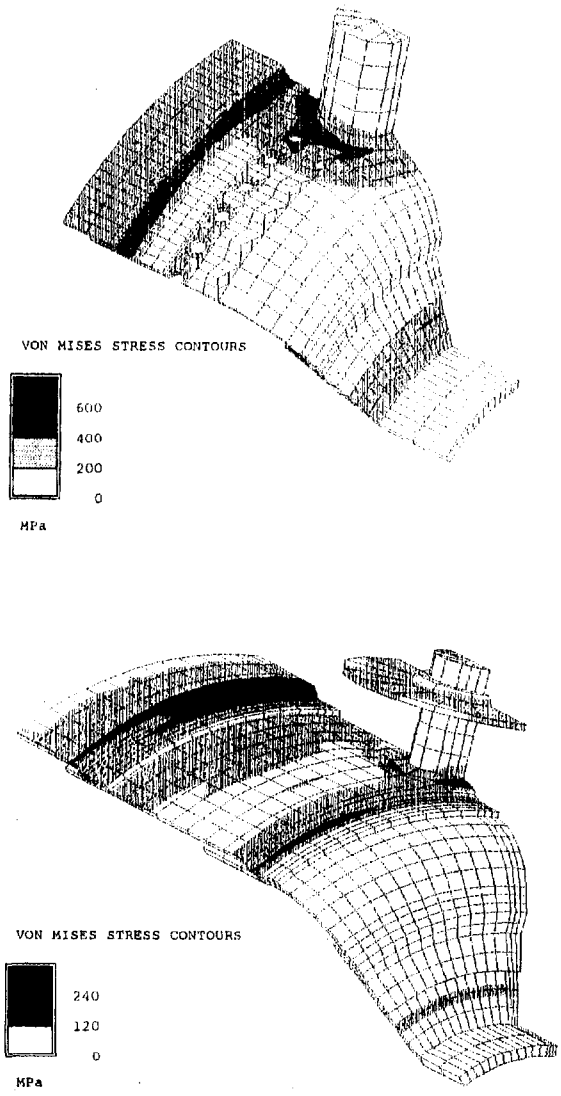

Fig. 7 Stress profiles for the original and redesigned HP combustors

this skirt would inevitably lead to failure and further improvements to the shutdown and trip procedures were deemed to be required.

The volume and size of the feed manifold to the injectors was significantly reduced on the HP unit. Recent experience

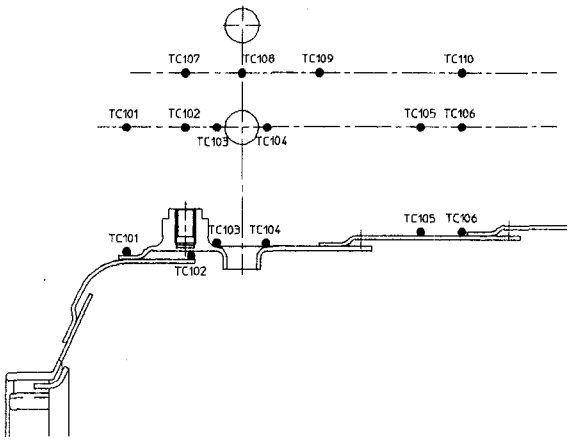

Fig. 8 On plant thermocouple locations: HP combustors

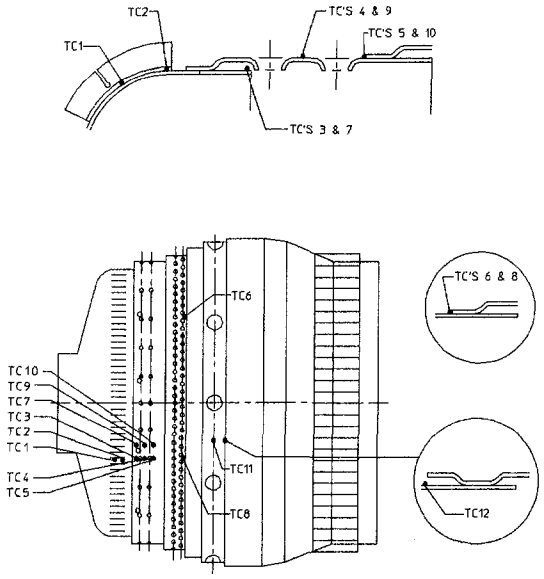

Fig. 9 On plant thermocouple locations: LP combustors

Table 10 Maximum metal temperatures—HP combustor (°C) (test date 9 July 1994)

	Couple No.	101	102	103	104	105	106	107	108	109	110
	Location	Domed Head	Cooling Skirt	P/Z U/S Holes	P/Z D/S Holes	Int. Sect.	D/S Int.	Cooling Skirt	Between P/Z Holes	D/S P/Z Holes	D/S Int.
NATURAL GAS	10 MW	409	406	353	477	-	445	453	453	560	446
	25 MW	399	392	344	461	-	422	439	433	538	423
	50 MW	385	371	334	451	-	410	418	422	524	404
	75 MW	374	359	326	443	-	398	403	412	517	390
	100 MW	342	334	298	407	-	374	366	381	482	356
	110 MW	334	332	290	395	-	363	353	373	474	344
FUEL OIL	10 MW	439	399	392	557	-	550	521	543	685	549
	25 MW	405	364	368	517	-	510	444	492	620	511
	50 MW	387	353	352	479	-	474	401	457	569	464
	75 MW	360	328	334	452	-	453	355	419	502	433
	100 MW	324	301	304	403	-	413	324	378	482	393
	110 MW	319	298	297	389	-	395	324	374	481	378
OVERALL MAXIMA		439	406	392	557	-	550	521	543	685	549

Table 11 Maximum metal temperatures—LP combustor (°C) (combustor No. 6 test date 9 July 1994)

Couple No.	1	2	3	4	5	6	7	8	9	10	11	12
Location	Domed Head	Domed Head	Cooling Skirt	Mid P/Z	D/S P/Z	D/S Int.	Cooling Skirt	D/S Int.	Mid P/Z	D/S P/Z	Mid Int. Sect.	D/S Int. Sect.
NATURAL GAS												
10 MW	478	495	427	452	481	502	374	455	461	507	402	442
25 MW	521	566	469	509	554	586	382	502	498	552	434	491
50 MW	523	576	475	533	588	634	392	532	515	578	462	533
75 MW	518	674	466	534	592	648	395	540	519	587	472	551
100 MW	499	569	448	517	577	628	383	527	514	581	461	550
110 MW	500	588	448	521	583	622	378	531	512	578	460	556
FUEL OIL												
10 MW	536	553	456	516	553	533	379	489	529	577	421	457
25 MW	598	646	503	613	658	651	399	575	657	727	478	539
50 MW	635	704	510	656	720	684	412	624	679	743	519	595
75 MW	675	777	498	650	736	787	401	623	672	751	547	634
100 MW	660	771	471	643	727	729	393	616	629	721	534	624
110 MW	642	770	465	628	701	699	391	606	626	713	527	620
OVERALL MAXIMA	675	777	510	656	736	787	412	624	679	751	547	634

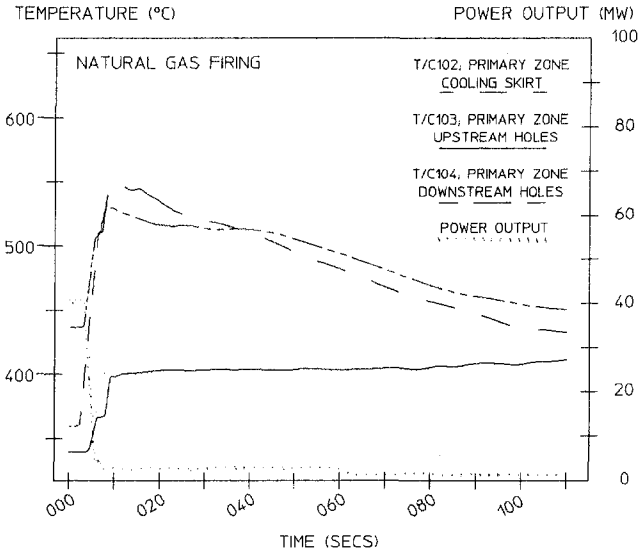

Fig. 10 HP combustor metal temperatures trip from 40 MW

has shown some improvement. Continued monitoring will, however, be necessary. Figure 10 shows the response of the most sensitive thermocouples to a trip from 40 MW on natural gas following modification in the fuel system (the LP combustor showed a similar level of response).

It can be seen that the HP skirt temperatures rise from some 371°C to 538°C (the LP rose from 454°C to 677°C). As the combustors are now cooler during normal operation and the HP temperature excursions are reduced, an improved combustor life is anticipated. This aspect of performance will continue to be monitored to check for any potential increase in steady-state temperatures that could be indicative of rolling of the cooling skirts. It also emphasises the attention CAES designers need to apply to the control of shutdown and trip procedures.

Emission measurements during natural gas operation taken prior to the weakening of the primary zone of the HP combustors for smoke emissions improvement, indicated overall NO_x emissions at between 99 and 101 ppmv, replicating almost exactly the prediction from rig testing, as shown in Table 12. Following modification to eliminate smoke from the HP, further emissions measurements were carried out and the current level of plant NO_x on natural gas is of the order of some 65 to 70 ppmv and CO and UHC emissions are some 5 and 1 ppmv, respectively.

Table 12 Performance targets: plant emissions

		SPECIFICATION		AIT PREDICTED	
		NATURAL GAS	DIESEL OIL	NATURAL GAS	DIESEL OIL
NO_x	kg/MWhr	1.04	1.50	0.82	1.27
NO_x	ppmv	128	181	100	154
CO	ppmv	50	50	≤ 12	≤ 12
UHC	ppmv	-	-	≤ 3	≤ 1

Summary

The CAES operating cycle presents the combustion designer with new problems in addition to those present within normal gas turbines.

First, the series operation of the LP combustor downstream of the HP expander and the attendant vitiation of its inlet air creates an increased propensity for dynamic pressure pulsations to occur when operating on natural gas. (Unvitiated tests at identical conditions on shop tests showed no problems with dynamic pressure pulsations.) The situation is further exacerbated by the introduction of water to control NO_x.

Second, the highly cyclic nature of operation, allied to the very high pressures in the HP unit, provides additional problems with regard to mechanical integrity and the high-pressure operation of the HP can add to the generation of exhaust smoke when using diesel fuel.

Third, the uncoupled nature of the compressor/turbine combination provides a challenge in adequately purging the fuel injectors on shutdown while limiting the propensity for overspeed of the expanders.

Last, the potential for posttrip/postshutdown combustion and the potential damage to the combustors should be minimized by attention to detail of the shutdown procedures as well as the specific design of the combustor and combustor cooling films.

Bearing in mind the above, it is not surprising that the Alabama CAES combustors have experienced problems as plant operation and power generation has progressed. However, as a result of the combustion modifications, the combustion system is now considered to be fully developed, provided that careful monitoring of metal temperatures to study the possible impact of posttrip combustion is continued.

The plant has now operated for over 3000 hours in compression and generation and has produced in excess of 70,000 MW of power.

Acknowledgments

The authors wish to express their appreciation to the Directors of Aero & Industrial Technology Limited and to Dresser Rand for permission to publish the paper and to colleagues at Aero & Industrial Technology Limited and Dresser Rand for the hard work and support during the development programme at Burnley and the field testing in Alabama. Additionally acknowledgment is made to Alabama Electric Co-operative, operators of the plant, to EPRI sponsors and supporters of the CAES principal, to Power Tech Associates for the provision of the engine monitoring instrumentation, and finally to ESPC for their assistance in Engine Data analysis.

References

1 Korinek, K., Hendry, D., and Howard, J., "Alabama Electric Co-operative Compressed Air Energy Storage Project," *Power-Gen '89,* Vol. III, p. 489.

2 Nakhamkin, M., Andersson, L., Swenson, E., Howard, J., Meyer, R., Schainker, R., Pollak, R., and Mehta, B., "AEC 110 MW CAES Plant Status of Project," *Proc. American Power Conference 53rd Annual Meeting,* April/May 1991, p. 743.

3 Totten, P. A., and Meyer, R., "CAES Old and New," *Power-Gen '89,* Vol. III, p. 495.